LASER SELECTIVE EXCITATION OF PRASEODYMIUM IONS IN HYDROGENATED FLUORITE CRYSTALS

A thesis

submitted for the degree

of

Doctor of Philosophy in Physics

in the

University of Canterbury

by

Roger J. Reeves

University of Canterbury

1987

To my family

ABSTRACT

The techniques of laser selective excitation have been successfully applied to study the multitude of spectroscopic sites present in hydrogenated $SrF_2:Pr^{3+}$ and $CaF_2:Pr^{3+}$ crystals. Many optical transitions of the tetragonally sited Pr^{3+} ions have been characterised using well defined polarisation rules, and comprehensive sets of energy levels have been established. For the hydrogenic C_{4v} Pr^{3+} sites, the predictions of a single frequency multiphonon relaxation theory show excellent agreement with the results of a temporal study of these sites. The results show that the relaxation of the Pr^{3+} electronic system is entirely determined by the hydrogenic ion local mode phonons.

Several low symmetry hydrogenic Pr^{3+} centres show the, new to inorganics, property of reversible bleaching. Two mechanisms have been identified, where a photoproduct is formed with a different site orientation or at a different excitation wavelength. Site configurations have been developed that successfully account for many of the observed bleaching effects.

ACKNOWLEDGEMENTS

This thesis is dedicated to my parents for their continuing encouragement and support, and who found they still had to support a dependent child far longer than most would consider reasonable.

I would particularly like to thank Dr Glynn Jones and Dr Rod Syme for their interest and guidance, and for unselfishly imparting their knowledge during their supervision of this project.

Others I also wish to thank include,

- Dr Roger Macfarlane who maintained a keen interest in this work and provided much from many stimulating discussions.
- My fellow research students, Nigel Cockroft, Thomas Han, Lai Kai Kien and Chris Tomblin for contributing to the productive research atmosphere of the group.
- Terry Rowe, Wayne Smith, Tom Walker and Ross Ritchie and other workshop staff who willingly provided the technical support necessary for this project.
- Fellow inmates of the tearoom and the Friday night session at the 'Bush'. We'll solve the worlds problems yet guys!
- Mrs Gill Evans for skillfully typing this thesis while coping with the demands of a sometimes harassed graduate student.
- Dr Neil Manson of the Australian National University for providing the opportunity and support for a visit to the A.N.U.

Finally I would like to thank Karyn for her understanding and support especially during the last few difficult months.

Financial assistance has been provided by a Postgraduate Scholarship from the New Zealand University Grants Committee and a

Teaching Assistantship from the Physics Department. A Royal Society of New Zealand Young Scientists Award enabled travel to the Eighth Annual Condensed Matter Physics Meeting, Wagga Wagga, Australia. Additional support during this project was provided by a bursary from the Royal Arch Chapter of Freemasons.

TABLE OF CONTENTS

		Page
CHAPTER I	INTRODUCTION	
I.1	Introduction	1
I.2	Rare-Earth Doped Alkaline Earth Fluoride Crystals	1
I.3	Hydrogenated Alkaline Earth Fluorides Containing Rare-Earth Ions	3
I.4	The Structure of this Work	4
CHAPTER II	REVIEW OF THE THEORY	
II.1	The Free Ion Hamiltonian	9
II.2	The C_{4v} Crystal Field	16
II.3	Energy Matrices for the Pr^{3+} Ion	18
CHAPTER III	EXPERIMENTAL CONSIDERATIONS	
III.1	Crystal Preparation	21
III.2	Optical Spectroscopy	25
	III.2.1 Optical Absorption	25
	III.2.2 Fluorescence Spectra	25
III.3	Time Domain Spectroscopy	28
III.4	Low Temperature Cryostats	30
CHAPTER IV	OPTICAL SPECTROSCOPY OF ALKALINE EARTH FLUORIDES CONTAINING PRASEODYMIUM	
IV.1	Crystal Field Level Structure and Selection Rules for Pr^{3+} Ions in a Field of C_{4v} Point Group Symmetry	32
	IV.1.1 Crystal Field Level Structure	32
	IV.1.2 Transition Selection Rules	40
	IV.1.3 Polarisation Ratios	42

Page

IV.2 Optical Spectroscopy of Pr^{3+} in SrF_2 45

IV.2.1 Introduction 45

IV.2.2 Absorption and Excitation of $SrF_2:Pr^{3+}$ 46

IV.2.3 Optical Emission of the C_{4v} F^- Site in $SrF_2:Pr^{3+}$ 54

IV.3 Optical Spectroscopy of Pr^{3+} in CaF_2 77

IV.3.1 Introduction 77

IV.3.2 Absorption and Excitation of $CaF_2:Pr^{3+}$ 78

IV.3.3 Optical Emission of the C_{4v} F^- Site in $CaF_2:Pr^{3+}$ 82

IV.4 Crystal Field Parameterisation for Pr^{3+} Ions in the C_{4v} Sites 98

CHAPTER V OPTICAL SPECTROSCOPY OF THE TETRAGONAL SITE IN HYDROGENATED SrF_2 AND CaF_2 CRYSTALS CONTAINING PRASEODYMIUM

V.1 The C_{4v} Hydrogenic Sites in $SrF_2:Pr^{3+}$ 104

V.1.1 Absorption and Excitation of the C_{4v} Hydrogenic Sites in $SrF_2:Pr^{3+}$ 104

V.1.2 Optical Emission of the C_{4v} Hydrogenic Sites in $SrF_2:Pr^{3+}$ 124

V.2 The C_{4v} Hydrogenic Sites in $CaF_2:Pr^{3+}$ 167

V.2.1 Absorption and Excitation of the C_{4v} Hydrogenic Sites in $CaF_2:Pr^{3+}$ 167

V.2.2 Optical Emission of the C_{4v} Hydrogenic Sites in $CaF_2:Pr^{3+}$ 176

Page

CHAPTER VI LOW SYMMETRY HYDROGENIC ION SITES IN $SrF_2:Pr^{3+}$ AND $CaF_2:Pr^{3+}$ CRYSTALS

VI.1 Introduction 211

VI.2 Optical Spectroscopy of the Rhombic Centres in Hydrogenated $SrF_2:Pr^{3+}$ 214

VI.2.1 The $C_s(1)$ Centre 216

VI.2.2 The $C_s(2)$ Centre 225

VI.2.3 The $C_s(4)$ Centre 236

VI.2.4 The $C_s(3)$ Centre 242

VI.3 Optical Spectroscopy of the Rhombic Centres in Hydrogenated $CaF_2:Pr^{3+}$ 246

VI.3.1 The $C_s(1)$ Centre 248

VI.3.2 The $C_s(2)$ Centre 252

VI.3.3 The $C_s(3)$ Centre 255

VI.4 Discussion of the Bleaching Effects 258

VI.4.1 Site Configurations 258

VI.4.2 Non-Resonant Photoproduct Formation 271

VI.5 Spectral Holeburning in the Hydrogenic $C_s(1)$ and $C_s(2)$ Centres of $SrF_2:Pr^{3+}:D^-$ 274

CHAPTER VII LOCAL MODE VIBRATION AND ELECTRON-PHONON INTERACTION EFFECTS IN HYDROGENATED $SrF_2:Pr^{3+}$ AND $CaF_2:Pr^{3+}$ CRYSTALS

VII.1 Introduction 279

VII.2 Vibrations of the Anharmonic Local Oscillator 281

VII.2.1 Background Theory 281

Page

VII.2.2 Analysis of the C_{4v} H^- Anharmonic Oscillator in $SrF_2:Pr^{3+}$ 292

VII.2.3 Calculation of the Potential for the Remaining C_{4v} Oscillators 299

VII.3 The Electron-Phonon Interaction 309

VII.4 Vibronic Splittings in the Local Mode Spectra 317

VII.4.1 Introduction 317

VII.4.2 Calculation of the First Order Splittings 328

VII.4.3 Calculation of the Second Order Splittings 335

CHAPTER VIII TEMPORAL STUDIES AND UPCONVERSION IN HYDROGENATED $SrF_2:Pr^{3+}$ AND $CaF_2:Pr^{3+}$ CRYSTALS

VIII.1 Introduction 343

VIII.1.1 Background 343

VIII.2 Fluorescent Lifetimes and Non-Radiative Decay in the Tetragonal Sites in $SrF_2:Pr^{3+}$ and $CaF_2:Pr^{3+}$ 346

VII.3 Upconversion in the C_{4v} Sites of $SrF_2:Pr^{3+}$ and $CaF_2:Pr^{3+}$ 361

CHAPTER IX SPECTRAL HOLEBURNING AND OPTICALLY DETECTED NUCLEAR MAGNETIC RESONANCE IN THE C_{4v} SITES OF $SrF_2:Pr^{3+}$ AND $CaF_2:Pr^{3+}$

IX.1 Introduction to Spectral Holeburning 376

IX.2 Review of Previous Work : ODNMR in the C_{4v} F^- Site of $CaF_2:Pr^{3+}$ 378

Page

IX.3 ODNMR in Hydrogenated Crystals of $CaF_2:Pr^{3+}$ and $SrF_2:Pr^{3+}$ 384

CHAPTER X CONCLUSIONS AND SUGGESTIONS FOR FUTURE WORK 392

REFERENCES 394

APPENDIX 399

LIST OF TABLES

		Page
Table II.3.1	Electrostatic energies for the f^2 electronic configuration.	18
Table II.3.2	Spin orbit matrix elements for the f^2 electronic configuration.	19
Table II.3.3	Matrix elements of the f^2 configuration interactions.	20
Table IV.1.1	Cubic crystal field wavefunctions, in $\|JJ_z\rangle$ basis states and energies for the levels of the $^3H_4$ multiplet.	34
Table IV.1.2	First order C_{4v} crystal field wavefunctions as $\|JJ_z\rangle$ states assigned to parent cubic Γ_a and C_{4v} γ_b irreps.	36
Table IV.1.3	Polarisation ratios for electric dipole transitions from the $^1D_2$ multiplet of the Pr^{3+} ion in the cubic CaF_2 type crystals.	44
Table IV.2.1	Electronic absorption transitions from the ground state to the crystal field levels of the $^3P_1$, $^3P_0$, $^1D_2$ and $^1G_4$ multiplets for the C_{4v} F^- site SrF_2:0.05%Pr^{3+}.	49

Page

Table IV.2.2 Excitation lines identified in the $^1D_2$ region for the C_{4v} F^- charge compensated site in SrF_2:0.05%Pr^{3+}. The zero-phonon electronic transitions of the Pr^{3+} ion identified are the D_1, D_2 and D_4 crystal field levels. 53

Table IV.2.3 Spectral data for the crystal field levels of the $^3H_4$ multiplet for the C_{4v} F^- site in SrF_2:Pr^{3+}. 60

Table IV.2.4 Spectral data for the crystal field levels of the $^3H_5$ multiplet for the C_{4v} F^- site in SrF_2:Pr^{3+}. 62

Table IV.2.5 Spectral data for the crystal field levels of the $^3H_6$ multiplet for the C_{4v} F^- site in SrF_2:Pr^{3+}. 66

Table IV.2.6 Spectral data for the crystal field levels of the $^3F_2$ multiplet for the C_{4v} F^- site in SrF_2:Pr^{3+}. 69

Table IV.2.7 Energy shifts from zero phonon lines, for vibronic transitions observed to the $^3F_2$ multiplet. 70

Table IV.2.8 Spectral data for the crystal field levels of the $^3F_3$ multiplet for the C_{4v} F^- site in SrF_2:Pr^{3+}. 72

Page

Table IV.2.9 Spectral data for the crystal field levels of the $^3F_4$ multiplet for the C_{4v} F^- site in $SrF_2:Pr^{3+}$. 74

Table IV.3.1 Wavelengths of absorption transitions and site assignments for a 0.02 mol% $CaF_2:Pr^{3+}$ crystal. 81

Table IV.3.2 Spectral data for the crystal field levels of the $^3H_4$ multiplet for the C_{4v} F^- site in $CaF_2:Pr^{3+}$. 85

Table IV.3.3 Spectral data for the crystal field levels of the $^3H_5$ multiplet for the C_{4v} F^- site in $CaF_2:Pr^{3+}$. 89

Table IV.3.4 Spectral data for the crystal field levels of the $^3H_6$ multiplet for the C_{4v} F^- site in $CaF_2:Pr^{3+}$. 91

Table IV.3.5 Spectral data for the crystal field levels of the $^3F_2$ multiplet for the C_{4v} F^- site in $CaF_2:Pr^{3+}$. 95

Table IV.3.6 Spectral data for the crystal field levels of the $^3F_3$ multiplet for the C_{4v} F^- site in $CaF_2:Pr^{3+}$. 97

Page

Table IV.3.7 Spectral data for the crystal field levels of the $^3F_4$ multiplet for the C_{4v} F^- site in $CaF_2:Pr^{3+}$. 99

Table V.1.1 Wavelengths of absorption transitions, recorded at 14 K, for the C_{4v} hydrogenic charge compensation ion sites in SrF_2:0.05%Pr^{3+} crystals. 107

Table V.1.2 $^1D_2$ excitation lines for the C_{4v} D^- site in $SrF_2:Pr^{3+}$ shown in Figure V.1.3. The crystal temperature was 14 K. 110

Table V.1.3 Polarisation rules for the absorption and emission in the C_{4v} sites for the two polarisation geometries x(yx)z and x(yy)z in a <100> oriented crystal. 113

Table V.1.4 Polarisation rules for the absorption when monitoring σ-polarised emission, in the C_{4v} sites for the two polarising geometries x(yy)z and x(zy)z in a <100> oriented crystal. 120

Table V.1.5 Electronic D^- ion local mode frequencies measured from the $^1D_2$ excitation spectrum for the C_{4v} D^- site in a SrF_2:0.05%Pr^{3+}:D^- crystal. Sample temperature was 14 K. 121

Page

Table V.1.6 Electronic energies for the $^3H_4$ multiplet of the hydrogenic C_{4v} sites in $SrF_2:Pr^{3+}$. The energy level uncertainties are ±1 cm^{-1} unless otherwise indicated. The polarisation of the transitions to these levels from $^1D_2(D_1)$ is also included. 133

Table V.1.7 Electronic and local mode vibronic level energies for the $^3H_5$ multiplet of the hydrogenic C_{4v} sites in $SrF_2:Pr^{3+}$. The energy level uncertainties are ±1 cm^{-1} and the observed polarisation for the transition from $^1D_2(D_1)$ is also included. 146

Table V.1.8 Lattice phonon frequencies in the hydrogenic C_{4v} Pr^{3+} ion sites in SrF_2Pr^{3+}, determined from vibronic line intervals from the $^1D_2(D_1)$ and $^3H_6(X_1)$ levels. 150

Table V.1.9 Electronic and local mode vibronic level energies for the $^3H_6$ multiplet of the Pr^{3+} ion in the hydrogenic C_{4v} sites in SrF_2. The polarisation of the transition from $^1D_2(D_1)$ is given for each level. 152

Page

Table V.1.10 Energies of the electronic and local mode vibronic levels of the $^3F_2$ multiplet for the Pr^{3+} ion in the hydrogenic C_{4v} sites of $SrF_2:Pr^{3+}$. The polarisation for transitions from $^1D_2(D_1)$ is also included. Level uncertainties are ± 1 cm^{-1}. 156

Table V.1.11 Energies of the electronic and local mode vibronic levels of the $^3F_3$ multiplet for the Pr^{3+} ion in the hydrogenic C_{4v} sites in SrF_2. The polarisation of the transition from $^1D_2(D_1)$ to the levels is also included where it is determined. Level uncertainties are ± 2 cm^{-1}. 164

Table V.1.12 Energy level scheme for the $^3F_4$ multiplet of the Pr^{3+} ion in the hydrogenic C_{4v} sites in $SrF_2:Pr^{3+}$. Level uncertainties are ± 2 cm^{-1}. 166

Table V.2.1 Absorption transition wavelengths from the ground state, recorded at 14 K, for the C_{4v} hydrogenic charge compensation ion sites in CaF_2:0.05%Pr^{3+} crystals. 169

Table V.2.2 Electronic level energies and D^- ion local mode frequencies measured, at 14 K, from the $^1D_2$ excitation spectrum for the C_{4v} D^- site in $CaF_2:Pr^{3+}:D^-$ crystal. 174

Page

Table V.2.3 Energies of the electronic and local mode vibrational levels of the $^3H_4$ multiplet for the C_{4v} hydrogenic ion sites in $CaF_2:Pr^{3+}$. The polarisation of the transition from the $D_1(\gamma_1)$ level to the various states is given. Energy level uncertainties are ±1 cm^{-1} unless otherwise indicated. 184

Table V.2.4 Energies of the electronic and local mode vibrational levels of the $^3H_5$ multiplet for the C_{4v} hydrogenic sites in $CaF_2:Pr^{3+}$. The energy level uncertainties are ± 1 cm^{-1}. 193

Table V.2.5 Energies of the electronic and local mode vibronic levels of the $^3H_6$ multiplet for the C_{4v} Pr^{3+}-hydrogenic ion sites in $CaF_2:Pr^{3+}$. Level uncertainties are ± 1 cm^{-1}. 199

Table V.2.6 Energies of the electronic and local mode vibronic levels of $^3F_2$ multiplet for the C_{4v} Pr^{3+}-hydrogenic ions sites in $CaF_2:Pr^{3+}$. Level uncertainties are ± 1 cm^{-1}. 202

Table V.2.7 Energies of the electronic and local mode vibronic levels for the $^3F_3$ multiplet of the C_{4v} D^- site in $CaF_2:Pr^{3+}$. Level uncertainties are ± 2 cm^{-1}. 209

Page

Table V.2.8 Energies of the electronic and local mode vibronic levels for the $^3F_4$ multiplet of the C_{4v} D^- site in $CaF_2:Pr^{3+}$. Level uncertainties are ± 2 cm^{-1}. 210

Table VI.2.1 Spectral data for the hydrogenic $C_s(1)$ site in $SrF_2:Pr^{3+}$. 218

Table VI.2.2 Spectral data for the hydrpgenic $C_s(2)$ site in $SrF_2:Pr^{3+}$. 229

Table VI.2.3 Spectral data for the hydrogenic $C_s(4)$ site in $SrF_2:Pr^{3+}$crystals 238

Table VI.2.4 Spectral data for the hydrogenic $C_s(3)$ site in $SrF_2:Pr^{3+}$. 244

Table VI.3.1 Spectral data for the hydrogenic $C_s(1)$ site in $C_aF_2:Pr^{3+}$. 251

Table VI.3.2 Spectral data for the hydrogenic $C_s(2)$ site in $CaF_2:Pr^{3+}$. 254

Table VI.3.3 Spectral data for the $C_s(3)$ D^- centre in $CaF_2:Pr^{3+}$. 257

Table VI.5.1 Hyperfine interaction parameter values for the $C_s(1)$ and centres measured in $SrF_2:0.05\%Pr^{3+}:D^-$. 278

Page

Table VII.2.1 Energy shift from the harmonic oscillator frequencies of the first few levels of the anharmonic oscillator in a site of C_{4v} symmetry. 285

Table VII.2.2 Excitation energies for the first few levels of the C_{4v} anharmonic oscillator. 286

Table VII.2.3 Fundamental and second harmonic local mode frequencies measured for the H^-, D^- and T^- anharmonic oscillators in $SrF_2:Pr^{3+}$ and $CaF_2:Pr^{3+}$ crystals. 295

Table VII.2.4 Anharmonic parameters calculated for the C_{4v} H^- oscillator in $SrF_2:Pr^{3+}$. 297

Table VII.2.5 Anharmonic parameters for the $SrF_2:Pr^{3+}:H^-$ data using the approximation $^g/_f = 1.0$, $^k/_h = 1.0$. 300

Table VII.2.6 Anharmonic constants for the two most likely assignments of the observed second harmonic frequencies for the C_{4v} H^- oscillator in $CaF_2:Pr^{3+}$. The quartic parameter ratios used were f = g, h = k and $^h/_f = 0.80$. 301

Table VII.2.7 Anharmonic parameters for the C_{4v} H^- oscillator in $CaF_2:Pr^{3+}$ with varying quartic ratios (f = g, h = k). 302

Page

Table VII.2.8 Anharmonic oscillator parameters for the C_{4v} D^- oscillator in $SrF_2:Pr^{3+}$. The three columns are the results for the three choices of energy level assignment. 305

Table VII.2.9 Anharmonic constants for the six choices of second harmonic level assignment for the $CaF_2:Pr^{3+}:D^-$ data. 306

Table VII.2.10 Anharmonic constants for the T^- oscillator in SrF_2Pr^{3+} and $CaF_2:Pr^{3+}$ using quartic parameter ratios of $^g/_f = 1.0$, $^k/_h = 1.0$, $^h/_f = 0.8$. 307

Table VII.2.11 Summary of the C_{4v} anharmonic oscillator for the H^-, D^- and T^- oscillators in $SrF_2:Pr^{3+}$ and $CaF_2:Pr^{3+}$ crystals using the quartic parameter ratios $^g/_f = 1.0$, $^k/_f = 1.0$, $^h/_f = 0.8$. 309

Table VII.4.1 Infrared absorption measurements for the H^- local modes in the tetragonal Pr^{3+}- H^- ion sites. 318

Table VII.4.2 Fundamental local mode frequencies, measured from fluorescence transitions to vibronic levels, for the tetragonal Pr^{3+} -hydrogenic ion sites. The sample temperature was 14 K. 325

Page

Table VII.4.3 First order energy shifts, due to the electron-phonon interaction, to the x,y vibronic levels. 334

Table VII.4.4 Vibronic states of the $^3H_4$ multiplet in the hydrogenic C_{4v} Pr^{3+} site having the same transformation properties as the fundamental x,y vibronic levels ψ_r. 337

Table VII.4.5 Constant A in equation VII.4.18 for the energy shifts ΔE_r of the vibronic states ψ_r. 339

Table VII.4.6 Energies of the two closest levels to the fundamental x,y vibronic states. 340

Table VII.4.7 Energy shifts to the ψ_1 and ψ_3 vibronic states due to second order effects from the $|\Gamma_3\gamma_3(000)\rangle$ and $|\Gamma_3\gamma_1(000)\rangle$ intermediate states. 341

Table VII.4.8 Calculated x,y vibronic level splittings to second order perturbation theory. 342

Table VIII.2.1 Fluorescent lifetimes measured at 14 K for C_{4v} Pr^{3+} ion sites in SrF_2 and CaF_2 host crystals. 348

Page

Table IX.3.1 ODNMR frequencies for nearest neighbour ^{19}F nuclei and various interstitial ions for the tetragonal charge compensated sites in $CaF_2:Pr^{3+}$ ans $SrF_2:Pr^{3+}$ crystals. 385

Table IX.3.2 ODNMR frequencies and nuclear g values for various interstitial ions in the C_{4v} sites of $CaF_2:Pr^{3+}$ and $SrF_2:Pr^{3+}$ crystals. 388

LIST OF FIGURES

Page

Figure I.1.1 Structure of the alkaline earth fluorides. 2

Figure I.2.1 A model of the RE^{3+} C_{4v} site. In the alkaline earth fluorides there are six equivalent interstitial positions for the charge compensating ion. 4

Figure I.4.1 Energy level diagram for the Pr^{3+} in the C_{4v} site in SrF_2. 6

Figure III.1.1 Experimental arrangement of the quartz components constructed for the tritiation of crystals. 23

Figure IV.1.1(a) Predicted energy level scheme of the Pr^{3+} ion for the 33 states of the ^3H multiplets for a crystal field increasing from cubic to the full axial value. 38

Figure IV.1.1(b) Predicted energy level scheme of the Pr^{3+} ion for the 21 states of the ^3F 39

Figure IV.2.1 Optical absorption, recorded at 14K, of transitions to the (a)$^3P_0$ and $^3P_1$,(b)$^1D_2$ and (c) $^1G_4$ multiplets for a SrF_2:0.05% Pr^{3+} crystal. 47

Figure IV.2.2 Transition coincidences with argon ion laser lines in SrF_2:Pr^{3+} crystals 50

Figure IV.2.3 14K excitation spectrum of $^3H_4 \rightarrow {}^1D_2$ transitions for the C_{4v} site in SrF_2:Pr^{3+} 52

Figure IV.2.4 14K polarised emission to the crystal field levels of the $^3H_4$ multiplet for the C_{4v} F^- site in SrF_2:Pr^{3+} from (a) the $^1D_2$ multiplet and (b) the $^3P_0$ crystal field level. 56

Figure IV.2.5 14K polarised emission to the crystal field levels of the $^3H_5$ multiplet for the C_{4v} F^- site in SrF_2:Pr^{3+} 61

Page

Figure IV.2.6 14K polarised emission to the crystal field levels of the $^3H_6$ multiplet 65

Figure IV.2.7 14K polarised emission to the crystal field levels of the $^3F_2$ multiplet 68

Figure IV.2.8 14K polarised emission to the crystal field levels of the $^3F_3(V_i)$ and $^3F_4(U_i)$ multiplets 71

Figure IV.2.9 (a) 14K $^3P_0 \rightarrow {}^1G_4$ emission for the C_{4v} F^- site in $SrF_2:Pr^{3+}$ and (b) the energy level scheme for this multiplet. 75

Figure IV.3.1 Optical absorption recorded at 14K, for tramsitions to the (a) $^3P_0$ and $^3P_1$ and (b) $^1D_2$ crystal field levels of the Pr^{3+} ion in the C_{4v} F^- site of $CaF_2:Pr^{3+}$. 79

Figure IV.3.2 14K laser excitation spectrum of the $^1D_2$ region for the C_{4v} F^- site in $CaF_2:Pr^{3+}$. 80

Figure IV.3.3 Polarised emission at 14K to the $^3H_4$ multiplet from the (a) $^1D_2$ and (b) $^3P_0$ levels for the C_{4v} F^- site 84

Figure IV.3.4 (a) and (b) polarised $^1D_2 \rightarrow {}^3H_5$ emission and (c) $^3P_0 \rightarrow {}^3H_5$ emission, for the C_{4v} F^- site in $CaF_2:Pr^{3+}$ at 14K. 87

Figure IV.3.5 (a) and (b) polarised $^1D_2 \rightarrow {}^3H_6$ emission and (c) $^3P_0 \rightarrow {}^3H_6$ emission 92

Figure IV.3.6 (a) and (b) polarised $^1D_2 \rightarrow {}^3F_2$ emission and (c) $^3P_0 \rightarrow {}^3F_2$ emission 93

Figure IV.3.7 (a) and (b) polarised $^1D_2 \rightarrow {}^3F_3$, $^3F_4$ emission and (c) $^3P_0 \rightarrow {}^3F_3$, $^3F_4$ emission 96

Page

Figure V.1.1 Optical absorption of the crystal field levels of the (a) $^3P_0$ and $^3P_1$ and (b) $^1D_2$ multiplets recorded at 14K for a hydrogenated $SrF_2:Pr^{3+}$ crystal. 105

Figure V.1.2 Broadband laser excitation spectrum of the $^1D_2$ region for a SrF_2:0.05%$Pr^{3+}:D^-$ crystal showing transitions of the F^- and D^- C_{4v} sites and several rhombic symmetry sites also containing D^- ions. 108

Figure V.1.3 14K $^1D_2$ excitation spectrum of the C_{4v} D^- site in $SrF_2:Pr^{3+}:D^-$ 109

Figure V.1.4 Polarised $^1D_2$ excitation spectra for the C_{4v} D^- site in a <100> oriented $SrF_2:Pr^{3+}:D^-$ crystal in the (a) x(yy)z and (b) x(yx)z polarisation geometries. The $^1D_2(D_1)\rightarrow{}^3H_5(\Gamma_3\gamma_1)$ transition being monitored at 14616 cm^{-1} has π-polarisation. 111

Figure V.1.5 Polarised $^1D_2$ excitation spectra for the C_{4v} D^- site in a <100> oriented $SrF_2:Pr^{3+}:D^-$ crystal recorded when monitoring the σ-polarised $^1D_2(D_1)\rightarrow{}^3H_5(\Gamma_4\gamma_5)$ transition at 14579 cm^{-1}. 112

Figure V.1.6 Polarised excitation spectra of the C_{4v} D^- site in $SrF_2:Pr^{3+}:D^-$, showing transitions to vibronic levels associated with local mode vibrations coupled to the $^1D_2(D_1)$ level. 115

Figure V.1.7 14K excitation spectrum for the C_{4v} D^- site in $SrF_2:Pr^{3+}:D^-$ showing local mode vibronic lines associated with vibrations coupled to the D_4 crystal field level. 118

Page

Figure V.1 8 Polarised excitation spectra for the C_{4v} D^- site in $SrF_2:Pr^{3+}:D^-$ showing local mode vibronic lines associated with second harmonic vibrations coupled to the D_1 crystal field level. 119

Figure V.1.9 Laser excitation of a praseodymium doped SrF_2 crystal showing lines from Nd^{3+} ions present as an impurity. 123

Figure V.1.10(a) 14K polarised fluorescence from the C_{4v} H^- site in $SrF_2:Pr^{3+}$ showing the $^1D_2 \rightarrow {}^3H_4$ electronic transitions •••• 127

Figure V.1.10(b) Polarised fluorescence from the C_{4v} H^- site in $SrF_2:Pr^{3+}$ on an expanded scale showing transitions to the local mode vibronic levels associated with the $^3H_4$ multiplet. 128

Figure V.1.11(a) Polarised $^1D_2 \rightarrow {}^3H_4$ fluorescence from the C_{4v} D^- site in $SrF_2:Pr^{3+}:D^-$ •••• 129

Figure V.1.11(b) Polarised fluorescence from the C_{4v} D^- site in $SrF_2:Pr^{3+}$ on an expanded scale •••• 130

Figure V.1.12(a) Polarised $^1D_2 \rightarrow {}^3H_4$ fluorescence from the C_{4v} T^- site in $SrF_2:Pr^{3+}$ •••• 131

Figure V.1.12.(b) Polarised fluorescence from the C_{4v} T^- site in $SrF_2:Pr^{3+}$ •••• 132

Figure V.1.13 $^3P_0 \rightarrow {}^3H_4$ upconverted emission, recorded at 14K from the C_{4v} D^- site in $SrF_2:Pr^{3+}$ with $^3H_4(Z_1) \rightarrow {}^1D_2(D_1)$ excitation •••• 139

Figure V.1.14 14K $^3P_0 \rightarrow {}^3H_4$ upconverted emission from the C_{4v} T^- site in $SrF_2:Pr^{3+}$ with $^3H_4(Z_1) \rightarrow {}^1D_2(D_1)$ excitation •••• 140

Figure V.1.15 14K $^1D_2 \rightarrow {}^3H_5$ polarised emission from the (a) H^-, (b) D^- and (c) T^- C_{4v} sites in $SrF_2:Pr^{3+}$. 142

Page

Figure V.1.16 $^3P_0 \rightarrow {}^3H_5$ fluorescence with $^3H_4(Z_1) \rightarrow {}^3P_0$ excitation from the C_{4v} D^- site in $SrF_2:Pr^{3+}$. 143

Figure V.1.17 14K $^1D_2 \rightarrow {}^3H_6$ polarised emission from the (a) H^-, (b) D^- and (c) T^- C_{4v} sites in $SrF_2:Pr^{3+}$. 147

Figure V.1.18 $^3P_0 \rightarrow {}^3H_6$ fluorescence from the C_{4v} D^- site $SrF_2:Pr^{3+}$ with $^3H_4(Z_1) \rightarrow {}^3P_0$ excitation. 148

Figure V.1.19 Polarised fluorescence at 14K, of the $^1D_2 \rightarrow {}^3F_2$ transitions from the C_{4v} D^- site in $SrF_2:Pr^{3+}$ 153

Figure V.1.20 $^3P_0 \rightarrow {}^3F_2$ fluorescence recorded with $^3H_4(Z_1) \rightarrow {}^3P_0$ excitation, from the C_{4v} D^- site in $SrF_2:Pr^{3+}$. 154

Figure V.1.21 $^1D_2 \rightarrow {}^3F_2$ fluorescence recorded at 14K from the C_{4v} H^- site in $SrF_2:Pr^{3+}$. 154

Figure V.1.22 Polarised $^1D_2 \rightarrow {}^3F_3, {}^3F_4$ emission from the C_{4v} H^- site in $SrF_2:Pr^{3+}$ 158

Figure V.1.23 14K Polarised $^1D_2 \rightarrow {}^3F_3, {}^3F_4$ emission from the C_{4v} D^- site in $SrF_2:Pr^{3+}$. 159

Figure V.1.24 14K $^3P_0 \rightarrow {}^3F_3, {}^3F_4$ emission from the C_{4v} D^- site in $SrF_2:Pr^{3+}$ with $^3H_4(Z_1) \rightarrow {}^3P_0$ excitation. 160

Figure V.1.25(a) 14K $^1D_2 \rightarrow {}^3F_3, {}^3F_4$ emission in the x(yy)z polarisation geometry showing the transitions of the C_{4v} D^- site on an expanded scale. 161

Figure V.1.25(b) 14K $^1D_2 \rightarrow {}^3F_3, {}^3F_4$ emission in the x(yx)z polarisation geometry 162

Figure V.1.26 14K $^1D_2 \rightarrow {}^3F_3, {}^3F_4$ emission on an expanded scale, from the C_{4v} H^- site in $SrF_2:Pr^{3+}$. 163

Figure V.2.1 Optical absorption of the (a) $^3P_0$ and $^3P_1$ levels and (b) $^1D_2$ crystal field levels for a CaF_2:0.05%Pr^{3+}:D^- crystal at 14K. 168

Page

Figure V.2.2 14K $^1D_2$ excitation spectrum for the C_{4v} D^- site in a CaF_2:0.05%Pr^{3+}:D^- crystal. 170

Figure V.2.3 Polarised excitation spectra of the C_{4v} D^- site in CaF_2:Pr^{3+}:D^-, showing transitions to D^- local mode vibronic levels •••• 172

Figure V.2.4 14K excitation spectrum for the C_{4v} D^- site in CaF_2:Pr^{3+} showing transitions to fundamental local mode vibronic lines •••• 175

Figure V.2.5(a) 14K polarised fuorescence from the C_{4v} H^- site in CaF_2:Pr^{3+}:H^- showing the $^1D_2 \rightarrow {}^3H_4$ electronic transitions of the Pr^{3+} ion •••• 178

Figure V.2.5(b) Polarised fluorescence from the C_{4v} H^- site in CaF_2:Pr^{3+}:H^- on an expanded •••• 179

Figure V.2.6(a) Polarised $^1D_2 \rightarrow {}^3H_4$ fluorescence from the C_{4v} D^- site in CaF_2:Pr^{3+}:D^- showing transitions to the electronic levels of the Pr^{3+} ion. 180

Figure V.2.6(b) Polarised fluorescence from the C_{4v} D^- site in CaF_2:Pr^{3+}:D^- on an expanded scale •••• 181

Figure V.2.7(a) Polarised fluorescence from the C_{4v} T^- site in CaF_2:Pr^{3+}:T^- showing the $^1D_2 \rightarrow {}^3H_4$ electronic transitions •••• 182

Figure V.2.7(b) Polarised fluorescence from the C_{4v} T^- site in CaF_2:Pr^{3+}:T^- •••• 183

Figure V.2.8 Polarised spectra of the $^1D_2 \rightarrow {}^3H_5$ emission from the C_{4v} H^- site in CaF_2:Pr^{3+}:H^- •••• 191

Figure V.2.9 $^1D_2 \rightarrow {}^3H_5$ polarised emission from the (a) C_{4v} D^- and (b) C_{4v} T^- sites in CaF_2:Pr^{3+} crystals. 192

Page

Figure V.2.10 $^1D_2 \rightarrow {}^3H_6$ polarised emission from the (a) C_{4v} H^-, (b) C_{4v} D^- and (c) C_{4v} T^- sites in $CaF_2:Pr^{3+}$. •••• 196

Figure V.2.11 Polarised $^1D_2 \rightarrow {}^3F_2$ emission from the (a) C_{4v} H^-, (b) C_{4v} D^- and (c) C_{4v} T^- sites in $CaF_2:Pr^{3+}$ crystals •••• 201

Figure V.2.12 Polarised $^1D_2 \rightarrow {}^3F_2$ emission from the C_{4v} D^- site in $CaF_2:Pr^{3+}:D^-$ ••• 203

Figure V.2.13 Polarised $^1D_2 \rightarrow {}^3F_3$, $^3F_4$ emission from the C_{4v} D^- site in $CaF_2:Pr^{3+}:D^-$ •••• 206

Figure V.2.14(a) x(yy)z polarised $^1D_2 \rightarrow {}^3F_3$, $^3F_4$ emission from the C_{4v} D^- site in $CaF_2:Pr^{3+}:D^-$ •••• 207

Figure V.2.14(b) x(yx)z polarised $^1D_2 \rightarrow {}^3F_3$, $^3F_4$ emission from the C_{4v} D^- site in $CaF_2:Pr^{3+}:D^-$ •••• 208

Figure VI.2.1 Broadband excitation spectrum of the $^1D_2$ region in a SrF_2:0.05%$Pr^{3+}:D^-$ crystal showing the transitions of several low symmetry sites studied. 215

Figure VI.2.2 14K $^1D_2 \rightarrow {}^3H_4$ emission spectra for the (a) H^-,(b) D^- and (c) T^- $C_s(1)$ centres in $SrF_2:Pr^{3+}$ crystals. 217

Figure VI.2.3 Fluorescence intensity as a function of time for a sequence of laser excitations in the two possible polarisation directions, V[001] and H[010], for the $C_s(1)$ centre in a <100> oriented $SrF_2:Pr^{3+}:D^-$ crystal. 222

Figure VI.2.4 Bleaching curves for the $C_s(1)$ centre in $SrF_2:Pr^{3+}:D^-$ at 14K. •••• 224

Figure VI.2.5 A series of excitation spectra for the $C_s(1)$ centre in a <100> oriented $SrF_2:Pr^{3+}:D^-$ crystal •••• 226

Page

Figure VI.2.6 14K $^1D_2 \rightarrow {}^3H_4$ emission spectra for the (a) H^-, (b) D^- and (c) T^- $C_s(2)$ centres in $SrF_2:Pr^{3+}$ crystals. 228

Figure VI.2.7 Sequences of bleaching curves for excitation of the $C_s(2)$ centre in a <100> oriented $SrF_2:Pr^{3+}:D^-$ crystal using the two orthogonal laser polarisations V[001] and H[010]. 232

Figure VI.2.8 14K laser excitation spectra of the $C_s(2)$ centre in $SrF_2:Pr^{3+}:D^-$ 235

Figure VI.2.9 (a) Bleaching curves in a <100> oriented crystal and (b) $^1D_2 \rightarrow {}^3H_4$ emission from the $C_s(4)$ centre in $SrF_2:Pr^{3+}:D^-$. 237

Figure VI.2.10 Laser excitation, at 14K, of the $C_s(4)$ centre in a $SrF_2:Pr^{3+}:D^-$ crystal. 241

Figure VI.2.11 (a) Bleaching curves in a <100> oriented crystal and (b) $^1D_2 \rightarrow {}^3H_4$ emission at 14K, for the $C_s(3)$ centre in $SrF_2:Pr^{3+}:D^-$. 243

Figure VI.2.12 Laser excitation at 14K of the $C_s(3)$ centre in $SrF_2:Pr^{3+}:D^-$. 247

Figure VI.3.1 Fluorescence intensity at 14K for a sequence of laser excitations of the $C_s(1)$ centre in a <100> oriented $CaF_2:Pr^{3+}:D^-$ crystal using the orthogonal V[001] and H[010] laser polarisations. 249

Figure VI.3.2 14K $^1D_2 \rightarrow {}^3H_4$ emission spectra for the (a) H^-, (b) D^- and (c) T^- $C_s(1)$ centres in $CaF_2:Pr^{3+}$ crystals. 250

Figure VI.3.3 (a) Bleaching curves in a <100> oriented crystal and (b) $^1D_2 \rightarrow {}^3H_4$ emission at 14K for the $C_s(2)$ centre in $CaF_2:Pr^{3+}:D^-$. 253

Page

Figure VI.3.4 (a) Bleaching curves in a <100> oriented crystal and (b) $^1D_2 \rightarrow {}^3H_4$ emission for the $C_s(3)$ centre in a $CaF_2:Pr^{3+}:D^-$ crystal. 256

Figure VI.4.1 Two possible site configurations for double hydrogenic-ion centres having near neighbour substitutional and interstitial hydrogenic ions. 259

Figure VI.4.2 Interstitialcy mechanism for the reorientation of the site configuration in Figure VI.4.1(a) to give an equivalent centre oriented at 90°. 260

Figure VI.4.3 Proposed site configuration for the hydrogenic ion $C_s(2)$ centre in $SrF_2:Pr^{3+}$ crystals. 264

Figure VI.4.4 (a) Simple interstitialcy mechanism for the reversible reorientation of the hydrogenic $C_s(2)$ centre 265

Figure VI.4.5 (a) Proposed model for the $C_s(4)$ hydrogenic ion centre in $SrF_2:Pr^{3+}$ crystals 268

Figure VI.4.6 Laser excitation at 14K of the $C_s(3)$ centre in $SrF_2:Pr^{3+}:D^-$ 272

Figure VI.4.7 Laser excitation at 14K of the $C_s(2)$ and $C_s(4)$ centres in a $SrF_2:Pr^{3+}:D^-$ crystal. 273

Figure VI.5.1 Persistent spectral holes burned in the (a) $C_s(1)$ and (b) $C_s(2)$ centres of a SrF_2:0.05%$Pr^{3+}:D^-$ crystal showing large pseudoquadrupole splittings in the ground state. 275

Figure VI.5.2 Schematic energy level diagram of the singlet electronic states of the C_s centres which exhibit close to axial symmetry, ... 276

Figure VII.2.1 The energy levels for the anharmonic oscillator with C_{4v} symmetry. 288

Page

Figure VII.2.2 Polarised emission at 14K from the C_{4v} H^- site in a <100> oriented $SrF_2:Pr^{3+}$ crystal •••• 290

Figure VII.2.3 Polarised emission at 14K from the C_{4v} D^- site in a <100> oriented $SrF_2:Pr^{3+}$ crystal •••• 291

Figure VII.2.4 Fluorescence at 14K from the C_{4v} H^- site in a $CaF_2:Pr^{3+}$ crystal showing transitions to the; (a) fundamental and (b) second harmonic vibronic levels. 293

Figure VII.2.5 Polarised emission, at 14K, from the C_{4v} D^- site in a <100> oriented $CaF_2:Pr^{3+}$ crystal •••• 294

Figure VII.4.1(a) Polarised emission from the C_{4v} H^- site in $SrF_2:Pr^{3+}$ recorded at 14K for the; •••• 319

Figure VII.4.1(b) Polarised emission to the fundamental local mode vibronic levels of the C_{4v} D^- site in $SrF_2:Pr^{3+}$. •••• 320

Figure VII.4.1(c) Polarised emission to the fundamental local mode vibronic levels of the C_{4v} T^- site in $SrF_2:Pr^{3+}$. •••• 321

Figure VII.4.2(a) Fluorescence recorded at 14K from the C_{4v} H^- site in $CaF_2:Pr^{3+}$ showing the spectral lines for transitions to the fundamental local mode vibronic levels. •••• 322

Figure VII.4.2(b) Polarised emission from the C_{4v} D^- site in $CaF_2:Pr^{3+}$ recorded at 14K •••• 323

Figure VII.4.2(c) Polarised emission to the fundamental local mode vibronic levels of the C_{4v} T^- site in $CaF_2:Pr^{3+}$. •••• 324

Figure VII.4.3 Some of the energy levels in the combined electronic-local mode phonon system for the $^3H_4$ multiplet of the Pr^{3+}-H^- C_{4v} site. 327

Page

Figure VIII.2.1 Fluorescent transients recorded for the $^3P_0$ and $^1D_2$ emitting levels of the C_{4v} site in $CaF_2:Pr^{3+}:D^-$. The crystal temperature was 14K. 347

Figure VIII.2.2 Fluorescence decay, recorded at 14K, of the $^1D_2(D_1)$ emitting level with $^3H_4(Z_1) \rightarrow {}^3P_0$ excitation for the (a) C_{4v} D^- and (b) C_{4v} H^- sites in $SrF_2:Pr^{3+}$. 352

Figure VIII.2.3 Fluorescent transients of the $^1D_2$ level for the (a) C_{4v} D^- and (b) C_{4v} H^- sites in $SrF_2:Pr^{3+}$ on an expanded time scale showing the risetime for emmision after $^3P_0$ excitation. 353

Figure VIII.3.1 Energy level diagram for the Pr^{3+} ion in the C_{4v} F^- site in $SrF_2:Pr^{3+}$. 363

Figure VIII.3.2 Upconverted $^3P_0 \rightarrow {}^3H_4$ emission , at 14K, from the C_{4v} F^- site in $SrF_2:Pr^{3+}$ with $^3H_4(Z_1) \rightarrow {}^1D_2(D_1)$ excitation. 365

Figure VIII.3.3 Polarised $^3P_0 \rightarrow {}^3H_4$ emission from the C_{4v} F^- site in $SrF_2:Pr^{3+}$ with direct $^3P_0$ excitation using the argon ion laser. 366

Figure VIII.3.4 Fluorescence decay, at 14K, of the upconverted $^3P_0$ emission from the C_{4v} F^- site in $SrF_2:Pr^{3+}$ for Pr^{3+} ion concentrations of (a) 0.5 mol%, (b) 0.1 mol% and (c) 0.05 mol%. 369

Figure IX.1.1 Schematic view of an inhomogeneously broadened spectral line formed from the envelope of much narrower homogeneous 'spin packets'. 377

Figure IX.2.1 Energy level diagram of the Pr^{3+} ion, of nuclear spin $I = {}^5/_2$, in the C_{4v} symmetry site showing the hyperfine and superhyperfine levels. 380

Page

Figure IX.2.2 Pictorial reperesentation of the physical model for holeburning in the C_{4v} site. •••• 381

Figure IX.3.1 ODNMR lines from resonances of nearest neighbour ^{19}F nuclei and interstitial F^- and H^- ions in $SrF_2:Pr^{3+}$ crystals. 386

Figure IX.3.2 ODNMR lines from resonances of nearest neighbour ^{19}F nuclei for several C_{4v} sites in $SrF_2:Pr^{3+}$ crystals having different interstitial ions. 390

CHAPTER I

INTRODUCTION

I.1 Introduction

The aim of this thesis is to report results from an experimental and theoretical investigation into alkaline earth fluoride crystals doped with both trivalent praseodymium (Z=59) and hydride ions. Alkaline earth fluorides form cubic crystals from an array of fluorine ions located at the corners of a cube, and alkaline earth ions at the centre of every alternate cube (Figure I.1.1). These crystals are excellent hosts for optically active impurity ions, such as the rare-earth ions, being transparent over a wide range of the electromagnetic spectrum and mechanically stable under a range of physical conditions. The optical transitions of a rare-earth ion are sensitive to the local environment and a study of its electronic system will yield information on its interactions and surroundings in the crystal.

I.2 Rare-Earth Doped Alkaline Earth Fluoride Crystals

The rare-earths form the lanthanide series which is characterised by the progressive filling of the 4f shell. Rare-earth ions introduced as impurities into MeF_2 crystals (Me = Ca, Sr, Ba) have been the subject of extensive investigations and it is now well established they substitutionally occupy a Me^{2+} site in either the divalent or trivalent state. When in the trivalent state some form of charge compensation is required to maintain crystal neutrality. This is provided by additional F^- ions occupying vacant interstitial sites in the lattice, the position of which may be remote or close to the RE^{3+} ion. Each charge compensation mechanism forms a different spectroscopic site having a unique set of energy levels.

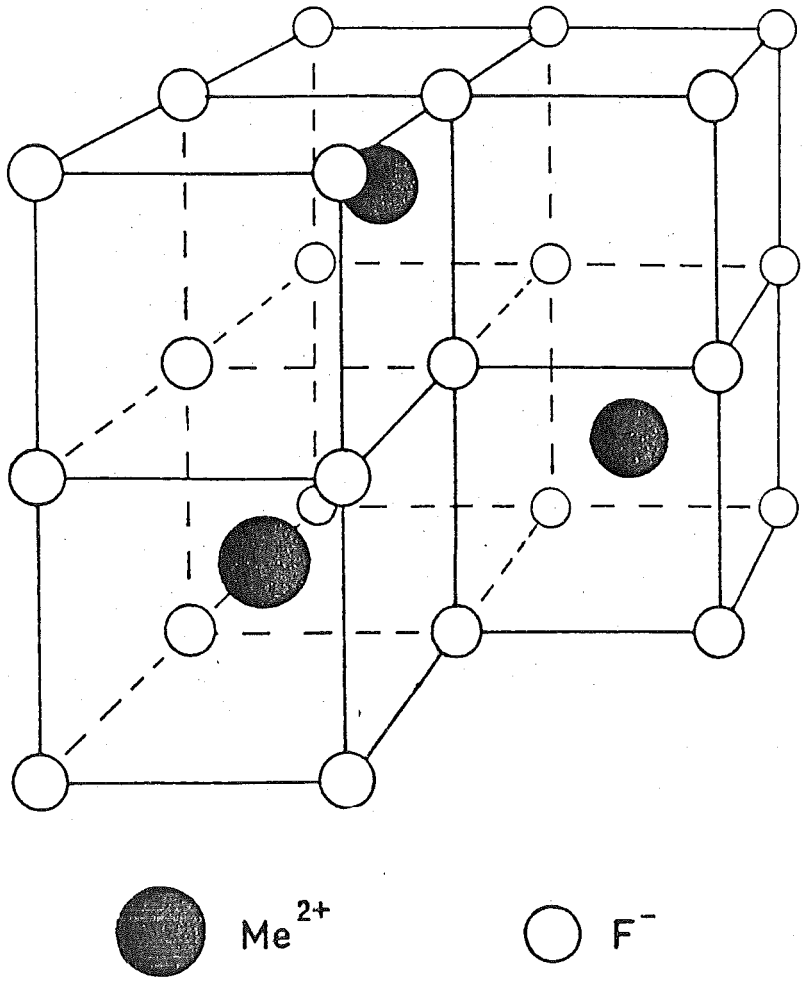

Figure I.1.1 Structure of the alkaline earth fluorides.

A common charge compensating arrangement for single rare-earth ions in MeF_2 crystals, has an interstitial F^- ion occupying one of the six vacant cubes adjacent to the rare-earth ion as shown in Figure I.2.1. Each of the pairs of RE^{3+} - F^- ions forms a site of tetragonal (C_{4v}) point group symmetry.

Through the lanthanide contraction that draws the 4f shell inside the closed $5s^2 5p^6$ shells (Wybourne [1965]), the f shell is relatively insensitive to the atomic environment and does not interact strongly with the lattice. Thus the optical transitions of a rare-earth ion are well defined and the absorption spectrum of crystals containing such ions consists of a superposition of sharp lines from the numerous discrete centres present.

I.3 Hydrogenated Alkaline Earth Fluorides Containing Rare Earth Ions

Using the techniques of Hall and Schumacher [1962], it is possible to introduce H^- ions (or its isotopes D^- and T^-) into $MeF_2{:}RE^{3+}$ lattices that substitute for some of the F^- ions present, including those taking part in the charge compensation process. Although subject to similar force constants to the fluoride ion which it replaces, the very much smaller mass of the H^- ion results in a vibrational frequency considerably higher than the maximum frequency the lattice can propagate and a localised mode of vibration is apparent. The localisation of the excitation is not as well defined for the D^- and T^- isotopes as they have lower frequencies of vibration, with their increase in mass, which are closer to the levels the lattice can propagate.

New lines appear in the optical and infrared spectra of hydrogenated $MeF_2{:}RE^{3+}$ crystals as H^- ions become involved in the charge compensation process. Jones et al [1969] carried out extensive

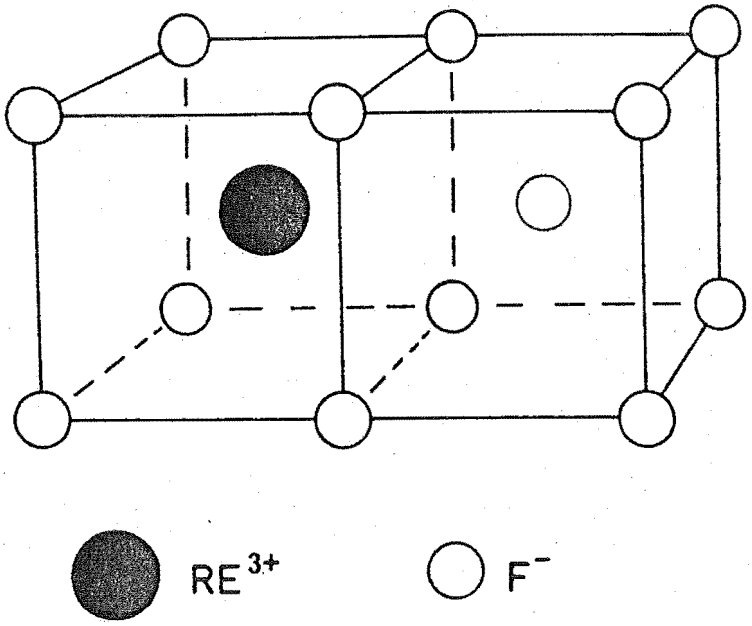

Figure I.2.1 A model of the RE^{3+} C_{4v} site. In the alkaline earth fluorides there are six equivalent interstitial positions for the charge compensating ion.

investigations of such crystals and presented results consistent with the formation of a tetragonal RE^{3+}- H^- site analogous to the RE^{3+}- F^- site described previously. The infrared spectrum of tetragonal H^- sites contains two fundamental local mode lines corresponding to the longitudinal and transverse modes of vibration. The equivalency of the two transverse directions of motion results in a degeneracy in the transverse local mode which in some special cases can be lifted by the electron-phonon interaction. Jacobs et al [1971] observed the lower frequency local mode line to split into two components for the Ce^{3+}-H^- site and three components for the Pr^{3+}- H^- site, confirming the assignment of this line as the transverse x,y local mode vibration.

In addition to the common tetragonal RE^{3+}- H^- site, hydrogenic ions can substitute for F^- ions at other positions to form further hydrogenic RE^{3+} ion sites (Edgar et al [1977] & [1979], Cockroft et al [1987b]). The asymmetry induced by the H^- ions in such sites lowers the crystal field symmetry on the RE^{3+} ion leading to a lifting of level degeneracies in some cases (Macfarlane et al [1987]).

I.4 The Structure of This Work

Whether in the parent or hydrogenated crystal, the tetragonal (C_{4v}) site is the dominant RE^{3+} centre in praseodymium doped fluorite crystals and most attention in this study was focussed on these centres. The powerful techniques of laser selective excitation were employed to study individual optically active centres. Also, these techniques were extended by using linearly polarised laser beams and oriented samples to obtain additional information on the energy levels of the Pr^{3+} ions.

Figure I.4.1 depicts the energy level scheme for the Pr^{3+} ion in the C_{4v} site in SrF_2. The extent of the crystal field splitting is represented by the thickness of the level. In common with the

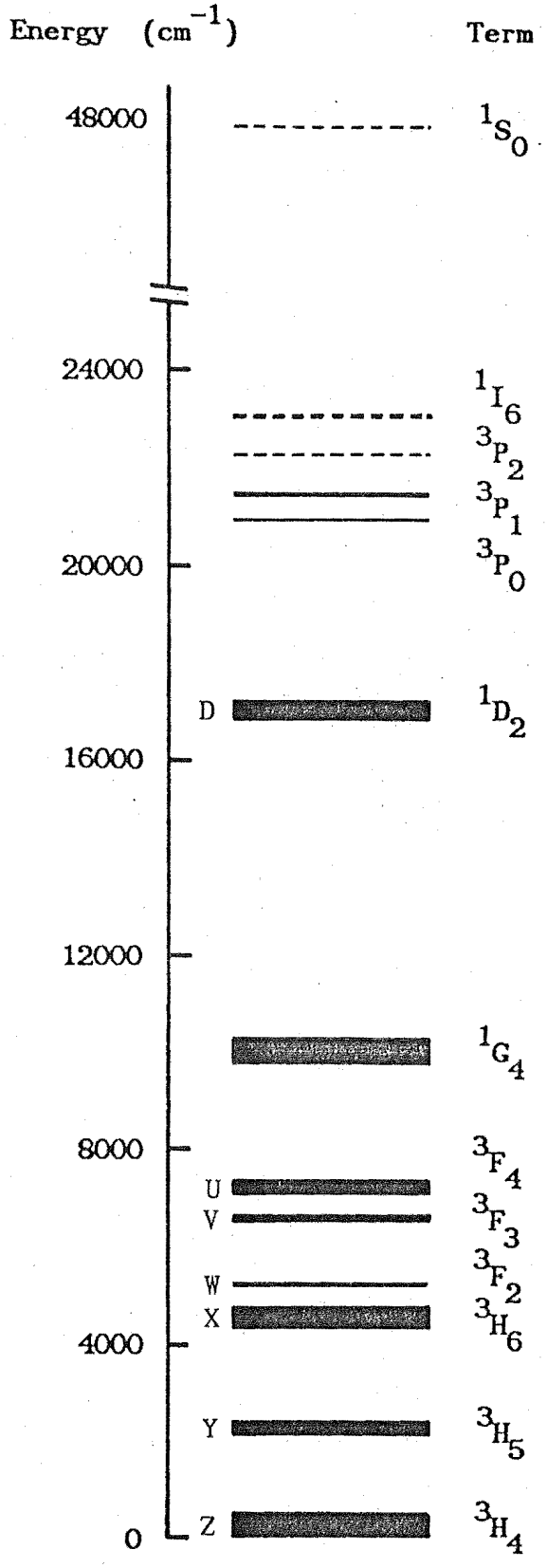

Figure I.4.1 Energy level diagram for the Pr^{3+} in the C_{4v} site in SrF_2.

nomenclature established for other rare-earth ions, the multiplets are labelled from the ground state in descending alphabetical order, i.e. the ground state $^3H_4$ multiplet is Z, the $^3H_5$ multiplet is Y etc. A departure from this scheme for Pr^{3+} gave the $^1D_2$ multiplet the label of D. The crystal field levels within a multiplet are numbered in ascending order from the lowest component. Thus, the absorption transition from the ground state to the lowest crystal field component of $^1D_2$ would be labelled by $Z_1 \longrightarrow D_1$.

The $^1D_2$ and $^3P_0$ multiplets are conveniently placed in the optical region for excitation using tunable dye lasers. Emission spectra from these levels reveals a multitude of sharp lines corresponding to transitions to the crystal field levels of the lower multiplets. A comprehensive survey of the absorption and emission spectra has established up to 49 out of the total of 70 energy levels for the C_{4v} sites in $SrF_2:Pr^{3+}$ and $CaF_2:Pr^{3+}$ crystals. The results of these experiments are presented in Chapter IV for the sites containing an F^- charge compensating ion and in Chapter V for the corresponding C_{4v} sites containing H^-, D^- and T^- ions.

Hydrogenated crystals of $SrF_2:Pr^{3+}$ and $CaF_2:Pr^{3+}$ have been found to contain a number of similar centres that are derived from the dominant C_{4v} H^- site by the addition of extra hydrogenic ions. A large number of such sites are apparent as there are many combinations possible for the placement of these extra ions. Such centres are found to be unstable under laser excitation and exhibit the interesting phenomena of reversible polarised bleaching (Cockroft et al [1987a]) and photoproduct formation (Macfarlane et al [1987]). These effects and some possible site configurations and bleaching mechanisms are discussed in Chapter VI.

The light H^- (or D^-, T^-) ions introduced into fluorite crystals undergo modes of vibration that are spatially localised at the ion

site. The effect on any nearby RE^{3+} ions is to modulate the crystal field and produce extra lines in its optical spectra. These lines are associated with transitions to local mode vibronic levels that are at energy intervals from a parent RE^{3+} electronic level corresponding to the local mode phonon frequency. For the C_{4v} Pr^{3+}- H^- site in SrF_2 and CaF_2 crystals a particular manifestation of the electron-phonon interaction is a lifting of the degeneracy of the transverse local mode vibration of the H^- ion. In Chapter VII a theoretical analysis shows the dominant contribution to the splitting arises from second order effects associated with nearby electronic levels.

The high frequency local mode vibrations of the charge compensating hydrogenic ions were found to completely determine the non-radiative contribution to the decay of a Pr^{3+} electronic level. Results are presented in Chapter VIII that show the changes in the fluorescent lifetime of an emitting level in the hydrogenic C_{4v} sites have an excellent correlation with the changes in the order of a multiphonon process describing the relaxation to the next lowest level. It was found that a single hydrogenic local mode phonon frequency was all that was required to explain the observed trends.

The C_{4v} Pr^{3+} sites in CaF_2 and SrF_2 crystals exhibit a novel holeburning mechanism where the population reservoirs are superhyperfine levels formed from the different configurations of neighbouring lattice F^- ion nuclear spins (Burum et al [1982]). The results of a preliminary study of spectral holeburning in the C_{4v} Pr^{3+}-hydrogenic sites are presented in Chapter IX and show that the electronically similar H^- and D^- ions occupy different physical positions in the lattice cube.

CHAPTER II

REVIEW OF THE THEORY

The electronic configuration of the neutral lanthanides is characterised by the progressive filling of the 4f shell inside the 6s and 5d shells containing two or three electrons. Ionization to the +3 state occurs by the successive removal of all the 6s and 5d electrons and frequently a 4f electron, to leave a common xenon structure and a $4f^N$ configuration with N = 1 for cerium increasing to N = 14 for lutecium. These valence 4f electrons are shielded from the effects of the external environment as the lanthanide contraction draws this shell inside the closed $5s^2 5p^6$ shells. Thus, the lanthanide ions show small crystal field splittings and a theoretical analysis of the crystal field can be treated using perturbation theory on the free ion Hamiltonian.

II.1 The Free Ion Hamiltonian

The non-relativistic Hamiltonian for an N electron atom is

$$H = \sum_{i=1}^{N} \left[-\frac{\hbar^2}{2m} \nabla_i^2 - \frac{Ze^2}{r_i} \right] + \sum_{i<j=1}^{N} \frac{e^2}{r_{ij}} \qquad \text{(II.1.1)}$$

where the symbols have their usual meanings. The presence of the second summation prevents exact solutions for systems of more than one electron and is also too large to be treated by perturbation theory. The problem becomes solvable using the central field approximation of Condon and Shortley [1935] where each electron is assumed to move independently in a spherically symmetric potential, $-U(r_i)/e$, arising from the spherically averaged potential fields of each of the other electrons.

The central field Hamiltonian is then

$$H_{central} = \sum_{i=1}^{N} \left[-\frac{\hbar^2}{2m} \nabla_i^2 + U(r_i) \right] \qquad (II.1.2)$$

where the remainder

$$H - H_{central} = \sum_{i=1}^{N} \left[-\frac{Ze^2}{r_i} - U(r_i) \right] + \sum_{i<j}^{N} \frac{e^2}{r_{ij}} \qquad (II.1.3)$$

is of such a size that it can be treated by perturbation theory. For each electron the Schrödinger equation is now readily separated into radial and angular equations, and by drawing an analogy with the hydrogen atom the normalised solutions for equation (II.1.2) take the form

$$\psi(k) = r^{-1} R_{nl}(r) Y_{lm_l}(\theta,\phi)\sigma_s \qquad (II.1.4)$$

where σ_s is a spin function corresponding to the two possible projections $m_s = \pm \frac{1}{2}$ of the electron spin along the z-axis. The $Y_{lm_l}(\theta,\phi)$ are spherical harmonics defined by

$$Y_{lm}(\theta,\phi) = (-1)^m \left\{ \frac{(2l+1)(l-m)!}{4\pi(l+m)!} \right\}^{\frac{1}{2}} P_l^m(\cos\theta) e^{im\phi} \qquad (II.1.5)$$

with

$$P_l^m(x) = \frac{(1-x^2)^{\frac{m}{2}}}{2^l l!} \frac{d^{l+m}}{dx^{l+m}} (x^2-1)^l \qquad (II.1.6)$$

the associated Legendre Polynomials. The angular part of (II.1.4) can

be solved exactly whereas the radial part $R_{nl}(r)$ depends upon the form of U(r).

The solutions of the Schrödinger equation for the atom are products of single electron solutions and can be written as

$$\Psi = \prod_{i=1}^{N} \psi(k_i) \qquad (II.1.7)$$

where k_i represents the quantum numbers $nlm_l m_s$ of the i^{th} electron. This is not a unique solution as any permutation of the coordinates of the N electrons also leads to a solution of the Schrödinger equation and linear combinations are required. However, to satisfy the Pauli exclusion principle the linear combination of these solutions must be chosen so that the resulting wavefunction is totally antisymmetric with respect to the simultaneous interchange of the spatial m_l and spin m_s coordinates of any pair of electrons. The resulting solution can be written as a determinantal product state

$$\{k_1, k_2, \cdots k_N\} = N^{-\frac{1}{2}} \sum_{P} (-1)^P \psi_1(k_1)\psi_2(k_2)\cdots\psi_N(k_N) \qquad (II.1.8)$$

where the sum is over all permutations P of the electrons' coordinates among the states defined by the quantum numbers $k_1, k_2 \cdots k_N$ and p is the parity of the permutation.

The eigenvalues of these solutions form the electronic configurations of the atom and are written as a sequence of the nl quantum numbers, a single electron state being degenerate with respect to m_l and m_s. These configurations will be highly degenerate in the determinental product states as the Hamiltonian is a symmetric function in the coordinates of the electrons. This degeneracy will be partially removed by the electrostatic perturbation potential given by

equation II.1.3.

$$H - H_{central} = V = \sum_{i=1}^{N} \left[-\frac{Ze^2}{r_i} - U(r_i) \right] + \sum_{i<j}^{N} \frac{e^2}{r_{ij}} \qquad (II.1.3)$$

The first summation is purely radial and will shift the levels of a configuration as a whole and is discarded as giving no information on the structure of the configuration. The remaining term

$$H_{coul} = \sum_{i<j}^{N} \frac{e^2}{r_{ij}} \qquad (II.1.9)$$

represents the repulsive Coulomb interaction between all pairs of electrons and will partially lift the degeneracy of the levels of the configuration. It has been shown by Condon and Shortley [1935] Chapter 6, that the contribution to the energy from the electrostatic interaction of closed shells is common to all states of the atom. As interest is usually centred only on the relative energy levels, the sum in (II.1.9) can be restricted to those electrons in valence shells.

The solutions of the Schrödinger equation which are certain linear combinations of the determinantal product states have been labelled up to now with single electron quantum numbers $nlm_l m_s$. It becomes convenient to label the states using the total orbital and total spin angular momenta of the electrons

$$\underset{\sim}{L} = \sum_i \underset{\sim}{l}_i \qquad \underset{\sim}{S} = \sum_i \underset{\sim}{s}_i \qquad (II.1.10)$$

as the Coulomb interaction H_{coul} commutes with $\underset{\sim}{L}^2$ and $\underset{\sim}{S}^2$.

Thus the matrix elements to be calculated

$$\langle\ \tau SL \left| \sum_{i<j} \frac{e^2}{r_{ij}} \right| \tau' SL\ \rangle \qquad \text{(II.1.11)}$$

will be diagonal in S and L but not necessarily τ, the remaining quantum numbers of the state. Following Condon and Shortley [1935], the interaction between each pair of electrons is expanded in Legendre Polynomials of the cosine of the angle between the vectors to the electrons, i.e.

$$\frac{e^2}{r_{ij}} = e^2 \sum \frac{r_<^k}{r_>^{k+1}} P_k(\cos \omega_{ij}) \qquad \text{(II.1.12)}$$

From the spherical harmonic addition theorem

$$P_k(\cos \omega_{ij}) = \frac{4\pi}{2k+1} \sum_q Y^*_{kq}(\theta_i,\phi_i)\ Y_{kq}(\theta_j,\phi_j) \qquad \text{(II.1.13)}$$

$$= \underset{\sim}{C}_i^{(k)} \cdot \underset{\sim}{C}_j^{(k)}$$

where

$$\underset{\sim}{C}_q^{(k)} = \sqrt{\frac{4\pi}{2k+1}}\, Y_{kq}$$

is a tensor operator of rank k of electron q. Thus equation II.1.11 becomes

$$\sum_k e^2 \langle\ \tau SL \left| \sum_{i<j} \frac{r_<^k}{r_>^{k+1}} \left[\underset{\sim}{C}_i^{(k)} \cdot \underset{\sim}{C}_j^{(k)} \right] \right| \tau' SL\ \rangle \qquad \text{(II.1.14)}$$

The radial part of this matrix element can be expressed in terms of

Slater integrals while the angular part can be evaluated using the tensor operator methods of Racah (see, for example Judd [1963]).

For an f^N configuration the electrostatic energy is written as a linear combination of Slater integrals F_k,

$$E = \sum_{k=0}^{6} f^k F_k(nf, nf) \qquad (II.1.15)$$

where k is even and the f^k's are the coefficients of the linear combination and represent the angular part of the interaction. It is more convenient to construct new operators having some simple transformation properties (Wybourne [1965]) and the matrix elements are then written as

$$E = \sum_{k=o}^{3} e_k E^k$$

where the e_k and E^k can be expressed as linear combinations of the f^k's and F_k's respectively. Nielson and Koster [1963] can be consulted for a complete tabulation of the electrostatic energy matrices for all the f^N configurations.

The largest relativistic correction to the perturbation potential II.1.3 is the spin orbit interaction

$$H_{so} = \sum_i \xi(r_i) \underset{\sim}{s}_i \cdot \underset{\sim}{l}_i \qquad (II.1.16)$$

where the radial function $\xi(r_i)$ depends upon the form of $U(r_i)$.

The spin orbit interaction commutes with $\underset{\sim}{J}^2$, where $\underset{\sim}{J}$ is the total angular momentum given by

$$\underset{\sim}{J} = \underset{\sim}{L} + \underset{\sim}{S} \quad ,$$

but not with $\underset{\sim}{L}^2$ or $\underset{\sim}{S}^2$. Hence its matrix elements are diagonal in J but not in L or S and the effect will be to split the ^{2S+1}L term into levels characterised by different values of J.

For many cases the spin orbit interaction is small compared with the Coulomb interaction and we have LS or Russell Saunders coupling with the states being labelled by the still good quantum numbers S and L. The splitting of a ^{2S+1}L term into its J components will be solely diagonal and given by the Lande interval rule

$$\begin{matrix}\text{spin orbit} \\ \text{matrix element}\end{matrix} \qquad \alpha \quad J(J+1) - L(L+1) - S(S+1)$$

If the strength of the interaction is appreciable, states of different L and S but the same J will be mixed and the LS coupling is broken. L and S will no longer be good quantum numbers and the eigenfunctions in this intermediate coupling scheme will now be linear combinations of terms having the same value of J. It is usual to choose the dominant $^{2S+1}L_J$ term as the label for that particular eigenfunction.

The matrix elements of the spin orbit interaction are given by (Wybourne [1965]),

$$\langle l^N \alpha SLJM | \xi_{nl} \sum_{i=1}^{N} \underset{\sim}{s}_i \cdot \underset{\sim}{l}_i | l^N \alpha' S'L'JM\rangle = \xi_{nl} (-1)^{J+L+S'} \begin{Bmatrix} L & L' & 1 \\ S' & S & J \end{Bmatrix}$$

$$\times \sqrt{l(l+1)(2l+1)}\, \langle l^N \alpha SL \| \underset{\sim}{V}^{(11)} \| l^N \alpha' S'L' \rangle \quad . \qquad \text{(II.2.17)}$$

The matrix elements for all the f^N configurations have been tabulated by Nielson and Koster [1963].

In some instances it becomes necessary to introduce the interaction between configurations in order to account for differences between observed and predicted energy levels. Wybourne [1965] contains a discussion of these configuration mixing effects and only the results required are included here. Rajnak and Wybourne [1963] showed the configuration interaction can be included using the expression

$$\alpha L(L+1) + \beta G(G_2) + \gamma G(R_7) \qquad \text{(II.1.18)}$$

where $G(G_2)$ and $G(R_7)$ are the eigenvalues of Casimirs operators for the groups G_2 and R_7 used to classify the states of the f^N configuration and α, β and γ are associated parameters. These eigenvalues are tabulated in Wybourne [1965] using integers (u_1u_2) and $(w_1w_2w_3)$ to label the irreducible representations of the groups G_2 and R_7. Nielson and Koster [1963] relate these integer labels of the irreps to the more familiar ^{2S+1}L terms for several electron configurations.

II.2. The C_{4v} Crystal Field

The electrons of rare-earth ions are sufficiently localised due to the lanthanide contraction that the crystal field can be treated as a perturbation on the states of the free ion. The (2J+1) fold degeneracy of each term of the free ion is destroyed and the term splits into several levels, the number of which depends upon the point symmetry about the ion. Just as the electrostatic repulsion between electron pairs in the Coulomb interaction could be written as a product of a radial function and an angular function expressed in terms of spherical harmonics, the electrostatic potential between a rare-earth electron and an ion or atom of the lattice can be written

in the same way. That is, the crystal field can be written

$$H_{CF} = \sum_{k,q} B_q^k \sum_{i=1}^{N} C_q^{(k)}(i) \qquad \text{(II.2.1)}$$

where the $C_q^{(k)}$ are Racah tensor operators related to the spherical harmonics Y_{kq} by

$$C_q^{(k)} = \sqrt{\frac{4\pi}{2K+1}}\, Y_{kq} \qquad \text{(II.2.2)}$$

All the radial information is contained in the B_q^k which are usually treated as adjustable parameters in a least squares fit of the experimentally determined crystal field energy levels.

The matrix elements of the crystal field for a f^N configuration are given by (Wybourne [1965])

$$\langle f^N \alpha SLJJ_Z | H_{CF} | f^N \alpha' SL'J'J'_Z \rangle = \sum_{k,q} B_q^k (-7) \begin{pmatrix} 3 & k & 3 \\ 0 & 0 & 0 \end{pmatrix} (-1)^{2J-J_Z+L'+S+k}$$
$$\times \sqrt{(2J+1)(2J'+1)} \begin{pmatrix} J & k & J' \\ -J_Z & q & J_Z' \end{pmatrix} \begin{Bmatrix} J & J' & k \\ L' & L & S \end{Bmatrix} \langle SL \| U^{(k)} \| SL' \rangle \qquad \text{(II.2.3)}$$

where the 3j and 6j symbols can be found in Rotenberg et al [1959] and the doubly reduced matrix elements are tabulated by Nielson & Koster [1963].

The crystal field Hamiltonian appropriate for C_{4v} symmetry is

$$H_{C_{4v}} = B_c^4 \left[C_0^{(4)} + \sqrt{\frac{5}{14}} \left[C_4^{(4)} + C_{-4}^{(4)} \right] \right] + B_c^6 \left[C_0^{(6)} - \sqrt{\frac{7}{2}} \left[C_4^{(6)} + C_{-4}^{(6)} \right] \right]$$
$$+ B_0^2 C_0^{(2)} + B_0^4 C_0^{(4)} + B_0^6 C_0^{(6)} \qquad \text{(II.2.4)}$$

where the first two terms represent the cubic crystal field and the remaining an axial perturbation. The crystal field wavefunctions,

which will be linear combinations of $|SLJJ_Z\rangle$ states can be labelled by the cubic O_h and tetragonal C_{4v} irreps Γ_i and τ_j respectively.

II.3 Energy Matrices for the Pr^{3+} Ion

Thirteen $^{2S+1}L_J$ terms constitute the $4f^2$ electronic configuration for the Pr^{3+} ion. The techniques of Condon and Shortley [1935] can be used to derive the ^{2S+1}L terms of any electronic configuration and the electrostatic energies for the terms of a configuration are tabulated by Nielson and Koster [1963]. Table II.3.1 gives these energies for the Pr^{3+} ion.

Table II.3.1

Electrostatic energies for the f^2 electronic configuration.

Term	Energy
^3P	$33E^3$
^3F	0
^3H	$-9E^3$
^1S	$9E^1$
^1D	$2E^1 + 286E^2 - 11E^3$
^1G	$2E^1 - 260E^2 - 4E^3$
^1I	$2E^1 + 70E^2 + 7E^3$

The spin orbit interaction, equation II.1.16, mixes states of the same J but different L and S. The matrix elements between free ion states in such an intermediate coupling scheme will consist of a linear combination of Slater radial integrals and spin orbit radial integrals and can be arranged in energy matrices, one for each value

of J. Using equation II.1.17 and the tables of Nielson and Koster [1963] the spin orbit matrix element for the Pr^{3+} ion in the f^2 configuration are given in Table II.3.2.

Table II.3.2

Spin orbit matrix element for the f^2 electronic configuration

J = 0

	$^3P_0$	$^1S_0$
$^3P_0$	-1	$-2\sqrt{3}$
$^1S_0$	$-2\sqrt{3}$	0

J = 1

	$^3P_1$
$^3P_1$	$-\frac{1}{2}$

J = 2

	$^3F_2$	$^1D_2$	$^3P_2$
$^3F_2$	-2	$-\sqrt{6}$	0
$^1D_2$	$-\sqrt{6}$	0	$\frac{3}{\sqrt{2}}$
$^3P_2$	0	$\frac{3}{\sqrt{2}}$	$\frac{1}{2}$

J = 3

	$^3F_3$
$^3F_3$	$-\frac{1}{2}$

J = 4

	$^3H_4$	$^3F_4$	$^1G_4$
$^3H_4$	-3	$-\sqrt{6}$	$-\sqrt{\frac{10}{3}}$
$^3F_4$	0	0	$\sqrt{\frac{11}{3}}$
$^1G_4$	$-\sqrt{\frac{10}{3}}$	$\sqrt{\frac{11}{3}}$	0

J = 5

	$^3H_5$
$^3H_5$	$-\frac{1}{2}$

J = 6

	$^3H_6$	$^1H_6$
$^3H_6$	$\frac{5}{2}$	$\sqrt{\frac{3}{2}}$
$^1I_6$	$\sqrt{\frac{3}{2}}$	0

The configuration interactions given in the expression II.1.18 are diagonal in L and S. Table II.3.3 gives the matrix elements of these

interactions for the f^2 configuration.

Table II.3.3

Matrix elements of the f^2 configuration interactions.

Term	L(L+1)	$G(G_2)$	$G(R_7)$
^3H	30	1	1
^3F	12	0.5	1
^1G	20	$\frac{7}{6}$	$\frac{7}{5}$
^1D	6	$\frac{7}{6}$	$\frac{7}{5}$
^3P	2	1	1
^1I	42	$\frac{7}{6}$	$\frac{7}{5}$
^1S	0	0	0

The matrix elements for the electrostatic, spin orbit and configuration interactions have been detailed above for the f^2 configuration appropriate to the Pr^{3+} ion. Particular values of the Slater integrals E^1, E^2, E^3, the spin orbit integral ξ and the parameters α, β, γ can be chosen to construct the complete free ion energy matrix. Diagonalisation of this matrix yields a set of eigenvalues and corresponding eigenvectors that can be used for a theoretical energy level scheme. The crystal field interaction, equation II.2.1, lifts the degeneracy of a $^{2S+1}L_J$ term and when included into the energy matrix will require the dimension of the matrix to be increased to its maximum multiplicity given by the combination $\begin{bmatrix} 2(2l+1) \\ x \end{bmatrix}$ for a configuration nl^x. Results of a crystal field calculation of the electronic states for the Pr^{3+} in the C_{4v} site in SrF_2 will be presented in Chapter IV.

CHAPTER III

EXPERIMENTAL CONSIDERATIONS

III.1 Crystal preparation

Single crystals of calcium fluoride and strontium fluoride containing trivalent praseodymium were either purchased from Optovac Inc. or grown in this institution from the melt using the Bridgeman technique. For the locally grown samples, measured amounts of pure alkaline earth fluoride and PrF_3 were placed in a graphite crucible and lowered through the temperature gradient produced by the work coil of a 38 kW Arther D. Little rf furnace. At a lowering rate of 4.1 mm per hour single crystals of diameter 10 mm and length 30 mm could be satisfactorily grown. A vacuum was maintained to better than 10^{-4} torr and under these conditions oxygen contamination was found to be insignificant in this work.

Samples for spectroscopic study or further treatment were either cut using a diamond saw or cleaved from the previously grown boules to a convenient thickness of typically 3 mm. A pair of parallel flats were ground on the edges of the crystal cylinder for the entry and exit of the laser beam. Successively finer grades of abrasive paper were used to shape these edges and the crystal faces. The crystals were polished to an optical finish on plastic sheet using 800 grade abrasive powder with water as a lubricant.

Oriented crystals for polarisation studies were cut from aligned boules. The cubic calcium fluoride type crystals cleave along (111) planes and the <100> cubic faces can be identified from the line of intersection between two cleavage planes. The crystal boules were cleaved in two (111) planes using a sharp chisel and then glued in a angled holder in preparation for cutting. In some cases <100> oriented crystals were purchased from Optovac Inc. The alignment of

the locally produced oriented crystals was not checked independently, however the good polarisation ratios of the spectra produced in this study indicate it was satisfactory.

Hydrogen, deuterium or tritium was introduced into the samples following the method of Hall & Schumacher [1962]. The crystals were sandwiched between coils of aluminium wire in alumina crucibles which were then placed in a 20 mm diameter quartz tube. The oxide layer had been previously scraped off the aluminium wire before forming the coils and care was taken to avoid handling the samples and coils after a thorough washing in acetone. The quartz tube was evacuated with a mercury diffusion pump to 10^{-3} mm Hg and after several flushings with the appropriate gas was sealed containing a gas pressure of 20 inches Hg absolute. The arrangement was heated to 850°C for times ranging from 24-68 hours. Various cooling methods were used depending upon the crystal requirements, and ranged from gradual cooldown to room temperature over a period of hours to the immediate immersion in liquid nitrogen.

For the preparation of the tritiated samples used in this study the small amount of gas available and its inclusion in a sealed glass container necessitated the design of a new quartz tube - the old arrangement displacing too much volume. The main design criterion was having the volume as small as possible to keep the partial pressure of the tritium gas high enough for a satisfactory treatment. Other requirements included external access in order to break the ampoule seal and that the arrangement be reusable as several treatments were planned. Figure III.1.1 details the design and glassware arrangement.

The internal quartz sleeve was introduced to hold the glass gas capsule. At the temperature of the treatment it was expected that the glass capsule would melt and either disturb the crystals or fuse to the walls of the outer quartz tube and destroy the integrity of the system when the arrangement was cooled.

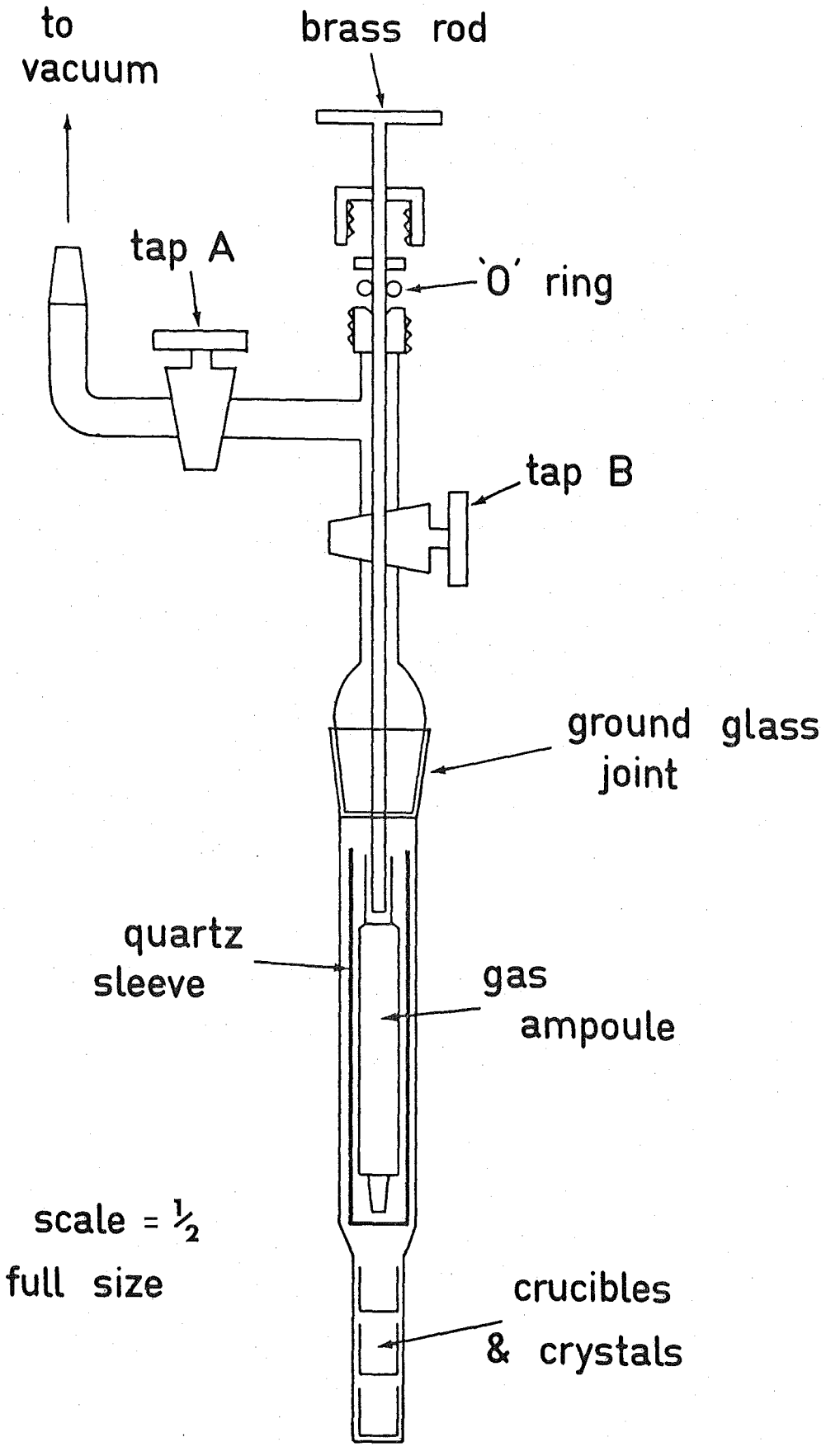

Figure III.1.1 Experimental arrangement of the quartz components constructed for the tritiation of crystals.

With the system ready for treatment it was calculated that the quartz tube to gas capsule volume ratio would reduce the tritium gas pressure from its original atmospheric value to around 3 inches Hg absolute. As this pressure is substantially lower than the standard treatment pressure of 20 inches Hg, a test treatment run was carried out using hydrogen gas at a pressure of 2 inches Hg. The samples from this treatment were analysed using infra-red absorption and found to contain hydride ions within a factor of two of the conventional treatment.

The seal on the capsule containing the tritium gas is broken by pushing the brass rod down through the open tap B while tap A to the vacuum pump is closed. As the gas will expand up into the area between taps A and B, the brass boss has to be vacuum tight as the rod moves up and down. A single, well greased 'O' ring was found to be sufficient to maintain the vacuum. The treatment process is started by withdrawing the rod past tap B, closing B and then heating the arrangement to 850^{o}C.

The inclusion of hydride ions or one of the other isotopes into these crystals is a process where contaminants such as oxygen can compete, reducing the number of desired ions in the crystal. In a normal hydrogenation or deuteration treatment, contaminants are removed by multiple flushings with the appropriate gas. The small amount of tritium gas available precluded this method for the tritation of the crystals. In the technique used, all components were washed with acetone and handled only while wearing clean plastic gloves. After assembly of the components in the quartz tube, the arrangement was allowed to outgas at 200^{o}C for 4 hours while open to the mercury diffusion pump. After multiple flushings with clean dry helium gas the system was again baked under vacuum for a further 4-5 hours before breaking open the capsule to start the treatment.

III.2 Optical Spectroscopy

III.2.1 Optical Absorption

Optical absorption spectra were measured photoelectrically on a Spex Industries Model 1700 single monochromator. This spectrometer operates in a Czerny-Turner configuration with a 0.75 m focal length and f/6.8 aperture. The single plane grating fitted has 1180 lines/mm and is blazed at 750.0 nm. Source radiation was supplied by a 100 W quartz iodine lamp regulated by a voltage stabilised 12 V power supply.

Absorption transitions to the levels of the $^1D_2$, $^3P_0$ and $^3P_1$ multiplets of the Pr^{3+} ion were detected using the spectrometer's second order reflection and an EMI 9558 QA photomultiplier tube thermoelectrically cooled to -25°C. Second order reflection was used as the grating suffered from an imperfection in the 495 nm region. Appropriately chosen Corning glass filters were used to eliminate unwanted first order radiation. The photomultiplier tube signal was measured on either a Jarrell-Ash electrometer or more recently a Keithley 610B electrometer and displayed on a strip chart recorder.

III.2.2 Fluorescence Spectra

Spectra of the fluorescent transitions from the $^1D_2$ levels of the Pr^{3+} centres were recorded using selective laser excitation. The exciting source was a Spectra Physics Model 375 tunable dye laser pumped with a Spectra Physics Model 171 15 Watt argon-ion laser. A Rhodamine 6G dye having a lasing range from 15400 to 17600 cm^{-1} and pumped with the 514.5 nm argon-ion laser line was appropriate for exciting transitions to the $^1D_2$ multiplet of the Pr^{3+} ion. Vibronic energy levels in the 18200 cm^{-1} region associated with the same $^1D_2$ multiplet were excited using a Coumarin 6 dye pumped with the 488.0 nm line of the argon-ion laser. Typical output powers used in the

experiments were 100 mW and 15 mW for the red and green dyes respectively.

Initially the dye laser was fitted with a tuning wedge and a fine tuning etalon giving a stated laser linewidth of 40 GHz. With both elements in the cavity continuous tuning of the laser frequency could only be achieved over 30 cm^{-1}, the free spectral range (FSR) of the fine tuning etalon. In March 1986 a Spectra Physics Model 573 three plate birefringent filter obtained from Dr Neil Manson of the Australian National University was assembled and installed by the author. This single tuning element replaces the two elements previously required and allows continuous tuning over the whole lasing range of the dye.

For the experiments using the tuning wedge and fine tuning etalon, an Anaspec 300S laser filter monochromator was placed in the dye laser beam path to reduce the intensity of the etalon sidebands located at the FSR either side of the laser line. This monochromator was no longer required when the laser was equipped with the birefringent filter.

Fluorescence spectra recorded before January 1984 were measured using a Jarrell-Ash Model 25-103 double monochromator. The photomultiplier tube signal was amplified by a PAR Model 1121 preamplifier and discriminator before processing by a PAR Model 1112 photon counter. The digital photon counter output was recorded on paper tape for further processing by a Burroughs B6900 mainframe computer. Details on the paper tape storage and retrieval system and the Jarrell-Ash spectrometer are given in the Ph.D. thesis of Tomblin [1983].

During January 1984 a Spex Industries 1403 double monochromator was installed. This spectrometer has a Czerny Turner configuration with a 0.85 m focal length and an aperture of f/7.8 and was equipped with holographic gratings having 1800 grooves/mm. The scanning range

was from 31000 to 11000 cm^{-1} with a reproducibility of ± 0.3 cm^{-1} and a linear dispersion of 10 cm^{-1}/mm at 514.5 nm. The stated resolution was 0.14 cm^{-1} at 579.0 nm with slit settings of 6/100/100/6 microns. Typical slitwidths for most spectra recorded here ranged between 20 μm and 150 μm. The spectrometer was operated in a stepping rather than a continuous scanning mode under the control of an Apple IIe microcomputer. Photoelectric detection of the signal used an RCA C31034 photomultiplier tube thermoelectrically cooled to -25°C. Numerical data from the photon counter were collected and stored by the microcomputer before being displayed on a digital plotter.

Fluorescence from the $^1D_2$ to the $^3F_{2,3,4}$ levels, in the region from 11600 cm^{-1} to 9000 cm^{-1}, was analysed by the Spex single monochromator equipped with an RCA 7102 photomultiplier tube cooled to -100°C in a PAR Model TE-176-RF liquid nitrogen refrigeration chamber. Photomultiplier tube signal was recorded with a Keithley 610B electrometer connected to a strip chart recorder. A Corning glass CS2-62 filter eliminated radiation from higher orders.

The installation of the birefringent filter to the dye laser allowed excitation spectra to be recorded where the laser frequency is scanned while monitoring fluorescence. The two Spex spectrometers and sample geometry were arranged so that emission could be detected simultaneously with both spectrometers. A single site excitation spectrum could be recorded by having either spectrometer stationary at the frequency of a particular fluorescence transition of that site. Alternatively all fluorescing levels for all sites could be detected by recording an excitation spectrum with the single monochromator tuned to monitor the direct zero order reflection. In these experiments the photomultiplier tube output from both spectrometers

was recorded using a Keithley 610B electrometer connected to a strip chart recorder. In most cases the dye laser was operated in light mode to maintain a constant power output and equalize the relative excitation efficiencies.

In the various polarisation measurements recorded, a Spectra Physics 310 polarisation rotator determined the linear polarisation direction of the dye laser while a conventional polaroid sheet was employed as an analyser in the visible region. For the infrared emission studies, infrared HRB polaroid sheet was used to analyse the fluorescence. Both spectrometers were equipped with Hanle quartz wedge polarisation scramblers to equalize the gratings' different spectral response with polarisation direction.

III.3 Time Domain Spectroscopy

Fluorescent lifetimes of transitions from the $^1D_2$ and $^3P_0$ excited state levels of the Pr^{3+} ion centres, were measured using a Photochemical Research Associates Model LN107 dye laser pumped by a PRA LN1000 pulsed nitrogen laser. The nitrogen laser has a wavelength of 337.1 nm, is of a single pass design and provides a 1 mJ laser pulse of width 600 ps (FWHM) at a maximum repetition rate of 20 Hz. The dye laser included an amplifier stage bringing its output up to 100 μJ for the more efficient dyes. Using a selection of dyes the spectral range of the dye laser output extended from 360 to 980 nm with a bandwidth of typically 0.04 nm. Wavelength selection was by way of the laser cavity end mirror rotating under stepper motor control to change the angle of incidence to a diffraction grating. Rhodamine 590 and Coumarin 481 dyes were appropriate for excitation to the $^1D_2$ and $^3P_0$ levels of the Pr^{3+} ion respectively.

The emission was analysed by the Spex single monochromator

equipped with an RCA C31034 photomultiplier tube thermoelectrically cooled to -25°C. This photomultiplier tube has a stated risetime of 7 ns which was sufficiently fast for the range of lifetimes measured. For some of the earlier measurements the anode terminal of the PMT was directly connected to the input of a low gain preamplifier that was supplied by the Chemistry Department of the University of Canterbury. More recently an ORTEC model 574 timing amplifier was purchased to replace this preamp. The 574 amplifier consists of four independent stages each having a nominal gain of 4.5 in a 50 Ω system and a rise time of typically 1.2 ns. Within the linear output range, the stages could be cascaded to provide a maximum gain of about 400. Signal output from either amplifier was analysed by a Stanford Research Systems (SRS) Model SR250 boxcar signal averager. The SR250 was controlled by an IBM personal computer running the SRS SR265.EXE data acquisition and control program through a SRS SR245 computer interface module. All the necessary parameters for recording a transient waveform including the boxcar width, delay scale and amount of averaging were specified by the user from the microcomputer.

Various methods were tried to obtain a signal for the boxcar trigger and the subsequent datum collection. A trigger output is available from the nitrogen laser 1 μs before lasing occurs, however this signal was found to be unsatisfactory for two reasons. Firstly, for lifetimes faster than 1 μs the delay was unacceptably long compared to the time base range necessary to give an accurate reproduction of the transient signal. Secondly and more importantly the delay was not constant, varying from 1.0 to 1.4 μs. This effect distorts the waveform as a stationary boxcar would be sampling a different section of the waveform with each laser pulse.

A second option was to trigger the laser and boxcar from an external source, however this was also found to be unsatisfactory as the delay from receipt of the trigger and the laser pulse was

13.2 ± .2 μs. By using a pulse delay generator the problem of a constant delay could be solved but the instability would still remain.

The method developed in these experiments, and found to be very satisfactory, was to obtain a signal from a pyroelectric detector placed in the laser beam exiting from the sample. This arrangement has the advantage of no significant time delay and also that data is only collected if the intensity of the laser pulse is above an acceptable level. In later experiments the detector was placed to directly sample a scattered portion of the nitrogen laser beam. This position for the detector would overcome any problems associated with the poor transmittance of a dark crystal.

Fluorescence spectra from the $^3P_0$ level were recorded for some of the centres using the pulsed laser as the exciting source. For these cases the spectrometer was scanned sufficiently slowly to allow the SR250 boxcar to average 30 samples before directing the output straight to a strip chart recorder.

III.4 Low Temperature Cryostats

All measurements were made on crystals cooled to low temperatures in several cryostats, the details of which are now presented.

Optical absorption spectra were recorded at liquid nitrogen and liquid helium temperatures using an Andonian Associates variable temperature optical dewar. This cryostat is of the cold finger design and attains a sample temperature of 15 K with a liquid helium refrigerant. Further details on the construction and operation of this dewar can be found in Tomblin [1983]. The crystal samples were clamped to a copper block at the base of the cold finger. Indium foil was used extensively to maximise thermal contact. Up to four crystals could be mounted and examined independently in one low temperature run.

The same Andonian dewar was also used for some of the early fluorescence experiments. The crystals were clamped in a vertical plane with the polished flats horizontal to allow the vertical laser beam to traverse the sample. The incident laser beam was reflected from horizontal using a 90^{o} glass prism and focussed on the sample with a 15 cm focal length glass lens. Light collection to the spectrometer used a two lens system that provided a close match to the f-number of the spectrometer. These lenses were mounted on micrometer driven x,y translating stages for precise optical alignment.

More recently a CTI-Cryogenics Model 21C two stage closed cycle helium refrigerator was used for all subsequent fluorescence and some absorption measurements. This refrigerator has a base temperature of 10 K as measured by a silicon diode mounted on the base of the second stage. A heater element was also provided for operation above the normal base temperature. Heater output and temperature readings were controlled by a Palm Beach Cryophysics Inc. Model 4025 Cryogenic Thermometer/Controller.

The cold head of the refrigerator was operated in a horizontal orientation allowing the use of a vertical laser beam. The samples were mounted vertically on a copper block that was attached to the second stage of the refrigerator. Measurements on two thermally populated levels indicated the crystal temperature to be in the range 12-14 K.

CHAPTER IV

OPTICAL SPECTROSCOPY OF ALKALINE-EARTH FLUORIDES CONTAINING PRASEODYMIUM

IV.1 Crystal Field Level Structure and Selection Rules for Pr^{3+} Ions in a Field of C_{4v} Point Group Symmetry

IV.1.1 Crystal Field Level Structure

Before commencing a discussion of the energy levels of the Pr^{3+} ion in a field of C_{4v} point group symmetry it is appropriate to describe the expected ordering of levels and the selection rules for transitions between them.

It was discussed earlier in Chapter II how the electronic energy levels of a rare-earth ion can be labelled by appropriate quantum numbers S,L,J as each interaction of the Hamiltonian is introduced. The energy level scheme for a free ion consists of several distinct $^{2S+1}L_J$ terms, each of degeneracy (2J+1) and having wavefunctions that can be labelled $|SLJJ_z\rangle$. The free ion Hamiltonian is invariant under the operations of the three dimensional rotation group R_3 and the irreducible representations of this group are described by Wigner [1959].

When the ion is placed in a crystal the symmetry is reduced from spherical to the point group appropriate for the ion site. This point group will be a subgroup of R_3 and the new Hamiltonian

$$H = H_{\text{free ion}} + V_{C.F.} \qquad \text{(IV.1.1)}$$

will be invariant under the operations of the point group. It is usual to label the wavefunctions with the particular irreducible

representation having the same transformation properties. For an even electron rare-earth ion such as praseodymium these irreps are $\tau_1,\tau_2,\tau_3,\tau_4$ and τ_5 of the single group. Under the operations of the new point group the R_3 representations are now reducible and a decomposition table of Koster et al [1963] will give the decomposition of the R_3 representations to the irreps of the new group.

The free ion ground state of Pr^{3+} is the $^3H_4$ term and is chosen as an example to illustrate the decomposition. In the reduction from R_3 to the cubic point group O, the decomposition table shows that the free ion irrep $D_4^{\pm}$ decomposes into 4 cubic irreps, $\Gamma_1,\Gamma_3,\Gamma_4$ and Γ_5. There will be four distinct eigenvalues and some degree of degeneracy will remain amongst the nine cubic field wavefunctions that now consist of linear combinations of the original $|SLJJ_z\rangle$ basis states. These linear combinations are obtained by diagonalising the crystal field matrix. Assignment of the appropriate combination of $|SLJJ_z\rangle$ basis states to a particular cubic irrep is achieved using the point group character table and the operations of the point group. The character of a particular irrep with respect to a point group operation is the trace of the matrix describing the transformation properties of the wavefunction under that operation.

Table IV.1.1 gives the cubic field wavefunctions, as linear combinations of $|JJ_z\rangle$ basis states, and calculated energies for the crystal field levels of the $^3H_4$ multiplet.

Table IV.1.1

Cubic crystal field wavefunctions, in $|JJ_z\rangle$ basis states and energies for the levels of the $^3H_4$ multiplet.

Cubic Wavefunction	Energy	Cubic Irrep
$\sqrt{\frac{1}{2}}\{\|42\rangle+\|4\text{-}2\rangle\}$	$48\ b_4 + 256\ b_6$	Γ_3
$\sqrt{\frac{7}{24}}\|44\rangle - \sqrt{\frac{10}{24}}\|40\rangle + \sqrt{\frac{7}{24}}\|4\text{-}4\rangle$	$48\ b_4 + 256\ b_6$	Γ_3
$\sqrt{\frac{1}{2}}\{\|42\rangle - \|4\text{-}2\rangle\}$	$-312\ b_4 - 80\ b_6$	Γ_5
$\sqrt{\frac{7}{8}}\{\|4\pm3\rangle - \sqrt{\frac{1}{8}}\|4\mp1\rangle$	$-312\ b_4 - 80\ b_6$	Γ_5
$\sqrt{\frac{1}{8}}\{\|4\pm3\rangle + \sqrt{\frac{7}{8}}\|4\mp1\rangle$	$168\ b_4 + 16\ b_6$	Γ_4
$\sqrt{\frac{1}{2}}\{\|44\rangle - \|4\text{-}4\rangle\}$	$168\ b_4 + 16\ b_6$	Γ_4
$\sqrt{\frac{5}{24}}\|44\rangle + \sqrt{\frac{14}{24}}\|40\rangle + \sqrt{\frac{5}{24}}\|4\text{-}4\rangle$	$336\ b_4 - 320\ b_6$	Γ_1

The b_4 and b_6 are crystal field parameters related to the more usual parameters B_c^4 and B_c^6 by

$$b_4 = \frac{-1}{2.3^2.11^2} B_c^4 \qquad b_6 = \frac{17}{3^2.11^2.13} B_c^6$$

The degeneracies group the $|JJ_z\rangle$ wavefunctions into their irreps and can aid in the identification in some cases. The Γ_1 irrep is the only non-degenerate irrep and can be identified with the $|JJ_z\rangle$ wavefunction of

$$\sqrt{\frac{5}{24}}\ |44\rangle + \sqrt{\frac{14}{24}}\ |40\rangle + \sqrt{\frac{5}{24}}\ |4\text{-}4\rangle$$

In a similar way the Γ_3 irrep is identified with the

$$\sqrt{\frac{1}{2}}\ \{|42\rangle + |4\text{-}2\rangle\}$$

$$\sqrt{\frac{7}{24}}\ |44\rangle - \sqrt{\frac{10}{24}}\ |40\rangle + \sqrt{\frac{7}{24}}\ |4\text{-}4\rangle$$

$|JJ_z\rangle$ wavefunctions as the only doubly degenerate level present. It only remains to discriminate between the two triply degenerate levels of the Γ_4 and Γ_5 irreps. The character table of the cubic point group shows a C_4 group operation will distinguish these two irreps. After manipulation of the appropriate coordinates the assignments in Table IV.1.1 are obtained. Once an assignment to an eigenvalue is complete the diagrams of Lea, Leask and Wolf [1962] can be consulted to estimate relative energy splittings and obtain initial estimates for the crystal field parameters.

The reduction from cubic to axial symmetry follows a similar path to the decomposition $R_3 \longrightarrow 0$. Under the operations of the new point group, C_{4v}, the cubic representations reduce to the C_{4v} irreps given by the decomposition table $O_h \longrightarrow C_{4v}$. Similar methods using the point group operations are used to identify the C_{4v} irreps. Table IV.1.2 summarises the wavefunction assignment to a cubic irrep Γ_a and C_{4v} irrep γ_b for the levels of the $^3H_4$ multiplet. The first order axial splittings are also given.

As there are now different energy levels with the same C_{4v} symmetry, there will be crystal field mixing between these levels and new linear combinations of $|JJ_z\rangle$ states would need to be constructed for a diagonal basis. The cubic wavefunctions are retained as the first order C_{4v} wavefunctions, as are the irrep labels, as they indicate the cubic parentage of the C_{4v} wavefunctions.

Table IV.1.2

First order C_{4v} crystal field wavefunctions as $|JJ_z\rangle$ states assigned to parent cubic Γ_a and C_{4v} γ_b irreps.

$\Gamma_a\gamma_b$	First Order Wavefunction	First Order Energy
$\Gamma_3\gamma_3$	$\sqrt{\frac{1}{2}}\left\{\|42\rangle + \|4\text{-}2\rangle\right\}$	$48b_4 + 256b_6 - 8b_2^0 - 132b_4^0 + 88b_6^0$
$\Gamma_3\gamma_1$	$\sqrt{\frac{7}{24}}\|44\rangle - \sqrt{\frac{10}{24}}\|40\rangle + \sqrt{\frac{7}{24}}\|4\text{-}4\rangle$	$48b_4 + 256b_6 + 8b_2^0 + 188b_4^0 - 24b_6^0$
$\Gamma_4\gamma_5$	$\sqrt{\frac{1}{8}}\|4\pm3\rangle + \sqrt{\frac{7}{8}}\|4\mp1\rangle$	$168b_4 + 16b_6 - 14b_2^0 + 63b_4^0 - 5b_6^0$
$\Gamma_4\gamma_2$	$\sqrt{\frac{1}{2}}\left\{\|44\rangle - \|4\text{-}4\rangle\right\}$	$168b_4 + 16b_6 + 28b_2^0 + 168b_4^0 + 16b_6^0$
$\Gamma_1\gamma_1$	$\sqrt{\frac{5}{24}}\|44\rangle + \sqrt{\frac{14}{24}}\|40\rangle + \sqrt{\frac{5}{24}}\|4\text{-}4\rangle$	$336b_4 - 320b_6 + 196b_4^0 - 40b_6^0$
$\Gamma_5\gamma_4$	$\sqrt{\frac{1}{2}}\left\{\|42\rangle - \|4\text{-}2\rangle\right\}$	$-312b_4 - 80b_6 - 8b_2^0 - 132b_4^0 + 88b_6^0$
$\Gamma_5\gamma_5$	$\sqrt{\frac{7}{8}}\|4\pm3\rangle - \sqrt{\frac{1}{8}}\|4\mp1\rangle$	$-312b_4 - 80b_6 + 4b_2^0 - 207b_4^0 - 59b_6^0$

New crystal field parameters are related to the more usual parameters by

$$b_2^0 = \frac{-2.13}{3^2.5^2.11} B_0^2 \qquad b_4^0 = \frac{-1}{2.3^2.11^2} B_0^4 \qquad b_6^0 = \frac{17}{3^2.11^2.13} B_0^6$$

The same methods of constructing the $|JJ_z\rangle$ wavefunctions and determining their symmetry can be used for the other J multiplets of the ion. For the multiplets with J larger than 4, some irreps of O appear more than once in the $R_3 \longrightarrow O$ decomposition and cubic crystal field mixing occurs at this stage. The linear combinations of $|JJ_z\rangle$ states for these repeating irreps are not unique and depend upon the relative strengths of the 4th and 6th degree components of the cubic crystal field. The desired linear combination for a particular 4th to 6th degree ratio can be obtained from the tables of Lea, Leask and Wolf [1962].

An alternative method to the use of point group operations as described above in determining the symmetry of the $|JJ_z\rangle$ wavefunctions, is to consult the tables of Butler [1981]. In these tables the 2J+1 wavefunctions of a J multiplet are given a set of labels, one label for each of the point groups in the chosen branching chain, and related to the linear combination of spherical harmonics $Y_J^m(\theta,\phi)$ appropriate for that wavefunction. By relating each $|JJ_z\rangle$ wavefunction to the appropriate linear combination of spherical harmonics the set of labels for that wavefunction can be obtained from the tables. Examination of the character tables for the point groups of the branching chain gives the conversion of the new labels to the more traditional Γ labels and identifies the symmetry of that $|JJ_z\rangle$ linear combination under the point group.

Figure IV.1.1 shows an initial estimate of the C_{4v} crystal field splittings for some multiplets of the Pr^{3+} ion. Once level symmetries have been established selection rules for the transitions can be calculated.

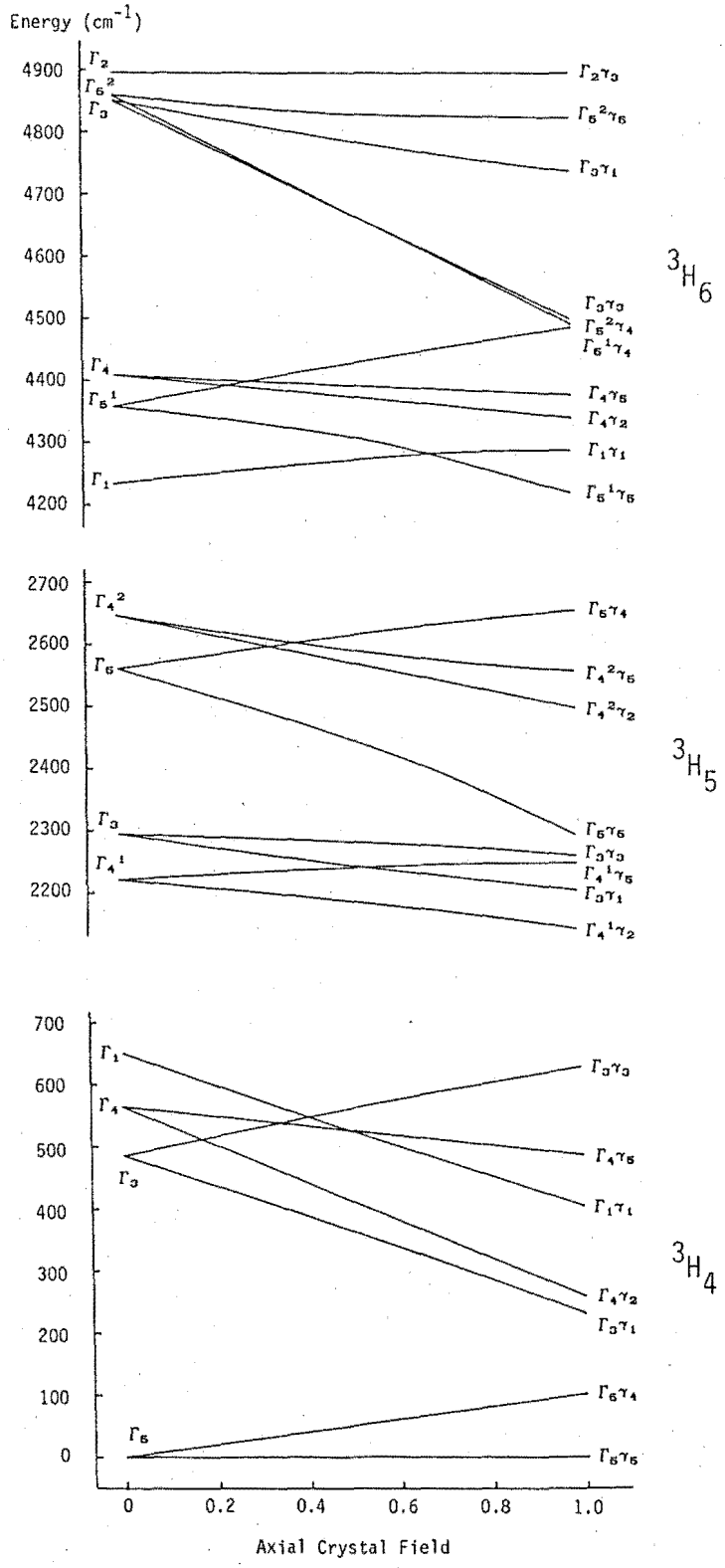

Figure IV.1.1(a) Predicted energy level scheme of the Pr^{3+} ion for the 33 states of the ^3H multiplets for a crystal field increasing from cubic to the full axial value.

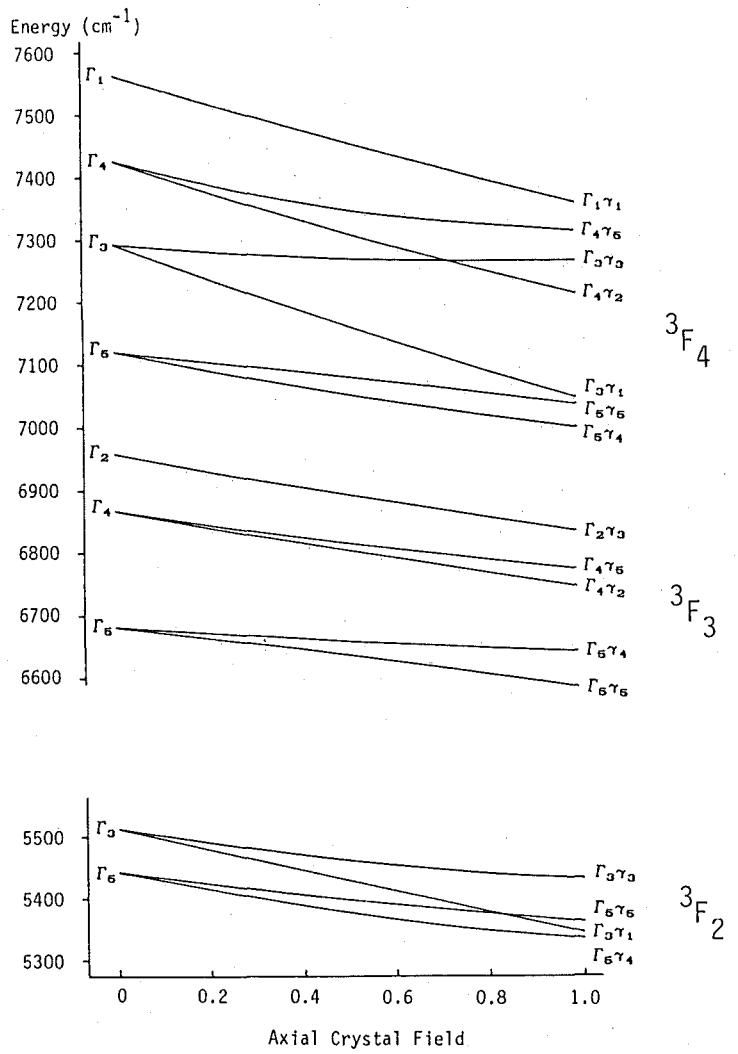

Figure IV.1.1(b) Predicted energy level scheme of the Pr^{3+} ion for the 21 states of the ^3F multiplets for a crystal field increasing from cubic to the full axial value.

IV.1.2 Transition Selection Rules

Electronic transitions can have electric-dipole, magnetic-dipole or electric-quadrupole character or may have contributions from more than one mode. Electric dipole transitions require a change in parity between initial and final states and are therefore forbidden between $4f^n$ states. However if the ion resides in a non-centrosymmetric static or in a dynamic crystal field, odd harmonics in the expansion of the crystal potential can introduce a small admixture of opposite parity states from a higher configuration into $4f^n$ thereby making electric dipole transitions allowed. Selection rules for electric dipole transitions include

$$\Delta\ell = \pm 1, \quad \Delta S = 0 \quad |\Delta L|, \quad |\Delta J| \leq 2\ell$$

In pure LS coupling magnetic dipole transitions are restricted by the selection rules

$$\Delta J \leq 1, \quad \Delta L = 0, \quad \Delta S = 0, \quad \Delta\ell = 0$$

and are allowed within states of an f^n configuration. Thus in absorption magnetic dipole transitions would only be seen from the ground state to the first excited state of the ground multiplet. With the addition of spin orbit coupling the L & S selection rules are relaxed and more transitions will be possible.

The majority of electronic transitions observed between $4f^n$ states of a rare-earth ion are of an electric-dipole character. For Pr^{3+} the spin selection rule forbids the absorption transitions from $^3H_4$ to $^1D_2$ and intensity for these transitions depends upon the J mixing of the triplet states $^3P_2$ and $^3F_2$ with $^1D_2$. The necessity of some admixing

process is reflected in the weak intensities observed for these transitions.

The x,y and z components of the electric dipole operator, $e \sum_i \underset{\sim}{r}_i$, transform as the components of the displacement vector under the operations of a point group. Examination of the bases for irreps in the character table of C_{4v} point group symmetry show that the components of the electric dipole operator transform as either the $\gamma_5(x,y)$ or the $\gamma_1(z)$ irreps for this group. Similarly the components for the magnetic dipole operator transform either as the $\gamma_5(S_x,S_y)$ or the $\gamma_2(S_z)$ irreps. A non-vanishing transition probability between initial and final states requires that

$$\Gamma_i \times \Gamma_{\substack{\text{dipole} \\ \text{operator}}} = \Gamma_f$$

with the rules obtainable from the C_{4v} multiplication table.

Optical absorption results, show the $^1D_2(D_1)$ and $^1D_2(D_2)$ levels of the Pr^{3+} ion in the C_{4v} F^- site of $SrF_2{:}Pr^{3+}$ to be separated by 19 cm^{-1}. A crystal field calculation shows these two levels have wavefunctions transforming as the $\Gamma_3\gamma_1$ and $\Gamma_3\gamma_3$ irreps but a definite assignment of level to irrep cannot be made. Assuming an emitting level transforming as the γ_1 irrep, electric dipole transitions will be observable from this level to terminating levels transforming as either γ_1 or γ_5 irreps. Magnetic dipole transitions would terminate on levels transforming as either γ_2 or γ_5 irreps. In the situation of the emitting level having γ_3 symmetry the terminating levels will transform as γ_3 or γ_5 irreps for electric dipole transitions and γ_4 or γ_5 irreps for magnetic dipole transitions. It readily becomes apparent that for each site, transitions to a considerable number of levels of a multiplet will not be observed and care must be taken in

the assignment of an energy level scheme. Polarisation can help with the assignment of level symmetries, however gaps in the energy level scheme will continue to exist.

IV.1.3 Polarisation Ratios

At first appearance no polarisation effects would be expected for the C_{4v} sites in CaF_2:RE^{3+} type crystals because of the three possible orientations of the principal C_4 axis of symmetry. However, due to the well defined selection rules for the transitions, some of the orientations are preferentially excited when polarised laser light is incident along a crystal symmetry direction. With plane polarised laser light incident along a [100] axis of the cubic host lattice, the fluorescence observed in a perpendicular direction is found to be well polarised. By understanding the observed intensity ratios such polarisation effects can aid in the identification of the crystal field energy levels.

The electric dipole selection rules for even electron ions, such as Pr^{3+}, in C_{4v} symmetry sites are:

	Γ_1	Γ_2	Γ_3	Γ_4	Γ_5
Γ_1	π				σ
Γ_2		π			σ
Γ_3			π		σ
Γ_4				π	σ
Γ_5	σ	σ	σ	σ	π

Here the polarisation labels σ and π correspond to the $\underset{\sim}{E}$ vector of the light being perpendicular or parallel to the z axis of the C_{4v} site.

The selection rules for magnetic dipole transitions are:

	γ_1	γ_2	γ_3	γ_4	γ_5
γ_1		π'			σ'
γ_2	π'				σ'
γ_3				π'	σ'
γ_4			π'		σ'
γ_5	σ'	σ'	σ'	σ'	π'

The labels σ' and π' now correspond to the $\underset{\sim}{B}$ vector of the light being perpendicular or parallel to the z axis of the C_{4v} site.

A nomenclature for the polarisation geometry is introduced to describe the effects. The polarisation geometry is specified by x(ab)z, where x is the direction of the incident laser beam, z the direction of propagation of the observed fluorescence, a(= y or z) the polarisation plane of the laser light and b(= x or y) the polarisation plane of the observed fluorescence.

For $CaF_2|SrF_2:Pr^{3+}$ crystals, the fourfold rotation (z) axis is defined by the position of the charge compensating ion and can be along the [100], [010] or [001] crystal axes. The polarisation effects arise as the particular Pr^{3+}-charge compensating ion site oriented with its z axis in the direction of laser beam propagation cannot show π-polarised absorption lines, nor can the site with its z axis in the direction of fluorescence propagation have π-polarised lines in emission. The selection rules show the transition from the Pr^{3+} ion ground state of γ_5 symmetry to the lowest $^1D_2$ level, whether it be of γ_1 or γ_3 symmetry, is allowed only in σ-polarisation. Then for laser beam propagation along the [100] axis it is possible to avoid exciting either those Pr^{3+} sites with their z axis along the

[010] axis or those sites with their z axis along the [001] axis by having the laser radiation polarised along [010] or [001] respectively.

With the laser radiation polarised along [010] the two site orientations excited, i.e. those with z axes along [100] and [001] have σ polarised emission and no π type when the fluorescence is analysed in [010]. With the fluorescence analysed in the [100] direction, site orientations with z axes along [001] contribute with σ-polarised transitions while those oriented along [100] contribute π-polarised transitions to the observed emission. By recording fluorescence spectra with the laser polarised [010] and the analyser in [100] and [010] a net polarisation effect is observed.

For the other incident laser light polarisation of [001] no net polarisation effects are observed as the two orientations excited contribute in both σ and π polarisations to the emission for both analyser positions. By examining the selection rules, these polarisation effects can be used to identify upper and lower level symmetries. The expected polarisation ratios for electric dipole transitions are summarised in Table IV.1.3.

Table IV.1.3

Polarisation ratios for electric dipole transitions from the $^1D_2$ multiplet of the Pr^{3+} ion in the cubic CaF_2 type crystals.

Polarisation Geometry	Terminating Level Symmetry	
	τ_a	τ_5
x(yx)z	1	1
x(yy)z	0	2
x(zx)z	1	1
x(zy)z	1	1

$\tau_a = \tau_1$ or τ_3 for an emitting level transforming as a τ_1 or τ_3 irrep respectively.

Magnetic dipole transitions will also show polarisation effects. Because of the orthogonality of the electric and magnetic fields, a polarised magnetic dipole transition will show the inverse of the electric dipole polarisation ratio. This will not be apparent for σ polarised transitions as the much stronger electric dipole transitions have the same selection rules. However, since the selection rules of π polarised transitions are different for the two modes of radiation,magnetic dipole transitions exhibiting these inverse polarisation ratios will be expected.

IV.2 Optical Spectroscopy of Pr^{3+} in SrF_2

IV.2.1 Introduction

Rare-earth ions stabilise in the trivalent state and in alkaline earth fluoride crystals such as SrF_2 they substitute for the divalent Me^{2+} ions. To maintain electrical neutrality of the crystal, some form of charge compensation is required. This is provided by additional F^- ions occupying vacant interstitial sites in the lattice, the position of which may be remote or close to the RE^{3+} ion. The former charge compensation mechanism leads to the RE^{3+} site having cubic symmetry while the symmetry for the latter case will be somewhat lower. Each charge compensation mechanism forms a different spectroscopic site having a unique set of energy levels. By examining these energy levels some insight may be gained on the point group symmetry the RE^{3+} ion resides in, which in turn gives some information on the host lattice.

For rare-earth ions at the beginning of the lanthanide series the dominant site formed in CaF_2 type crystals has a charge compensating F^- ion occupying the immediate neighbouring interstitial site in the

(100) direction and Pr^{3+} is no exception to this rule. The RE^{3+} ion resides in a crystal field of C_{4v} symmetry which can be specified by a relatively simple crystal field Hamiltonian (Chapter II) offering some hope for a successful theoretical analysis.

The C_{4v} F^- site in $SrF_2:Pr^{3+}$ has been identified previously in absorption (Jacobs [1971]) and emission (Syme et al [1984]). Having an f^2 configuration the Pr^{3+} ion has 91 electronic states which reduces to 70 distinct levels in a crystal field of C_{4v} symmetry. An extensive investigation of this site, the results of which are presented in this chapter, has identified the energy and electronic state of 49 of these levels.

IV.2.2 Absorption and Excitation of $SrF_2:Pr^{3+}$

The $^1D_2$ multiplet of the Pr^{3+} ion lies in the spectral range of a rhodamine 6G dye laser making it appropriate to record the absorption spectrum in this region before attempting laser excitation studies. Other multiplets in the optical region of the spectrum are the $^3P_0$, $^3P_1$, $^3P_2$, $^1I_6$ multiplets and the $^1G_4$ multiplet which lies in the 1 μm region. Figures IV.2.1 (a), (b) and (c) show the absorption to the $^3P_0$ and $^3P_1$, $^1D_2$ and $^1G_4$ multiplets respectively for a SrF_2:0.05%Pr^{3+} crystal. The absorption spectra of the $^3P_2$ and $^1I_6$ multiplets consisted of a number of broad features and was not studied further as little information was obtainable. Electric dipole transitions from the $^3H_4$ ground state to the $^1D_2$ levels are spin forbidden making the observed lines somewhat weaker than those for transitions to $^3P_0$.

The absorption transitions of the Pr^{3+} ion in the C_{4v}- F^- ion charge compensated site are indicated in the figures. Jacobs [1971] has previously identified the transitions to the $^3P_0$ and $^3P_1$ multiplets but this is the first identification of the $^1D_2$ and $^1G_4$ levels. Clearly from the $^3P_0$ absorption other absorbing sites are present but, due to time constraints were not studied in this work.

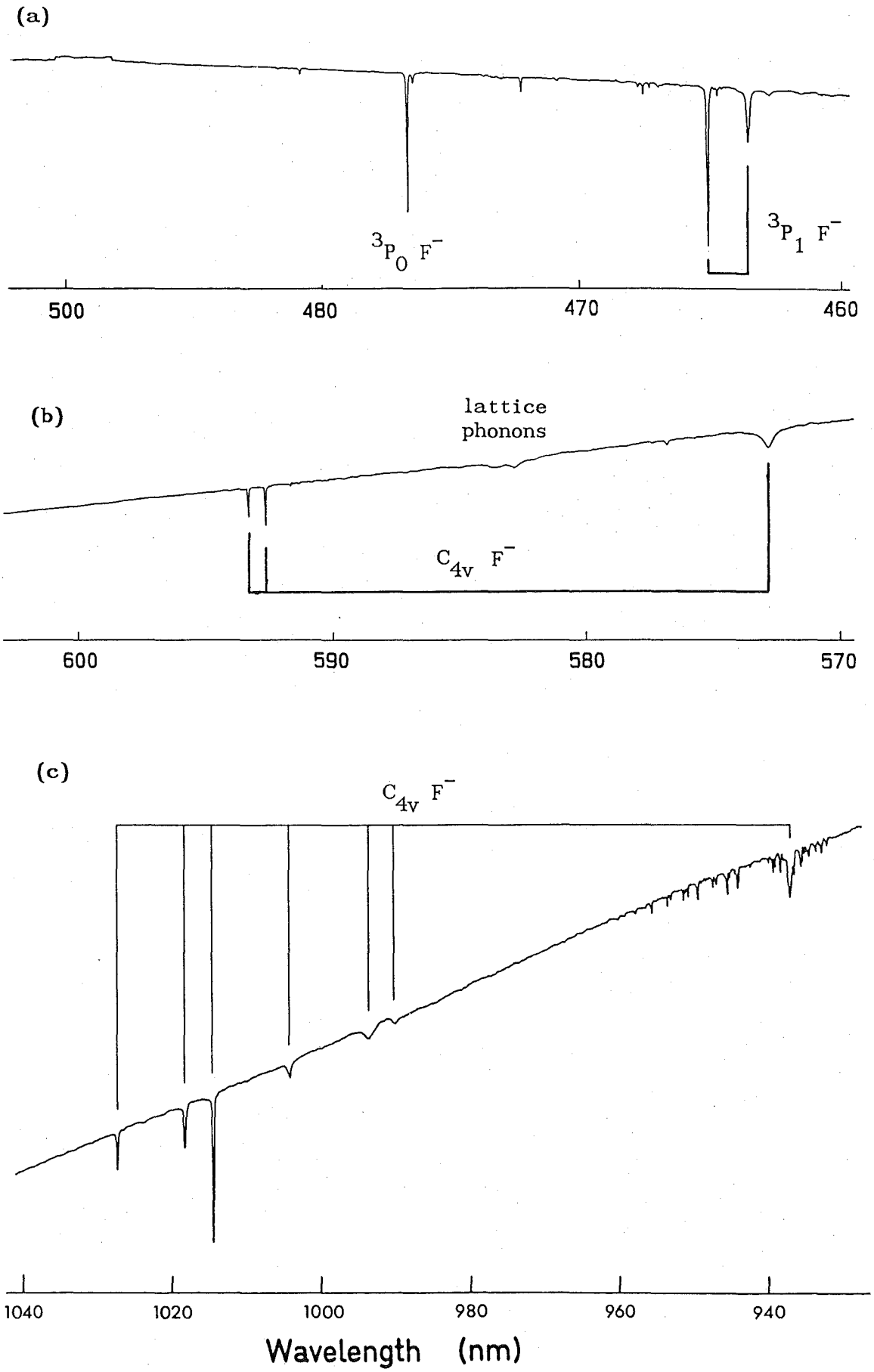

Figure IV.2.1 Optical absorption, recorded at 14K, of transitions to the (a) $^3P_0$ and $^3P_1$, (b) $^1D_2$ and (c) $^1G_4$ multiplets for a SrF_2:0.05% Pr^{3+} crystal.

Absorption transitions to three of the four crystal field levels of the $^1D_2$ multiplet have been identified. Assignment of the broad line at 572.6 nm to the D_4 crystal field level was subsequently confirmed by laser excitation studies. The missing D_3 component is presumably one of the lines in the band of broad features in the region between D_2 and D_4. These features are not particularly well resolved in the absorption spectrum but are more easily defined in the excitation spectrum which will be discussed later.

Six of the seven transitions to the crystal field levels of the $^1G_4$ multiplet appear in the 980-1030 nm region. The seventh was identified at 935.91 nm amidst structure found to be due to the quartz iodine light source. A crystal field calculation subsequently confirmed this large splitting and identified the level at 935.91 nm as the $\Gamma_1\gamma_1$ state of $^1G_4$. The absorption transitions identified for the C_{4v} F^- ion charge compensated site are summarised in Table IV.2.1.

An interesting feature with the results in the table is that the $^3H_4(Z_1) \longrightarrow {}^3P_0$ transition for the C_{4v} F^- site at 476.52 nm is in near coincidence with the blue 476.5 nm line of the argon ion laser (Syme et al [1984]). Furthermore, for the multiple H^- ion $C_s(3)$ centre to be discussed in Chapter VI, the $^3H_4(Z_1) \longrightarrow {}^3P_0$ transition is in near coincidence with the 488.0 nm argon laser line. Through a slight change in frequency due to the isotope shift, this transition for the corresponding $C_s(3)$ centre containing deuterium ions, falls within the profile of the 488.0 nm argon laser line. Figure IV.2.2 shows the $^3P_0$ absorption spectra recorded for these centres as a small amount of the appropriate laser line was simultaneously scattered into the spectrometer. In each of the cases, these coincidences were used to excite the ions of the centre for the recording of their fluorescence spectra. The Pr^{3+} ion in the C_{4v} F^- site is known to exhibit holeburning with hyperfine and superhyperfine structure visible for

some transitions (Macfarlane et al [1981]). In principle such high resolution studies could be achieved by Zeeman sweeping the transitions through a single mode argon ion laser. Using the g-value for $CaF_2:Pr^{3+}$ of 5.44 MHz/G (Macfarlane et al [1984]) a magnetic field of 5 kG would be all that was required to achieve coincidence of the $^3H_4(Z_1) \rightarrow {}^3P_0$ C_{4v} F^- transition and the 476.5 nm argon ion laser line.

Table IV.2.1

Electronic absorption transitions from the ground state to the crystal field levels of the $^3P_1$, $^3P_0$, $^1D_2$ and $^1G_4$ multiplets for the C_{4v} F^- site $SrF_2:0.05\%Pr^{3+}$.

C_{4v} F^- charge compensation site

Crystal Field level		Wavelength of Absorption line (nm)
$^3P_1$	$\Gamma_4\gamma_2$	463.36
	$\Gamma_4\gamma_5$	464.92
$^3P_0$	$\Gamma_1\gamma_1$	476.52
$^1D_2$	$\Gamma_5\gamma_4$	572.56
		592.53
		593.18
$^1G_4$	$\Gamma_1\gamma_1$	935.91
		988.24
		992.47
		1003.24
		1013.49
		1017.30
		1026.34

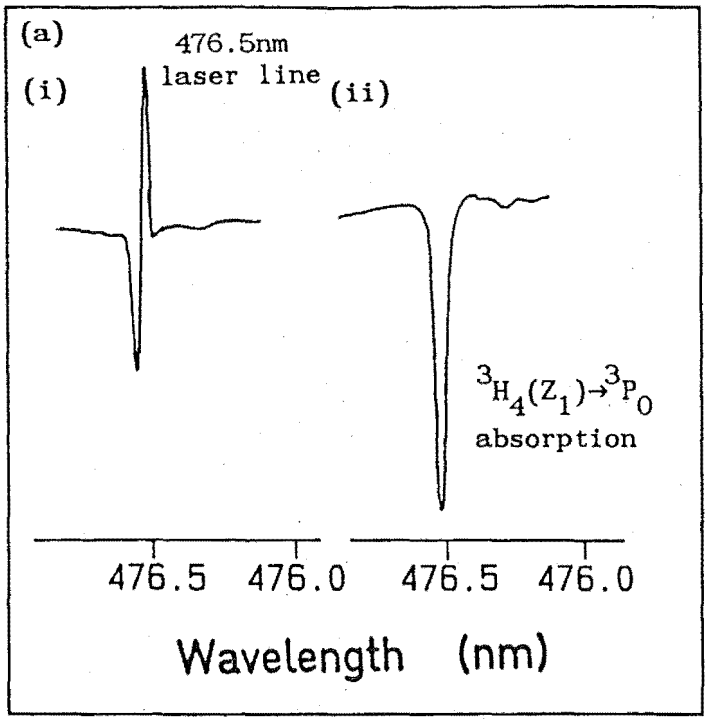

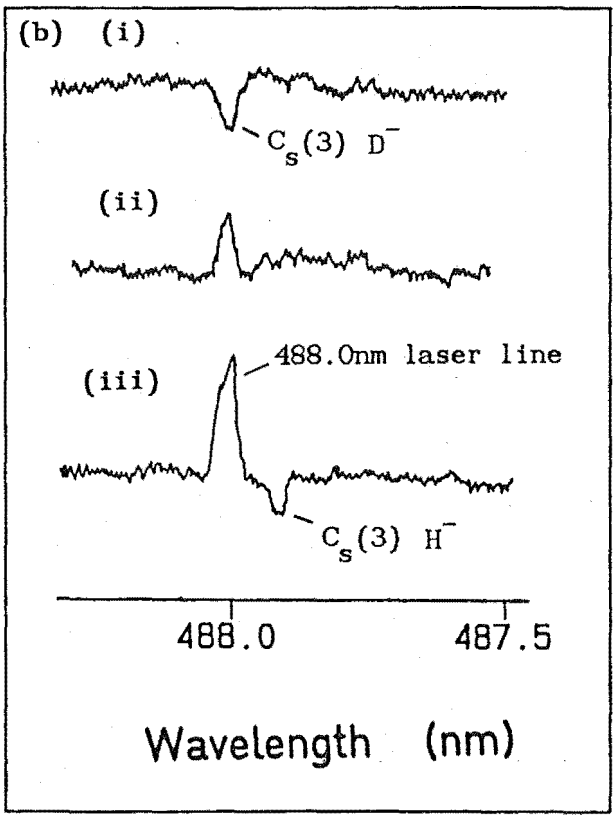

Figure IV.2.2 Transition coincidences with argon ion laser lines in $SrF_2:Pr^{3+}$ crystals (a) Near coincidence of the $^3H_4(Z_1) \rightarrow {}^3P_0$ transition in the C_{4V} F^- site (b) (i) $^3H_4(Z_1) \rightarrow {}^3P_0$ absorption line for the $C_S(3)$ D^- centre, (ii) line profile is coincident with scattered laser light, (iii) the isotope shift for the $C_S(3)$ H^- site removes the centre from coincidence.

Near the end of the period of this work, a 3 plate birefringent filter was obtained for the cw dye laser and installed by the author. With this element installed the laser frequency could be continuously scanned over the spectral range of the dye enabling laser excitation spectra to be recorded. This technique differs from laser fluorescence in that the laser is continuously scanned rather than the spectrometer. The emitted light can be analysed by a spectrometer tuned to a particular transition to record the excitation spectrum of a single site or broad band detection can be used to detect all sites in a similar way to absorption. While having a vastly superior sensitivity compared to absorption, laser excitation records the emitted light and line intensities depend upon the quantum efficiency of the fluorescing species. Thus, a particular absorbing species may be known to exist in large numbers but gives a weak excitation signal if non-radiative processes dominate their decay. This is the situation for the hydrogenic charge compensated sites where, similar numbers of H^- and D^- centres are expected to exist, but the excitation spectrum obtained for the H^- case is considerably degraded compared to the D^- site as the higher local mode frequency induces a greater contribution from non-radiative decay.

Figure IV.2.3 shows the $^1D_2$ excitation spectrum for the C_{4v} F^- site in $SrF_2:Pr^{3+}$. The D_2 and D_4 crystal field levels identified in absorption are indicated. The $Z_1 \rightarrow D_1$ excitation line is not apparent as this was the transition being monitored by the spectrometer. The broad phonon bands that were weakly visible in the absorption spectrum are now seen to comprise a number of distinct lines. Table IV.2.2 lists the frequencies of these features and their energy shifts from the D_1 and D_2 crystal field levels. These lines are transitions to vibronic states originating from lattice phonons coupling to the D_1 and D_2 levels. The richness of this band shows that a large number of

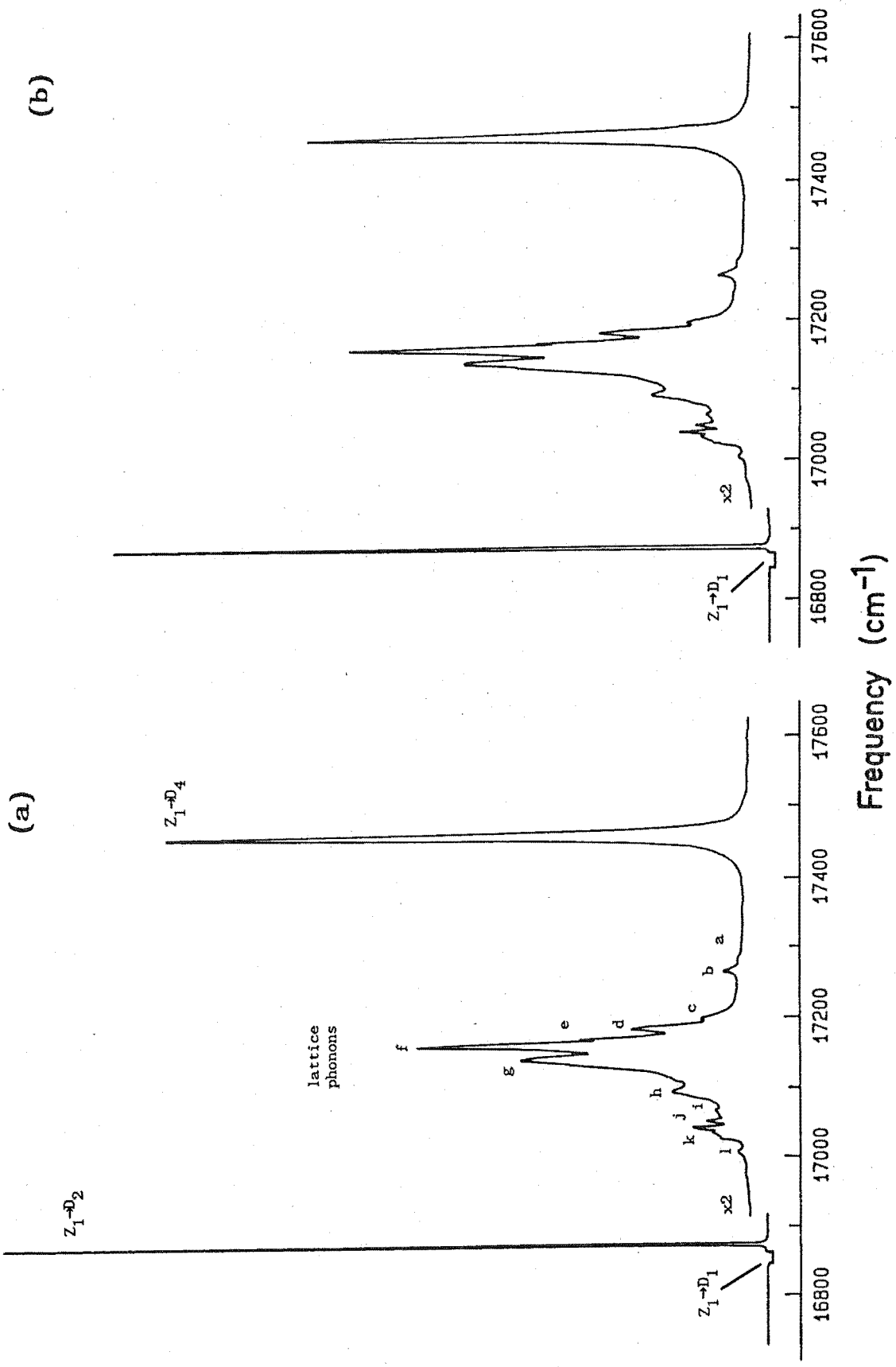

Figure IV.2.3 14K excitation spectrum of $^3H_4 \rightarrow {}^1D_2$ transitions for the C_{4v} site in $SrF_2:Pr^{3+}$ with (a) the spectrometer tuned to exactly match the $D_1 \rightarrow Z_1$ transition and (b) when slightly tuned off this frequency some changes in relative intensities are observed.

phonons exist and the energy of each is given by the interval from the parent electronic line.

Table IV.2.2

Excitation lines identified in the $^1D_2$ region for the C_{4v} F^- charge compensated site in SrF_2:0.05%Pr^{3+}. The zero-phonon electronic transitions of the Pr^{3+} ion identified are the D_1, D_2 and D_4 crystal field levels.

Transition Identification	Line Frequency (±2 cm^{-1})	Energy Shift from	
		$D_1(cm^{-1})$	$D_2(cm^{-1})$
D_4	17459	605	587
a	17276	422	404
b	17259	405	387
c	17193	339	321
d	17176	322	304
e	17164	320	292
f	17154	300	282
g	17135	281	263
h	17087	233	215
i	17058	204	186
j	17044	190	172
k	17035	181	163
l	17001	147	129
D_2	16872	18	0
D_1	16854	0	- 18

The same phonon can couple to both D_1 and D_2 levels to give two vibronic transitions separated by the $D_1 - D_2$ splitting. This is reflected in the equality of some of the entries in the two columns of Table IV.2.2 such as f and g, but some uncertainty will remain as to whether it is the same phonon or one of a slightly different energy.

This doubt would be removed by observing the same band coupled to a different electronic line such as D_4 but this particular region lies beyond the spectral range of the rhodamine dye laser. Presumably this would also identify the D_3 crystal field component as the line of that frequency interval would be absent.

Figure IV.2.3(a) was recorded with the spectrometer tuned to exactly match the $D_1 \longrightarrow Z_1$ transition for the C_{4v} F^- site. The spectrum shown in Figure IV.2.3(b) was recorded after the spectrometer was moved a small increment to lower energy so as to decrease the site emission signal by half. A corresponding increase in the gain restored the two spectra to a similar intensity. A change in the relative intensity between the phonon band and the D_4 crystal field level is apparent. When tuned off the $D_1 \longrightarrow Z_1$ transition, the spectrometer is sampling relatively more of the broad background that is evident in the fluorescence spectra. The changes in Figure IV.2.3(b) indicate the phonon band is relatively more efficient at pumping the background than the D_4 crystal field component. This means the lattice phonons giving rise to the phonon structure are also responsible for the broad background features that are apparent in the fluorescence spectra. It would be expected that the D_3 component would follow the same relative intensity trends as D_4 since they both resonantly excite the Pr^{3+} ion. As no other line shows similar trends to D_4, the D_3 component does not appear to be one of the tabulated transitions.

IV.2.3 Optical Emission of the C_{4v} F^- Site in SrF_2:Pr^{3+}

Fluorescence spectra of emission from the $^1D_2$ and $^3P_0$ multiplets to the crystal field levels of the $^3H_{4,5,6}$ and $^3F_{2,3,4}$ multiplets for the Pr^{3+} ion in the C_{4v} F^- charge compensating ion site were recorded at low temperatures. In most cases a 0.05mol% Pr^{3+} doped crystal was

studied and no evidence of cross relaxation to other distinct centres was observed at this concentration. Selective excitation of the ion to the $^1D_2$ multiplet used a Rhodamine 6G dye laser tuned to match an absorption transition, usually the lowest crystal field component at 16853.7 cm^{-1}. The near coincidence of the $^3H_4(Z_1) \longrightarrow {}^3P_0$ transition at 476.52 nm to the 476.5 nm argon ion laser line, enabled the argon laser to be used as the exciting source of the ion to the $^3P_0$ level. For both emitting levels the exciting laser could be linearly polarised and analysis of the polarised emission aided in the identification of the terminating level symmetries. The crystal field levels of the various multiplets will be described by the labels $\Gamma_\alpha\gamma_\beta$ where the first symmetry label represents the representation label of the wavefunction in the parent O_h crystal field and the second symmetry label is the irrep in the C_{4v} point group. The spectra of emission to each multiplet will now be discussed separately.

The $^3H_4$ multiplet

Figures IV.2.4(a) and (b) show the polarised emission to the levels of the $^3H_4$ multiplet from the $^1D_2$ and $^3P_0$ multiplets respectively. The spectra were recorded at 14 K from a <100> oriented crystal for the two polarisation geometries x(yy)z and x(yx)z. The lines in Fig.IV.2.4(a) are labelled by Z_j corresponding to the transition from the $^1D_2(D_1)$ crystal field level to the $^3H_4(Z_j)$ level. Where the D_2 component is the emitting level this is labelled explicitly. In Fig.IV.2.4(b) of the $^3P_0 \longrightarrow {}^3H_4$ emission there is only one emitting level and the lines are labelled only by their terminating level. The line evident at 16873 cm^{-1} in Figure IV.2.4(a) corresponds to the transition $^1D_2(D_2) \longrightarrow {}^3H_4(Z_1)$ and is at a higher frequency than that of the laser. Its appearance indicates that the fluorescent lifetime of the D_1 level is sufficiently long for a Boltzmann distribution to

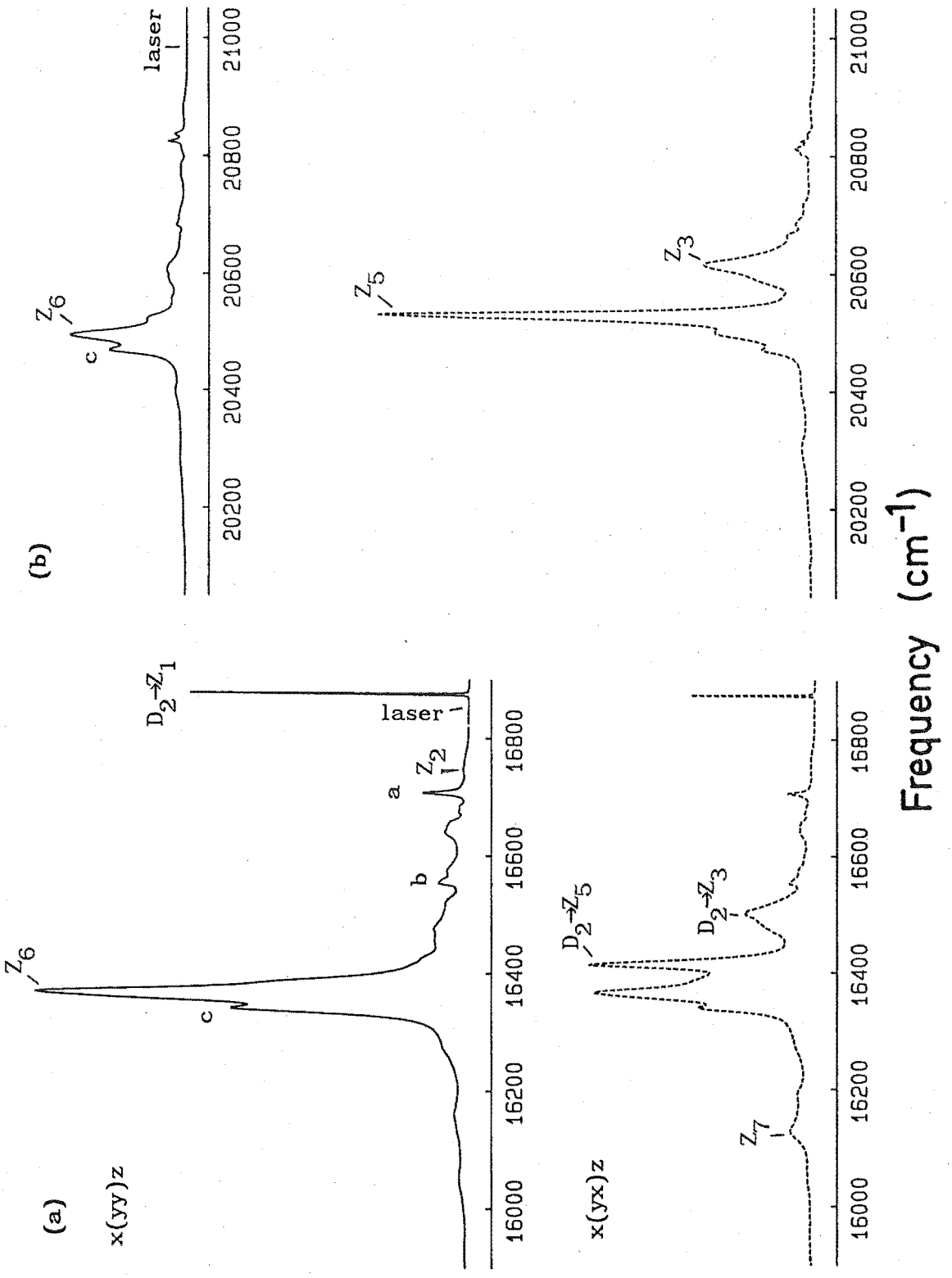

Figure IV.2.4 14K polarised emission to the crystal field levels of the $^3H_4$ multiplet for the C_{4v} F^- site in SrF_2:Pr^{3+} from (a) the $^1D_2$ multiplet and (b) the $^3P_0$ crystal field level.

be established between the D_1 and D_2 levels. This emission line is observed to have σ-polarisation but this does not establish the symmetry of the D_2 level since this polarisation will be common to both $^1D_2(\Gamma_3\gamma_1) \longrightarrow {}^3H_4(\Gamma_5\gamma_5)$ and $^1D_2(\Gamma_3\gamma_3) \longrightarrow {}^3H_4(\Gamma_5\gamma_5)$ transitions.

The dominant feature of Figure IV.2.4(b) is the spectral line at 20520 cm^{-1}, previously observed by Jacobs [1971]. With J = 0 the $^3P_0$ level is singly degenerate and will transform as the γ_1 irrep of the C_{4v} group. The π-polarisation of the line at 20520 cm^{-1} requires that the terminating level transforms as the same irrep, i.e. γ_1. Inspection of the calculated energy scheme for $^3H_4$ (Figure IV.1.1) indicates this level to be the $\Gamma_1\gamma_1$ state. Of particular interest is that a transition to this level is **not** observed from the D_1 level of $^1D_2$. From D_1 this transition would be expected at a frequency of 16394 cm^{-1}, but instead a line is observed at the higher frequency of 16413 cm^{-1}. The 19 cm^{-1} difference shows the observed line at 16413 cm^{-1} originates from the D_2 level and not from D_1. This is confirmed by spectra recorded at higher temperatures showing that the line at 16413 cm^{-1} increases in relative intensity with increasing temperature. The absence of a line at 16394 cm^{-1} indicates the $^1D_2(D_1) \longrightarrow Z_5(\Gamma_3\gamma_1)$ transition is forbidden which identifies the D_1 level to be the $^1D_2(\Gamma_3\gamma_3)$ state. Then the D_2 level must be the $^1D_2(\Gamma_3\gamma_1)$ state and the $D_2 \longrightarrow Z_5(\Gamma_1\gamma_1)$ transition has the expected π-polarisation. A similar situation occurs for the spectral lines at 16501 cm^{-1} in Fig IV.2.4(a) and 20608 cm^{-1} in Fig IV.2.4(b), being transitions from $^1D_2(D_2)$ and $^3P_0$ to $Z_3(\Gamma_3\gamma_1)$ respectively.

In both Fig IV.2.4(a) and (b) the transitions to the $Z_6(\Gamma_4\gamma_5)$ level are observed at a frequency interval of 490 cm^{-1} from the pump transition and have the expected σ-polarisation from both $^1D_2(D_1)$ and $^3P_0$ levels. The origin of the side line labelled c at an interval of 516 cm^{-1} is unexplained at this time. A transition to an electronic

level is not expected in this region with this polarisation. The line is present in spectra from both emitting levels and its character does not change relative to other lines under variable pumping conditions. One possible explanation is a transition to a vibronic line associated with a lattice phonon. It will be shown later that the Z_2 crystal field level, which is the $^3H_4(\Gamma_5\gamma_4)$ state, has an energy of 108 cm^{-1} above the ground state. The energy interval from this Z_2 level at 108 cm^{-1} and the level at 516 cm^{-1} is 408 cm^{-1}. A lattice phonon close to this energy was identified in the excitation spectrum. (Table IV.2.2.)

The transition to the $Z_7(\Gamma_3\gamma_3)$ level will be π-polarised from $^1D_2(\Gamma_3\gamma_3)$ but will be forbidden from $^3P_0(\Gamma_1\gamma_1)$. A line present in the $^1D_2 \longrightarrow {}^3H_4$ spectrum in the expected region and fitting this polarisation requirement is observed at 16128 cm^{-1}.

Inspection of the C_{4v} point group multiplication table reveals that the $Z_2(\Gamma_5\gamma_4)$ level cannot be reached from either the $^1D_2$ or $^3P_0$ emitting levels by an electric dipole transition. However under the C_{4v} group operations

$$\gamma_3 \times \gamma_2 = \gamma_4$$

and the z component of the magnetic dipole radiation field, transforming as the γ_2 irrep, will provide a non-vanishing transition probability between the $^1D_2(\Gamma_3\gamma_3)$ and $Z_2(\Gamma_5\gamma_4)$ states. Emission through this component of the magnetic dipole field will be π-polarised corresponding to the magnetic field $\underset{\sim}{B}$ being parallel to the z axis of the C_{4v} site. However, the polarisation ratio will be opposite to the electric dipole transitions from the orthogonality of the magnetic and electric field vectors, i.e. the x(yy)z:x(yx)z polarisation ratio will be 1:0 rather than 0:1 which is observed for a π-polarised electric dipole transition. In the $^1D_2 \longrightarrow {}^3H_4$ emission

spectrum a weak line in the expected region having the required polarisation dependence is observed at 16746 cm^{-1}.

The remaining $^3H_4$ level to be assigned is the $Z_4(\Gamma_4\gamma_2)$ state. Transitions will be allowed to this level from $^3P_0(\Gamma_1\gamma_1)$ and $^1D_2(\Gamma_3\gamma_1)$ by magnetic dipole radiation but are expected to be weak. Due to the number of broad phonon related features in the same region of the spectrum the energy of this level remains unassigned at this time.

The two lines labelled a and b in Fig IV.2.4(a) appear to correspond to vibronic transitions associated with a 149 cm^{-1} lattice phonon and its 302 cm^{-1} second harmonic respectively. Similar lines have been observed in the C_{4v} hydrogenic sites in $SrF_2:Pr^{3+}$ crystals at a slightly different frequency. These lines show a polarisation dependence and so must have some well defined symmetry properties in these sites.

Table IV.2.3 summarises the transitions observed to the crystal field levels of the $^3H_4$ multiplet and the energy level scheme.

The $^3H_5$ Multiplet

Figures IV.2.5(a) and (b) show the polarised emission spectra of transitions to the crystal field levels of the $^3H_5$ multiplet from the $^1D_2$ and $^3P_0$ levels respectively. The transitions are labelled using the labels Y_i appropriate for $^3H_5$ as the second to lowest multiplet. Using similar arguments to those detailed in the previous section to identify the level symmetries, the energy level scheme for $^3H_5$ can be established. Table IV.2.4 summarises those transitions observed and gives the energy level scheme for this multiplet.

Interesting points to note include a magnetic dipole transition to the $Y_1(\Gamma_4^{(1)}\gamma_2)$ level from the γ_1 symmetry levels of the $^3P_0$ and $^1D_2$ multiplets, and the existence of the transition to $Y_4(\Gamma_3\gamma_3)$ from $^1D_2(\Gamma_3\gamma_3)$ but not from $^3P_0$. These two points further support the assignment of the lowest crystal field component of $^1D_2$ as the

Table IV.2.3

Spectral data for the crystal field levels of the $^3H_4$ multiplet for the C_{4v} F^- site in $SrF_2:Pr^{3+}$.

Transition	Frequency ($\pm$ 1 cm^{-1})	Polarisation Observed	Predicted
$D_2(\Gamma_3\gamma_1) \longrightarrow Z_1(\Gamma_5\gamma_5)$	16872.1 $\pm$ 0.1	σ	σ
$D_1(\Gamma_3\gamma_3) \longrightarrow Z_1(\Gamma_5\gamma_5)$	16853.7 $\pm$ 0.1	σ	σ
$D_1 \longrightarrow Z_2(\Gamma_5\gamma_4)$	16746	π'(md) [1]	π'(md)
$D_2 \longrightarrow Z_3(\Gamma_3\gamma_1)$	16499	π	π
$D_2 \longrightarrow Z_5(\Gamma_1\gamma_1)$	16411	π	π
$D_1 \longrightarrow Z_6(\Gamma_4\gamma_5)$	16364	σ	σ
$D_1 \longrightarrow Z_7(\Gamma_3\gamma_3)$	16128	π	π
$^3P_0(\Gamma_1\gamma_1) \longrightarrow Z_1(\Gamma_5\gamma_5)$	20980	σ	σ
$\longrightarrow Z_3(\Gamma_3\gamma_1)$	20608	π	π
$\longrightarrow Z_5(\Gamma_1\gamma_1)$	20520	π	π
$\longrightarrow Z_6(\Gamma_4\gamma_5)$	20491	σ	σ

$^3H_4$ Energy Levels ($\pm$ 1cm^{-1})

$Z_1(\Gamma_5\gamma_5)$	0
$Z_2(\Gamma_5\gamma_4)$	108
$Z_3(\Gamma_3\gamma_1)$	373 $\pm$ 2
$Z_4(\Gamma_4\gamma_2)$	-
$Z_5(\Gamma_1\gamma_1)$	461
$Z_6(\Gamma_4\gamma_5)$	490
$Z_7(\Gamma_3\gamma_3)$	726 $\pm$ 2

[1] (yy):(yx) polarisation ratio of 1:0 associated with a π-polarised magnetic dipole transition.

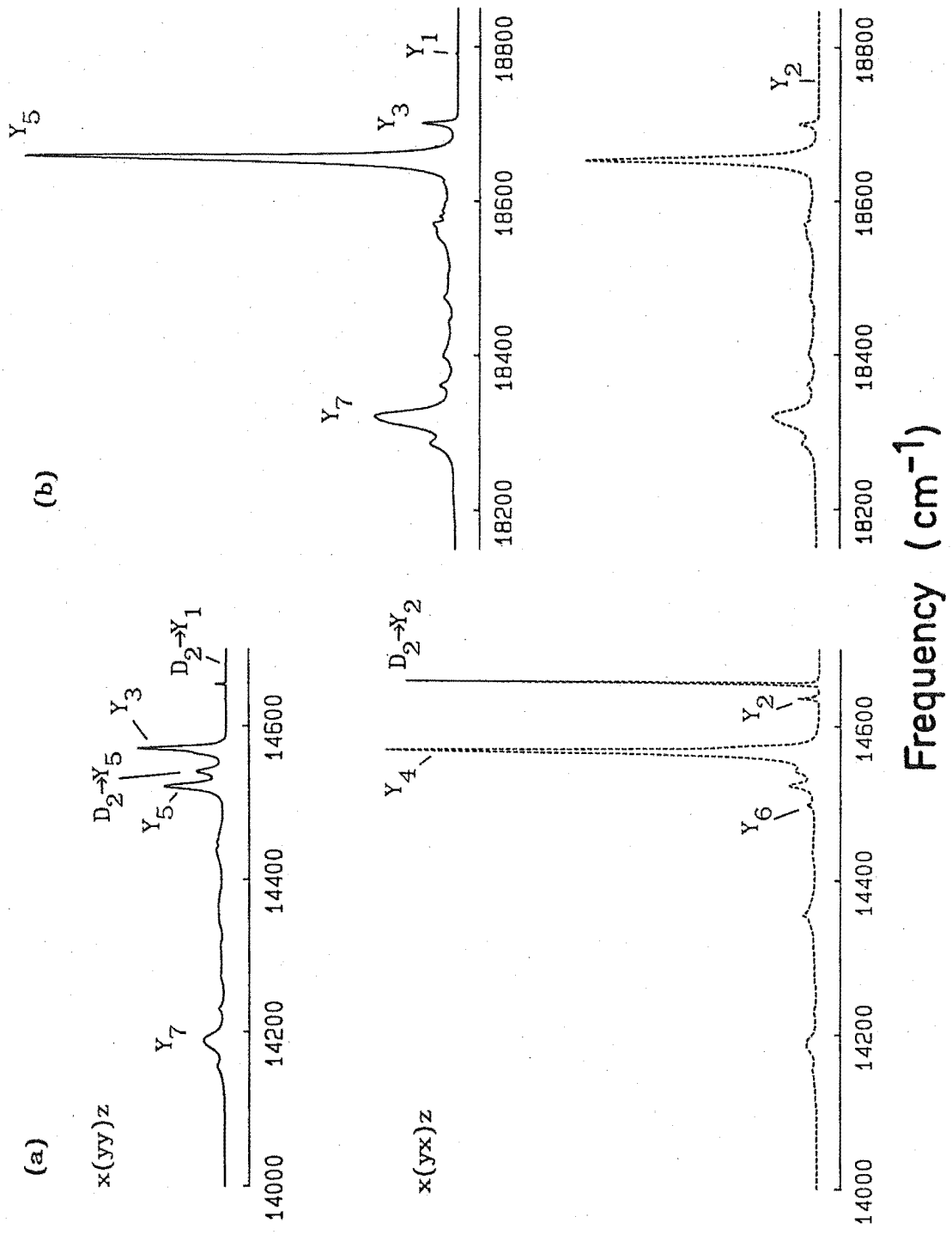

Figure IV.2.5 14K polarised emission to the crystal field levels of the $^3H_5$ multiplet for the C_{4v} F^- site in SrF_2:Pr^{3+} from (a) the $^1D_2$ and (b) the $^3P_0$ multiplets.

Table IV.2.4

Spectral data for the crystal field levels of the $^3H_5$ multiplet for the C_{4v} F^- site in $SrF_2:Pr^{3+}$.

Transition	Frequency ($\pm$ 1 cm^{-1})	Polarisation Observed	Predicted
$D_2(\Gamma_3\gamma_1) \longrightarrow Y_1(\Gamma_4{}^1\gamma_2)$	14678	π'(md) [1]	π'(md)
$D_2 \longrightarrow Y_2(\Gamma_3\gamma_1)$	14652	π	π
$D_1(\Gamma_3\gamma_3) \longrightarrow Y_2(\Gamma_3\gamma_1)$	14633	π	– [2]
$D_1 \longrightarrow Y_3(\Gamma_4{}^1\gamma_5)$	14569	σ	σ
$D_1 \longrightarrow Y_4(\Gamma_3\gamma_3)$	14562	π	π
$D_2 \longrightarrow Y_5(\Gamma_4{}^2\gamma_5)$	14539	σ	σ
$D_1 \longrightarrow Y_5(\Gamma_4{}^1\gamma_5)$	14520	σ	σ
$D_1 \longrightarrow Y_6(\Gamma_4{}^2\gamma_2)$	14497	π	π'(md) [3]
$D_1 \longrightarrow Y_7(\Gamma_5\gamma_5)$	14186	π	π
$^3P_0(\Gamma_1\gamma_1) \longrightarrow Y_1(\Gamma_4{}^1\gamma_2)$	18785	π'(md) [1]	π'(md)
$^3P_0 \longrightarrow Y_2(\Gamma_3\gamma_1)$	18759	π	π
$\longrightarrow Y_3(\Gamma_4{}^1\gamma_5)$	18695	σ	σ
$\longrightarrow Y_5(\Gamma_4{}^2\gamma_5)$	18647	σ	σ
$\longrightarrow Y_7(\Gamma_5\gamma_5)$	18315	σ	σ

$^3H_5$ Energy Levels ($\pm$ 1cm^{-1})

$Y_1(\Gamma_4{}^1\gamma_2)$	: 2195
$Y_2(\Gamma_3\gamma_1)$	: 2221
$Y_3(\Gamma_4{}^1\gamma_5)$	: 2285
$Y_4(\Gamma_3\gamma_3)$	: 2292
$Y_5(\Gamma_4{}^2\gamma_5)$	: 2334
$Y_6(\Gamma_4{}^2\gamma_2)$	: 2359 [3]
$Y_7(\Gamma_5\gamma_5)$	: 2668 $\pm$ 2
$Y_8(\Gamma_5\gamma_4)$	: –

[1] (yy):(yx) polarisation ratio of 1:0 associated with a π-polarised magnetic dipole transition.

[2] Transition forbidden by electric and magnetic dipole radiation.

[3] Tentative assignment.

$^1D_2(\Gamma_3\gamma_3)$ state.

The observed transitions to the $Y_2(\Gamma_3\gamma_1)$ crystal field level deserve some comment. For emission from the $^1D_2$ multiplet the transition probabilities must be very high as the line from the thermally populated $D_2(\Gamma_3\gamma_1)$ level is strong and there is some breakthrough of the forbidden $D_1(\Gamma_3\gamma_3) \longrightarrow Y_2(\Gamma_3\gamma_1)$ line. Conversely a π-polarised electric dipole transition is allowed from $^3P_0(\Gamma_1\gamma_1)$ but is barely visible on the intensity scale used in Fig.IV.2.5. A calculation of transition probabilities may provide some insight into the reasons for this discrepancy.

A tentative assignment has been made for the $Y_6(\Gamma_4{}^{(2)}\gamma_2)$ level based on a magnetic dipole transition observed in the $^3P_0 \longrightarrow {}^3H_5$ spectrum. Other similarly weak lines are observed in this region but do not have the polarisation expected for this transition.

A prominant feature in the emission spectrum from $^1D_2$ for some crystals, and observed in Figure IV.2.5(a) at 14353 cm^{-1}, can be assigned to the $(^5D_0)^1\Gamma_{1g} \longrightarrow (^7F_1)^3\Gamma_{4g}$ transition of the divalent Sm^{2+} ion. Wood and Kaiser [1962] characterised the absorption and emission spectra of Sm^{2+} in SrF_2, CaF_2 and BaF_2 lattices. As the absorption profile of Sm^{2+} shows a broad absorption, extending from 15000 cm^{-1} to 20000 cm^{-1}, in the same spectral region as the sharp $^1D_2$ absorption transitions of the Pr^{3+} ion, the excitation of the Sm^{2+} ion becomes unavoidable. The origin of the Sm^{2+} ion impurity can be traced to the growth of the crystal where it is included as one of the impurity ions in the praseodymium dopant material. The contamination of the optical spectra by the Sm^{2+} emission can become enhanced in hydrogenated crystals as the quantum yields of the hydrogenic centres are generally weaker than those of the F^- centres.

The $^3H_6$ Multiplet

Polarised emission spectra of transitions to the crystal field levels of the $^3H_6$ multiplet from the $^1D_2$ and $^3P_0$ multiplets are shown in Figures IV.2.6(a) and (b) respectively. The crystal field labels of X_i appropriate for the $^3H_6$ multiplet are used to indicate the origin of the lines in the spectra. The $^3H_6$ manifold is split by the C_{4v} crystal field into ten component levels of which eight have been assigned to an observed transition. The energy level scheme and those transitions observed are summarised in Table IV.2.5.

Figure IV.2.6(b), showing the $^3P_0 \longrightarrow {}^3H_6$ transitions, also contains lines corresponding to $^1D_2 \longrightarrow {}^3H_4$ transitions for the C_{4v} F^- site and additional lines from two other distinct centres. The transitions identified, and labelled a,b,c and d in the spectra are: $^1D_2(D_2) \longrightarrow {}^3H_4(Z_1)$ and $^1D_2(D_1) \longrightarrow {}^3H_4(Z_1)$ for the C_{4v} F^- centre, the $^1D_2(D_1) \longrightarrow {}^3H_4(Z_1)$ for the C_{4v} D^- centre and the $^1D_2(D_1) \longrightarrow {}^3H_4(Z_2)$ transition for the rhombic $C_s(1)$ D^- centre that will be described in a later chapter. The crystal from which these spectra were recorded had been deuterated and centres containing D^- charge compensating ions were known to exist. Of particular significance to the $^1D_2 \longrightarrow {}^3H_4$ transitions observed, is the greater intensity of the D^- centre lines relative to those from the F^- centre even though the C_{4v} F^- centre was being selectively excited. The $^3P_0$ levels of the C_{4v} D^- and $C_s(1)$ D^- sites are known to be at a lower energy than the C_{4v} F^- centre. Energy in the $^3P_0$ level of the C_{4v} F^- site is diverted by the multitude of lattice phonons to excite the Pr^{3+} ion in the D^- centres to its $^3P_0$ level. Emission from $^1D_2$ is obtained as the Pr^{3+} ion decays non-radiatively at least to the higher levels of the $^1D_2$ multiplet. The local mode vibrations of the D^- ions extend the phonon spectrum to higher frequencies to provide a lower order $^3P_0 \longrightarrow {}^1D_2$ non-radiative decay process. This can greatly increase the relative

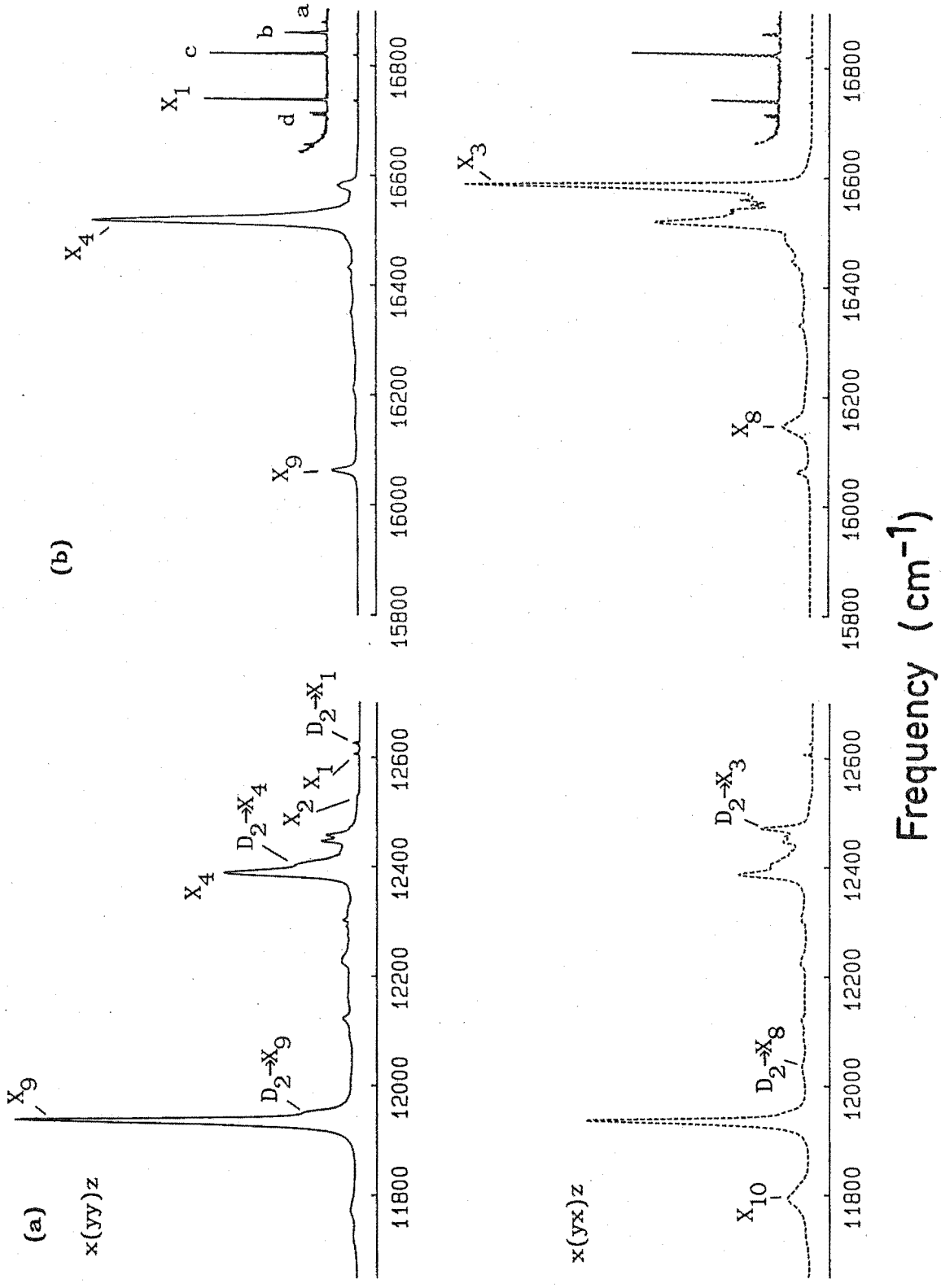

Figure IV.2.6 14K polarised emission to the crystal field levels of the $^3H_6$ multiplet for the C_{4v} F^- site in SrF_2:Pr^{3+} from (a) the $^1D_2$ and (b) the $^3P_0$ multiplets.

Table IV.2.5

Spectral data for the crystal field levels of the $^3H_6$ multiplet for the C_{4v} F^- site in $SrF_2:Pr^{3+}$.

Transition	Frequency ($\pm$ 1 cm^{-1})	Polarisation Observed	Predicted
$D_2(\Gamma_3\gamma_1) \longrightarrow X_1(\Gamma_5{}^1\gamma_5)$	12623	σ	σ
$D_1(\Gamma_3\gamma_3) \longrightarrow X_1(\Gamma_5{}^1\gamma_5)$	12604	σ	σ
$D_1 \longrightarrow X_2(\Gamma_5{}^1\gamma_4)$	12524	π'(md)[1]	π'(md)
$D_2 \longrightarrow X_3(\Gamma_1\gamma_1)$	12467	π	π
$D_2 \longrightarrow X_4(\Gamma_4\gamma_5)$	12402	σ	σ
$D_1 \longrightarrow X_4(\Gamma_4\gamma_5)$	12383	σ	σ
$D_2 \longrightarrow X_8(\Gamma_3\gamma_1)$	12034	π	π
$D_2 \longrightarrow X_9(\Gamma_5{}^2\gamma_5)$	11950	σ	σ
$D_1 \longrightarrow X_9(\Gamma_5{}^2\gamma_5)$	11931	σ	σ
$D_1 \longrightarrow X_{10}(\Gamma_2\gamma_3)$	11790	π	π
$^3P_0(\Gamma_1\gamma_1) \longrightarrow X_1(\Gamma_5{}^1\gamma_5)$	16730	σ	σ
$\longrightarrow X_3(\Gamma_3\gamma_1)$	16575	π	π
$\longrightarrow X_4(\Gamma_4\gamma_5)$	16509	σ	σ
$\longrightarrow X_5(\Gamma_4\gamma_2)$	16425	π'(md)[1]	π'(md)
$\longrightarrow X_8(\Gamma_3\gamma_1)$	16140	π	π
$\longrightarrow X_9(\Gamma_5{}^2\gamma_5)$	16057	σ	σ

$^3H_6$ Energy Levels ($\pm$ 1cm^{-1})

$X_1(\Gamma_5{}^1\gamma_5)$	: 4250
$X_2(\Gamma_5{}^1\gamma_4)$	: 4330
$X_3(\Gamma_1\gamma_1)$	: 4405
$X_4(\Gamma_4\gamma_5)$	: 4471
$X_5(\Gamma_4\gamma_2)$	: 4555 [2]
$X_6(\Gamma_3\gamma_3)$	: -
$X_7(\Gamma_5{}^2\gamma_4)$	: -
$X_8(\Gamma_3\gamma_1)$	: 4840
$X_9(\Gamma_5{}^2\gamma_5)$	: 4923
$X_{10}(\Gamma_2\gamma_3)$	: 5064 $\pm$ 2

[1] x(yy)z:x(yx)z polarisation ratio of 1:0 for a magnetic dipole transition.

[2] Tentative assignment.

probabilities of $^1D_2$ emission after $^3P_0$ excitation producing the differences in line intensities between the D^- and F^- centres.

The $^3F_2$ Multiplet

The $^3F_2$ multiplet splits into four levels in a crystal field of C_{4v} symmetry (Figure IV.1.1). Transitions to three of these levels have been observed in the C_{4v} F^- site of $SrF_2:Pr^{3+}$ with a tentative assignment proposed for the fourth. Polarised emission spectra of the transitions from the $^1D_2$ and $^3P_0$ multiplets to the $^3F_2$ levels are shown in Figures IV.2.7(a) and (b). Table IV.2.6 summarises the energy level scheme and those transitions observed. The observation of a strong $^1D_2(D_2) \longrightarrow {}^3F_2(\Gamma_3\gamma_1)$ π-polarised transition adds further support to the assignment of the D_1 and D_2 levels of $^1D_2$ as being the $\Gamma_3\gamma_3$ and $\Gamma_3\gamma_1$ states respectively.

Transitions from both D_1 and D_2 to $W_3(\Gamma_5\gamma_5)$ are observed to be σ-polarised consistent with the level symmetries. The W_4 crystal field level has γ_3 symmetry and a π-polarised $D_1(\Gamma_3\gamma_3) \longrightarrow W_3(\Gamma_3\gamma_3)$ transition is observed in Fig IV.2.7(a). As expected a transition is not visible to this level from $^3P_0(\Gamma_1\gamma_1)$. A π-polarised magnetic dipole transition is allowed to the $W_1(\Gamma_5\gamma_4)$ level from $D_1(\Gamma_3\gamma_3)$ and a weak feature at 859.6 nm is tentatively assigned to this transition.

With the electronic energy levels spanning an energy range of only 150 cm^{-1} the $^3F_2$ multiplet provides an ideal situation for further examination of the vibronic levels associated with lattice phonons. Table IV.2.7 summarises the vibronic intervals observed from the four zero-phonon lines of this multiplet.

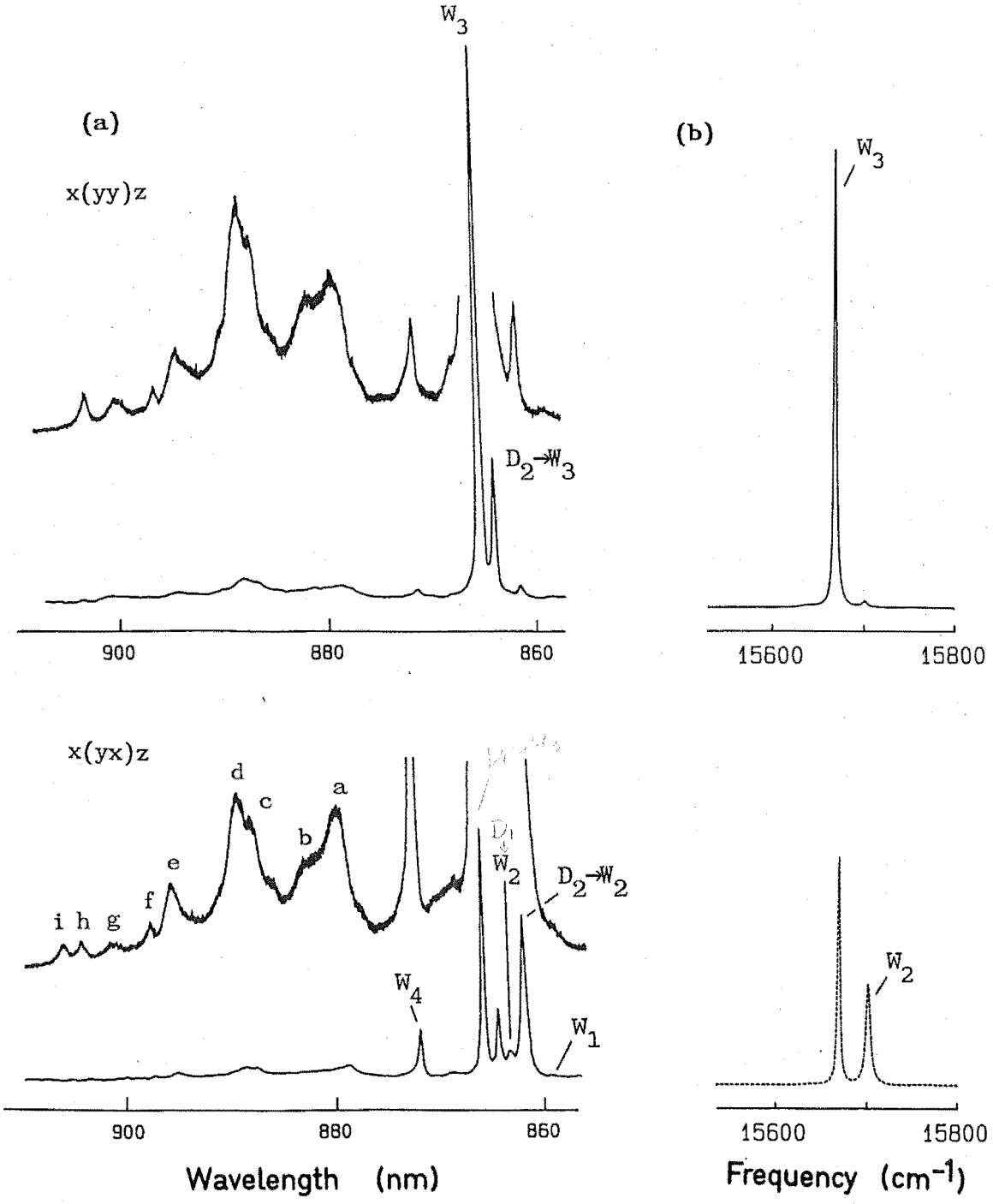

Figure IV.2.7 14K polarised emission to the crystal field levels of the $^3F_2$ multiplet for the C_{4v} F^- site in $SrF_2:Pr^{3+}$ from (a) the $^1D_2$ and (b) the $^3P_0$ multiplets.

Table IV.2.6

Spectral data for the crystal field levels of the $^3F_2$ multiplet for the C_{4v} F^- site in $SrF_2:Pr^{3+}$.

Transition	Air Wavelength (± .1 nm)	Polarisation Observed	Polarisation Predicted
$D_1(\Gamma_3\gamma_3) \longrightarrow W_1(\Gamma_5\gamma_4)$	859.6 [1]	π'(md)	π'(md)
$D_2(\Gamma_3\gamma_1) \longrightarrow W_2(\Gamma_3\gamma_1)$	861.9	π	π
$D_1 \longrightarrow W_2(\Gamma_3\gamma_1)$	863.3	π	- [2]
$D_2 \longrightarrow W_3(\Gamma_5\gamma_5)$	864.3	σ	σ
$D_1 \longrightarrow W_3(\Gamma_5\gamma_5)$	865.8	σ	σ
$D_1 \longrightarrow W_4(\Gamma_3\gamma_3)$	872.3	π	π
	Frequency(±1cm^{-1})		
$^3P_0(\Gamma_1\gamma_1) \longrightarrow W_2(\Gamma_3\gamma_1)$	15705	π	π
$\longrightarrow W_3(\Gamma_5\gamma_5)$	15672	σ	σ

$^3F_2$ Energy Levels (± 2cm^{-1})
$W_1(\Gamma_5\gamma_4)$: 5225
$W_2(\Gamma_3\gamma_1)$: 5275
$W_3(\Gamma_5\gamma_5)$: 5308
$W_4(\Gamma_3\gamma_3)$: 5394

[1] Tentative assignment from a weak magnetic dipole transition.

[2] Weak transition forbidden by electric or magnetic dipole radiation.

Table IV.2.7

Energy shifts from zero phonon lines for vibronic transitions observed to the $^3F_2$ multiplet.

Vibronic Lines		Parent zero phonon line (±.1 nm)			
Label	Wavelength (±.1 nm)	860.3	864.0	866.5	873.0
a	880.0	261	210	177	91
b	882.1	287	237	205	118
c	888.1	364	313	281	195
d	889.2	378	327	295	209
e	895.7	459	410	377	290
f	898.0	487	438	404	319
g	901.6	532	482	450	363
h	904.7	571	520	488	401
i	906.6	594	544	510	425

The $^3F_3$ and $^3F_4$ Multiplets

Spectra of polarised emission from the $^1D_2$ and $^3P_0$ multiplets to the $^3F_3$ and $^3F_4$ crystal field levels are shown in Figure IV.2.8 for the C_{4v} F^- site in $SrF_2:Pr^{3+}$. A complete energy level scheme is obtained for the $^3F_3$ multiplet as transitions have been identified to all levels. Table IV.2.8 summarises the details of these transitions and gives the energy level scheme for this multiplet.

Several magnetic dipole transitions are observed that support the D_1 and D_2 level symmetries as $\Gamma_3\gamma_3$ and $\Gamma_3\gamma_1$ respectively. A line to the $V_2(\Gamma_5\gamma_4)$ level is observed in Fig.IV.2.8(a) but not (b). This transition originates from $D_1(\Gamma_3\gamma_3)$ and has the expected x(yy)z:x(yx)z polarisation ratio of 1:0 consistent with a π-polarised magnetic dipole transition.

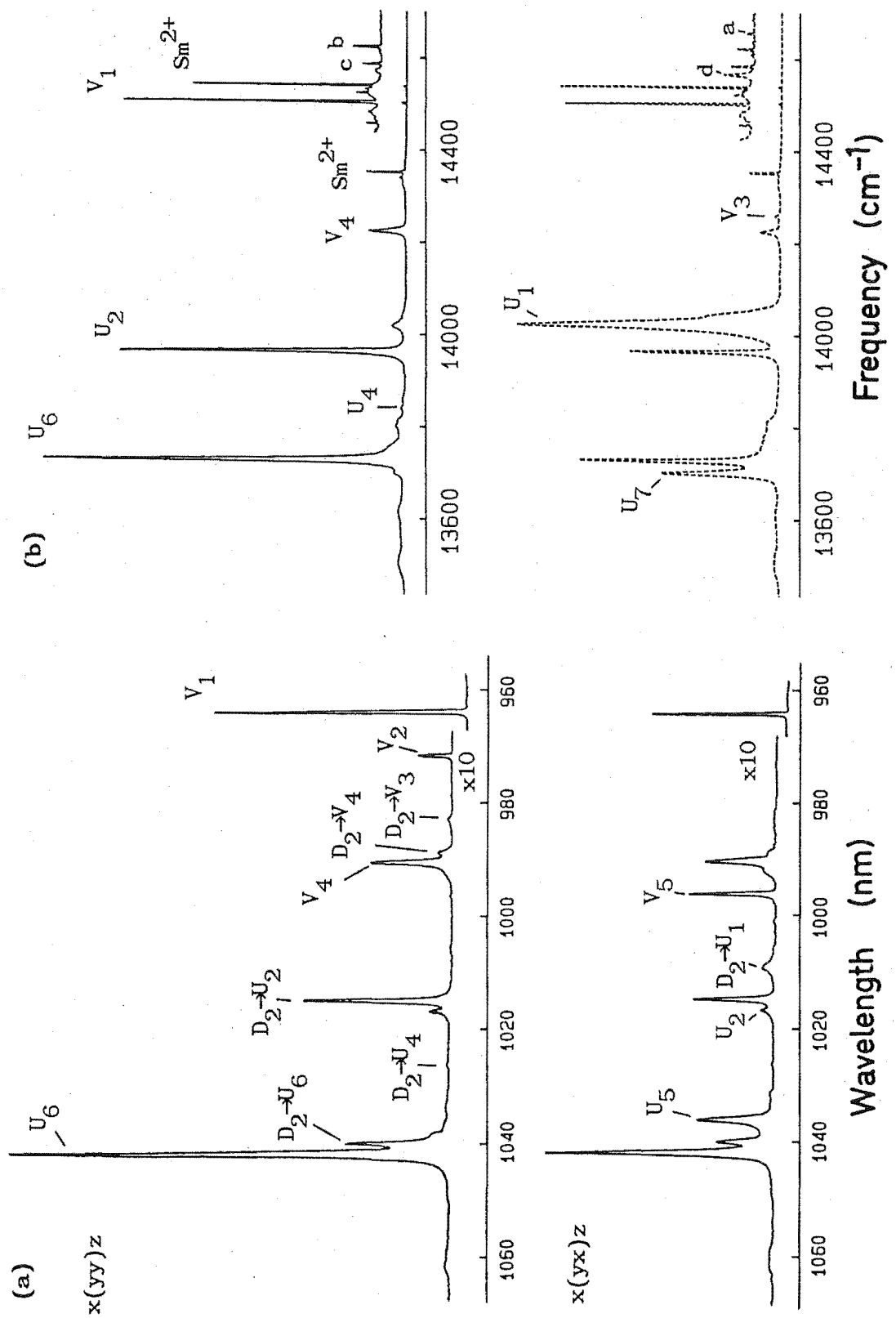

Figure IV.2.8 14K polarised emission to the crystal field levels of the $^3F_3(V_i)$ and $^3F_4(U_i)$ multiplets for the C_{4v} F^- site in $SrF_2:Pr^{3+}$ from (a) the $^1D_2$ and (b) the $^3P_0$ multiplets.

Table IV.2.8

Spectral data for the crystal field levels of the $^3F_3$ multiplet for the C_{4v} F^- site in $SrF_2:Pr^{3+}$.

Transition	Air Wavelength (± 0.2 nm)	Polarisation Observed	Polarisation Predicted
$D_2(\Gamma_3\gamma_1) \longrightarrow V_1(\Gamma_5\gamma_5)$	962.2	σ	σ
$D_1(\Gamma_3\gamma_3) \longrightarrow V_1(\Gamma_5\gamma_5)$	963.9	σ	σ
$D_1 \longrightarrow V_2(\Gamma_5\gamma_4)$	971.5	π'(md)[1]	π'(md)
$D_2 \longrightarrow V_3(\Gamma_4\gamma_2)$	982.8	π'(md)[1]	π'(md)
$D_2 \longrightarrow V_4(\Gamma_4\gamma_5)$	988.6	σ	σ
$D_1 \longrightarrow V_4(\Gamma_4\gamma_5)$	990.5	σ	σ
$D_1 \longrightarrow V_5(\Gamma_2\gamma_3)$	996.3	π	π
	Frequency(±1cm^{-1})		
$^3P_0(\Gamma_1\gamma_1) \longrightarrow V_1(\Gamma_5\gamma_5)$	14496	σ	σ
$\longrightarrow V_3(\Gamma_4\gamma_2)$	14278	π'(md)[1]	π'(md)
$\longrightarrow V_4(\Gamma_4\gamma_5)$	14218	σ	σ

$^3F_3$ Energy Levels (± 2cm^{-1})
$V_1(\Gamma_5\gamma_5)$: 6484
$V_2(\Gamma_5\gamma_4)$: 6565
$V_3(\Gamma_4\gamma_2)$: 6702
$V_4(\Gamma_4\gamma_5)$: 6762
$V_5(\Gamma_2\gamma_3)$: 6821

[1] (yy):(yx) polarisation ratio of 1:0 associated with a π-polarised magnetic dipole transition.

Transitions to $V_3(\Gamma_4\gamma_2)$ are apparent in both Figures IV.2.8(a) and (b) but the wavelength of the line in (a) requires the originating level to be D_2. With level symmetries of $^3P_0(\Gamma_1\gamma_1)$ and $D_2(\Gamma_3\gamma_1)$ the $^3P_0 \longrightarrow V_3$ and $D_2 \longrightarrow V_3$ lines are expected and found to be π-polarised magnetic dipole transitions.

In the same manner to that described earlier, emission from $^1D_2$ levels of D^- sites can occur after $^3P_0$ excitation in crystals that have been subject to the deuteration process. The Transitions $D_2 \rightarrow Y_2$ and $D_2 \rightarrow Y_4$ for the C_{4v} F^- site and $D_1 \rightarrow Y_2$ and $D_1 \rightarrow Y_3$ for the C_{4v} D^- site are labelled a, d, b and c respectively in Figure IV.2.8(b). As before the D^- site lines have a similar intensity to those from the F^- site again illustrating the efficient quenching of $^3P_0$ excitation by local mode phonons. A number of other lines present cannot be assigned, however the transitions of the $C_s(1)$ D^- centre, and other centres of this type, are not known in this region.

Transitions to $^3F_4$ crystal field levels are also shown in Fig IV.2.8 and the results are detailed in Table IV.2.9. A transition to $U_5(\Gamma_3\gamma_3)$ is observed from $D_1(\Gamma_3\gamma_3)$ but not $^3P_0(\Gamma_1\gamma_1)$ consistent with the level symmetries. Similarly transitions to $U_1(\Gamma_3\gamma_1)$ are observed from $D_2(\Gamma_3\gamma_1)$ and $^3P_0(\Gamma_1\gamma_1)$ but not $D_1(\Gamma_3\gamma_3)$. The $U_3(\Gamma_5\gamma_4)$ level remains unassigned at this time.

The $^1G_4$ Multiplet

The ability to selectively excite the $^3P_0$ level of the Pr^{3+} ion in the C_{4v} F^- site with the 476.5 nm argon ion laser line enabled emission to be detected to some of the levels of the $^1G_4$ multiplet. Optical absorption establishes the $^1G_4$ levels to be centred near 1000.0 nm so emission to these levels will be around 910.0 nm. Figure IV.2.9(a) shows the emission recorded in this region with the polarisation of each line indicated.

Table IV.2.9

Spectral data for the crystal field levels of the $^3F_4$ multiplet for the C_{4v} F^- site in $SrF_2:Pr^{3+}$.

Transition	Air Wavelength (± .2 nm)	Polarisation Observed	Predicted
$D_2(\Gamma_3\gamma_1) \longrightarrow U_1(\Gamma_3\gamma_1)$	1009.1	π	π
$D_2 \longrightarrow U_2(\Gamma_5\gamma_5)$	1015.0	σ	σ
$D_1(\Gamma_3\gamma_3) \longrightarrow U_2(\Gamma_5\gamma_5)$	1016.9	σ	σ
$D_2 \longrightarrow U_4(\Gamma_4\gamma_2)$	1027.8	$\pi'(md)$[1]	$\pi'(md)$
$D_1 \longrightarrow U_5(\Gamma_3\gamma_3)$	1036.1	π	π
$D_2 \longrightarrow U_6(\Gamma_4\gamma_5)$	1040.0	σ	σ
$D_1 \longrightarrow U_6(\Gamma_4\gamma_5)$	1041.9	σ	σ
	Frequency (± $1cm^{-1}$)		
$^3P_0(\Gamma_1\gamma_1) \longrightarrow U_1(\Gamma_3\gamma_1)$	14014	π	π
$\longrightarrow U_2(\Gamma_5\gamma_5)$	13956	σ	σ
$\longrightarrow U_4(\Gamma_4\gamma_2)$	13834	$\pi'(md)$[1]	$\pi'(md)$
$\longrightarrow U_6(\Gamma_4\gamma_5)$	13720	σ	σ
$\longrightarrow U_7(\Gamma_1\gamma_1)$	13694	π	π

$^3F_4$ Energy Levels (± $2cm^{-1}$)	
$U_1(\Gamma_3\gamma_1)$:	6966
$U_2(\Gamma_5\gamma_5)$:	7024
$U_3(\Gamma_5\gamma_4)$:	-
$U_4(\Gamma_4\gamma_2)$:	7146
$U_5(\Gamma_3\gamma_3)$:	7206
$U_6(\Gamma_4\gamma_5)$:	7260
$U_7(\Gamma_1\gamma_1)$:	7286

[1] (yy):(yx) polarisation ratio of 1:0 associated with a π-polarised magnetic dipole transition.

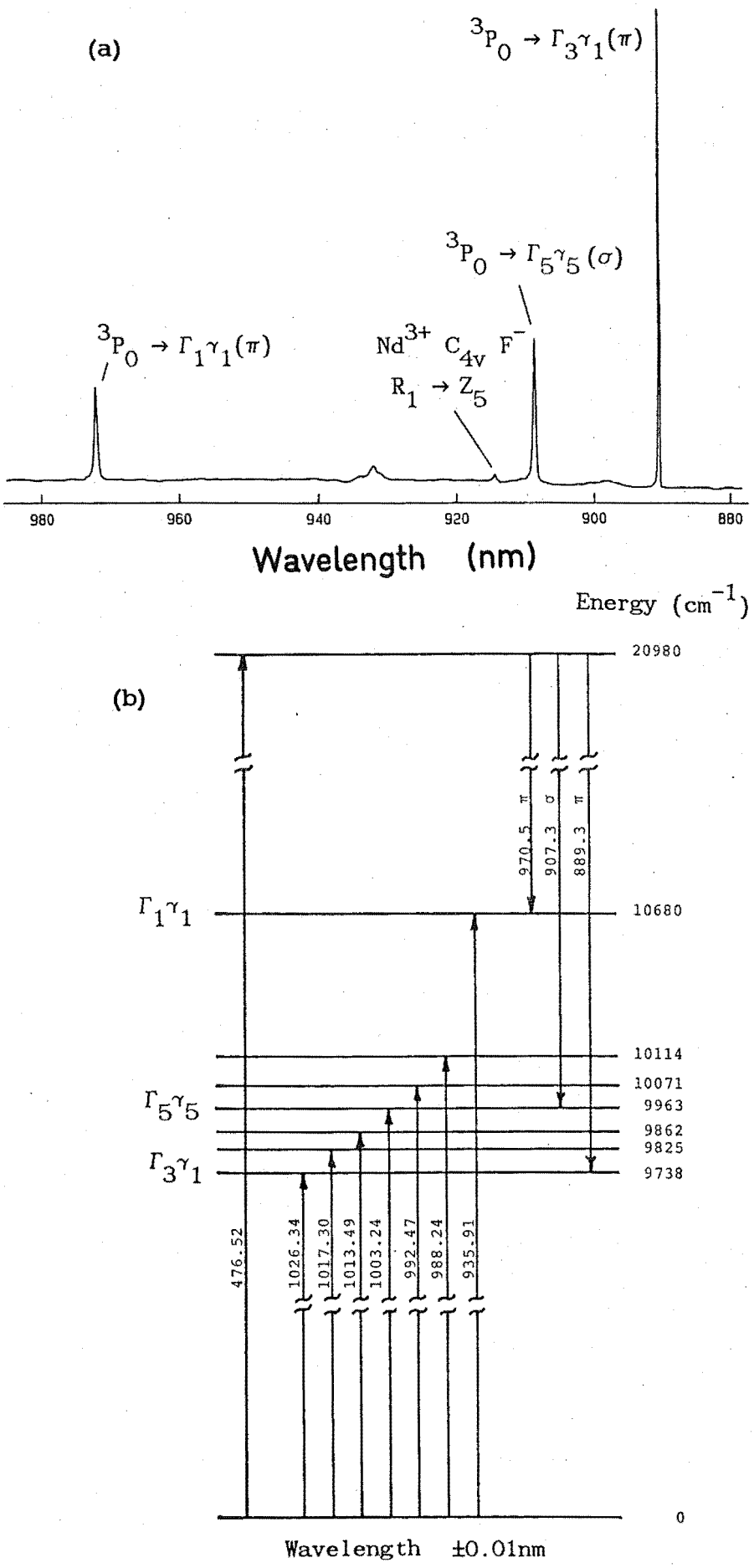

Figure IV.2.9 (a) 14K $^3P_0 \rightarrow {}^1G_4$ emission for the C_{4v} F^- site in $SrF_2:Pr^{3+}$ and (b) the energy level scheme for this multiplet.

Figure IV.2.9(b) summarises the $^1G_4$ energy level scheme and shows those transitions observed. The π-polarisation of the emission from the $^3P_0(\Gamma_1\gamma_1)$ level to the lowest component of $^1G_4$ requires this level to transform as the γ_1 irrep and can be assigned to the $\Gamma_3\gamma_1$ state. Similarly the transition to the highest crystal field level is π-polarised consistent with the assignment of this level to be the $\Gamma_1\gamma_1$ state discussed earlier. The third transition observed is σ-polarised. The terminating level for this transition is most likely to be the $^1G_4(\Gamma_5\gamma_5)$ state.

In addition to praseodymium ion transitions, lines originating from the Nd^{3+} ion in the C_{4v} F^- site are also apparent in this region of the spectrum. These lines can be identified from the results of Freeth and Jones [1982]. Like the Sm^{2+} impurity, Nd^{3+} ions are included in the crystal from the praseodymium dopant material during its growth. This infrared region is the main region of Nd^{3+} fluorescence and the small number of ions present contribute emission on a scale comparable to that of the Pr^{3+} ions. Nd^{3+} ion transitions have also been observed in absorption and details of these lines will be presented in the next chapter.

Upconversion

At a 4000 fold increase in sensitivity over that used for recording the normal $^1D_2 \longrightarrow {}^3H_4$ emission , fluorescence is observed from the $^3P_0$ level of the C_{4v} F^- site when the laser is tuned to excite the Pr^{3+} ion to the $^1D_2$ multiplet, i.e. upconverted emission is obtained (Jones et al [1987], Lezama et al [1986]). New results reported in this work include upconversion in the C_{4v} D^- and T^- sites in SrF_2:Pr^{3+}. Upconversion is common between pairs of rare-earth ions forming cluster sites where the interaction is short range. The mechanism for the upconversion observed here may be different as the

single ion nature of the centres and the dilute dopant concentrations require the interaction to be over a longer range. For the Pr^{3+} F^- C_{4v} site, pumping with the 476.5 nm argon laser line allows the directly excited $^3P_0 \longrightarrow {}^3H_4$ emission to be compared with the upconverted $^3P_0 \longrightarrow {}^3H_4$ emission to show the equality of the two spectra. As this effect is common to other centres in these crystals further discussion will be reserved until Chapter VIII and all the results have been presented.

IV.3 Optical Spectroscopy of Pr^{3+} in CaF_2

IV.3.1 Introduction

As in $SrF_2:Pr^{3+}$ crystals, the C_{4v} F^- site is the dominant spectroscopic centre in $CaF_2:Pr^{3+}$ however in this case other centres take on an increasing importance. Extensive investigations in $CaF_2:Pr^{3+}$ crystals have identified many distinct sites (Kliava et al [1981], Lezama et al [1986] and references therein). The C_{4v} F^- site has recently been subjected to high resolution laser studies (Burum et al [1982], Macfarlane et al [1984]) that provide direct evidence of the positioning of the charge compensating F^- ion in the neighbouring interstitial position. A novel spectral holeburning mechanism arises from the large difference in Pr^{3+} magnetic moment between the ground and $^1D_2$ excited states (Macfarlane et al [1981]).

In a similar manner to the $SrF_2:Pr^{3+}$ crystals, a detailed study of the energy levels of the C_{4v} F^- site in $CaF_2:Pr^{3+}$ was attempted. However, due to differences in the symmetry of the $^1D_2$ emitting level between these two crystals, the survey in $CaF_2:Pr^{3+}$ was not nearly as successful. Of the 70 crystal field levels comprising the Pr^{3+} configuration, energies of 35 levels have been measured.

IV.3.2 Absorption and Excitation of $CaF_2:Pr^{3+}$

In common with most other rare-earth ions in the fluorite crystals the optical absorption spectrum in the CaF_2 host contains more structure than in the SrF_2 host and praseodymium doped crystals are no exception. Figures IV.3.1(a) and (b) show the absorption to the $^3P_0$ and $^3P_1$ and $^1D_2$ multiplets respectively for a 0.02 mol%Pr^{3+} doped crystal. The wavelengths of the observed transitions are tabulated in Table IV.3.1 with the site assignments if they are known. Only the C_{4v} F^- site was singled out for laser excitation studies.

Figure IV.3.2 shows the $^1D_2$ laser excitation spectrum for the C_{4v} F^- site in $CaF_2:Pr^{3+}$. The D_1, D_2 and D_4 crystal field levels have been indicated. As for the C_{4v} F^- site in $SrF_2:Pr^{3+}$ a broad band of phonon structure is visible in the region between D_2 and D_4, although in this case the structure is less well resolved.

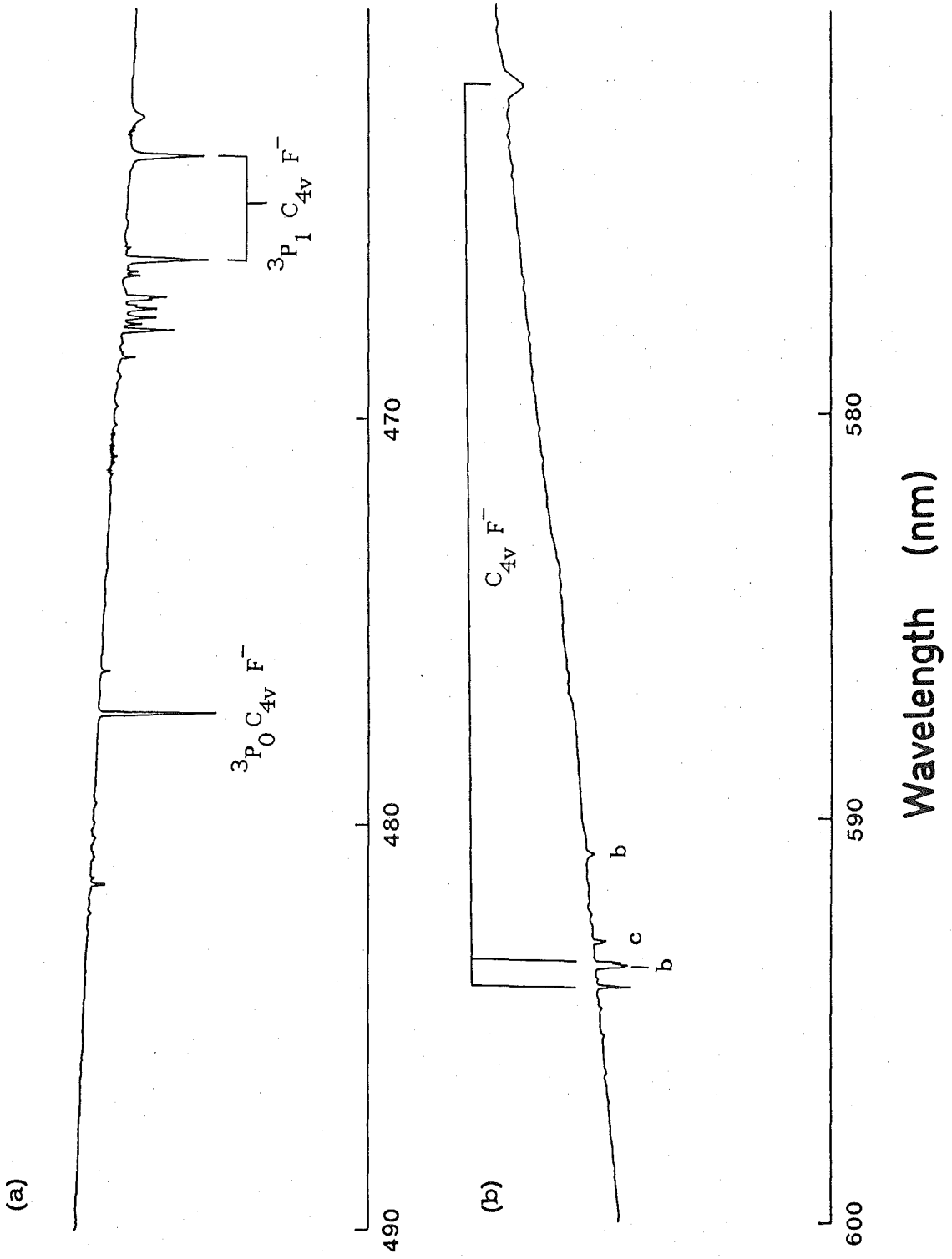

Figure IV.3.1 Optical absorption recorded at 14K, for transitions to the (a) $^3P_0$ and $^3P_1$ and (b) $^1D_2$ crystal field levels of the Pr^{3+} ion in the C_{4v} F^- site of $CaF_2:Pr^{3+}$.

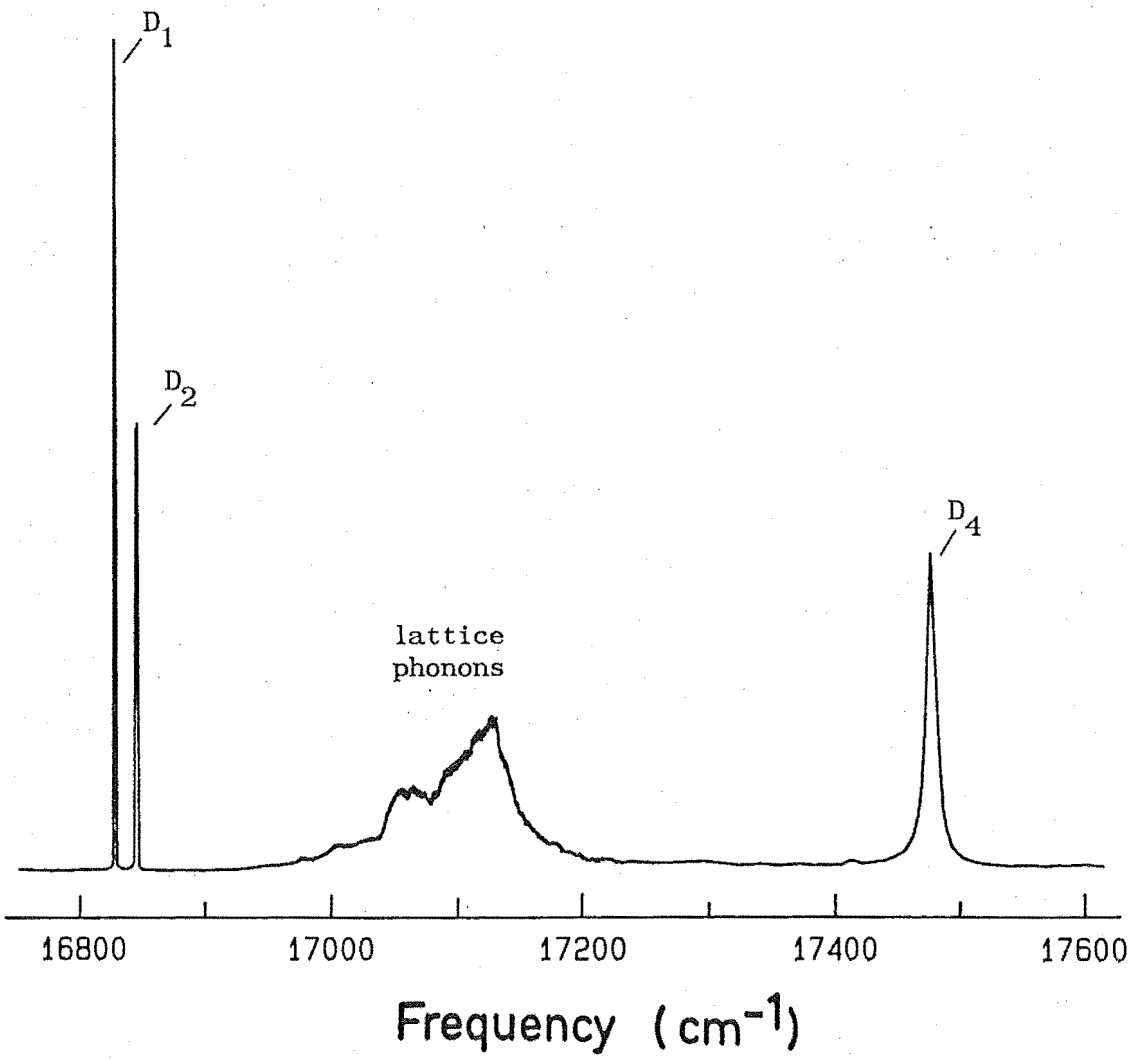

Figure IV.3.2 14K laser excitation spectrum of the $^1D_2$ region for the C_{4v} F^- site in $CaF_2:Pr^{3+}$.

Table IV.3.1

Wavelengths of absorption transition and site assignments for a 0.02 mol% $CaF_2:Pr^{3+}$ crystal.

Absorption Line Wavelength (±.01 nm)	Site Assignment	Relative Intensity
$^3P_1$ multiplet		
462.55		11
463.49	C_{4v}	63
465.11		3
465.65		2
465.76		4
465.86		3
466.05	C_{4v}	73
466.24		4
466.34		11
466.43		15
466.96		37
467.02		24
467.17		11
467.25		28
467.47		28
467.62		17
467.76		46
468.41		13
469.63		4
470.06		4
$^3P_0$ multiplet		
476.05		8
477.14	C_{4v}	100
481.17		4
481.33		13
482.05		3

Table IV.3.1 continued next page.....

Table IV.3.1, continued

Absorption Line Wavelength (±.01 nm)	Site Assignment	Relative Intensity
$^1D_2$ multiplet		
571.99 (D_4)	C_{4v},A,a	57
590.90	G,b	24
592.34		7
593.01	H,c	38
593.06	H,c	30
593.56 (D_2)	C_{4v},A,a	78
593.60	C,b	95
593.04	H,c	88
593.96		10
594.10 (D_1)	C_{4v},A,a	100
594.67		7

The capital letters A,G,H refer to site assignments of Lezama et al [1986] while the small letters a,b and c are the labels of Kliava et al [1978].

IV.3.3 Optical Emission of the C_{4v} F^- Site in $CaF_2:Pr^{3+}$

Spectra of the emission from the $^1D_2$ and $^3P_0$ multiplets to the crystal field levels of the $^3H_{4,5,6}$ and $^3F_{2,3,4}$ multiplets were recorded for the Pr^{3+} ion in the C_{4v} F^- site of a $CaF_2:Pr^{3+}$ crystal. Praseodymium ion concentrations used were typically 0.05 mol% and the spectra were recorded at a temperature of 14 K. The Pr^{3+} ion was excited to the $^1D_2$ multiplet by a Rhodamine 6G dye laser tuned to match an absorption transition, usually the lowest crystal field component at 16827.6 cm^{-1}. The $^3P_0$ level is outside the spectral range of the cw tunable dye laser and recording the emission of the ion from this level was achieved in several ways. Irradiation with a tunable pulsed dye laser using Coumarin 481 dye enabled selective excitation of the ion to the $^3P_0$ level but emission spectra had to be

recorded at high sensitivities due to the low light levels obtained. Following Chryschoos [1984], excitation with the 457.9 nm argon ion laser line produced emission from the $^3P_0$ state. At low Pr^{3+} ion concentrations this emission will mostly originate from the C_{4v} F^- site. Irradiation with other argon laser lines and the use of several crystals with different growth histories, clarified the emission from the C_{4v} F^- site. A third method of observing emission from the $^3P_0$ level, and possibly that giving the most information, is through the upconversion process. Like the C_{4v} F^- site in $SrF_2:Pr^{3+}$, polarisation information is retained in the upconverted emission, however the weak nature of this process restricts its usefulness.

Using Zeeman studies, Macfarlane et al [1984] identified the lowest crystal field component of $^1D_2$ as transforming as the γ_1 irrep of C_{4v}. This is in contrast to the C_{4v} F^- site in $SrF_2:Pr^{3+}$ where it was determined in this work that the D_1 level transforms as the γ_3 irrep. The fluorescence transitions observed that led to this assignment for $SrF_2:Pr^{3+}$ are **not** observed for $CaF_2:Pr^{3+}$ thus supporting the assignment of a different symmetry for the emitting level in the two hosts.

The spectra of emission to each multiplet will now be discussed in turn.

The $^3H_4$ Multiplet

Figures IV.3.3(a) and (b) show the polarised emission to the levels of the $^3H_4$ multiplet from the $^1D_2$ and $^3P_0$ multiplets respectively. Table IV.3.2 summarises the transitions identified and the energy level scheme for this multiplet. This confirms the assignment of both $^1D_2(D_1)$ and $^3P_0$ emitting levels as transforming as the γ_1 irrep as both have the same selection rules for emission from the two levels. The spectra show transitions to the same $^3H_4$ levels only from

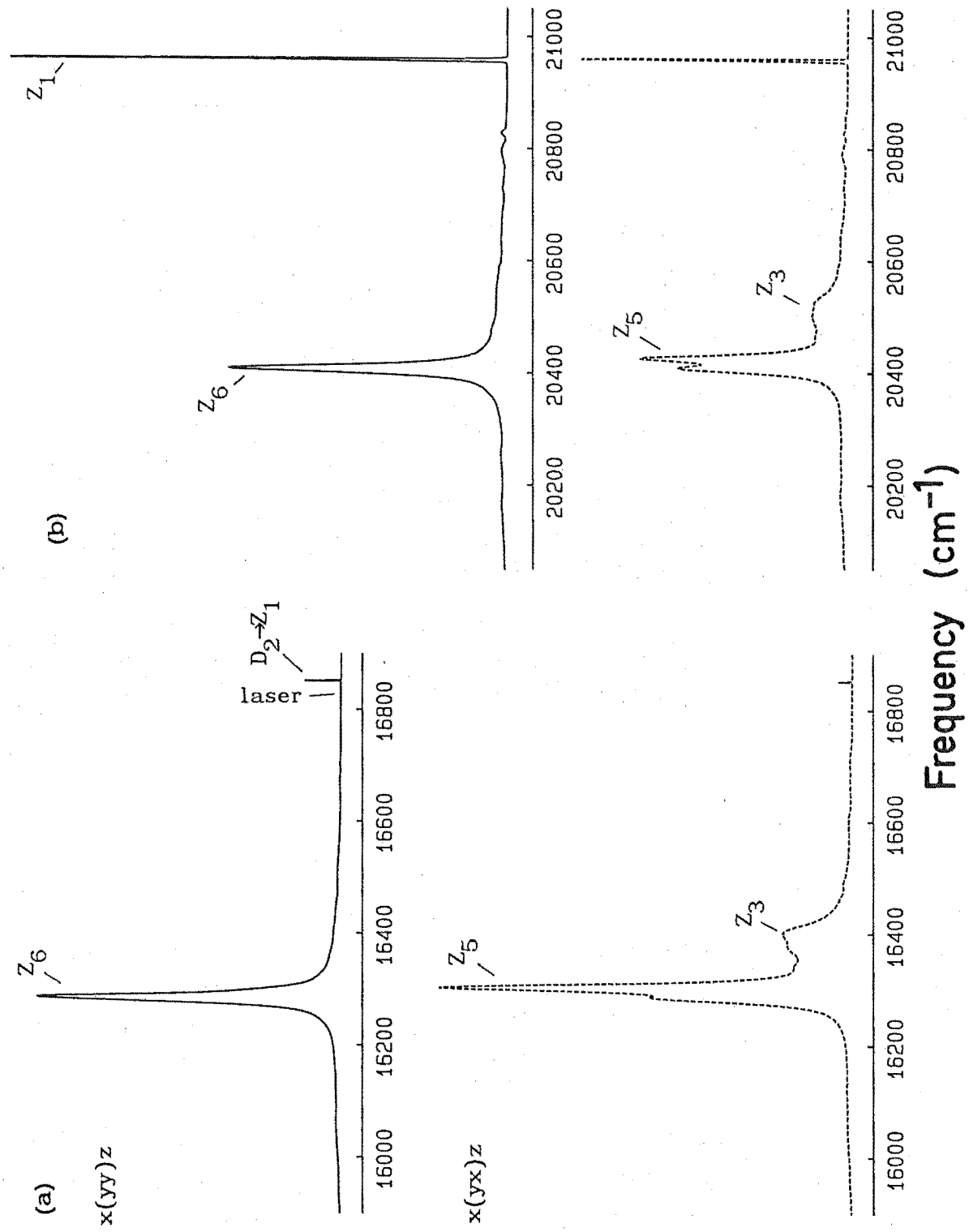

Figure IV.3.3 Polarised emission at 14K to the $^3H_4$ multiplet from the (a) $^1D_2$ and (b) $^3P_0$ levels for the C_{4v} F^- site in a <100> oriented $CaF_2:Pr^{3+}$ crystal. The $^3P_0 \rightarrow {}^3H_6$ emission depicted in (b) is upconverted having been produced using $Z_1 \rightarrow D_1$ excitation.

Table IV.3.2

Spectral data for the crystal field levels of the $^3H_4$ multiplet for the C_{4v} F^- site in $CaF_2:Pr^{3+}$.

Transition	Frequency ($\pm$ 1cm^{-1})	Polarisation Observed	Predicted
$D_2(\Gamma_3\gamma_3) \longrightarrow Z_1(\Gamma_5\gamma_5)$	16844.3 $\pm$ .1	σ	σ
$D_1(\Gamma_3\gamma_1) \longrightarrow Z_1(\Gamma_5\gamma_5)$	16827.6 $\pm$ .1	σ	σ
$D_1 \longrightarrow Z_3(\Gamma_3\gamma_1)$	16381 $\pm$ 10 [1]	π	π
$D_1 \longrightarrow Z_4(\Gamma_4\gamma_2)$	16344 [2]	π'(md)	π'(md)
$D_1 \longrightarrow Z_5(\Gamma_1\gamma_1)$	16294	π	π
$D_1 \longrightarrow Z_6(\Gamma_4\gamma_5)$	16276	σ	σ
$D_2 \longrightarrow Z_7(\Gamma_3\gamma_3)$	16116 [2]	π	π
$^3P_0(\Gamma_1\gamma_1) \longrightarrow Z_1(\Gamma_5\gamma_5)$	20954	σ	σ
$\longrightarrow Z_3(\Gamma_3\gamma_1)$	20506 $\pm$ 10 [1]	π	π
$\longrightarrow Z_4(\Gamma_4\gamma_2)$	20470 [2]	π'(md)	π'(md)
$\longrightarrow Z_5(\Gamma_1\gamma_1)$	20420	π	π
$\longrightarrow Z_6(\Gamma_4\gamma_5)$	20403	σ	σ

$^3H_4$ Energy Levels ($\pm$ 1cm^{-1})	
$Z_1(\Gamma_5\gamma_5)$:	0
$Z_2(\Gamma_5\gamma_4)$:	-
$Z_3(\Gamma_3\gamma_1)$:	447 $\pm$ 10 [1]
$Z_4(\Gamma_4\gamma_2)$:	484 [2]
$Z_5(\Gamma_1\gamma_1)$:	534
$Z_6(\Gamma_4\gamma_5)$:	552
$Z_7(\Gamma_3\gamma_3)$:	728 [2]

[1] The fluorescent transitions to the $Z_3(\Gamma_3\gamma_1)$ level are broad and a single well resolved peak is not apparent.

[2] Tentative assignment.

D_1 and $^3P_0$ and these lines have similar polarisation ratios.

With both emitting levels transforming as the γ_1 irrep, the emission spectra do not show the diversity of transitions observed for the C_{4v} F^- site in $SrF_2:Pr^{3+}$ and the energy level scheme is harder to determine. Electric dipole transitions are allowed and have been observed from $D_1(\Gamma_1\gamma_1)$ to the $Z_3(\Gamma_3\gamma_1)$, $Z_5(\Gamma_1\gamma_1)$ and $Z_6(\Gamma_4\gamma_5)$ crystal field levels. The transitions to γ_1 symmetry states are π-polarised and show the x(yy)z:x(yx)z polarisation ratio of 0:1 expected. The $D_1(\Gamma_1\gamma_1) \longrightarrow Z_6(\Gamma_4\gamma_5)$ line has a polarisation ratio of 2:1 consistent with the σ-polarisation of this transition. An electric dipole $D_2(\Gamma_3\gamma_3) \longrightarrow Z_7(\Gamma_3\gamma_3)$ transition will be allowed in π-polarisation but its observation depends upon the $D_2(\Gamma_3\gamma_3)$ level being thermally populated. The fluorescent lifetime of the $^1D_2$ level for the C_{4v} F^- site was measured to be 5 times faster in $CaF_2:Pr^{3+}$ than $SrF_2:Pr^{3+}$ (Chapter VIII) and the 'hot' emission lines from D_2 will be relatively weaker in this host. A transition to $Z_7(\Gamma_3\gamma_3)$ is not allowed from $^3P_0(\Gamma_1\gamma_1)$. A line satisfying the polarisation and selection rules is observed at 16116 cm^{-1} giving a tentative assignment of the $Z_7(\Gamma_3\gamma_3)$ level at 728 cm^{-1}.

Magnetic dipole transitions to the $Z_4(\Gamma_4\gamma_2)$ and $Z_2(\Gamma_5\gamma_4)$ levels are allowed from states transforming as the γ_1 and γ_3 irreps respectively. A possible candidate for the transition to the $Z_4(\Gamma_4\gamma_2)$ level gives the energy of this state as 484 cm^{-1} but the energy of the $Z_2(\Gamma_5\gamma_4)$ level remains undetermined at this time.

The $^3H_5$ Multiplet

The spectra of emission to the crystal field levels of the $^3H_5$ multiplet from the $^1D_2$ and $^3P_0$ multiplets are shown in Figure IV.3.4. Note the scale change in Fig.IV.3.4(b). Polarised emission was available for spectra recorded from $^1D_2$ but not $^3P_0$ as this level was

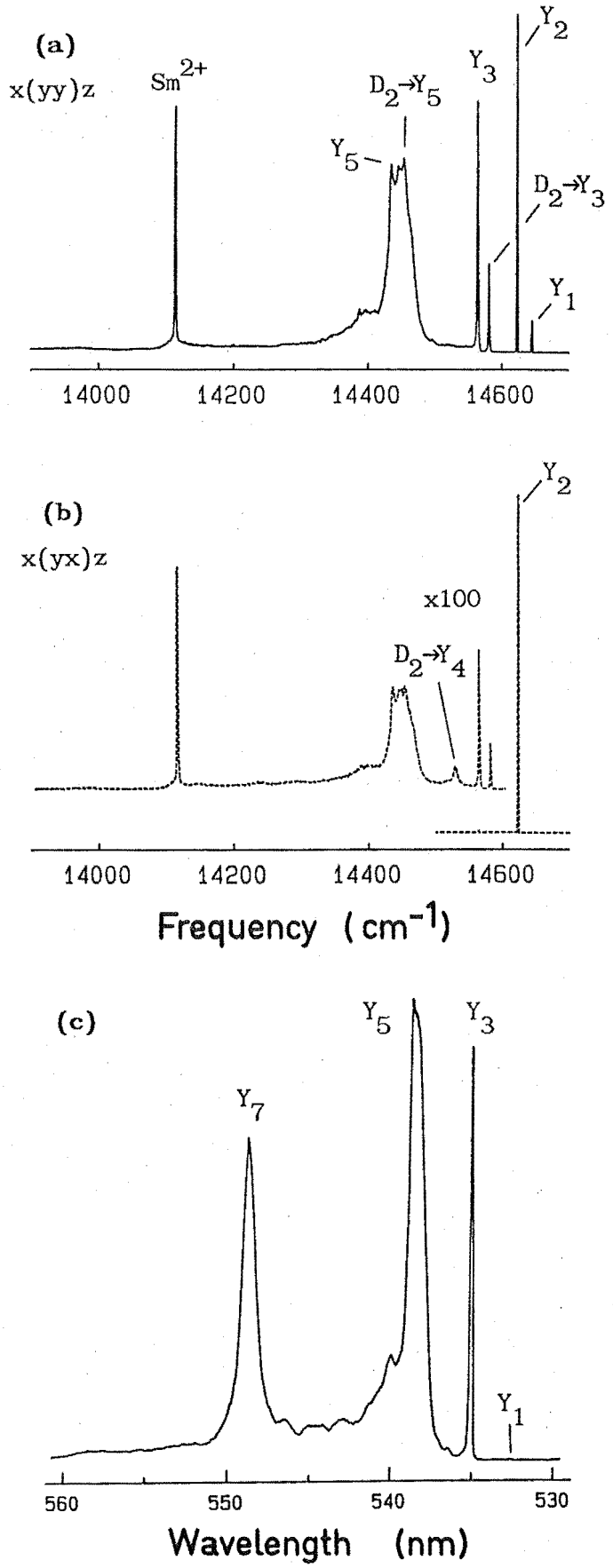

Figure IV.3.4 (a) and (b) polarised $^1D_2 \rightarrow {}^3H_5$ emission and (c) $^3P_0 \rightarrow {}^3H_5$ emission, for the C_{4v} F^- site in CaF_2:Pr^{3+} at 14K.

excited using the tunable pulsed laser. Those transitions observed, and the energy level scheme determined are summarised in Table IV.3.3 for the $^3H_5$ multiplet.

A weak magnetic dipole transition has been observed to the $Y_1(\Gamma_4^{(1)}\gamma_2)$ level from both $^1D_2(\Gamma_3\gamma_1)$ and $^3P_0(\Gamma_1\gamma_1)$ levels at 14639 cm^{-1} and 532.73 nm respectively. A very strong π-polarised $D_2(\Gamma_3\gamma_1) \longrightarrow Y_2(\Gamma_3\gamma_1)$ transition is apparent at 14617 cm^{-1} but the corresponding transition from $^3P_0(\Gamma_1\gamma_1)$ appears to be nonexistent in Fig IV.3.4(b). This line from $^3P_0$ was also very weak in the spectrum for the C_{4v} F^- site in $SrF_2:Pr^{3+}$. Transitions to the $Y_3(\Gamma_4^{(1)}\gamma_5)$ level are observed from the $^3P_0(\Gamma_1\gamma_1)$, $D_2(\Gamma_3\gamma_3)$ and $D_1(\Gamma_3\gamma_1)$ levels at 535.10 nm, 14575 and 14558 cm^{-1} respectively, in σ-polarisation for those originating from $^1D_2$. An assignment of the Y_4 level energy is made from the observation of the $D_2(\Gamma_3\gamma_3) \longrightarrow Y_4(\Gamma_3\gamma_3)$ transition at 14521 cm^{-1} in the expected π-polarisation.

The broad feature centred at 14438 cm^{-1} is σ-polarised and contains transitions to the $Y_5(\Gamma_4^{(2)}\gamma_5)$ level from both D_1 and D_2 components of $^1D_2$. The spectral line from $^3P_0$ appears asymmetrical but peaks at 538.81 nm corresponding to the same energy interval as the $D_1 \longrightarrow Y_5$ line. Further structure apparent around 14390 cm^{-1} in Fig.IV.3.4(a) and 540 nm in Fig.IV.3.4(b) has no electronic origin, but may originate from transitions to vibronic levels associated with lattice phonons.

Not visible in Figure IV.3.4(a) but present in (b), is the transition to the $Y_7(\Gamma_5\gamma_5)$ level. The $^3P_0(\Gamma_1\gamma_1) \longrightarrow Y_7(\Gamma_5\gamma_5)$ wavelength of 548.80 nm would place the $^1D_2(\Gamma_3\gamma_1) \longrightarrow Y_7(\Gamma_5\gamma_5)$ transition close to the sharp line at 14099 cm^{-1}. This line is attributed to the $(4f^5 5d)$ $A_{1u} \longrightarrow (4f^6)^7F_0$ transition of the Sm^{2+} ion in this host crystal (Feofilov & Kaplyanskii [1961], Kaiser et al [1961]). The excitation of the Sm^{2+} ion involves the same mechanism as that proposed earlier,

Spectral data for the crystal field levels of the $^3H_5$ multiplet for the C_{4v} F^- site in $CaF_2:Pr^{3+}$.

Transition	Frequency ($\pm$ 1cm^{-1})	Polarisation Observed	Predicted
$D_1(\Gamma_3\gamma_1) \longrightarrow Y_1(\Gamma_4{}^1\gamma_2)$	14639	π'(md)[1]	π'(md)
$D_1 \longrightarrow Y_2(\Gamma_3\gamma_1)$	14617	π	π
$D_2(\Gamma_3\gamma_3) \longrightarrow Y_3(\Gamma_4{}^1\gamma_5)$	14575	σ	σ
$D_1 \longrightarrow Y_3(\Gamma_4{}^1\gamma_5)$	14558	σ	σ
$D_2 \longrightarrow Y_4(\Gamma_3\gamma_3)$	14521	π	π
$D_2 \longrightarrow Y_5(\Gamma_4{}^2\gamma_5)$	14447 [2]	σ	σ
$D_1 \longrightarrow Y_5(\Gamma_4{}^2\gamma_5)$	14429 [2]	σ	σ
	Air Wavelength ($\pm$ 0.05 nm)		
$^3P_0(\Gamma_1\gamma_1) \longrightarrow Y_1(\Gamma_4{}^1\gamma_2)$	532.73	- [3]	π'(md)
$\longrightarrow Y_3(\Gamma_4{}^1\gamma_5)$	535.10	-	σ
$\longrightarrow Y_5(\Gamma_4{}^2\gamma_5)$	538.81	-	σ
$\longrightarrow Y_7(\Gamma_5\gamma_6)$	548.80	-	σ

$^3H_5$ Energy Levels ($\pm$ 1cm^{-1})	
$Y_1(\Gamma_4{}^1\gamma_2)$	: 2189
$Y_2(\Gamma_3\gamma_1)$	: 2211
$Y_3(\Gamma_4{}^1\gamma_5)$	: 2270
$Y_4(\Gamma_3\gamma_3)$	: 2324
$Y_5(\Gamma_4{}^2\gamma_5)$	: 2399 [2]
$Y_6(\Gamma_4{}^2\gamma_2)$	: -
$Y_7(\Gamma_5\gamma_5)$	: 2738
$Y_8(\Gamma_5\gamma_4)$	: -

[1] x(yy)z:x(yx)z polarisation ratio of 1:0 associated with a π'-polarised magnetic dipole transition.

[2] Broad line containing unassigned structure.

[3] Polarised spectra not recorded for $^3P_0 \longrightarrow {}^3H_5$ emission.

i.e. excitation through the broad absorption band of Sm^{2+} in the same region as the sharp $^3H_4 \longrightarrow {}^1D_2$ Pr^{3+} transitions. Discrimination of the Pr^{3+} emission against the Sm^{2+} emission could be achieved in the time domain by using the fast 2 μsec lifetime of the Sm^{2+} fluorescence (Kaiser et al [1961]).

The $^3H_6$ Multiplet

The energy level scheme for the $^3H_6$ multiplet summarised in Table IV.3.4 was established using the fluorescence spectra from the $^1D_2$ and $^3P_0$ levels shown in Figure IV.3.5. Of the ten crystal field levels for the $^3H_6$ multiplet in C_{4v} point group symmetry, transitions to only five will be allowed by electric dipole radiation from the $^1D_2(\Gamma_3\gamma_1)$ and $^3P_0(\Gamma_1\gamma_1)$ emitting levels and four of these have been identified. The σ-polarised lines at 12623 cm^{-1}, 12320 cm^{-1} and 11859 cm^{-1} and the π-polarised spectral line at 11932 cm^{-1} are the transitions from the $D_1(\Gamma_3\gamma_1)$ level to the $X_1(\Gamma_5{}^{(1)}\gamma_5)$, $X_4(\Gamma_4{}^{(1)}\gamma_5)$, $X_9(\Gamma_5{}^{(2)}\gamma_5)$ and $X_8(\Gamma_3\gamma_1)$ states respectively. The fifth allowed transition to the $X_3(\Gamma_1\gamma_1)$ state is hidden by the broad structure centred around 12360 cm^{-1}. This band consists of transitions to vibronic levels formed from the coupling of lattice phonons to the $X_1(\Gamma_5{}^{(1)}\gamma_5)$ level, and is the mirror image of the phonon band observed in the excitation spectrum. As will become apparent later, a band of this type appears in this region for all the C_{4v} sites studied including the hydrogenic centres.

The $^3F_2$ Multiplet

Fluorescence transitions to three of the four crystal field levels of the $^3F_2$ multiplet have been observed for this site. Figure IV.3.6 shows the fluorescence spectra to the $^3F_2$ levels from the $^1D_2$ and $^3P_0$

Table IV.3.4

Spectral data for the crystal field levels of the $^3H_6$ multiplet for the C_{4v} F^- site in $CaF_2:Pr^{3+}$.

Transition	Frequency ($\pm$ 1cm^{-1})	Polarisation Observed	Predicted
$D_2(\Gamma_3\gamma_3) \longrightarrow X_1(\Gamma_5{}^1\gamma_5)$	12640	σ	σ
$D_1(\Gamma_3\gamma_1) \longrightarrow X_1(\Gamma_5{}^1\gamma_5)$	12623	σ	σ
$D_1 \longrightarrow X_3(\Gamma_1\gamma_1)$	12360 $\pm$ 10 [1]	π	π
$D_1 \longrightarrow X_4(\Gamma_4\gamma_5)$	12320	σ	σ
$D_1 \longrightarrow X_8(\Gamma_3\gamma_1)$	11932	π	π
$D_2 \longrightarrow X_9(\Gamma_5{}^2\gamma_5)$	11874	σ	σ
$D_1 \longrightarrow X_9(\Gamma_5{}^1\gamma_5)$	11859	σ	σ
	Air Wavelength ($\pm$ 0.05 nm)		
$^3P_0(\Gamma_1\gamma_1) \longrightarrow X_1(\Gamma_5{}^1\gamma_5)$	596.97	- [2]	σ
$\longrightarrow X_3(\Gamma_1\gamma_1)$	606.5 $\pm$ .1 [1]	-	π
$\longrightarrow X_4(\Gamma_4\gamma_5)$	608.06	-	σ
$\longrightarrow X_8(\Gamma_3\gamma_1)$	639.98	-	π
$\longrightarrow X_9(\Gamma_5{}^2\gamma_5)$	625.43	-	σ

$^3H_6$ Energy Levels ($\pm$ 1cm^{-1})

$X_1(\Gamma_5{}^1\gamma_5)$	: 4205
$X_2(\Gamma_5{}^1\gamma_4)$	: -
$X_3(\Gamma_1\gamma_1)$	: 4468 $\pm$ 10
$X_4(\Gamma_4\gamma_5)$	: 4508
$X_5(\Gamma_4\gamma_2)$	: -
$X_6(\Gamma_3\gamma_3)$	: -
$X_7(\Gamma_5{}^2\gamma_4)$	: -
$X_8(\Gamma_3\gamma_1)$	: 4896
$X_9(\Gamma_5{}^2\gamma_5)$	: 4954
$X_{10}(\Gamma_2\gamma_3)$	: -

[1] Broad line containing structure.

[2] Polarised spectra not recorded for $^3P_0 \longrightarrow {}^3H_6$ emission.

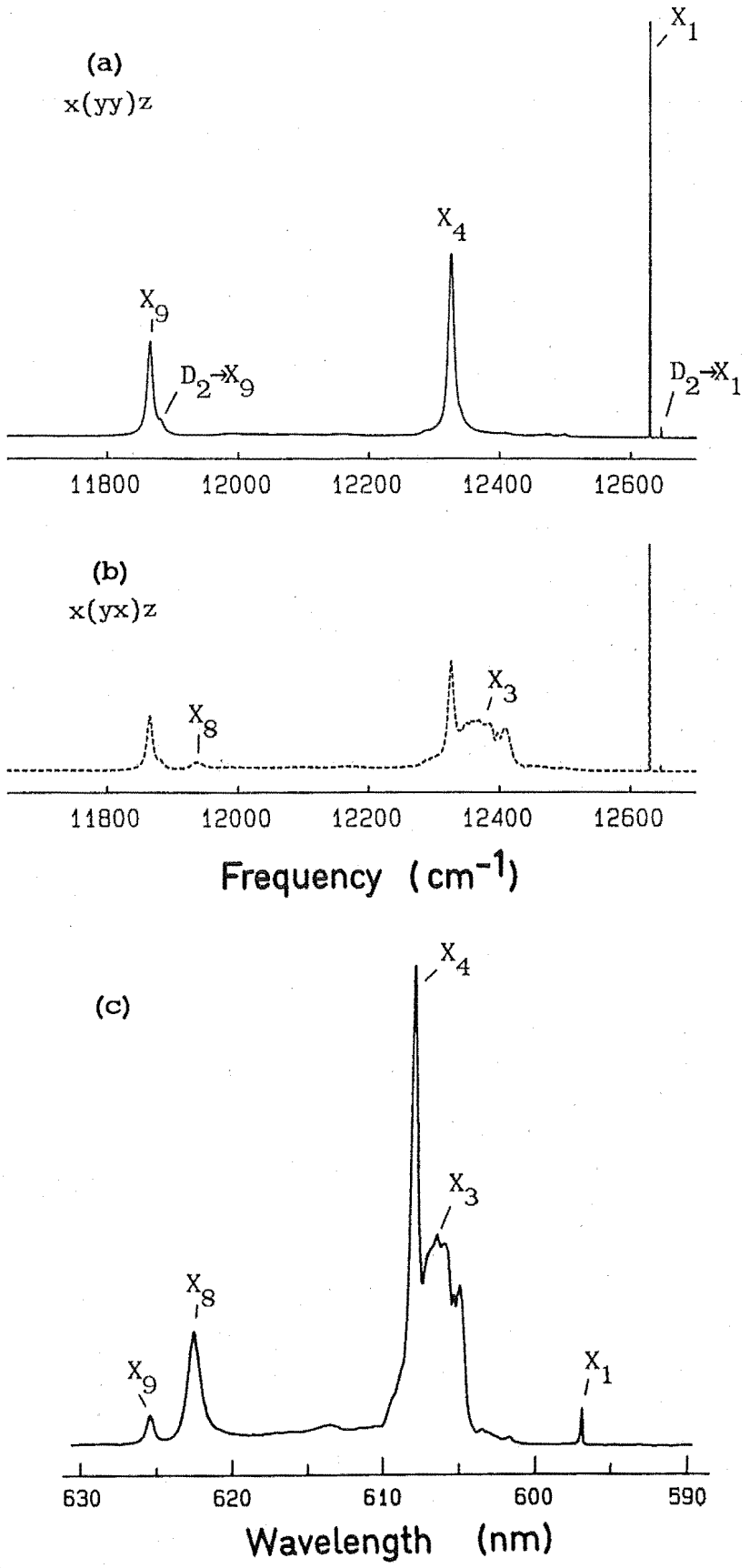

Figure IV.3.5 (a) and (b) polarised $^1D_2 \rightarrow {}^3H_6$ emission and (c) $^3P_0 \rightarrow {}^3H_6$ emission for the C_{4v} F^- site in $CaF_2:Pr^{3+}$ at 14K.

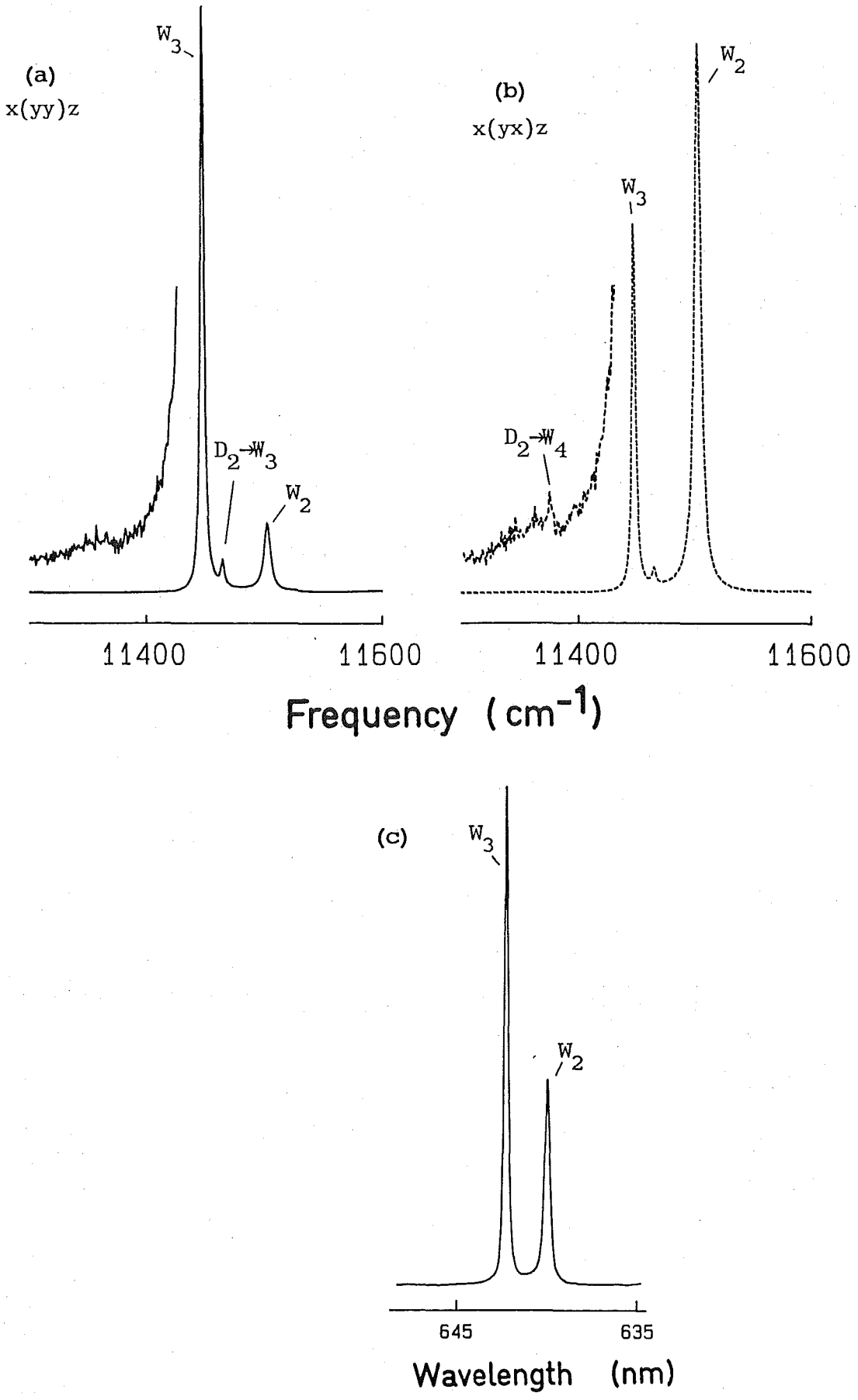

Figure IV.3.6 (a) and (b) polarised $^1D_2 \rightarrow {}^3F_2$ emission and (c) $^3P_0 \rightarrow {}^3F_2$ emission for the C_{4v} F^- site in $CaF_2:Pr^{3+}$ at 14K.

multiplets. The energy level scheme and those transitions observed are summarised in Table IV.3.5.

Electric dipole transitions are expected and have been observed from $D_1(\Gamma_3\gamma_1)$ and $^3P_0(\Gamma_1\gamma_1)$ to the $U_2(\Gamma_3\gamma_1)$ and $U_3(\Gamma_5\gamma_5)$ levels of $^3F_2$. The x(yy)z:x(yx)z polarisation ratios of 0:1 and 2:1 for the transitions to the U_2 and U_3 levels respectively, are appropriate for π and σ-polarised transitions and identify the level symmetries. An electric dipole transition from $D_2(\Gamma_3\gamma_3)$ to $U_4(\Gamma_3\gamma_3)$ is allowed but is expected to be weak from this thermally populated level, however a line with the required π-polarisation is observed at 11367 cm^{-1}.

The $^3F_3$ and $^3F_4$ Multiplets

Emission from $^1D_2$ and $^3P_0$ multiplets to the crystal field levels of the $^3F_3$ and $^3F_4$ multiplets is shown in Figure IV.3.7 for the C_{4v} F^- site in $CaF_2:Pr^{3+}$. The fluorescence from $^3P_0$ was obtained by using the 457.9 nm line of the argon ion laser to indirectly excite the $^3P_0$ level of this site. As a result emission lines from other centres are apparent in Fig.IV.3.7(c) as Pr^{3+} ions in other sites are also excited.

The unusual situation arises of having a complete energy level scheme for the $^3F_3$ multiplet as transitions are observed to all crystal field levels. Table IV.3.6 summarises those transitions observed and details the energy level scheme. Magnetic dipole transitions are allowed, and have been observed, to the $V_2(\Gamma_5\gamma_4)$ and $V_3(\Gamma_4\gamma_2)$ levels from $D_2(\Gamma_3\gamma_4)$ and $D_1(\Gamma_3\gamma_1)$ respectively. These lines have a x(yy)z:x(yx)z polarisation ratio of 1:0 associated with a π-polarised transition. At this point it is interesting to compare the spectra in Fig.IV.3.7 with those in Fig.IV.2.8 showing the corresponding transitions for the C_{4v} F^- site in $SrF_2:Pr^{3+}$. The relative intensities of these two magnetic dipole transitions show

Table IV.3.5

Spectral data for the crystal field levels of the $^3F_2$ multiplet for the C_{4v} F^- site in $CaF_2:Pr^{3+}$.

Transition	Frequency (± 1 cm^{-1})	Polarisation Observed	Predicted
$D_1(\Gamma_3\gamma_1) \longrightarrow U_2(\Gamma_3\gamma_1)$	11496	π	π
$D_2(\Gamma_3\gamma_3) \longrightarrow U_3(\Gamma_5\gamma_5)$	11458	σ	σ
$D_1 \longrightarrow U_3(\Gamma_5\gamma_5)$	11441	σ	σ
$D_2 \longrightarrow U_4(\Gamma_3\gamma_3)$	11367	π	π
	Air Wavelength (± 0.02 nm)		
$^3P_0(\Gamma_1\gamma_1) \longrightarrow U_2(\Gamma_3\gamma_1)$	639.98	- [1]	π
$\longrightarrow U_3(\Gamma_5\gamma_5)$	642.32	-	σ

$^3F_2$ Energy Levels (± 1cm^{-1})	
$U_1(\Gamma_5\gamma_4)$:	-
$U_2(\Gamma_3\gamma_1)$:	5332
$U_3(\Gamma_5\gamma_5)$:	5387
$U_4(\Gamma_3\gamma_3)$:	5478 ± 2

[1] Polarised $^3P_0 \longrightarrow {}^3F_2$ emission was not recorded.

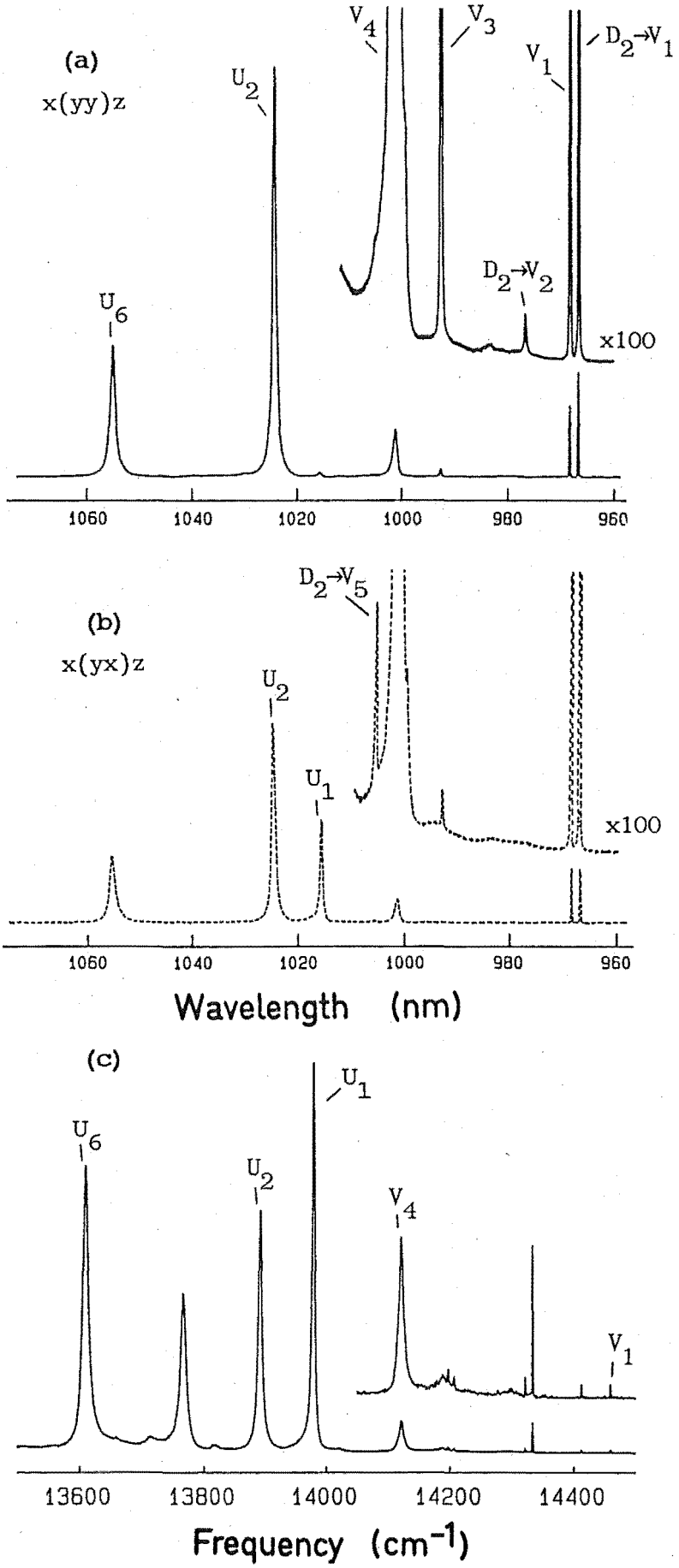

Figure IV.3.7 (a) and (b) polarised $^1D_2 \rightarrow {}^3F_3$, $^3F_4$ emission and (c) $^3P_0 \rightarrow {}^3F_3$, $^3F_4$ emission for the C_{4v} F^- site in $CaF_2:Pr^{3+}$ at 14K.

Table IV.3.6

Spectral data for the crystal field levels of the $^3F_3$ multiplet for the C_{4v} F^- site in $CaF_2:Pr^{3+}$.

Transition	Air Wavelength (± 0.2 nm)	Polarisation Observed	Polarisation Predicted
$D_2(\Gamma_3\gamma_3) \longrightarrow V_1(\Gamma_5\gamma_5)$	966.3	σ	σ
$D_1(\Gamma_3\gamma_1) \longrightarrow V_1(\Gamma_5\gamma_5)$	967.9	σ	σ
$D_2 \longrightarrow V_2(\Gamma_5\gamma_4)$	976.4	π'(md) [1]	π'(md)
$D_1 \longrightarrow V_3(\Gamma_4\gamma_2)$	992.3	π'(md) [1]	π'(md)
$D_2 \longrightarrow V_4(\Gamma_4\gamma_5)$	999.2	σ	σ
$D_1 \longrightarrow V_4(\Gamma_4\gamma_5)$	1000.8	σ	σ
$D_2 \longrightarrow V_5(\Gamma_2\gamma_3)$	1005.1	π	π
	Frequency (± 1 cm^{-1})		
$^3P_0(\Gamma_1\gamma_1) \longrightarrow V_1(\Gamma_5\gamma_5)$	14459	- [2]	σ
$\longrightarrow V_4(\Gamma_4\gamma_5)$	14119	-	σ

$^3F_3$ Energy Levels (± 1cm^{-1})
$V_1(\Gamma_5\gamma_5)$: 6500
$V_2(\Gamma_5\gamma_4)$: 6607
$V_3(\Gamma_4\gamma_2)$: 6754
$V_4(\Gamma_4\gamma_5)$: 6840
$V_5(\Gamma_2\gamma_3)$: 6900

[1] x(yy)z:x(yx)z polarisation ratio of 1:0 associated with a π-polarised magnetic dipole transition.

[2] Polarised spectra not recorded for $^3P_0 \longrightarrow {}^3F_3$ emission.

considerable differences. The transition to $V_2(\Gamma_5\gamma_4)$ is symmetry allowed from $^1D_2(\Gamma_3\gamma_3)$ which is the D_1 level for the site in $SrF_2:Pr^{3+}$. The line in $CaF_2:Pr^{3+}$ is much weaker as the emitting level, D_2, is not directly excited but thermally populated only. The transitions to $V_3(\Gamma_4\gamma_2)$ show the opposite behaviour, being stronger in $CaF_2:Pr^{3+}$ where the lower D_1 emitting level has the appropriate symmetry. These differences provide unequivocal evidence that the D_1 levels in the C_{4v} F^- site in $CaF_2:Pr^{3+}$ and $SrF_2:Pr^{3+}$ have a different symmetry. Additional support is provided by the transitions to the $V_5(\Gamma_2\gamma_3)$ level where the emitting level in $SrF_2:Pr^{3+}$ is $D_1(\Gamma_3\gamma_3)$ and the line is relatively stronger.

Energies can be assigned to only four crystal field levels of the $^3F_4$ multiplet. Those lines observed correspond to electric dipole transitions from $D_1(\Gamma_3\gamma_1)$ and $^3P_0(\Gamma_1\gamma_1)$. The energy level scheme is summarised in Table IV.3.7. The assignment of the $U_7(\Gamma_1\gamma_1)$ level requires some comment. Based on the experience with the C_{4v} F^- site in $SrF_2:Pr^{3+}$ and the hydrogenic C_{4v} sites in $CaF_2:Pr^{3+}$ to follow, a strong π-polarised transition is expected to this level from $^3P_0(\Gamma_1\gamma_1)$. As no line is observed, there may be overlap with the transition to the $U_6(\Gamma_4\gamma_5)$ level and a tentative assignment is made with these two levels having equal energy.

IV.4 Crystal Field Parameterisation for Pr^{3+} Ions in the C_{4v} Sites

Despite having a comprehensive set of experimental energy levels a crystal field analysis of the C_{4v} sites in $SrF_2:Pr^{3+}$ and $CaF_2:Pr^{3+}$ crystals has not been spectacularly successful. Various degrees of complexity were tried, starting from the analysis of a single multiplet and culminating in the diagonalisation of the 91x91 matrix

Table IV.3.7

Spectral data for the crystal field levels of the $^3F_4$ multiplet for the C_{4v} F^- site in $CaF_2:Pr^{3+}$.

Transition	Air Wavelength (± 0.2 nm)	Polarisation Observed	Polarisation Predicted
$D_1(\Gamma_3\gamma_1) \longrightarrow U_1(\Gamma_3\gamma_1)$	1015.2	π	π
$\longrightarrow U_2(\Gamma_5\gamma_5)$	1024.4	σ	σ
$\longrightarrow U_6(\Gamma_4\gamma_5)$	1054.8	σ	σ
	Frequency(±1cm^{-1})		
$^3P_0(\Gamma_1\gamma_1) \longrightarrow U_1(\Gamma_3\gamma_1)$	13974	- [1]	π
$\longrightarrow U_2(\Gamma_5\gamma_5)$	13886	-	σ
$\longrightarrow U_6(\Gamma_4\gamma_5)$	13604	-	σ

$^3F_4$ Energy Levels (± 1cm^{-1})

$U_1(\Gamma_3\gamma_1)$	6980
$U_2(\Gamma_5\gamma_5)$	7068
$U_3(\Gamma_5\gamma_4)$	-
$U_4(\Gamma_4\gamma_2)$	-
$U_5(\Gamma_3\gamma_3)$	-
$U_6(\Gamma_4\gamma_5)$	7350
$U_7(\Gamma_1\gamma_1)$	7350 ± 10 [2]

[1] Polarised spectra for $^3P_0 \longrightarrow {}^3F_4$ emission was not recorded.

[2] Tentative assignment (refer to text).

representing all the electronic states of the f^2 configuration. Interactions included in this matrix were discussed in Chapter II, and are the electrostatic repulsion, spin-orbit interaction, configuration mixing and the crystal field.

Initial attempts concentrated on the 33 states of the $^3H_4$, $^3H_5$ and $^3H_6$ multiplets. Problems associated with this approach centred on the close proximity of the ^3F multiplets and the large degree of mixing to the $^3H_4$ states from $^3F_4$ and $^1G_4$. An intermediate coupling calculation subsequently found the $^3H_4$, $^3F_4$ and $^1G_4$ multiplets to be 95%, 72% and 70% pure respectively. The strong mixing between the $^3F_4$ and $^1G_4$ multiplets arises from their small energy separation, being only 3000 cm^{-1} apart. As a large number of levels had been measured, it was considered that the easiest method of including the perturbing effects described above was to construct the matrix for all the states of the configuration, considering that with a dimension of 91 the size was still reasonable.

Before including the crystal field splitting, it was necessary to determine the free ion parameters. A least squares program was written to fit the 10 experimentally determined centres of gravity for the C_{4v} F^- site in $SrF_2:Pr^{3+}$. It was found that the configuration mixing interaction had to be included to obtain the correct ordering of the multiplets. The crystal field interaction was then included and the 91x91 matrix diagonalised to yield the calculated energy level scheme. This scheme was then least squares fitted to the 49 experimentally determined crystal field levels. As part of the fitting routine the calculated levels were identified with $|SLJJ_z\rangle$ wavefunctions having a particular symmetry in the C_{4v} group and these were constrained to maintain their correct ordering relative to the experimental data. The results are summarised in Table IV.4.1.

Table IV.4.1

Free Ion and Crystal Field Parameters determined for the C_{4v} F^- site in $SrF_2:Pr^{3+}$.

Electrostatic Parameters	E^1	=	4581.6 cm^{-1}
	E^2	=	22.11 cm^{-1}
	E^3	=	471.97 cm^{-1}
Spin-Orbit	ξ	=	736.76 cm^{-1}
Configuration Mixing Parameters	α	=	23.10 cm^{-1}
	β	=	-904.55 cm^{-1}
	γ	=	1625.4 cm^{-1}
Crystal Field Parameters	B_0^2	=	430.3 cm^{-1}
	B_0^4	=	1569 cm^{-1}
	B_0^6	=	681.2 cm^{-1}
	B_c^4	=	-2546 cm^{-1}
	B_c^6	=	478.4 cm^{-1}
Deviation	σ	=	69 cm^{-1}

The parameters determined compare favourably with the results obtained for other systems. Similar free ion parameters were obtained by Carnall et al [1968] for the Pr^{3+} ion in LaF_3. Also, the crystal field parameters determined here are similar to those obtained for a number of rare-earth ions in CaF_2 and SrF_2 crystals (Freeth and Jones [1982]).

While a deviation of 69 cm^{-1} does not appear unreasonable given that 49 energy levels are being fitted, deviations of some individual levels were as large as 130 cm^{-1}. Comparison with other systems shows

that the results are consistent, however a degree of caution should be maintained. Investigations are continuing on the other C_{4v} Pr^{3+} sites and to isolate the reasons for some of these large individual deviations.

CHAPTER V

OPTICAL SPECTROSCOPY OF THE TETRAGONAL SITE IN HYDROGENATED SrF_2 AND CaF_2 CRYSTALS CONTAINING PRASEODYMIUM

In Chapter IV the spectroscopy of the Pr^{3+} ion charge compensated by an interstitial ion in the tetragonal symmetry site was described for SrF_2 and CaF_2 crystals. It is well known that H^- ions, or corresponding isotopes D^- and T^-, can be introduced into these fluorite crystals to participate in the charge compensation process for any rare-earth ions present. In Pr^{3+} doped crystals the major role of the H^- ions in this process is the simple substitution of the interstitial F^- ion of the C_{4v} site to produce the corresponding H^- C_{4v} site. In these hydrogenic ion sites, additional effects arise from the high frequency localised modes of vibration of the light H^- ion coupling to the Pr^{3+} electronic system through the electron-phonon interaction. Extra sharp lines appear in the optical spectra that are transitions to local mode vibronic levels. These lines appear at energy intervals from their parent electronic transition corresponding to the local mode phonon frequency and are typically 1% of the intensity of the parent line. Other manifestations of the electron-local mode phonon interaction are discussed in later chapters.

The C_{4v} H^- centre in $SrF_2:Pr^{3+}$ and $CaF_2:Pr^{3+}$ crystals was first observed by Jacobs [1971] using infrared absorption where the local modes of the H^- ion were identified. Optical transitions to the $^3P_0$ and $^3P_1$ levels for the C_{4v} H^- and D^- sites in $CaF_2:Pr^{3+}$ were observed,but transitions were not identified for these sites in $SrF_2:Pr^{3+}$. Fluorescence spectra recorded in this work have been used to identify the crystal field levels of the $^3H_{4,5,6}$ and $^3F_{2,3,4}$ multiplets for the C_{4v} sites in both $SrF_2:Pr^{3+}$ and $CaF_2:Pr^{3+}$ with H^-,

D^- and T^- charge compensating ions. In addition transitions have been observed to many local mode vibronic levels in these multiplets that identify the local mode frequencies for the H^-, D^- and T^- ions.

This chapter is divided into two sections corresponding to hydrogenic sites in $SrF_2:Pr^{3+}$ or $CaF_2:Pr^{3+}$ crystals. Subsections within these parts describe the spectra associated with, firstly absorption transitions and secondly fluorescence transitions. The emission spectra are described on a multiplet by multiplet basis and the energy level schemes are summarised in this manner.

V.1 The C_{4v} Hydrogenic Sites in $SrF_2:Pr^{3+}$

V.1.1 Absorption and Excitation of the C_{4v} Hydrogenic Sites in $SrF_2:Pr^{3+}$

Absorption transitions to the $^1D_2$, $^3P_0$ and $^3P_1$ multiplets were recorded in $SrF_2:Pr^{3+}:H^-$ and $SrF_2:Pr^{3+}:D^-$ crystals. Samples containing tritium ions were not studied in absorption due to the small number of T^- ions contained in the particular crystals available. Comparison of the absorption spectrum from a hydrogenated crystal with the spectrum of an untreated parent crystal shows a large number of new absorption lines, particularly in the $^3P_0$ region, that can be associated with sites containing hydrogenic ions. The assignment of a site as hydrogenic is based on the observation of an isotope shift of the Pr^{3+} ion electronic transitions in crystals containing different hydrogen isotopes and by the observation of local mode vibronic lines in the emission spectra of the site. Figures V.1.1(a) and (b) show the absorption transitions to the $^3P_0$ and $^3P_1$ and the $^1D_2$ levels respectively for a SrF_2:0.05%$Pr^{3+}:H^-$ crystal, recorded at 14 K.

Transitions to the $^3P_0$ and $^3P_1$ levels of the Pr^{3+} ion identified by Jacobs [1971] have been indicated in Figure V.1.1(a). The C_{4v} H^-

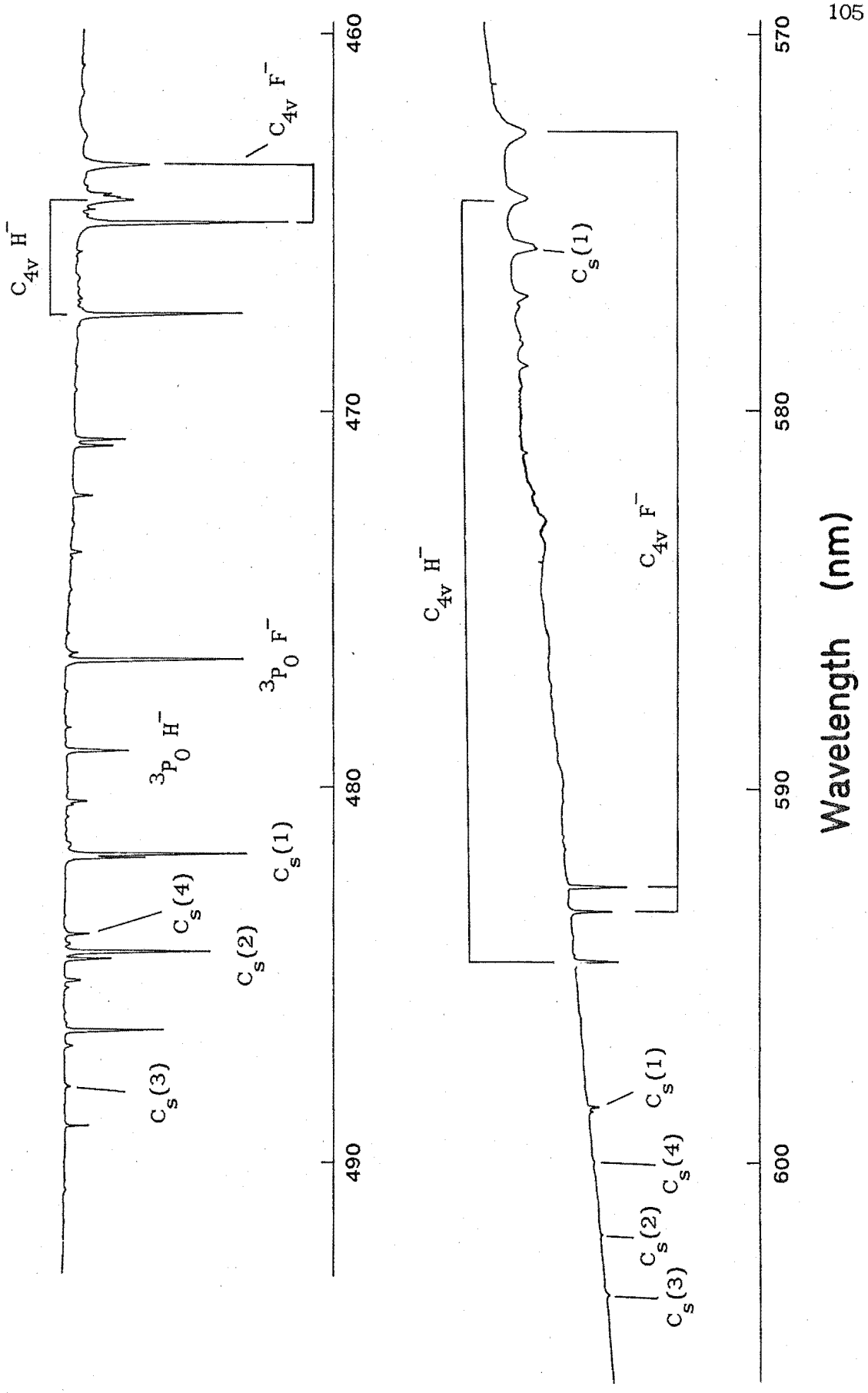

Figure V.1.1 Optical absorption of the crystal field levels of the (a) $^3P_0$ and $^3P_1$ and (b) $^1D_2$ multiplets recorded at 14K for a hydrogenated $SrF_2:Pr^{3+}$ crystal.

site is identified as the major hydrogenic site in the spectrum of absorption to the $^1D_2$ multiplet (Figure V.1.1(b)). Confirmation that the transitions indicated belong to the C_{4v} H^- site was subsequently made by fluorescence studies. It is apparent from Figure V.1.1(a) showing the absorption to the $^3P_0$ multiplet, that there are a number of other centres containing hydrogenic ions. Some of these transitions belong to centres observed to contain multiple hydrogenic ions and these sites will be discussed in Chapter VI.

Absorption spectra recorded at higher temperatures to that at which Figure V.1.1 was recorded, show no evidence of transitions originating from a Z_2 level for the C_{4v} sites. The maximum temperature used of 85 K, places a lower limit of ~100 cm^{-1} on the Z_1-Z_2 splitting for this centre. Also absent from the $^1D_2$ absorption spectrum is the transition to the second crystal field component, i.e. the D_2 level, of this multiplet. Results that will be presented later concerning the C_{4v} H^- site in $CaF_2:Pr^{3+}:H^-$, show evidence of a weak $^3H_4(Z_1) \longrightarrow {}^1D_2(D_2)$ transition 36 cm^{-1} higher in energy than the $^3H_4(Z_1) \longrightarrow {}^1D_2(D_1)$ line. If this trend of a doubling in the D_1-D_2 splitting from C_{4v} F^- to C_{4v} H^- sites applies to the $SrF_2:Pr^{3+}:H^-$ system, then the D_2 level of the hydrogenic sites would nearly coincide with the D_1 level of the C_{4v} F^- site making its observation difficult.

Table V.1.1 summarises the absorption transitions for the C_{4v} H^- and D^- sites in $SrF_2:Pr^{3+}$. The value for the C_{4v} T^- site also included was determined from laser excitation studies.

Table V.1.1

Wavelengths of absorption transitions, recorded at 14 K, for the C_{4v} hydrogenic charge compensation ion sites in SrF_2:0.05%Pr^{3+} crystals.

Crystal Field Level		Charge Compensating Ion Isotope		
		H^-	D^-	T^-
$^1D_2$	D_1	594.55 nm	594.55 nm	594.54 nm
	D_4	574.3 nm	574.4 nm	
$^3P_0$	$\Gamma_1\gamma_1$	478.94 nm	479.00 nm	
$^3P_1$	$\Gamma_4\gamma_5$	467.32 nm	467.45 nm	
	$\Gamma_2\gamma_2$	464.30 nm	464.23 nm	

The absorption from the $^3H_4$ multiplet to the $^1D_2$ levels is spin forbidden and the spectra from $SrF_2:Pr^{3+}:H^-$ crystals do not show the wide diversity of sites shown in the $^3P_0$ region. By having a considerably greater sensitivity, laser excitation enhances the underlying features and illustrates the richness of the spectra. Figure V.1.2 of the $^1D_2$ zero order excitation spectrum of a $SrF_2:Pr^{3+}:D^-$ crystal, shows the multitude of sites expected from the $^3P_0$ absorption. Excitation spectra of the C_{4v} site was recorded by tuning the spectrometer to a specific fluorescence transition of this site. Figure V.1.3 shows a typical spectrum with the D_1 and D_4 crystal field levels indicated. In common with the C_{4v} F^- site a number of phonon bands are apparent. The frequencies of the lines in this band and their energy interval from the D_1 crystal field level are tabulated in Table V.1.2.

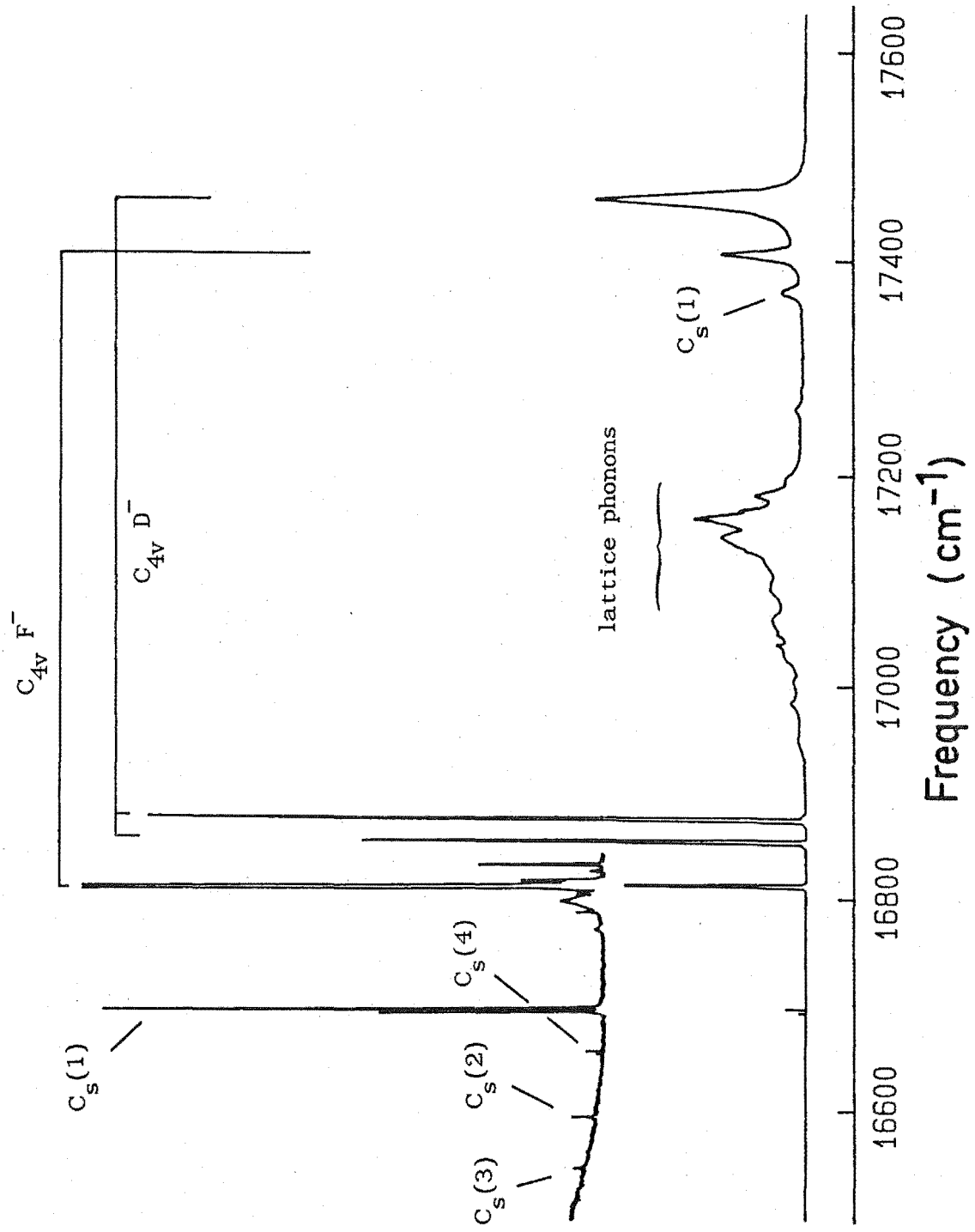

Figure V.1.2 Broadband laser excitation spectrum of the $^1D_2$ region for a SrF_2:0.05%Pr^{3+}:D^- crystal showing transitions of the F^- and D^- C_{4v} sites and several rhombic symmetry sites also containing D^- ions.

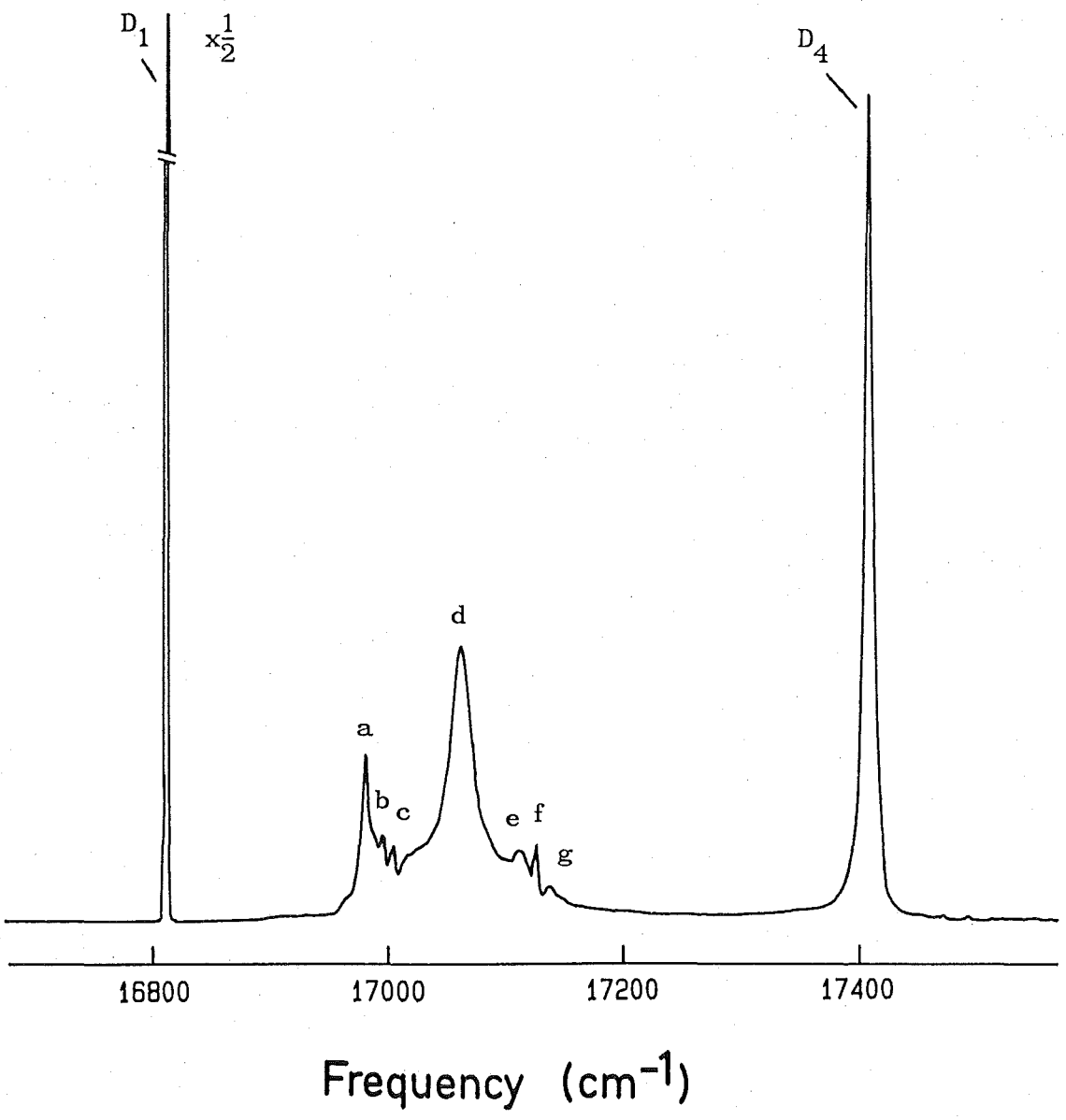

Figure V.1.3 14K $^1D_2$ excitation spectrum of the C_{4v} D^- site in $SrF_2:Pr^{3+}:D^-$ showing the electronic transtitions D_1 and D_4 and lattice phonon vibronic lines labelled a-g.

Table V.1.2

$^1D_2$ excitation lines for the C_{4v} D^- site in $SrF_2:Pr^{3+}$ shown in Figure V.1.3. The crystal temperature was 14 K

Label	Line Frequency ($\pm$ .5 cm^{-1})	Interval from $^1D_2(D_1)$ ($\pm$ .5 cm^{-1})
D_1	16815.2	0
a	16980.4	165.2
b	16992.2	177.0
c	17001.7	186.5
d	17058.7	243.5
e	17106.2	291.0
f	17118.4	303.2
g	17133.0	317.8
D_4	17411.9	596.7

Additional information is available from polarised excitation spectra. Figures V.1.4(a) and (b) show the C_{4v} D^- site excitation spectra, for the two polarisation geometries x(yy)z and x(yx)z in a <100> oriented crystal, when monitoring the π-polarised $^1D_2(D_1) \longrightarrow {}^3H_5(\Gamma_3\gamma_1)$ transition at 14616 cm^{-1}. Similar spectra are shown in Figures V.1.5(a) and (b) where the σ-polarised $^1D_2(D_1) \longrightarrow {}^3H_5(\Gamma_4\gamma_5)$ transition at 14579 cm^{-1} was monitored. From the two figures it is clear that the polarisation behaviour of the D_1 and D_4 crystal field levels differs from that of the lines in the phonon band. When monitoring the π-polarised transition, the D_1 and D_4 components show a close to 0:1 ratio for the $x(\overset{y}{\wedge})z:x(\overset{x}{\wedge})z$ polarisation geometries in contrast to the 1:0 ratio of the phonon band. The polarisation is not perfectly clean as there is a small polarisation breakthrough in the monitored transition. Alternatively monitoring the σ-polarised transition the polarisation ratio x(yy)z:x(yx)z is 2:1 for the D_1 and D_4 lines but 0:1 for the phonon band.

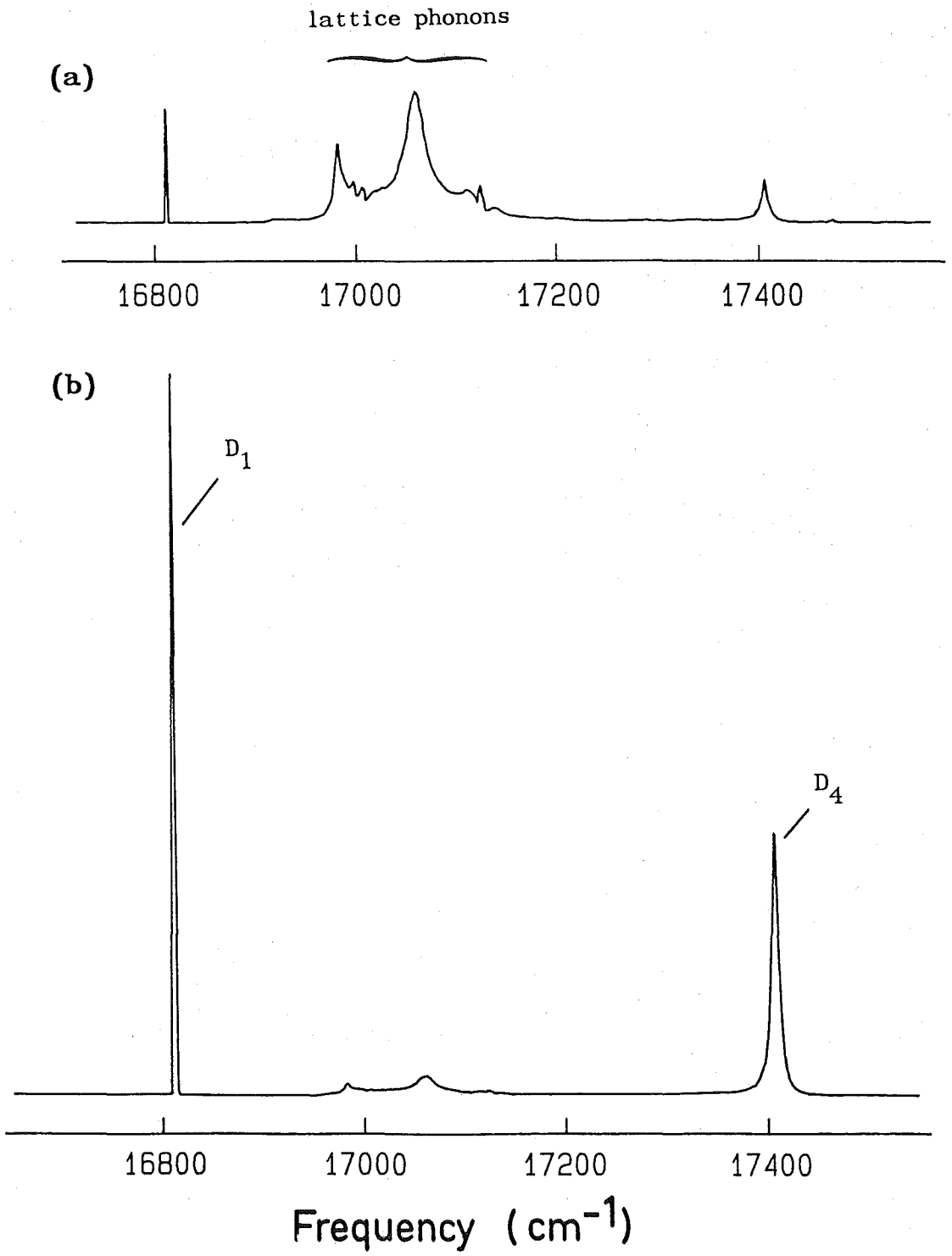

Figure V.1.4 Polarised $^1D_2$ excitation spectra for the C_{4v} D^- site in a <100> oriented $SrF_2:Pr^{3+}:D^-$ crystal in the (a) x(yy)z and (b) x(yx)z polarisation geometries. The $^1D_2(D_1)\rightarrow{}^3H_5(\Gamma_3\gamma_1)$ transition being monitored at 14616 cm^{-1} has π-polarisation.

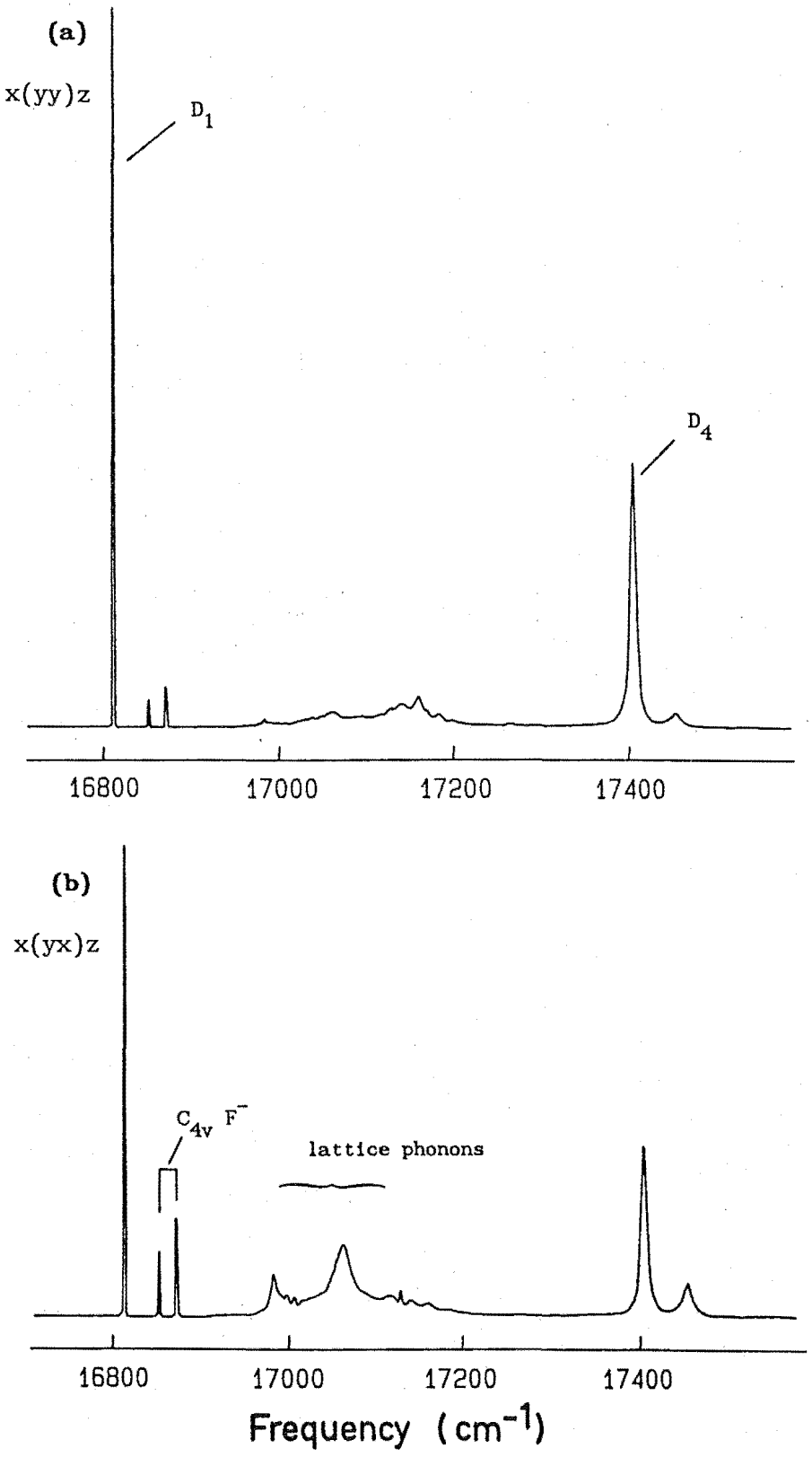

Figure V.1.5 Polarised $^1D_2$ excitation spectra for the C_{4v} D^- site in a <100> oriented $SrF_2:Pr^{3+}:D^-$ crystal recorded when monitoring the σ-polarised $^1D_2(D_1) \rightarrow {}^3H_5(\Gamma_4{}^7\gamma_5)$ transition at 14579 cm^{-1}.

These results can be understood by analysing the polarisation absorption and selection rules for these C_{4v} sites. The three orthogonal orientations of the C_{4v} site, as defined by their C_4 axes can be labelled in a similar way to the polarisation geometry, ie the orientation with its C_4 axis parallel to the x axis of the polarisation geometry can be labelled as the X orientation. Then with a laser propagation direction of x and polarisation plane of y , the two site orientations that absorb in σ-polarisation will be X and Z. Table V.1.3 summarises the absorption and emission rules for the two polarisation geometries shown in Figures V.1.4 and V.1.5.

Table V.1.3

Polarisation rules for the absorption and emission in the C_{4v} sites for the two polarisation geometries x(yx)z and x(yy)z in a <100> oriented crystal.

Polarisation of $^1D_2$ absorption transition	Polarisation of $^1D_2 \longrightarrow {}^3H_5$ emission line	X,Y,Z site orientations contributing to the emission for the polarisation geometries		Relative Intensity Ratio
		x(yx)z	x(yy)z	(yx):(yy)
σ	σ	Z	X,Z	1:2
	π	X	-	1:0
π	σ	Y	-	1:0
	π	-	Y	0:1

Using the rules from Table V.1.3 it can be concluded that the observed changes are consistent with the electronic transitions to D_1 and D_4 absorbing in σ-polarisation and the phonon band in π-polarisation. A crystal field analysis shows that D_1 must transform

as either a γ_1 or γ_3 irrep of C_{4v} and will absorb in σ-polarisation from the γ_5 symmetry ground state through the $\gamma_5(x,y)$ electric dipole operator. The D_4 crystal field component is expected to transform as a γ_4 irrep which will also absorb in σ-polarisation from the ground state.

The the D_3 crystal field level appears to be either masked by the phonon band or is one of the lines in the band. This level will transform as a γ_5 irrep of C_{4v} and will only absorb from the γ_5 symmetry ground state in π-polarisation through the $\gamma_1(z)$ electric dipole operator. The spectra show that all the lines comprising the phonon band absorb in π-polarisation hence an unequivocal assignment of D_3 cannot be made.

Apparent in Figure V.1.5 are the D_1 and D_2 excitation lines of the C_{4v} F^- site. These arise as the line being monitored at 14579 cm^{-1} has a slight overlap with the 14562 cm^{-1} $^1D_2 \longrightarrow {}^3H_5$ emission line of the C_{4v} F^- site. The opposite polarisation behaviour of the D^- and F^- site lines in Figures V.1.5(a) and (b) reflect the different polarisations of the monitored line; the 14579 cm^{-1} line of the D^- site and the 14562 cm^{-1} line of the F^- site being polarised σ and π respectively.

In an excitation spectrum of the C_{4v} D^- site recorded with an increased intensity scale, a number of lines are observed close to the D_4 crystal field level. Figures V.1.6(a) and (b) show the x(yy)z and x(yx)z polarised excitation spectra for this region in a <100> oriented crystal. The frequency interval from the D_1 crystal field level identifies the excitation lines at 17479.2 and 17501.8 cm^{-1} as being D^- ion local mode vibronic lines associated with the transverse (x,y) and longitudinal (z) local mode vibrations respectively. In a similar manner to emission, local mode vibronic lines can be observed in absorption, or excitation in this case, at energy intervals of the

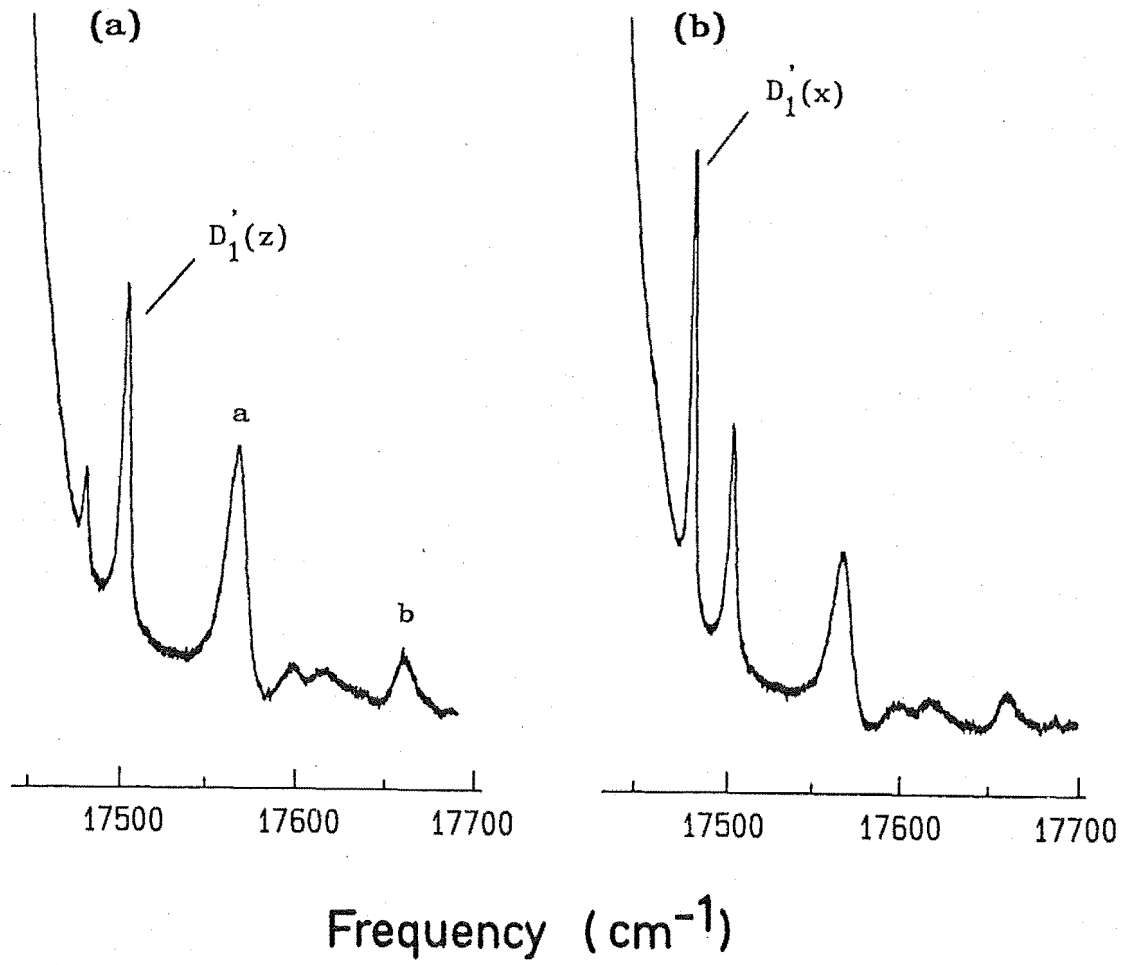

Figure V.1.6 Polarised excitation spectra of the C_{4v} D^- site in $SrF_2:Pr^{3+}:D^-$, showing transitions to vibronic levels associated with local mode vibrations coupled to the $^1D_2(D_1)$ level. The spectra are for the (a) x(yy)z and (b) x(yx)z polarisation geometries in a <100> oriented crystal.

vibrational frequencies from the parent electronic line. For absorption however, they appear at higher frequencies than the electronic line as necessary for the creation of a phonon. Also, since the local mode vibration is coupling to a different electronic wavefunction the vibrational frequencies may be different from those measured in emission.

The two vibronic lines at 17479.2 and 17501.8 cm^{-1} show polarisation effects which can be interpreted using similar arguments to those presented previously. Figure V.1.6 was recorded when monitoring the $^1D_2(D_1) \longrightarrow {}^3H_4(Z_1)$ transition at 16815.2 cm^{-1} known to have σ-polarisation. The polarisation changes of the vibronic levels can be predicted from the C_{4v} group multiplication rules. The transverse and longitudinal local modes transform as the γ_5 or γ_1 irrep of C_{4v} respectively and a crystal field analysis shows D_1 will transform as either the γ_1 or γ_3 irrep of the C_{4v} group. Then the C_{4v} group multiplication rules show the x,y vibronic level coupled to D_1 will transform as the γ_5 irrep and the z level as either the γ_1 or γ_3 irrep depending upon the symmetry of D_1. The absorption polarisations expected from a ground state having γ_5 symmetry are π for the x,y level and σ for the z level. Examination of Table V.1.3 predicts the x(yy)z:x(yx)z polarisation ratios to be 0:1 for the transverse (x,y) vibronic line and 2:1 for the longitudinal (z) vibronic line. These polarisation ratios are, in fact, observed for the two vibronic lines indicated in Figure V.1.6.

In addition to the D^- local mode vibronic lines a number of other lines are present in Figure V.1.6, the two most pronounced being at 17562 cm^{-1} and 17647 cm^{-1} labelled 'a' and 'b' respectively. The most likely origin of these lines concerns their energy shift from the D_4 electronic line. Individual lines in the phonon band previously described, are observed at intervals of 165 cm^{-1} and 244 cm^{-1} from D_1.

The lines at 17562 and 17647 cm^{-1} are shifted 150 and 235 cm^{-1} respectively from the D_4 transition and could be the same phonons shifted in frequency due to their coupling to a different electronic level.

Extending the range of the laser excitation spectrum into the 18100-18500 cm^{-1} region by using a green dye laser, reveals further structure. Figure V.1.7 shows the excitation spectrum in this region obtained when monitoring the $^1D_2(D_1) \longrightarrow {}^3H_4(Z_1)$ transition of the C_{4v} D^- site at 16815.2 cm^{-1}. Two lines immediately apparent at 18076 and 18088 cm^{-1} are vibronic lines associated with D^- ion local mode vibrations coupling to the D_4 electronic level. The frequency intervals are 664 cm^{-1} and 676 cm^{-1} for the transverse (x,y) and longitudinal (z) local modes respectively. At higher gain, vibronic lines associated with second harmonics of the local modes coupled to D_1 are observed. Figures V.1.8(a) and (b) show the polarised excitation spectra recorded for the x(yy)z and x(zy)z polarisation geometries in a <100> oriented crystal. Those second harmonic vibronic lines identified can be associated with; two x,y vibrations (xx) for the line at 18147 cm^{-1}, the combination x,y and a z vibration (xz) for the transition at 18157 cm^{-1} and two z vibrations (zz) at 18179 cm^{-1}. Although the laser polarisation plane has been rotated in these polarised spectra, a similar analysis to that presented previously for different analyser planes is appropriate. Table V.1.4 summarises the selection rules for the two polarisation geometries presented in the spectra. The line being monitored is the σ-polarised $^1D_2(D_1) \longrightarrow {}^3H_4(Z_1)$ transition.

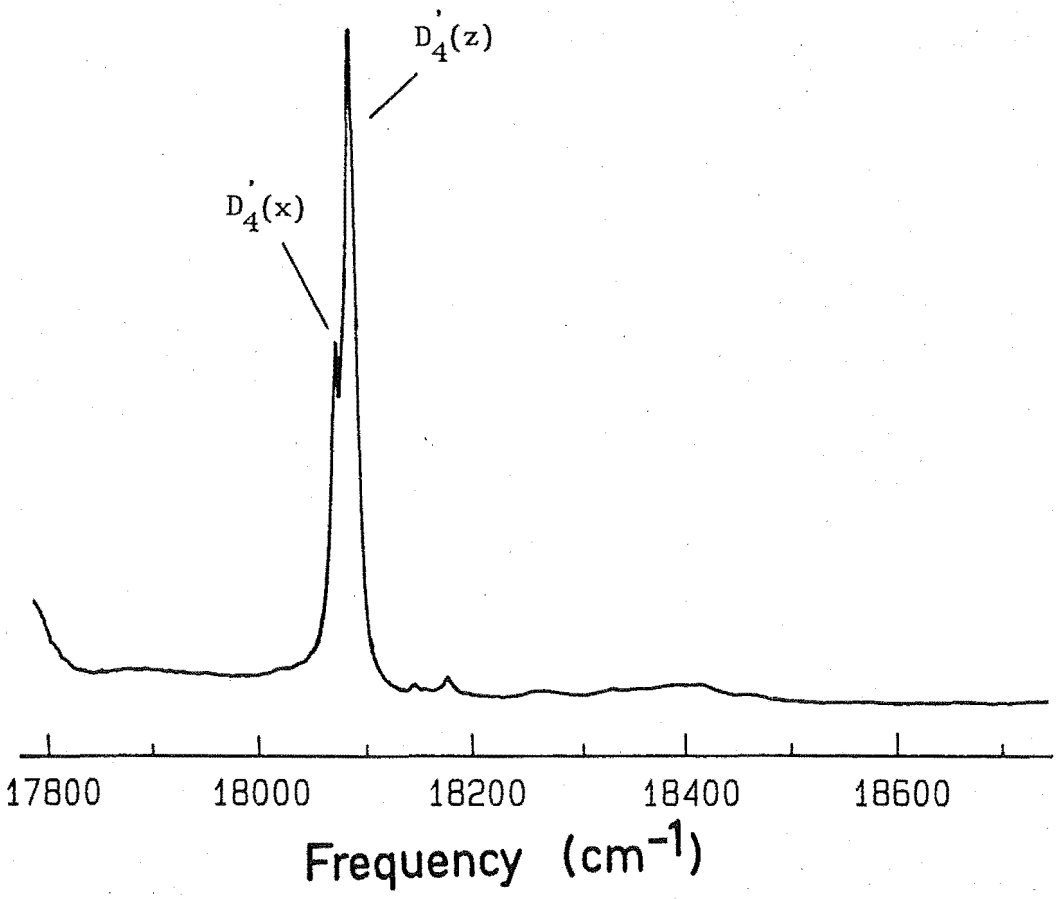

Figure V.1 7 14K excitation spectrum for the C_{4v} D^- site in $SrF_2:Pr^{3+}:D^-$ showing local mode vibronic lines associated with vibrations coupled to the D_4 crystal field level.

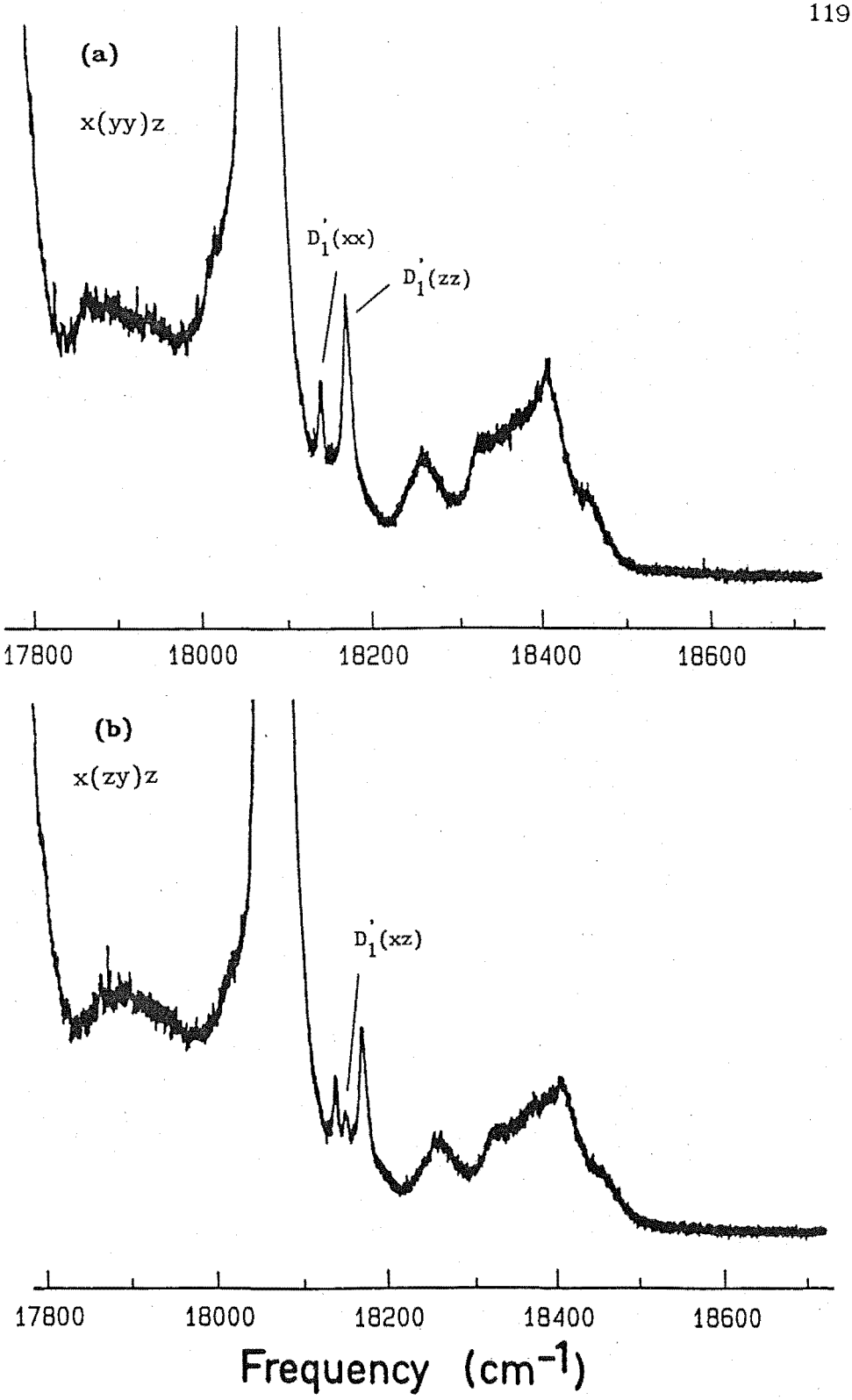

Figure V.1 8 Polarised excitation spectra for the C_{4v} D^- site in $SrF_2:Pr^{3+}:D^-$ showing local mode vibronic lines associated with second harmonic vibrations coupled to the D_1 crystal field level.

Table V.1.4

Polarisation rules for the absorption when monitoring σ-polarised emission, in the C_{4v} sites for the two polarising geometries x(yy)z and x(zy)z in a <100> oriented crystal.

Polarisation of $^1D_2$ absorption transition	X,Y,Z site orientations contributing to the emission for the polarisation geometries		Relative Intensity Ratio
	x(yy)z	x(zy)z	(yy):(zy)
σ	X,Z	X	2:1
π	-	Z	0:1

Previously it was shown that the vibronic level associated with the single transverse local mode coupled to D_1 at 17479.2 cm^{-1}, is doubly degenerate and transforms as the γ_5 irrep of C_{4v}. The coupling of a second degenerate transverse vibration produces an (xx) second harmonic local mode comprising four levels as in the C_{4v} group

$$\gamma_5 \times \gamma_5 = \gamma_1 + \gamma_2 + \gamma_3 + \gamma_4 \quad .$$

Excitation lines from the vibronic ground state which transforms as a γ_5 irrep, are allowed to all four (xx) second harmonic levels in σ-polarisation through the $\gamma_5(x,y)$ electric dipole operator. As only one transition is observed the splitting of these levels appears to be very small. The spectra in Figure V.1.8 show this transition has a x(yy)z:x(zy)z polarisation ratio of 2:1 as predicted by the selection rules in Table V.1.4.

A similar polarisation ratio is expected for the (zz) second harmonic vibronic level. The two z local mode vibrations, each transforming as the γ_1 irrep, couple to D_1 to produce a (zz) vibronic

level having the same symmetry as D_1. The D_1 crystal field level will transform as either a γ_1 or γ_3 irrep and the $^3H_4(Z_1) \longrightarrow {}^1D_2(D_1)$ transition is expected and is known to be σ-polarised.

The addition of a z local mode vibration to an x,y local mode vibronic produces a single, doubly degenerate (xz) second harmonic local mode level transforming as the γ_5 irrep of C_{4v}. The excitation line from the γ_5 symmetry ground state will be π-polarised, through absorption by the $\gamma_1(z)$ component of the electric dipole operator. This line in Figure V.1.8 has the x(yy)z:x(zy)z polarisation ratio of 0:1 predicted by the selection rules in Table V.1.4.

Table V.1.5 summarises the Pr^{3+} ion electronic and D^- ion local mode frequencies measured using laser excitation for the C_{4v} D^- site in $SrF_2:Pr^{3+}$.

Table V.1.5

Electronic and D^- ion local mode frequencies measured from the $^1D_2$ excitation spectrum for the C_{4v} D^- site in a SrF_2:0.05%Pr^{3+}:D^- crystal. Sample temperature was 14 K.

$^1D_2$ Electronic Frequency (cm^{-1})	Local Mode Vibronic Intervals (cm^{-1})	Second Harmonic Local Mode Vibronic Intervals (cm^{-1})
D_1=16815.2±0.1	x,y : 664.0±0.5 z : 686.6±0.5	xx : 1332±2 xz : 1342±2 zz : 1364±2
D_4=17411.9±0.5	x,y : 664±2 z : 676±2	- -

Also appearing in Figure V.1.8 are a number of broad lines having a different character to the second harmonic local mode transitions. The most likely origin of these features are vibronic lines associated with lattice phonons coupling to the D^- ion local mode vibronic levels at 18076 and 18088 cm^{-1}. These phonon energies would be in the range of 170-350 cm^{-1}. A band of lattice phonons in this frequency range is apparent in the excitation spectrum of Figure V.1.3. Similar bands of lattice phonons would also be expected to appear coupled to the D_4 crystal field level. Unfortunately the appropriate region is outside the spectral range of the exciting laser, but as Figure V.1.7 shows some structure is starting to appear at the low energy spectral limit of the green dye laser.

The previous chapter described the problem of Sm^{2+} contamination in crystals containing nominally only praseodymium dopant rare-earth ions. Figure V.1.9 demonstrates the sensitivity of the laser excitation technique by showing the excitation spectrum of impurity Nd^{3+} ions occupying the C_{4v} F^- site in a crystal containing praseodymium dopant material. Identification of the impurity as Nd^{3+} was confirmed by data made available by Han [1987]. The excitation lines in the figure correspond to transitions from the $^4I_{9/2}(Z_1)$ ground state to the crystal field levels of the $^2G_{7/2}$ and $^2G_{5/2}$ multiplets. The excellent signal to noise in Figure V.1.9 illustrates how laser spectroscopy can detect impurity rare-earth ions to a few parts in 10^4.

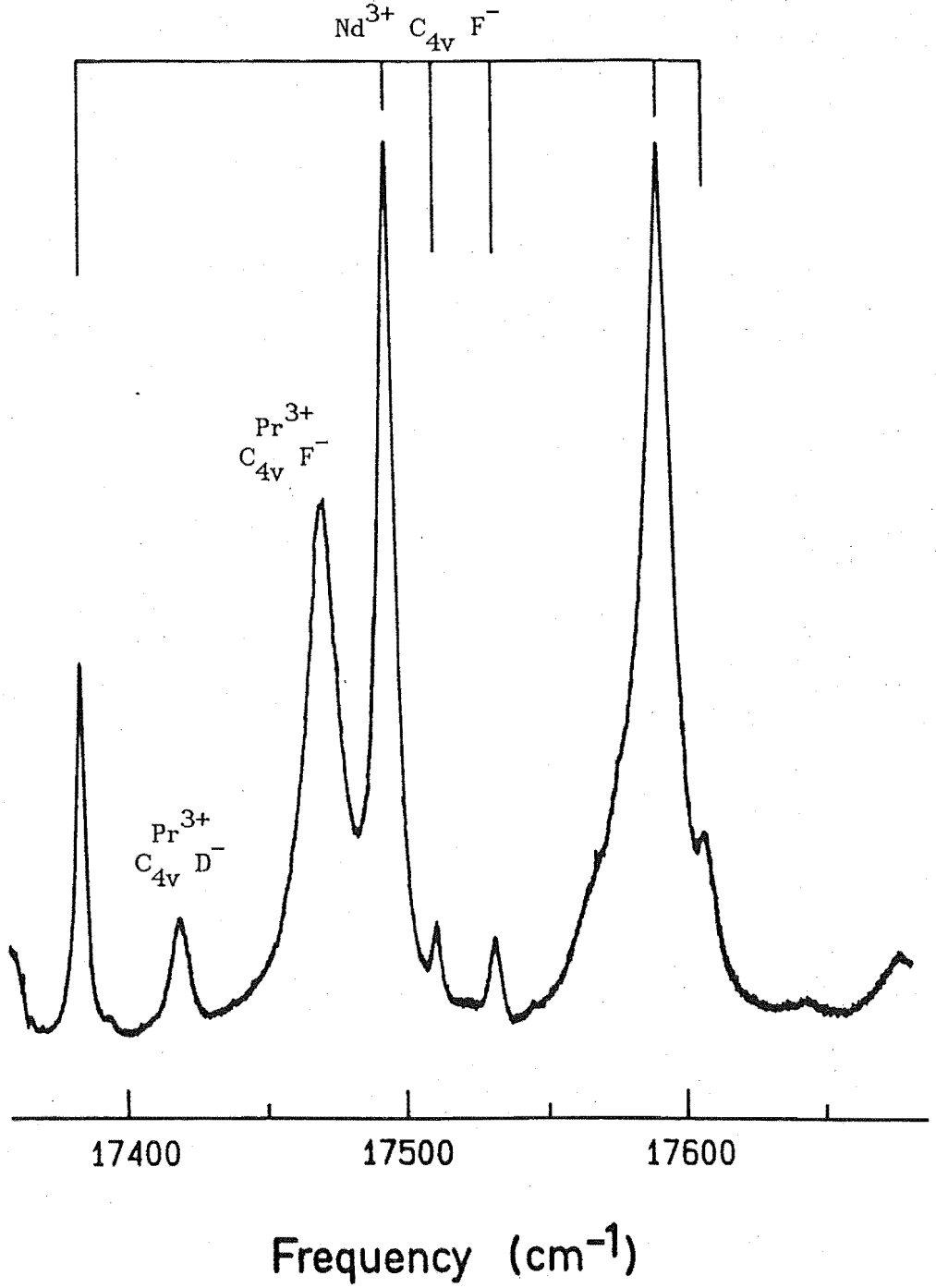

Figure V.1.9 Laser excitation of a praseodymium doped SrF_2 crystal showing lines from Nd^{3+} ions present as an impurity.

V.1.2 Optical Emission of the C_{4v} Hydrogenic Sites in $SrF_2:Pr^{3+}$

Fluorescence spectra from the $^1D_2$ multiplet and in some cases from the $^3P_0$ multiplet, to the crystal field levels of the $^3H_{4,5,6}$ and $^3F_{2,3,4}$ multiplets of the Pr^{3+} ion were recorded for the C_{4v} hydrogenic charge compensating ion sites. The spectral range scanned for each multiplet was considerably extended from the F^- sites, as vibronic lines associated with local mode phonons of the hydrogenic ion were visible at energies several hundreds of wavenumbers lower than their parent Pr^{3+} ion electronic transitions. A Rhodamine 6G dye laser operating with typical powers of 50-200 mW, was appropriate for selective excitation of the Pr^{3+} ion to the $^1D_2$ multiplet and was usually tuned to match the absorption transition of the lowest crystal field component. For the C_{4v} D^- site, fluorescence from the $^3P_0$ multiplet was recorded using a nitrogen pumped pulsed dye laser as the exciting source. As polarisation studies had been found useful for identifying energy level symmetries, most fluorescence spectra were recorded using <100> oriented samples containing typically 0.05 mol% of praseodymium. The polarisation selection rules for Pr^{3+} ions in C_{4v} F^- sites have been derived previously and will be applicable to the transitions observed in the hydrogenic C_{4v} sites.

Identification of the $^1D_2$ emitting level symmetry is not as straight forward for the hydrogenic sites as it was for the C_{4v} F^- site. It was shown in Chapter IV how the observation of transitions from the $^3P_0(\Gamma_1\gamma_1)$ level that were common to transitions from the $^1D_2(D_2)$ level established the $^1D_2$ level symmetries for the C_{4v} F^- site as $\Gamma_3\gamma_3$ and $\Gamma_3\gamma_1$ for the D_1 and D_2 levels respectively. No fluorescence transitions from, nor absorption transitions to, the D_2 level have been observed for the hydrogenic sites in $SrF_2:Pr^{3+}$ crystals. The $^3P_0 \rightarrow {}^3H_4$ emission spectrum has been recorded for the

C_{4v} D^- and T^- ion sites by way of the upconversion process and the $^3P_0$ level has been excited directly in the C_{4v} D^- ion site using the nitrogen pulsed laser. The frequency intervals of the transitions from the $^3P_0$ level were found to be the same as those from the $^1D_2(D_1)$ level implying a similar symmetry for the two emitting levels. A π-polarised magnetic dipole transition observed from both $^3P_0$ and $^1D_2(D_1)$ levels to the $^3H_5(\Gamma_4^{(1)}\gamma_2)$ crystal field level indicates a D_1 level transforming as the γ_1 irrep. However, there is conflicting evidence to this assignment as several π-polarised transitions are observed terminating on levels transforming as the γ_3 irrep indicating an emitting level of this symmetry.

Some insight may be gained from a discussion of the results for the $CaF_2:Pr^{3+}$ system. In Chapter IV it was shown the D_1-D_2 splitting was 17 cm^{-1} for the C_{4v} F^- site with the D_1 level transforming as the γ_1 irrep. Results to be presented later in this chapter will show this splitting increases to 37 cm^{-1} for the hydrogenic C_{4v} sites. If this change is interpreted as the $D_2(\Gamma_3\gamma_3)$ level moving 20 cm^{-1} to higher energy relative to the $D_1(\Gamma_3\gamma_1)$ level from F^- to H^- ion substitution, then the same interpretation for the $SrF_2:Pr^{3+}$ C_{4v} sites would see the $D_1(\Gamma_3\gamma_3)$ - $D_2(\Gamma_3\gamma_1)$ splitting of 19 cm^{-1} for the F^- site close to ~1 cm^{-1} for the hydrogenic ion sites. If the two states were this close together, considerable mixing could occur from second order effects and the emitting level may exhibit characteristics of both symmetries. However, there was no evidence of a second line closeby in the excitation spectra discussed in the previous section but beyond this contention an explanation of the observed polarisations is difficult.

The details of the electronic and vibrational energy level structure for the hydrogenic ion C_{4v} sites in $SrF_2:Pr^{3+}$ will now be discussed for each multiplet in turn. For archival purposes spectra for all three H^-, D^- and T^- isotopic variations of the hydrogenic site

are included even though some spectral features are similar.

The $^3H_4$ Multiplet

Spectra showing the polarised emission to the crystal field levels of the $^3H_4$ multiplet are given in Figures V.1.10, V.1.11 and V.1.12 for the Pr^{3+} ion in a C_{4v} site charge compensated by an H^-, D^- or T^- ion respectively. The spectra were recorded at 14 K using <100> oriented samples and show the emission for the x(yy)z and x(yx)z polarisation geometries in (i) and (ii) of each figure respectively. The convention used to label the lines in the spectra uses the traditional Z_i label to indicate the terminating level of an electronic transition while the label $Z_i^{\prime}(\alpha)$, where α = x or z, indicates a transition terminating on a local mode vibronic level. For these vibronic lines the parent electronic level is the Z_i level and the type of local mode is transverse for α = x and longitudinal for α = z. The electronic and local mode vibronic level energies are summarised in Table V.1.6 for the $^3H_4$ multiplet of the hydrogenic C_{4v} Pr^{3+} ion site in SrF_2:Pr^{3+}. The spectra in Figure V.1.10 of the emission from the Pr^{3+}-H^- C_{4v} site are chosen for discussion.

Polarised emission to the Z_3, Z_5, Z_6 and Z_7 crystal field levels is readily identified in Figure V.1.10(a). The x(yy)z:x(yx)z polarisation ratio of the transition to the Z_6 crystal field level is 2:1 indicating a σ-polarisation for this transition consistent with the Z_6 level assignment of τ_5 symmetry. The transitions to the Z_3 and Z_5 crystal field levels have a x(yy)z:x(yx)z polarisation ratio of 0:1. Experience of the C_{4v} F^- site suggests these levels transform as the τ_1 irrep of C_{4v} and their π-polarised transitions and the C_{4v} site selection rules require the D_1 emitting level to also have τ_1 symmetry.

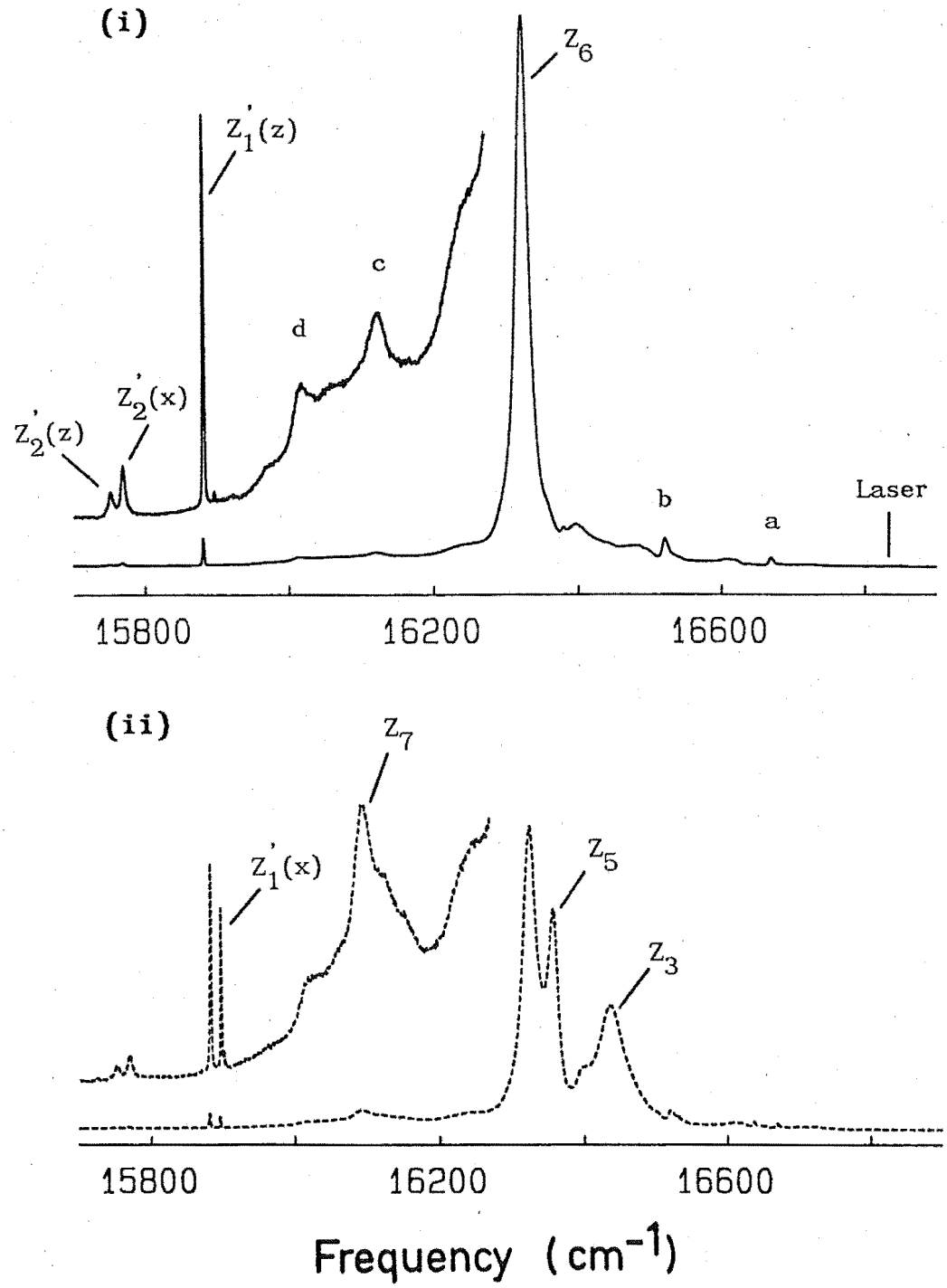

Figure V.1.10(a) 14K polarised fluorescence from the C_{4v} H^- site in $SrF_2:Pr^{3+}$ showing the $^1D_2 \rightarrow {}^3H_4$ electronic transitions of the Pr^{3+} ion for the (i) x(yy)z and (ii) x(yx)z polarisation geometries in a <100> oriented crystal.

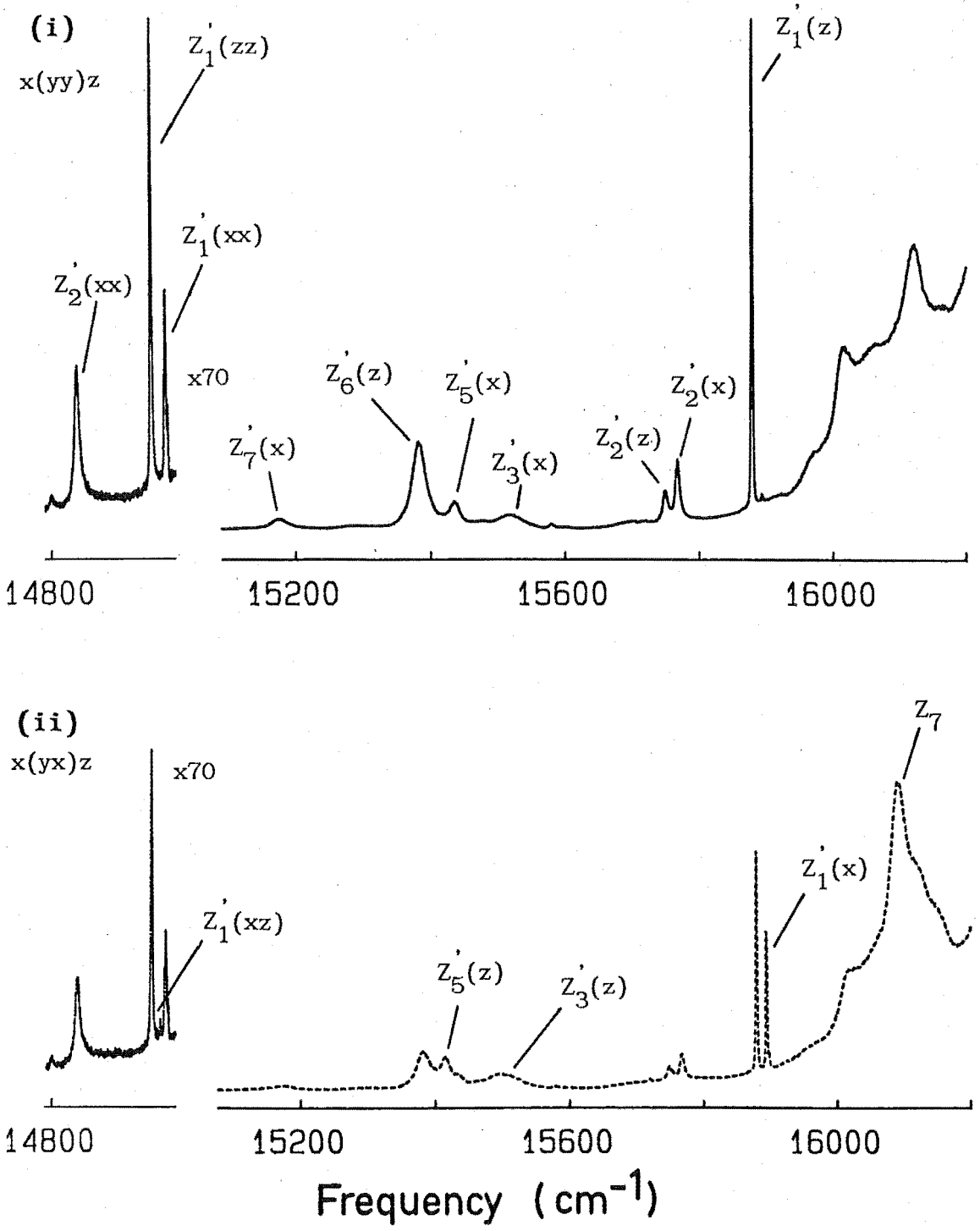

Figure V.1.10(b) Polarised fluorescence from the C_{4v} H^- site in $SrF_2:Pr^{3+}$ on an expanded scale showing transitions to the local mode vibronic levels associated with the $^3H_4$ multiplet.

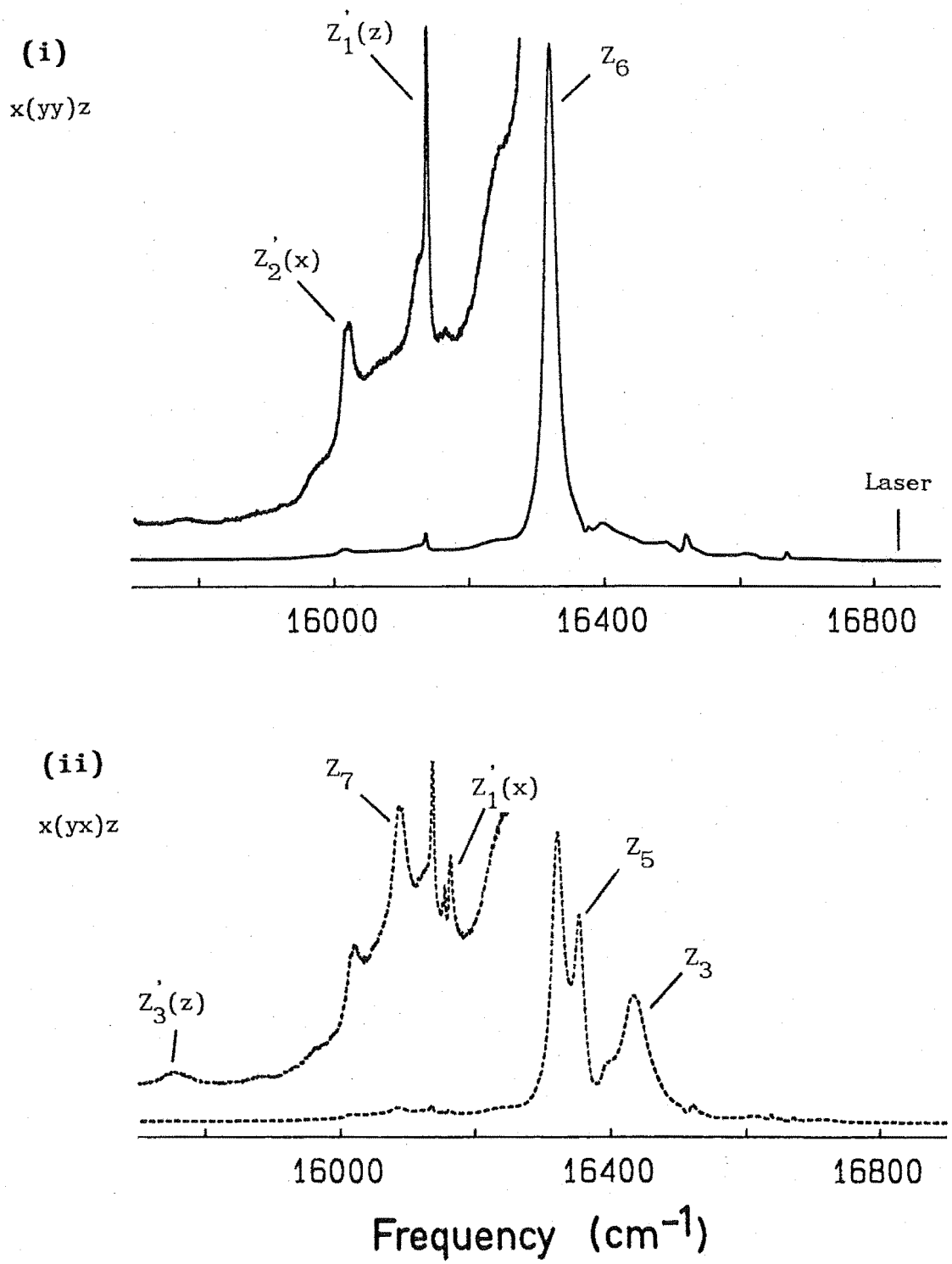

Figure V.1.11(a) Polarised $^1D_2 \rightarrow {}^3H_4$ fluorescence from the C_{4v} D^- site in $SrF_2:Pr^{3+}:D^-$ showing transitions to the electronic levels of the Pr^{3+} ion.

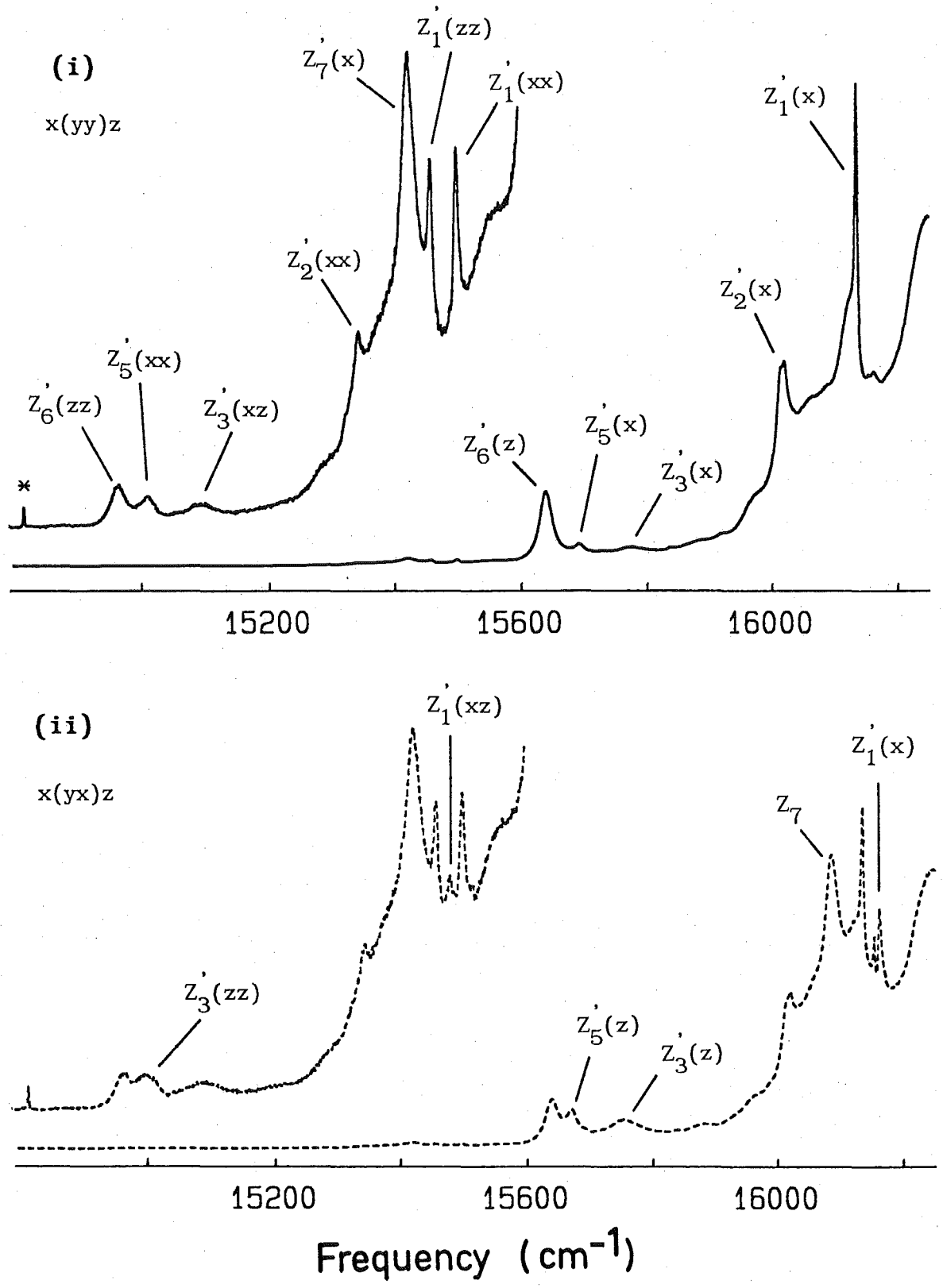

Figure V.1.11(b) Polarised fluorescence from the C_{4v} D^- site in $SrF_2:Pr^{3+}$ on an expanded scale showing transitions to the local mode vibronic levels. The line labelled * is not related to this site.

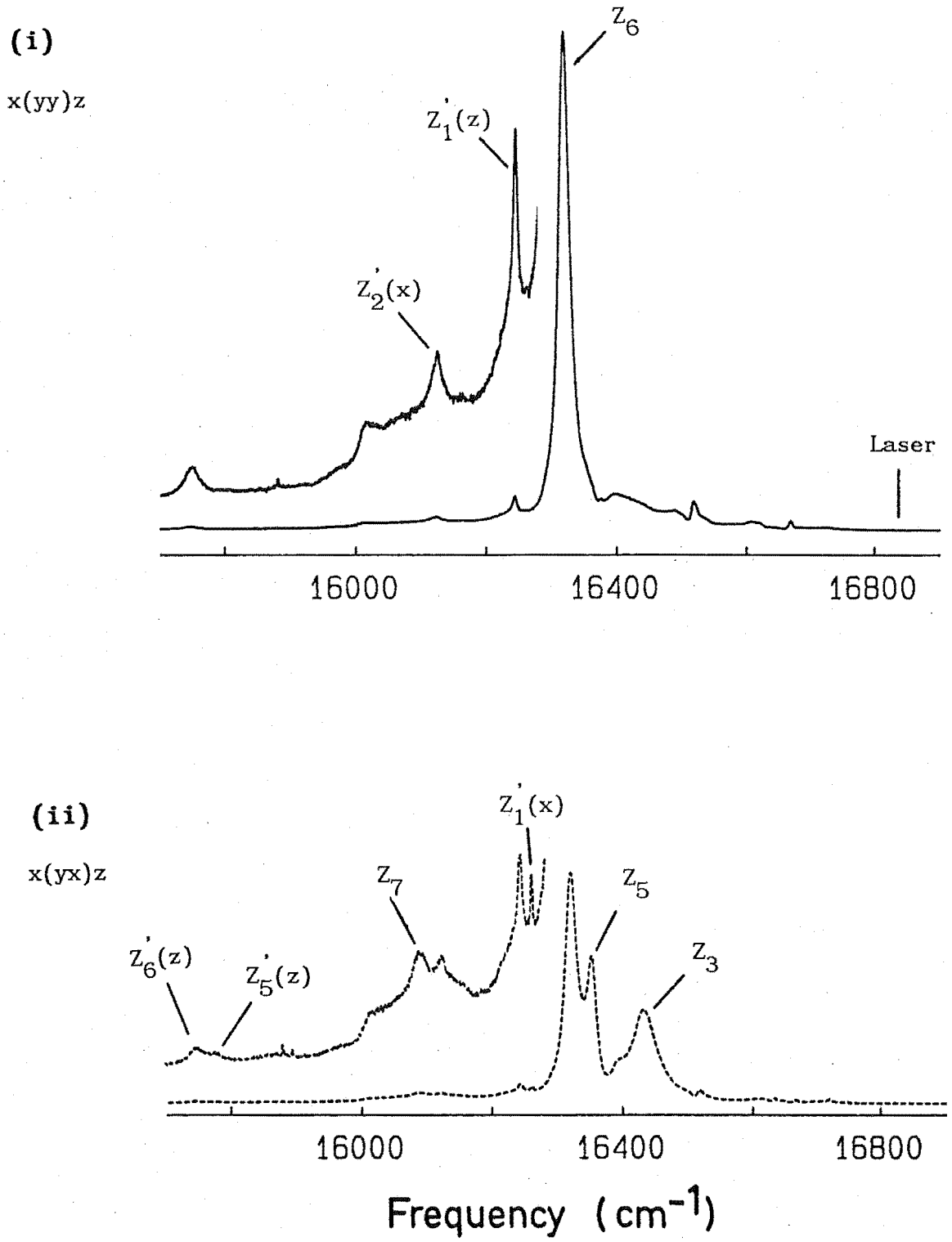

Figure V.1.12(a) Polarised $^1D_2 \rightarrow {}^3H_4$ fluorescence from the C_{4v} T^- site in $SrF_2:Pr^{3+}$ showing transitions to the electronic levels of the Pr^{3+} ion.

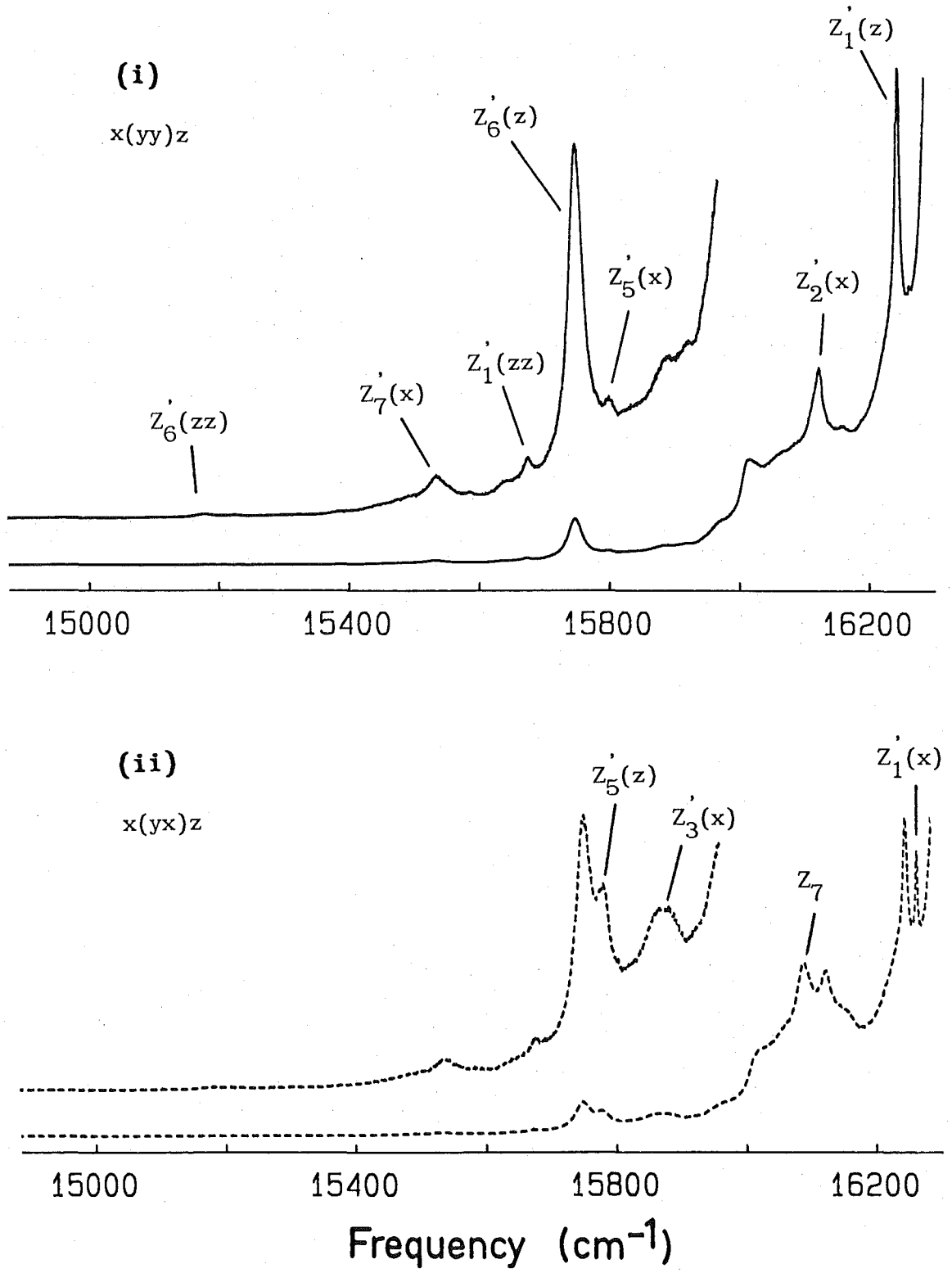

Figure V.1.12.(b) Polarised fluorescence from the C_{4v} T^- site in $SrF_2:Pr^{3+}$ showing transitions to the local mode vibronic levels.

Table V.1.6

Electronic energies for the $^3H_4$ multiplet of the hydrogenic C_{4v} sites in $SrF_2:Pr^{3+}$. The energy level uncertainties are ±1 cm^{-1} unless otherwise indicated. The polarisation of the transitions to these levels from $^1D_2(D_1)$ is also included.

Electronic state symmetry and polarisation	C_{4v} H^- Electronic level energy (cm^{-1})	C_{4v} H^- Vibronic level mode, energy (cm^{-1}) and polarisation	C_{4v} D^- Electronic level energy (cm^{-1})	C_{4v} D^- Vibronic level mode, energy (cm^{-1}) and polarisation	C_{4v} T^- Electronic level energy (cm^{-1})	C_{4v} T^- Vibronic level mode, energy (cm^{-1}) and polarisation
$Z_1(\tau_5)$, σ	0	x: 921.6±.5 (π) 925.1±.5 (π) z: 939.6±.5 (σ) xx:1846.2±.5 (σ) 1849.2±.5 (σ) 1851.2±.5 (σ) xz:1857.7±.5 (π) zz:1870.7±.5 (σ)	0	x: 658.4±.5 (π) 666.9±.5 (π) z: 684.9±.5 (σ) xx:1322.9±.5 (σ) xz:1342.4±.5 (π) zz:1363.9±.5 (σ)	0	x:558 (π) z:575 (σ) xx: - xz:1131 (π) zz:1144 (σ) third harmonic :1708±2 (σ)
$Z_2(\tau_4)$ [a]	138±5	x:1052.1±.5 (σ) z:1069.6±.5 (σ) xx:1983.9±.5 (σ) xz:2021.7±.5 (σ)	139±3	x:801 (σ)	137±3	x:695 (σ) z: - xz:1233 (σ)
$Z_3(\tau_1)$, π	386±2	x:1302 (σ) z:1320 (π)	387±2	x:1047 (σ) z:1069 (π) xz:1729±2 (σ)	387±2	x:929 (σ) z:950 (π) zz:1515±2 (π)

Table V.1.6 continued next page...

Table V.1.6 continued...

Electronic state symmetry and polarisation	C_{4v} H^- Electronic level energy (cm^{-1})	Vibronic level mode, energy (cm^{-1}) and polarisation	C_{4v} D^- Electronic level energy (cm^{-1})	Vibronic level mode, energy (cm^{-1}) and polarisation	C_{4v} T^- Electronic level energy (cm^{-1})	Vibronic level mode, energy (cm^{-1}) and polarisation
$Z_4(\tau_2)$	-		-		-	
$Z_5(\tau_1)$, σ	466	x:1385 (σ) z:1405 (π)	467	x:1130 (σ) z:1150 (π) xz:1812 (σ) zz:1826±2 (π)	467	x:1020 (σ) z:1042 (π) xz:1593±2 (σ) zz:1603±2 (π)
$Z_6(\tau_5)$, σ	498	x: - z:1437 (σ)	499	x: - z:1182 (σ) zz:1858 (σ)	498	x: - z:1072 (σ) zz:1640±2 (σ)
$Z_7(\tau_3)$, π	729±2	x:1644 (σ)	736±2	x:1399 (σ) xz:2083±2 (σ)	732±2	x:1286 (σ) xz:1857±2 (σ)

[a] Electronic level position inferred from observation of local mode vibronic transitions.

In the C_{4v} F^- site the Z_7 level transformed as the τ_3 irrep of C_{4v} and an electric dipole allowed, π-polarised, $D_1(\tau_3) \longrightarrow Z_7(\tau_3)$ transition was observed. For the C_{4v} hydrogenic sites, a weak line is observed in the appropriate region for a $D_1 \longrightarrow Z_7(\tau_3)$ transition. This π-polarised transition indicates a τ_3 symmetry to the emitting level conflicting with the assignment in the previous paragraph. Clearly there appears to be some relaxation of the strict C_{4v} transition rules.

The hydrogenic ion local mode vibrations can couple to the electronic levels of the Pr^{3+} ion to produce vibronic levels. Fluorescence transitions will be observed to these vibronic levels at lower frequencies than the parent electronic transition with an interval equivalent to the frequency of the local mode vibration. In some cases fluorescence transitions to vibronic levels associated with second harmonic vibrations of the hydrogenic ion are observed. Using infrared absorption the C_{4v} site local mode frequencies have been measured for the H^- ion coupled to the ground state of the Pr^{3+} ion (Edgar, Freeth and Jones [1977]) and these can be used as a starting point for analysing the complicated local mode vibronic spectra observed in fluorescence.

The selection rules for polarised emission to the local mode vibronic levels can be derived using the C_{4v} point group multiplication rules and the electronic level and local mode vibration symmetries. The vibronic levels associated with the ground electronic state can be taken as a specific example. The longitudinal (z) local mode vibration transforms as the τ_1 irrep of C_{4v} and the Pr^{3+} ion electronic ground state has been shown in this work to transform as the τ_5 irrep for these C_{4v} sites. The coupling between the electronic ground state and the longitudinal local mode phonon produces a

vibronic level in the combined electronic-local mode phonon system transforming as the $\tau_1 \times \tau_5 = \tau_5$ irrep. The ground state of the local mode phonon system transforms as the τ_1 irrep and all the electronic zero-phonon levels will retain their original symmetry in the combined system. Therefore a fluorescence transition from $^1D_2(D_1)$ to this z local mode vibronic level should be σ-polarised and have a 2:1 x(yy)z:x(yx)z polarisation ratio. This is, in fact, observed and the transition has been indicated with the label $Z_1'(z)$ in Fig. V.1.10(b).

The transverse (x,y) vibronic level is particularly interesting because of the combination of two degenerate levels. The doubly degenerate electronic ground state and x,y local mode vibration combine to form four vibronic levels, as in the C_{4v} point group

$$\tau_5 \times \tau_5 = \tau_1 + \tau_2 + \tau_3 + \tau_4 \quad .$$

In principle, these four vibronic levels will have different energies but not all components may be resolvable. Using infrared absorption Jacobs [1971] observed a splitting in this fundamental x,y local mode vibration for the C_{4v} H^- site in both $CaF_2:Pr^{3+}$ and $SrF_2:Pr^{3+}$ crystals. Although not apparent on the scale used in Figures V.1.10 and V.1.11, two components split by 3.5 cm^{-1} and 8.5 cm^{-1} have been observed in the emission to the x,y vibronic level for the H^- and D^- C_{4v} sites respectively. Only one component is observed for the T^- site. Transitions to only two of the four levels are visible, but on the basis of the observed electronic lines it is likely that fluorescence will be allowed only to the two vibronic levels transforming as the τ_1 and τ_3 irreps. However, absorption by electric dipole radiation will be allowed to all four vibronic levels from the τ_5 symmetry vibronic ground state and all four lines could be observed. A theoretical analysis will be presented in Chapter VII that shows the dominant contribution to this splitting is due to second order effects arising from the close proximity of nearby

electronic levels.

The polarisation dependence of transitions to other vibronic levels can be analysed in a similar way. Using these methods and matching energy intervals, the origin of most of the vibronics can be identified and is indicated on the spectra.

In some cases the observation of vibronic transitions can aid the assignment of a forbidden parent zero-phonon line. A direct transition has not been observed to the Z_2 crystal field level for any of the hydrogenic C_{4v} sites, however an energy can be assigned to this level from the observation of its local mode vibronic lines (Table V.1.6). In a similar way, the appearance of the $D_1 \longrightarrow Z_7'(x)$ transition confirms the assignment of the weak π-polarised transition at 16086 cm^{-1} as terminating on the Z_7 crystal field level.

For all three H^-, D^- and T^- charge compensating ions transitions have been observed to vibronic levels associated with second harmonic local mode vibrations of the hydrogenic ion. In a site having C_{4v} potential, the hydrogenic ion oscillator will have five second harmonic local modes as the anharmonic terms to the potential split the transverse (x,y) vibrations (Newman [1973]). Three of these second harmonic vibrations will be infrared active and have been measured for the C_{4v} H^- sites containing Gd^{3+}, Tm^{3+} and Y^{3+} rare-earth ions in CaF_2 crystals (Jones et al [1969]). On an expanded frequency scale to that used in Figure V.1.10(b), the low frequency (xx) second harmonic vibronic transition $Z_1'(xx)$, is observed to contain three components and we have the unique situation of a complete set of five second harmonic frequencies. In Chapter VII these results and those from the hydrogenic sites in $CaF_2:Pr^{3+}$ are discussed and the form of the anharmonic potential is derived in some cases.

Several weak lines in Figure V.1.10(a) cannot be assigned to transitions in the Pr^{3+}-H^- vibronic system. Two lines having energy shifts of 151 and 301 cm^{-1} from the $D_1 \longrightarrow Z_1$ transition are labelled with the letters a and b respectively. These lines appear to be transitions to vibronic levels associated with a fundamental and second harmonic lattice phonon. Of interest is the comparable strength of these two lines and their polarisation, indicating some symmetry to the phonon. Similar lines were observed in the $^1D_2 \longrightarrow {}^3H_4$ emission spectrum of the C_{4v} F^- site in SrF_2:Pr^{3+} at frequency intervals of 149 and 302 cm^{-1}. It appears the same phonon is involved and that its frequency is not greatly influenced by the charge compensating ion. Results of spectral holeburning experiments to be presented in Chapter IX, show that the fluorine lattice in the immediate neighbourhood of the Pr^{3+} and interstitial ion is distorted when the charge compensating ion varies amongst the F^-, H^-, D^- isotopes. As there is little change to the frequency it can be concluded that the 150 cm^{-1} phonon is not very localised at the ion site and extends beyond the range of this distortion. The lines labelled c and d in Figure V.1.9 are vibronic lines coupled to the Z_6 crystal field level associated with lattice phonons of energy 200 and 300 cm^{-1} respectively. Inspection of Figures V.1.10, V.1.11 and V.1.12 show that these lines are apparent in the spectra for all three H^-, D^- and T^- C_{4v} sites.

The C_{4v} site upconversion described in Chapter IV for the F^- sites is also observed in the C_{4v} D^- and T^- sites in SrF_2:Pr^{3+} but at an efficiency several orders of magnitude lower. Figures V.1.13 and V.1.14 show the polarised $^3P_0 \longrightarrow {}^3H_4$ upconverted emission for the C_{4v} D^- and T^- sites in SrF_2:Pr^{3+} respectively. The same labels used for the direct emission indicate the transitions to the various

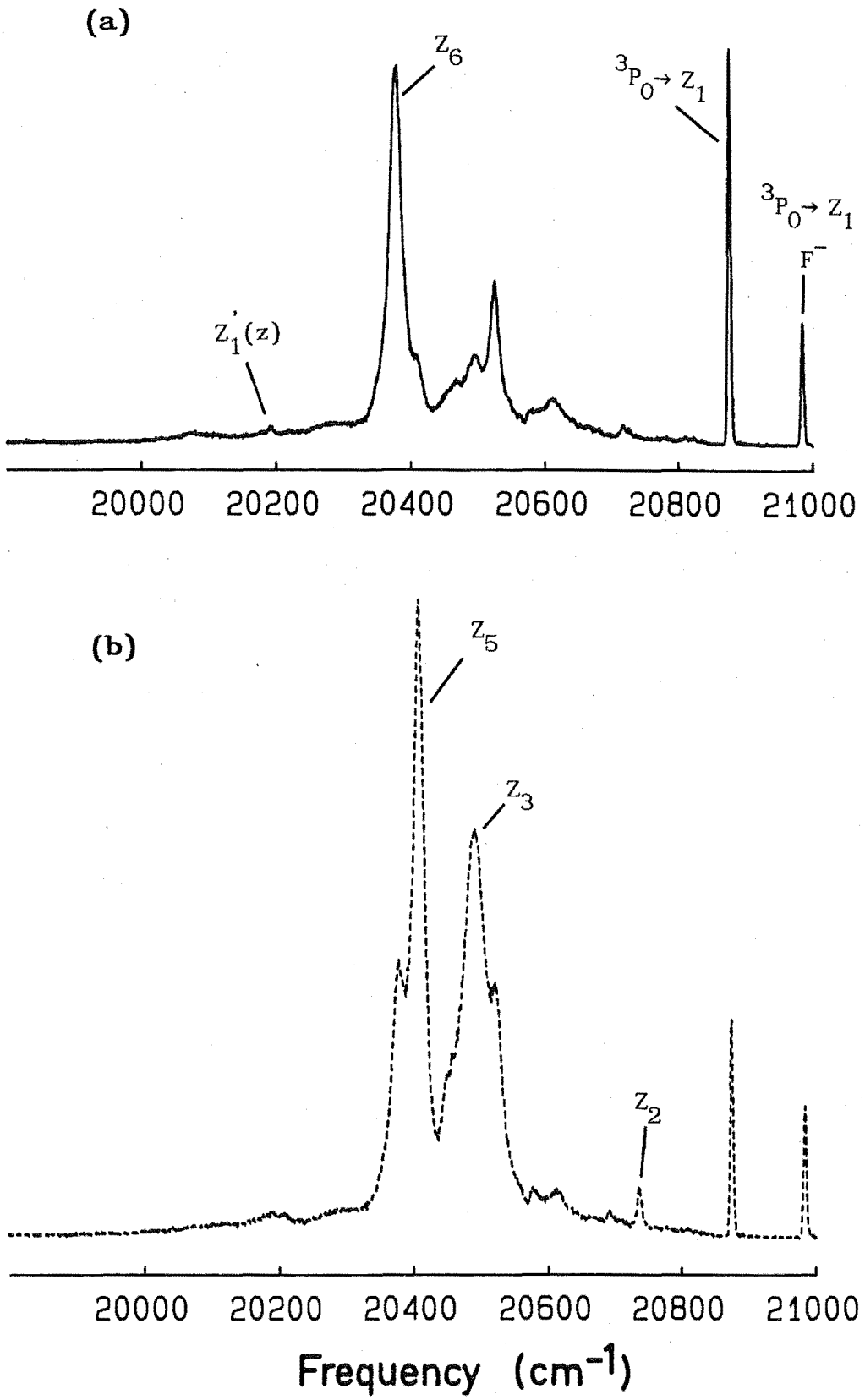

Figure V.1.13 $^3P_0 \rightarrow {}^3H_4$ upconverted emission, recorded at 14K from the C_{4v} D^- site in $SrF_2:Pr^{3+}$ with $^3H_4(Z_1) \rightarrow {}^1D_2(D_1)$ excitation for the (a) x(yy)z and (b) x(yx)z polarisation geometries.

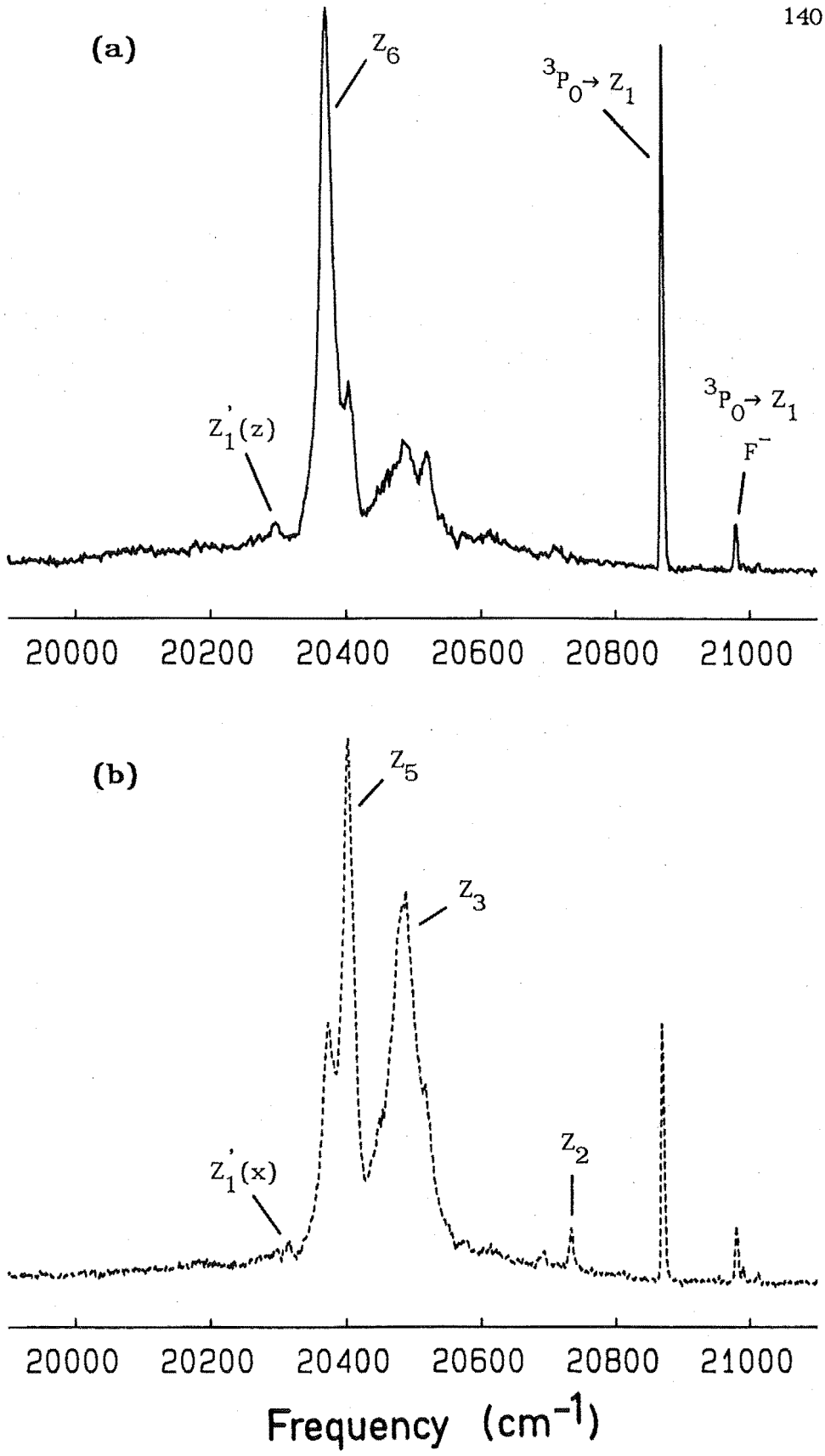

Figure V.1.14 14K $^3P_0 \rightarrow {}^3H_4$ upconverted emission from the C_{4v} T^- site in $SrF_2:Pr^{3+}$ with $^3H_4(Z_1) \rightarrow {}^1D_2(D_1)$ excitation for the (a) x(yy)z and (b) x(yx)z polarisation geometries.

crystal field levels. Although there are some relative intensity changes, notably the transitions to $^3H_4$ levels transforming as the γ_1 irrep being more intense, the observed lines show similar polarisation to the direct emission for both sites. Contrasting to this is the $^3P_0 \longrightarrow {}^3H_4(Z_1)$ transition for the C_{4v} F^- site, visible in both spectra at 20986 cm^{-1}, that shows no polarisation changes. This line is present, as under the intense excitation conditions used to produce these spectra, the Pr^{3+} ions in the C_{4v} F^- sites are being excited to the $^1D_2$ multiplet and participate in their independent upconversion process. The polarisation effects in these C_{4v} sites arise through the ability to selectively excite particular orthogonal orientations of the sites and the retention of polarisation characteristics for the upconverted C_{4v} D^- and T^- emission, and not the C_{4v} F^- in this case, indicates that only those sites originally excited participate in the process. This has significance in limiting the number of possible mechanisms for the upconversion in these supposedly single ion sites. Additional results using a pulsed excitation source and discussion on the possible mechanisms will be presented in Chapter VIII.

The $^3H_5$ Multiplet

Spectra of the polarised emission from $^1D_2$ to the crystal field levels of the $^3H_5$ multiplet are shown in Figure V.1.15 for the (a) H^-, (b) D^- and (c) T^- hydrogenic C_{4v} sites in $SrF_2:Pr^{3+}$. Fluorescence to the $^3H_5$ levels from $^3P_0$ was recorded for the C_{4v} D^- site only and is shown in Figure V.1.16. The same convention is used for labelling the observed spectral lines with Y_i being the appropriate label for the $^3H_5$ multiplet.

More prominant in the spectra of the hydrogenic sites than it was for the fluorine sites is the transition at 14353 cm^{-1}, identified in Chapter IV as the $(^5D_0)^1\Gamma_{1g} \longrightarrow (^3F_1)^3\Gamma_{4g}$ transition of the Sm^{2+} ion.

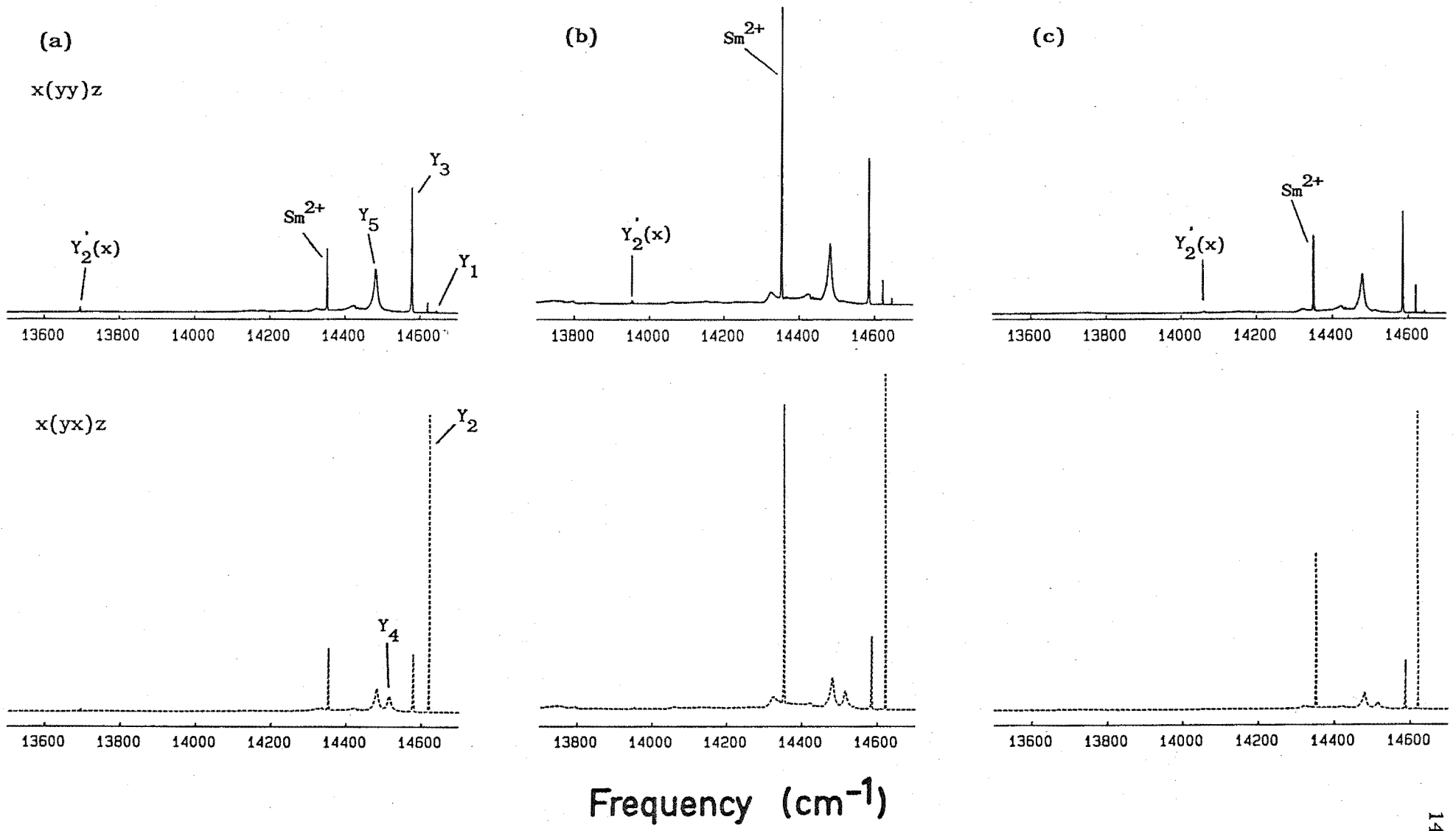

Figure V.1.15 14K $^1D_2 \rightarrow {}^3H_5$ polarised emission from the (a) H^-, (b) D^- and (c) T^- C_{4v} sites in $SrF_2:Pr^{3+}$.

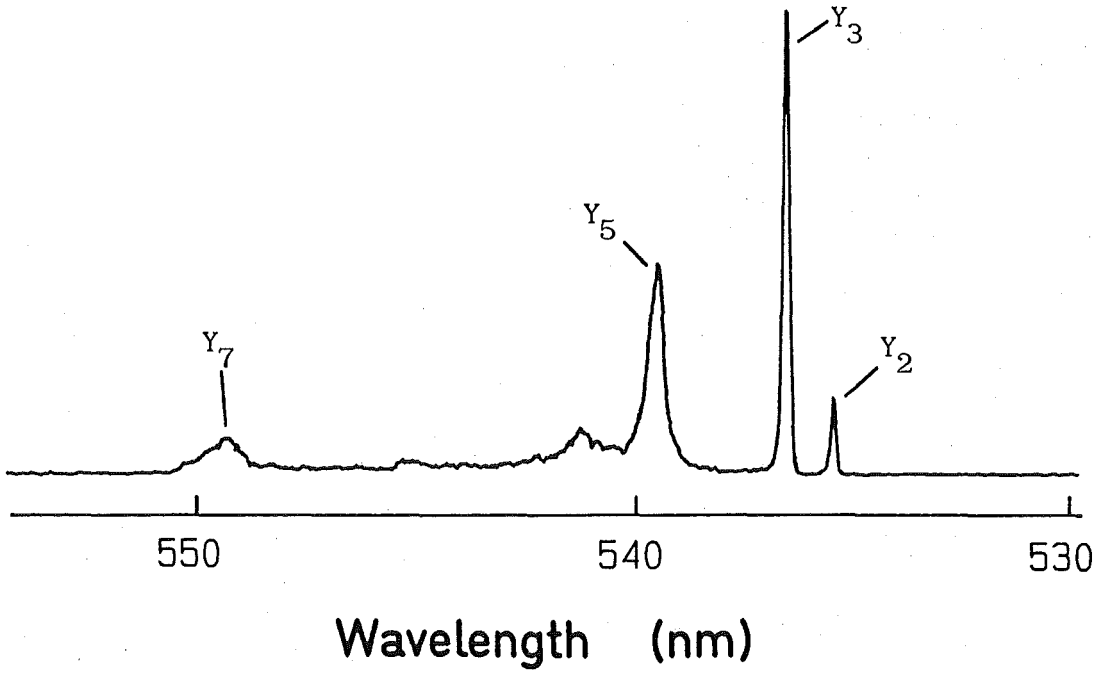

Figure V.1.16 $^3P_0 \rightarrow {}^3H_5$ fluorescence with $^3H_4(Z_1) \rightarrow {}^3P_0$ excitation from the C_{4v} D^- site in $SrF_2:Pr^{3+}$.

Possible reasons for the greater prominance are the weaker quantum efficiencies of the hydrogenic sites and an increase in the Sm^{2+} ion population by reduction of Sm^{3+} in the hydrogenation process. Associated with the strong narrow line at 14353 cm^{-1} are a number of broad features, more pronounced in Figure V.1.15(b) of the D^- C_{4v} site emission. These are readily identified with the Sm^{2+} ion emission using the published spectra of Wood and Kaiser [1962].

The $^3H_5$ multiplet of the Pr^{3+} ion splits into eight crystal field levels in a site of C_{4v} symmetry. Figure IV.1.1 can be referenced for an estimate of the ordering and splitting of these levels. In this figure a crystal field analysis predicts the lowest crystal field level to transform as the τ_2 irrep of C_{4v} which was found to be the case for the C_{4v} F^- site. The same assignment is made for the hydrogenic C_{4v} sites as the x(yy)z:x(yx)z polarisation ratio of 1:0 for the $D_1 \longrightarrow Y_1$ transition is appropriate for a magnetic dipole transition terminating on a level transforming as the τ_2 irrep. The emitting level symmetry of τ_1 required for this transition polarisation, conflicts with the assignment required for the transition to the Y_4 level. The Y_4 crystal field level has τ_3 symmetry (Figure IV.1.1) requiring the emitting level to also have τ_3 symmetry to account for the observed π-polarisation of the $D_1 \longrightarrow Y_4$ transition.

Five of the eight crystal field levels of the $^3H_5$ multiplet have been conclusively identified and a likely assignment can be made to one other. A broad feature around 549.3 nm in Figure V.1.16 showing the $^3P_0 \longrightarrow {}^3H_5$ emission, is tentatively assigned to the $Y_7(\tau_5)$ level. The transition to this level is not particularly obvious in the $^1D_2 \longrightarrow {}^3H_5$ spectra but there is structure in the region having the correct polarisation.

As in the $^3H_4$ multiplet, local mode vibronic lines appear at energy intervals from the parent electronic line corresponding to the local mode frequency. The strongest local mode vibronic line observed is that of the transverse (x,y) vibration coupled to the $Y_2(\gamma_1)$ electronic level. Other vibronic lines are apparent in spectra recorded at a higher gain.

The energy levels of the $^3H_5$ multiplet for the three variations of the hydrogenic Pr^{3+} ion C_{4v} site in SrF_2 are summarised in Table V.1.7. The local mode vibronic levels are included as is the polarisation of the particular transitions observed. The polarisation of the vibronic levels are all consistent with the rules derived in the previous section and their parent electronic level symmetry. For example the γ_5 symmetry transverse (x,y) local mode couples with the $Y_2(\gamma_1)$ electronic level to produce a vibronic level transforming as the γ_5 irrep. Then the transition from $^1D_2$ to this level is expected, and is observed, to be σ-polarised. Conversely, the transition to the x,y vibronic level coupled to the $Y_3(\gamma_5)$ electronic state has π-polarisation consistent with the vibronic level symmetry of $\gamma_1 + \gamma_2 + \gamma_3 + \gamma_4$.

The $^3H_6$ Multiplet

The $^3H_6$ multiplet has the most crystal field levels of all the multiplets studied having ten components in a crystal field of C_{4v} symmetry (Fig. IV.1.1). It has also been the least successful for establishing a complete energy level scheme as transitions to only five of the ten levels have been unambiguously identified. The polarised emission to the $^3H_6$ levels from the $^1D_2$ multiplet is given in Figure V.1.17 for the C_{4v} H^-, D^- and T^- sites. Figure V.1.18 shows the $^3P_0 \longrightarrow {}^3H_6$ emission recorded for the C_{4v} D^- site. The lines in the spectra are labelled with X_i representing the $^3H_6$ terminating crystal field level.

Table V.1.7

Electronic and local mode vibronic level energies for the $^3H_5$ multiplet of the hydrogenic C_{4v} sites in $SrF_2:Pr^{3+}$. The energy level uncertainties are ±1 cm^{-1} and the observed polarisation for the transition from $^1D_2(D_1)$ is also included.

Electronic state symmetry and polarisation	C_{4v} H^- Electronic level energy (cm^{-1})	C_{4v} H^- Vibronic level mode, energy (cm^{-1}) and polarisation	C_{4v} D^- Electronic level energy (cm^{-1})	C_{4v} D^- Vibronic level mode, energy (cm^{-1}) and polarisation	C_{4v} T^- Electronic level energy (cm^{-1})	C_{4v} T^- Vibronic level mode, energy (cm^{-1}) and polarisation
$Y_1(\tau_2)$, π [a](md)	2177	x: -	2175	x:2844	2174	x:2733 (σ)
$Y_2(\tau_1)$, π	2200	x:3124 (σ)	2199	x:2867 (σ) z:2886 (π)	2197	x:2755 (σ)
$Y_3(\tau_5)$, σ	2243	x:3169 (π) z:3201 (σ)	2236	x:2904 (π) z:2935 (σ)	2232	x: - z:2816 (σ)
$Y_4(\tau_3)$, π	2306	x:3221 (σ) z:3245 (π)	2305		2304	x:2856 (σ)
$Y_5(\tau_5)$, σ	2339	x:3257 (π) z:3279 (σ)	2339		2338	x: - z:2911 (σ)
$Y_6(\tau_2)$	-		-		-	
$Y_7(\tau_5)$, σ	2667±3 [b]		2667±3 [b]		2664±3 [b]	
$Y_8(\tau_4)$	-		-		-	

[a] Polarisation for a magnetic dipole transition

[b] Tentative assignment only

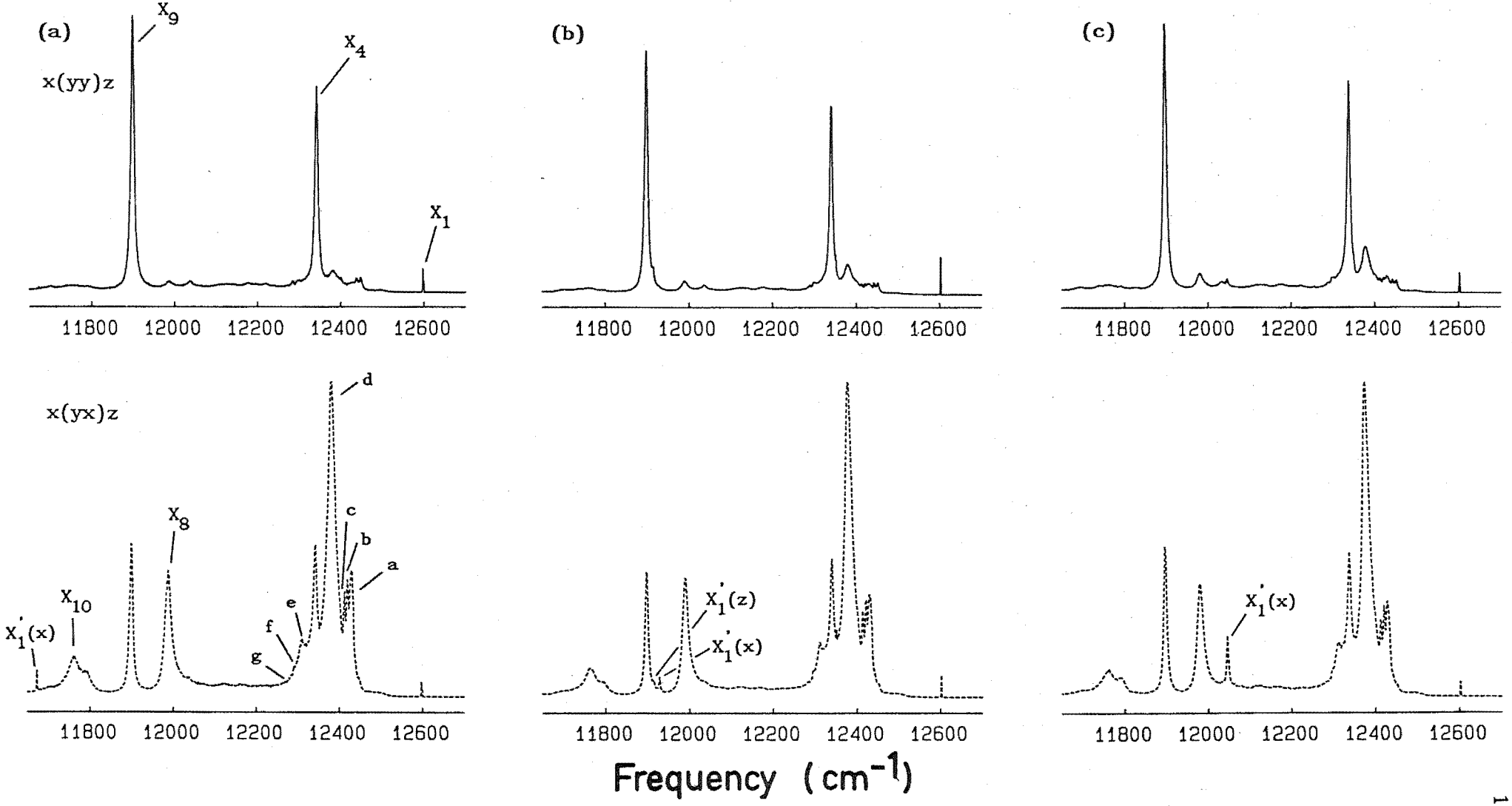

Figure V.1.17 14K $^1D_2 \rightarrow {}^3H_6$ polarised emission from the (a) H^-, (b) D^- and (c) T^- C_{4v} sites in $SrF_2:Pr^{3+}$.

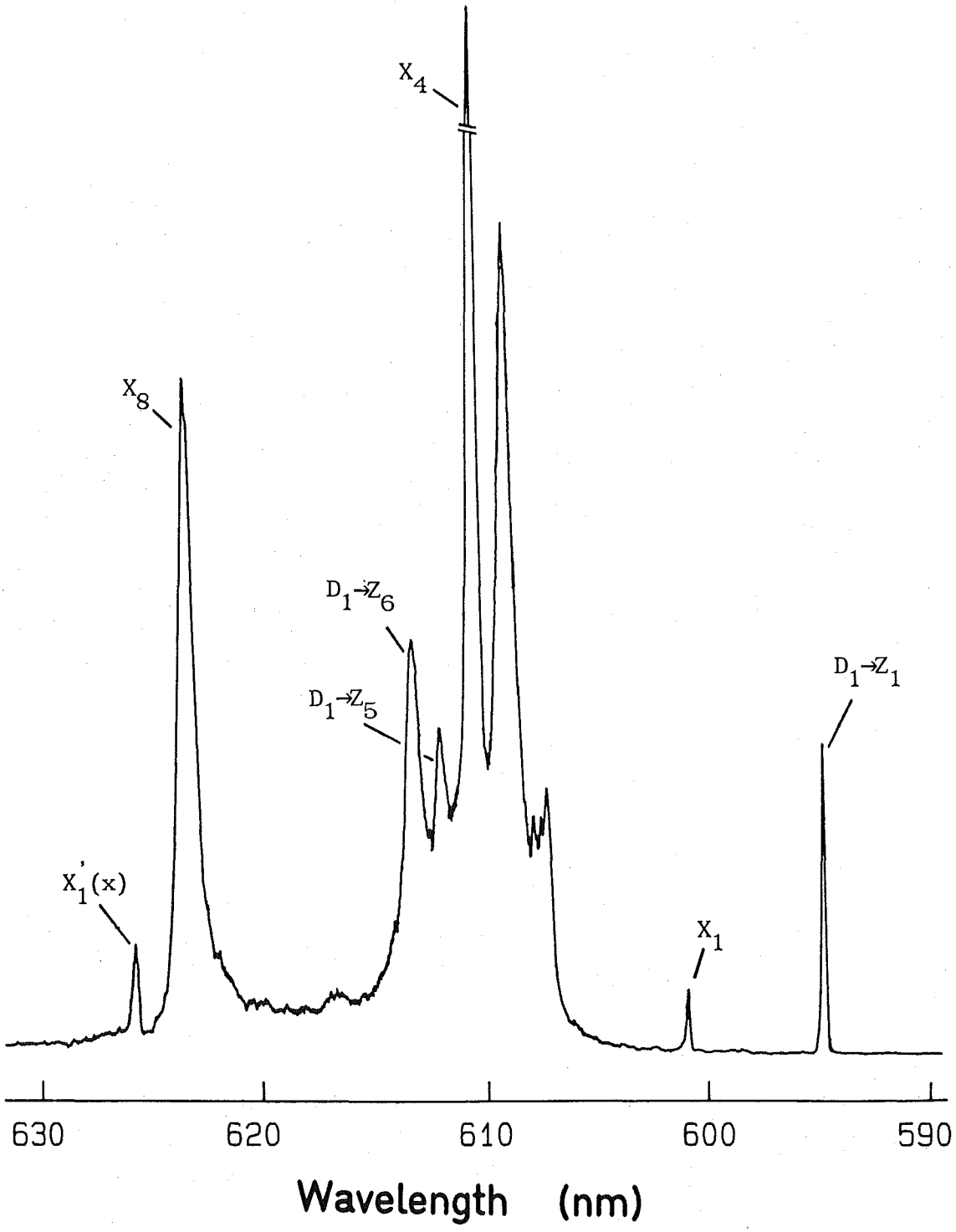

Figure V.1.18 $^3P_0 \rightarrow {}^3H_6$ fluorescence from the C_{4v} D^- site $SrF_2:Pr^{3+}$ with $^3H_4(Z_1) \rightarrow {}^3P_0$ excitation. The $^1D_2 \rightarrow {}^3H_4$ emission is in the same spectral region and some of these transitions are observed.

Those transitions positively assigned are to the $X_1(\tau_5)$, $X_4(\tau_5)$, $X_8(\tau_1)$, $X_9(\tau_5)$ and $X_{10}(\tau_3)$ crystal field levels and have been indicated in the spectra. The observed x(yy)z:x(yx)z polarisation ratios of 2:1 for the X_1, X_4, X_9 levels and of 0:1 for the X_8, X_{10} levels are consistent with the selection rules for transitions to these levels.

Only a tentative assignment can be made to the $X_2(\tau_1)$ crystal field level with the relevant transition labelled 'd' in Figure V.1.17(a). The π-polarisation of this transition is appropriate for a terminating level having τ_1 symmetry but an alternative explanation of this line and others at a slightly higher frequency can be invoked using lattice phonons. The group of three lines labelled a, b and c in Figure V.1.17(a) has no purely electronic origin and along with the line labelled 'd', appear in the spectra for all three sites. This band of lines bears a resemblance to the lattice phonon vibronic band that was described in Section V.1.2 showing the $^1D_2$ excitation spectra. Comparison with Figure V.1.3 from that section reveals the similar polarisation and character of the two bands. The parent electronic level in the $^3H_6$ multiplet is the $X_1(\tau_5)$ level. Table V.1.8 gives the frequency intervals from the two electronic levels for the individual vibronic lines in the band. The differences in the frequencies between the two states of the C_{4v} D^- site could arise as the phonons couple to two different electronic levels. The changes of an individual phonon frequency with the three hydrogenic ion isotopes, reflect the distortions of the lattice to compensate for the different physical characteristics of the ions.

Table V.1.8

Lattice phonon frequencies in the hydrogenic C_{4v} Pr^{3+} ion sites in $SrF_2:Pr^{3+}$, determined from vibronic line intervals from the $^1D_2(D_1)$ and $^3H_6(X_1)$ electronic levels.

Vibronic line label in Figure V.1.17	Vibronic line intervals from the electronic states			
	$^1D_2(D_1)$ C_{4v} D^-	$^3H_6(X_1)$ C_{4v} H^-	$^3H_6(X_1)$ C_{4v} D^-	$^3H_6(X_1)$ C_{4v} T^-
a	165	170	173	174
b	177	180	181	182
c	187	187	189	190
d	244	218	223	224
e	291	287	291	292
f	303	298	303	303
g	318	313	313	-

Vibronic lines associated with local mode phonons are also observed coupled to several electronic levels, the most prominant being associated with the $X_1(\tau_5)$ level. An interesting point is the comparable strength of the (x) vibronic line and its parent X_1 line in the spectra of Figure V.1.17. The intensity of the line to X_1 is unusually small as typically, vibronic lines are 1% of their parent line strength. The transition to X_1 from $^3P_0$ has a similar relative intensity (Figure V.1.18.). Transitions from $^3P_0$ and $^1D_2(D_1)$ to $X_1(\tau_5)$ are not forbidden by electric dipole radiation and investigations into the oscillator strengths may be worthwhile to reveal the origin of the weaker than expected strength.

A comparison between Figures V.1.17 and V.1.18 shows three extra lines are present in the spectrum of $^3P_0 \rightarrow {}^3H_6$ emission. The wavelengths of the extra lines identify their origin as $^1D_2 \rightarrow {}^3H_4$

transitions. This assignment is confirmed by the longer fluorescent lifetime of these lines as the $^3P_0$ level has a shorter lifetime than the $^1D_2(D_1)$ level (Chapter VIII). The mechanism for populating the $^1D_2$ multiplet from $^3P_0$ excitation appears to involve hydrogenic ion local mode vibrations as emission from $^1D_2$ following $^3P_0$ excitation is practically nonexistent for the C_{4v} F^- site. The extension of the phonon spectrum to higher frequencies by the hydrogenic ion local modes can provide a much lower order process for the non-radiative decay of the upper level leading to the efficient quenching of the emission. Another manifestation of this process is the difference in the fluorescent lifetime of an emitting level across the C_{4v} site series with the H^- sites being fastest. Although a spectrum was not recorded, a consequence of this mechanism would be that the $^1D_2 \longrightarrow {}^3H_4$ transitions would have a greater strength relative to the $^3P_0 \longrightarrow {}^3H_6$ transitions in the C_{4v} H^- site version of Figure V.1.18, as the higher frequency H^- local modes would be more efficient at quenching the $^3P_0$ excitation. Further discussion of these dynamical aspects to the decay will be presented in Chapter VIII.

The energy levels of the $^3H_6$ multiplet for the three hydrogenic C_{4v} sites in $SrF_2:Pr^{3+}$ are summarised in Table V.1.9. The transition polarisations are also included as are the local mode vibronic levels.

The $^3F_2$ Multiplet

Spectra of the emission from the $^1D_2$ multiplet to the crystal field levels and vibrational levels of the $^3F_2$ multiplet were recorded at 14 K for the Pr^{3+} ion in the C_{4v} H^- and D^- centres. Only the electronic transitions were recorded for the C_{4v} T^- site. Figure V.1.19 shows the polarised emission from a <100> oriented crystal for the Pr^{3+} ion in the C_{4v} D^- site. The $^3P_0 \longrightarrow {}^3F_2$ emission is shown in Figure V.1.20 for this site. Although the polarised emission was recorded for the C_{4v} H^- site the signal to noise was low and the total

Table V.1.9

Electronic and local mode vibronic level energies for the $^3H_6$ multiplet of the Pr^{3+} ion in the hydrogenic C_{4v} sites in SrF_2. The polarisation of the transition from $^1D_2(D_1)$ is given for each level.

Electronic state symmetry and polarisation	C_{4v} H^- Electronic level energy (cm^{-1})	C_{4v} H^- Vibronic level mode, energy (cm^{-1}) and polarisation	C_{4v} D^- Electronic level energy (cm^{-1})	C_{4v} D^- Vibronic level mode, energy (cm^{-1}) and polarisation	C_{4v} T^- Electronic level energy (cm^{-1})	C_{4v} T^- Vibronic level mode, energy (cm^{-1}) and polarisation
$X_1(\tau_5)$, σ	4222	x:5149(π) xx:6042±5	4218	x:4892 (π) z:4907 (σ)	4215	x:4771 (π) z:4783 (σ)
$X_2(\tau_1)$, π	4440 [a]		4441 [a]		4439 [a]	
$X_3(\tau_4)$	-		-		-	
$X_4(\tau_5)$, σ	4479		4480		4479	
$X_5(\tau_2)$	-		-		-	
$X_6(\tau_3)$	-		-		-	
$X_7(\tau_4$	-		-		-	
$X_8(\tau_1)$, π	4834		4831		4837	
$X_9(\tau_5)$, σ	4922	z:5857±5	4923	z:5606±5 (σ)	4921	
$X_{10}(\tau_3)$,π	5057	x:5979±5	5057		5057	

[a] Tentative assignment to line labelled 'd' in Figure V.1.17.

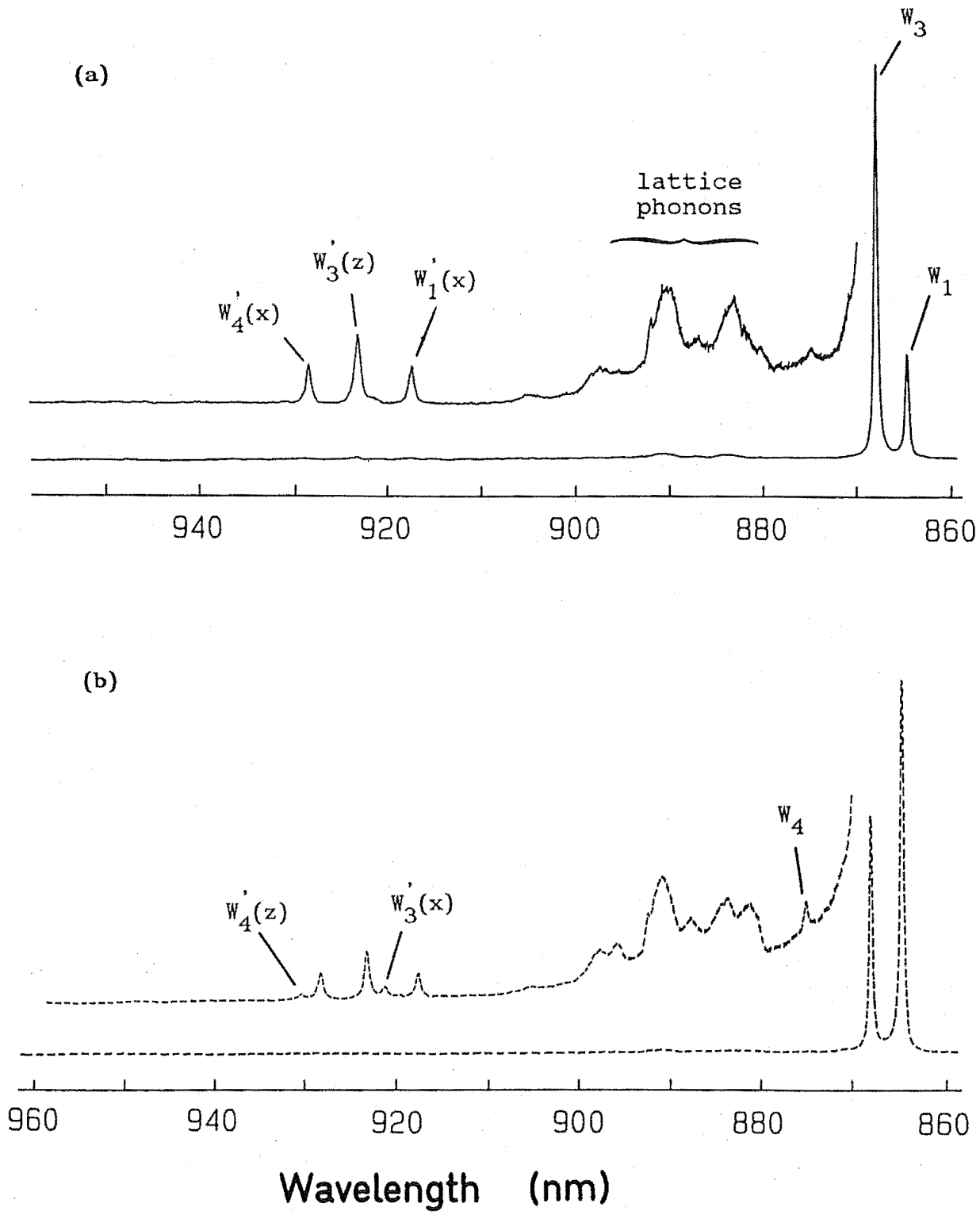

Figure V.1.19 Polarised fluorescence at 14K, of the $^1D_2 \rightarrow {}^3F_2$ transitions from the C_{4v} D^- site in $SrF_2:Pr^{3+}$ for the (a) x(yy)z and (b) x(yx)z polarisation geometries.

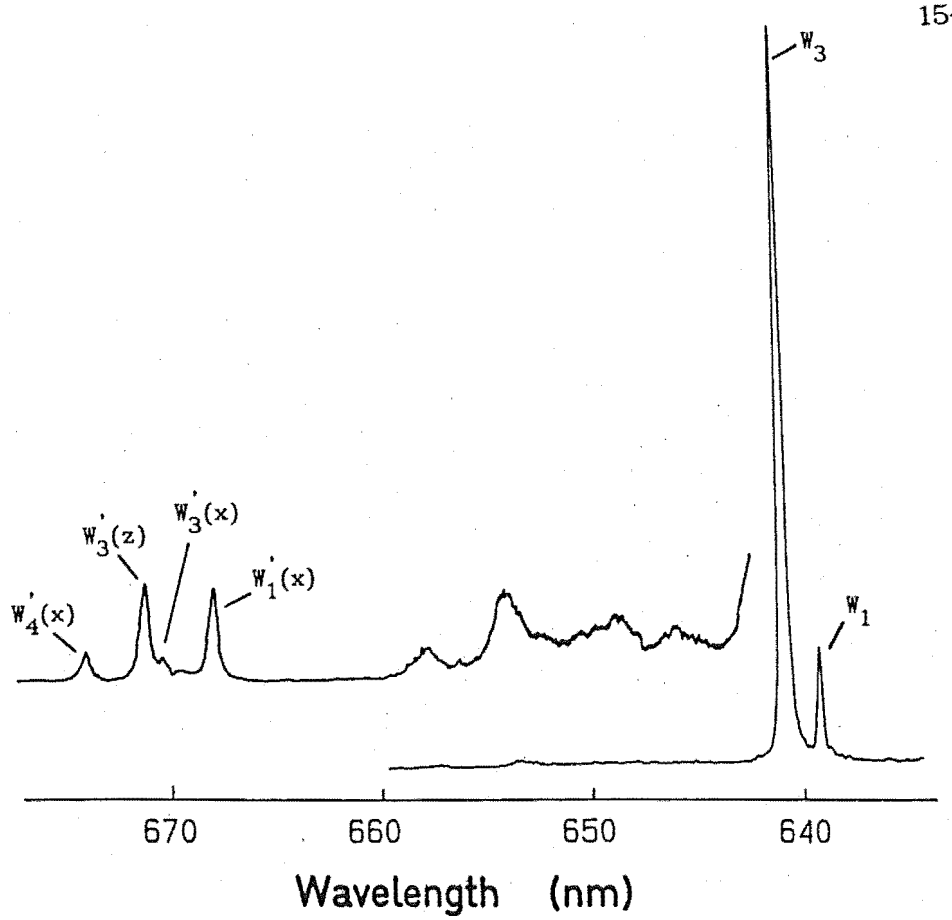

Figure V.1.20 $^3P_0 \rightarrow {}^3F_2$ fluorescence recorded with $^3H_4(Z_1) \rightarrow {}^3P_0$ excitation, from the C_{4v} D^- site in $SrF_2:Pr^{3+}$.

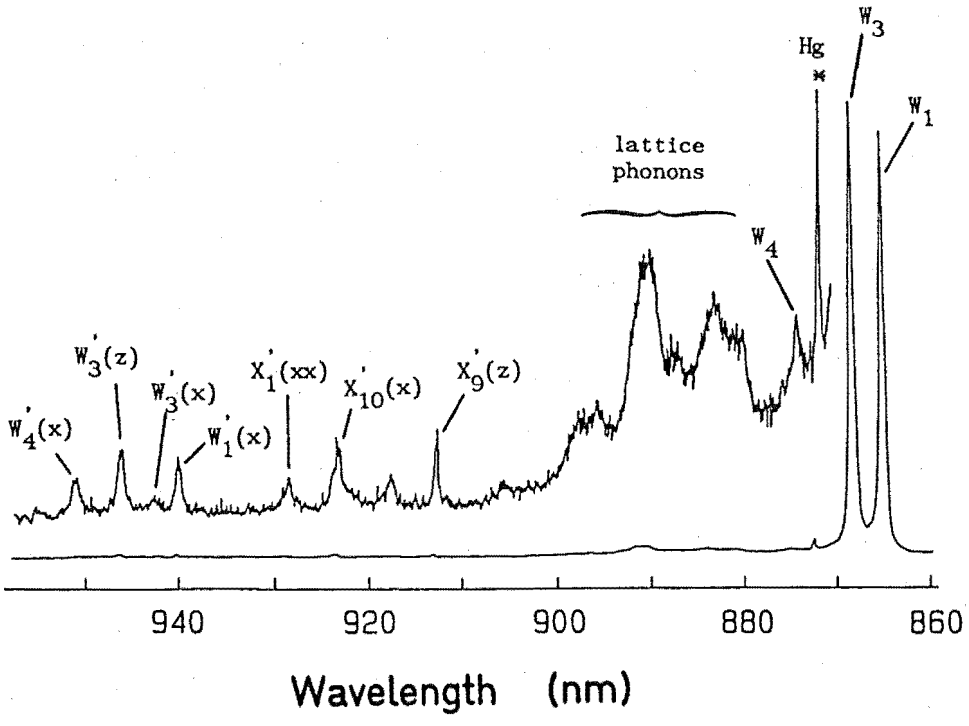

Figure V.1.21 $^1D_2 \rightarrow {}^3F_2$ fluorescence recorded at 14K from the C_{4v} H^- site in $SrF_2:Pr^{3+}$.

emission is depicted here in Figure V.1.21 to illustrate the features.

The energies of the electronic levels and local mode vibronic levels for the $^3F_2$ multiplet are summarised in Table V.1.10 for the hydrogenic C_{4v} sites in $SrF_2:Pr^{3+}$. Polarisation of the transitions to the various levels has also been included where it can be determined.

Transitions to three of the four crystal field levels have been identified in the spectra and are indicated using the W_i labels appropriate for this multiplet. The polarisations of the transitions observed are consistent with the level symmetries and the selection rules for electric dipole radiation. The lowest crystal field component has been assigned to the level transforming as the γ_1 irrep but the ordering of the remaining three is somewhat arbitrary as the position of the γ_4 level has yet to be established.

Several local mode vibronic transitions are apparent in the spectra including lines that correspond to vibrations coupled to $^3H_6$ electronic levels. This is particularly pronounced for the C_{4v} H^- site but not so for the D^- centre where such lines have merged with the broad lattice phonon structure. The origin of those local mode vibronic lines identified, is indicated in the spectra. Due to time constraints, the emission of the C_{4v} T^- site was not studied using the infrared emission spectrometer and local mode frequencies are not available for this multiplet.

The $^3F_3$ and $^3F_4$ Multiplets

The transitions to the levels of the $^3F_3$ and $^3F_4$ multiplets will be discussed together as the small separation between these two multiplets makes it convenient to record their emission spectra together. Emission to these levels from $^1D_2$ was recorded at 14 K for the C_{4v} H^- and D^- sites and from $^3P_0$ for the C_{4v} D^- site. The tritiated sample was not examined in this region of the spectrum.

Table V.1.10

Energies of the electronic and local mode vibronic levels of the $^3F_2$ multiplet for the Pr^{3+} ion in the hydrogenic C_{4v} sites of $SrF_2:Pr^{3+}$. The polarisation for transitions from $^1D_2(D_1)$ is also included. Level uncertainties are ± 1 cm^{-1}.

Electronic state symmetry and polarisation	C_{4v} H^- Electronic level energy (cm^{-1})	C_{4v} H^- Vibronic level mode, energy (cm^{-1}) and polarisation	C_{4v} D^- Electronic level energy (cm^{-1})	C_{4v} D^- Vibronic level mode, energy (cm^{-1}) and polarisation	C_{4v} T^- Electronic level energy (cm^{-1})	C_{4v} T^- Vibronic level mode, energy (cm^{-1}) and polarisation
$W_1(\tau_1)$, π	5249	x,y:6174 (π)	5246	x,y:5915 (σ)	5243	–
$W_2(\tau_4)$	–		–		–	
$W_3(\tau_5)$, σ	5291	x,y:6220 (π) z:6241 (σ)	5290	x,y:5959 (π) z:5983 (σ) xx:664 (π) zz:6661 (σ)	5287	–
$W_4(\tau_3)$, π	5380	x,y:6296 (σ)	5380	x,y:6043 (σ) z:6068 (π)	5373±5	–

Figures V.1.22 and V.1.23 show the polarised $^1D_2 \rightarrow {}^3F_3$, $^3F_4$ emission from a <100> oriented crystal for the C_{4v} H^- and D^- sites respectively. The emission from $^3P_0$ for the C_{4v} D^- site is depicted in Figure V.1.24. In common with other multiplets, transitions to hydrogenic ion local mode vibronic levels are apparent in spectra recorded with an expanded intensity scale. Figure V.1.25 shows these details in polarised spectra for the C_{4v} D^- site while Figure V.1.26 records the total emission for the H^- centre. Where it can be established the origin of each electronic and vibronic line is indicated with the labels V_i and U_i representing the levels of the $^3F_3$ and $^3F_4$ multiplet respectively. The poor signal to noise for the H^- site and the absence of spectra for the T^- site make cross-checking of local mode frequencies difficult and some vibronic level assignments may be subsequently found to be in error. The spectra of the $^3F_3$ multiplet will be discussed first.

Transitions have been observed to all five crystal field levels of the $^3F_3$ multiplet for both H^- and D^- C_{4v} sites and Table V.1.11 summarises the electronic and local mode vibronic level energies for this multiplet. The spectral lines to the V_2 and V_3 levels transforming as the τ_4 and τ_2 irreps respectively, have a x(yy)z:x(yx)z polarisation ratio of 1:0 consistent with magnetic dipole transitions to these levels. However the observation of both transitions again illustrates the relaxation of the strict selection rules as the emitting level must transform as both τ_1 and τ_3 irreps for the appearance of these two lines. The x(yy)z:x(yx)z ratio is 2:1 for the V_1 and V_4 levels indicating σ-polarised transitions and a level symmetry of τ_5 for these states. The remaining V_5 level transforms as the τ_3 irrep and shows a 0:1 polarisation ratio consistant with a π-polarised transition from $^1D_2(D_1)$.

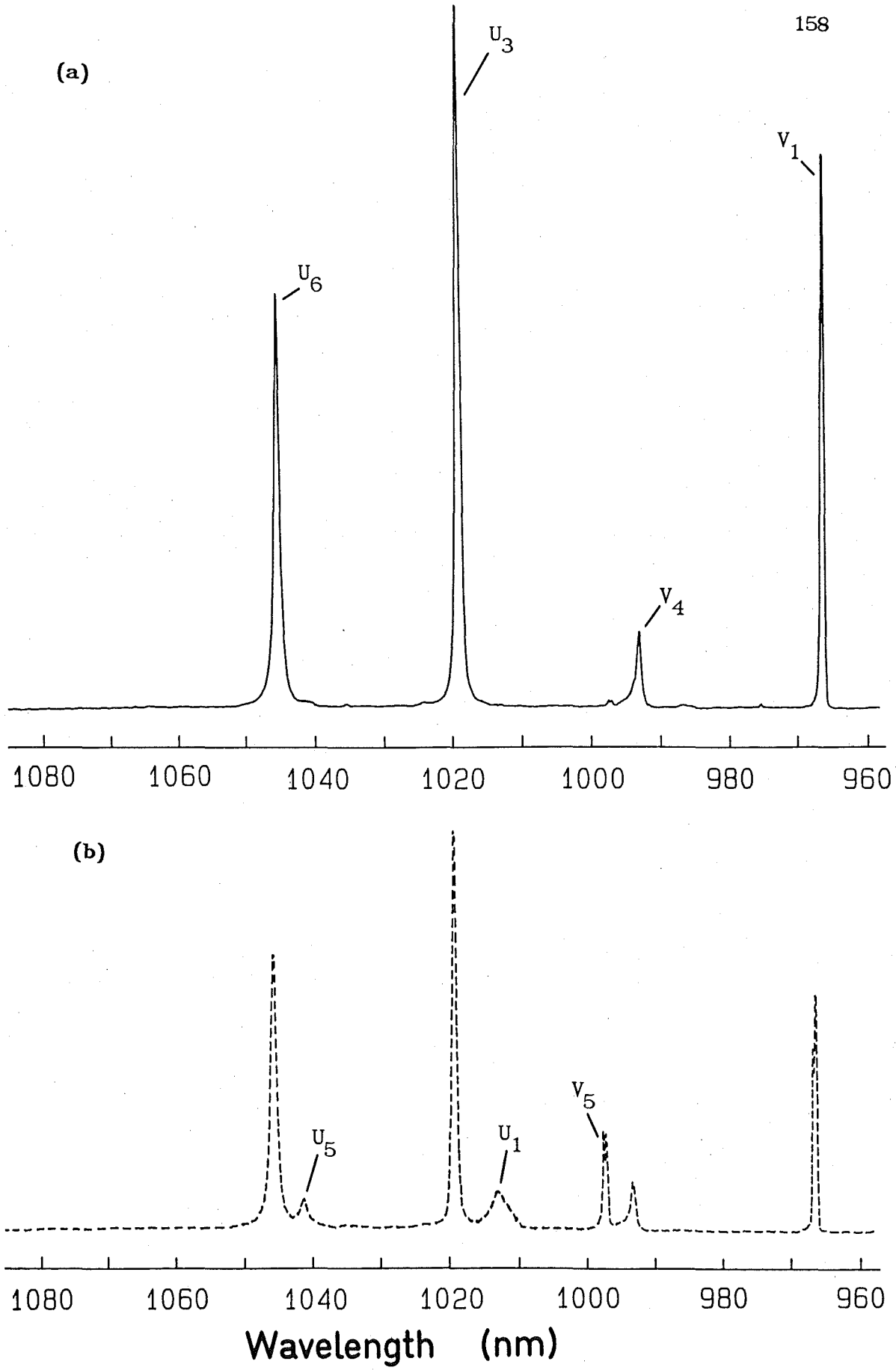

Figure V.1.22 Polarised $^1D_2 \rightarrow {}^3F_3, {}^3F_4$ emission from the C_{4v} H^- site in $SrF_2:Pr^{3+}$ recorded at 14K with (a) x(yy)z and (b) x(yx)z polarisation geometries.

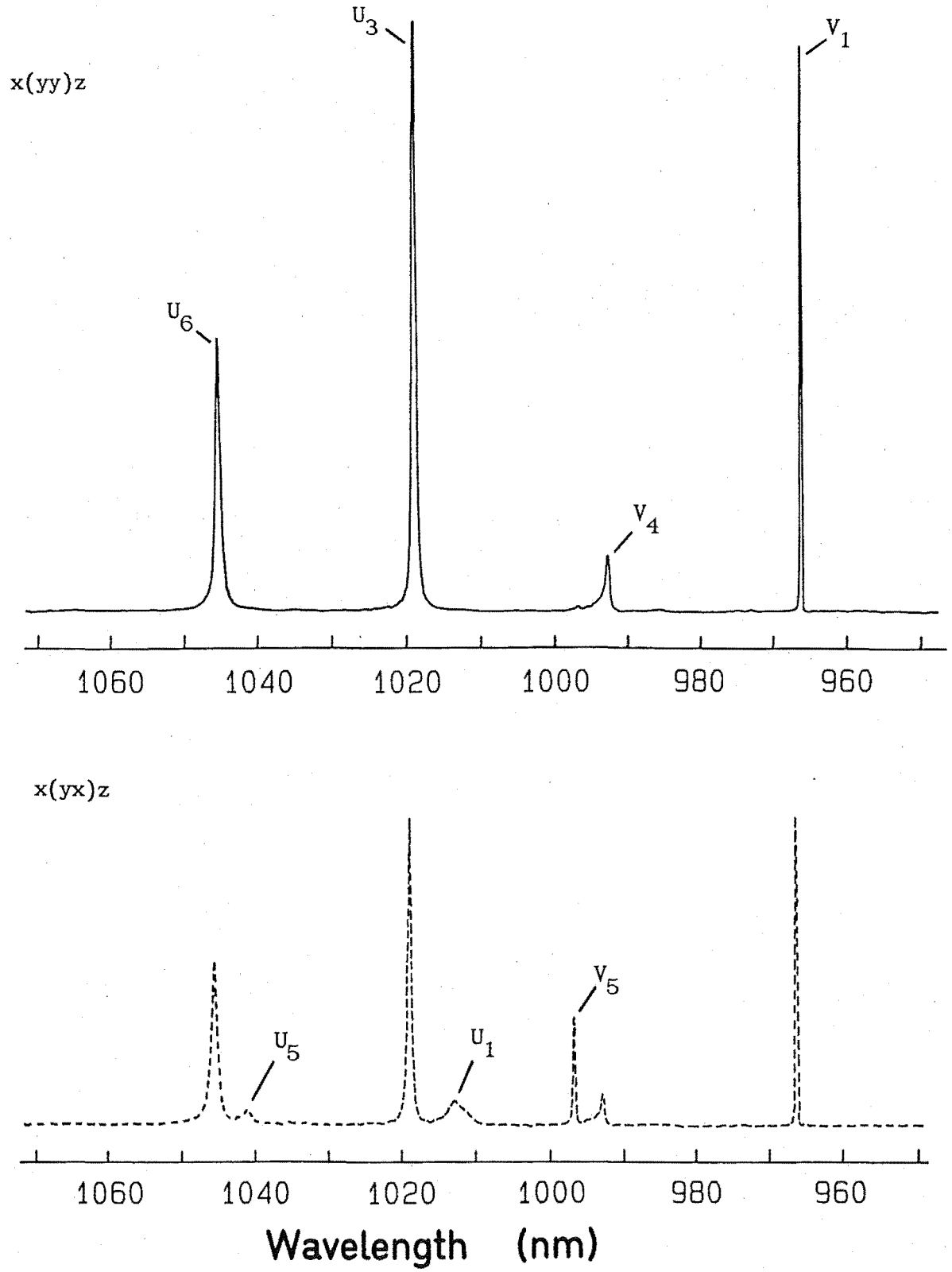

Figure V.1.23 14K Polarised $^1D_2 \rightarrow {}^3F_3, {}^3F_4$ emission from the C_{4v} D^- site in $SrF_2:Pr^{3+}$.

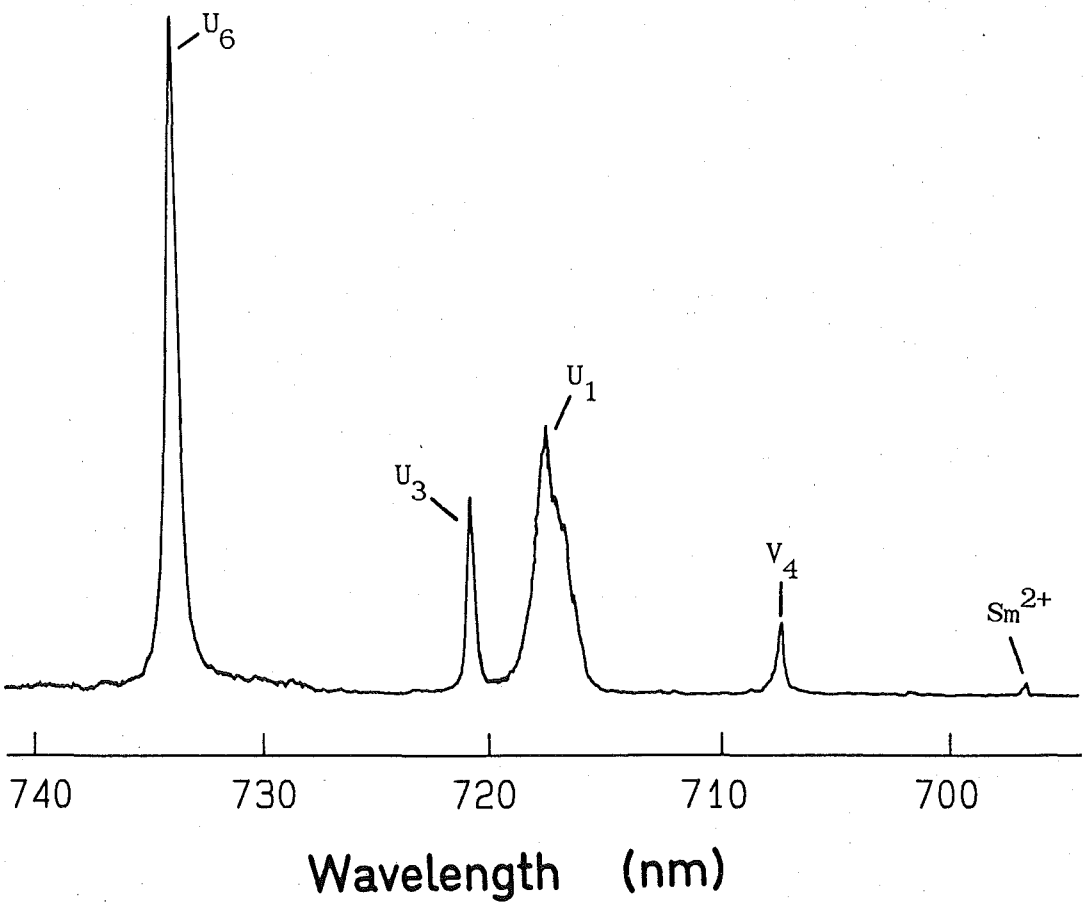

Figure V.1.24 14K $^3P_0 \rightarrow {}^3F_3, {}^3F_4$ emission from the C_{4v} D^- site in $SrF_2:Pr^{3+}$ with $^3H_4(Z_1) \rightarrow {}^3P_0$ excitation.

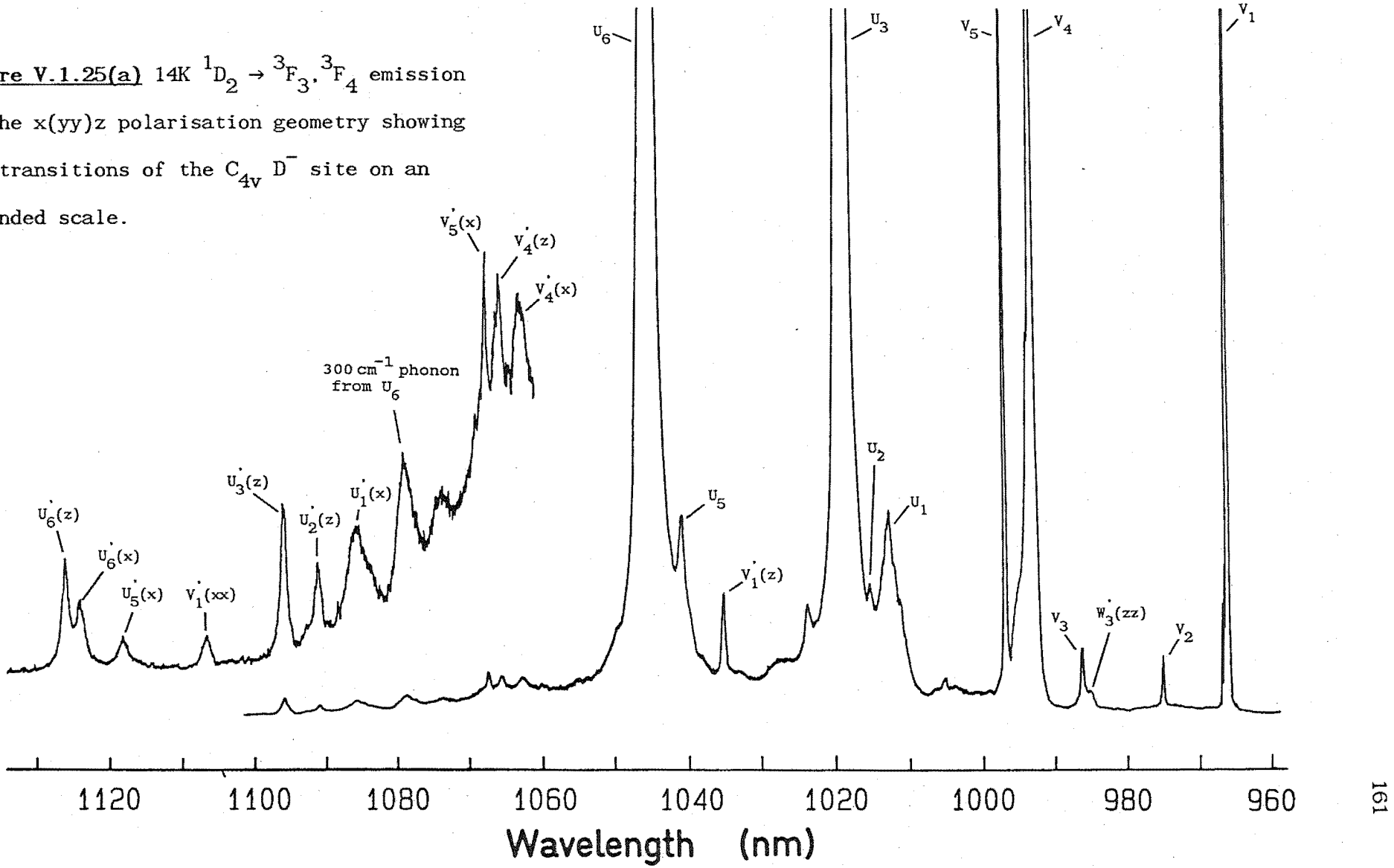

Figure V.1.25(a) 14K $^1D_2 \rightarrow {}^3F_3, {}^3F_4$ emission in the x(yy)z polarisation geometry showing the transitions of the C_{4v} D^- site on an expanded scale.

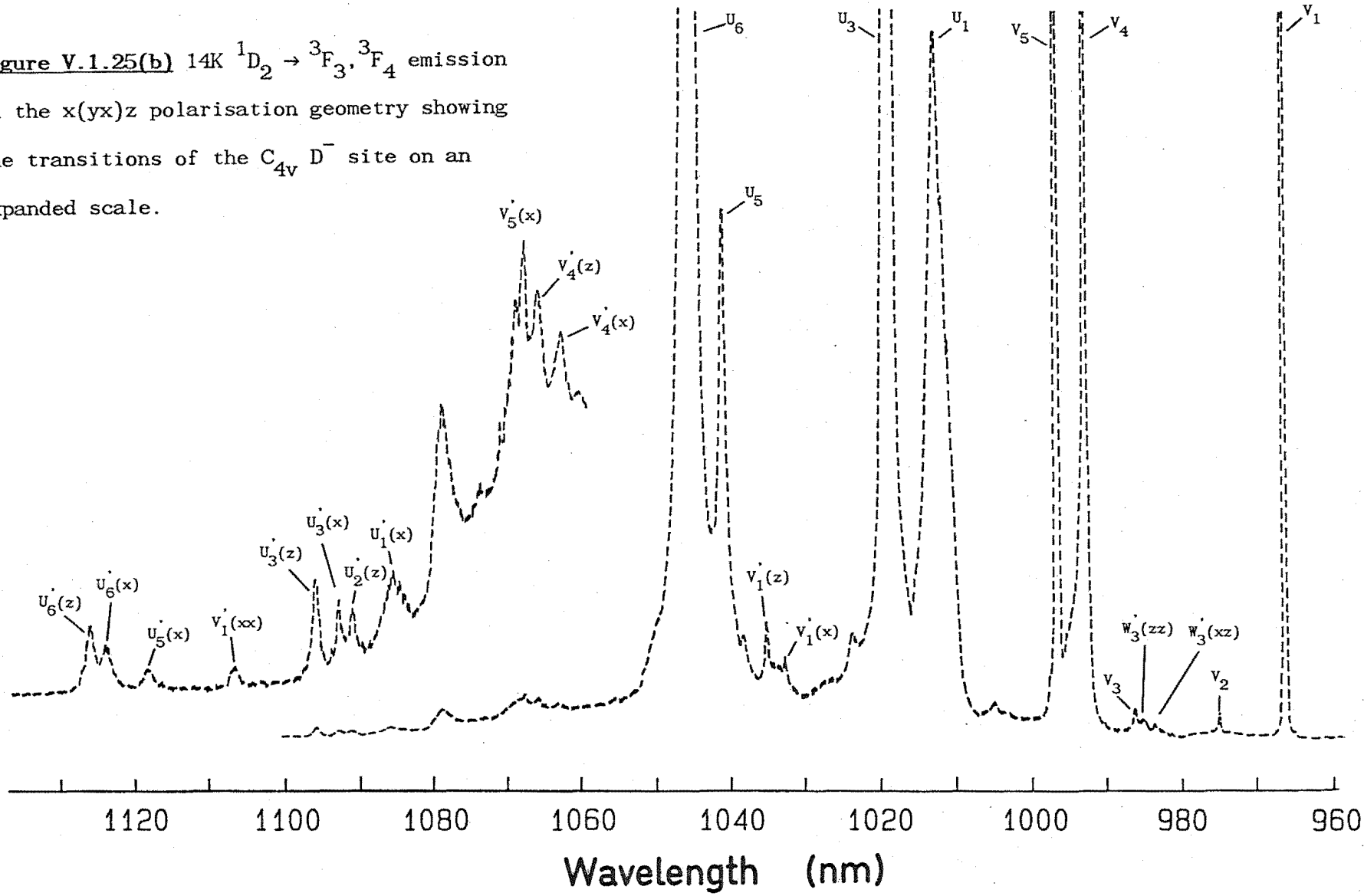

Figure V.1.25(b) 14K $^1D_2 \rightarrow {}^3F_3, {}^3F_4$ emission in the x(yx)z polarisation geometry showing the transitions of the C_{4v} D^- site on an expanded scale.

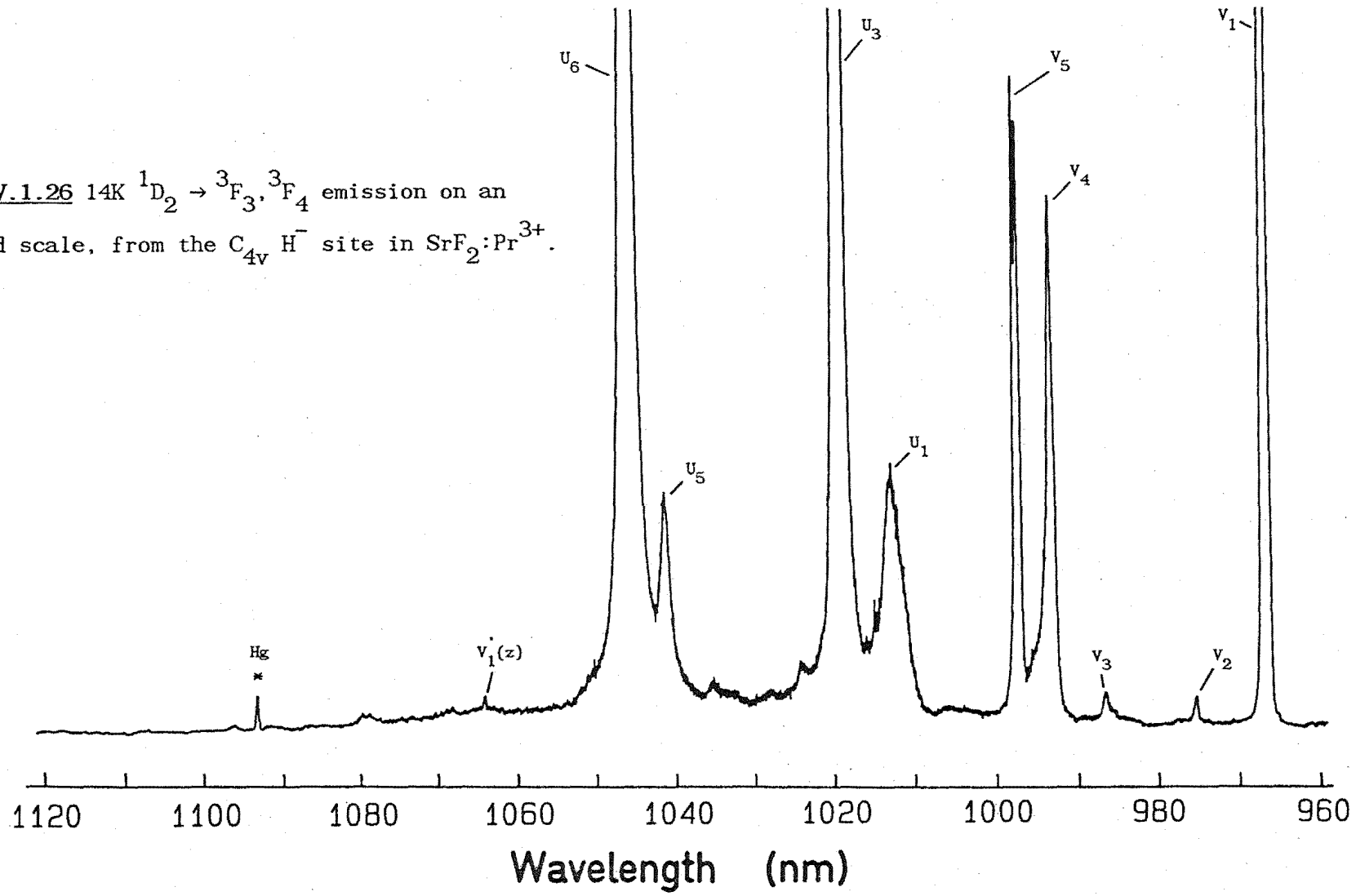

Figure V.1.26 14K $^1D_2 \rightarrow {}^3F_3, {}^3F_4$ emission on an expanded scale, from the C_{4v} H^- site in $SrF_2:Pr^{3+}$.

Table V.1.11

Energies of the electronic and local mode vibronic levels of the $^3F_3$ multiplet for the Pr^{3+} ion in the hydrogenic C_{4v} sites in SrF_2. The polarisation of the transition from $^1D_2(D_1)$ to the levels is also included where it is determined. Level uncertainties are ± 2 cm^{-1}.

Electronic symmetry polarisation	C_{4v} H^-		C_{4v} D^-	
	Electronic level energy (cm^{-1})	Vibronic level mode, energy (cm^{-1}) and polarisation	Electronic level energy (cm^{-1})	Vibronic level mode, energy (cm^{-1}) and polarisation
$V_1(\gamma_5)$, π	6460	z:7412	6461	x,y: 7129(π) z: 7153(σ) xx: 7775
$V_2(\gamma_4)$, π'(md)[a]	6554	-	6556	-
$V_3(\gamma_2)$, π'(md)[a]	-		6672	x,y: 7338
$V_4(\gamma_5)$, σ	6740		6740	x,y: 7404 z: 7430
$V_5(\gamma_1)$, σ	6781	-	6780	x,y: 7447

[a] Magnetic dipole transition

The transitions to the V_1 and V_5 levels for the C_{4v} H^- site comprise two components separated by 0.3 and 0.4 nm respectively (Figure V.1.22). This effect was repeatable on the particular day the spectra in the figure were recorded. As other equally narrow lines are not observed to show such a splitting instrumental effects can be discounted. It is difficult to envisage a mechanism that would produce these splittings in only a few of the observed transitions. A splitting has been observed in the optical transitions of the R site in CaF_2:Er^{3+}:D^- (Reeves et al [1987]) where the lines were observed to comprise two components separated by the rather smaller amount of 11

GHz and to appear in most of the spectral lines of the site. The explanation invoked has the interstitial hydrogenic ion occupying two stable positions within the lattice cube. A small splitting is observed in the transitions as the rare-earth ion is sensitive to the changes in the crystal field between the two hydrogenic ion sites. A similar explanation could be used to explain the Pr^{3+}- H^- site results but must also consider why only the transitions to V_1 and V_5 are sensitive to the changes. Clearly more experimental data are required.

Five of the seven crystal field levels and numerous local mode vibronic lines have been identified for the $^3F_4$ multiplet of the Pr^{3+} ion in the hydrogenic C_{4v} sites. The transitions have been indicated in the figures with the labels U_i using the same convention of the other multiplets. In common with the C_{4v} F^- site in SrF_2:Pr^{3+} the transition to the U_1 crystal field level is relatively stronger from the $^3P_0$ level than the $^1D_2$ level and is also uncharacteristically broad for a transition to the lowest crystal field component of a multiplet. The larger than usual linewidth probably arises from the efficient non-radiative decay from this level across the small energy separation between the $^3F_3$ and $^3F_4$ multiplets. As the separation is only about 150 cm^{-1}, it is unlikely the high frequency hydrogenic ion local modes would substantially contribute to the decay and the linewidth is expected, and observed, to be similar for the fluorine and hydrogenic ion sites.

Table V.1.12 summarises the energy level scheme for the $^3F_4$ multiplet including those local mode vibronic levels identified. Transitions to the U_3 and U_6 levels are σ-polarised consistent with their τ_5 level symmetry while the transition to U_5 has a x(yy)z:x(yx)z polarisation ratio close to 0:1 indicating a terminating level symmetry of either τ_1 or τ_3. The level symmetry is chosen to be

τ_3 based on the C_{4v} F^- site where the $D_1 \longrightarrow U_7(\tau_1)$ transition was observed on the low energy side of the $D_1 \longrightarrow U_6(\tau_5)$ line.

In Figure V.1.25 some of the vibronic lines do not show the well defined polarisation that is apparent for levels in other multiplets. This may be associated with polarisation breakthrough as the efficiency of the analyser decreases for these longer wavelength transitions.

Table V.1.12

Energy level scheme for the $^3F_4$ multiplet for the hydrogenic C_{4v} sites in $SrF_2:Pr^{3+}$. Level uncertainties are ± 2 cm^{-1}

Electronic state symmetry and polarisation	C_{4v} H^- Electronic level energy (cm^{-1})	C_{4v} D^- Electronic level energy (cm^{-1})	C_{4v} D^- Vibronic level mode, energy (cm^{-1}) and polarisation
$U_1(\tau_1)$, σ	6937	6938	x,y: 7603
$U_2(\tau_4)$, π'(md)[a]	-	6963	z: 7649
$U_3(\tau_5)$, σ	6998	6999	x,y: 7663 z: 7689
$U_4(\tau_2)$	-	-	
$U_5(\tau_3)$, π	7209	7208 x,	,y: 7870
$U_6(\tau_5)$, σ	7246	7245	x,y: 7916 z: 7932
$U_7(\tau_1)$	-	-	

[a] magnetic dipole transition

V.2 The C_{4v} Hydrogenic Sites in $CaF_2:Pr^{3+}$

V.2.1 Absorption and Excitation of the C_{4v} Hydrogenic Sites in $CaF_2:Pr^{3+}$

Optical absorption to the crystal field levels of the $^1D_2$, $^3P_0$ and $^3P_1$ multiplets was measured for hydrogenated and deuterated crystals of $CaF_2:Pr^{3+}$. Figure V.2.1 shows the absorption spectra recorded for transitions to the $^1D_2$, $^3P_0$ and $^3P_1$ levels for a CaF_2:0.05%$Pr^{3+}:D^-$ crystal. The transitions to the $^3P_0$ and $^3P_1$ levels of the C_{4v} sites identified by Jacobs [1971] are indicated in the spectra, as are the $^1D_2$ levels for this site assigned from results obtained in this work. Absorption transitions of several low symmetry hydrogenic ion sites have been identified in the $^1D_2$ and $^3P_0$ spectra with the $C_s(i)$ labels. The assignment of the $^3P_0$ lines is not complete as technical difficulties prevented laser excitation studies in this region. It has been established that these rhombic symmetry centres contain multiple numbers of hydrogenic ions and that they have some very interesting bleaching effects (Macfarlane, Reeves and Jones [1987], Cockroft et al [1987a]). Further discussion on these centres is reserved until Chapter VI.

A weak absorption transition is visible to the D_2 crystal field component of the $^1D_2$ multiplet at 595.38 nm. The 17 cm^{-1} D_1-D_2 splitting of the C_{4v} F^- site has been increased to 40 cm^{-1} for the C_{4v} D^- site, by the stronger axial crystal field. A similar effect is apparent for the two levels of the $^3P_1$ multiplet where the splitting has increased from 118 cm^{-1} for the C_{4v} F^- site (Table IV.3.1) to 200 cm^{-1} for the D^- site. A crystal field analysis shows that, to first order, this splitting is equal to $\frac{3}{10} B_0^2$, where B_0^2 is the second degree axial crystal field parameter. The substitution of the charge compensating F^- ion by a hydrogenic ion increases the axial crystal field on the rare-earth ion by 70%.

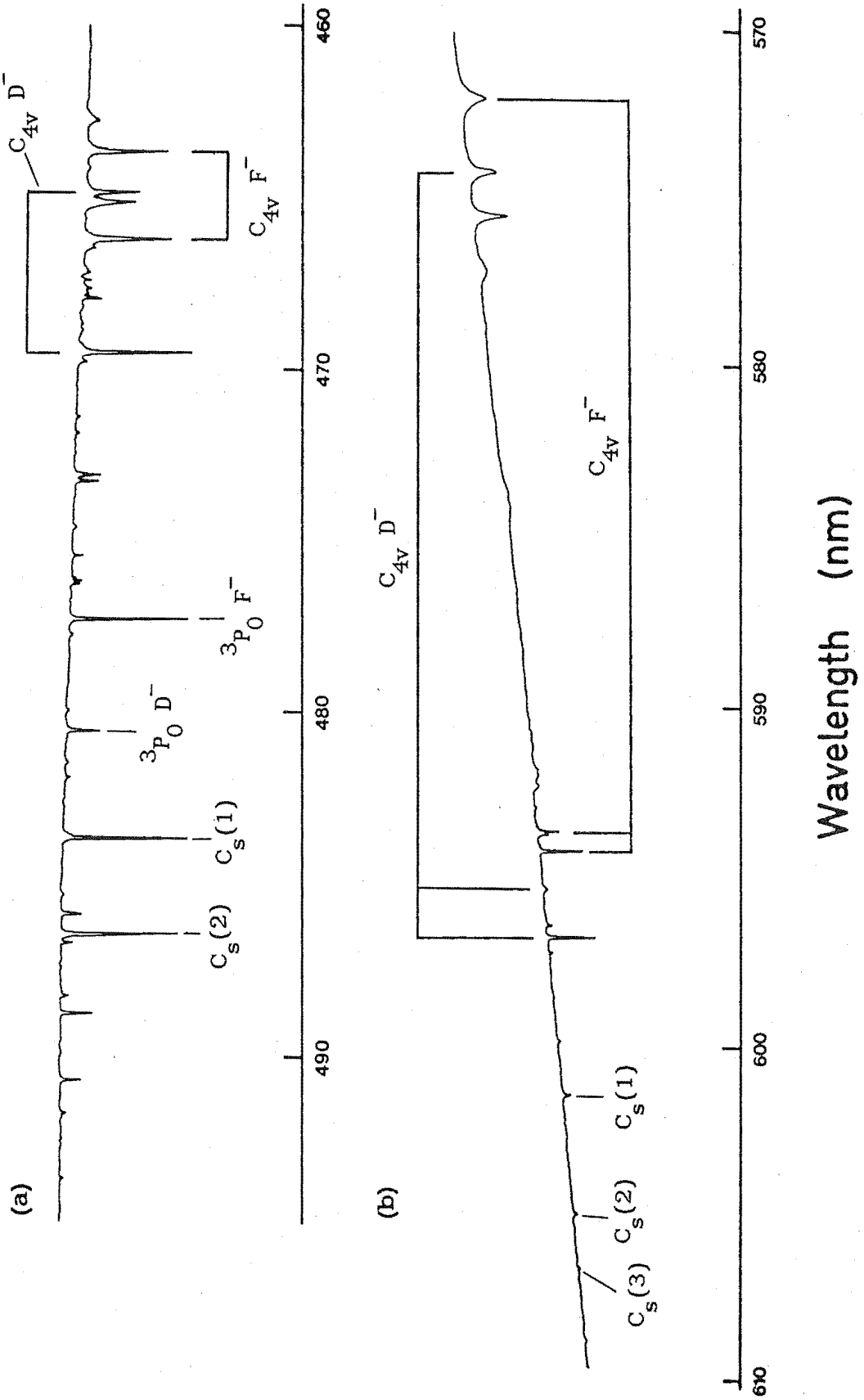

Figure V.2.1 Optical absorption of the (a) $^3P_0$ and $^3P_1$ levels and (b) $^1D_2$ crystal field levels for a CaF_2:0.05%Pr^{3+}:D^- crystal at 14K.

The symmetry of the D_1 and D_2 crystal field levels for the hydrogenic sites will be the same as that for the C_{4v} F^- site, i.e. the D_1 and D_2 levels will transform as the τ_1 and τ_3 irreps of C_{4v} respectively. Table V.2.1 summarises the absorption transitions measured for the hydrogenic ion C_{4v} sites in $CaF_2:Pr^{3+}$ crystals. The data for the C_{4v} T^- site were measured by laser excitation and are included for comparison.

Table V.2.1

Absorption transition wavelengths from the ground state, recorded at 14 K, for the C_{4v} hydrogenic charge compensation ion sites in CaF_2:0.05%Pr^{3+} crystals.

Crystal Field Level		Charge Compensating Ion		
		H^-	D^-	T^-
$^1D_2$	$D_1(\tau_1)$	596.68 nm	596.69 nm	596.69 nm
	$D_2(\tau_3)$	595.38 nm	595.28 nm	595.24 nm
	$D_4(\tau_4)$	574.22 nm	574.13 nm	-
$^3P_0$	(τ_1)	480.28 nm	480.36 nm	-
$^3P_1$	(τ_5)	469.40 nm	469.32 nm	-
	(τ_2)	465.05 nm	464.96 nm	-

The transition identifying the D_2 crystal field level is much more apparent in an excitation spectrum than in absorption, as shown in Figure V.2.2 depicting the $^1D_2$ excitation spectrum of the Pr^{3+}- D^- C_{4v} site in $CaF_2:Pr^{3+}$. In addition to the D_1, D_2 and D_4 crystal field levels, a number of lines associated with other sites are also visible. These lines can be discounted from belonging to the C_{4v} site

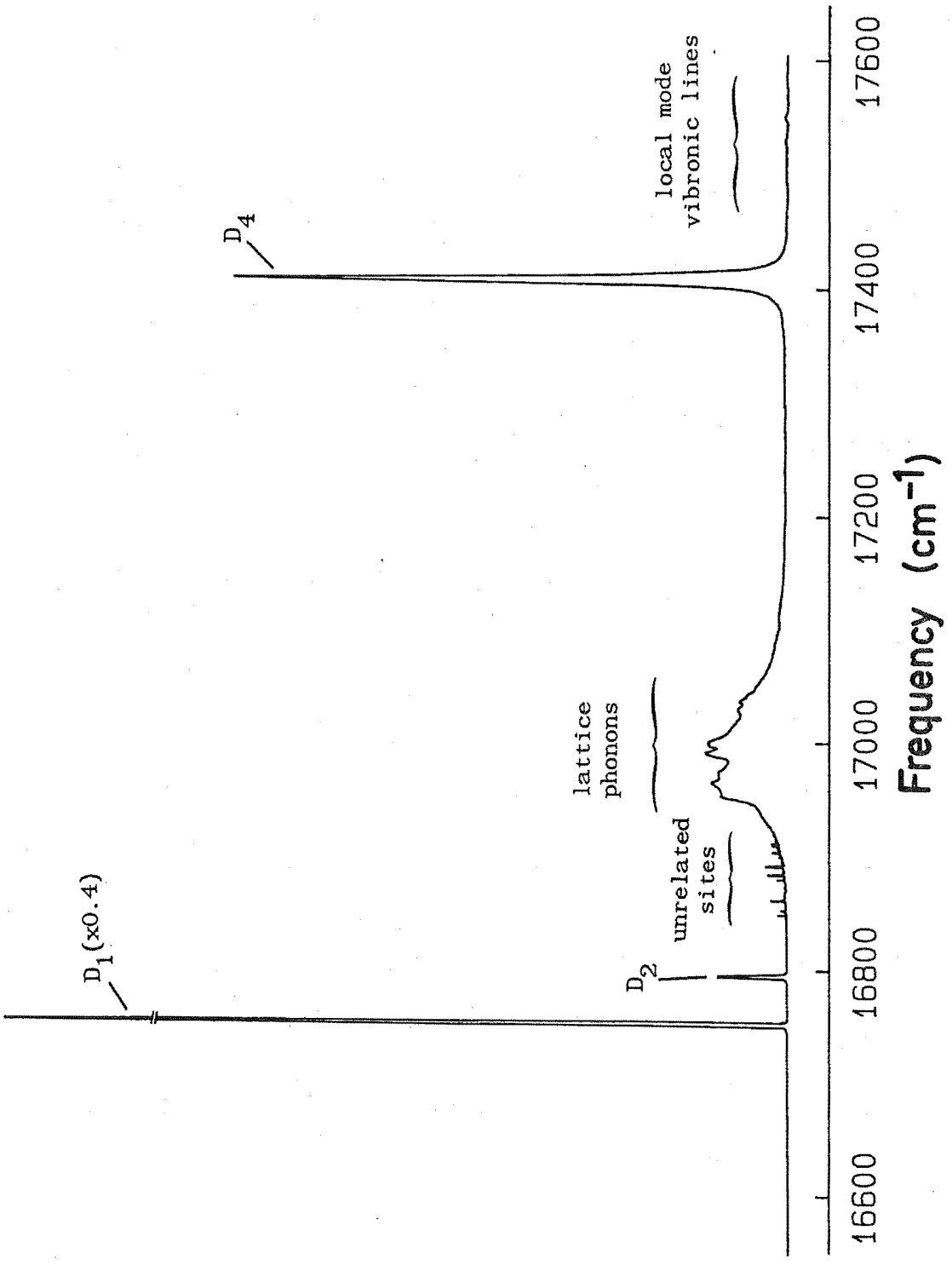

Figure V.2.2 14K $^1D_2$ excitation spectrum for the C_{4v} D^- site in a CaF_2:0.05%Pr^{3+}:D^- crystal.

by comparing relative intensities of lines under various excitation conditions. Also visible and apparently part of the C_{4v} site is a broad band of lattice phonons, similar in character to that previously described for the $SrF_2:Pr^{3+}$ crystals.

On an expanded scale, transitions to local mode vibronic levels that are coupled to the D_1 and D_2 crystal field components are observed at frequencies just higher than the D_4 crystal field level. Polarised excitation spectra can yield information on these lines. Figure V.2.3 shows the 14 K polarised excitation spectra of these vibronic transitions for the C_{4v} Pr^{3+} - D^- site in a <100> oriented $CaF_2:Pr^{3+}:D^-$ crystal. Using the energy intervals from the D_1 and D_2 electronic lines, the local mode vibronic transitions have been identified and are indicated in the spectra. The transition to the $D_2'(z)$ vibronic level is not apparent.

The polarisation of these lines can be understood as follows. The transverse local mode vibration will couple to the $D_1(\gamma_1)$ and $D_2(\gamma_3)$ crystal field levels to produce x,y vibronic levels transforming as the γ_5 irrep of C_{4v}. Absorption transitions to these levels will be π-polarised from the γ_5 symmetry ground state and are expected to show a x(yy)z:x(yx)z polarisation ratio of 0:1, which is observed. Similarly, the longitudinal (z) local mode vibration will couple to D_1 and D_2 levels to produce z vibronic levels transforming as the γ_1 and γ_3 irrep respectively. Absorption transitions to these z-vibronic levels will be σ-polarised and are expected to give the 2:1 x(yy)z:x(yx)z polarisation ratio observed.

The $D_1'(x)$ vibronic line at 17475 cm^{-1} almost coincides with the D_4 crystal field level of the C_{4v} F^- site at 17477 cm^{-1}. This coincidence becomes apparent when the spectrometer monitoring the C_{4v} D^- site fluorescence is tuned away from the position of peak intensity. The line at 17475 cm^{-1} increases its relative intensity

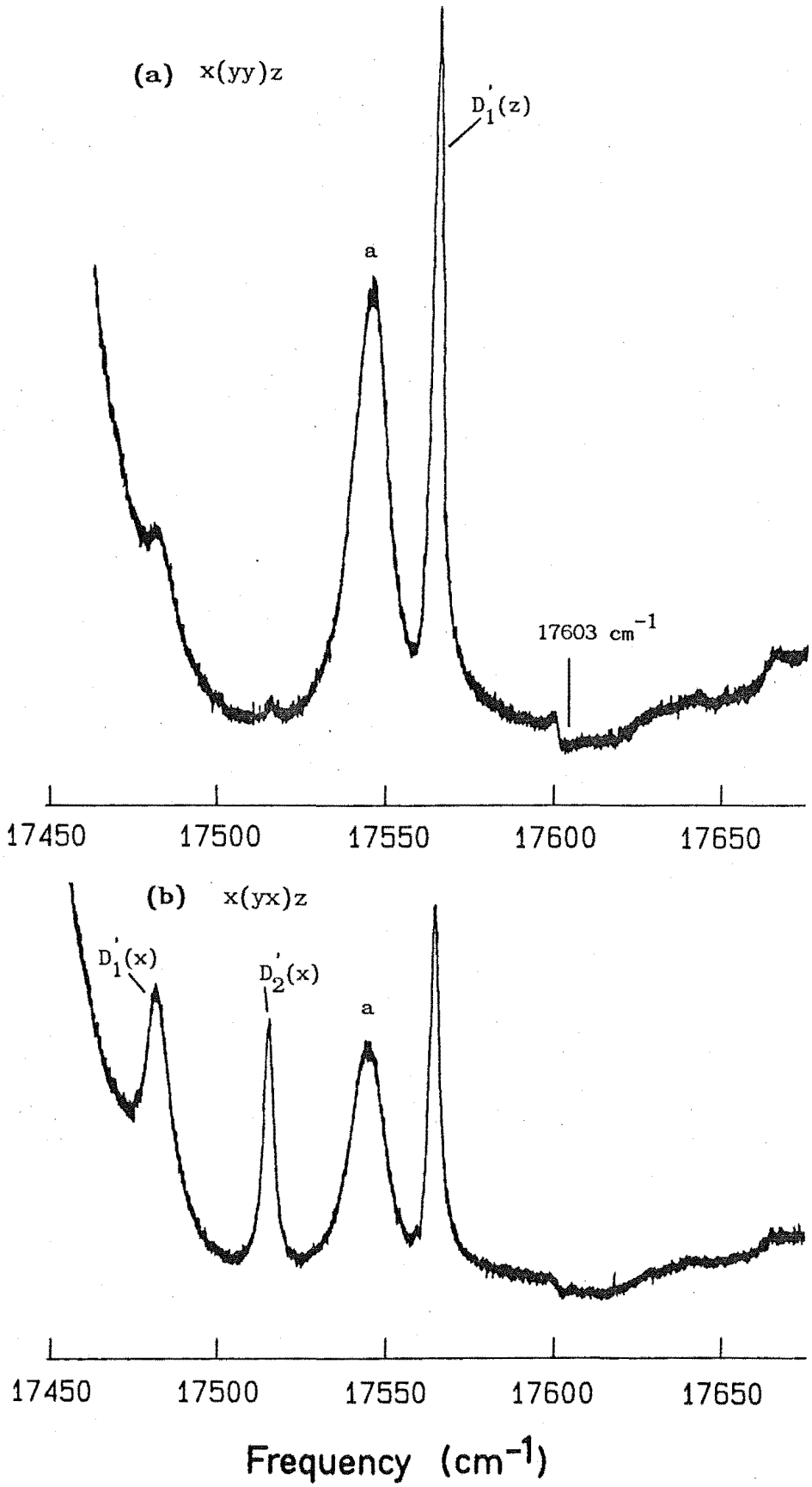

Figure V.2.3 Polarised excitation spectra of the C_{4v} D^- site in $CaF_2:Pr^{3+}:D^-$, showing transitions to D^- local mode vibronic levels associated with the $^1D_2(D_1)$ and $^1D_2(D_2)$ crystal field levels.

compared with the other vibronic transitions, but this is attributed to breakthrough of the C_{4v} F^- site emission. The well defined π-polarisation of this line in Figure V.2.3 catorgorically supports its assignment as the $D_1'(x)$ transition since the transition to the D_4 level of the C_{4v} F^- site is σ-polarised.

The line at 17544 cm^{-1} in Figure V.2.3 does not fit into the expected local mode vibronic level scheme even though it has a well defined polarisation. One possible assignment would have this line as the transition to the $D_1'(z)$ level while the line at 17564 cm^{-1} would be the transition to the $D_2'(z)$ level, however this does not seem likely as the z local mode frequencies would be 790 and 770 cm^{-1} for the vibrations coupled to the D_1 and D_2 levels respectively. This line is definitely related to this site as it maintains a consistent relative intensity with the vibronic lines under various excitation conditions. Its most probable origin is a lattice vibronic line associated with a phonon of energy 132 cm^{-1} coupling to the D_4 crystal field level at 17412 cm^{-1}.

The transition to the $D_2'(z)$ vibronic line does not appear in the excitation spectrum in Figure V.2.3. With a ground state of τ_5 symmetry, transitions to all symmetry states are allowed. Using the known z local mode frequency the $D_2'(z)$ transition is expected around 17603 cm^{-1}, the position of which is marked in the figure. Clearly some sort of irregularity is apparent in this region, probably arising from non-linearities in the laser frequency. The excitation spectra in this work were recorded using a dye laser fitted with a 3 plate birefringent filter. This filter was obtained in a disassembled state, realigned and installed by the author and may not meet the exact specifications of the manufacturers. While giving satisfactory results across most of the spectral range it appears that some discontinuities exist near the upper limit of the range where the

the spectra in Figure V.2.3 were recorded. Consequently the frequency of 17603 cm^{-1} required to excite the $D_2'(z)$ vibronic level may not be obtainable.

Using a green dye laser the excitation spectrum of the vibronic levels coupled to D_4 and second harmonic levels coupled to D_1 and D_2 was recorded and is shown in Figure V.2.4. Transitions to the x,y and z vibronic levels coupled to D_4 are visible at frequency intervals close to the known local mode frequencies. Only two second harmonic lines are apparent, those to the $D_1'(zz)$ and $D_2'(xx)$ vibronic levels. The lower frequency lines such as $D_1'(xx)$, $D_2'(xx)$ etc are hidden by the strong transitions of $D_4'(x)$ and $D_4'(z)$. The $D_2'(zz)$ transition would be expected around 18414 cm^{-1} but does not appear in the spectrum. This region is clear of other lines and there may be some underlying selection rule that explains the nonappearance of either the $D_2'(z)$ or $D_2'(zz)$ transitions. Table V.2.2 summarises the electronic and D^- ion local mode frequencies measured using laser excitation for the C_{4v} D^- site in $CaF_2:Pr^{3+}$

Table V.2.2

Electronic level energies and D^- ion local mode frequencies measured, at 14 K, from the $^1D_2$ excitation spectrum for the C_{4v} D^- site in $CaF_2:Pr^{3+}:D^-$ crystal.

$^1D_2$ Electronic Frequency (cm^{-1})	D^- Ion Local Mode Vibronic Intervals (cm^{-1})
D_1 = 16754.4 ± 0.1	x,y : 721 ± 1 z : 810 ± 1 zz : 1620 ± 2
D_2 = 16794.2 ± 0.1	x,y : 721 ± 1
D_4 = 17411.6 ± 0.1	x,y : 721 ± 2 z : 804 ± 2

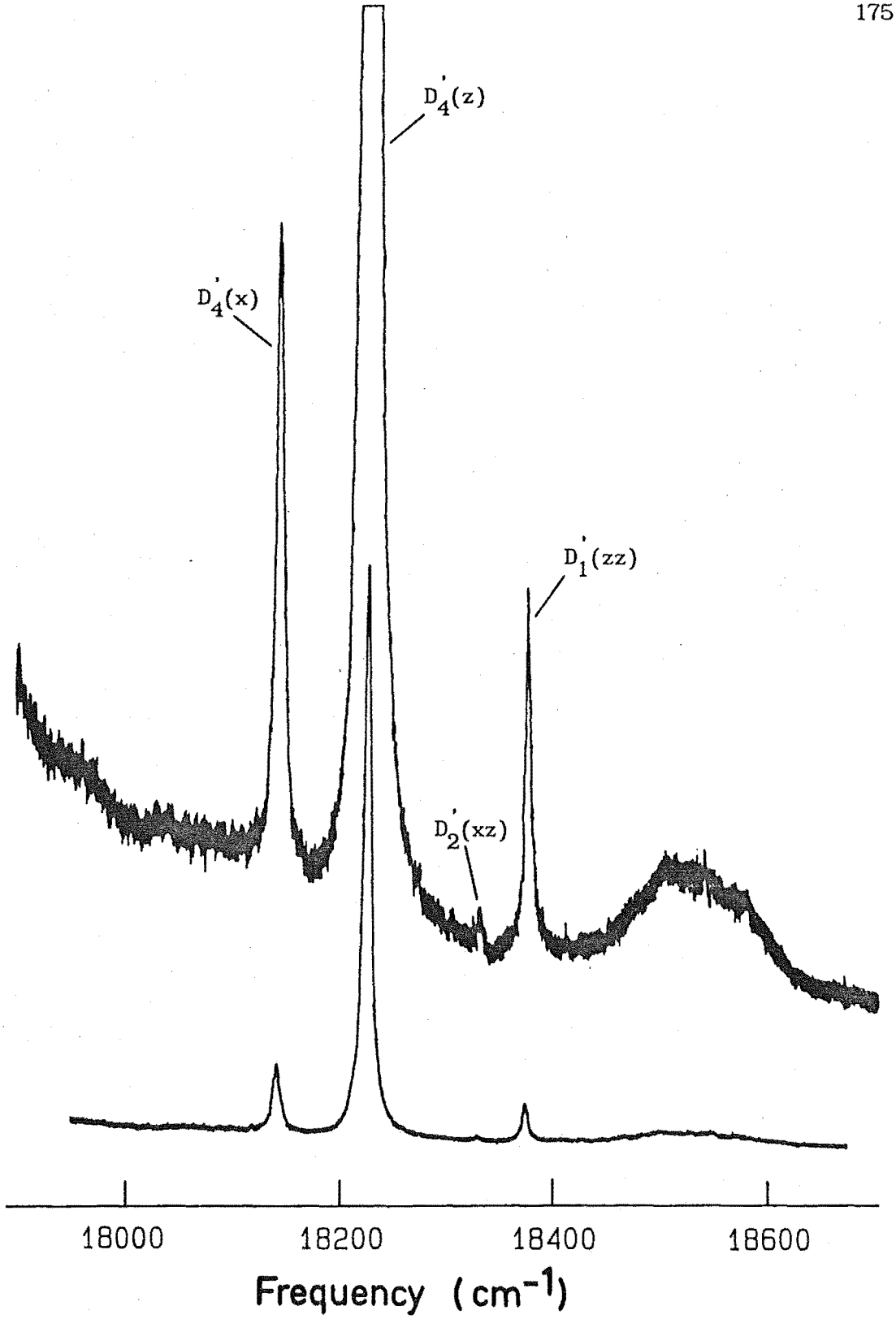

Figure V.2.4 14K excitation spectrum for the C_{4v} D^- site in $CaF_2:Pr^{3+}:D^-$ showing transitions to fundamental local mode vibronic lines associated with the $^1D_2(D_4)$ crystal field level and to second harmonic vibronic lines associated with the $^1D_2(D_1)$ and $^1D_2(D_2)$ levels.

V.2.2 Optical Emission of the C_{4v} Hydrogenic Sites in $CaF_2:Pr^{3+}$

The optical emission from the $^1D_2$ multiplet for the hydrogenic C_{4v} sites in $CaF_2:Pr^{3+}$ was recorded using similar techniques to those described in Section V.1 of this chapter. The results obtained however, are not as complete as those obtained for the C_{4v} sites in $SrF_2:Pr^{3+}$ crystals. The spectra themselves are generally not as rich in lines and the weak quantum efficiency for the H^- site precluded the recording of the emission spectra to the levels of the $^3F_3$ and $^3F_4$ multiplets. In some regions, spectra free from transitions belonging to other sites could not be recorded. Especially troublesome was the Sm^{2+} impurity as the broad absorption profile of this ion in the excitation region did not allow an opportunity to improve the discrimination by varying the pumping conditions. Also appearing in the C_{4v} H^- site spectra are emission lines from a fluorine ion compensated site that has an excitation frequency very close to that of the H^- site. Discriminating the H^- site emission from these lines can be achieved by tuning the laser frequency to optimise the relative intensities rather than tuning for maximum overall intensity.

The spectral contamination of the H^- site emission does not arise from an increase in impurity ions but through its very low quantum efficiency. The $^1D_2$ lifetime has been measured for this site to be 380 ± 20 nsecs compared with the C_{4v} F^- site lifetime of 420 ± 10 μsec. This change of three orders of magnitude is a vivid demonstration of the importance of the hydrogenic ion local mode vibrations in the non-radiative decay of the praseodymium ion. At the sensitivities required to measure the hydride ion site emission, transitions from any fluorine sites unintentionally excited will be apparent in the spectra due to their much greater quantum yields.

In Section V.2.1 it was shown that absorption transitions to both D_1 and D_2 crystal field levels of $^1D_2$ are observed and that the D_1 - D_2 splitting increases from 17 cm^{-1} to around 40 cm^{-1} with the substitution of the fluorine charge compensating ion by a hydrogenic ion. The D_1 and D_2 level symmetries will be the same as they were for the C_{4v} F^- site, i.e. transforming as τ_1 and τ_3 irreps respectively, and the selection rules for transitions and polarisation ratios are therefore expected to be the same. The details of transitions to the electronic and local mode vibronic levels will now be discussed for each multiplet in turn.

The $^3H_4$ Multiplet

Polarised emission from the $^1D_2$ multiplet to the crystal field levels of the $^3H_4$ multiplet, was recorded for the hydrogenic C_{4v} sites in $CaF_2:Pr^{3+}$ and is shown in Figures V.2.5, V.2.6 and V.2.7 for the H^-, D^- and T^- charge compensating ions respectively. The spectra were recorded at 14 K using a <100> oriented crystal and show the emission for the (i) x(yy)z and (ii) x(yx)z polarisation geometries. Details of the local mode vibronic spectra are included in part (b) of each figure. The origin of the various electronic and local mode vibronic lines observed are indicated using the nomenclature introduced in Section V.1.2. The energies of the electronic and local mode vibronic levels for the $^3H_4$ multiplet are summarised in Table V.2.3 for the three isotopic variations of the hydrogenic C_{4v} site. The polarisation of the transition from the $^1D_2(D_1)$ level to the various $^3H_4$ levels has been included in the table where it can be determined.

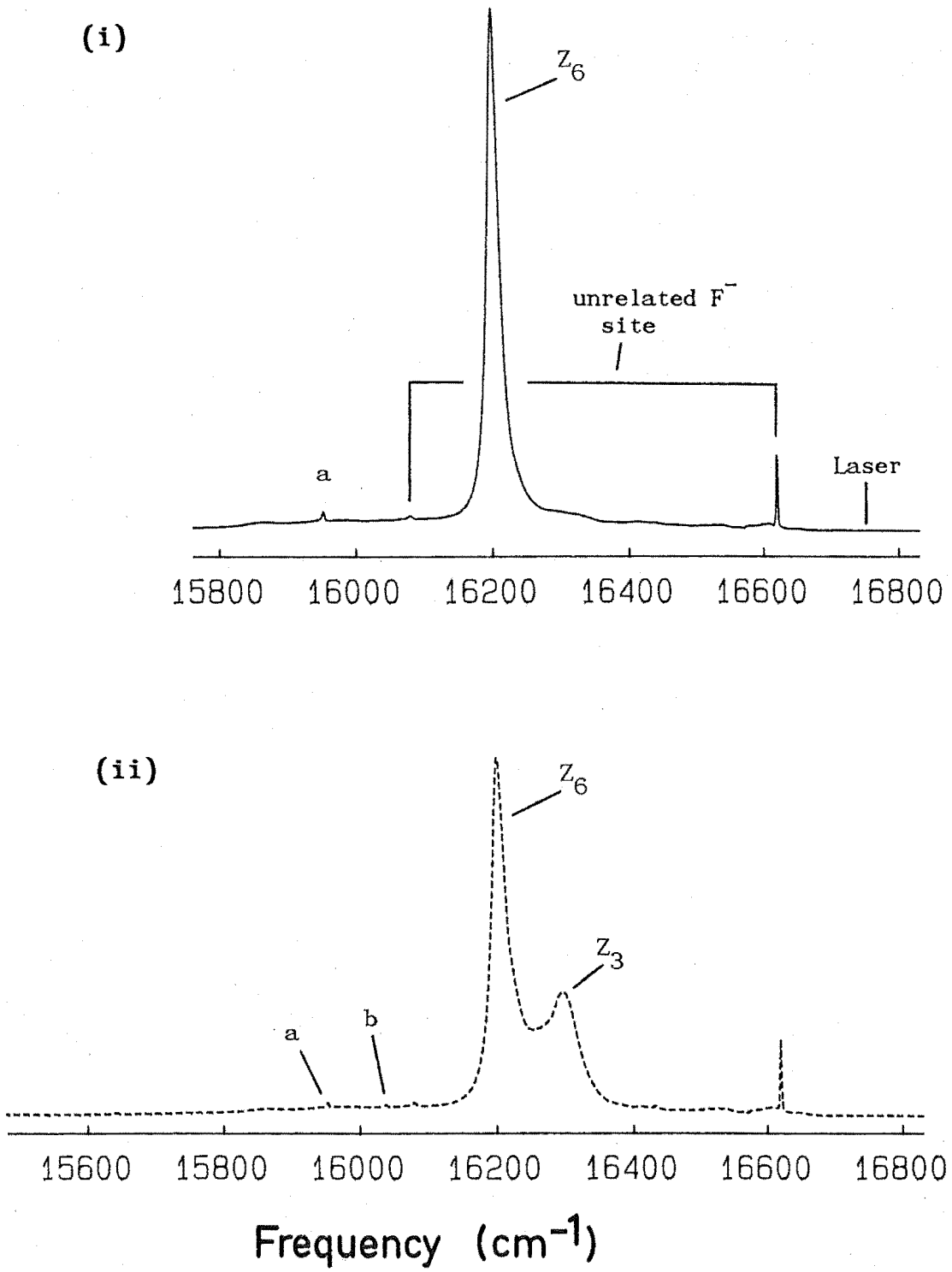

Figure V.2.5(a) 14K polarised fuorescence from the C_{4v} H^- site in $CaF_2:Pr^{3+}:H^-$ showing the $^1D_2 \rightarrow {}^3H_4$ electronic transitions of the Pr^{3+} ion for the (i) x(yy)z and (ii) x(yx)z polarisation geometries in a <100> oriented crystal.

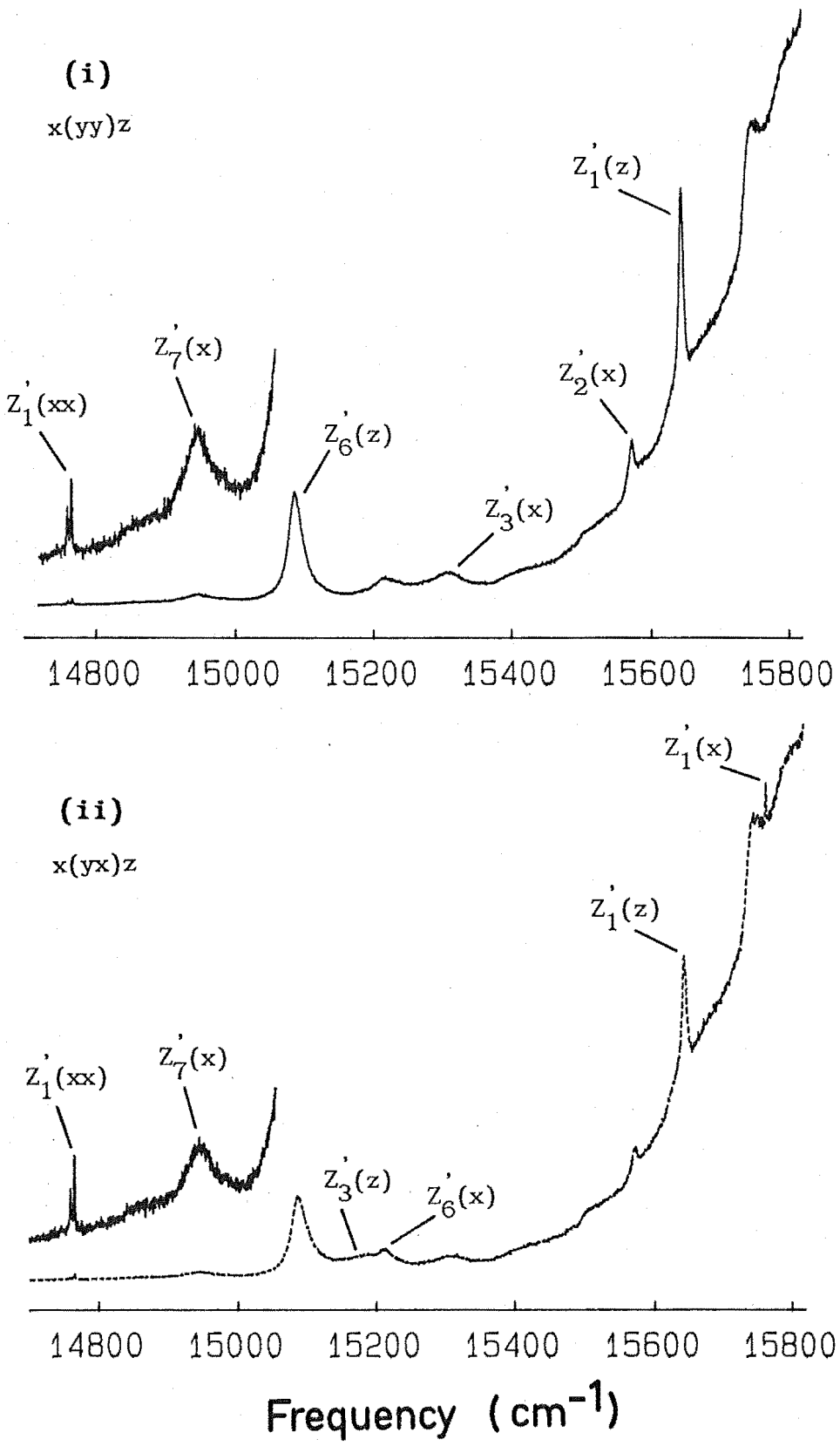

Figure V.2.5(b) Polarised fluorescence from the C_{4v} H^- site in $CaF_2:Pr^{3+}:H^-$ on an expanded scale showing the transitions to the local mode vibronic levels of the $^3H_4$ multiplet.

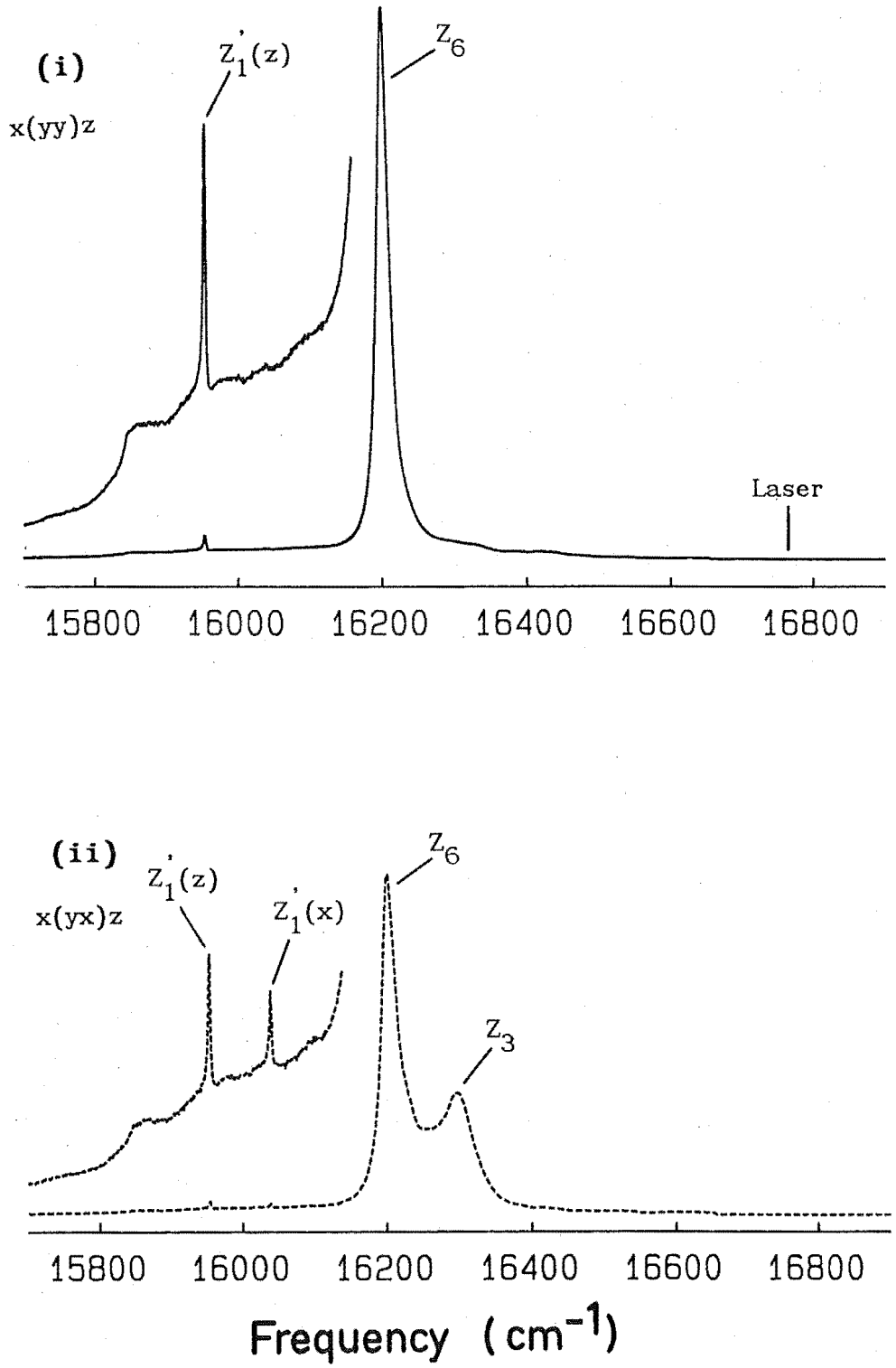

Figure V.2.6(a) Polarised $^1D_2 \rightarrow {}^3H_4$ fluorescence from the C_{4v} D^- site in $CaF_2:Pr^{3+}:D^-$ showing transitions to the electronic levels of the Pr^{3+} ion.

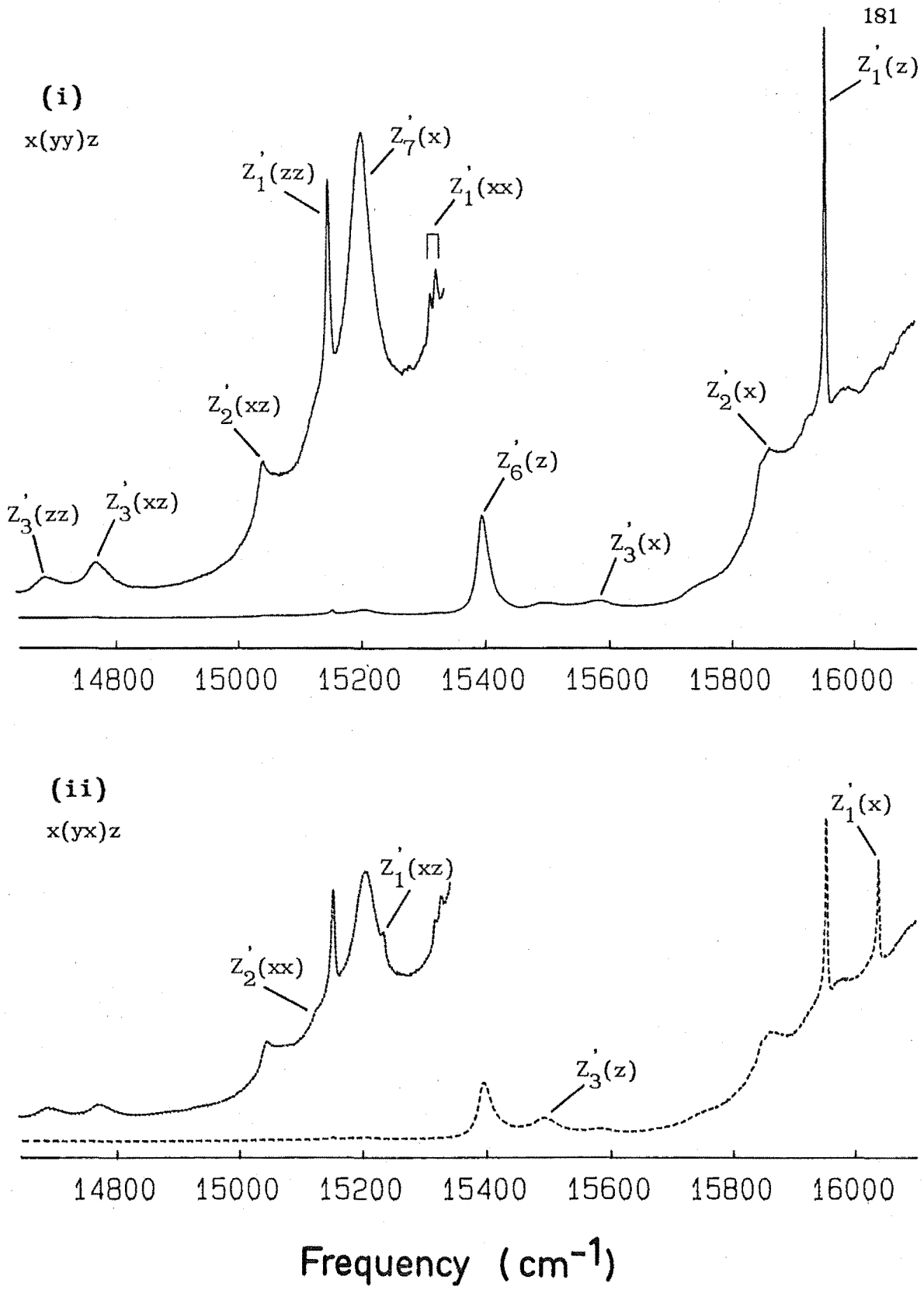

Figure V.2.6(b) Polarised fluorescence from the C_{4v} D^- site in $CaF_2:Pr^{3+}:D^-$ on an expanded scale showing the transitions to the local mode vibronic levels.

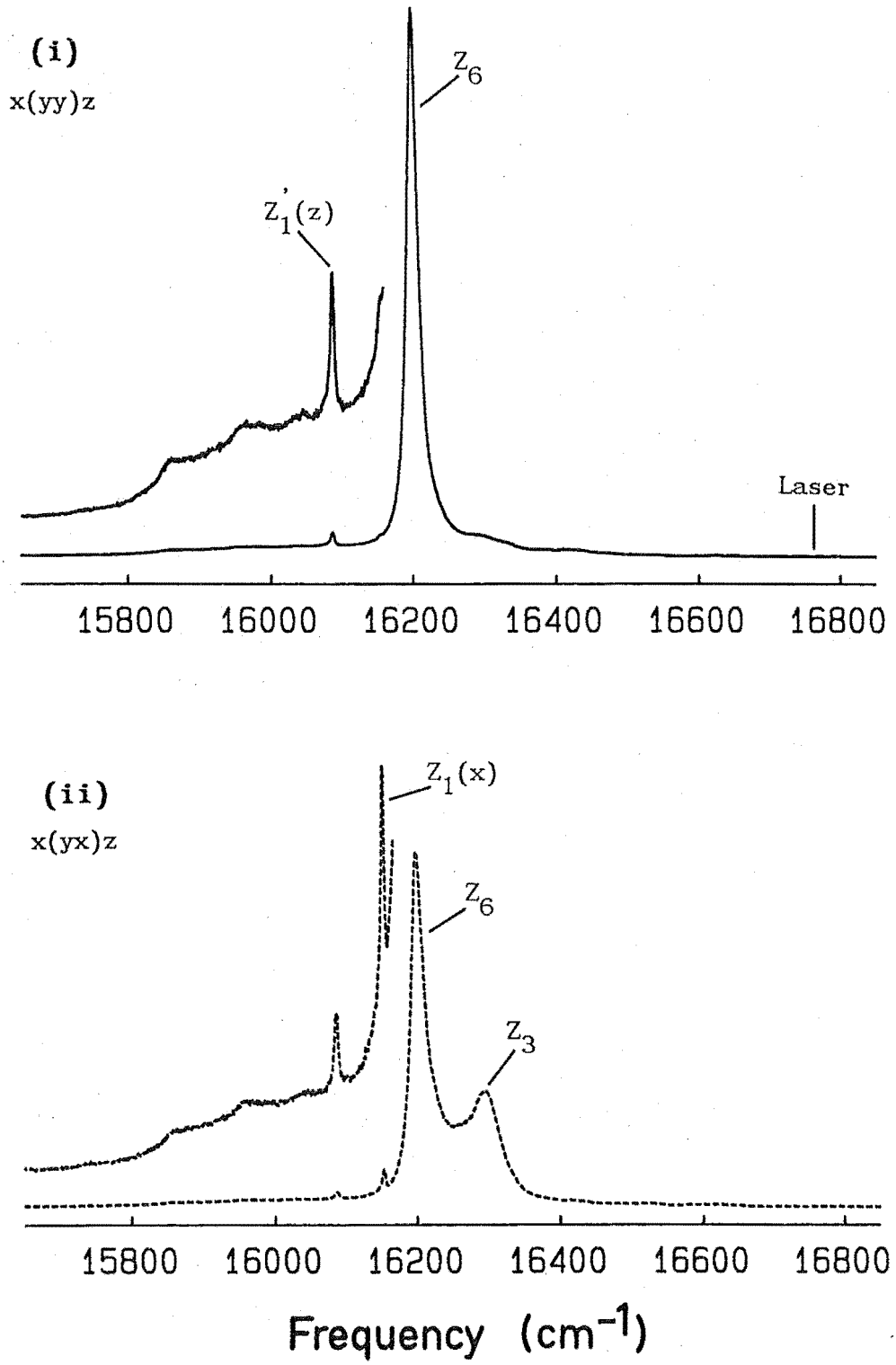

Figure V.2.7(a) Polarised fluorescence from the C_{4v} T^- site in $CaF_2:Pr^{3+}:T^-$ showing the $^1D_2 \rightarrow {}^3H_4$ electronic transitions of the Pr^{3+} ion.

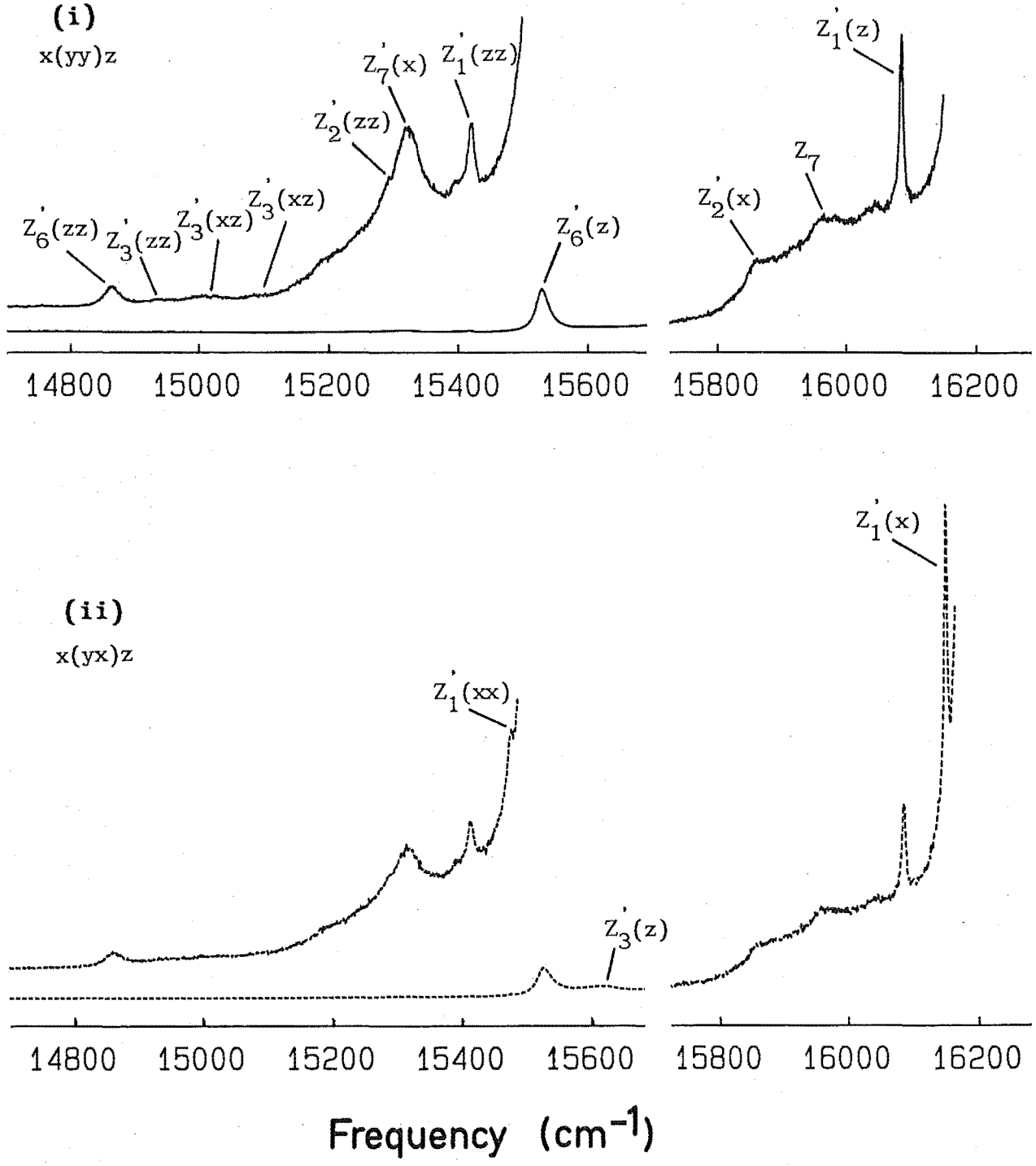

Figure V.2.7(b) Polarised fluorescence from the C_{4v} T^- site in $CaF_2:Pr^{3+}:T^-$ showing the transitions to the local mode vibronic levels.

Table V.2.3

Energies of the electronic and local mode vibrational levels of the $^3H_4$ multiplet for the C_{4v} hydrogenic ion sites in $CaF_2:Pr^{3+}$. The polarisation of the transition from the $D_1(\tau_1)$ level to the various states is given. Energy level uncertainties are ±1 cm^{-1} unless otherwise indicated.

Electronic state symmetry and polarisation	C_{4v} H^-		C_{4v} D^-		C_{4v} T^-	
	Electronic level energy (cm^{-1})	Vibronic level mode, energy (cm^{-1}) and polarisation	Electronic level energy (cm^{-1})	Vibronic level mode, energy (cm^{-1}) and polarisation	Electronic level energy (cm^{-1})	Vibronic level mode, energy (cm^{-1}) and polarisation
$Z_1(\tau_5)$, σ	0	x,y: 996.5±.5(π) 997.3±.5(π) 1002.5±.5(π) z:1117.5±.5(σ) xx:1992.3±.5(σ) 1998.3±.5(σ) xz:2107 zz:2222	0	x,y:722.8±.5(π) z:808.1±.5(σ) xx:1435 (σ) 1444 (σ) xz:1528 (π) zz:1606 (σ)	0	x,y:606 (π) z:673 (σ) xx: - xz:1275 (π) zzz:2004 (σ)
$Z_2(\tau_4)$ [a]	191±5	x,y:1189 (σ)	195±5	x,y:902±5 (σ) z: - xx:1637 (π) xz:1717 (σ)	192±5	x,y:793±2(σ) z: - xz:1467 (σ)
$Z_3(\tau_1)$ π	462	x,y:1456 (σ) z:1575 (π)	463	x,y:1176 (σ) z:1268 (π) xz:1990 (σ) zz:2073 (σ)	464	x,y: - z:1135 (π) xx:1668 (σ) xz:1741 (σ)

Table V.2.3 continued next page...

Table V.2.3 continued....

Electronic state symmetry and polarisation	C_{4v} H^-		C_{4v} D^-		C_{4v} T^-	
	Electronic level energy (cm^{-1})	Vibronic level mode, energy (cm^{-1}) and polarisation	Electronic level energy (cm^{-1})	Vibronic level mode, energy (cm^{-1}) and polarisation	Electronic level energy (cm^{-1})	Vibronic level mode, energy (cm^{-1}) and polarisation
$Z_4(\tau_2)$	-		-		-	
$Z_5(\tau_1)$ [b]	560±20		559±20		559±20	
$Z_6(\tau_5)$, σ	560	x,y:1550 (π) z:1676 (σ)	559	x,y: - z:1365 (σ)	559	x,y: - z:1229 (σ) zz:1894 (σ)
$Z_7(\tau_3)$ [a]	821±5	x,y:1818 (σ)	834±5	x,y:1557 (σ)	831±5	x,y:1437 (σ)

[a] Position inferred from position of local mode vibronic levels.

[b] Transition to this level is not resolvable from the linewidth of the Z_6 level.

Only two strong electronic transitions are apparent in the spectra and are assigned to transitions to the Z_3 and Z_6 levels. The σ-polarised line close to 16200 cm^{-1} has a x(yy)z:x(yx)z polarisation ratio of 2:1 consistent with a transition terminating on the Z_6 level which transforms as the τ_5 irrep of C_{4v}. The broad π-polarised line close to 16300 cm^{-1} has been assigned to the Z_3 crystal field level rather than to the Z_5 level which would also have this polarisation. This justification is based on the similar characteristics of this line and the transition terminating on the Z_3 level of the C_{4v} F^- site. An electric dipole transition is allowed to the Z_5 level of this site but is not observed in any of the three hydrogenic sites. As there are also no transitions visible to local mode vibronic levels coupled to Z_5 a possible reason for its absence may be an accidental coincidence with another transition, the most likely being that to the Z_6 level. In this case the local mode vibronic lines would also be coincident. Therefore the energy of Z_5 has been given the same energy as the Z_6 level with an uncertainty sufficiently large to cover the linewidth.

Although the positions of only two electronic levels can be measured directly the energy of others can be inferred from their local mode vibronic levels. For all three H^-, D^- and T^- variations of the hydrogenic C_{4v} site a transition to the $Z_7'(x)$ level is apparent. From the known x,y local mode frequency, the energy of the Z_7 level can be estimated to a few wavenumbers. A greater uncertainty is required since the phonon frequency used was that of the x,y vibration coupled to the ground state. The choice of the x,y vibration as being the applicable phonon is made from the observed polarisation. The x,y(τ_5) and z(τ_1) local mode phonons will couple to the τ_3 symmetry Z_7 level to produce vibronic levels transforming as τ_5 and τ_3 irreps

respectively. The observed x(yy)z:x(yx)z polarisation ratio of 2:1 is that expected for the σ-polarised transition to the $Z_7'(x)$ vibronic level.

Another electronic level that can have its energy estimated from local mode vibronic levels is the Z_2 state. An electric dipole transition to this level which transforms as the τ_4 irrep of C_{4v}, is symmetry forbidden from the $D_1(\tau_1)$ emitting level. A lower limit of ~100 cm^{-1} can be inferred from the non-appearance of absorption transitions from Z_2 at temperatures up to 85 K. In Figure V.2.5 of the C_{4v} H^- site emission, a line is apparent at 15566 cm^{-1} that is assigned to the transition terminating on the $Z_2'(x)$ vibronic level. Although lines from other sites are present in the H^- ion site spectra, the assignment of the 15566 cm^{-1} line as belonging to the C_{4v} site can be made from its consistent behaviour under various excitation conditions. This assignment as a transition terminating on the $Z_2'(x)$ level is also consistent with the observed polarisation. The $x,y(\tau_5)$ local mode phonon will couple with the $Z_2(\tau_4)$ level to form a $Z_2'(x)$ state transforming as the τ_5 irrep. A transition from $D_1(\tau_1)$ to this level will be σ-polarised and show a x(yy)z:x(yx)z polarisation ratio of 2:1. The frequency interval of the 15566 cm^{-1} line from the $Z_1'(x)$ line at 15757 cm^{-1} gives a Z_1-Z_2 interval of 191 cm^{-1}.

A similar analysis for the D^- and T^- sites is not as straightforward, as a transition to a fundamental vibronic level of Z_2 is not observed. Nevertheless, some information can be gained from second harmonic transitions. The weak lines at 15117 and 15037 cm^{-1} for the C_{4v} D^- site are assigned as transitions to $Z_2'(xx)$ and $Z_2'(xz)$ second harmonic vibronic levels respectively. Subtraction of these frequencies from the relevant vibronic levels coupled to Z_1 gives a Z_1-Z_2 splitting averaging 193 cm^{-1}, close to that estimated for the H^- C_{4v} site. Furthermore, the observed polarisations of the 15117 and

15037 cm^{-1} transitions are consistent with the $Z_2'(xx)$ and $Z_2'(xz)$ assignments. Weak transitions to these same levels can be identified at 15391 and 15287 cm^{-1} for the C_{4v} T^- site. The frequency interval of the $Z_2'(xz)$ line from the $Z_1'(xz)$ line at 15479 cm^{-1} gives a Z_1-Z_2 splitting of 192 cm^{-1}. These energies for the Z_2 level have been estimated using the local mode frequencies for vibronic levels coupled to the ground state. As the frequencies will vary for vibronic levels coupled to different electronic states, the energy of the Z_2 levels is given with an increased uncertainty.

Already mentioned are transitions to second harmonic local mode vibronic levels coupled to the ground state and their frequencies are tabulated in Table V.2.3. For the C_{4v} H^- and D^- sites two of the three (xx) second harmonic frequencies can be measured, however inconsistencies arise as the D^- site splitting is greater than that of the H^- site. This conflicts with the expected decrease in frequency by the isotopic mass ratio. This problem will be discussed further in Chapter VII.

The polarisation of the second harmonics and also the fundamentals can be understood using the by now familiar C_{4v} group multiplication and selection rules. The combination of two γ_5 symmetry (x,y) vibrations with the γ_5 symmetry ground state will produce three xx second harmonic vibronic levels, all transforming as the γ_5 irrep. Details for the other levels will not be discussed here as they have been previously derived for the C_{4v} hydrogenic sites in $SrF_2:Pr^{3+}$ suffice to say that the observed polarisations are generally consistent with the model.

The splitting of the fundamental (x,y) vibronic level observed in the hydrogenic C_{4v} sites in $SrF_2:Pr^{3+}$ is not as readily apparent in the $CaF_2:Pr^{3+}$ sites. There is some indication of more than one component for the H^- site, but none at all for the D^- and T^- sites.

Jacobs [1971], using infrared absorption, was able to measure these splittings for the H^- site in both $SrF_2:Pr^{3+}$ and $CaF_2:Pr^{3+}$ crystals. The difficulty in observing the separate components here may be related to the selection rules for transitions, as they are more restrictive for emission from the $D_1(\tau_1)$ level than in absorption from a ground state transforming as the τ_5 irrep. These splittings originate from the electron-phonon interaction and are analysed in Chapter VII for the hydrogenic C_{4v} sites in both $CaF_2:Pr^{3+}$ and $SrF_2:Pr^{3+}$ crystals.

In Figure V.2.5 of the C_{4v} H^- emission, lines to the x,y and z vibronic levels of the D^- C_{4v} site have been indicated. The lines were identified from their frequency and polarisation. The particular crystal used was **not** subjected to the deuteration process. The appearance of these lines gives a dramatic demonstration of the sensitivity of the laser excitation technique. The hydrogen gas used in the treatment of the samples is known to contain approximately one part in 6000 of deuterium, the ions of which will also diffuse in to the crystal to form the corresponding D^- charge compensating ion sites. In $CaF_2:Pr^{3+}$ the isotope shift for the $Z_1 \longrightarrow D_1$ transition between the C_{4v} H^- and D^- sites is 0.2 cm^{-1} and it is difficult to avoid exciting the small number of C_{4v} D^- sites present when pumping the H^- site. Consequently the electronic transitions will have H^- and D^- site components and an isotope splitting may be observed for some narrow lines. Although it is expected that there is only one D^- site for every 6000 H^- sites in this crystal, the D^- site lines appear at a greater relative intensity than would be indicated by this ratio. The same reasoning used before in discussing the breakthrough of fluorine site emission is appropriate here. The fluorescent lifetime of the C_{4v} D^- site was measured in this work to be 95 ± 3 μsec which is two orders of magnitude slower than the H^- site value of 380 ± 20 ns.

With the much greater quantum yield associated with the difference between the two lifetimes, the D^- site breakthrough is more prominant than would be expected from the relative numbers of sites. Transitions of the D^- site are apparent in the spectra of other multiplets as well. In order to optimise the signal from the H^- sites it was necessary to tune on a transition associated with an H^- local mode vibronic level.

The $^3H_5$ Multiplet

Spectra depicting the polarised emission from the $^1D_2$ multiplet to the crystal field levels of the $^3H_5$ multiplet are given in Figures V.2.8 for the H^- C_{4v} site and V.2.9 for the C_{4v} D^- and T^- sites in $CaF_2:Pr^{3+}$ <100> oriented crystals. The origin of the observed spectral lines are indicated by the labels Y_i for electronic transitions and $Y_i'(\alpha)$ for local mode vibronic transitions using the same convention for the indices as used in the multiplets discussed previously. Table V.2.4 summarises the energies of the electronic and local mode vibronic levels of the $^3H_5$ multiplet in the C_{4v} Pr^{3+}-hydrogenic ion sites of $CaF_2:Pr^{3+}$. Also included in the table is the polarisation of the transition from $^1D_2(D_1)$ to the levels of the multiplet.

There are several missing entries to the table as transitions to some crystal field levels have not been observed. The Y_4 and Y_8 levels transform as τ_3 and τ_4 irreps of C_{4v} respectively and from symmetry arguments cannot be terminating levels for electric dipole transitions originating from the $D_1(\tau_1)$ state. The remaining unassigned component, the Y_6 level, transforms as the τ_2 irrep of C_{4v} and is symmetry allowed as a terminating level for a magnetic dipole transition from $D_1(\tau_1)$. Such transitions tend to be weak and it is not surprising that a transition is not observed in this case.

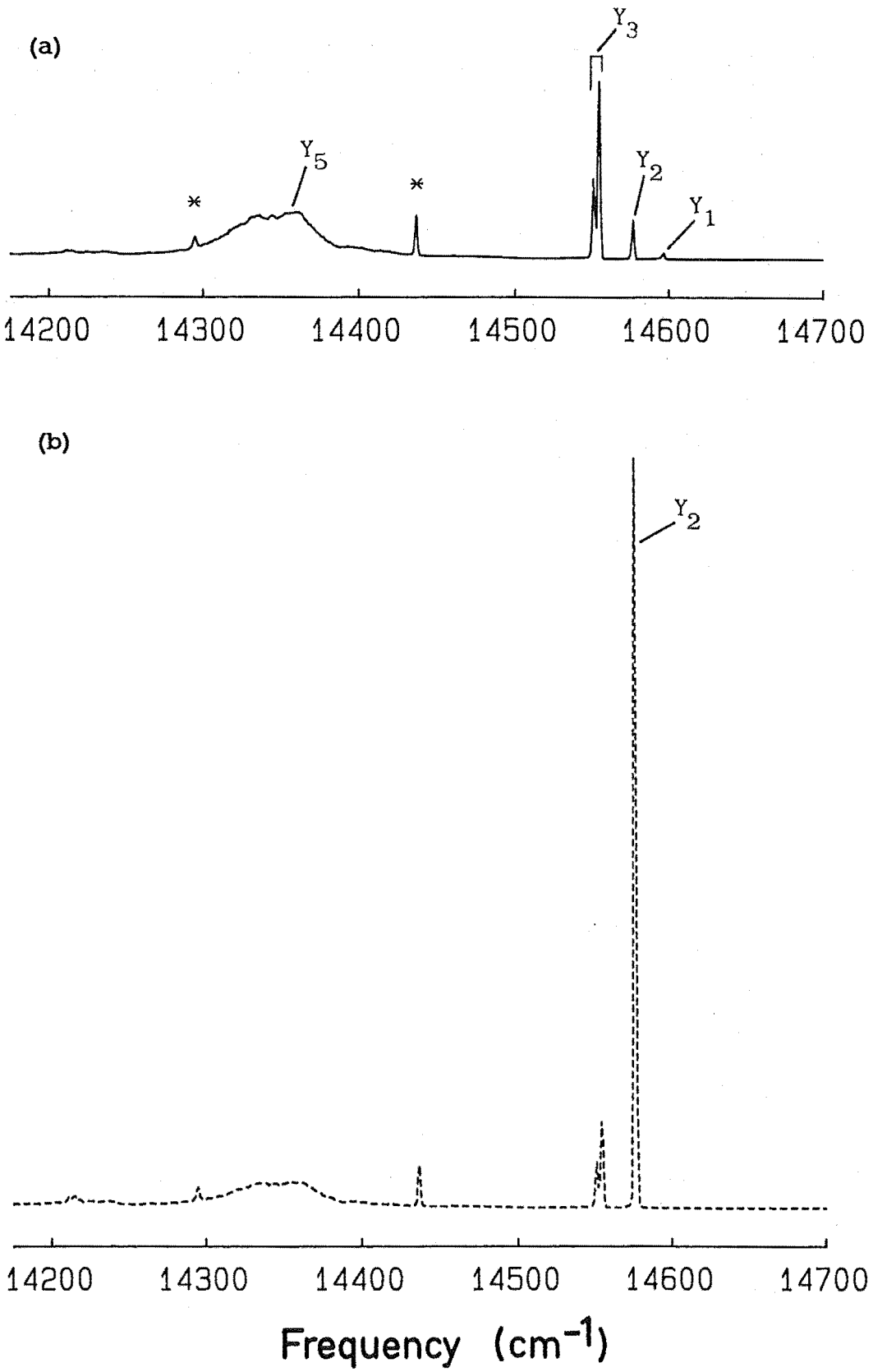

Figure V.2.8 Polarised spectra of the $^1D_2 \rightarrow {}^3H_5$ emission from the C_{4v} H^- site in $CaF_2:Pr^{3+}:H^-$ for the (a) x(yy)z and (b) x(yx)z polarisation geometries in a <100> oriented crystal.

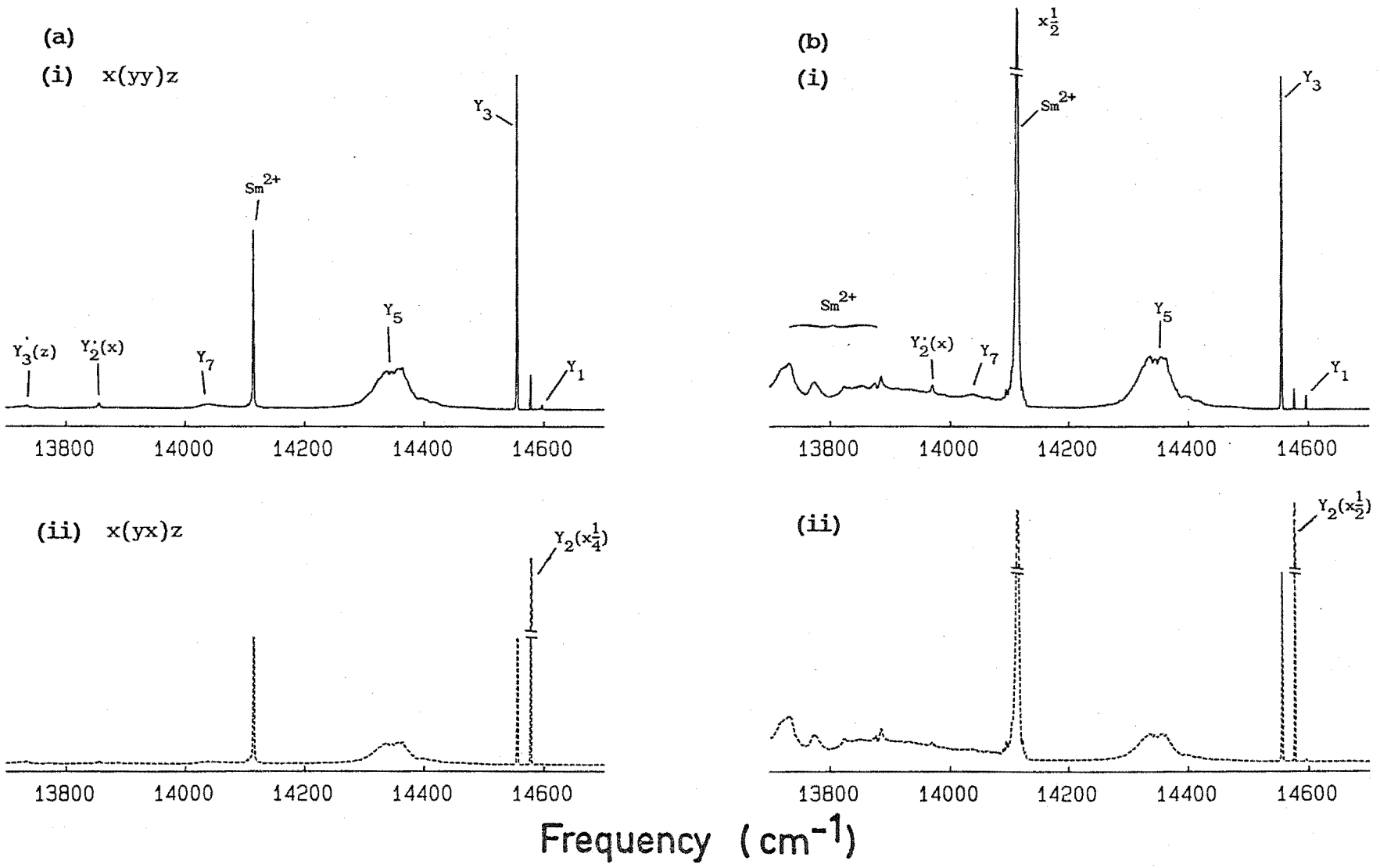

Figure V.2.9 $^1D_2 \rightarrow {}^3H_5$ polarised emission from the (a) C_{4v} D^- and (b) C_{4v} T^- sites in $CaF_2:Pr^{3+}$ crystals.

Table V.2.4

Energies of the electronic and local mode vibrational levels of the $^3H_5$ multiplet for the C_{4v} hydrogenic sites in $CaF_2:Pr^{3+}$. The energy level uncertainties are ± 1 cm^{-1}.

Electronic state symmetry and polarisation	C_{4v} H^-	C_{4v} D^-		C_{4v} T^-	
	Electronic level energy (cm^{-1})	Electronic level energy (cm^{-1})	Vibronic level mode, energy (cm^{-1}) and polarisation	Electronic level energy (cm^{-1})	Vibronic level mode, energy (cm^{-1}) and polarisation
$Y_1(\tau_2)$, π(md)[a]	2166	2164		2162	
$Y_2(\tau_1)$, π	2185	2183	x:2906(σ) z:2994(π)	2182	x:2788(σ)
$Y_3(\tau_5)$, σ	2211	2206	z:3027(σ)	2203	
$Y_4(\tau_3)$	-	-		-	
$Y_5(\tau_5)$, σ	2420±20	2425±20		2410±20	
$Y_6(\tau_2)$	-	-		-	
$Y_7(\tau_5)$, σ	-	2723		2719	
$Y_8(\tau_4)$	-	-		-	

[a] Magnetic dipole transition

However, of the transitions that have been observed, one is a magnetic dipole transition that terminates on the Y_1 crystal field level. This line has been observed for all the C_{4v} sites examined in both $CaF_2:Pr^{3+}$ and $SrF_2:Pr^{3+}$ crystals. The Y_1 level also transforms as the τ_2 irrep of C_{4v} and a transition through the z-component of the magnetic dipole radiation field is symmetry allowed from the $D_1(\tau_1)$ state. The observed x(yy)z:x(yx)z polarisation ratio of 1:0 is that expected for a π-polarised magnetic dipole transition. Note that this is the inverse ratio to a π-polarised electric dipole transition since the magnetic and electric field vectors of the radiation field are orthogonal. It appears that the observation of this magnetic dipole transition is aided by the very low background of the emission at this point.

Spectral lines of a normal character are observed to the Y_2 and Y_3 crystal field levels and their polarisation indicate electric dipole transitions terminating on τ_1 and τ_5 symmetry levels respectively. However the σ-polarised transition to the Y_5 level is very broad and appears to contain some structure. The energy interval of this line from the very strong $D_1 \longrightarrow Y_2$ transition corresponds to the frequency of a band of lattice phonons previously shown to occur in these sites and some of the structure may be due to these phonons. A similar situation was discussed for the hydrogenic sites in $SrF_2:Pr^{3+}$ where a lattice phonon band was observed coupled to the X_1 crystal field level of the $^3H_6$ multiplet. As such, the $D_1 \longrightarrow Y_5$ transition cannot be unequivocally identified and the Y_5 level has been given with an increased uncertainty. In Figure V.2.8, the $D_1 \longrightarrow Y_3$ transition for the C_{4v} H^- site comprises two components separated by ~4 cm^{-1}. The second line is the $D_1 \longrightarrow Y_3$ transition for the C_{4v} D^- site breaking through and is well resolved for this transition due to the large isotope shift (Table V.2.4).

The $(4f^5 5d)\ A_{1u} \longrightarrow (4f^6)\,^7F_0$ emission line of the Sm^{2+} ion at 14099 cm^{-1} dominates the $^1D_2 \longrightarrow {}^3H_5$ emission spectra in some crystals and along with the related structure of this emission swamps some vibronic transitions. Because the Sm^{2+} absorption is broad in the region of excitation, variable pumping conditions will not improve the hydrogenic site discrimination, however the difference in lifetimes may do so. The fluorescent lifetime of the Sm^{2+} emission was measured by Wood and Kaiser [1962] to be 2 μsec. For the C_{4v} D^- site in $CaF_2:Pr^{3+}$, the $^1D_2$ level has a lifetime of 95 μsec and the Sm^{2+} emission could be removed from the spectrum by using a pulsed excitation source and gating the sampling interval until, say 10 μsec after the laser pulse. At this delay, e^{-5} or less than 1% of the Sm^{2+} emission would remain at the expense of a 10% reduction in the D^- site emission. Although the C_{4v} T^- site lifetime has not been measured it is expected to be longer than the D^- site value and the same technique could be used there. A different method would be required for the C_{4v} H^- site as its fluorescent lifetime of 380 nsec is faster than that of the Sm^{2+} ion. For this site some enhancement in the H^- signal could be achieved, in principle, by using a narrow sampling interval at a very short time delay from the exciting laser pulse. The enhancement is due to the sampling interval recording emission for a greater proportion of the H^- lifetime then the Sm^{2+} lifetime. The maximum possible increase in relative intensity of H^- emission is given by the ratio of the lifetimes, which is approximately 5, although in reality something less than this would be expected.

The $^3H_6$ Multiplet

Spectra showing polarised emission from the $^1D_2$ multiplet to the crystal field levels of the $^3H_6$ multiplet are shown in Figure V.2.10 for the C_{4v} H^-, D^- and T^- sites in $CaF_2:Pr^{3+}$. The origin of the spectral lines have been indicated using the labels X_i appropriate for

Figure V.2.10 $^1D_2 \rightarrow {}^3H_6$ polarised emission from the (a) C_{4v} H^-, (b) C_{4v} D^- and (c) C_{4v} T^- sites in $CaF_2:Pr^{3+}$. The spectra are recorded with (i) x(yy)z and (ii) x(yx)z polarisation geometries in a <100> oriented crystal. The lines labelled * do not originate from the C_{4v} site.

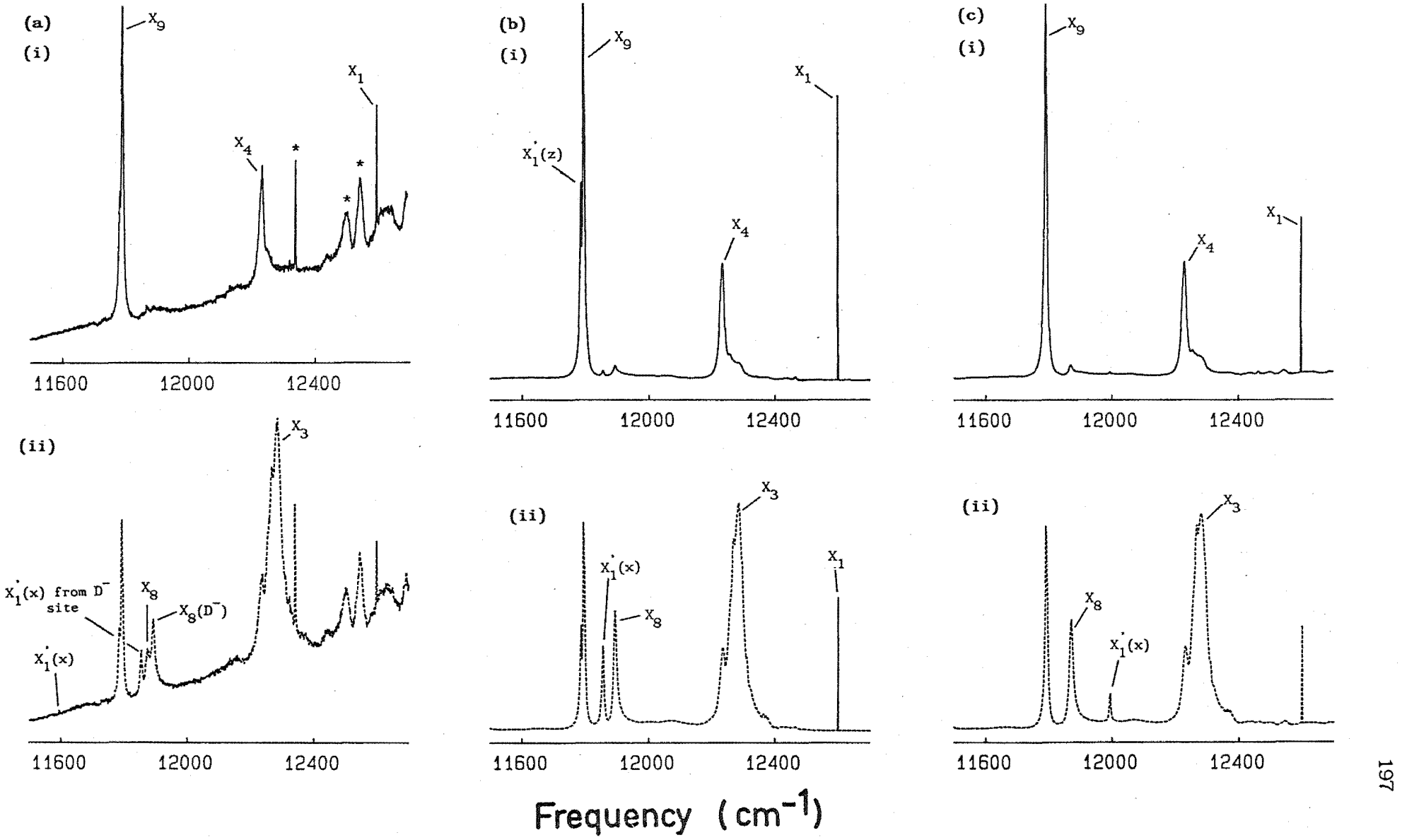
(a)
(i)
X9
X4
X1
*
*
*
11600
12000
12400
(ii)
X3
X1(x) from D⁻ site
X8
X8(D⁻)
X1(x)
11600
12000
12400
(b)
(i)
X9
X1(z)
X1
X4
11600
12000
12400
(ii)
X3
X1(x)
X8
X1
11600
12000
12400
(c)
(i)
X9
X1
X4
11600
12000
12400
(ii)
X3
X8
X1(x)
11600
12000
12400
Frequency (cm⁻¹)

levels of the $^3H_6$ multiplet and the conventions previously discussed. The energies of the electronic and local mode vibronic levels of the $^3H_6$ multiplet are summarised in Table V.2.5.

The $^3H_6$ multiplet proves itself the most difficult to obtain a complete energy level scheme for as only five of the ten crystal field levels have symmetries that allow electric dipole transitions. For the C_{4v} hydrogenic sites in $CaF_2:Pr^{3+}$ it is only these levels for which a transition is observed and a level assignment made. Three σ-polarised transitions to the X_1, X_4 and X_9 levels identify their symmetry as τ_5 while π-polarisations for the $D_1 \longrightarrow X_3$ and $D_1 \longrightarrow X_8$ transitions confirm the τ_1 symmetry of these two levels. A similar problem in the assignment of the $D_1 \longrightarrow X_3$ transition is apparent as was encountered for this transition in the hydrogenic C_{4v} sites of $SrF_2:Pr^{3+}$. A band of lattice phonons, having a frequency centred close to 300 cm^{-1}, couple to the X_1 electronic level to produce a vibronic band in the region of the X_3 crystal field level. The X_3 level has been assigned to the strongest line within this band, but with the realisation that another component may be the correct transition.

Some discussion is warranted on the position of the X_8 crystal field level as the table shows the energy does not follow the isotopic trends. For the C_{4v} D^- site the position of this level appears to be strongly perturbed out of sequence, probably by the influence of the nearby $X_1'(x)$ level. Being formed from the coupling of two doubly degenerate states, the $X_1'(x)$ vibronic level comprises four components, as in the C_{4v} group

$$\tau_5 \times \tau_5 = \tau_1 + \tau_2 + \tau_3 + \tau_4$$

The same lifting of the degeneracy was discussed for the $Z_1'(x)$ level, although splittings were not generally observed. The absence of an

Table V.2.5

Energies of the electronic and local mode vibronic levels of the $^3H_6$ multiplet for the C_{4v} Pr^{3+}-hydrogenic ion sites in $CaF_2:Pr^{3+}$. Level uncertainties are ± 1 cm^{-1}.

Electronic state symmetry and polarisation	C_{4v} H^-		C_{4v} D^-		C_{4v} T^-	
	Electronic level energy (cm^{-1})	Vibronic level mode, energy (cm^{-1}) and polarisation	Electronic level energy (cm^{-1})	Vibronic level mode, energy (cm^{-1}) and polarisation	Electronic level energy (cm^{-1})	Vibronic level mode, energy (cm^{-1}) and polarisation
$X_1(\tau_5)$, σ	4167	x:5166(π)	4163	x:4907(π) z:4976(σ) zz:5782(σ)	4160	x:4764(π)
$X_2(\tau_4)$	-		-		-	
$X_3(\tau_1)$, π	4477		4476		4476	
$X_4(\tau_5)$, σ	4528		4528		4528	
$X_5(\tau_2)$	-		-		-	
$X_6(\tau_3)$	-		-		-	
$X_7(\tau_4)$	-		-		-	
$X_8(\tau_1)$, π	4891		4869		4888	
$X_9(\tau_5)$, σ	4970		4967	z:5771(σ)	4968	
$X_{10}(\tau_3)$	-		-		-	

observable splitting in the $Z_1'(x)$ level, even though it should be resolvable (see the analysis of Chapter VII), is suggested to be the result of the transition selection rules that will allow a transition to only one of the four components. The strong interaction between the $X_1'(x)$ vibronic level and the X_8 level that is sufficient to perturb the X_8 level out of the isotope series would also be expected to produce a large splitting in the four components comprising the $X_1'(x)$ level. It is unfortunate that the same selection rules that precluded the observation of a splitting in the $Z_1'(x)$ level appear to be doing the same here. As the $^3H_6$ multiplet is within reach of infrared absorption spectrometers, it may be interesting to measure the infrared absorption to the X_8 and $X_1'(x)$ levels as the selection rules for absorption from the ground state allow transitions to all components.

In the $^1D_2 \rightarrow {}^3H_6$ spectra for the C_{4v} H^- site, lines from the C_{4v} D^- site are also apparent, such as transitions to the X_8, $X_1'(x)$ and $X_1'(z)$ levels. Although emission from both isotopic sites are present, the only line to show any substantial splitting associated with the isotope shift is the X_8 level, and as was discussed earlier the main contribution to this shift is from second order effects associated with the nearby $X_1'(x)$ level of the D^- site.

The $^3F_2$ Multiplet

Optical emission was recorded from the $^1D_2$ multiplet to the Pr^{3+} ions electronic levels of the $^3F_2$ multiplet for all three isotopic varieties of the hydrogenic C_{4v} site in $CaF_2:Pr^{3+}$. As the deuterated sample was the only crystal examined using the infrared emission spectrometer, the vibronic levels are available for the C_{4v} D^- site only. Figure V.2.11 shows the polarised $^1D_2 \rightarrow {}^3F_2$ emission spectra of the electronic levels for the H^-, D^- and T^- C_{4v} sites using a <100>

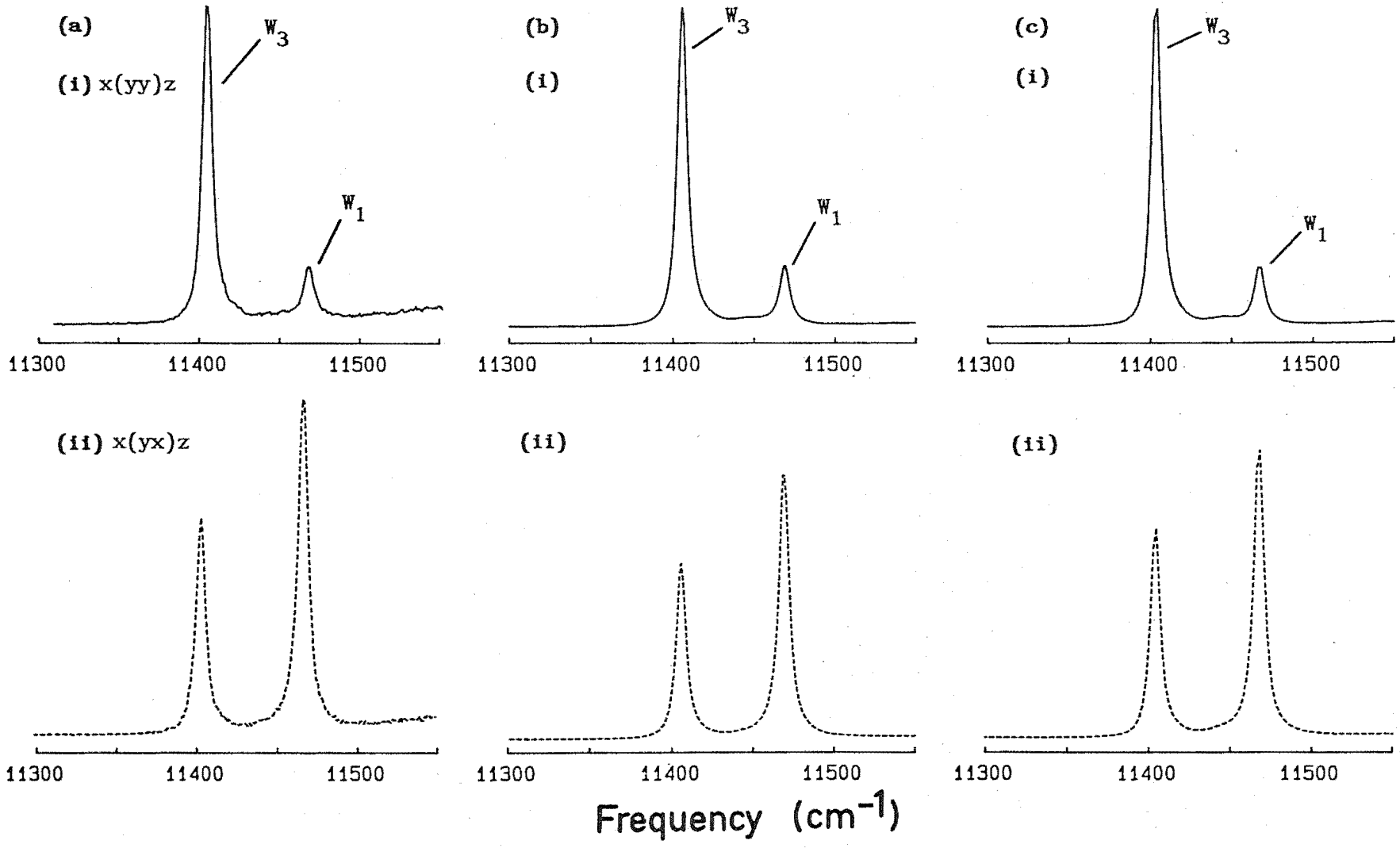

Figure V.2.11 Polarised $^1D_2 \rightarrow {}^3F_2$ emission from the (a) C_{4v} H^-, (b) C_{4v} D^- and (c) C_{4v} T^- sites in CaF_2:Pr^{3+} crystals showing the two principal electronic transitions.

oriented crystal. The C_{4v} D^- site emission spectra is also shown in Figure V.2.12 where the local mode vibronic details are observed in spectra with an expanded scale. The $^3F_2$ terminating level for each transition from $^1D_2(D_1)$ is indicated on the spectra using the labels W_i for electronic transitions and $W_i'(\alpha)$ for local mode vibronic levels. The energies of the electronic and local mode vibronic levels are summarised in Table V.2.6 for the $^3F_2$ multiplet.

Table V.2.6

Energies of the electronic and local mode vibronic levels of $^3F_2$ multiplet for the C_{4v} Pr^{3+}-hydrogenic ion sites in $CaF_2:Pr^{3+}$. Level uncertainties are ± 1 cm^{-1}.

Electronic symmetry and Polarisation	C_{4v} H^- (cm^{-1}) Electronic	C_{4v} D^- Electronic level energy (cm^{-1})	C_{4v} D^- Vibronic level mode energy (cm^{-1}) and polarisation	C_{4v} T^- (cm^{-1}) Electronic
$W_1(\gamma_1),\pi$	5297	5293	z:6106	5290
$W_2(\gamma_4)$	-	-		-
$W_3(\gamma_5),\sigma$	5360	5357	x,y:6079(π) z:6178(σ)	5354
$W_4(\gamma_3)$, [a]	-	5448	x,y:6171(σ)	-

[a] Electronic level energy inferred from the local mode vibronic transition.

Well polarised electronic transitions are observed to two $^3F_2$ levels for each site and have been assigned to transitions from $^1D_2(D_1)$ terminating on the $W_1(\gamma_1)$ and $W_3(\gamma_5)$ crystal field levels.

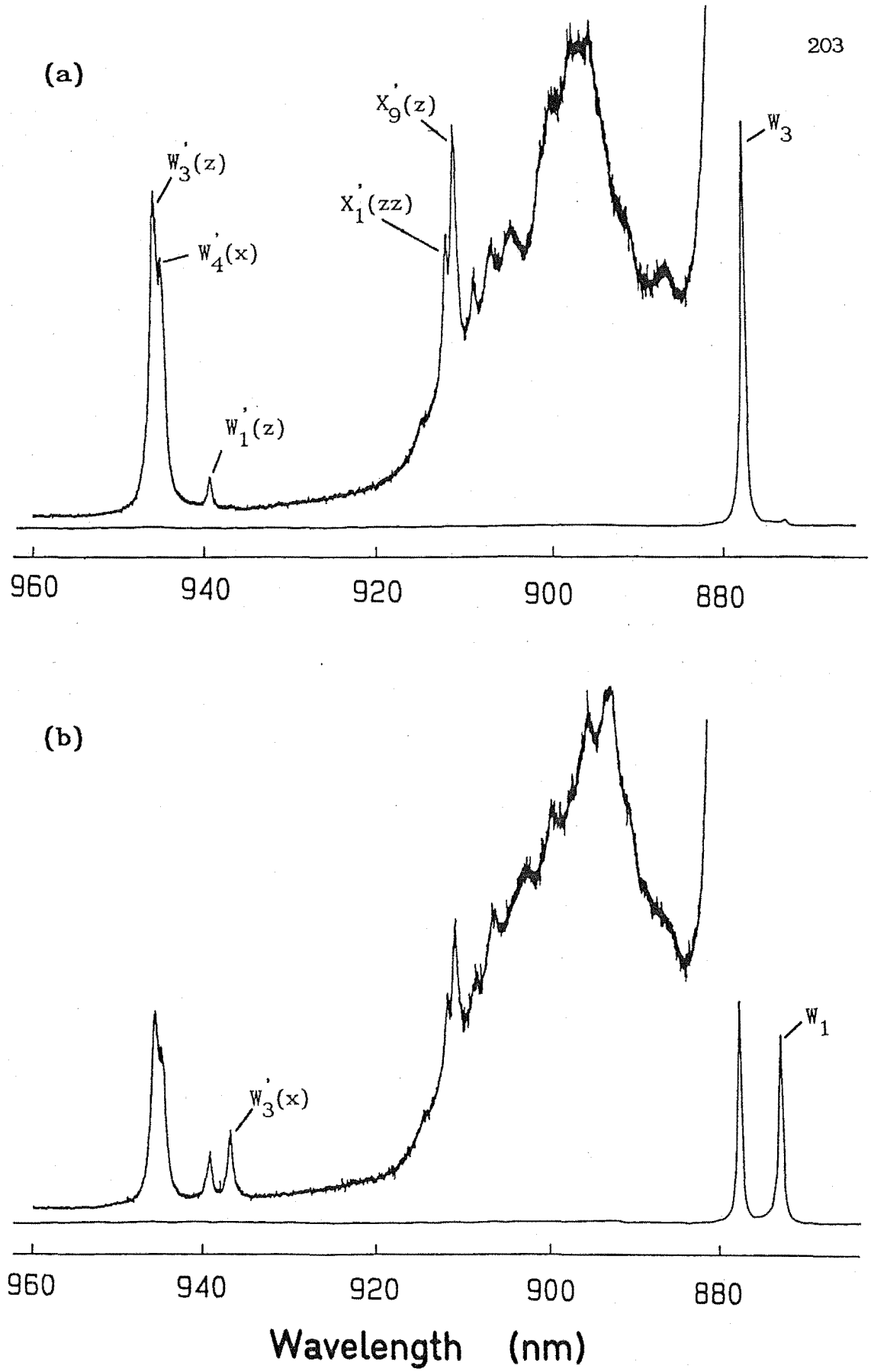

Figure V.2.12 Polarised $^1D_2 \rightarrow {}^3F_2$ emission from the C_{4v} D^- site in $CaF_2:Pr^{3+}:D^-$ showing details of the local mode vibronic transitions . The spectra are recorded for the (a) x(yy)z and (b) x(yx)z polarisation geometries in a <100> oriented crystal.

The polarisations of π and σ for the two lines are appropriate for electric dipole transitions originating from a γ_1 symmetry state and terminating on γ_1 and γ_5 symmetry levels respectively. Note that in the spectra of Figure V.2.11 there is some deviation from the x(yy)z:x(yx)z polarisation ratios of 0:1 and 2:1 expected for these π and σ polarised lines. This breakthrough results from the use of an analyser appropriate for the visible region of the spectrum in the particular spectra shown in Figure V.2.11. A polarisation analyser designed for the infrared region was used in the spectra of Figure V.2.12 and here the polarisation ratios are very close to those predicted.

Using symmetry arguments, electric dipole transitions are not expected to the W_2 and W_4 crystal field levels from the $D_1(\gamma_1)$ emitting level, however a tentative assignment of the W_4 level position can be made from a local mode vibronic level. In Figure V.2.12 two vibronic lines are observed close together at 946 nm, both having σ-polarisation. Either of these has an energy interval from the W_3 transition appropriate for a transition to the $W_3'(z)$ level. There is no reason why a second line should be associated with W_3 in this region, and the origin of this line could be a transition to the $W_4'(x)$ vibronic level which would also be expected to have σ-polarisation. With the somewhat arbitrary assignment of the $W_3'(z)$ transition as being the strongest line of the pair, and using the x,y local mode frequency of 723 cm^{-1} a tentative assignment of the W_4 level is made at 5448 cm^{-1}. At first glance a Zeeman experiment would not aid in the assignment of the two lines at 946 nm as both are doubly degenerate. However the degeneracy of the $W_3'(z)$ line is electronic in nature and would be split by the relevant electronic g-value, while the degeneracy of the $W_4'(x)$ level is phonon related and may split differently.

The $^3F_3$ and $^3F_4$ Multiplets

Spectra of emission from the $^1D_2$ multiplet to the $^3F_3$ and $^3F_4$ levels were recorded for the C_{4v} D^- site only as the deuterated $CaF_2:Pr^{3+}$ crystal was the only sample examined using the infrared emission spectrometer. Figure V.2.13 shows the polarised $^1D_2 \rightarrow {}^3F_3, {}^3F_4$ emission for this site recorded at 14 K using a <100> oriented crystal. Transitions to local mode vibronic levels are apparent in spectra recorded with an expanded intensity scale and these are given in Figure V.2.14. The spectral lines for transitions to the levels of the $^3F_3$ and $^3F_4$ multiplet are indicated using the V_i and U_i labels respectively.

The two strong σ-polarised lines in the $^1D_2 \rightarrow {}^3F_3$ region are assigned to transitions to the V_1 and V_4 crystal field levels as this polarisation is consistent with a terminating level symmetry of γ_5. In Figure V.2.14 a weak transition exhibiting a x(yy)z:x(yx)z polarisation ratio of 1:0 is assigned to the V_3 crystal field level. This level transforms as the γ_2 irrep of C_{4v} and the line has the appropriate polarisation for a transition through the z component of the magnetic dipole radiation field.

There does not appear to be a line in the spectra that can be associated with the $D_1 \rightarrow V_5$ transition. Both D_1 and V_5 transform as γ_1 irreps of C_{4v} and the transition is allowed by π-polarised electric dipole radiation and was observed as such for the C_{4v} F^- site in $CaF_2:Pr^{3+}$. Consequently, it is reasonable to assume it would be observed for the C_{4v} D^- site if not hidden by another transition through some accidental degeneracy. The most likely level for coincidence is V_4, and V_5 is given the same energy as V_4 with an increased uncertainty. Only a few local mode vibronic lines have been observed coupled to $^3F_3$ transitions as the $^1D_2 \rightarrow {}^3F_4$ transitions occur in the same region,. Table V.2.7 summarises the energies of the electronic and local mode vibronic levels for the $^3F_3$ multiplet.

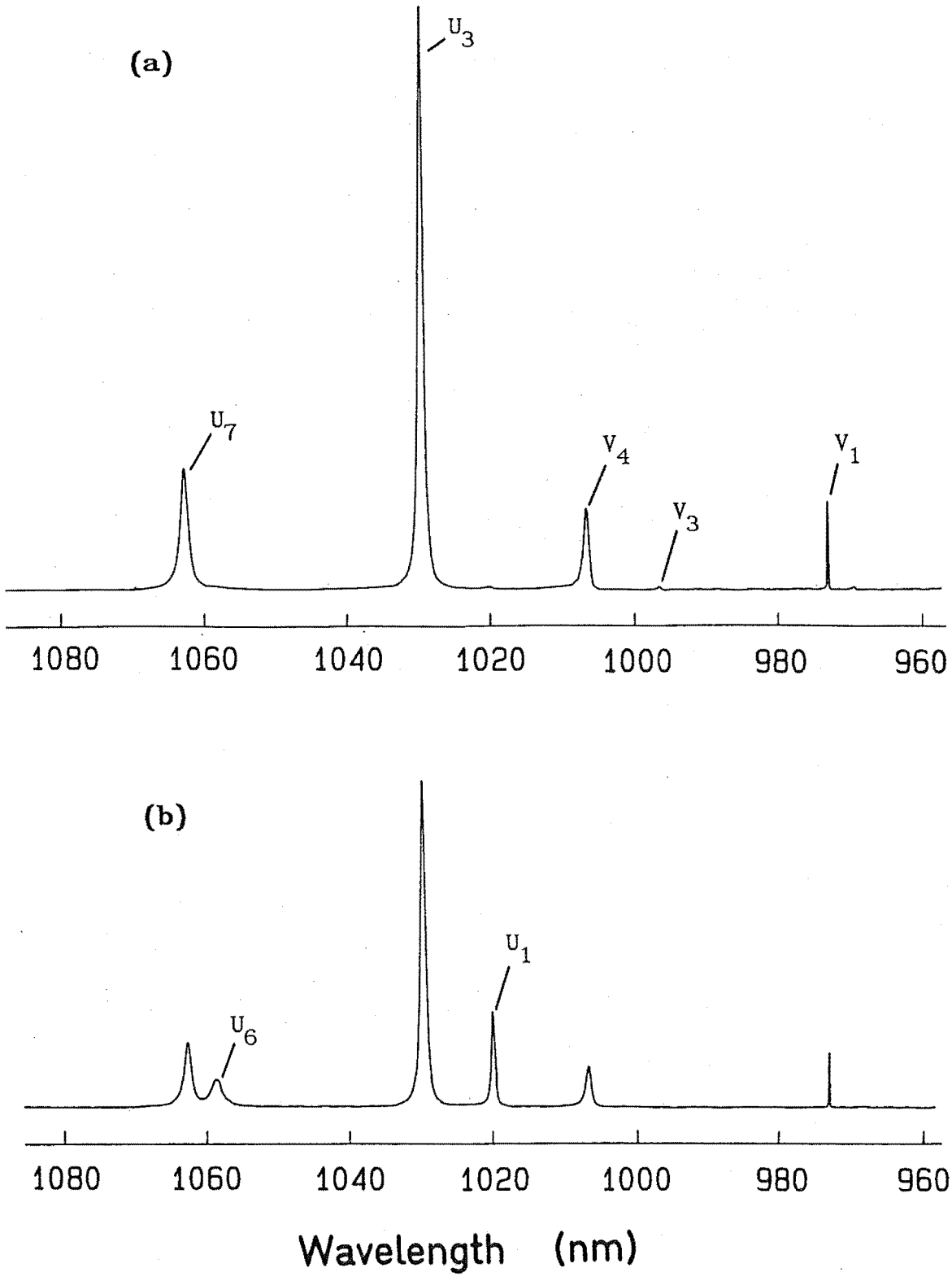

Figure V.2.13 Polarised $^1D_2 \rightarrow {}^3F_3, {}^3F_4$ emission from the C_{4v} D^- site in $CaF_2:Pr^{3+}:D^-$ recorded with (a) x(yy)z and (b) x(yx)z polarisation geometries.

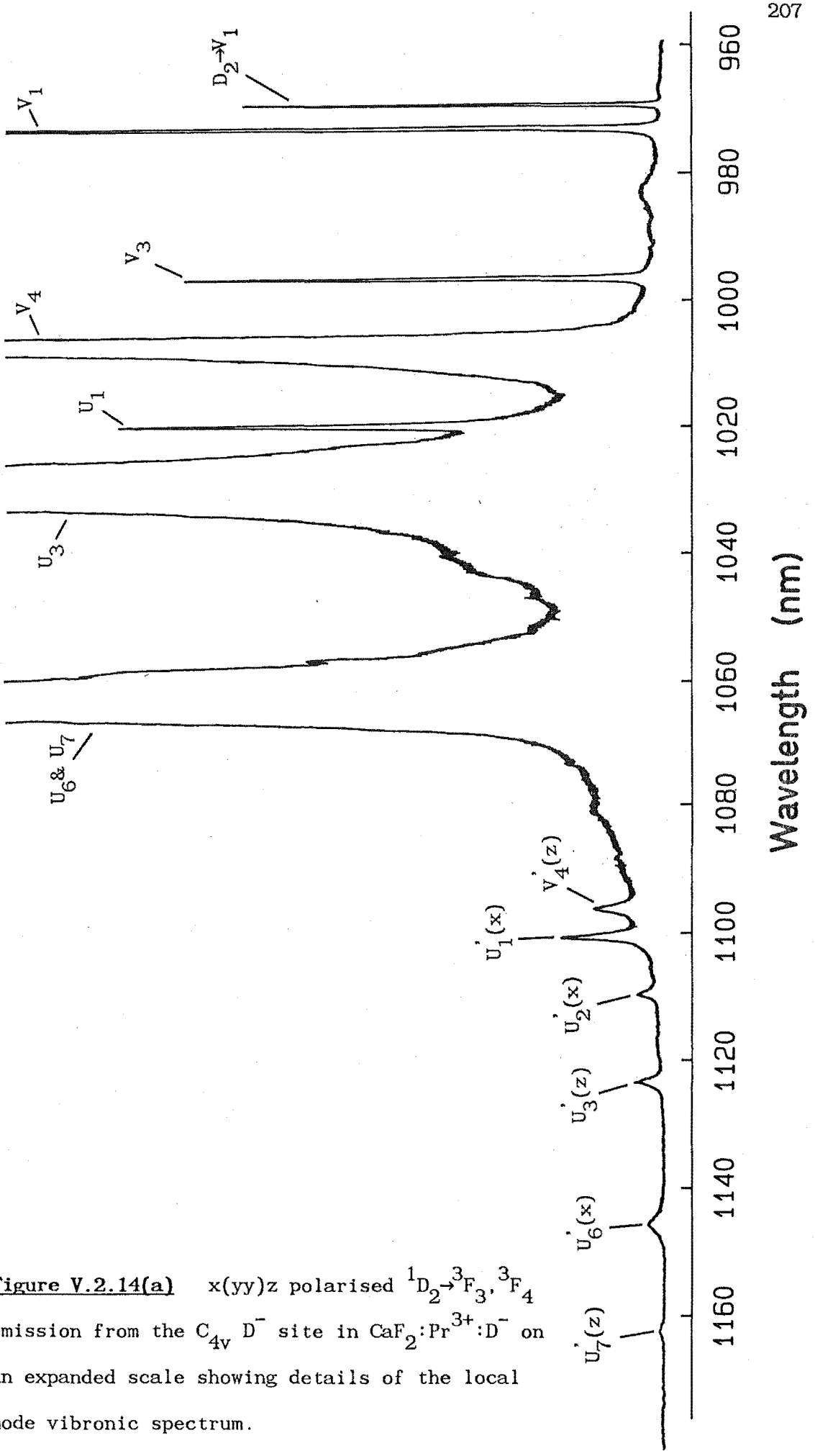

Figure V.2.14(a) x(yy)z polarised $^1D_2 \rightarrow {}^3F_3, {}^3F_4$ emission from the C_{4v} D^- site in $CaF_2:Pr^{3+}:D^-$ on an expanded scale showing details of the local mode vibronic spectrum.

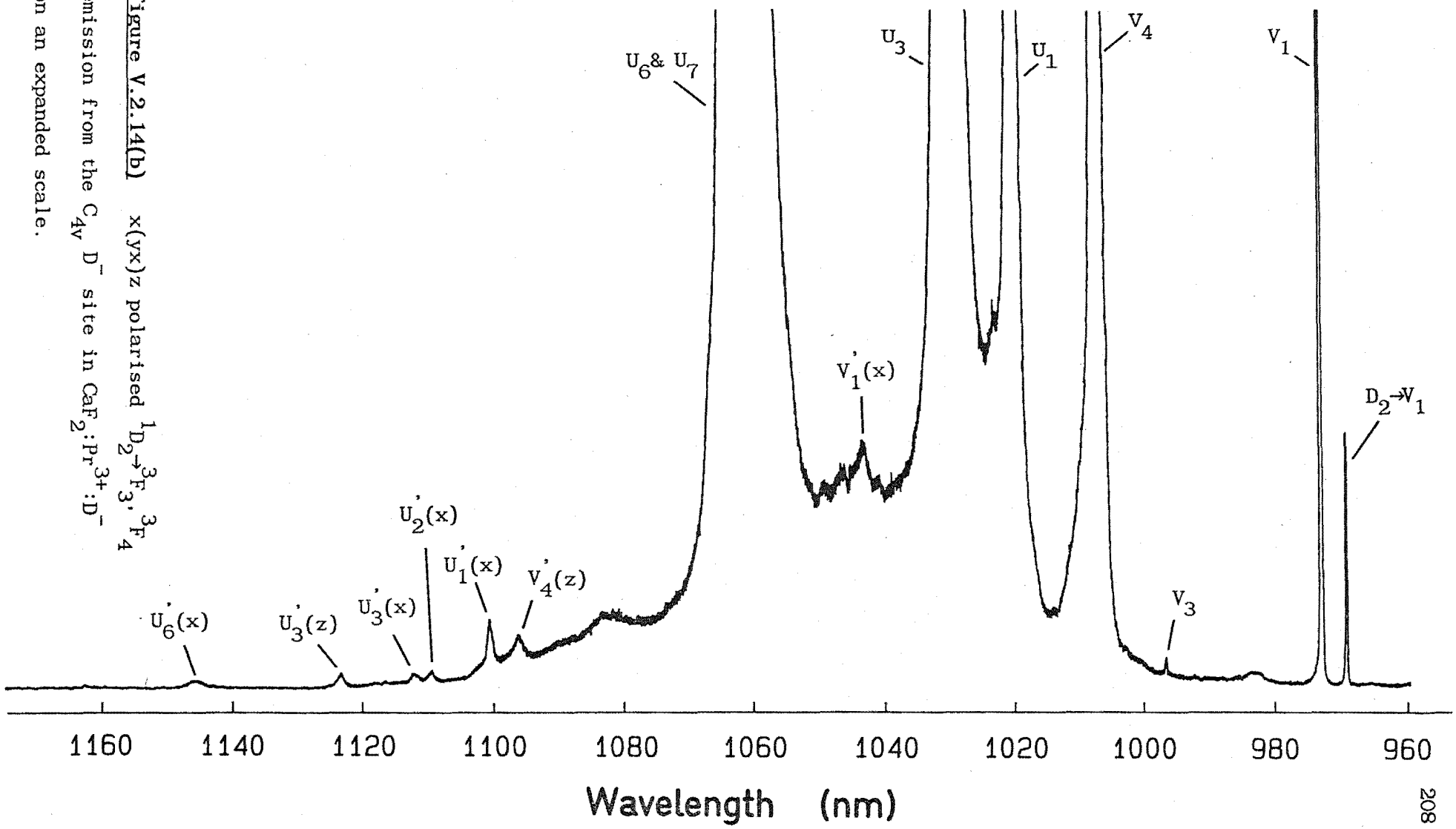

Figure V.2.14(b) x(yx)z polarised $^1D_2 \rightarrow {}^3F_3, {}^3F_4$ emission from the C_{4v} D^- site in $CaF_2:Pr^{3+}:D^-$ on an expanded scale.

Table V.2.7

Energies of the electronic and local mode vibronic levels for the $^3F_3$ multiplet of the C_{4v} D^- site in $CaF_2:Pr^{3+}$. Level uncertainties are ± 2 cm^{-1}.

Electronic state, symmetry and polarisation	C_{4v} D^- Electronic level energy (cm^{-1})	Vibronic level mode, energy (cm^{-1}) and polarisation
$V_1(\gamma_5)$, σ	6473	x:7195(π)
$V_2(\gamma_4)$	-	
$V_3(\gamma_2)$, π(md) [a]	6719	-
$V_4(\gamma_5)$, σ	6820	z:7630(σ)
$V_5(\gamma_1)$	6820±10	-

[a] polarisation for a magnetic dipole transition.

Four Pr^{3+} ion electronic energy levels of the $^3F_4$ multiplet have been assigned from direct transitions with the position of another one being inferred from a local mode vibronic level. The energy of the electronic and local mode vibronic levels are summarised in Table V.2.8 for the $^3F_4$ multiplet of the C_{4v} D^- site.

Table V.2.8

Energies of the electronic and local mode vibronic levels for the $^3F_4$ multiplet of the C_{4v} D^- site in $CaF_2:Pr^{3+}$. Level uncertainties are ± 2 cm^{-1}.

Electronic state, symmetry and polarisation	C_{4v} D^- Electronic level energy (cm^{-1})	Vibronic level mode, energy (cm^{-1}) and polarisation
$U_1(\gamma_1)$ π	6947	x:7666(σ)
$U_2(\gamma_4)$ [a]	7017±5	x:7739(σ)
$U_3(\gamma_5)$, σ	7040	x:7760 z:7851(σ)
$U_4(\gamma_2)$	-	
$U_5(\gamma_3)$	-	
$U_6(\gamma_1)$, π	7307	x:8025
$U_7(\gamma_5)$, σ	7343	z:8151(σ)

[a] electronic level energy assigned from position of vibronic level.

Transitions to the U_1,U_3,U_6 and U_7 crystal field levels are all electric dipole allowed from $D_1(\gamma_1)$ and have π,σ,π and σ-polarisations respectively, consistent with their symmetry assignments. A transition to the U_2 crystal field level was not observed directly but its energy can be inferred from the position of the $U_2'(x)$ vibronic level. The choice of the x,y vibration as the appropriate phonon was made on the basis of the observed σ-polarisation of the $D_1 \longrightarrow U_2'(x)$ transition. Note that the U_6 crystal field level is now resolvable from the U_7 level after they were almost coincident in the C_{4v} F^- site. The observed π-polarisation of the $D_1 \longrightarrow U_6$ transition is consistent with the U_6 level transforming as a γ_1 irrep of C_{4v}.

CHAPTER VI

LOW SYMMETRY HYDROGENIC ION SITES IN $SrF_2:Pr^{3+}$ AND $CaF_2:Pr^{3+}$ CRYSTALS.

VI.1 Introduction

Previous studies of hydrogenated and deuterated crystals of calcium and strontium fluorides containing low concentrations of rare-earth ions, revealed the existence of several low-symmetry sites derived from the hydrogenic C_{4v} site (Edgar, Freeth and Jones [1977], Edgar, Jones and Presland [1979]). Several of these rhombic symmetry sites in hydrogenated $SrF_2:Pr^{3+}$ and $CaF_2:Pr^{3+}$ crystals have been characterised in the optical region using laser selective excitation techniques and are found to be modified from the C_{4v} H^- site by the addition of a second and in some cases several, extra hydrogenic ions. The observation of strong local mode vibronic transitions infers that the second hydrogenic ion substitutes for a lattice F^- ion in the first coordination shell of the Pr^{3+} ion. In addition, the centre retains its regular charge compensating hydrogenic ion in the 100 interstitial position. A total of thirteen centres containing multiple hydrogenic ions have been identified in $SrF_2:Pr^{3+}$ and $CaF_2:Pr^{3+}$ crystals. All these centres have been found to be unstable under laser excitation as the site emission bleaches under constant pumping conditions.

On pumping Pr^{3+} ion electronic transitions in these centres, the intensity of the fluorescence is observed to decrease by typically factors of five in times ranging from a few seconds to several minutes depending upon the particular site. The fluorescence is quickly restored on illuminating a virgin piece of the crystal only for it to rapidly decay again. All three H^-, D^- and T^- isotopic variations of these centres show the effect and the site of a light isotope gives a more rapid decrease of fluorescence than the corresponding centre of a

heavier isotope. This bleaching is persistent at low temperatures showing only a slight recovery (<5%) after 2 hours at 14 K. Spectral holes burnt into the absorption line of the $C_s(1)$ centre in $SrF_2:Pr^{3+}:D^-$ show no degradation after 1 hour at a temperature of 1.6 K (Macfarlane, Reeves and Jones [1987]). For this same site the broadband bleaching time increases with temperature up to 100 K where no fluorescence decay effects are observed. Thermal cycling of the crystal to a temperature above 100 K also restores the initial level of fluorescence from a previously bleached centre.

The bleaching effects in these rhombic Pr^{3+} centres result from constituent hydrogenic ions of the site migrating to new positions which removes the centre from resonance with the laser and leads to photoproduct formation. This mechanism is analogous to photochemical holeburning which is common for many organic systems and molecules in glasses (Friedrich and Haarer [1984]). In the cubic fluorite crystals studied here, the ions are observed to migrate either to different positions to form a photoproduct centre at a different excitation wavelength or to equivalent positions where the photoproduct is an equivalent centre reoriented by 90^o (Macfarlane, Reeves and Jones [1987]). In both cases the motion is observed to be reversible as excitation of the photoproduct leads to restoration of the original centre. A similar reversible switching between discrete photoproducts is the proton transfer in metal-free pthalocyanine (Gorokhovskii et al [1974]) and porphin (Volker et al [1977]) which leads to spectral holeburning. When the photoproduct is an equivalent centre reoriented by 90^o an unusual phenomenon of reversible polarised bleaching is observed (Cockcroft et al [1987a]). This effect results from the independence of the absorption cross-sections of the three possible orientations of a [100] oriented $RE^{3+}-H^-$ ion pair. In a <100> oriented crystal adherence to the transition selection rules results in a preferential excitation of some site orientations. A similar

independence of site orientations was shown recently using photochemical holeburning of CN^- molecules in cubic alkali halide crystals (Spitzer, Ambrose and Sievers [1986]).

The reversible polarised bleaching is clearest for <100> oriented crystals with the laser light incident parallel to the [100] unit cell edge. After bleaching with the laser polarised in the [001] direction, fluorescence could be substantially restored by switching the laser polarisation to the [010] direction and bleaching the fluorescence with this geometry. Moreover, by suitable sequential pumping with the laser polarised in these two directions an apparently indefinite sequence of bleaching and recovery of the fluorescence could be accomplished.

A discussion on the mechanisms for bleaching and possible site configurations will be presented in Section VI.4 of this chapter and only a brief description follows. The reversible bleaching observations can be understood on a model of reorientation of [100] oriented Pr^{3+}- H^- ion pairs. Selective excitation with one laser polarisation induces H^- ion migration to form an equivalent centre in either of the two orientations at 90^o to the original alignment. Subsequent excitation with the second polarisation returns some ions to their previous positions and the reversibility is complete. As there are three equivalent [100] directions but only two possible laser polarisation directions there is a preferential excitation of some site orientations. This results in a net loss of centres able to be driven by the laser field as the third orientation is either depleted, for σ-polarised absorption, or populated, for π-polarised absorption, and a less than 100% recovery of fluorescence is expected with each polarisation cycle. For the centres where a discrete photoproduct is formed there is no reorientation of the Pr^{3+}- H^- pairs and the fluorescence from the two laser polarisations bleaches independently.

Two centres in both $SrF_2:Pr^{3+}$ and $CaF_2:Pr^{3+}$ are found to exhibit reversible polarised bleaching while the remaining bleach through photoproduct formation. In the next two sections the optical spectroscopy of these centres is discussed, firstly with those found in $SrF_2:Pr^{3+}$, and then some thoughts on the bleaching mechanism and site configurations are presented in Section VI.4. Finally some results on the persistent spectral holeburning observed for two centres in $SrF_2:Pr^{3+}:D^-$ are presented.

VI.2 Optical Spectroscopy of the Rhombic Centres in Hydrogenated $SrF_2:Pr^{3+}$

The optical spectroscopy of the four principle rhombic hydrogenic centres was studied using both continuous and pulsed laser techniques. These sites were labelled $C_s(1)$, $C_s(2)$, $C_s(3)$ and $C_s(4)$ in the chronological order in which they were examined. More recent experiments using a vastly superior detection technique for laser excitation revealed the existence of at least a further five centres of this type including photoproducts of some of the original four sites studied. Figure VI.2.1 depicts a broad band excitation spectrum of the appropriate $^1D_2$ region in a $SrF_2:Pr^{3+}:D^-$ crystal and shows the $Z_1 \longrightarrow D_1$ excitation lines of the sites studied. In the reduction to rhombic C_s symmetry, the degenerate ground state of the parent C_{4v} site is split and for some sites the separation is sufficiently small for a $Z_2 \longrightarrow D_1$ excitation line to be observed. The photoproduct centres are not visible in this spectrum as the centres have yet to be bleached. The spectroscopy of each of the four centres studied will now be discussed on an individual basis.

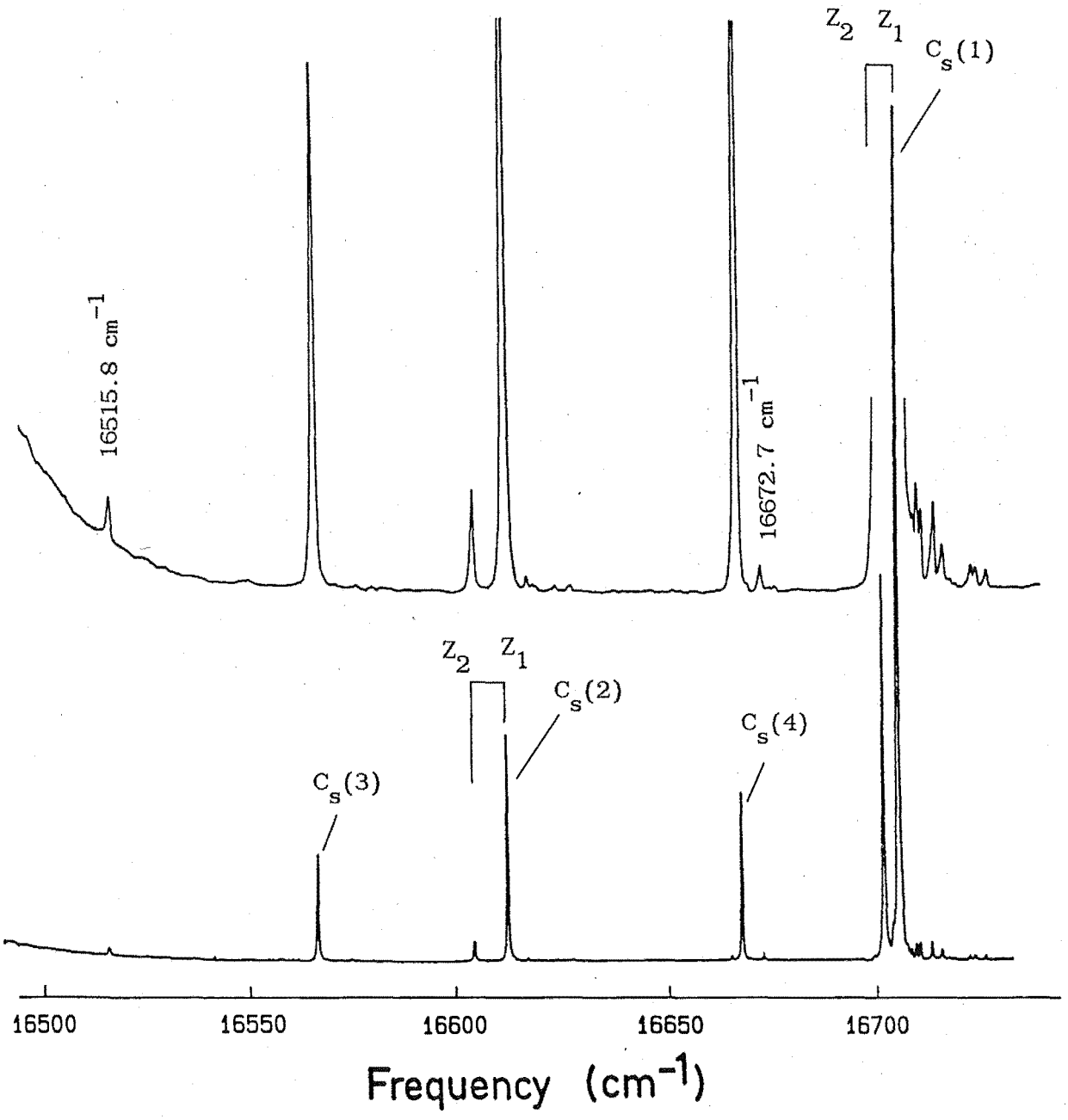

Figure VI.2.1 Broadband excitation spectrum of the $^1D_2$ region in a SrF_2:0.05%Pr^{3+}:D^- crystal showing the transitions of several low symmetry sites studied.

VI.2.1 The $C_s(1)$ Centre

As Figure VI.2.1 shows the $C_s(1)$ centre is the dominant multiple hydrogenic ion centre and was the most studied during the period of this work. Its absorption is several times stronger than the other rhombic centres and about the same order of magnitude weaker than the C_{4v} hydrogenic site. For the $C_s(1)$ D^- centre the $Z_1 - Z_2$ splitting has been measured to be 3.3 ± 0.1 cm^{-1} and an excitation line correponding to the $Z_2 \longrightarrow D_1$ transition is observed in Figure VI.2.1 at the crystal temperature of 14 K.

In Figure V.1.1 showing the absorption of a $SrF_2:Pr^{3+}:H^-$ crystal, transitions to the $^3P_0$ level were indicated for some of the rhombic C_s centres. The assignment of these absorption lines to a particular rhombic centre studied in the $^1D_2$ region was made on the basis of the same $Z_1 - Z_2$ splitting and the correct frequency for the $D_1 \longrightarrow Z_1$ emission when the $^3P_0$ level was excited with a pulsed nitrogen pumped tunable dye laser. For the $C_s(1)$ site the $Z_1 \longrightarrow {}^3P_0$ transition was measured to be 481.57 nm and 481.37 nm for the D^- and H^- varieties respectively.

All three isotopic variations of the $C_s(1)$ site were studied in emission. Figure VI.2.2 shows the $^1D_2 \longrightarrow {}^3H_4$ fluorescence spectra recorded at 14 K, and Table VI.2.1 summarises the spectral data for the $C_s(1)$ sites.

A definite assignment can be made to seven crystal field levels of the $^3H_4$ multiplet. The electronic transitions have been indicated with appropriate Z_i labels in the spectra of Figure VI.2.2 according to the order of electronic levels given in the table. Local mode vibronic lines are labelled a-f and in some cases transitions to vibronic levels associated with excited $^3H_4$ levels are observed. The transition to the Z_2 level is not apparent due to the action of the shutter mechanism on the spectrometer protecting the photomultiplier

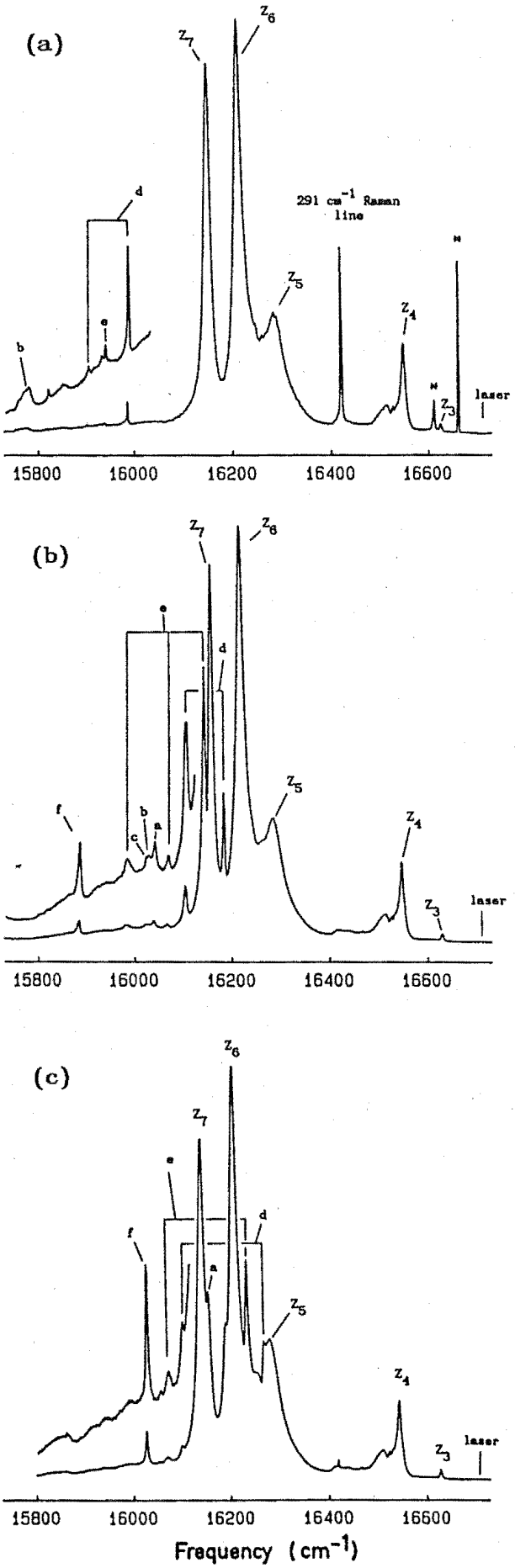

Figure VI.2.2 14K $^1D_2 \rightarrow {}^3H_4$ emission spectra for the (a) H^-, (b) D^- and (c) T^- $C_s(1)$ centres in $SrF_2:Pr^{3+}$ crystals.

tube from scattered laser light.

Table VI.2.1

Spectral data for the hydrogenic $C_s(1)$ site in $SrF_2:Pr^{3+}$

Site		$C_s(1)$ H^-	$C_s(1)$ D^-	$C_s(1)$ T^-
$Z_1 \rightarrow D_1$ transition and Z_1-Z_2 splitting ($\pm$ 0.1 cm^{-1})		16707.6 3±1	16706.7 3.3	16706.3 3±1
Other Pr^{3+} ion electronic energy levels ($\pm$ 1 cm^{-1})		85 163 427 499 561	83 165 427 495 555	80 165 427 501 567
Interstitial ion local mode vibration intervals ($\pm$ 1 cm^{-1})	a b c	[1] 934	673 685 691	553 [2] [2]
Substitutional ion local mode vibration intervals ($\pm$ 1cm^{-1})	d e f	723 774 -	529 569 829	439 474 682
$Z_1 \rightarrow {}^3P_0$ transition ($\pm$ 0.01 nm)		481.37	481.57	-

[1] Broad line of width 30 cm^{-1} and appearing to contain structure.

[2] Obscured by electronic level at 567 cm^{-1}.

The electronic transitions to the Z_6 and Z_7 levels exhibit a large isotope shift between the sites that does not follow the expected H^-:D^-:T^- trend (Table VI.2.1). Firstly the magnitude of the shifts is much greater than it was for the hydrogenic C_{4v} sites due to a stronger electron-phonon interaction. This coupled with the large intensity of some local mode vibronic transitions suggests that a

constituent hydrogenic ion of the centre is closer to the Pr^{3+} ion than is the case for the C_{4v} site. The anomalous isotope shifts arise from second order effects due to the close proximity of these strong local mode vibronics to the electronic transitions (Figure VI.2.2).

Apparent in Figure VI.2.2 (a) and (c) showing the emission spectra for the H^- and T^- $C_s(1)$ sites is a sharp line at an interval of 291 cm^{-1} from the laser line. This line corresponds to the first order Raman scattering transition of the SrF_2 lattice (Denham et al [1970]).

The $C_s(1)$ site bleaches under continuous laser excitation and it was of interest to see whether the same was true under pulsed laser excitation. If the bleaching occurred on a purely energetic basis then the decay time of 30 seconds for the D^- centre at a cw laser power of 100 mW would correspond to 3J of energy received. At 100 μJ per pulse and a repetition rate of 10 Hz the pulsed excitation bleaching time would be approximately 50 minutes. For this site, degradation of the fluorescent transient was observed in qualitative agreement with this time scale.

The fluorescent lifetime of the $^1D_2$ level was measured to be 60 ± 5 μsecs for the $C_s(1)$ D^- site. This value contrasts with the corresponding C_{4v} site lifetime of 405 μsec. The factor of ten reduction arises as a further non-radiative relaxation path is provided by the second D^- ion in the centre. Generation of local mode phonons through the coupling of the electron-phonon interaction efficiently channels the Pr^{3+} excitation into non-radiative processes giving a reduction in the fluorescent lifetime. Further results on the role of local mode phonons in the relaxation of the Pr^{3+} ion are to be presented in Chapter VIII.

Vibronic Transitions of the $C_s(1)$ Site

Several strong local mode vibronic lines are visible in the

emission spectra depicted in Figure VI.2.2 and can be distinguished from the electronic lines by their characteristic large shift in frequency with hydrogenic ion isotope. These vibronic lines are much more intense than those previously observed for the hydrogenic C_{4v} sites and their frequency and strength can yield information on the positions of the hydrogenic ions in the centre.

An interstitial charge compensating ion in an approximately C_{4v} symmetry position is inferred from the observation of vibronic lines similar to those of the C_{4v} site. Discussing the $C_s(1)$ D^- centre as being representative, the interstitial ion local mode intervals of 673, 685 and 691 cm^{-1} measured for the $C_s(1)$ D^- site are close to the C_{4v} site frequencies of 658.4, 666.9 and 684.9 cm^{-1} (Chapter V). Three distinct local mode frequencies are expected for the interstitial ion of the $C_s(1)$ site as the degenerate transverse vibration of the C_{4v} site is split into two modes in the reduction to rhombic C_s symmetry.

It is inferred from the greater intensity of its vibronic transitions that a second D^- ion has substituted for a lattice F^- ion in the first coordination shell of the Pr^{3+} ion. These vibronic transitions show vibrational intervals of 529, 569 and 829 cm^{-1} and have a mean frequency close to 642 cm^{-1}, the frequency of an isolated D^- ion occupying a regular T_d symmetry lattice anion site (Harrington et al [1970]). The three observed local mode frequencies of this ion arise from the combined effects of the neighbouring Pr^{3+} ion and the interstitial charge compensating ion in lifting the three fold degeneracy of the T_d site vibration at 642 cm^{-1}.

Using infrared absorption, the local mode frequencies for the H^- ions in the $C_s(1)$ site of $SrF_2:Pr^{3+}$ have been measured (Edgar, Freeth & Jones [1977]). Their two low frequency vibrations of 721.0 and 772.7 cm^{-1} correspond to the 529 and 569 cm^{-1} vibrations discussed above for the D^- site and have been observed here as transitions to

vibronic levels for all three varieties of the $C_s(1)$ site. However a line has not been observed in the optical spectra corresponding to their 951.5 cm^{-1} vibration. Moreover the high frequency substitutional ion vibration observed here, at 829 cm^{-1} for the D^- site, was not observed in the infrared. This local mode is definitely established in the optical spectra as a fluorescence transition to a vibronic level coupled to Z_1 at intervals of 829 and 682 cm^{-1} for the D^- and T^- sites respectively and as a vibronic level coupled to the D_4 crystal field level of $^1D_2$ in absorption. The $C_s(1)$ D^- centre could be excited by tuning a green dye laser to 18201 cm^{-1}, corresponding to a level 827 cm^{-1} higher in energy than the $Z_1 \longrightarrow D_4$ absorption at 17374 cm^{-1} for this centre. In a similar manner this centre could be excited with this laser tuned to a level at a frequency interval of 525 cm^{-1} above the $Z_1 \longrightarrow D_4$ absorption.

Bleaching in the $C_s(1)$ Centre

The $C_s(1)$ centre is observed to undergo reversible polarised bleaching in a <100> oriented crystal when excited from either of the Z_1 or Z_2 crystal field levels. Figure VI.2.3 shows the fluorescence intensity when exciting from Z_1 for a sequence of laser excitations of the $C_s(1)$ D^- site. The intensity is observed to recover between the two possible laser polarisations, V[001] and H[010], to a level better than 95%. The origin of the asymmetry in intensity between the two polarisations is not clear but may originate in misalignments from the ideal geometry in both the sample and the laser/spectrometer geometry or from polarisation effects. Bleaching curves recorded with an analyser in the fluorescence path may yield information on this effect.

During the early part of the decay the bleaching curve shows a single exponential behaviour with a characteristic time of ~30 seconds for the D^- site with 100 mW of laser power. For the H^- site the time

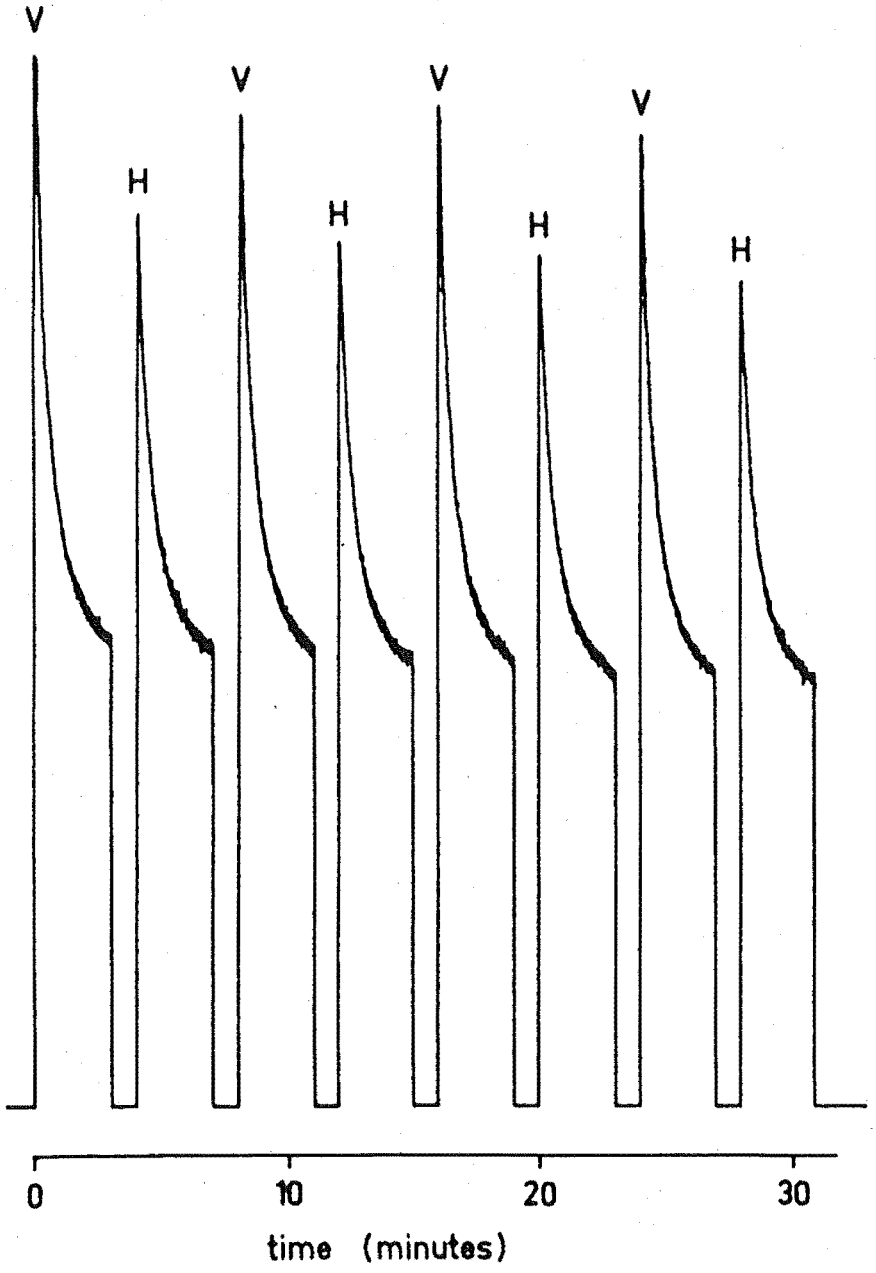

Figure VI.2.3 Fluorescence intensity as a function of time for a sequence of laser excitations in the two possible polarisation directions, V[001] and H[010], for the $C_s(1)$ centre in a <100> oriented $SrF_2:Pr^{3+}:D^-$ crystal.

reduces dramatically to 3 seconds. The H^- site bleaches more rapidly than the D^- site due to the much greater mobility of H^- ions. Preliminary studies show an inverse power dependence of the bleaching time consistent with a model where the rate of decay is determined by the incident light flux.

The $C_s(1)$ D^- site shows bleaching effects up to temperatures of 100 K with the bleaching time becoming longer as the temperature is elevated. Warming the crystal above 100 K rejuvenates the previously bleached fluorescence of this site. This observation appears to be applicable to all the rhombic centres studied. With the crystal held at 14 K for two hours some recovery of the fluorescence was recorded for the $C_s(1)$ centres previously bleached. Figure VI.2.4 shows the bleaching curves for the $C_s(1)$ D^- site (a) for regular bleaching and (b) after 2 hours held at 14 K with no irradiation. The bleaching in (b) is much faster than the regular bleaching shown in (a). This indicates that some of the centres are more mobile than others and restore their equilibrium populations more quickly. As the figure shows they also bleach quickly and experiments on the reversible bleaching at very fast times may be useful.

Excitation Spectra of the $C_s(1)$ Centre

For some of the C_s rhombic centres a photoproduct site at a different excitation frequency is formed when the centre is bleached (Macfarlane Reeves and Jones [1987]). After bleaching the $Z_1 \longrightarrow D_1$ transition of the $C_s(1)$ D^- site the broadband excitation spectrum was scanned over a wide frequency range but failed to find evidence of any new photoproduct site. This indicates that the dominant bleaching mechanism for the $C_s(1)$ centre is the reversible process and the only photoproducts are equivalent centres oriented at 90^o to each other.

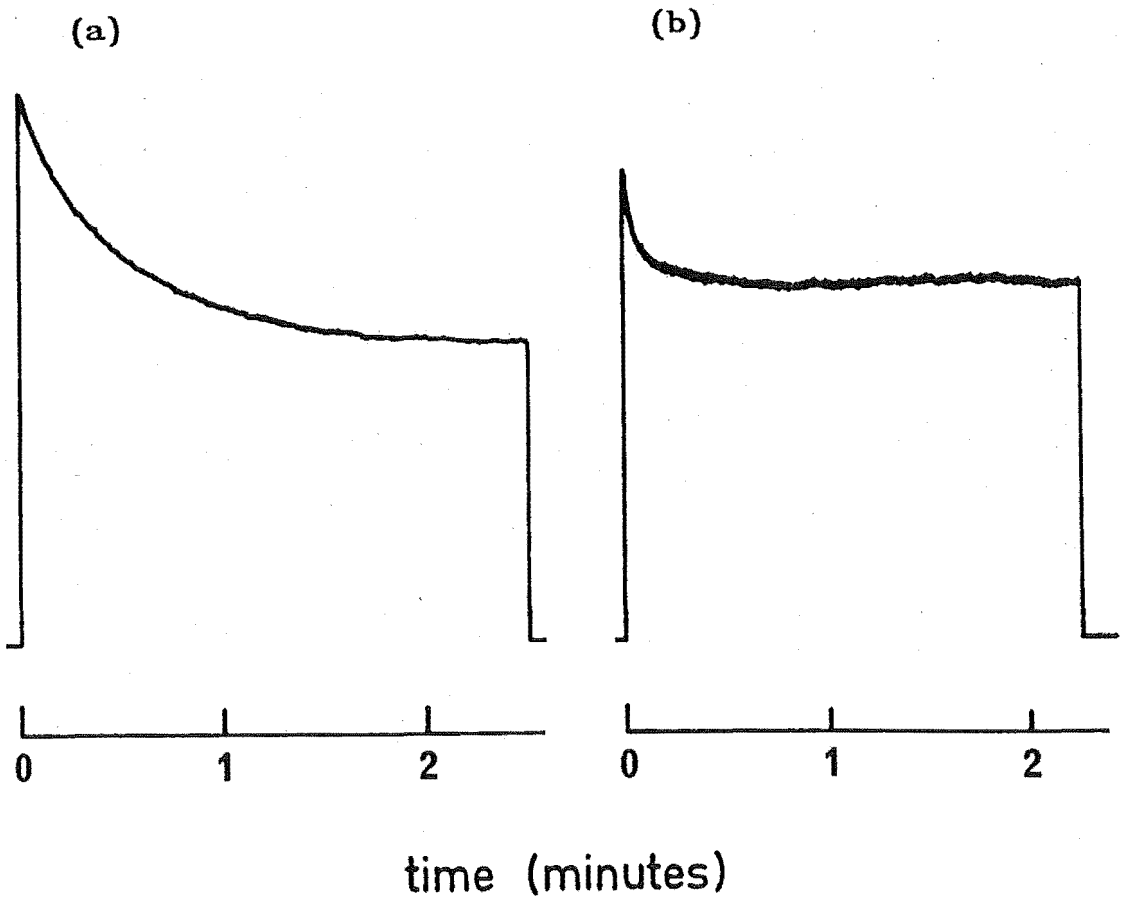

Figure VI.2.4 Bleaching curves for the $C_s(1)$ centre in $SrF_2:Pr^{3+}:D^-$ at 14K. The regular bleaching is shown in (a) while (b) shows some recovery to the previously bleached fluorescence after the crystal was held at 14K for 2 hours with no irradiation.

Figure VI.2.5 shows a series of excitation spectra for the $Z_1 \rightarrow D_1$ and $Z_2 \rightarrow D_1$ transitions of the $C_s(1)$ D^- site, recorded at 14 K in a <100> oriented $SrF_2:Pr^{3+}:D^-$ crystal. A laser power of 5 mW was used when probing these excitation transitions to minimise any bleaching effects at this stage. Parts (i) and (ii) of the figure show the transitions for the probe laser polarised in the V[001] and H[010] planes respectively. In Figure VI.2.5(a) the excitation lines are shown in their equilibrium state before any bleaching has occurred. After bleaching for 5 minutes at a power of 50 mW and laser polarisation V[001], the excitation lines probed in polarisation V[001] show a loss of intensity while showing little change when probed in polarisation H[010] (Fig. VI.2.5(b)). Reversing the bleaching polarisation to H[010] restores the lost intensity from V[001] but at the expense of that in H[010] (Fig. VI.2.5(c)). This sequence of reversible switching continues indefinitely as shown by the decay curves discussed earlier.

VI.2.2 The $C_s(2)$ Centre

When excited from the Z_1 crystal field level of the Pr^{3+} ion the $C_s(2)$ centre exhibits reversible polarised bleaching, however for excitation from the Z_2 level the initial bleaching is non-reversing. This result shows that the absorption transitions determine some bleaching properties and care is required in the classification of a particular centre as reversible or non-reversible. Spectra recording the $^1D_2 \rightarrow {}^3H_4$ fluorescence are shown in Figure VI.2.6 for the three isotopic varieties of the $C_s(2)$ centre and Table VI.2.2 summarises the spectral data for this site.

Figure VI.2.5 A series of excitation spectra for the $C_s(1)$ centre in a <100> oriented $SrF_2:Pr^{3+}:D^-$ crystal probed with (i) V[001] and (ii) H[010] laser polarisation planes.

(a) $Z_1 \rightarrow D_1$ and $Z_2 \rightarrow D_1$ excitation lines for the two polarisation geometries before any bleaching of the centre,

(b) after bleaching for 5 minutes at 50mW in polarisation V[001] the intensity in this geometry has decreased but shows no change in the orthogonal geometry H[010],

(c) bleaching in polarisation H[010] restores the lost intensity in V[001] but at the expense of the intensity in its own geometry.

Subsequent bleaching with the polarisation switched between these two planes will see an indefinite continuation of the spectra in (a) and (b).

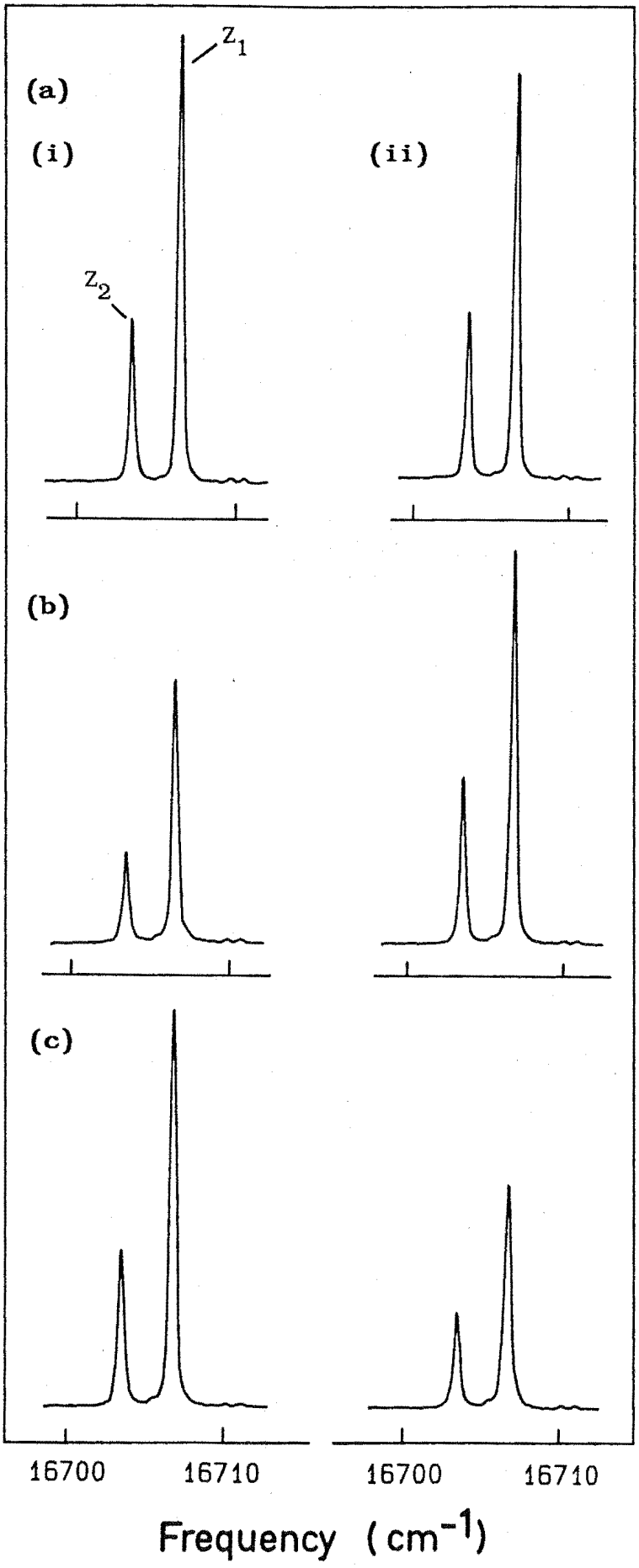
(a)
(i)
z_1
z_2
(ii)
(b)
(c)
16700
16710
16700
16710
Frequency (cm^{-1})

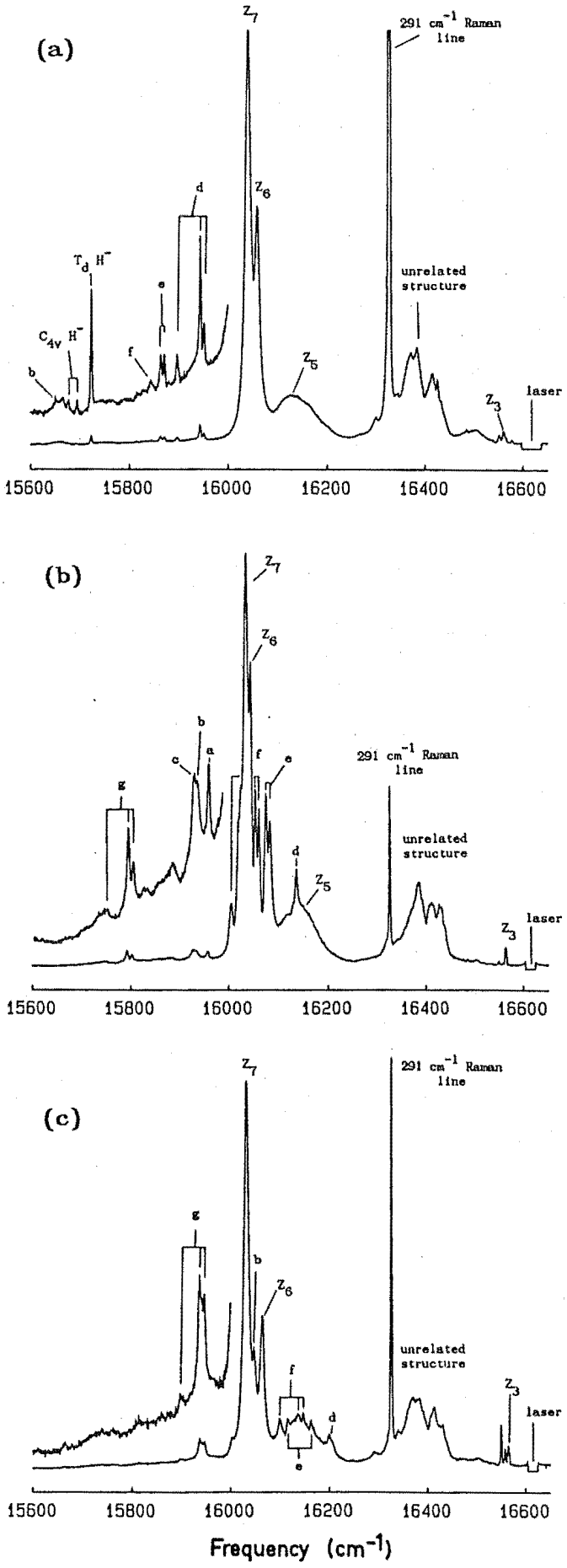

Figure VI.2.6 14K $^1D_2 \rightarrow {}^3H_4$ emission spectra for the (a) H^-, (b) D^- and (c) T^- $C_s(2)$ centres in $SrF_2:Pr^{3+}$ crystals.

Table VI.2.2

Spectral data for the hydrogenic $C_s(2)$ site in $SrF_2:Pr^{3+}$

Site		$C_s(2)$ H^-	$C_s(2)$ D^-	$C_s(2)$ T^-
$Z_1 \rightarrow D_1$ transition and Z_1-Z_2 splitting ($\pm$ 0.1 cm^{-1})		16612.4 8±1	16612.8 7.6	16613.0 8±1
Other Pr^{3+} ion electronic energy levels ($\pm$ 1 cm^{-1})		37 491±5 559 576	51 475±5 571 581	49±5 477±5 550 582
Interstitial ion local mode vibration intervals ($\pm$ 1 cm^{-1})	a b c	951 [1]	658 682 687	567 [2]
Substitutional ion local mode vibration intervals ($\pm$ 1 cm^{-1})	d e f g	665 745 773 -	480 533 554 812	410 452 468 666
$Z_1 \rightarrow {}^3P_0$ transition ($\pm$ 0.01 nm)		484.23	484.32	-
Photoproduced $Z_1 \rightarrow D_1$ transition and Z_1-Z_2 splitting ($\pm$ 0.1 cm^{-1})		-	16664.3 16.6	-

[1] broad line with some structure

[2] other lines obscured by electronic transitions

Six electronic energy levels have been identified for this centre and the corresponding transitions have been indicated in the spectra. The $Z_1 - Z_2$ splitting in the ground state was measured to be 7.6±0.1 cm^{-1} for the D^- site with the third component of the cubic Γ_5 level residing at 51 cm^{-1}. Like the $C_s(1)$ centre, the electronic levels of the $C_s(2)$ site show a large isotope shift which for some

lines does not follow the expected $H^-:D^-:T^-$ site trend. Comparing the energy of the level around 560 cm^{-1} (Table VI.2.2) the D^- site shows anomalous behaviour. Second order effects from the close proximity of the substitutional ion local mode vibronic levels perturb the D^- site level from the expected isotopic trend. For the H^- and T^- sites the local mode levels are further away and their energies for this electronic level are similar.

Vibronic Transitions of the $C_s(2)$ Centre

A similar vibronic spectrum is obtained for the $C_s(2)$ centre to that for the $C_s(1)$ centre, with evidence for substitutional and interstitial hydrogenic ions. In this site local mode vibronic transitions are characterised by the splitting pattern of the three lowest electronic levels. The same local mode phonon will couple to the Z_1, Z_2 and Z_3 levels to produce vibronic lines separated by the 0:8:51 cm^{-1} pattern. The transitions to the D^- site levels will be discussed as being representative.

An interstitial charge compensating ion is inferred from the observation of three vibronic lines with intervals of 658, 682 and 687 cm^{-1} similar to those for a D^- ion in a C_{4v} symmetry site. The separation of these three frequencies is greater than it was for the $C_s(1)$ site possibly indicating a greater distortion from C_{4v}. Strong local mode vibronic transitions at intervals of 533, 554 and 812 cm^{-1} indicate the presence of a substitutional D^- ion in the first coordination shell of the Pr^{3+} ion. These three frequencies are close to those of the $C_s(1)$ site and similarly average to a value close to the 642 cm^{-1} frequency of the isolated T_d site. For this site however, a fourth substitutional ion vibronic line is observed at an interval of 480 cm^{-1} and is confirmed as having a hydrogenic ion origin by the observation of the same mode in the H^- and T^- sites at 665 cm^{-1} and 410 cm^{-1} respectively. As there are only three degrees

of freedom for each ion, a fourth substitutional ion local mode vibration requires there to be more than one such ion. As will be discussed later the bleaching effects in this centre suggest the site configuration contains three hydrogenic ions.

A number of lines appearing in the vibronic spectra of the $C_s(2)$ H^- site are in fact Raman scattering from local mode vibrations of other H^- ion sites. The dominant line at an interval of 893 cm^{-1} originates from H^- ions in the T_d symmetry site (Harrington et al [1970]) and additional Raman lines are observed from the C_{4v} H^- site, the next most prevalent centre. This is the first observation of Raman scattering from H^- local modes in hydrogenic rare-earth ion sites. The measured frequencies of 922 and 939 cm^{-1} correspond to those measured in the laser excitation studies (Chapter V). At the resolution used to record the spectra in Figure VI.2.6 the x,y splitting of the degenerate transverse local mode (Chapter VII) is not resolved.

Bleaching of the $C_s(2)$ Centre

The $C_s(2)$ centre has some peculiar bleaching properties which will now be described. Excitation of the Pr^{3+} ion from the Z_1 crystal field level induces the familiar reversible polarised bleaching, however the bleaching when exciting from the Z_2 level is non-reversible. Figure VI.2.7 shows a series of bleaching curves for excitation from the Z_1 and Z_2 crystal field levels for the $C_s(2)$ D^- site. In both cases the bleaching was initiated in a new piece of crystal that had not been previously irradiated. For excitation from the Z_1 level the extent of recovery is observed to drop dramatically so that after only four cycles the recoverable fluorescence is less than half that initially recorded. As will be shown in the next section this decay is associated with a second bleaching mechanism where a photoproduct with a different excitation frequency is formed.

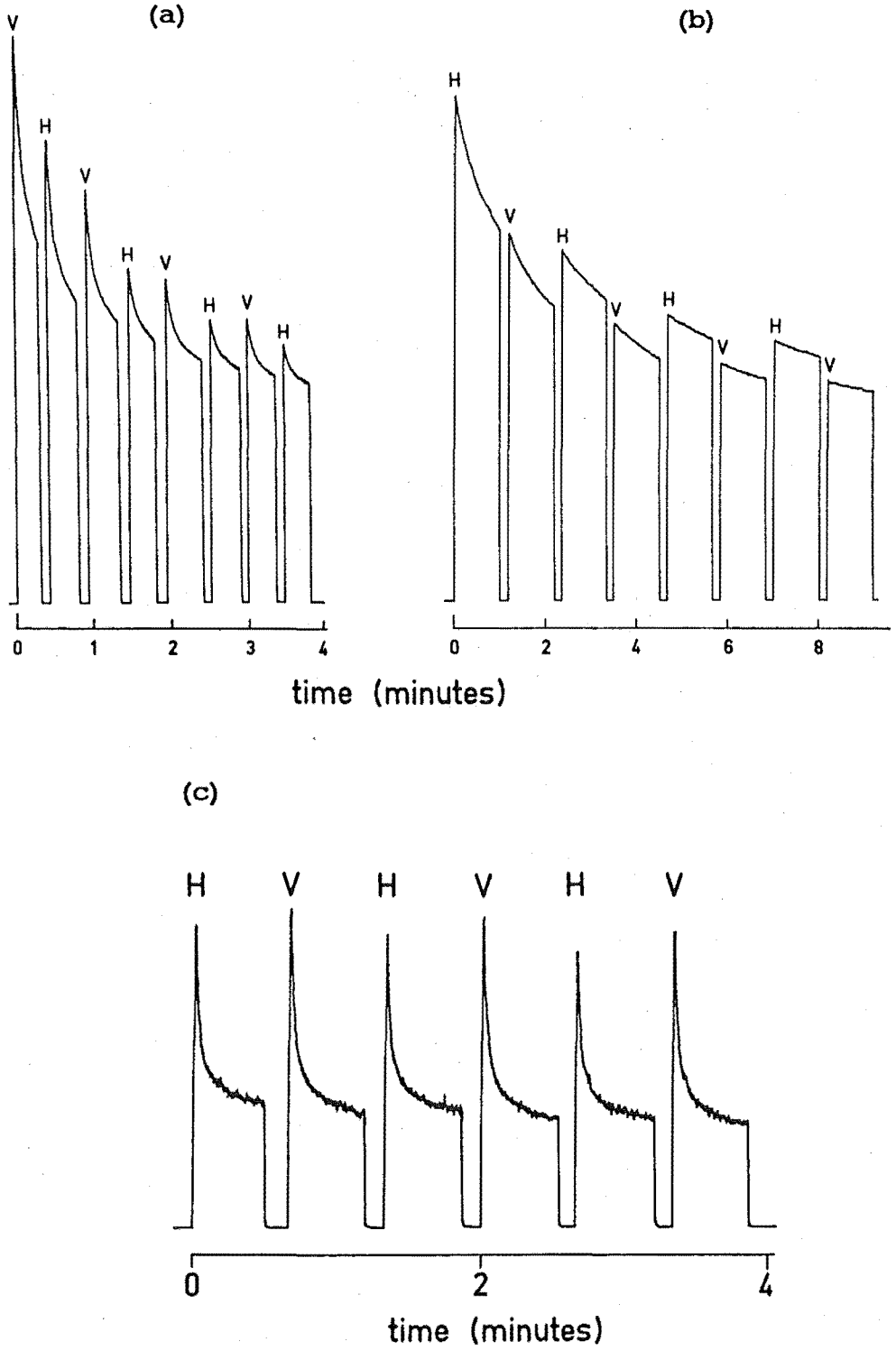

Figure VI.2.7 Sequences of bleaching curves for excitation of the $C_s(2)$ centre in a <100> oriented $SrF_2:Pr^{3+}:D^-$ crystal using the two orthogonal laser polarisations V[001] and H[010].

(a) with the laser tuned to the $Z_1 \rightarrow D_1$ transition the bleaching is reversible and shows a decay associated with photoproduct formation, (b) the bleaching is non-reversible when tuned to the $Z_2 \rightarrow D_1$ transition and (c) after 30 minutes of bleaching the $Z_1 \rightarrow D_1$ transition the centre shows excellent recovery levels for reversible bleaching.

After many such bleaching cycles the curves show a similar pattern to the $C_s(1)$ centre with recovery levels better than 95% (Fig. VI.2.7(c)). When excited from Z_2 this centre shows non-reversible bleaching characteristics (Fig. VI.2.7(b)). The different characters for the bleaching when the ion is excited from the Z_1 or Z_2 level is particularly interesting as it shows that the division between reversible and non-reversible sites is not always obvious. Recall from the discussion in the introduction that reversible polarised bleaching originates from the selective excitation of a subset of all the centres that are distinguished by the orientations of their principle C_4 axis. Non-reversible bleaching was described as a migration of the ions so as to completely remove the centre from resonance with the laser in either polarisation.

In the non-reversible bleaching observed for excitation from the Z_2 level of the $C_s(2)$ centre it seems unlikely that the only ion migration occuring is that which forms an inequivalent photoproduct given the excellent reversibility of the Z_1 level. The most probable mechanism has sites in all three orientations of the C_4 axis being equivalently excited so that there is no net transfer of population between orientations and the bleaching arises only from photoproduct formation. This situation could arise if the excitation transition from Z_2 has very well defined selection rules in C_3 rather than C_4 symmetry. A rare-earth ion at the centre of a lattice cube has a three fold rotation axis in the [111] crystallographic direction. Then in a <100> oriented crystal where all three orientations of the C_4 axis are equivalently aligned to the [111] direction, a transition exhibiting well defined C_3 symmetry will exhibit no polarisation dependence.

It was established from the vibronic spectra that at least one substitutional hydrogenic ion resides in the first coordination shell.

This ion may be the origin of the C_3 symmetry but since it is replacing an F^- ion of the same charge its influence is expected to be small. Other perturbations may arise from the presence of more ions in the centre than at first realised. An extra local mode vibronic line, one more than the six expected for two hydrogenic ions, was observed and could correspond to a third hydrogenic ion.

The non-reversibility of the site when pumping from the Z_2 level suggests a few points that need further investigation. Since the decay has no reversible component, the observed bleaching solely represents the rate of photoproduct centre production. Analysis of the bleaching curve under various excitation conditions may yield information on the ionic motion and the form of the photoproduct. Also the bleaching curve for excitation from Z_1 shows that not all the site is converted to the photoproduct and a subset remains in resonance with the laser to undergo reversible bleaching (Figure VI.2.7). Then the hypothesis discussed for the Z_2 excitation case would have the fluorescence reaching a steady state level once the photoproduct was formed which can be easily tested experimentally.

Excitation of the $C_s(2)$ Centre

The $C_s(2)$ centre was observed to undergo anomalous bleaching behaviour with two saturation mechanisms apparent. One mechanism is associated with the production of a new photoproduct centre. Figure VI.2.8 shows excitation spectra of the $C_s(2)$ D^- site after various bleaching experiments. In all cases the lines were probed at a low laser power to avoid inducing additional bleaching. Figure VI.2.8(a) shows the excitation lines of the $Z_1 \longrightarrow D_1$ and $Z_2 \longrightarrow D_1$ transitions before any bleaching has been induced. The strong line near 16670 cm^{-1} is the $C_s(4)$ rhombic centre that will be discussed in the next section and the small line is a further centre, that has yet to be examined.

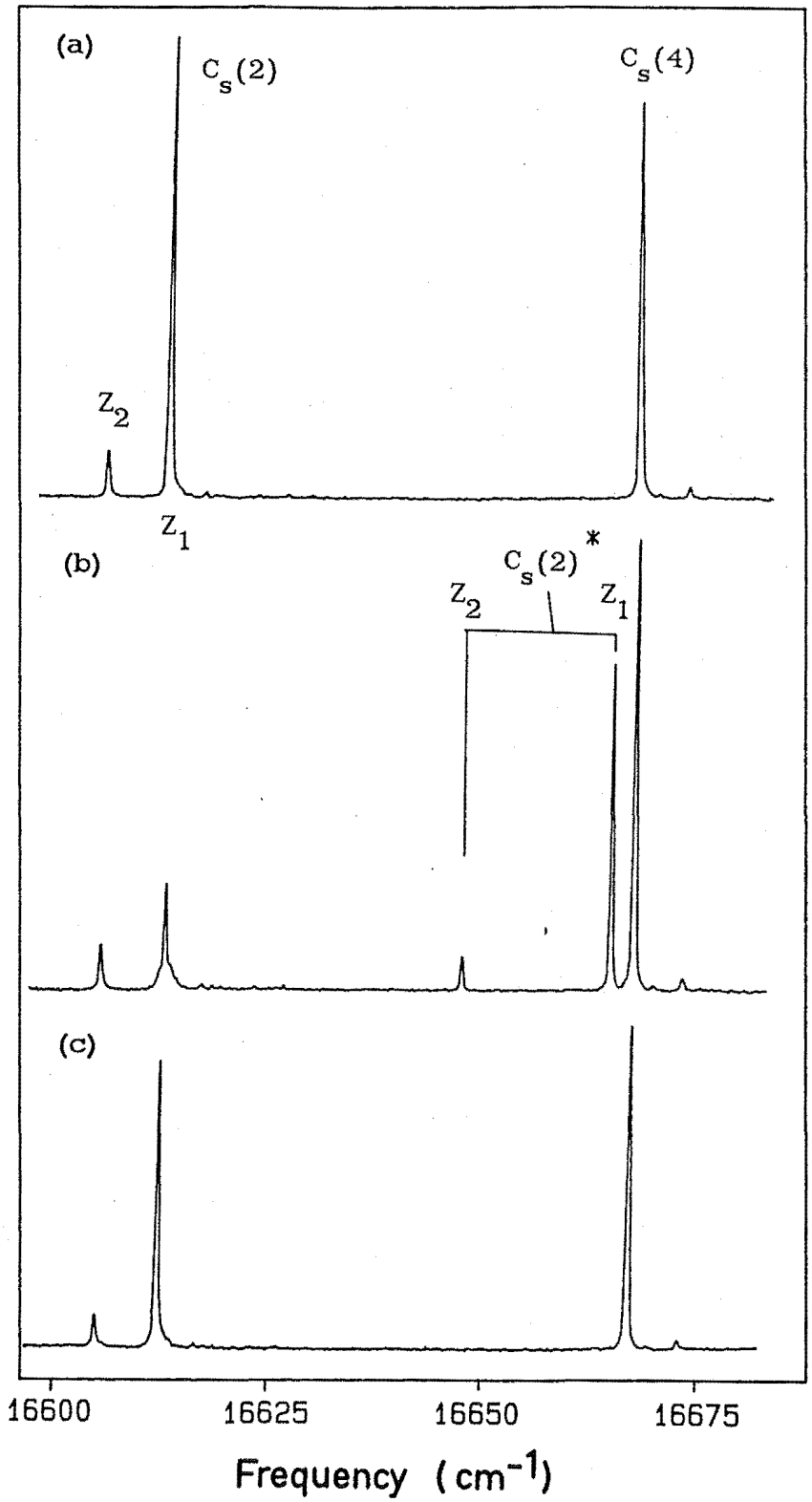

Figure VI.2.8 14K laser excitation spectra of the $C_s(2)$ centre in $SrF_2:Pr^{3+}:D^-$.

(a) before bleaching,

(b) after bleaching for several minutes at 50mW laser power a photoproduct $C_s(2)^*$ is produced at 16664.3 cm^{-1},

(c) subsequent bleaching of $C_s(2)^*$ restores almost all the lost intensity of the $C_s(2)$ centre.

After bleaching the $Z_1 \longrightarrow D_1$ transitions for several minutes at 50 mW laser power the spectrum shown in (b) was obtained. A photoproduct centre, labelled $C_s(2)^*$, has appeared absorbing at 16664.3 cm^{-1}. The second new line is the $Z_2 \longrightarrow D_1$ transition of the photoproduct centre $C_s(2)^*$. Subsequent irradiation of $C_s(2)^*$ at 16664.3 cm^{-1} completely bleaches the photoproduct and restores almost all the lost intensity of the $C_s(2)$ centre (Figure VI.2.8(c)). No other line appears indicating the ion migration between $C_s(2)$ and $C_s(2)^*$ is completely reversible and any model for the site configurations must take this into consideration.

An attempt to record the $^1D_2 \longrightarrow {}^3H_4$ emission spectrum of the $C_s(2)^*$ centre met with no success. For the parent rhombic centres some residual fluorescence remains after bleaching and the spectrum can be recorded, however for the photoproduct centres there is complete bleaching and the fluorescence drops to zero very quickly.

Another noticable point in Figure VI.2.8 is that the $Z_2 \longrightarrow D_1$ transition undergoes very little change during these bleaching cycles. This is a further manifestation of the very different bleaching characteristics of these two levels discussed earlier. The difference is so dramatic that initially this transition was considered to belong to another centre but was subsequently found to give an identical emission spectrum.

VI.2.3 The $C_s(4)$ Centre

The $C_s(4)$ centre is another member of the multiple hydrogenic ion sites that exhibits bleaching properties. In a <100> oriented crystal the fluorescence has a non-reversing character between the V[001] and H[010] laser polarisations when the Pr^{3+} ion of the site is excited from the Z_1 crystal field level, the only level that was tested. Figure VI.2.9(a) shows the fluorescence intensity recorded at 14 K for

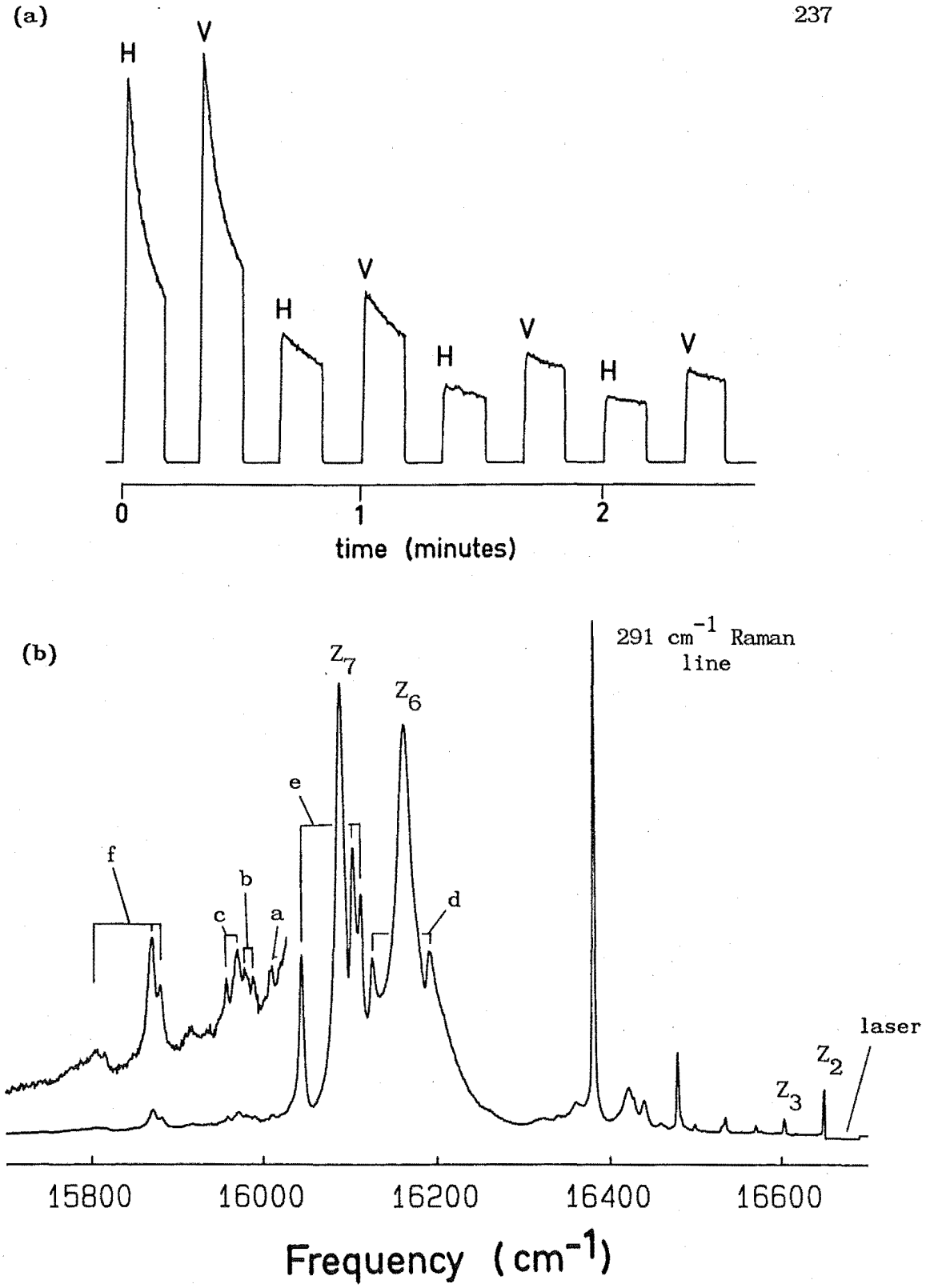

Figure VI.2.9 (a) Bleaching curves in a <100> oriented crystal and (b) $^1D_2 \rightarrow {}^3H_4$ emission from the $C_s(4)$ centre in $SrF_2:Pr^{3+}:D^-$.

a sequence of laser polarisations for the $C_s(4)$ D^- site. The decay is very fast and is probably instrument limited during the initial period. Based on the experience with the $C_s(2)$ site this decay would suggest photoproduct formation which is indeed observed.

The $^1D_2 \longrightarrow {}^3H_4$ emission spectrum is shown in Figure VI.2.9(b) for the $C_s(4)$ D^- site recorded at 14 K. The emission from the corresponding H^- and T^- sites was monitored but is not included here as complete spectra were not generally recorded due to the poor fluorescence levels. The spectral data for the sites are summarised in Table VI.2.3.

Table VI.2.3

Spectral data for the hydrogenic $C_s(4)$ site in $SrF_2:Pr^{3+}$ crystals

Site	$C_s(4)$ H^-	$C_s(4)$ D^-	$C_s(4)$ T^-
$Z_1 \longrightarrow D_1$ transition and Z_1-Z_2 splitting ($\pm$ 0.1 cm^{-1})	16665.9 -	16667.0 9±1	16667.6
Other Pr^{3+} ion electronic energy levels ($\pm$ 1 cm^{-1})	- 515 578	68 508 582	66 513 585
Interstitial ion local mode vibration intervals ($\pm$ 1 cm^{-1}) a b c	[1]	659 681 699	539
Substitutional ion local mode vibration intervals ($\pm$ 1 cm^{-1}) d e f	[1]	479 558 789	411 456 648
$Z_1 \longrightarrow {}^3P_0$ transition ($\pm$ 0.01 nm)	483.58	483.77	-
Photoproduct $Z_1 \longrightarrow D_1$ transition and Z_1Z_2 splitting ($\pm$0.1cm^{-1})	-	16676.5 11.7	-

[1] Sensitivity not sufficient to measure H^- local mode vibronic intervals.

Up to five Pr^{3+} electronic levels have been identified from transitions in the spectra, but as Figure VI.2.9(b) shows there are many lines yet to be assigned. The difficulty arises as the H^- and T^- sites do not provide a sufficiently clean spectrum to be able to make comparisons between any but the strongest transitions. The $Z_1 - Z_2$ splitting has been measured only for the D^- site.

In a similar manner to the $C_s(1)$ and $C_s(2)$ sites a substitutional hydrogenic ion can be inferred from three local mode vibronic lines at intervals of 479, 558 and 789 cm^{-1} for the D^- site. These frequencies

average to 609 cm^{-1} which is further away from the isolated T_d frequency of 642 cm^{-1} than for the other two C_s sites. If the local mode frequencies of the substitutional ion are compared between the three sites a trend emerges. A high frequency vibration is apparent for all three sites and this is balanced by one of a low frequency for the $C_s(2)$ and $C_s(4)$ sites. However it is not clear whether this low frequency local mode vibration originates from the same ion. Between these extremes are two modes having a similar frequency. Apart from the high frequency mode the energies of these vibrations do not change much between sites indicating that the substitutional ion experiences a similar environment in all three cases. Thus any configurations for these sites must require the substitutional ions to reside in positions of similar symmetry.

The situation regarding the interstitial hydrogenic ion is more complicated than for the other C_s sites with many lines being observed in the appropriate region. Although some order has been obtained and frequencies determined for one ion (Table VI.2.3) it was necessary to assign lines to local mode phonons coupled to several low lying Z levels. This was not required for the other sites, where three lines were observed to be dominant, and may hide the fact that a second interstitial ion is present in the centre.

Excitation Spectra of the $C_s(4)$ Centre

The rapid, non-reversible decay of the $C_s(4)$ fluorescence is an indication that photoproduct formation plays a dominant role in the bleaching of this centre. An excitation spectrum recorded after bleaching of the centre shows that photoproducts are formed by the appearance of two extra lines in the spectrum.

Figure VI.2.10 shows series of excitation spectra recorded at 14 K for the $C_s(4)$ D^- centre. A laser power of 2 mW was used in the probe beam to avoid redistributing the displaced site populations. In Figure VI.2.10(a) the $Z_1 \longrightarrow D_1$ transition of this centre is shown before any irradiation of the crystal. Although the Z_2 level at 9 ± 1 cm^{-1} should be thermally populated at the temperature of 14 K, there is no visible $Z_2 \longrightarrow D_1$ transition. The two small lines at 16672.7 cm^{-1} and 16669.4 cm^{-1} are as yet uncharacterised centres that also exhibit bleaching properties.

After bleaching the $Z_1 \longrightarrow D_1$ transition of $C_s(4)$ for 2 minutes at 50 mW laser power the excitation spectrum revealed two new photoproduct lines labelled P_1 and P_2, at 16676.5 and 16664.8 cm^{-1} respectively (Figure VI.2.10(b)). The lower energy line of this pair, P_2, almost exactly coincides with the photoproduct of the $C_s(2)$ centre at 16664.3 cm^{-1}, but is a separate entity as it can be observed as a sideline to $C_s(2)^*$ in an excitation spectrum containing both photoproducts. Some of the lost intensity in $C_s(4)$ is restored on bleaching the photoproduct P_1 (Figure VI.2.10(c)). Note that the photoproducts P_1 and P_2 are not independent as the intensity of P_2 has dropped in this spectrum. This result can be explained if P_1 and P_2 are the Z_1 and Z_2 transitions of a single photoproduct centre. The separation of 11.7 cm^{-1} is sufficiently small for the Z_2 level to be populated at this temperature although for this explanation the $Z_2 \longrightarrow D_1$ and $Z_1 \longrightarrow D_1$ transition probabilities must be sufficiently

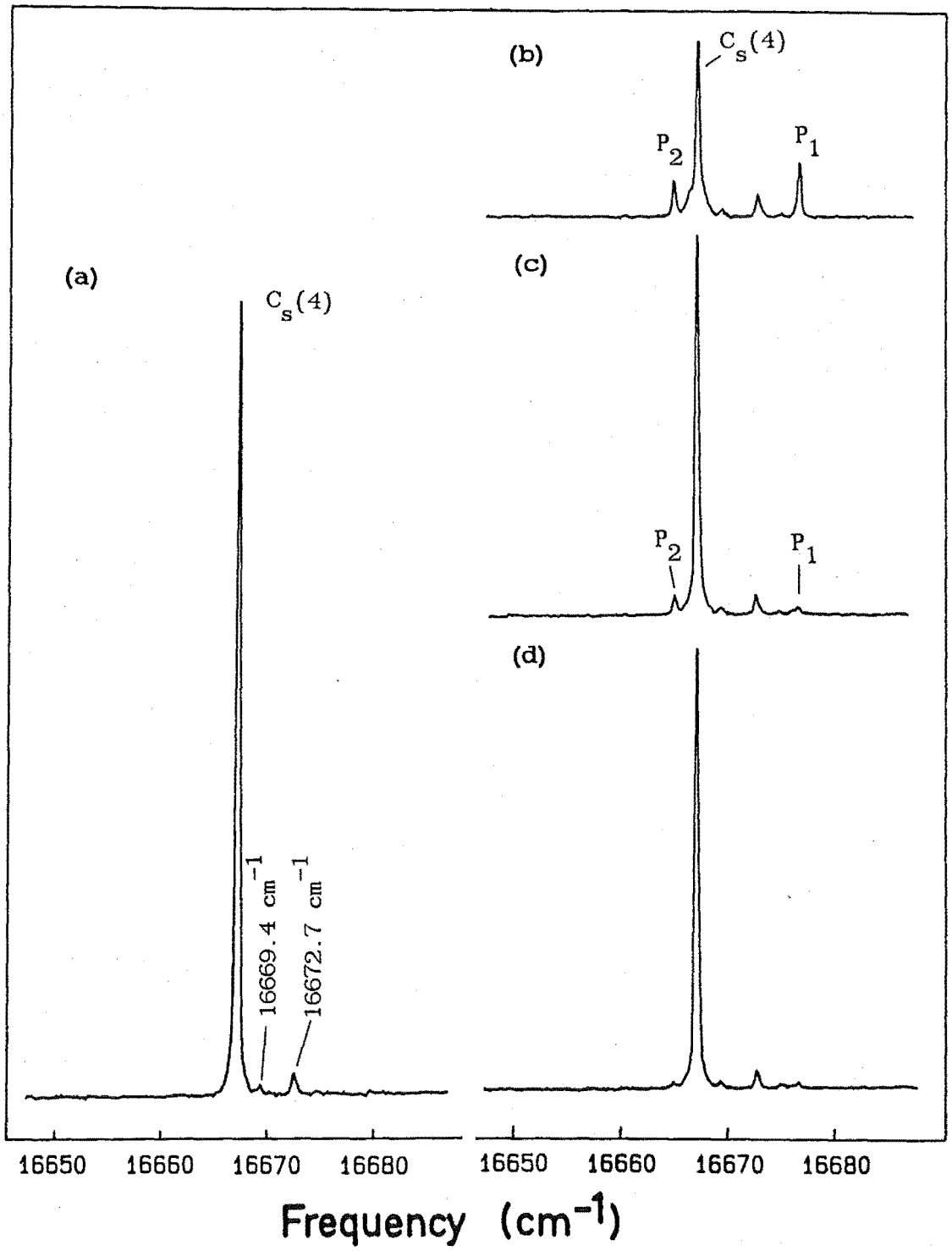

Figure VI.2.10 Laser excitation, at 14K, of the $C_s(4)$ centre in a $SrF_2:Pr^{3+}:D^-$ crystal.

(a) before bleaching,

(b) after bleaching $C_s(4)$ for 2 minutes at 50mW laser power photoproduct lines P_1 and P_2 appear,

(c) bleaching of P_1 restores some of the lost intensity to $C_s(4)$,

(d) subsequent bleaching of P_2 continues to restore intensity to $C_s(4)$.

different to explain their almost equal intensities. If P_2 is not the Z_2 level of the photoproduct P_1 then the almost coincident frequencies of the $C_s(2)^*$ and P_2 lines would suggest that these two sites were closely related even to the point where interconversion might be expected between them. If this was the case then some doubt would arise as to the independence of their parent sites, the $C_s(2)$ and $C_s(4)$ centres. As no obvious interconversion is observed between any centres other than with their photoproducts it is most likely that P_2 is the Z_2 level of the single photoproduct centre P_1. This conclusion is supported in Figure VI.2.10(d) where bleaching of the P_2 line has added only to the $C_s(4)$ intensity rather than to P_1 as well, which would be expected if P_1 and P_2 were discrete centres.

VI.2.4 The $C_s(3)$ Centre

The spectroscopy of the $C_s(3)$ centre indicates that this site contains more hydrogenic ions than the three C_s sites discussed earlier. Multiple local mode vibronics, both substitutional and interstitial are observed in the emission spectrum. Unfortunately the emission from this site is weak making it difficult to record spectra from the H^- and T^- sites. For this reason some doubt exists with the identification of levels and the total number of vibronics. However, using the measured $Z_1:Z_2:Z_3$ electronic level splitting of 0:16:40 cm^{-1} a tentative assignment has been made that has nine local mode vibrations. This would require that at least three hydrogenic ions would constitute this site. Table VI.2.4 summarises the spectral data for the $C_s(3)$ site while Figure VI.2.11(b) shows the $^1D_2 \longrightarrow {}^3H_4$ emission spectrum for the $C_s(3)$ D^- site recorded at 14 K.

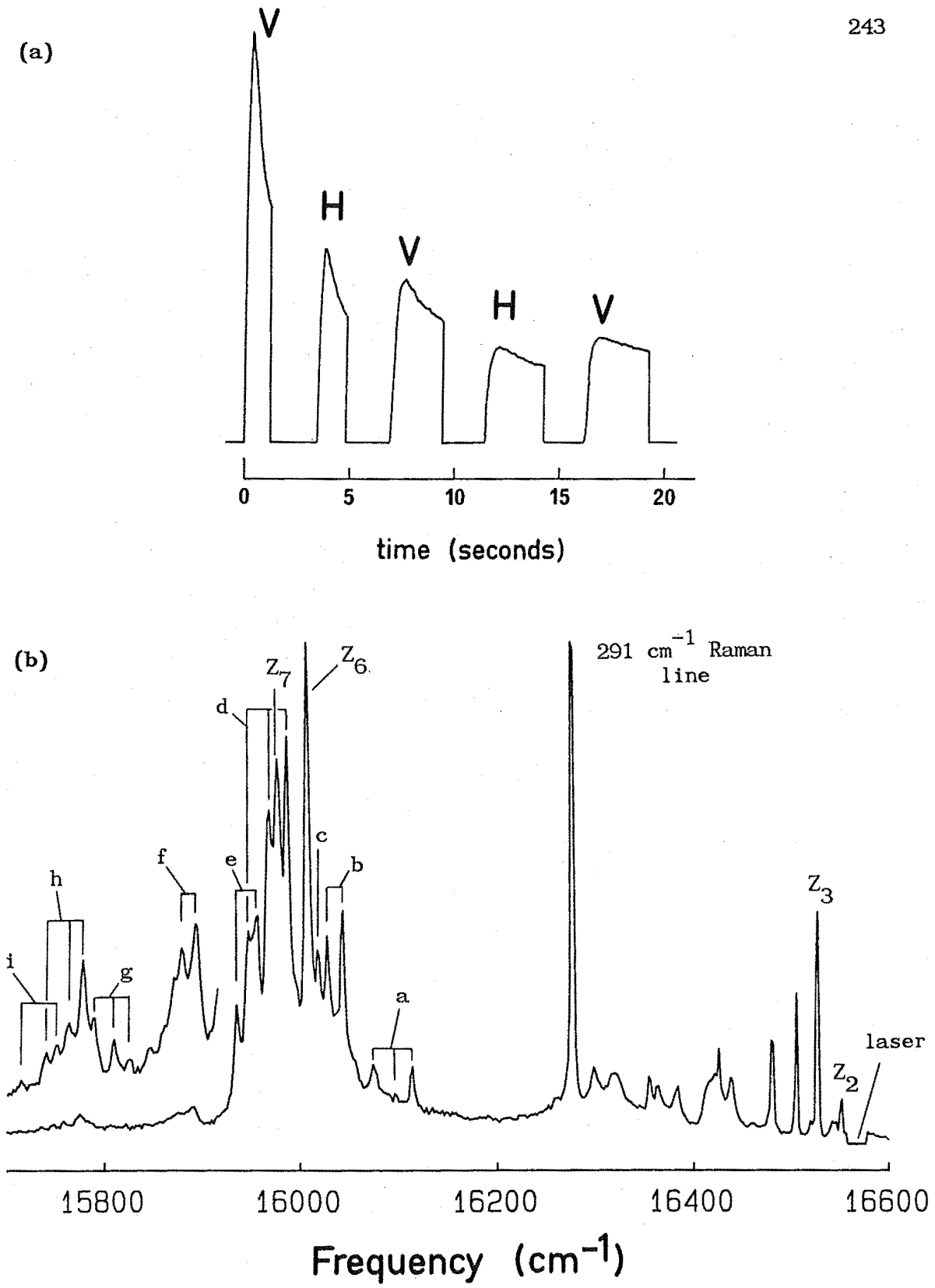

Figure VI.2.11 (a) Bleaching curves in a <100> oriented crystal and (b) $^1D_2 \rightarrow {}^3H_4$ emission at 14K, for the $C_s(3)$ centre in $SrF_2:Pr^{3+}:D^-$.

Table VI.2.4

Spectral data for the hydrogenic $C_s(3)$ site in $SrF_2:Pr^{3+}$

Site	$C_s(3)$ D^-	$C_s(3)$ H^-
$Z_1 \rightarrow D_1$ transition	16566.5 [1]	16564.8
and Z_1-Z_2 splitting ($\pm$ 0.1 cm^{-1})	16±2	
Other Pr^{3+} ion electronic energy levels ($\pm$ 2 cm^{-1})	40 558 590	43 573 597
$Z_1 \rightarrow {}^3P_0$ transition ($\pm$ 0.01 nm)	487.99	487.90
Photoproduct Centre $Z_1 \rightarrow D_1$ transition	16568.7	-
Z_1-Z_2 splitting ($\pm$ 0.1 cm^{-1})	13.6	

Parent Electronic Transition	Local Mode	D^- ion Vibronic Interval ($\pm$2 cm^{-1})
$D_1 \rightarrow Z_1$		454
$D_1 \rightarrow Z_2$	a	454
$D_1 \rightarrow Z_3$		452
$D_1 \rightarrow Z_1$	b	524
$D_1 \rightarrow Z_2$		522
$D_1 \rightarrow Z_1$	c	458
$D_1 \rightarrow Z_1$		580
$D_1 \rightarrow Z_2$	d	582
$D_1 \rightarrow Z_3$		580
$D_1 \rightarrow Z_1$	e	610
$D_1 \rightarrow Z_2$		614

Table VI.2.4 continued next page....

Table VI.2.4 continued....

$D_1 \rightarrow Z_1$	f	676
$D_1 \rightarrow Z_2$		674
$D_1 \rightarrow Z_1$		744
$D_1 \rightarrow Z_2$	g	744
$D_1 \rightarrow Z_3$		740
$D_1 \rightarrow Z_1$		792
$D_1 \rightarrow Z_2$	h	790
$D_1 \rightarrow Z_3$		790
$D_1 \rightarrow Z_1$	i	819
$D_1 \rightarrow Z_3$		816

[1] $Z_1 \rightarrow D_1$ transition for the $C_s(3)$ T^- site measured as 16566.9 cm^{-1}.

Like the other centres of this type the $C_s(3)$ centre exhibits bleaching of its fluorescence which shows a non-reversible character between the two laser polarisations in a <100> oriented crystal (Figure VI.2.11(a)). The bleaching time is very fast being only a few seconds for the D^- site. The non-recoverable decay suggests photoproduct formation which was subsequently observed in the excitation spectrum.

The $Z_1 \rightarrow {}^3P_0$ transition wavelength for this centre is very close to the 488.0 nm line of the argon ion laser and for the D^- analogue appears to be coincident (Chapter IV). For this site the $^3P_0$ level of the Pr^{3+} ion could be excited with this laser line although when excited in this way no fluorescence is observed from the $^3P_0$ level. The hydrogenic ions of the centre provide an efficient non-radiative relaxation path to the lower $^1D_2$ multiplet. Creation of their high frequency local mode vibrations lowers the order of the multiphonon

decay process and substantially increases the probability of non-radiative decay. Further discussion on the influence of local mode phonons in the decay of RE^{3+}-hydrogenic sites is presented in Chapter VIII.

Excitation Spectra of the $C_s(3)$ Centre

An excitation spectrum recorded before and after bleaching the $C_s(3)$ centre confirms the observation from the decay curves that photoproduct formation is the dominant bleaching mechanism. Figure VI.2.12 shows a series of excitation spectra of the $C_s(3)'$ D^- centre recorded at 14 K using a laser power of 2 mW in the probe beam. Before bleaching the main $Z_1 \longrightarrow D_1$ transition and a weak $Z_2 \longrightarrow D_1$ transition 16 cm^{-1} lower in energy are visible in the spectrum (Figure VI.2.12(a)). The spectrum shown in (b) was recorded after bleaching the $Z_1 \longrightarrow D_1$ $C_s(3)$ transition for 2 minutes at a laser power of 50 mW. Two photoproduct lines have appeared at 16568.7 and 16555.1 cm^{-1}. Bleaching the first of these two lines restores a substantial amount of the lost intensity of the $C_s(3)$ $Z_1 \longrightarrow D_1$ line (Figure VI.2.12(c)). The lower energy photoproduct line has also been bleached indicating this line is the $Z_2 \longrightarrow D_1$ transition of the photoproduct. In a similar way to the other C_s centres exhibiting photoproducts the return mechanism is very selective and no other lines appear.

VI.3 Optical Spectroscopy of the Rhombic Centres in Hydrogenated $CaF_2:Pr^{3+}$

Three centres containing multiple hydrogenic ions were studied in $CaF_2:Pr^{3+}$. Although not examined to the same extent as the $SrF_2:Pr^{3+}$ centres some correlations can be made about the site configurations and bleaching characteristics. The excitation spectra were not recorded for the $CaF_2:Pr^{3+}$ centres and while photoproduct centres are expected their transition frequencies and bleaching properties have

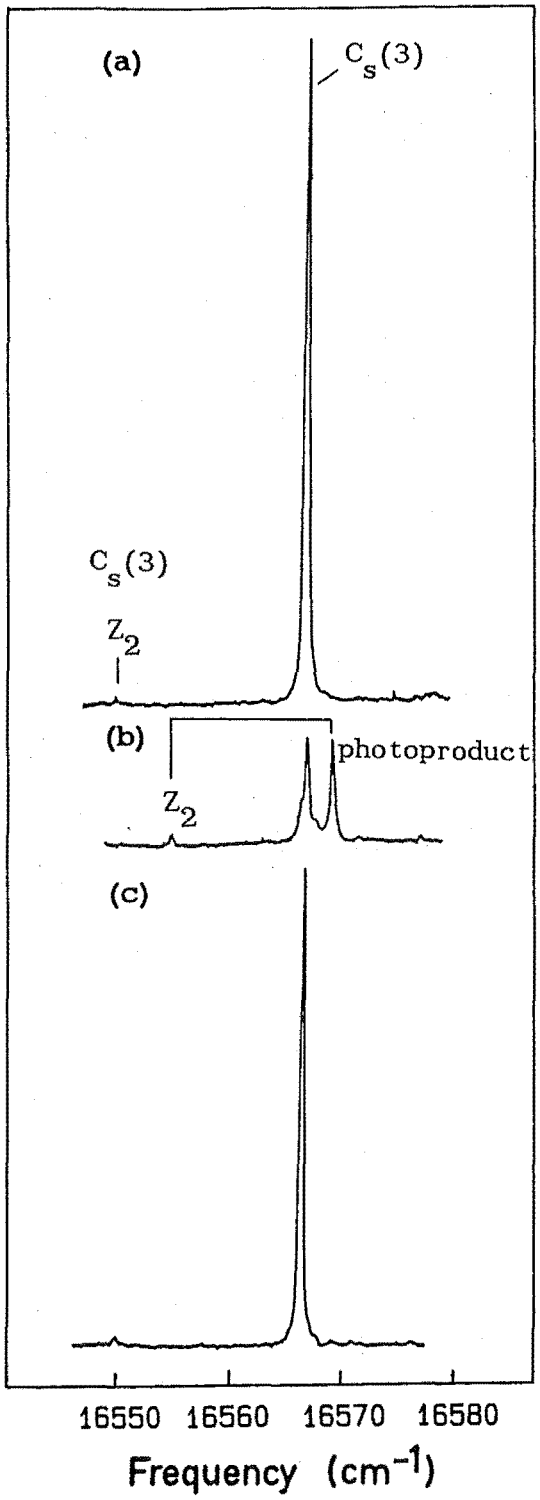

Figure VI.2.12 Laser excitation at 14K of the $C_s(3)$ centre in $SrF_2:Pr^{3+}:D^-$.

(a) before bleaching,

(b) after bleaching $C_s(3)$ for 2 minutes at 50mW laser power a photoproduct centre at 16568.7cm^{-1} is produced.

(c) Irradiation of the photoproduct substantially restores the lost intensity in the $C_s(3)$ centre.

yet to be observed. The centres studied will now be discussed on an individual basis.

VI.3.1 The $C_s(1)$ Centre

The $C_s(1)$ centre in $CaF_2:Pr^{3+}$ exhibits reversible polarised bleaching in a <100> oriented crystal and appears to be the analogue of the $C_s(1)$ centre in $SrF_2:Pr^{3+}$. Both these sites form the dominant centre of the multiple hydrogenic ion type. The bleaching decay time for the two $C_s(1)$ centres is also similar, both having a characteristic time of about 30 secs for the D^- centres with 100 mW of laser power. The recovery level is better than 90% during the reversible bleaching and based on the results from the $SrF_2:Pr^{3+}$ centres this would indicate that the dominant bleaching mechanism involves the formation of equivalent centres oriented at 90^o. Figure VI.3.1 shows a sequence of bleaching curves for the $C_s(1)$ D^- site in a <100> oriented crystal.

The $^1D_2 \longrightarrow {}^3H_4$ emission spectrum was recorded at 14 K and is shown in Figure VI.3.2 for the H^-, D^- and T^- varieties of this site. The spectral data are summarised in Table VI.3.1.

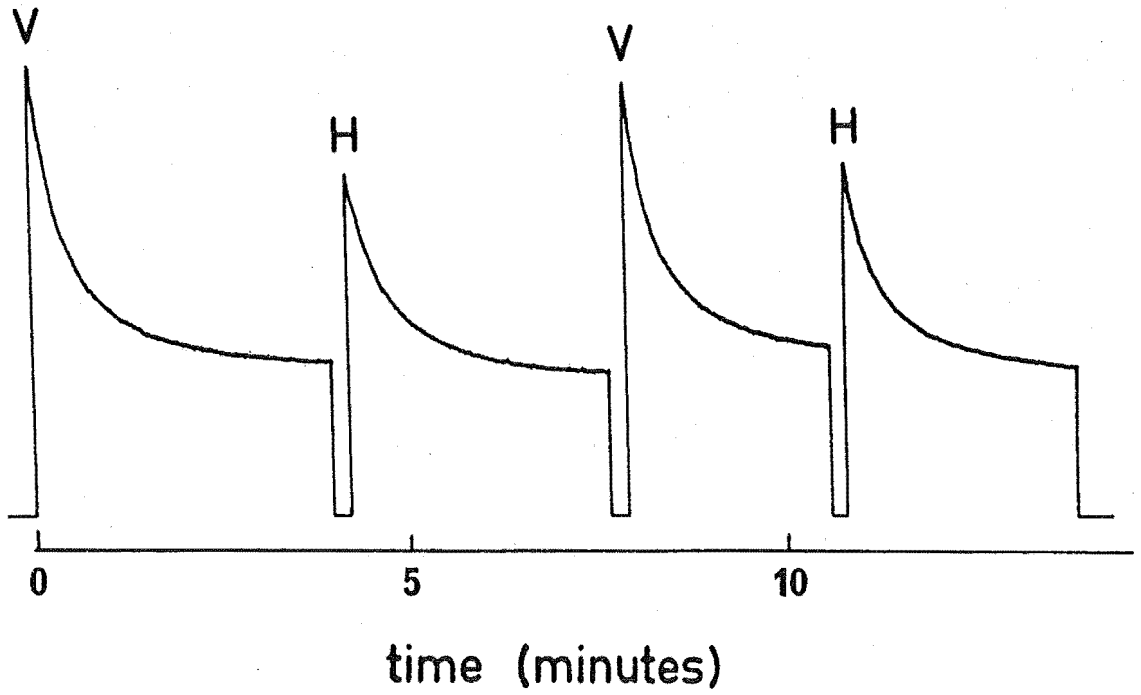

Figure VI.3.1 Fluorescence intensity at 14K for a sequence of laser excitations of the $C_s(1)$ centre in a <100> oriented $CaF_2:Pr^{3+}:D^-$ crystal using the orthogonal V[001] and H[010] laser polarisations.

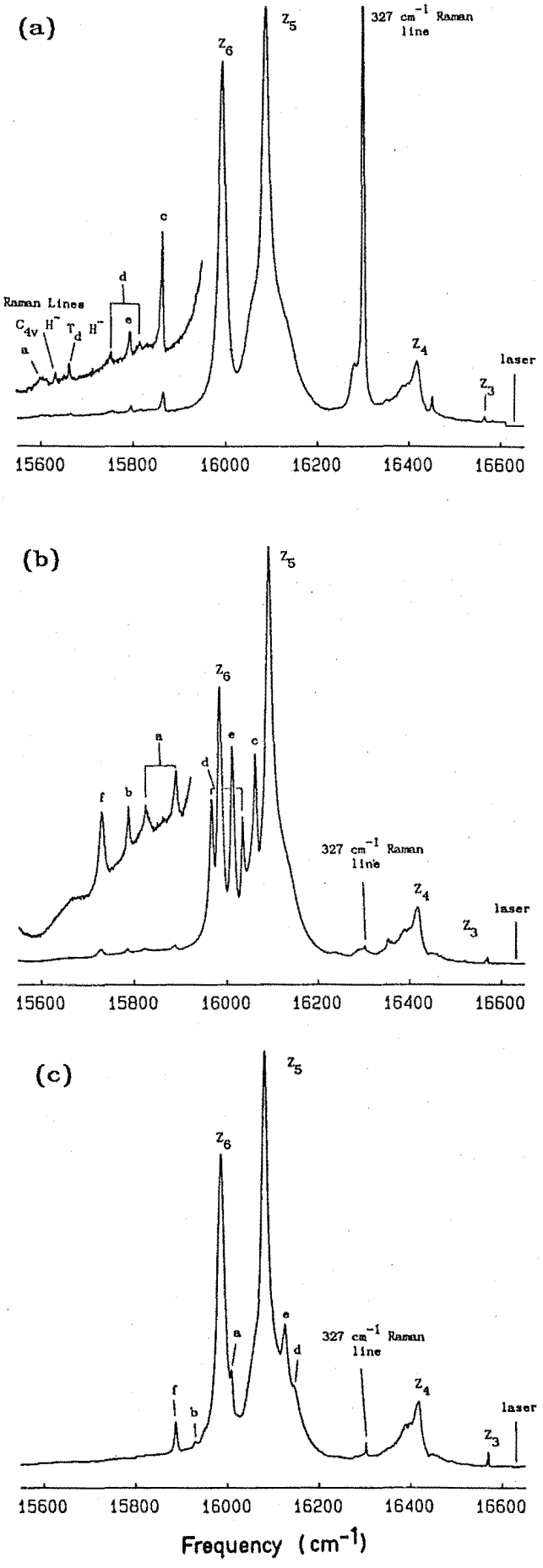

Figure VI.3.2 14K $^1D_2 \rightarrow {}^3H_4$ emission spectra for the (a) H^-, (b) D^- and (c) T^- $C_s(1)$ centres in $CaF_2:Pr^{3+}$ crystals.

Table VI.3.1

Spectral data for the hydrogenic $C_s(1)$ site in $C_aF_2:Pr^{3+}$

Site		$C_s(1)$ H^-	$C_s(1)$ D^-	$C_s(1)$ T^-
$Z_1 \longrightarrow D_1$ transition and Z_1-Z_2 splitting ($\pm$ 0.1 cm^{-1})		16625.2	16624.9 $\leq$ 2	16625.3
Other Pr^{3+} ion electronic energy levels ($\pm$ 1 cm^{-1})	Z_3	64	62	62
	Z_4	212	212	213
	Z_5	542	536	547
	Z_6	636	644	642
Interstitial ion local mode vibration intervals ($\pm$ 1 cm^{-1})	a	1027	743	621
	b	1174	844	701
Substitutional ion local mode vibration intervals ($\pm$ 1 cm^{-1})	c	765	568	-
	d	814	596	486
	e	834	618	504
	f	-	901	742

Six electronic levels are identified from transitions in Figure VI.3.2 and following the $SrF_2:Pr^{3+}$ centres large isotope shifts are apparent in some cases. For the D^- ion site, nearby local mode vibronic lines perturb the electronic levels out of the expected H^-: D^-: T^- sequence. The Z_2 level has not been measured accurately but is estimated to be $\leq$2 cm^{-1} from the absorption spectrum.

Parallel reasoning to that used in the previous section infers that a charge compensating interstitial ion and a nearby substitutional ion are principal constituents of this centre. The vibronics for the D^- centre will be discussed as being representative. Three strong local mode vibronic lines at intervals of 568, 596 and 618 cm^{-1} and a fourth at an interval of 901 cm^{-1} are assigned to the vibrations of a substitutional hydrogenic ion in the first coordination shell.

The two interstitial ion frequencies measured are 743 and 844 cm^{-1} for the D^- site. These are shifted further from the C_{4v} site frequencies of 723 and 808 cm^{-1} than was observed for the $C_s(1)$ centre of $SrF_2:Pr^{3+}$. The measured frequencies of 1027 and 1174 cm^{-1} for the H^- centre correspond to the local mode frequencies measured by infrared absorption for the B site of $CaF_2:Pr^{3+}:H^-$ (Cockroft et al [1987b]). In that work results were presented that correlated the infrared B site of $CaF_2:Er^{3+}:H^-$ to the R site of the optical spectra which was observed as a rhombic symmetry site by EPR (Edgar, Jones and Presland [1979]). The same correlation can be made here as the $C_s(1)$ and B sites have the same local mode frequencies. Thus the R site of the Er^{3+} crystal and the $C_s(1)$ centre in both $CaF_2:Pr^{3+}$ and $SrF_2:Pr^{3+}$ appear to correspond to the same site.

VI.3.2 The $C_s(2)$ Centre of $CaF_2:Pr^{3+}$

The $C_s(2)$ hydrogenic centre in $CaF_2:Pr^{3+}$ also exhibits reversible polarised bleaching in a <100> oriented crystal however the extent of recovery between cycles is not as great as it was for the $C_s(1)$ centre (Figure VI.3.3(a)). From the experience with the $SrF_2:Pr^{3+}$ centres this would suggest that photoproduct formation as well as site reorientation is determining the bleaching. The $Z_1 - Z_2$ splitting was measured to be 10 cm^{-1} for the D^- site and is apparent as the interval between pairs of local mode vibronic levels. Figure VI.3.3(b) depicts the $^1D_2 \longrightarrow {}^3H_4$ emission for the D^- centre recorded at 14 K. The H^- and T^- sites were studied but their spectra are not included here as they were not always scanned continuously. The spectral data for this site are summarised in Table VI.3.2.

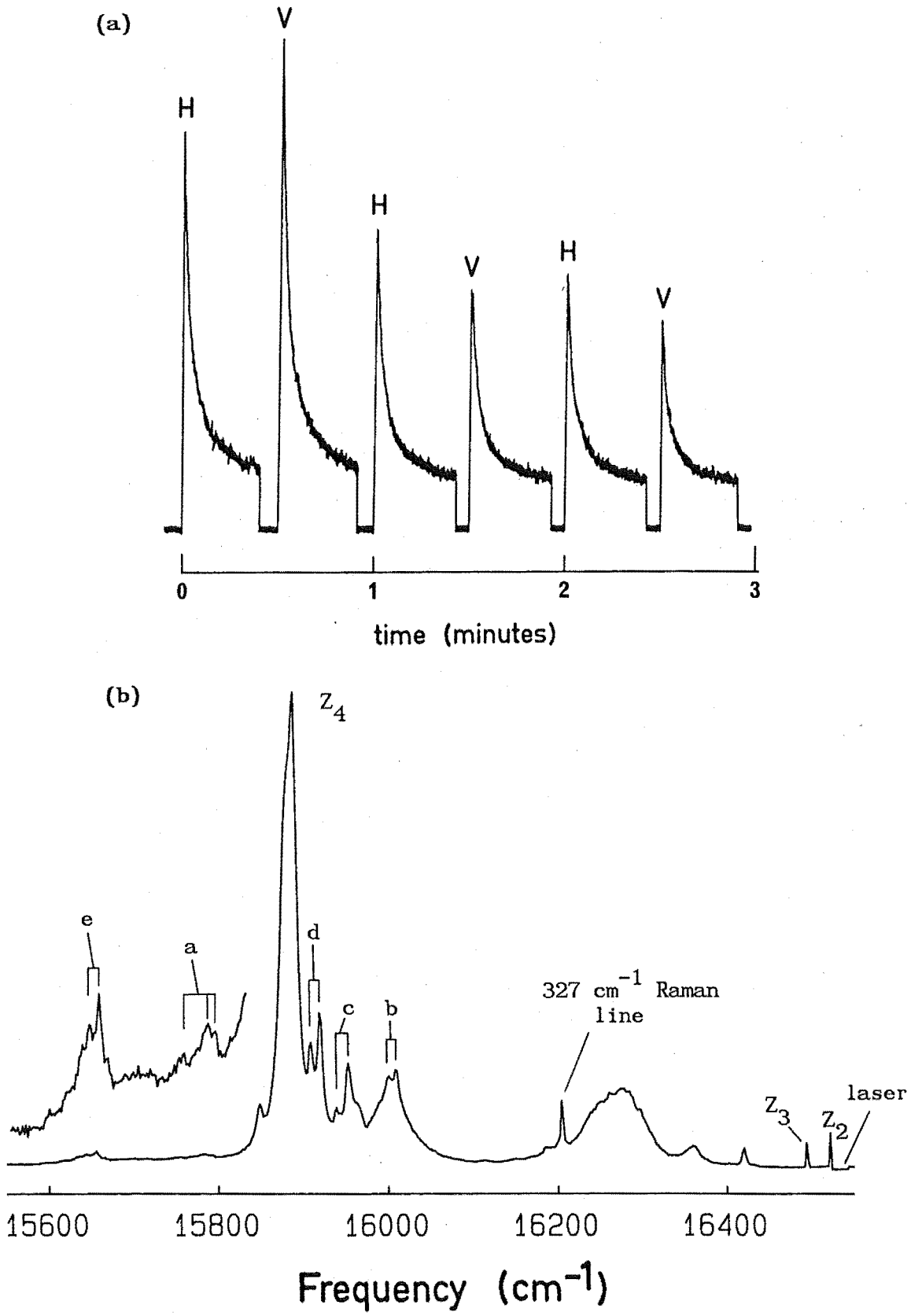

Figure VI.3.3 (a) Bleaching curves in a <100> oriented crystal and (b) $^1D_2 \rightarrow {}^3H_4$ emission at 14K for the $C_s(2)$ centre in $CaF_2:Pr^{3+}:D^-$.

Local mode vibronic transitions can be identified by their isotopic shift and again indicate that a substitutional and an interstitial hydrogenic ion are contained in this centre. The limited number of vibronic lines in the $C_s(1)$ and $C_s(2)$ spectra indicate that these two sites form a set that as will be shown in the next section has different properties from the $C_s(3)$ centre.

Table VI.3.2

Spectral data for the hydrogenic $C_s(2)$ site in $CaF_2:Pr^{3+}$

Site		$C_s(2)$ H^-	$C_s(2)$ D^-	$C_s(2)$ T^-
$Z_1 \longrightarrow D_1$ transition and Z_1-Z_2 splitting ($\pm$ 0.1 cm^{-1})		16527.5	16528.5 10±1	16527.9
Other Pr^{3+} ion electronic energy levels ($\pm$ 2 cm^{-1})	Z_3 Z_4 Z_5	- 625 645	39 645 [1]	37 641 651
Interstitial ion local mode vibration intervals ($\pm$ 2 cm^{-1})	a	-	741	619
Substitutional ion local mode vibration intervals ($\pm$ 2 cm^{-1})	b c d e	-	525 581 615 877	 526 723

[1] line at 645 cm^{-1} has a shoulder indicating a possible accidental degeneracy.

VI.3.3 The $C_s(3)$ Centre in $CaF_2:Pr^{3+}$

The $C_s(3)$ centre in this crystal has a different character when compared to the $C_s(1)$ and $C_s(2)$ sites showing non-reversible polarised bleaching (Figure VI.3.4(a)) and appearing to have a greater number of local mode vibronic lines in the emission spectrum Along with the $C_s(3)$ centre in $SrF_2:Pr^{3+}$ this site forms a separate entity from $C_s(1)$ and $C_s(2)$, probably distinguished by the addition of further hydrogenic ions. The rapid, non-recoverable decay of the fluorescence suggests photoproduct formation as the determining factor in the bleaching.

Figure VI.3.4(b) depicts the $^1D_2 \longrightarrow {}^3H_4$ emission for the $C_s(3)$ D^- site recorded at 14 K and the spectral data are summarised in Table VI.3.3. The emission spectra for the H^- and T^- sites have yet to be recorded and the vibronic line assignments are made on the apparent $Z_1:Z_2:Z_3$ splitting pattern. Such a method is at best unreliable and the local mode vibrations determined should be treated at tentative assignments. For this reason the intervals of the vibronic levels coupled to the Z_2 and Z_3 levels are also included in the table.

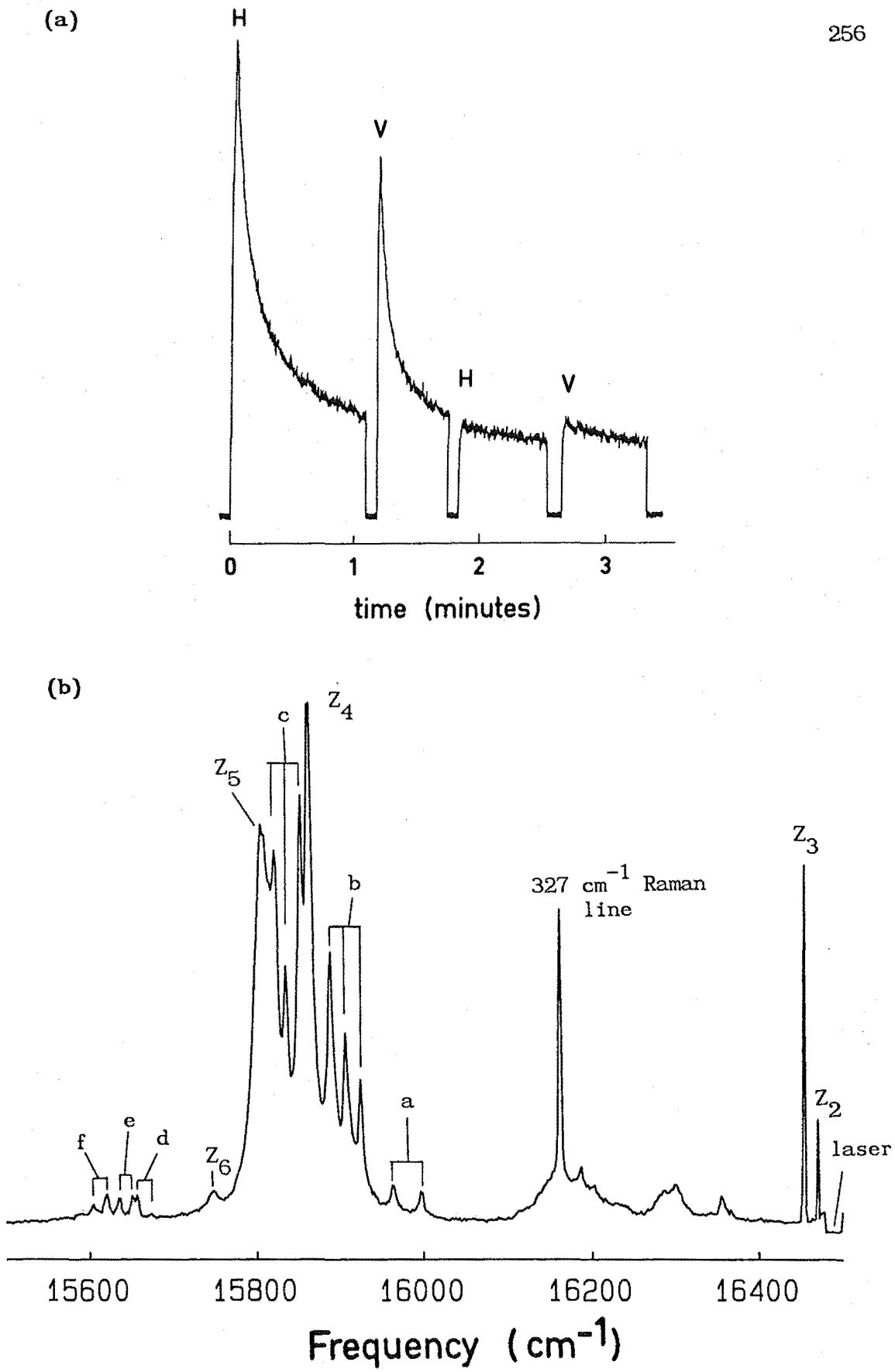

Figure VI.3.4 (a) Bleaching curves in a <100> oriented crystal and (b) $^1D_2 \rightarrow {}^3H_4$ emission for the $C_s(3)$ centre in a $CaF_2:Pr^{3+}:D^-$ crystal.

Table VI.3.3

Spectral data for the $C_s(3)$ D^- centre in $CaF_2:Pr^{3+}$.

$Z_1 \longrightarrow D_1$ transition and Z_1-Z_2 splitting (± 0.1 cm^{-1})		16483.9 19 ± 2
Other Pr^{3+} ion electronic levels (± 2 cm^{-1})	Z_3 Z_4 Z_5 Z_6	35 627 685 741

Parent electronic transition	Local Modes	Vibronic Interval (± 2 cm^{-1})
$D_1 \longrightarrow Z_1$	a	493
$D_1 \longrightarrow Z_3$		490
$D_1 \longrightarrow Z_1$	b	565
$D_1 \longrightarrow Z_2$		564
$D_1 \longrightarrow Z_3$		566
$D_1 \longrightarrow Z_1$	c	637
$D_1 \longrightarrow Z_2$		636
$D_1 \longrightarrow Z_3$		634
$D_1 \longrightarrow Z_1$	d	815
$D_1 \longrightarrow Z_2$		814
$D_1 \longrightarrow Z_1$	e	839
$D_1 \longrightarrow Z_2$		836
$D_1 \longrightarrow Z_1$	f	869
$D_1 \longrightarrow Z_2$		866

VI.4 Discussion of the Bleaching Effects

VI.4.1 Site Configurations

Critical to any discussion of the bleaching mechanism and ion pathways is the exact nature of the centre configuration. The experimental results discussed in earlier sections suggest that the most simple site configuration has a charge compensating hydrogenic ion in the regular [100] direction and a second hydrogenic ion substituting for a lattice F^- ion in the first coordination shell. The two possible site models fulfilling these criteria are illustrated in Figure VI.4.1. In one model the substitutional hydrogenic ion is on the side of the coordination cube closest to the interstitial (Figure VI.4.1(a)) and in the other the substitutional hydrogenic ion is opposite the interstitial (Figure VI.4.1(b)). Clearly from the large number of other centres observed there must be many other site configurations. The most important mechanism that any model must explain is that of reversible polarised bleaching.

A possible mechanism for reversible polarised bleaching is shown in Figure VI.4.2 using the site configuration of Figure VI.4.1(a). The substitional hydrogenic ion moves to a vacant interstitial position and is replaced by the original charge compensating ion to complete the reorientation. There are two possible vacant interstitial positions the substitutional ion can move to and in both cases the end product is the equivalent centre reoriented by 90^o required for reversible polarised bleaching. An alternative mechanism leading to the same reorientation would have the charge compensating H^- (or D^-, T^-) ion moving directly along a [110] direction. Both these mechanisms have been discussed as possible processes for the reorientation of the RE^{3+}-F^-(i) dipole of the C_{4v} site, observed at elevated temperatures in ionic thermocouple and dielectric loss

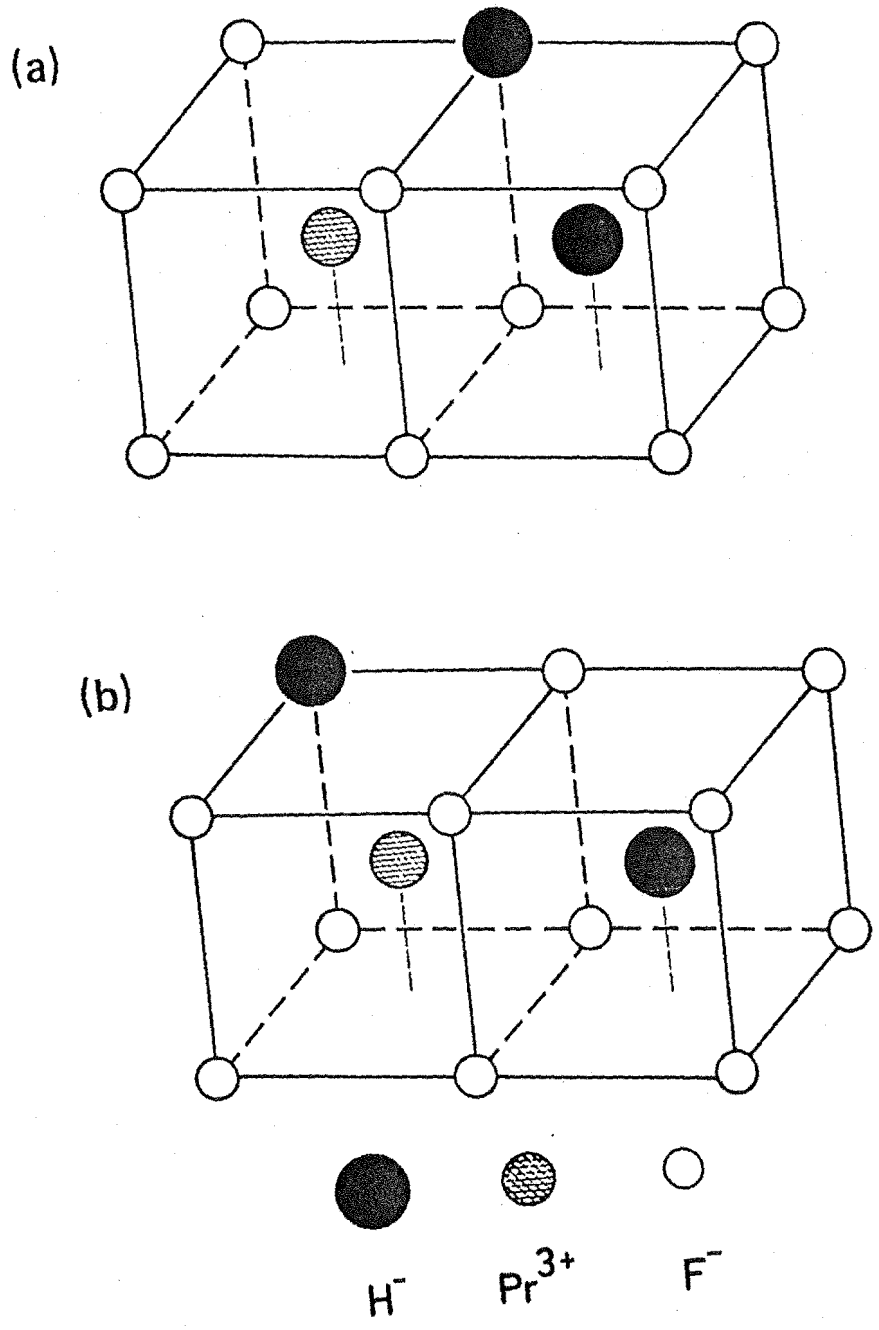

Figure VI.4.1 Two possible site configurations for double hydrogenic-ion centres having near neighbour substitutional and interstitial hydrogenic ions.

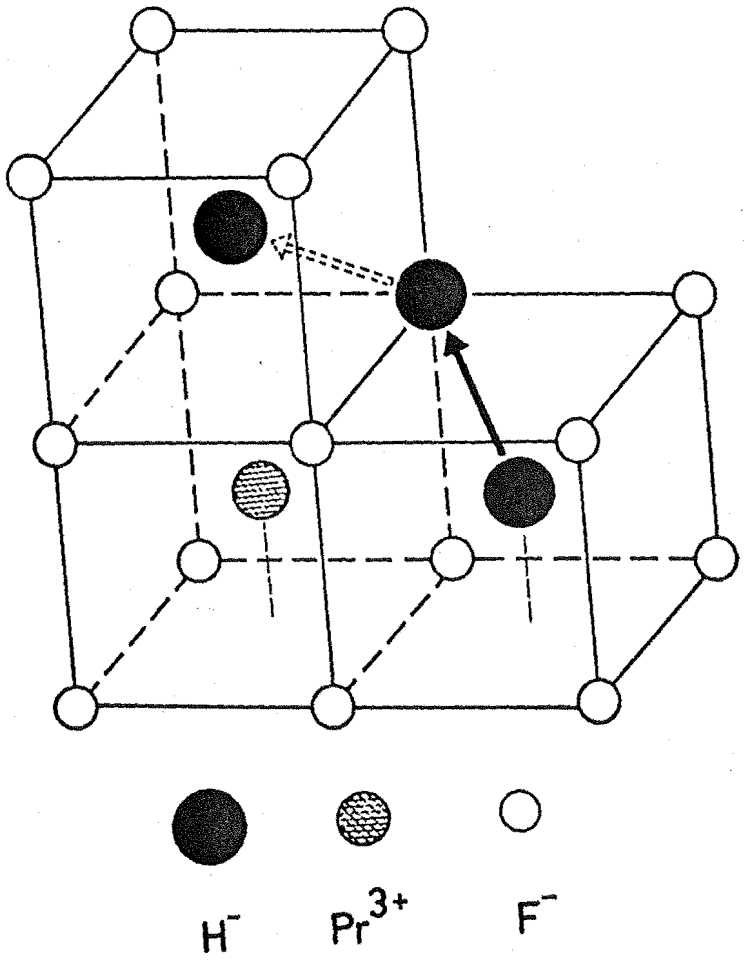

Figure VI.4.2 Interstitialcy mechanism for the reorientation of the site configuration in Figure VI.4.1(a) to give an equivalent centre oriented at 90°.

experiments (Bollmans et al [1970], Nauta-Leefers and den Hartog [1979] and references therein). By allowing a degree of relaxation in the lattice Catlow [1976] calculated that both mechanisms have a similar activation energy. Results from Edgar & Welsh [1975] for $CaF_2:Gd^{3+}$ crystals showed that the activation energy of the C_{4v} H^- site was very similar to that of the C_{4v} F^- site. As the extra mobility of the H^- ion did not appear to make a significant contribution it was concluded that the interstitialcy mechanism was dominant for these centres. In the double hydrogenic ion site depicted in Figure VI.4.1(a), the direct jump mechanism may be facilitated by local mode vibrations of the substitutional hydrogenic ion and make a greater contribution to the reorientation. Since bleaching is not observed for either of the C_{4v} F^- or H^- sites at low temperatures, the activation energy for dipole reorientation in the C_s centres must be much lower than for the C_{4v} sites.

Similar mechanisms to show reversible polarised bleaching are not so easy to find for the site configuration depicted in Figure VI.4.1(b). The interstitial hydrogenic ion is surrounded by a coordination cube containing eight F^- ions and other than small perturbations from the distant substitutional hydrogenic ion is in the same environment as the interstitial ion in the C_{4v} H^- site. Other than invoking some complicated interstitialcy type mechanism involving F^- ion motion, the only way to reorient this configuration to an equivalent centre would be by a [110] migration of the interstitial ion. The four possible directions for this motion would produce two different sites; one being an equivalent reoriented centre and the other of the configuration shown in Figure VI.4.1(a). Since the interstitial ion is in a very similar environment to the C_{4v} H^- site which does not bleach, any decay through this mechanism would be very slow as it relies on some perturbation of the F^- ion shell by

the substitutional hydrogenic ion to allow the migration. Also interconversion between the four principal centres of this type in $SrF_2:Pr^{3+}$ was searched for but no evidence of any transfer was found.

Through the correlation of local mode frequencies, the $C_s(1)$ centre in $SrF_2:Pr^{3+}$ and $CaF_2:Pr^{3+}$ is the same centre as the R_1 site (Edgar, Freeth and Jones [1977]) and the B site (Cockroft et al [1987b]) observed in EPR and infrared absorption respectively. Both the R_1 and B sites were assigned the site configuration depicted in Figure VI.4.1(b). The correlation of the two $C_s(1)$ centres in the optical region is confirmed by their similar bleaching characteristics where they both have a bleaching rate an order of magnitude slower than the other centres and by far the best recovery levels of the reversible centres. However the bleaching characteristics of the $C_s(1)$ centre in $SrF_2:Pr^{3+}$ are incompatible with the site configuration depicted in Figure VI.4.1(b). The reversible polarised bleaching in this configuration requires that a discrete photoproduct, the configuration of Figure VI.4.1(a), is produced at the same rate as the equivalent, reoriented centre. This requirement is not supported by the experimental results where a discrete photoproduct of the $C_s(1)$ centre was searched for, including amongst the other rhombic centres, but not found.

The results of this work suggest that the site configuration of the $C_s(1)$ centres is that depicted in Figure VI.4.1(a). For this model a direct jump mechanism can only produce an equivalent, reoriented centre in either of the two orthogonal directions. This conjecture assumes that a jump through a cube edge between two F^- ions is improbable as deduced from the stability of the C_{4v} H^- site. An interstitialcy type mechanism will produce the same reoriented centres. Both these mechanisms could produce a centre with the two hydrogenic ions along a [111] direction, one in the next nearest neighbour (nnn) interstitial position. However since the regular

single charge compensating ion site of this type, i.e. an F^- (or H^-) ion in the nnn position, is not found in praseodymium doped crystals (Andeen et al [1981]), this photoproduct centre is not stabilised.

The original assignment of the B site to the configuration proposed in Figure VI.4.1(b) was made on the basis of the magnitude of the splitting in the transverse (x,y) local mode vibration of the charge compensating hydrogenic ion (Edgar, Freeth and Jones [1977]). The reassignment of the site to the model in Figure VI.4.1(a) is still consistent with these results while now satisfying the effects observed in the optical region.

A further site assignment that can be proposed is that of the $C_s(2)$ centre in $SrF_2:Pr^{3+}$. This centre exhibited reversible polarised bleaching but was also found to display photoproduct formation. For the same reasons as before regarding its inability to explain reversible polarised bleaching satisfactorally, the model depicted in Figure VI.4.1(b) has to be discarded for this centre. Instead the model depicted in Figure VI.4.3 is proposed. This configuration contains three hydrogenic ions with two residing in the first coordination shell of the Pr^{3+} ion and sharing a common edge to the lattice cube. These two positions are equivalent and the two substitutional ions will have the same local mode frequencies. The charge compensating hydrogenic ion is still in an approximately C_{4v} symmetry site as all surrounding ions remain electrically equivalent however a greater departure from C_{4v} would be expected with respect to the $C_s(1)$ centre. This is in fact observed as the transverse (x,y) local mode vibration of the interstitial ion shows a greater splitting in this centre.

The bleaching results can be understood as follows. Reversible polarised bleaching can occur by either the direct jump or interstitialcy type mechanism and is illustrated in Figure VI.4.4(a).

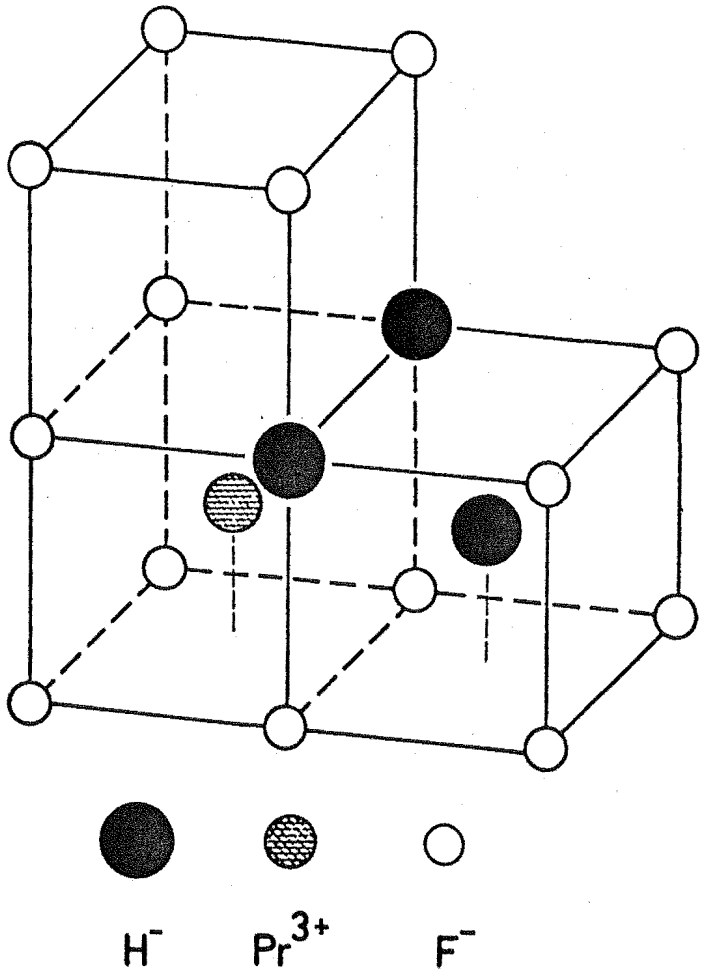

Figure VI.4.3 Proposed site configuration for the hydrogenic ion $C_s(2)$ centre in $SrF_2:Pr^{3+}$ crystals.

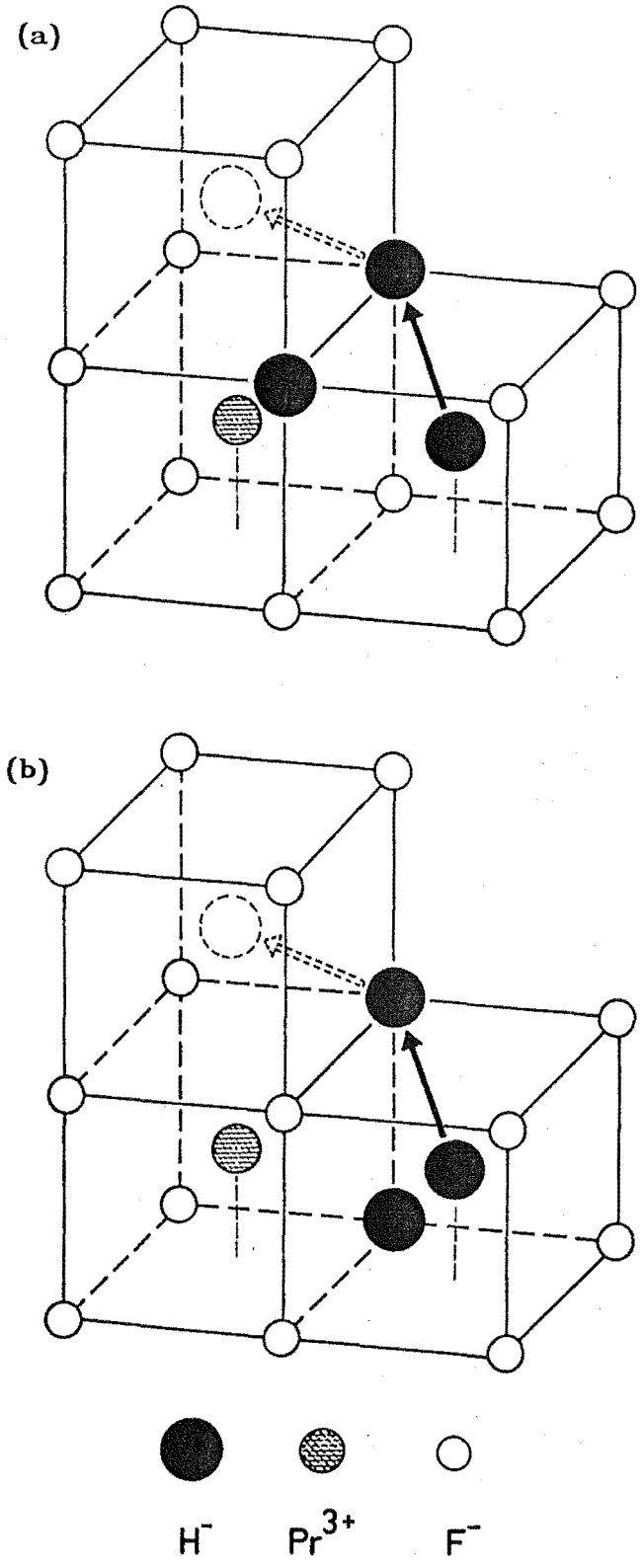

Figure VI.4.4 (a) Simple interstitialcy mechanism for the reversible reorientation of the hydrogenic $C_s(2)$ centre and (b) a mechanism for the $C_s(2)$ centre that would produce a single, discrete photoproduct centre.

In agreement with the experimental results, this reorientation is expected to be much faster than it was for the $C_s(1)$ centre as there are two pathways for the interstitialcy motion through either of the substitutional hydrogenic ions. The direct jump mechanism would also be more probably as the local mode vibrbations of two hydrogenic ions on a common cube edge could substantially lower the potential barrier for migration in that direction.

This reversible process differs from that of the $C_s(1)$ centre in that there is only one equivalent centre oriented at 90^o for each particular site. A reorientation in the third direction leads to a formation of a photoproduct at a different excitation wavelength in accordance with the experimental results (Figure VI.4.4(b)). Invoking an interstitialcy or a direct jump mechanism the figure shows that only one photoproduct can be formed assuming a jump can only occur through a cube edge containing a substitutional hydrogenic ion. Moreover, under the same conditions there is only one possible return path for the interstitial ion motion of the photoproduct and that is back to the configuration of the original centre. This agrees with the observed characteristics of the photoproduct that showed the migration was strictly reversible and no other centres were formed.

The bleaching curves for the $C_s(2)$ centre show a rapid decay in the recovery level of the fluorescence but it gets proportionally better after some time (Figure VI.2.7). Presumably the decay is associated with the photoproduct formation as centres are entirely removed from resonance with the laser frequency. The model described above for this centre can explain this decay but is unsuccessful in predicting an improvement in the recovery level. At this stage the rate of photoproduct formation must have decreased. The site configuration of Figure VI.4.3 predicts a constant rate of photoproduct formation. The improvement in the recovery level can be

explained if there are some centres that have a predisposition towards the reversible bleaching mechanism. After the bulk of the centres have formed the photoproduct during many cycles, these other centres continue to reversibly bleach with a reduced loss of intensity.

The bleaching characteristics of the $C_s(4)$ centre in $SrF_2:Pr^{3+}$ give some clues as to a possible site model. Recall that this centre does not undergo reversible polarised bleaching but does exhibit photoproduct formation. However throughout this discussion is should be realised that the bleaching characteristics were checked only for excitation from the Z_1 level, which as evidenced by the $C_s(2)$ centre may not give the overall picture. Nevertheless, it appears safe to assume that this site is totally non-reversible. As with the $C_s(2)$ site the two hydrogenic ion configuration of Figure VI.4.1(b) is found to be inadequate to explain the bleaching characteristics. The only photoproduct that can be formed from a simple interstitialcy mechanism in this model has the same configuration as that depicted in Figure VI.4.1(a) which has already been assigned to the $C_s(1)$ centre. An excitation spectrum showed that the photoproduct of the $C_s(4)$ centre is discrete from any of the other main centres and there was also no evidence of any conversion between the $C_s(4)$ and $C_s(1)$ centres. The site model proposed for the $C_s(4)$ centre is depicted in Figure VI.4.5(a).

As with the $C_s(2)$ centre this configuration has two substitutional hydrogenic ions in the first coordination shell. The positions are equivalent and will not be distinguished in the local mode vibrational spectrum. The charge compensating ion resides in a site of approximate C_{4v} symmetry and will show local mode vibrations similar to those of the $C_s(2)$ centre. This is in fact observed as Table VI.2.2 and VI.2.3 show. The bleaching properties can be explained using this model as follows. A simple interstitalcy type motion

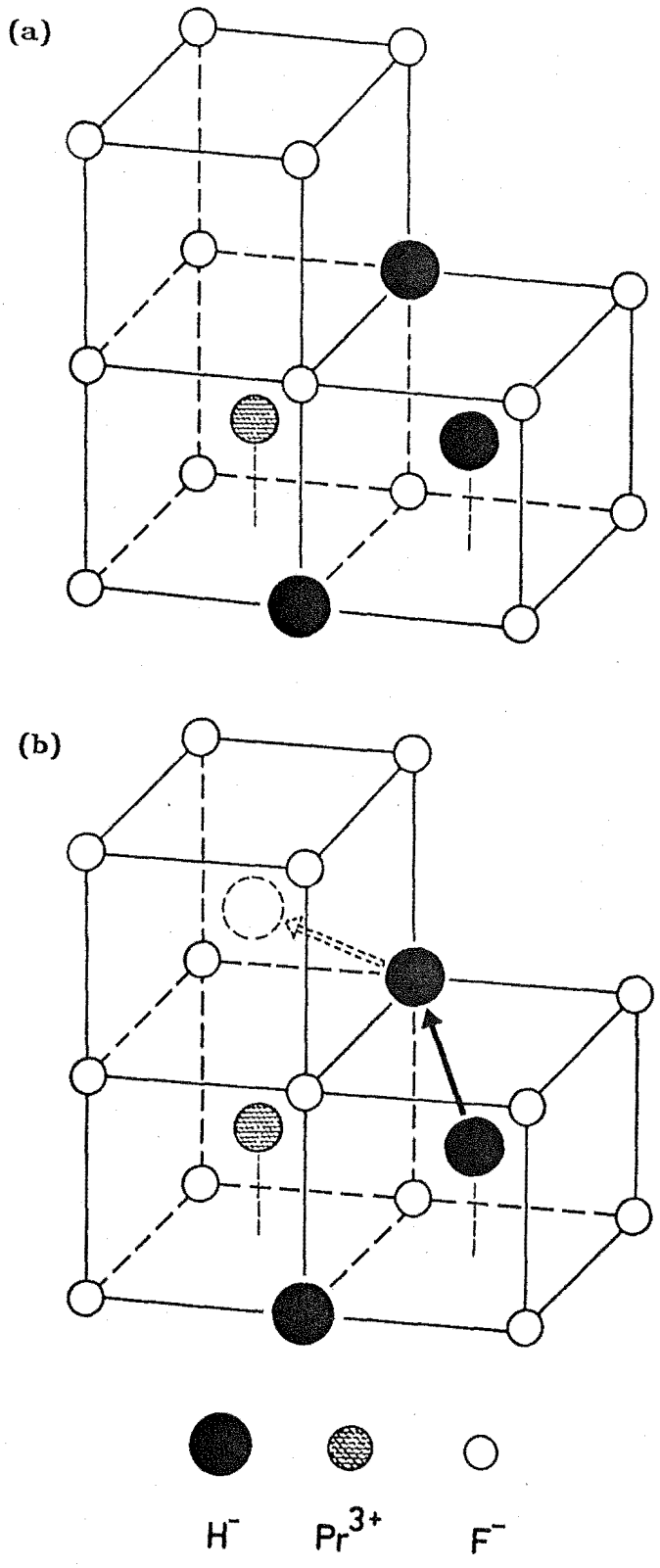

Figure VI.4.5 (a) Proposed model for the $C_s(4)$ hydrogenic ion centre in $SrF_2:Pr^{3+}$ crystals and (b) a simple interstitialcy mechanism for this site configuration that will produce a single, discrete photoproduct centre.

involving the interstitial ion and either of the substitutional ions will produce the photoproduct depicted in Figure VI.4.5(b) which places the Pr^{3+} ion in a different crystal field and out of resonance with the laser frequency. Similarly a direct jump through any of the four cube edges will produce the same photoproduct site. Without invoking some complicated interstitialcy mechanism there is no way for this configuration to reversibly reorient and there is only one possible photoproduct that can be formed. The experimental results require both these properties in a site model of the $C_s(4)$ centre. Excitation of the photoproduct will produce either an equivalent reoriented photoproduct centre or a centre of the original configuration. This gives a result that can be checked experimentally as the photoproduct should undergo reversible polarised bleaching. The effect, however, may not be dramatic as all the photoproducts so far observed are unstable under any excitation and appear to have a preference for returning to their originating configuration. In the unlikely event of the $C_s(4)$ centre showing reversible polarised bleaching for excitation from the Z_2 level the models depicted in Figure VI.4.5 are still applicable only their roles are reversed, i.e. the photoproduct centre would have the configuration depicted in Figure VI.4.5(a).

The question as to why the photoproduct centres are not found in a virgin crystal can now be addressed. Comparison between the three models proposed, Figures VI.4.1(a), VI.4.3 and VI.4.5(a), show that they are the simplest configurations involving one or two substitutional and one interstitial hydrogenic ions where these ions are grouped as close together as possible. If there is a preference for such clustering at low temperatures then the photoproducts, in which the hydrogenic ions are more dispered, may be unstable and

preferentially return to their original configurations. At higher temperatures a different distribution of centres may be energetically favourable and the photoproduct centres may exist in their own right.

In summary three site models have been proposed for the $C_s(1)$, $C_s(2)$ and $C_s(4)$ centres in $SrF_2:Pr^{3+}$ that are successful in explaining the observed spectral and bleaching characteristics. Experimental verification of two equivalent substitutional hydrogenic ions in the $C_s(2)$ and $C_s(4)$ centres could possibly be obtained with Zeeman experiments that may lift the vibrational degeneracy of the local mode vibronic lines observed in a fluorescence spectra. The remaining centre in $SrF_2:Pr^{3+}$ to be discussed is the $C_s(3)$ site that is clearly separated from the other three by the observation of multiple local mode vibronic lines. There are many positions where further hydrogenic ions could be added to the basic site configuration to explain the observed features and no firm model can be proposed on the basis of the present experimental data. However this site appears to produce only one photoproduct centre and this observations may help to shed some light on a possible configuration.

The C_s sites in $CaF_2:Pr^{3+}$ were not studied to the same extent as those in $SrF_2:Pr^{3+}$ however some correlations can be made. As previously discussed the $C_s(1)$ centres in both crystals have been correlated using the local mode frequencies measured in infrared absorption. The bleaching properties are also similar making it reasonable to assume they have the same site configurations. The $C_s(2)$ centre in $CaF_2:Pr^{3+}$ exhibited reversible polarised bleaching and also had a decay characteristic of photoproduct formation. Thus it is reasonable to assume it has the same configuration as the $C_s(2)$ centre in $SrF_2:Pr^{3+}$, i.e. that depicted in Figure VI.4.3. The remaining $CaF_2:Pr^{3+}$ centre is similar to the $C_s(3)$ centre of $SrF_2:Pr^{3+}$ in exhibiting many local mode vibronic lines. There is insufficient

information available to correlate these two sites but some connection is likely.

VI.4.2 Non-resonant Photoproduct Formation

During some of the excitation experiments performed on the rhombic centres in $SrF_2:Pr^{3+}$ it was noticed that intensity is lost from photoproduct lines if the crystal was subject to intense laser irradiation. Figure VI.4.6 shows a series of laser excitation spectra for the $C_s(3)$ D^- centre in $SrF_2:Pr^{3+}$. The unbleached intensity of the $Z_1 \longrightarrow D_1$ transition for this centre shown in Figure VI.4.6(a) reduces to that in (b) after laser excitation of the centre for several minutes and the photoproduct appears. The recovery observed in (c) was produced by an intense burst of excitation into the C_{4v} F^- site for only 10 seconds at a laser power of 50 mW.

The effect was greatest if the laser was tuned to the C_{4v} F^- site but was also apparent for the C_{4v} D^- site and there were some indications that it did not even need to be tuned to any electronic transition. One possible mechanism may be a result of crystal heating under the intense excitation conditions inducing ion migration. A new distribution of site populations is subsequently 'frozen in' by the cooling after the excitation is removed. The C_{4v} F^- site has the strongest absorption of all the sites and may be expected to produce the greatest local heating via non-radiative decay.

As well as decreasing photoproduct concentrations the process can work in the opposite direction to create photoproduct centres. The excitation spectrum of the $C_s(2)$ and $C_s(4)$ centres in $SrF_2:Pr^{3+}:D^-$ is shown for a new piece of crystal in Figure VI.4.7(a) and for the same piece in (b) after irradiating the C_{4v} F^- site for 3 minutes at 100 mW of laser power. Photoproducts of both $C_s(2)$ and $C_s(4)$ are formed and are indicated in the spectra.

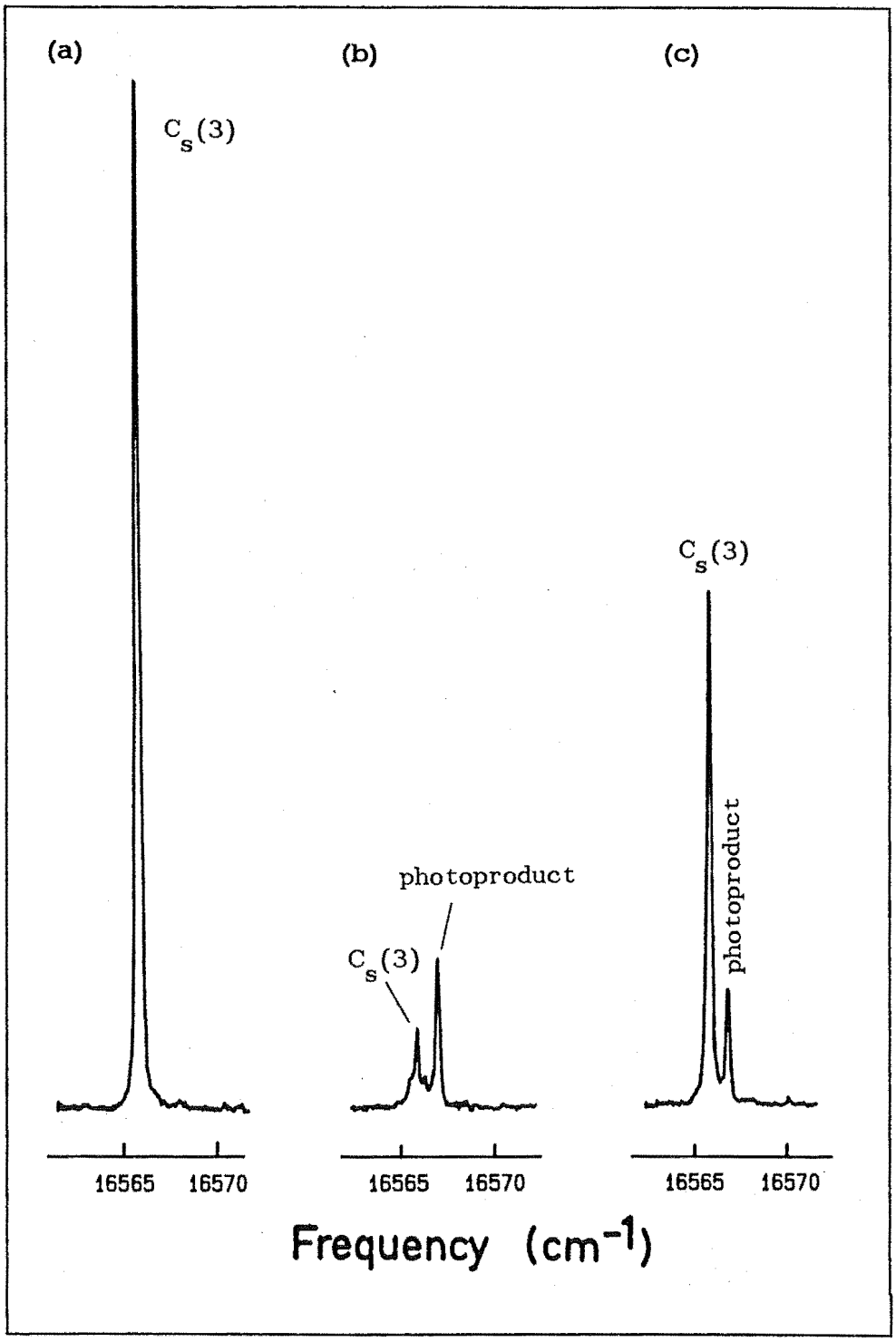

Figure VI.4.6 Laser excitation at 14K of the $C_s(3)$ centre in $SrF_2:Pr^{3+}:D^-$ (a) Before bleaching, (b) after bleaching at 50mW laser power for several minutes, (c) recovery of some $C_s(3)$ intensity produced by a 10 sec burst of C_{4v} F^- irradiation in the same piece of crystal using 50mW laser power.

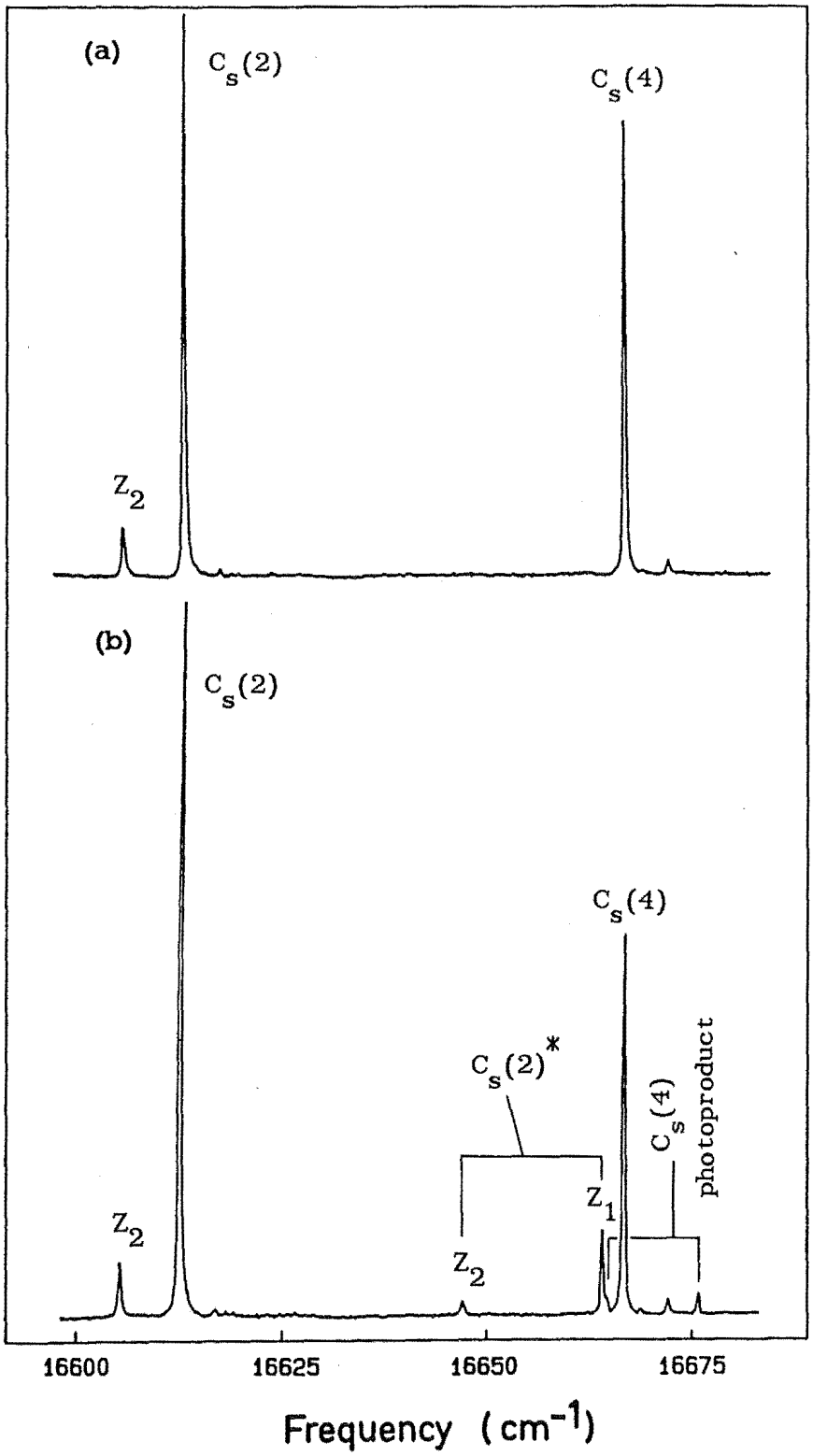

Figure VI.4.7 Laser excitation at 14K of the $C_s(2)$ and $C_s(4)$ centres in a $SrF_2:Pr^{3+}:D^-$ crystal.

(a) for a new piece of crystal, (b) after 3 minutes of irradiation into the C_{4v} F^- site using 100mW of laser power photoproducts of both $C_s(2)$ and $C_s(4)$ are produced.

VI.5 Spectral Holeburning in the Hydrogenic $C_s(1)$ and $C_s(2)$ Centres of $SrF_2:Pr^{3+}:D^-$.

As the two dominant centres of the multiple hydrogenic ion type, the $C_s(1)$ and $C_s(2)$ sites of a $SrF_2:Pr^{3+}:D^-$ crystal were chosen for high resolution spectral holeburning studies. The holeburning experiments were performed by Dr Roger Macfarlane at the IBM Almaden Research Center, California, and the results (Macfarlane, Reeves and Jones [1987]) have been accepted for publication in the September 1987 issue of Optics Letters, published by the Optical Society of America. A preprint of this publication is included in Appendix 1.

Persistent spectral holes were observed to exist for at least one hour at a temperature of 1.6 K, in the $Z_1 \longrightarrow D_1$ absorption line of both $C_s(1)$ and $C_s(2)$ centres. The persistent holeburning is attributed to the same mechanism proposed for the broadband bleaching where the centre is removed from resonance with the laser by D^- migration. The holeburning spectra obtained is shown in Figure VI.5.1 for the $C_s(1)$ centre at 598.40 nm and $C_s(2)$ centre at 601.80 nm.

In addition to the central hole at the laser frequency there are six side holes which have their origin in the hyperfine splittings in the ground and excited states. For the ^{141}Pr ion of nuclear spin $I = {}^5/_2$, the Z_1 and D_1 electronic singlet states are each comprised of three hyperfine levels with splittings in the ratio 2:1. Figure VI.5.2(a) reproduced from Macfarlane, Reeves and Jones [1987] shows a schematic diagram of the level structure, with the three transitions shown, which conserve M_I, being the strongest. This scheme will give the pattern of holes shown in Figure VI.5.2(b), with the central hole three times as strong, and satisfactorally accounts for the observed pattern.

Because of the small separation between the Z_1 and Z_2 electronic states, the hyperfine splittings are dominated by the very large

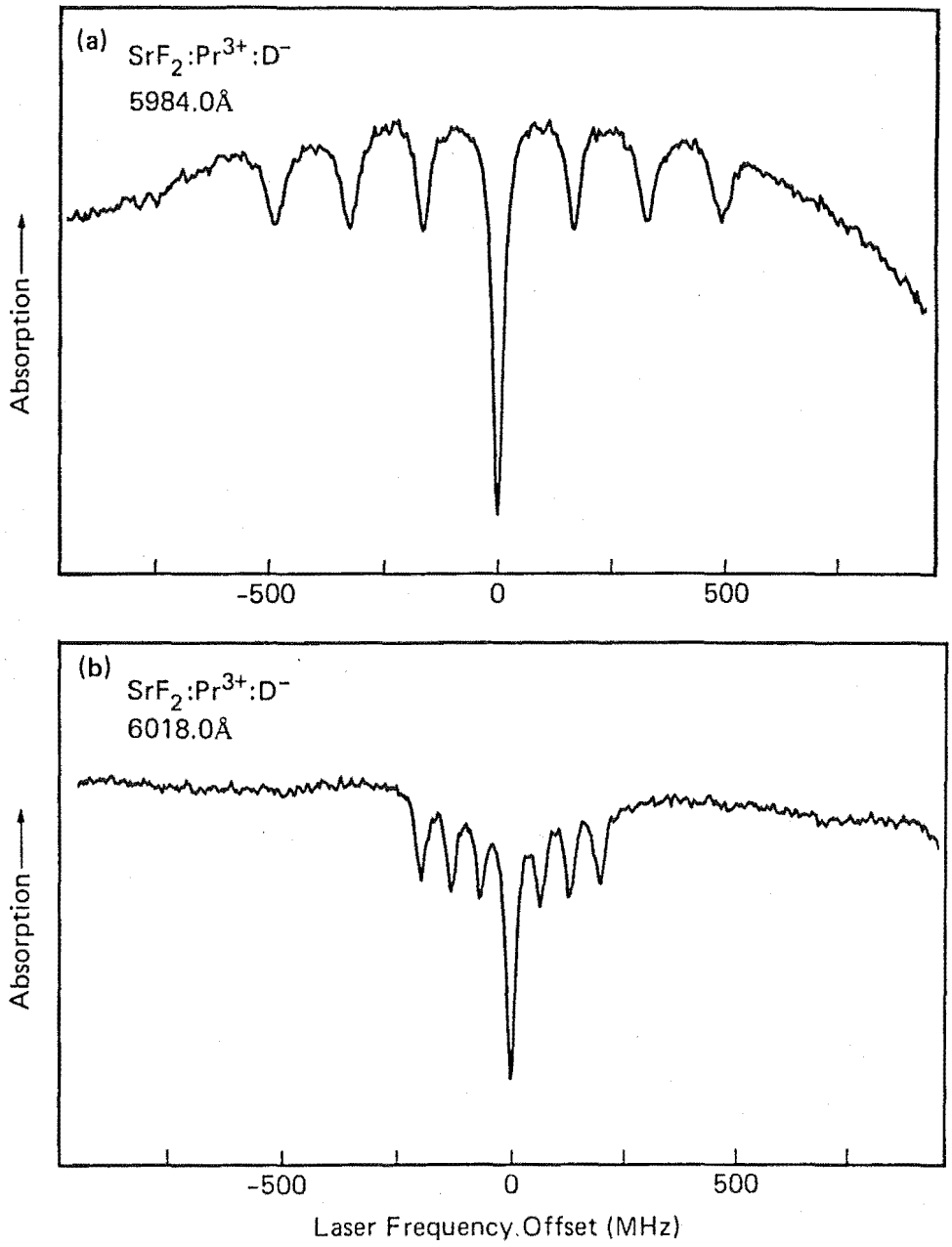

Figure VI.5.1 Persistent spectral holes burned in the (a) $C_s(1)$ and (b) $C_s(2)$ centres of a SrF_2:0.05%Pr^{3+}:D^- crystal showing large pseudoquadrupole splittings in the ground state.

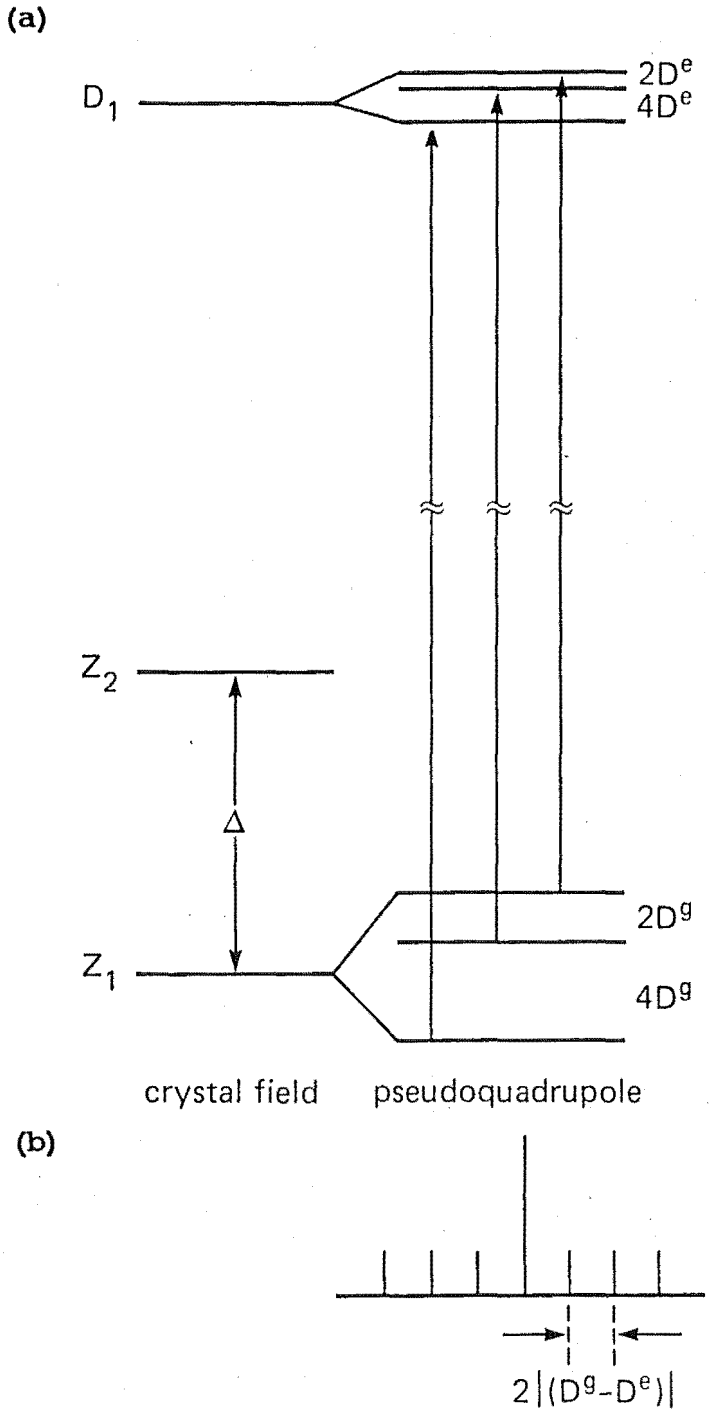

Figure VI.5.2 Schematic energy level diagram of the singlet electronic states of the C_s centres which exhibit close to axial symmetry, (b) pattern of spectral holes expected in the axial approxiamation.

pseudoquadrupole (Baker and Bleaney [1958]) contributions in the ground state. This contribution arises as the excited Z_2 state has a non-zero hyperfine interaction matrix element with the ground Z_1 state giving an energy correction of

$$\frac{\langle Z_1 | \underset{\sim}{J} \cdot \underset{\sim}{I} | Z_2 \rangle}{\Delta}$$

where Δ is the energy separation between the two levels. For the C_{4v} D^- site of $CaF_2:Pr^{3+}$ the $^1D_2$ state has a very small hyperfine splitting (Macfarlane, Burum and Shelby [1984]) and it is reasonable to assume that in these rhombic sites derived from the C_{4v} site the observed splittings arise solely from the ground state. Assuming an axial behaviour to the pseudoquadrupole contribution the hyperfine splitting is (Teplov [1968])

$$D^g = - A_J^2 \frac{\langle Z_1 | J_z | Z_2 \rangle^2}{\Delta}$$

where the ^{141}Pr magnetic hyperfine interaction constant A_J = 1093 MHz (Abragam and Bleaney [1970]). Then for the two C_s sites the relative hyperfine splittings should be inversely proportional to Δ since the matrix elements of J_z are not expected to change significantly. This is, in fact, observed with the appropriate ratios being

$$\frac{|D^g - D^e|_{5984}}{|D^g - D^e|_{6081}} = 2.6 \qquad \text{and} \qquad \frac{\Delta_{6018}}{\Delta_{5984}} = 2.3$$

Assuming that the matrix element of J_z between the Z_1 and Z_2 levels is $(g_{\|}\beta/2g_J)$ where $g_{\|}$ = 3.9 for the ground state of the C_{4v} site (Macfarlane et al [1984]), the absolute magnitude of the splitting can

be calculated. Table VI.5.1 reproduced from Macfarlane, Reeves and Jones [1987] summarises the observed and calculated splittings and shows the agreement is rather good.

Table VI.5.1

Hyperfine interaction parameter values for the $C_s(1)$ and $C_s(2)$ centers measured in SrF_2:0.05%Pr^{3+}:D^-.

Centre Wavelength (Å)	$2D^g$ (calc) (MHz)	$\|2(D^g-D^e)\|$(obs) (MHz)
$C_s(1)$ 5984.0	-142	164
$C_s(2)$ 6018.0	-61	64

In the holeburning experiments discussed here an oriented crystal was not used and antiholes were not observed. The broadband bleaching results show that distinct photoproducts are formed in some cases and in an oriented crystal can be reversibly reoriented. With the ability to be able to excite a selected subset of ions within the inhomogeneous linewidth, high resolution studies on these sites in oriented crystals may be productive in confirming site configurations and ion pathways.

CHAPTER VII

LOCAL MODE VIBRATION AND ELECTRON-PHONON INTERACTION EFFECTS IN HYDROGENATED $SrF_2:Pr^{3+}$ AND $CaF_2:Pr^{3+}$ CRYSTALS

VII.1 Introduction

In previous chapters the electronic properties of the Pr^{3+} ion in the hydrogenic sites were discussed with little attention paid to the properties of the H^- ion itself, suffice to say a brief description of vibronic transitions. Some of this imbalance will be redressed in this chapter.

The inclusion of point defects into a lattice destroys the translational symmetry and the normal vibrational modes are modified. As has been described earlier, hydride impurity ions in CaF_2 type crystals exhibit vibrational modes spatially localised at the ion site. The modes are localised as these ions are somewhat lighter than the ions of the host crystal with little change in the bond strength due to its ionic nature. With their larger masses the localisation will be less satisfactory for the deuterium and tritium isotopes and their modes will extend further into the lattice. In a similar way to the F^- ions, H^- ions participate in the charge compensation process of any rare-earth ions present and trends can be followed by the infrared absorption of the localised modes.

Investigations of rare-earth-hydride ion pairs in CaF_2 crystals by Jones et al [1969] established three hydride ion sites. Of particular interest to this chapter is the site identified as the tetragonal C_{4v} charge compensating hydride ion site found for all the rare-earth ions. Two fundamental local mode vibration lines exist for this site and three second harmonics have also been observed in some cases (Jones et al [1969]). ENDOR measurements on $CaF_2:Ce^{3+}$ and $CaF_2:Gd^{3+}$ (Kiro, et al [1969a], 1969b], Baker, Davies & Reddy [1969]) and more

recently on $CaF_2:Pr^{3+}$ (Burum, Shelby & Macfarlane [1982]) have shown that the point group symmetry is C_{4v} with the H^- ions in the adjacent interstitial sites. The corresponding C_{4v} sites have been observed in hydrogenated SrF_2 crystals for rare-earth ions up to holmium in the lanthanide series by Edgar et al [1977].

In this chapter the transitions of the H^- ion in the Pr^{3+}-H^- C_{4v} site will be addressed along with a particular aspect of the coupling between the two ions.

Since the H^- impurity ion is significantly lighter than the lattice ions it can be treated as an anharmonic oscillator in an effectively static potential well. Observation of the fundamental and harmonic vibrations can provide sufficient data in some cases to determine the anharmonic constants. Local mode vibrational frequencies have been measured for the H^-, D^- and T^- anharmonic oscillators in $CaF_2:Pr^{3+}$ and $SrF_2:Pr^{3+}$ crystals. For some sites more than the five transitions normally expected from infrared absorption have been observed due to the greater sensitivity of the laser excitation technique. In the case of the H^- oscillator in $SrF_2:Pr^{3+}$ all seven fundamental and second harmonic frequencies have been measured. The analysis of these anharmonic oscillators is presented in Section VII.2 of this chapter.

The observation of vibronic transitions comprising a localised vibration mode of the hydride ion and a rare-earth ion electronic transition provides direct evidence that the two ions do not exist in isolation. The interaction connecting the two is the electron-phonon interaction and arises from the change in the crystal field on the rare-earth ion due to the movement of the surrounding lattice ions. Although all lattice ions contribute to the interaction, interest can be focussed on those changes caused by the substitution of the different isotopes of hydrogen as the charge compensating ion.

In this case, only the motion of the hydrogenic ion need be considered as the remaining lattice ions will contribute equally for all three isotopes.

A splitting of the x,y vibronic level has been observed for the C_{4v} H^- site in $CaF_2:Ce^{3+}$ and $SrF_2:Ce^{3+}$ (Jacobs et al [1971]) and $CaF_2:Pr^{3+}$ and $SrF_2:Pr^{3+}$ (Jacobs [1971]). These results are extended in Section VII.4 of this chapter by observations from deuterated and tritiated samples of $CaF_2:Pr^{3+}$ and $SrF_2:Pr^{3+}$

VII.2 Vibrations of the anharmonic Local Oscillator

VII.2.1 Background Theory

The Hamiltonian for a single particle oscillator may be written as

$$H = \frac{p^2}{2m} + \frac{1}{2}\sum A_{ij}Q_iQ_j + \sum B_{ijk}Q_iQ_jQ_k + \sum C_{ijkl}Q_iQ_jQ_kQ_l + \ldots . \quad \text{(VII.2.1)}$$

where $\frac{p^2}{2m}$ is the kinetic energy of the particle having mass m and the Q_i's are the normal coordinates for the vibrations. The first two terms of equation VII.2.1 form the Hamiltonian for a harmonic oscillator and the remaining relatively small anharmonic terms are usually treated as perturbations, with the shifts and splittings of energy levels determined by perturbation theory.

Of particular interest to this work are the local mode vibrations of the H^- ion in the Pr^{3+}- H^- pair comprising the C_{4v} hydrogenic site. The normal coordinates for the H^- motion are the cartesian coordinates x,y and z of the displacement of the H^- ion from its equilibrium position. As the potential must transform as the totally symmetric representation of the point group of the defect site, group theory can be used to determine the possible forms for the Hamiltonian. The H^- ion in the Pr^{3+}- H^- pair of interest resides in

a site having C_{4v} point group symmetry. Using the transformation properties of the point group operations it can be shown that the potential for this symmetry is

$$V(x,y,z) = a(x^2+y^2) + bz^2 + cz^3 + dz(x^2+y^2) + f(x^4+y^4) + gz^4 + hz^2(x^2+y^2) + kx^2y^2 \qquad \text{(VII.2.2)}$$

Newman [1973] gives an extensive review of perturbed harmonic oscillators for C_{4v} and other symmetries. The anharmonic terms can be expressed in the creation/annihilation operator formalism using

$$x = y = \sqrt{\frac{\hbar}{2mw_x}}\ (a^\dagger + a) = \sqrt{\alpha}\ (a^\dagger + a)$$

and (VII.2.3)

$$z = \sqrt{\frac{\hbar}{2mw_z}}\ (b^\dagger + b) = \sqrt{\beta}\ (b^\dagger + b)$$

where $a^\dagger, a, b^\dagger$ and b are the creation and annihilation operators for the local mode phonons. In this formalism the action of an operator on a phonon state $|n\rangle$ is given by

$$x|n\rangle = \sqrt{\alpha}\ \{\ \sqrt{n+1}\,|n+1\rangle + \sqrt{n}\,|n-1\rangle\ \} \qquad \text{(VII.2.4)}$$

The cubic terms in the potential give non-zero matrix elements only in second order perturbation theory and the quartic terms which do have elements in first order perturbation theory will be of comparable size.

The wavefunctions of the three dimensional harmonic oscillator are $|n_1n_2n_3\rangle$ where n_1, n_2 and n_3 are integers and represent the phonon occupation numbers of the x,y,z oscillators respectively.

In the axial symmetry case here, the harmonic energies are

$$E_{n_1 n_2 n_3} = (n_1+n_2+1)\ \hbar w_x + (n_3+\tfrac{1}{2})\hbar w_z \quad . \qquad \text{(VII.2.5)}$$

Wavefunctions for the anharmonic oscillator can be chosen as particular linear combinations of the harmonic oscillator wavefunctions $|n_1 n_2 n_3\rangle$, transforming as the symmetric representations of the point group, using basis functions that appear in tables such as those found in Koster [1963]. Such wavefunctions can be labelled by $|n_1 n_2 n_3 \gamma_r\rangle$ when that linear combination transforms as the γ_r irreducible representation of the point group. Inspection of the appropriate character table of Koster reveals the following wavefunctions for the C_{4v} anharmonic oscillator

$$|000\gamma_1\rangle = |000\rangle$$
$$|100\gamma_5\rangle = |100\rangle \text{ and } |010\rangle$$
$$|001\gamma_1\rangle = |001\rangle$$
$$|110\gamma_4\rangle = |110\rangle$$
$$|101\gamma_5\rangle = |101\rangle \text{ and } |011\rangle$$
$$|200\gamma_3\rangle = \sqrt{\tfrac{1}{2}}\ \{\ |200\rangle - |020\rangle\ \}$$
$$|200\gamma_1\rangle = \sqrt{\tfrac{1}{2}}\ \{\ |200\rangle + |020\rangle\ \}$$
$$|002\gamma_1\rangle = |002\rangle.$$

Group theory can be applied to determine the selection rules for electric dipole transitions between the anharmonic oscillator energy levels. The electric dipole operator transforms as the components of the displacement vector, x,y or z. Thus in the harmonic approximation electric dipole transitions will be allowed only between levels with $\Delta n_i = \pm 1$, i.e. only from the ground state $|000\rangle$ to the fundamentals $|100\gamma_5\rangle$ and $|001\gamma_1\rangle$. However, the anharmonic terms mix all states of the same symmetry to allow second and third harmonics to appear.

The anharmonic shifts for the C_{4v} oscillator have been calculated by Maradudin & Peretti [1967] and more recently by Freeth [1974] with some differences in results apparent. The results calculated in this work, and listed in Table VII.2.1, are in substantial agreement with those of Freeth except for his contention that Maradudin & Peretti omitted the cross-terms

$$\frac{\frac{1}{2}\langle 200|dz(x^2+y^2)|001\rangle\langle 001|dz(x^2+y^2)|020\rangle}{2\hbar w_x - \hbar w_z}$$

$$+\frac{\frac{1}{2}\langle 020|dz(x^2+y^2)|001\rangle\langle 001|dz(x^2+y^2)|200\rangle}{2\hbar w_x - \hbar w_z}$$

in their second order perturbation calculation. The second order shifts calculated here were found to agree with those of Maradudin and Peretti. Analysis in this work has shown that Freeth omitted the cross terms

$$\frac{\frac{1}{2}\langle 200|dz(x^2+y^2)|221\rangle\langle 221|dz(x^2+y^2)|020\rangle}{-2\hbar w_x - \hbar w_z}$$

$$+\frac{\frac{1}{2}\langle 020|dz(x^2+y^2)|221\rangle\langle 221|dz(x^2+y^2)|200\rangle}{-2\hbar w_x - \hbar w_z}$$

from his analysis of the second order energy corrections. Using these results, the corrected excitation frequencies for the anharmonic oscillator levels obtained by subtraction of the ground state energy level and its energy shifts from the others, are listed in Table VII.2.2.

Table VII.2.1 Energy shift from the harmonic oscillator frequencies of the first few levels of the anharmonic oscillator in a site of C_{4v} symmetry.

$$\Delta E_{(000\gamma_1)} = 6f\alpha^4 + 3g\beta^4 + 2h\alpha^2\beta^2 + k\alpha^4 - \left\{ \frac{11c^2\beta^6 + 12cd\alpha^2\beta^4 + 4d^2\alpha^4\beta^2}{\hbar w_z} + \frac{4d^2\alpha^4\beta^2(2w_x - w_z)}{\hbar(4w_x^2 - w_z^2)} \right\}$$

$$\Delta E_{(100\gamma_5)} = 18f\alpha^4 + 3g\beta^4 + 4h\alpha^2\beta^2 + 3k\alpha^4 - \left\{ \frac{11c^2\beta^6 + 24cd\alpha^2\beta^4 + 16d^2\alpha^4\beta^2}{\hbar w_z} + \frac{8d^2\alpha^4\beta^2(2w_x - w_z)}{\hbar(4w_x^2 - w_z^2)} \right\}$$

$$\Delta E_{(001\gamma_1)} = 6f\alpha^4 + 15g\beta^4 + 6h\alpha^2\beta^2 + k\alpha^4 - \left\{ \frac{71c^2\beta^6 + 36cd\alpha^2\beta^4 + 4d^2\alpha^4\beta^2}{\hbar w_z} + \frac{4d^2\alpha^4\beta^2(6w_x - w_z)}{\hbar(4w_x^2 - w_z^2)} \right\}$$

$$\Delta E_{(110\gamma_4)} = 30f\alpha^4 + 3g\beta^4 + 6h\alpha^2\beta^2 + 9k\alpha^4 - \left\{ \frac{11c^2\beta^6 + 36cd\alpha^2\beta^4 + 36d^2\alpha^4\beta^2}{\hbar w_z} + \frac{12d^2\alpha^4\beta^2(2w_x - w_z)}{\hbar(4w_x^2 - w_z^2)} \right\}$$

$$\Delta E_{(101\gamma_5)} = 18f\alpha^4 + 15g\beta^4 + 12h\alpha^2\beta^2 + 3k\alpha^4 - \left\{ \frac{71c^2\beta^6 + 72cd\alpha^2\beta^4 + 16d^2\alpha^4\beta^2}{\hbar w_z} + \frac{8d^2\alpha^4\beta^2(6w_x - w_z)}{\hbar(4w_x^2 - w_z^2)} \right\}$$

$$\Delta E_{(200\gamma_3)} = 42f\alpha^4 + 3g\beta^4 + 6h\alpha^2\beta^2 + 3k\alpha^4 - \left\{ \frac{11c^2\beta^6 + 36cd\alpha^2\beta^4 + 36d^2\alpha^4\beta^2}{\hbar w_z} + \frac{12d^2\alpha^4\beta^2(2w_x - w_z)}{\hbar(4w_x^2 - w_z^2)} \right\}$$

$$\Delta E_{(200\gamma_1)} = 42f\alpha^4 + 3g\beta^4 + 6h\alpha^2\beta^2 + 7k\alpha^4 - \left\{ \frac{11c^2\beta^6 + 36cd\alpha^2\beta^4 + 36d^2\alpha^4\beta^2}{\hbar w_z} + \frac{4d^2\alpha^4\beta^2(6w_x - 5w_z)}{\hbar(4w_x^2 - w_z^2)} \right\}$$

$$\Delta E_{(002\gamma_1)} = 6f\alpha^4 + 39g\beta^4 + 10h\alpha^2\beta^2 + k\alpha^4 - \left\{ \frac{191c^2\beta^6 + 60cd\alpha^2\beta^4 + 4d^2\alpha^4\beta^2}{\hbar w_z} + \frac{4d^2\alpha^4\beta^2(10w_x - w_z)}{\hbar(4w_x^2 - w_z^2)} \right\}$$

Table VII.2.2 Excitation energies for the first few levels of the C_{4v} anharmonic oscillator.

$$\hbar\Omega_{(100\gamma_5)} = \hbar w_x + (12f\alpha^4 + 2h\alpha^2\beta^2 + 2k\alpha^4) - \left\{ \frac{12cd\alpha^2\beta^4 + 12d^2\alpha^4\beta^2}{\hbar w_z} + \frac{4d^2\alpha^4\beta^2(2w_x - w_z)}{\hbar(4w_x^2 - w_z^2)} \right\}$$

$$\hbar\Omega_{(001\gamma_1)} = \hbar w_z + (12g\beta^4 + 4h\alpha^2\beta^2) - \left\{ \frac{60c^2\beta^6 + 24cd\alpha^2\beta^4}{\hbar w_z} + \frac{16d^2\alpha^4\beta^2 w_x}{\hbar(4w_x^2 - w_z^2)} \right\}$$

$$\hbar\Omega_{(110\gamma_4)} = 2\hbar w_x + (24f\alpha^4 + 4h\alpha^2\beta^2 + 8k\alpha^4) - \left\{ \frac{24cd\alpha^2\beta^4 + 32d^2\alpha^4\beta^2}{\hbar w_z} + \frac{8d^2\alpha^4\beta^2(2w_x - w_z)}{\hbar(4w_x^2 - w_z^2)} \right\}$$

$$\hbar\Omega_{(101\gamma_5)} = \hbar(w_x + w_z) + (12f\alpha^4 + 12g\beta^4 + 10h\alpha^2\beta^2 + 2k\alpha^4) - \left\{ \frac{60c^2\beta^6 + 60cd\alpha^2\beta^4 + 12d^2\alpha^4\beta^2}{\hbar w_z} + \frac{4d^2\alpha^4\beta^2(10w_x - w_z)}{\hbar(4w_x^2 - w_z^2)} \right\}$$

$$\hbar\Omega_{(200\gamma_3)} = 2\hbar w_x + (36f\alpha^4 + 4h\alpha^2\beta^2 + 2k\alpha^4) - \left\{ \frac{24cd\alpha^2\beta^4 + 32d^2\alpha^4\beta^2}{\hbar w_z} + \frac{8d^2\alpha^4\beta^2(2w_x - w_z)}{\hbar(4w_x^2 - w_z^2)} \right\}$$

$$\hbar\Omega_{(200\gamma_1)} = 2\hbar w_x + (36f\alpha^4 + 4h\alpha^2\beta^2 + 6k\alpha^4) - \left\{ \frac{24cd\alpha^2\beta^4 + 32d^2\alpha^4\beta^2}{\hbar w_z} + \frac{16d^2\alpha^4\beta^2(w_x - w_z)}{\hbar(4w_x^2 - w_z^2)} \right\}$$

$$\hbar\Omega_{(002\gamma_1)} = 2\hbar w_z + (36g\beta^4 + 8h\alpha^2\beta^2) - \left\{ \frac{180c^2\beta^6 + 48cd\alpha^2\beta^4}{\hbar w_z} + \frac{32d^2\alpha^4\beta^2 w_x}{\hbar(4w_x^2 - w_z^2)} \right\}$$

The two second harmonic states $|200\gamma_1\rangle$ and $|002\gamma_1\rangle$ transform as the same irreducible representation of C_{4v} and can be mixed through the $hz(x^2+y^2)$ anharmonic term. The matrix element connecting these two states is

$$\langle 200\gamma_1 | hz(x^2+y^2) | 002\gamma_1 \rangle = 2\sqrt{2}\alpha^2\beta^2 h$$

and the admixture is obtained from the diagonalisation of the matrix:

	$\|200\gamma_1\rangle$	$\|002\gamma_1\rangle$
$\|200\gamma_1$	$\hbar\Omega_{(200\gamma_1)}$	$2\sqrt{2}\alpha^2\beta^2 h$
$\|002\gamma_1\rangle$	$2\sqrt{2}\alpha^2\beta^2 h$	$\hbar\Omega_{(002\gamma_1)}$

For small values of h, as the anharmonic shifts are expected to be, the corrected energies for these two states are

$$|200\gamma_1\rangle = \hbar\Omega_{(200\gamma_1)} - \frac{8\alpha^4\beta^4 h^2}{2\hbar w_x - 2\hbar w_z}$$

$$|002\gamma_1\rangle = \hbar\Omega_{(002\gamma_1)} + \frac{8\alpha^4\beta^4 h^2}{2\hbar w_x - 2\hbar w_z}$$

where the energy denominators have been approximated by the harmonic energies. Using the anharmonic wavefunctions as labels for the states, the energy level scheme is given in Figure VII.2.1.

Two fundamentals and three second harmonics are the only transitions expected to appear in an absorption spectrum and a unique solution of the six anharmonic parameters c,d,f,g,h & k in the oscillator potential (equation VII.2.2) cannot be obtained from the five pieces of experimental data. Several models to reduce the number of independent constants have been tried by Freeth [1974] with some success.

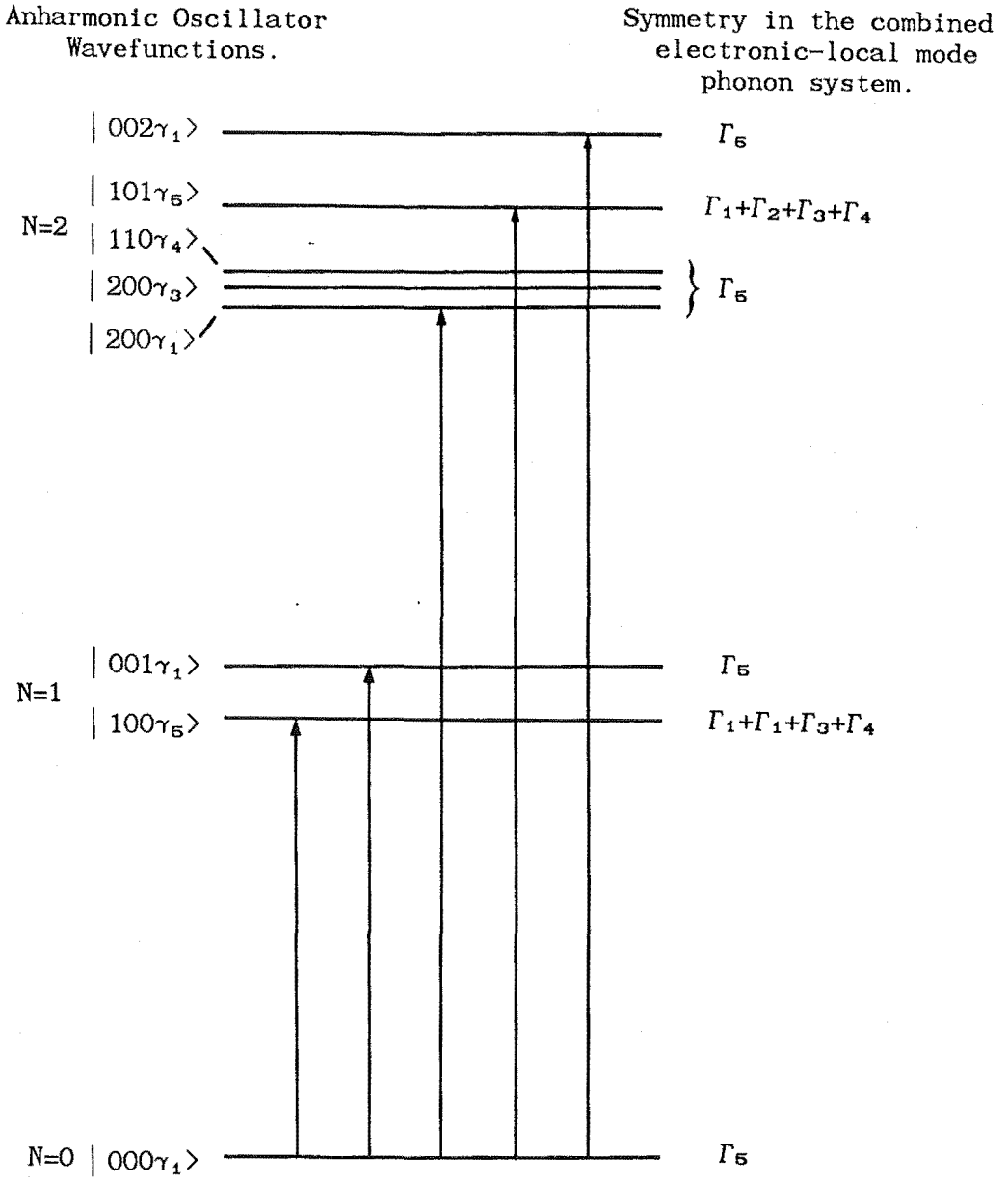

Figure VII.2.1 The energy levels for the anharmonic oscillator with C_{4v} symmetry. The electric dipole transitions shown are allowed for the isolated oscillator.

It was discussed in Chapter V how local mode vibrations of the light, charge compensating H^- ion are manifest in the optical emission spectra of the Pr^{3+} ion. Fluorescence transitions are visible to vibronic levels which are the energy levels of the combined electronic-local mode vibration system. The vibronic wavefunctions are products of the appropriate electronic and phonon states and transform as the product of the irreducible representation of the combining states. With the electronic ground state of the Pr^{3+} ion in the C_{4v} site transforming as the γ_5 irrep, the C_{4v} group multiplication table can be used to establish the symmetries of the vibronic levels. The symmetries for the H^- local mode levels in the combined system are indicated in Figure VII.2.1.

There is a possibility of a vibronic splitting of the $|100\gamma_5\rangle$ and $|101\gamma_5\rangle$ levels as these two doubly degenerate γ_5 symmetry phonon states combine with the degenerate electronic ground state to form each a set of four distinct vibronic states. Such a splitting has been observed in the $|100\gamma_5\rangle$ level for the C_{4v} Pr^{3+}- H^- site and is discussed in a later section.

Inspection of the level symmetries in Figure VII.2.1 reveals that electric dipole transitions will be allowed to all levels in the combined system from the ground state and from the $|D_1(000)\rangle$ emitting level of the $^1D_2$ multiplet. Since the electron-phonon interaction is small the transition probabilities for absorption would be expected to follow those of the anharmonic oscillator, i.e. only three second harmonic transitions would be readily observable. However for emission the observed lines are transitions between levels of the combined system where the selection rules appear relaxed to some extent and all second harmonics are detected in some cases.

Figures VII.2.2 and VII.2.3 show the emission spectra of transitions from the $|D_1(000)\rangle$ emitting level of $^1D_2$ to the

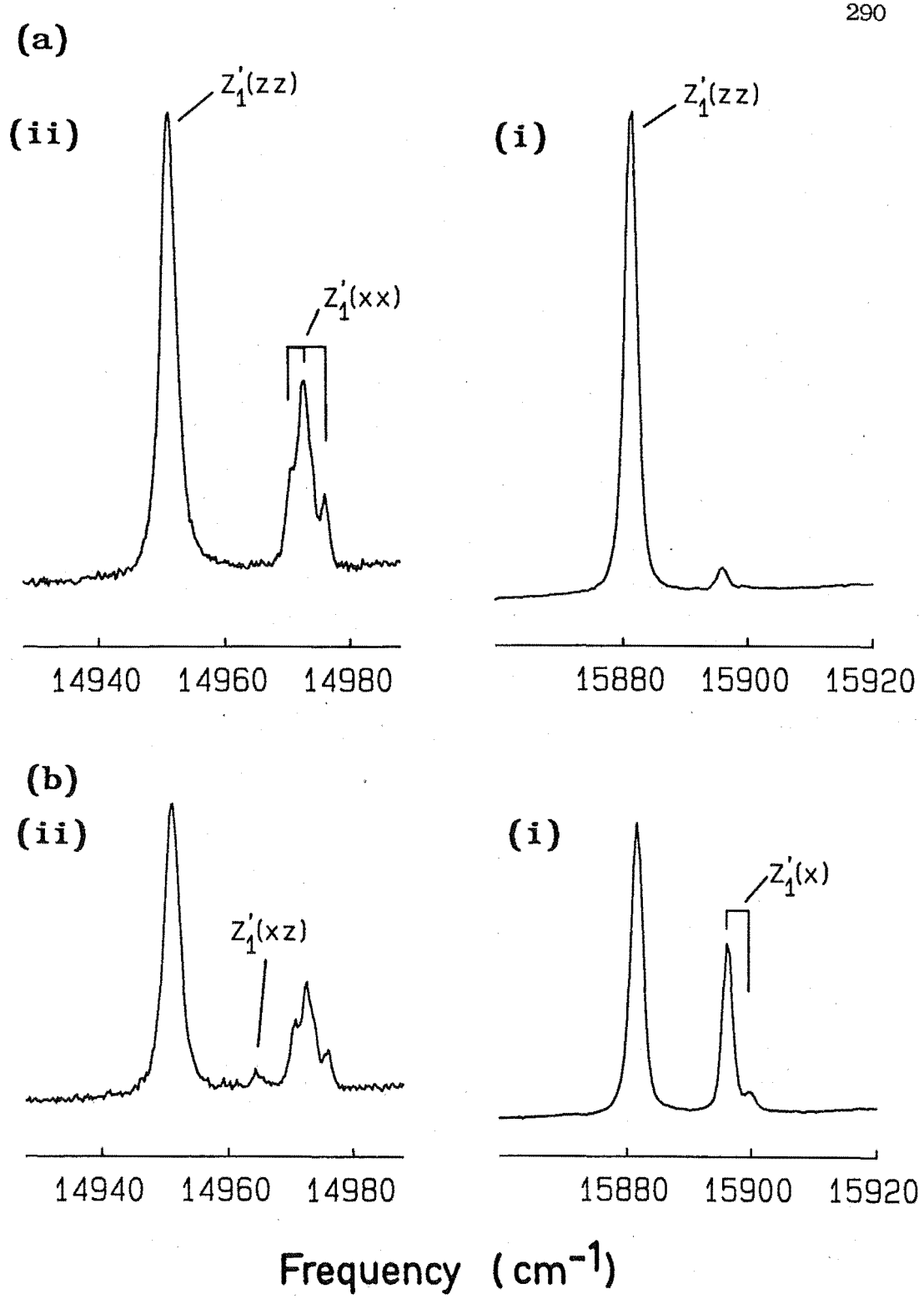

Figure VII.2.2 Polarised emission at 14K from the C_{4v} H^- site in a <100> oriented $SrF_2:Pr^{3+}$ crystal for the; (a) x(yy)z and (b) x(yx)z polarisation geometries. The spectral lines are transitions to the (i) fundamental vibronic levels and (ii) second harmonic vibronic levels of the H^- oscillator.

fundamental and second harmonic vibronic levels of the C_{4v} Pr^{3+} site in SrF_2 crystals with H^-, and D^- charge compensating ions respectively. Figures VII.2.4 and VII.2.5 show similar spectra for the hydrogenic C_{4v} sites in $CaF_2:Pr^{3+}$ crystals. Table VII.2.3 summarises the local mode phonon frequencies measured from fluorescence spectra. Where a splitting of the fundamental $|100\gamma_5>$, vibronic level has been observed an average frequency is given. The energies of the three (xx) second harmonic states differ in anharmonic shifts only and the assignment of an observed trasition to a particular state cannot be made on the experimental results alone.

VII.2.2 Analysis of the C_{4v} H^- Anharmonic Oscillator in $SrF_2:Pr^{3+}$.

Energies for all seven fundamental and second harmonic levels are available for the H^- oscillator in $SrF_2:Pr^{3+}$ with a lesser number having been determined for the other cases. As such this oscillator offers the best opportunity for determining the anharmonic constants with the minimum assumptions possible. While offering promise in some situations the model shows conflict in others. Two (xx) second harmonic transitions have been identified for the H^- and D^- oscillators in $CaF_2:Pr^{3+}$. The splitting between these two states is greater for the D^- oscillator than for the H^- oscillator, in contrast to the predictions of the model where the splittings will decrease by the isotope mass ratio.

In order to analyse these results and determine the form of the potential, several assumptions need to be made to reduce the number of independent parameters in the anharmonic oscillator Hamiltonian. Freeth [1974], in attempting to fit levels observed in infrared

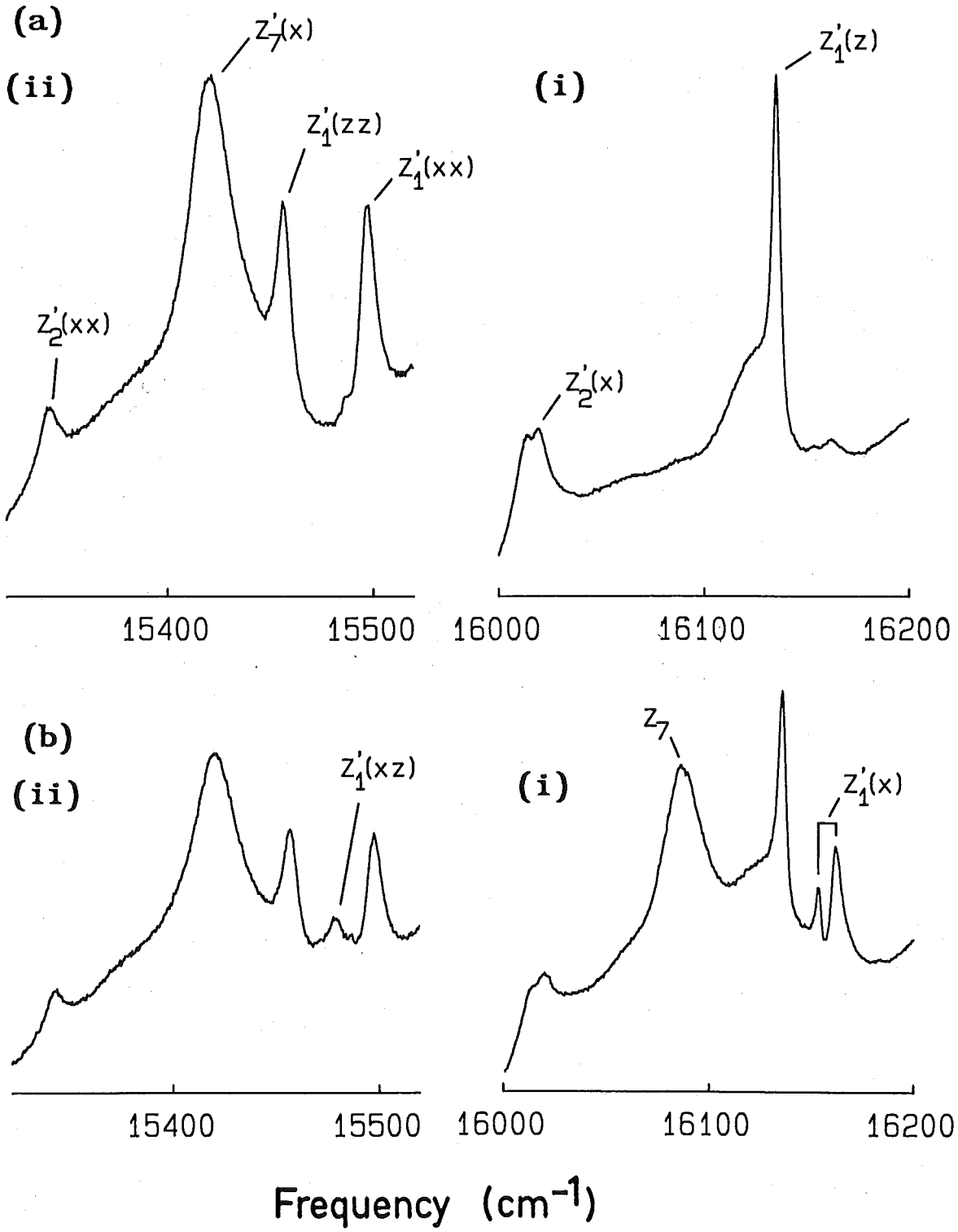

Figure VII.2.3 Polarised emission at 14K from the C_{4v} D^- site in a <100> oriented $SrF_2:Pr^{3+}$ crystal for the; (a) x(yy)z and (b) x(yx)z polarisation geometries. Transitions to fundamental and second harmonic vibronic levels of the D^- oscillator are shown in (i) and (ii) respectively.

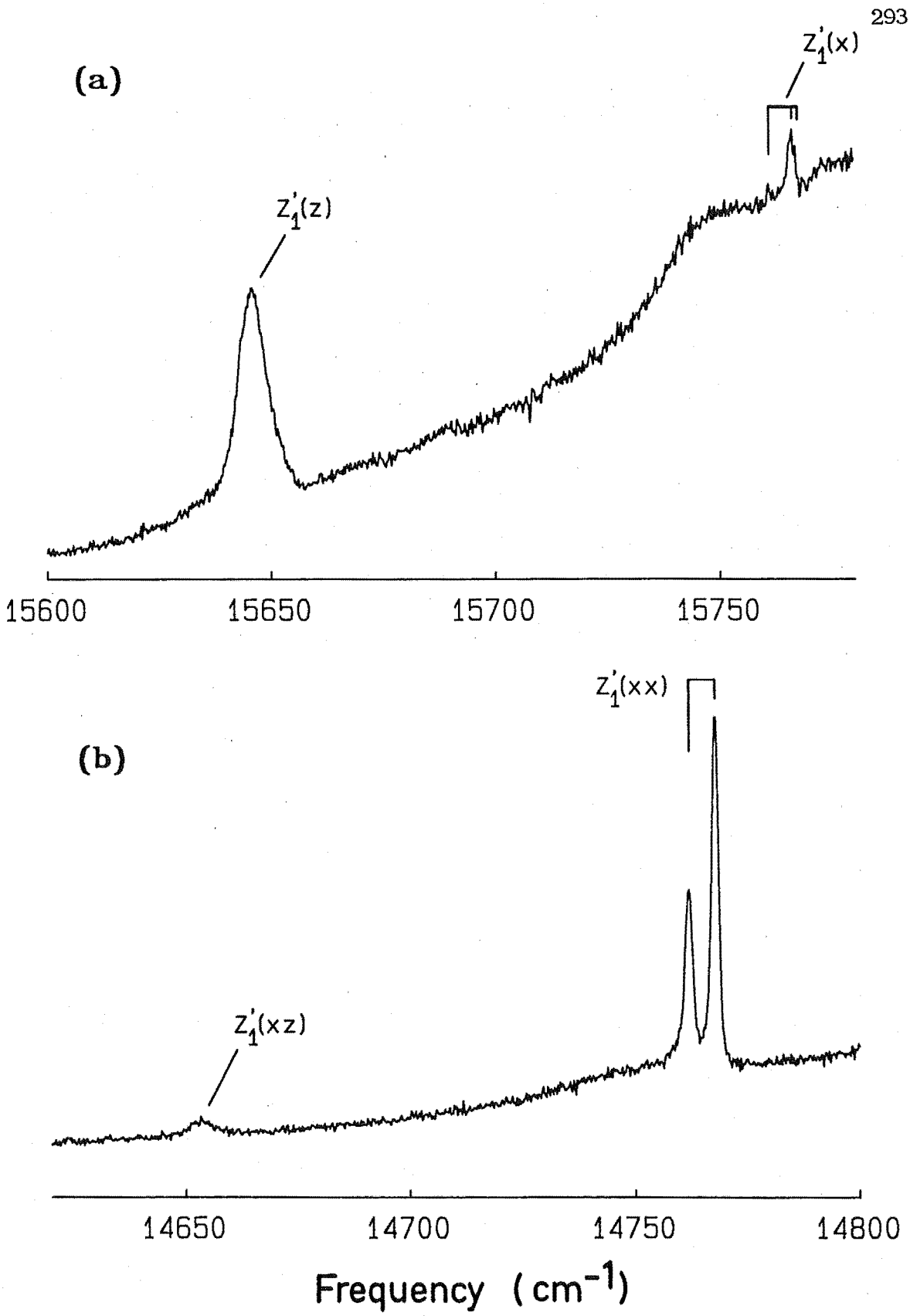

Figure VII.2.4 Fluorescence at 14K from the C_{4v} H^- site in a $CaF_2:Pr^{3+}$ crystal showing transitions to the; (a) fundamental and (b) second harmonic vibronic levels.

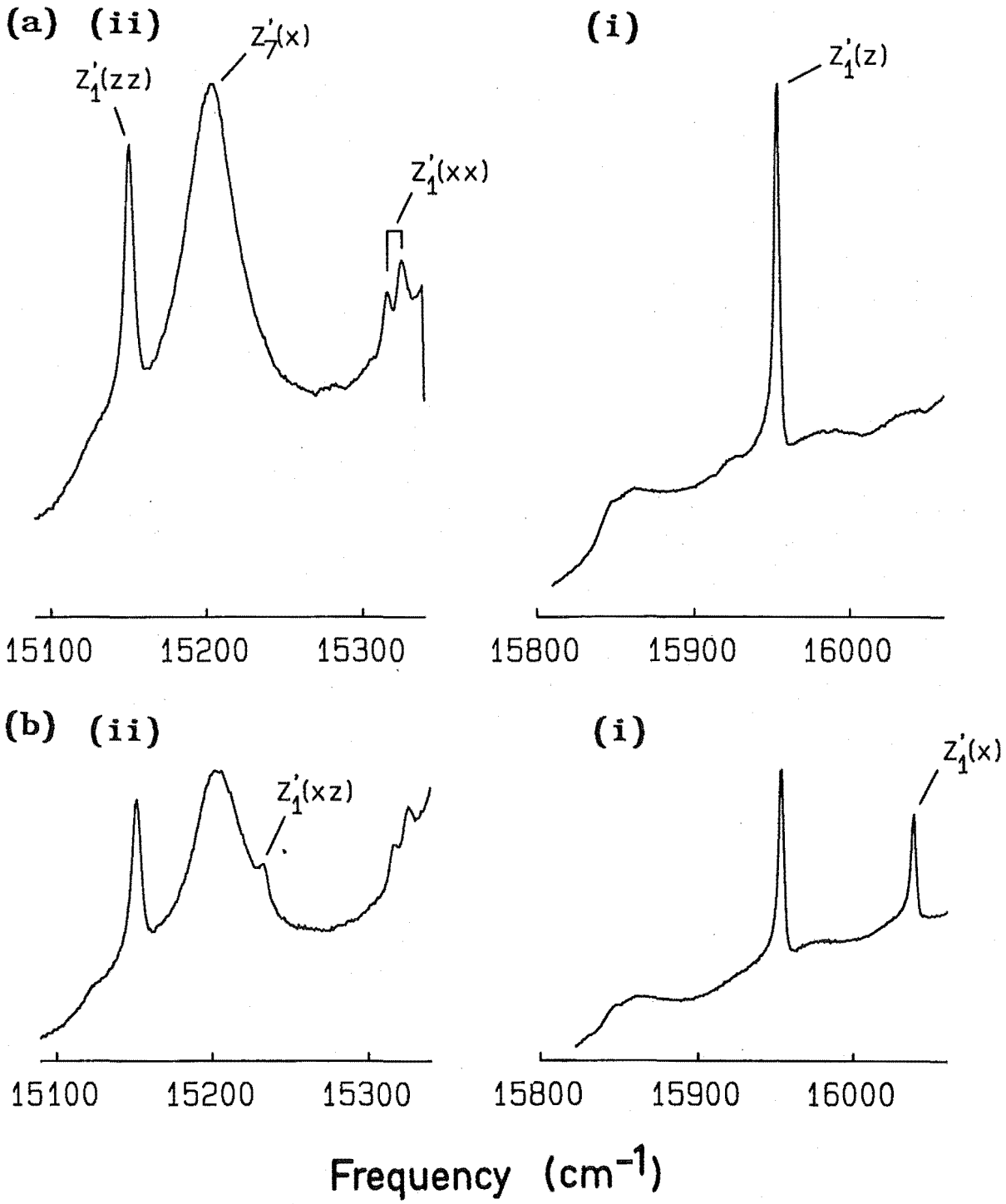

Figure VII.2.5 Polarised emission, at 14K, from the C_{4v} D^- site in a <100> oriented CaF_2:Pr^{3+} crystal for the; (a) x(yy)z and (b) x(yx)z polarisation geometries. Transitions to fundamental and second harmonic vibronic levels of the D^- oscillator are shown in (i) and (ii) respectively.

Table VII.2.3

Fundamental and second harmonic local mode frequencies measured for the H^-, D^- and T^- anharmonic oscillators in $SrF_2:Pr^{3+}$ and $CaF_2:Pr^{3+}$ crystals.

Anharmonic Local Mode Level	$SrF_2:Pr^{3+}$			$CaF_2:Pr^{3+}$		
	H^- ($\pm.5cm^{-1}$)	D^- ($\pm.5cm^{-1}$)	T^- ($1cm^{-1}$)	H^- ($\pm.5cm^{-1}$)	D^- ($\pm.5cm^{-1}$)	T^- ($\pm1cm^{-1}$)
$\|100\tau_5\rangle$	923.4	662.7	558	997.3	772.8	606
$\|001\tau_1\rangle$	939.6	684.9	575	1117.5	808.1	673
$\|110\tau_4\rangle$	1846.1		a	1992.3	1435±1	a
$\|200\tau_3\rangle$	1849.1	1322.9	a	1998.3	1444±1	a
$\|200\tau_1\rangle$	1851.1		a			a
$\|101\tau_5\rangle$	1857.6	1342.4	1131	2107±1	1528±1	1275
$\|002\tau_1\rangle$	1870.6	1363.9	1144	2222±1	1606±1	1341

[a] All three (xx) second harmonics obscured by the $|^1D_2D_1(000)\rangle \rightarrow |^3H_4\Gamma_4\tau_5(001)\rangle$ vibronic transition.

absorption, used the method of quartic ratios where the equalities f=g and h=k were invoked and the energy equations solved for the five parameters a,b,c,d & f for varying ratios of $^{h}/_{f}$. Alternatively, models for the potential such as the point charge model and the dipole model can be developed to determine some of the parameter ratios (Freeth [1974]).

The energy equations of Table VII.2.2 were fitted to the seven experimentally observed transitions for the H^- oscillator in $SrF_2:Pr^{3+}$. This site was chosen for the initial analysis as it has the greatest number of experimentally determined levels. Although all the levels are determined a reduction in the number of independent parameters is still required for a unique solution. The least restrictive assumption was considered to be equating the quartic terms having similar form, i.e. setting f=g and h=k. Although only one of these equalities is required to specify a unique solution, both were included to retain some generality to the fit. A least squares computer program was written to fit the excitation energies, generated by a subroutine calculating the C_{4v} oscillator energy levels, to the measured frequencies. The subroutine was similar to that used by Freeth [1974] with the previously discussed corrections made to the appropriate states. The results of the least squares fit to the levels of the C_{4v} H^- anharmonic oscillator in $SrF_2:Pr^{3+}$ are given in Table VII.2.4.

Table VII.2.4

Anharmonic parameters calculated for the C_{4v} H^- oscillator in $SrF_2:Pr^{3+}$.

Local Mode State	Experimental Data (cm^{-1})	Shifts from the Harmonic levels for the	
		Cubic Terms (cm^{-1})	Quartic Terms (cm^{-1})
$\|100\gamma_5\rangle$	923.4	-5.4	6.7
$\|001\gamma_1\rangle$	939.6	-20.0	6.4
$\|110\gamma_4\rangle$	1846.1	-12.6	15.0
$\|200\gamma_3\rangle$	1849.1	-12.6	18.0
$\|200\gamma_1\rangle$	1851.1	-11.9	19.4
$\|101\gamma_5\rangle$	1857.6	-32.3	14.5
$\|002\gamma_1\rangle$	1870.6	-54.7	17.6

$w_x = 921.76 \pm .02\ cm^{-1}$ S.D. = $0.04\ cm^{-1}$

$w_z = 954.01 \pm .02\ cm^{-1}$

$c = (127.30 \pm .02) \times 10^{10}\ ergs/cm^3$

$d = (116.82 \pm .08) \times 10^{10}\ ergs/cm^3$

$f = g = (264.7 \pm .5) \times 10^{17}\ ergs/cm^4$

$h = k = (224.5 \pm .1) \times 10^{17}\ ergs/cm^4$

The rather strange units of $ergs/cm^3$ and $ergs/cm^4$ are used to retain the comparison with the parameters determined by Freeth [1974].

It is apparent from the results in the table that the anharmonic shifts can be very large for some levels with the cubic terms contributing shifts of opposite sign and in some cases several times greater than the quartic terms. The observed frequency of the $|001\gamma_1\rangle$ state at 939.6 cm^{-1} is markedly different from the harmonic w_z frequency of 954.0 cm^{-1} with most of this difference arising from the cz^3 cubic term.

Since the cubic terms contribute only in second order perturbation theory, the absolute signs of c and d are not determined from this analysis. However the relative sign is conclusively shown to be positive and an identical fit to that presented in Table VII.2.4 is obtained with c and d taking negative values of the magnitudes listed. The sign of c and d is needed to interpret isotope shifts and is required to be negative to explain the observed shifts for gadolinium (Zdansky & Edgar [1971]), cerium (Jacobs et al [1971]) and erbium (Edgar, Jones and Presland [1979]).

The least squares fit results of Table VII.2.4 used parameter ratios of $^{g}/_{f} = 1.0$ and $^{k}/_{h} = 1.0$ to obtain a deviation of 0.04 cm^{-1}. The deviation could be minimised further using other ratios and for $^{g}/_{f} = 1.0$ and $^{k}/_{h} = 0.74$ a deviation of 0.0006 cm^{-1} was obtained, far exceeding the precision of the experimental data. The chosen ratios of $^{g}/_{f} = 1.0$ and $^{k}/_{h} = 1.0$ more than adequately fit the experimental data and will be retained for subsequent analyses.

The ordering of the (xx) second harmonic states depicted in Table VII.2.4, was determined using the results of the least squares fitting program. The assignment of these three states cannot be resolved spectroscopically in emission since all three vibronic states transform as the same irrep of C_{4v}. In principle, the $|200\gamma_1\rangle$ level would be the only (xx) second harmonic reached in infrared absorption but this measurement has yet to be attempted for Pr^{3+} doped crystals. With the local mode states assigned in any alternative scheme to that indicated in the table, the results of the least squares fit showed, either that no satisfactory fit was obtainable, or that anharmonic parameters having similar form, such as c and d, did not retain the same order of magnitude as expected.

In order to analyse those C_{4v} oscillators where fewer experimental

results are available, the number of independent parameters must be reduced further from the present six. This is best achieved by fixing the ratio $^{h}/_{f}$ to leave only f as the independent parameter for the quartic terms. Analysis of the $SrF_2:Pr^{3+}:H^-$ crystal with its seven pieces of experimental data, using this approximation will give an idea of the validity of the approach and define an appropriate range for the $^{h}/_{f}$ ratio. Table VII.2.5 contains the results of a least squares fit for different $^{h}/_{f}$ ratios. The data in the table suggest that the ratio produces valid results in the range $\frac{1}{3} \leq \frac{h}{f} \leq \frac{3}{2}$ and gives minimum deviation at $^{h}/_{f} = 0.80$.

The analysis so far has concentrated on the C_{4v} H^- anharmonic oscillator in $SrF_2:Pr^{3+}$ where all the fundamental and second harmonic frequencies have been experimentally determined. The extra frequencies available over those obtainable from infrared absorption allow the validity of various assumptions concerning parameter ratios to be tested. These relations can now be used for the analysis of other C_{4v} anharmonic oscillators where a complete set of frequencies is not available.

VII.2.3 Calculation of the Potential for the Remaining C_{4v} Oscillators

The C_{4v} H^- oscillator in $CaF_2:Pr^{3+}$

Two (xx) second harmonic frequencies have been measured for the C_{4v} H^- anharmonic oscillator in $CaF_2:Pr^{3+}$ (Table VII.2.3) giving six choices for the assignment of these frequencies to the possible states. A least squares fitting of the six energy level schemes, using the parameter ratios of f = g, h = k and $^{h}/_{f} = 0.80$ determined from the $SrF_2:Pr^{3+}:H^-$ data, reveals two plausible level assignments

Table VII.2.5

Anharmonic parameters for the $SrF_2:Pr^{3+}:H^-$ data using the approximation $^g/_f = 1.0$, $^k/_h = 1.0$

Ratio $\frac{h}{f}$	a cm^{-1}	b cm^{-1}	c ($x10^{10}$ ergs/cm^3)	d ($x10^{10}$ ergs/cm^3)	f ($x10^{17}$ ergs/cm^4)	S.D. cm^{-1}
-5.0	930.5	955.2	105.2	118.6	44.2	1.08
-3.0	929.6	955.1	107.9	114.7	69.9	.98
-2.0	928.6	954.9	110.3	112.2	94.0	.88
-1.0	927.2	954.6	114.1	110.3	133.6	.72
-0.5	926.1	954.4	116.7	110.3	161.6	.59
-0.33	925.7	954.3	117.6	110.7	172.5	.53
-0.2	925.3	954.3	118.4	111.2	181.2	.49
0.0	924.8	954.1	119.6	112.2	195.2	.41
0.2	924.3	954.0	120.9	113.7	209.6	.33
0.33	923.9	953.9	121.7	114.9	218.9	.26
0.5	923.5	953.8	122.7	116.9	230.8	.18
1.0	922.5	953.6	125.1	125.5	258.6	.13
2.0	923.9	953.7	122.1	148.5	224.9	.81
3.0	928.7	954.3	110.2	157.7	101.1	1.22
5.0	932.2	955.1	100.8	151.7	8.1	1.37
0.80	922.8	953.6	124.3	121.6	249.3	0.04

and the results are given in Table VII.2.6.

Table VII.2.6

Anharmonic constants for the two most likely assignments of the observed second harmonic frequencies for the C_{4v} H^- oscillator in $CaF_2:Pr^{3+}$. The quartic parameter ratios used were f = g, h = k and $^h/_f$ = 0.80.

Anharmonic constants	$\|110\gamma_4\rangle$ = 1992.3 cm^{-1} $\|200\gamma_3\rangle$ = 1998.3 cm^{-1}	$\|110\gamma_4\rangle$ = 1992.3 $\|200\gamma_1\rangle$ = 1998.3
w_x	993.4 cm^{-1}	997.7 cm^{-1}
w_z	1138.2 cm^{-1}	1138.3 cm^{-1}
c	$216x10^{10}$ ergs/cm^3	$201x10^{10}$ ergs/cm^3
d	$176x10^{10}$ ergs/cm^3	$176x10^{10}$ ergs/cm^3
f	$498x10^{17}$ ergs/cm^4	$300x10^{17}$ ergs/cm^4
S.D.	.5 cm^{-1}	.3 cm^{-1}
	$\|200\gamma_1\rangle$ = 2001.5	$\|200\gamma_3\rangle$ = 1995.8

The level assignment in the second column gave the smaller deviation and was chosen for further analysis regarding the variation of the ratio $^h/_f$. Table VII.2.7 contains the results of the least squares fitting procedure for this analysis. With this assignment the deviation minimises at a ratio of $^h/_f = -0.33$ but within the precision of the data the range is $-3.0 < {}^h/_f < 2.0$. The value of $^h/_f$ is less well determined here than for $SrF_2:Pr^{3+}:H^-$ as less data are available. Comparison between Tables VII.2.5 and VII.2.7 shows that the anharmonic constants for the two H^- oscillators are of similar magnitude.

Table VII.2.7

Anharmonic parameters for the C_{4v} H^- oscillator in $CaF_2:Pr^{3+}$ with varying quartic ratios (f=g, h=k).

$h_{/f}$	w_x cm^{-1}	w_z cm^{-1}	c ($x10^{10}$ ergs/cm^3)	d ($x10^{10}$ ergs/cm^3)	f ($x10^{17}$ ergs/cm^4)	S.D. cm^{-1}	$\|200\Gamma_3\rangle$ cm^{-1}
5.0	1000.6	1139.4	194	245	186	1.08	1989.6
3.0	998.2	1138.8	199	222	260	.76	1991.5
2.0	997.5	1138.5	201	202	287	.55	1993.2
1.0	997.6	1138.3	201	180	300	.32	1995.3
0.5	997.9	1138.3	200	169	299	.20	1996.4
0.33	998.0	1138.3	200	166	298	.16	1996.7
0.2	998.1	1138.3	200	163	297	.13	1997.0
0.0	998.3	1138.3	200	159	294	.08	1997.4
-0.2	998.6	1138.3	199	155	291	.04	1997.8
-0.33	998.7	1138.3	199	153	289	.01	1998.0
-0.5	998.9	1138.3	199	150	286	.03	1998.3
-1.0	999.6	1138.4	197	142	274	.13	1999.1
-2.0	1000.9	1138.6	195	129	247	.32	2000.4
-3.0	1002.2	1138.8	192	121	219	.48	2001.2
-5.0	1004.1	1139.2	188	114	169	.70	2002.0

Analysis of the deuterium and tritium anharmonic oscillators has not been previously attempted, in general due to the difficulty in observing sufficient numbers of infrared absorption transitions. Local mode frequencies have been measured from emission spectra for the C_{4v} D^- and T^- anharmonic oscillators in $SrF_2:Pr^{3+}$ and $CaF_2:Pr^{3+}$ crystals (Table VII.2.3). These oscillators will be briefly examined in turn.

The C_{4v} D^- oscillator in $SrF_2:Pr^{3+}$

Only one (xx) second harmonic was observed for the $SrF_2:Pr^{3+}:D^-$ oscillator at 1322.9 cm^{-1}. Since all three were observed for the H^- ion the most likely reason for their absence is insufficient spectral resolution. With all three (xx) second harmonic state energies set to the one observed frequency the following anharmonic constants were determined:

$$w_x = 668.6 \text{ cm}^{-1}$$
$$w_z = 695.8 \text{ cm}^{-1}$$
$$c = 120 \times 10^{10} \text{ ergs/cm}^3$$
$$d = 190 \times 10^{10} \text{ ergs/cm}^3$$
$$f = -81 \times 10^{17} \text{ ergs/cm}^4$$
$$\text{S.D.} = 0.2 \text{ cm}^{-1}.$$

The sign of f is negative here as the observed (xx) second harmonic at 1322.9 cm^{-1} is at a frequency less than twice the fundamental frequency, calculated to be 668.6 cm^{-1}. This difference in sign from the H^- results suggests that the constants determined are not representing a similar physical situation. If the harmonic parameter w_x is held at a value close to the observed fundamental frequency,

which can be justified from the results of the H^- oscillator in $SrF_2:Pr^{3+}$ and $CaF_2:Pr^{3+}$ (Tables VII.2.4 and VII.2.6), the results obtained for the three possible choices of energy level assignment are shown in Table VII.2.8.

The constants determined in the first and second schemes compare favourably with those determined for the H^- case (Table VII.2.4). In addition, the calculated level schemes show small separations between the three (xx) second harmonic levels that would be difficult to resolve, giving the appearance of a single second harmonic transition.

The C_{4v} D^- oscillator in $CaF_2:Pr^{3+}$.

Two (xx) second harmonic local mode transitions were observed for the D^- oscillator in $CaF_2:Pr^{3+}$. However the splitting of 9 cm^{-1} between these two levels is greater than that of 6 cm^{-1} for the H^- case when it should be reduced by the isotopic mass ratio. As the selection rules will be the same in each case, there appears to be no reason for the observed transitions to be terminating on different vibrational states in order to explain the different splittings. This difficulty with the splitting is manifested in the least squares fit results with satisfactory convergence only being obtained with the level symmetries inverted from the assignment of the H^- oscillator.

The two (xx) second harmonics at 1435 and 1444 cm^{-1} can be individually assigned to the three states $|200\gamma_1\rangle$, $|200\gamma_3\rangle$ and $|110\gamma_4\rangle$ to give six choices of an energy level scheme. Fixing the value of w_x at the observed fundamental frequency of 722.8 cm^{-1}, the six choices of levels were subject to a least squares fit and the results are given in Table VII.2.9.

Table VII.2.8

Anharmonic oscillator parameters for the C_{4v} D^- oscillator in $SrF_2:Pr^{3+}$. The three columns are the results for the three choices of energy level assignment.

Anharmonic Constants	$\|200\gamma_1\rangle$ = 1322.9 cm^{-1}	$\|200\gamma_3\rangle$ = 1322.9 cm^{-1}	$\|110\gamma_4\rangle$ = 1322.9 cm^{-1}
w_x (cm^{-1})	662.7	662.7	662.7
w_z (cm^{-1})	693.2	694.0	695.5
c ($ergs/cm^3$)	130 x 10^{10}	138 x 10^{10}	154 x 10^{10}
d ($ergs/cm^3$)	132 x 10^{10}	146 x 10^{10}	174 x 10^{10}
f ($ergs/cm^4$)	129 x 10^{17}	195 x 10^{17}	352 x 10^{17}
S.D. (cm^{-1})	0.7	0.6	0.4
	$\|200\gamma_3\rangle$ = 1322.6 cm^{-1}	$\|100\gamma_1\rangle$ = 1324.3 cm^{-1}	$\|200\gamma_1\rangle$ = 1326.8 cm^{-1}
	$\|110\gamma_4\rangle$ = 1321.8 cm^{-1}	$\|110\gamma_4\rangle$ = 1322.2 cm^{-1}	$\|200\gamma_3\rangle$ = 1325.3 cm^{-1}

Table VII.2.9

Anharmonic constants for the six choices of second harmonic level assignment for the $CaF_2:Pr^{3+}:D^-$ data.

Anharmonic Constants	(1)	(2)	(3)	(4)	(5)	(6)
w_x (cm^{-1})	722.8	722.8	722.8	722.8	722.8	722.8
w_z (cm^{-1})	809.8	815.8	817.3	820.7	820.0	819.7
c($x10^{10}$ ergs/cm^3)	187	190	197	236	230	227
d($x10^{10}$ ergs/cm^3)	-359	-141	-81	107	90	83
f($x10^{17}$ ergs/cm^4)	145	-332	-346	116	62	40
dev (cm^{-1})	1.6	1.6	1.5	.3	.4	.4
$\|200\gamma_1\rangle$ (cm^{-1})	1439	1436	1435 †	1445	1445	1444 †
$\|200\gamma_3\rangle$ (cm^{-1})	1436	1435 †	1436	1445	1444 †	1444
$\|200\gamma_4\rangle$ (cm^{-1})	1435 †	1438	1438	1444 †	1444	1444

† Second harmonic level that was held fixed to an observed frequency in the least squares fit.

Satisfactory convergence is obtained when the second harmonic at 1444 cm^{-1} is assigned to any one of the three states. Also the parameters determined in these cases are of a similar magnitude to those determined from the H^- data (Table VII.2.6). The model does not appear to be able to cope with the observed transition at 1435 cm^{-1}, either singly nor in conjunction with the second transition at 1444 cm^{-1}. However, the position and polarisation of the observed line provides convincing evidence that 1435 cm^{-1} is a second harmonic frequency of the D^- oscillator. The inability of this simple model to cope with the observed splitting may indicate the presence of a higher order effect, possibly from the close proximity of other levels.

The C_{4v} T^- oscillators in $SrF_2:Pr^{3+}$ and $CaF_2:Pr^{3+}$.

Only four local mode frequencies were measured for the C_{4v} T^- anharmonic oscillator in both $CaF_2:Pr^{3+}$ and $SrF_2:Pr^{3+}$ crystals (Table VII.1.3) as all (xx) second harmonic transitions are obscured by the $^1D_2D_1(000)\rangle \longrightarrow |^3H_4\Gamma_4\gamma_5(001)\rangle$ vibronic transition. In principle the missing frequencies could be obtained by observing vibronic transitions to states of a more clearcut multiplet such as $^3F_2$ but this is difficult as these transitions appear in the near infrared region and generally tend to be stronger when coupled to the ground state of the Pr^{3+} ion.

To circumvent the problems of an over parameterised Hamiltonian, the harmonic parameter w_x was equated to the observed fundamental frequency. This approximation is reasonable, as w_x has converged to a value close to the observed fundamental frequency in the previous analyses. The results from a least squares fit of w_z,c,d and f for the C_{4v} T^- anharmonic oscillator in the two lattices are given in Table VII.2.10.

Table VII.2.10

Anharmonic constants for the T^- oscillator in $SrF_2:Pr^{3+}$ and $CaF_2:Pr^{3+}$ using quartic parameter ratios of $^g/_f = 1.0$, $^k/_h = 1.0$, $^h/_f = 0.8$.

Anharmonic Constants	$SrF_2:Pr^{3+}:T^-$	$CaF_2:Pr^{3+}:T^-$
w_x (cm^{-1}) [1]	558	606
w_z (cm^{-1})	583	682
c $(ergs/cm^3)$	$179x10^{10}$	$251x10^{10}$
d $(ergs/cm^3)$	$119x10^{10}$	$263x10^{10}$
f $(ergs/cm^4)$	$236x10^{17}$	$657x10^{17}$

[1] w_x parameter fixed to the observed fundamental frequency.

The anharmonic oscillator Hamiltonian of equation VII.2.2 is over parameterized even with all seven fundamental and second harmonic frequencies determined. The number of independent parameters must be reduced to have any success at comparing theory with experiment. The two fundamental and three second harmonic frequencies can be measured by infrared absorption, but for some of the anharmonic oscillators in praseodymium doped crystals additional second harmonic frequencies can be measured from emission spectra. The validity of the assumptions used to reduce the number of independent parameters can be tested for these cases as the inclusion of the extra experimental results provides information on the quality of the parameters obtained.

As well as having its successes the simple anharmonic oscillator model represented by equation VII.2.2 also has it failures. Two second harmonic transitions in the D^- oscillator of $CaF_2:Pr^{3+}$ show an energy separation larger than for the H^- oscillator. If the two transitions for these oscillators are to the same vibronic states, the anharmonic oscillator model predicts the energy separation should decrease by the isotopic mass ratio. Second order effects from nearby levels would need to be introduced to reconcile the model with these results.

The anharmonic constants calculated for the H^-, D^- and T^- oscillators in $SrF_2:Pr^{3+}$ and CaF_2Pr^{3+} are summarised in Table VII.2.11.

Table VII.2.11

Summary of the C_{4v} anharmonic oscillator constants for the H^-, D^- and T^- oscillators in $SrF_2:Pr^{3+}$ and $CaF_2:Pr^{3+}$ crystals using the quartic parameter ratios $^g/_f = 1.0$, $^k/_f = 1.0$, $^h/_f = 0.8$

Anharmonic Constants	$SrF_2:Pr^{3+}:H^-$	$SrF_2:Pr^{3+}:D^-$	$SrF_2:Pr^{3+}:T^-$
w_x (cm^{-1})	922.8	662.7	558
w_z (cm^{-1})	953.6	695.5	583
c ($ergs/cm^3$)	$124x10^{10}$	$154x10^{10}$	$179x10^{10}$
d ($ergs/cm^3$)	$122x10^{10}$	$174x10^{10}$	$119x10^{10}$
f ($ergs/cm^4$)	$124x10^{17}$	$154x10^{17}$	$179x10^{17}$

Anharmonic Constants	$CaF_2:Pr^{3+}:H^-$	$CaF_2:Pr^{3+}:D^-$	$CaF_2:Pr^{3+}:T^-$
w_x (cm^{-1})	997.7	722.8	606
w_z (cm^{-1})	1138.3	820.7	682
c ($ergs/cm^3$)	$201x10^{10}$	$236x10^{10}$	$251x10^{10}$
d ($ergs/cm^3$)	$176x10^{10}$	$107x10^{10}$	$263x10^{10}$
f ($ergs/cm^4$)	$300x10^{17}$	$116x10^{17}$	$657x10^{17}$

VII.3 The Electron-Phonon Interaction

It is clear from the observation of local mode vibronic transitions, that there is an interaction between the 4f electrons of the rare-earth ion and the local mode oscillations of the hydrogenic

ion in an adjacent site. This interaction is the electron-phonon interaction and arises from the modulation of the crystal field at the rare-earth ion site by the motion of all the surrounding ions of the lattice. In addition to the appearance of vibronic transitions in the optical spectra other manifestations of the electron-phonon interaction in the hydrogenic sites are:-

1) small isotope shifts in the zero-phonon transitions of the rare-earth ion when paired with an H^-, D^- or T^- ion,
2) shifts in the local mode frequencies when vibronic levels are coupled to different electronic levels,
3) the lifting of the degeneracy for the x,y local mode for some rare-earth ions.

This last effect will be discussed in Section VII.4 of this chapter in light of new experimental results available for the tetragonal hydrogenic sites in $SrF_2:Pr^{3+}$ and $CaF_2:Pr^{3+}$ crystals.

The electron-phonon interaction is the difference between the instantaneous crystal field at the rare-earth ion site and the static crystal field produced with the ions at their equilibrium positions. Since this interaction will be small compared to the rare-earth ion electronic energy levels and the energies of any phonons involved, the adiabatic approximation (see for example Fong [1976]) can be invoked to separate the fast electronic system from the slower vibrational system. Following Pollack and Satten [1962] the electron-phonon interaction Hamiltonian is written as

$$V_{ev} = \sum_i f_i^{\alpha} Q_i^{\alpha} + \sum_{i,j} g_{ij}^{\alpha\beta} Q_i^{\alpha} Q_j^{\beta} + \ldots \qquad \text{(VII.3.1)}$$

where the f_i^{α} and $g_{ij}^{\alpha\beta}$ are functions of the coordinates of the rare-earth ion 4f electrons, and the Q_i^{α} are phonon normal coordinates

which transform according to the αth irreducible representation of the point group of the rare-earth ion site. As a Hamiltonian, V_{ev} spans the totally symmetric representation of this point group and the coordinate functions f_i^{α} and $g_{ij}^{\alpha\beta}$ must transform as the complex conjugate representations to those of Q_i^{α} and $Q_i^{\alpha}Q_j^{\beta}$ respectively, i.e. to those of Γ^{α} and $\Gamma^{\alpha} \times \Gamma^{\beta}$.

The electron-phonon interaction effects of interest involve the localised modes of the hydrogen, deuterium and tritium ions and only the normal coordinates of these phonons need be considered as the regular lattice modes are expected to be similar for all three cases. For the hydrogenic ion in an essentially static environment, the phonon normal coordinates are just X, Y and Z, the displacements of the light ion from its equilibrium position. The particular Pr^{3+}-H^{-} ion pairs of interest are those forming the tetragonal site making it convenient to group the displacement coordinate terms so that they form basis functions for the irreducible representations of the C_{4v} group. Then to quadratic terms in these coordinates, the electron-local mode phonon interaction is for C_{4v} symmetry

$$\begin{aligned} V_{ev} = {} & f_x X + f_y Y + f_z Z + \tfrac{1}{2}(g_{xx} + g_{yy})(X^2 + Y^2) \\ & + \tfrac{1}{2}(g_{xx} - g_{yy})(X^2 - Y^2) + g_{xy}XY + g_{xz}XZ + g_{yz}YZ \\ & + g_{zz}Z^2 \end{aligned} \qquad \text{(VII.3.2)}$$

The form of the electronic coordinate functions f_i and g_{ij} depend on the particular model chosen for the electron-phonon interaction, the simplest being that of the point charge model where the potential energies of the rare-earth ions' 4f electrons are evaluated in the electric field of the hydride ion treated as a point charge. Another model is the dipole model where the energies of the 4f electrons are

evaluated in the dipole field of the hydride ion. Both models have been discussed for electron-phonon interaction effects in Ce^{3+} - H^- centres by Jacobs et al [1971].

The crystal field potential may be expanded as a Taylor series in the hydride ion displacements to give

$$V_c = V_{co} + \sum_i \left[\frac{\partial V_{co}}{\partial X_i} \right] \Delta X_i + \frac{1}{2} \sum_{i,j} \left[\frac{\partial^2 V_{co}}{\partial X_i \partial X_j} \right] \Delta X_i \Delta X_j + \ldots \qquad \text{(VII.3.3)}$$

where V_{co} is crystal field potential with all lattice ions at their equilibrium positions. Then the electron-phonon interaction is

$$V_{ev} = \sum_i \left[\frac{\partial V}{\partial X_i} \right] \Delta X_i + \frac{1}{2} \sum_{i,j} \left[\frac{\partial^2 V}{\partial X_i \partial X_j} \right] \Delta X_i \Delta X_j + \ldots \qquad \text{(VII.3.4)}$$

Comparing equations VII.3.2 and VII.3.4 the electronic functions f_i and g_{ij} can thus be obtained by the differentiation of the crystal field potential with respect to the hydride ion coordinates.

Using a point charge model the electrostatic potential $V(r,\theta,\phi)$ at a point (r,θ,ϕ) from a charge q_j at a point $\underset{\sim}{R}_j$ is

$$V(r,\theta,\phi) = k \frac{q_j}{|\underset{\sim}{R}_j - \underset{\sim}{r}|} \qquad \text{(VII.3.5)}$$

If ω is the angle between $\underset{\sim}{R}_j$ and $\underset{\sim}{r}$ then

$$\frac{1}{|\underset{\sim}{R}_j - \underset{\sim}{r}|} = \sum_{n=0}^{\infty} \frac{r^n}{R^{(n+1)}} P_n^{\,o}(\cos\omega) \qquad \text{(VII.3.6)}$$

where the $P_n^{\,o}$ are the Legendre polynomials related to spherical

harmonics by

$$P_n^{\,o}(\cos\omega) = \frac{4\pi}{(2n+1)} \sum_{m=-n}^{n} (-1)^m \, Y_n^{-m}(\theta_j,\phi_j) \, Y_n^{\,m}(\theta_i,\phi_i) \qquad \text{(VII.3.7)}$$

Then the potential at (r,θ,ϕ) due to a single charge q_j is

$$V(r,\theta,\phi) = \sum_{n} \sum_{m=-n}^{n} r^n \, \gamma_{nm} \, Y_n^m(\theta,\phi) \qquad \text{(VII.3.8)}$$

where

$$\gamma_{nm} = \frac{4\pi}{(2n+1)} \frac{k\, q_j}{R_j^{(n+1)}} (-1)^m \, Y_n^{-m}(\theta_j,\phi_j)$$

The spherical harmonics $Y_n^{\,m}(\theta,\phi)$ are related to the Racah tensor operators $C_q^{(k)}$ by

$$C_q^{(k)} = \sqrt{\frac{4\pi}{2k+1}} \, Y_k^{\,q} \qquad \text{(VII.3.9)}$$

and equation VII.3.8 takes on the familiar tensor operator expansion for the crystal field of

$$V = \sum_{n=0}^{\infty} \sum_{m=-n}^{n} B_m^{\,n} \, C_m^{(n)} \qquad \text{(VII.3.10)}$$

with

$$B_m^{\,n} = q_j \frac{r^n}{R_j^{(n+1)}} \sqrt{\frac{4\pi}{2n+1}} \; (-1)^m \, Y_n^{-m}(\theta_j,\phi_j)$$

This form of the potential using spherical harmonics is commonly

used for the calculation of the crystal field of point charges. However for crystal fields using dipole moments or for the calculations of the coefficients of the electron-phonon interaction, derivatives of the potential function with respect to the cartesion coordinates are required and it is more convenient to use tesseral harmonics. For this calculation we will use the solid harmonics defined by Zdansky and Edgar [1971] as

$$T^{m}_{n,x} = r^{n} P^{m}_{n}(\cos\theta) \cos m\phi$$
$$T^{m}_{n,y} = r^{n} P^{m}_{n}(\cos\theta) \sin m\phi \qquad \text{(VII.3.11)}$$

for n,m positive integers and $m \leq n$. Here r,θ,ϕ are the spherical polar coordinates for the 4f electrons and the $P^{m}_{n}(\xi)$ are the associated Legendre polynomials

$$P^{m}_{n}(\xi) = (-1)^{n} \frac{(1-\xi^{2})^{\frac{m}{2}}}{2^{n}n!} \frac{d^{n+m}}{d\xi^{n+m}} (\xi^{2}-1)^{n} \qquad \text{(VII.3.12)}$$

Note that these solid harmonics differ from the more usual definition of tesseral harmonics by the inclusion of the factor r^{n}.

The solid harmonics of equation VII.3.11 are easily differentiated with respect to the cartesion coordinates x, y and z using the following recurrence relations reproduced from Zdansky and Edgar [1971]

$$\frac{\partial}{\partial z} T^{m}_{n,x} = (n+m) T^{m}_{n-1,x} \quad , \qquad \frac{\partial}{\partial z} T^{m}_{n,y} = (n+m) T^{m}_{n-1,y}$$

for $n, m \geq 0$,

and

$$
\begin{aligned}
2\frac{\partial}{\partial x} T^{m}_{n,x} &= -(n+m)(n+m-1)T^{m-1}_{n-1,x} + T^{m+1}_{n-1,x} \,, \\
2\frac{\partial}{\partial x} T^{m}_{n,y} &= -(n+m)(n+m-1)T^{m-1}_{n-1,y} + T^{m+1}_{n-1,y} \,, \\
2\frac{\partial}{\partial y} T^{m}_{n,x} &= +(n+m)(n+m-1)T^{m-1}_{n-1,y} + T^{m+1}_{n-1,y} \,, \\
2\frac{\partial}{\partial y} T^{m}_{n,y} &= -(n+m)(n+m-1)T^{m-1}_{n-1,x} - T^{m+1}_{n-1,x}
\end{aligned}
\qquad \text{(VII.3.13)}
$$

for $n \geq 0$, $m \geq 1$, and

$$
\frac{\partial}{\partial x} T^{0}_{n,x} = T^{1}_{n-1,x} \,, \qquad \frac{\partial}{\partial y} T^{0}_{n,x} = T^{1}_{n-1,y}
$$

for $n \geq 0$ ($m=0$). Here it is understood that $T^{m}_{n,i} = 0$ for $m > n$.

The Coulomb potential at $\underset{\sim}{r}$ of a unit point charge at $\underset{\sim}{R}$ can now be written in terms of solid harmonics for $|\underset{\sim}{R}| > |\underset{\sim}{r}|$ as

$$
\frac{1}{|\underset{\sim}{R}-\underset{\sim}{r}|} = \Sigma\, M_n^{\,m} \frac{1}{R^{(2n+1)}} \left[T^{m}_{n,x}(\underset{\sim}{R}) T^{m}_{n,x}(\underset{\sim}{r}) + T^{m}_{n,y}(\underset{\sim}{R}) T^{m}_{n,y}(\underset{\sim}{r}) \right] \qquad \text{(VII.3.14)}
$$

where

$$
M_n^{\,m} = 2\frac{(n-m)!}{(n+m)!} \qquad \text{for } m \neq 0
$$

$$
M_n^{\,m} = 1 \qquad \text{for } m = 0
$$

Also the expansion VII.3.14 can be used to derive the dipole moment potential at $\underset{\sim}{r}$ due to a dipole moment at $\underset{\sim}{R}$ as

$$
\underset{\sim}{p} \cdot \operatorname{grad} \frac{1}{|\underset{\sim}{R}-\underset{\sim}{r}|} = p_x \frac{\partial}{\partial x} \frac{1}{|\underset{\sim}{R}-\underset{\sim}{r}|} + p_y \frac{\partial}{\partial y} \frac{1}{|\underset{\sim}{R}-\underset{\sim}{r}|} + p_z \frac{\partial}{\partial z} \frac{1}{|\underset{\sim}{R}-\underset{\sim}{r}|} \qquad \text{(VII.3.15)}
$$

The electronic functions f_i and g_{ij} can be obtained from the derivatives of the potential, evaluated using the recursion relations

VII.3.13. The appropriate derivatives have been developed by Zdansky & Edgar [1971] with corrected versions summarised by Edgar [1974]. Using these derivatives and the $C_{\infty v}$ and C_{4v} group tables the following relations can be established between the f_i and g_{ij} electronic functions and the solid harmonics $T_{n,x}^{m}$ and $T_{n,y}^{m}$ (Jacobs et al [1971])

$$\begin{aligned} f_z &= a_{0n}\, T_n^0 \quad , & g_{zz} &= b_{0n}\, T_n^0 \\ f_x &= a_{1n}\, T_{n,x}^1 \quad , & (g_{xx} + g_{yy}) &= c_{on}\, T_n^0 \\ f_y &= a_{1n}\, T_{n,y}^1 \quad , & g_{xz} &= b_{1n}\, T_{n,x}^1 \\ & & g_{yz} &= b_{1n}\, T_{n,y}^1 \\ & & g_{xx} - g_{yy} &= b_{2n}\, T_{n,x}^2 \\ & & g_{xy} &= c_{2n}\, T_{n,y}^2 \end{aligned} \qquad \text{(VII.3.16)}$$

where the constants a_{in}, b_{in} and c_{in} depend on the particular model chosen for the light ion interaction. The form of these constants has been derived by Jacobs et al [1971] for the point charge model, the dipole moment model and the polarisation of the fluorine ion model. Since the Racah tensor operators $C_m^{(n)}$ are related to the solid harmonics by

$$C_{\pm m}^{(n)} = \frac{1}{r^n} \left[\frac{(n-m)!}{(n+m)!} \right]^{\frac{1}{2}} \left(T_{n,x}^{m} \pm i T_{n,y}^{m} \right) \qquad \text{(VII.3.17)}$$

expansions of the f_i and g_{ij} in the $C_q^{(n)}$'s can easily be found. Then the matrix elements of the f_i and g_{ij} functions between the electronic states of the rare-earth ions' 4f electrons can be evaluated using the techniques of Wybourne [1965]. Symmetry arguments restrict the values of n to 2, 4 and 6 as the electronic states here are states of an $\ell = 3$ configuration

VII.4 Vibronic splittings in the local mode spectra

VII.4.1 Introduction

For a hydrogenic ion in a C_{4v} symmetry site the x,y local mode vibration has a two fold degeneracy. However in this site the hydrogenic ion does not exist in isolation and for rare-earth ions possessing degenerate ground states the electron-phonon interaction between the rare-earth electrons and the hydrogenic ion local mode can produce a splitting of the degenerate x,y vibronic level. Such splittings have been previously reported for tetragonal Ce^{3+}- H^- ion pairs (Jacobs et al [1971]) and Pr^{3+}- H^- ion pairs (Jacobs [1971]) in calcium and strontium fluorides. Quantitative calculations on the extent of these splittings have been reasonably successful for the Ce^{3+}- H^- case but past attempts for the Pr^{3+}- H^- centres were hindered by there being little information available on the crystal field levels of the ground state multiplet. Table VII.4.1 reproduced from Jacobs [1971] lists the hydrogenic local mode frequencies measured from infra-red absorption for the tetragonal Pr^{3+}- H^- ion pairs in calcium and strontium fluorides.

Local mode vibrations can be observed in emission spectra as transitions to vibronic levels, each having an energy interval from the parent zero phonon line corresponding to the local mode frequency. Results discussed in Chapter V showed that fluorescence transitions have been observed to x,y vibronic levels coupled to several zero phonon lines for the tetragonal Pr^{3+}- H^-, D^- and T^- sites in calcium and strontium fluorides, but splittings have been observed only in the x,y vibronic levels coupled to the ground state.

Table VII.4.1

Infrared absorption measurements for the H^- local modes in the tetragonal Pr^{3+}-H^- ion sites.

Crystal	Mode	Frequency (cm^{-1})	Linewidth (cm^{-1})	Relative Intensity
$CaF_2:Pr^{3+}:H^-$	w_{xy}	996.1	0.9	1.0
		996.7	0.9	2.0
		999.5	1.2	1.0
	w_z	1117.5	7.5	4.8
$SrF_2:Pr^{3+}:H^-$	w_{xy}	921.5	1.2	3.0
		922.9	1.0	1.0
	w_z	939.7	1.2	3.4

Figure VII.4.1 shows the polarised emission spectra of transitions to vibronic levels coupled to the ground state for the tetragonal Pr^{3+} sites in SrF_2 crystals with H^-, D^- and T^- charge compensating ions, recorded at 14 K using <100> oriented crystals.

Splittings can be resolved in the x,y vibronic level for the Pr^{3+}- H^- and Pr^{3+}- D^- sites but not for the Pr^{3+}- T^- site. Also apparent is the increasing linewidth along the H^-, D^-, T^- series as the local mode vibrations become less well localised for the heavier isotopes. Similar spectra for the tetragonal sites in $CaF_2:Pr^{3+}$ are shown in Figure VII.4.2. No splittings are apparent for the D^- and T^- ion sites but some structure is observed for the H^- site. The local mode frequencies measured in this work, from fluorescence transitions to ground-state-coupled vibronic levels, are tabulated in Table VII.4.2.

For some sites the splittings measured here are different to those measured by Jacobs [1971]. Possible reasons include instrumental

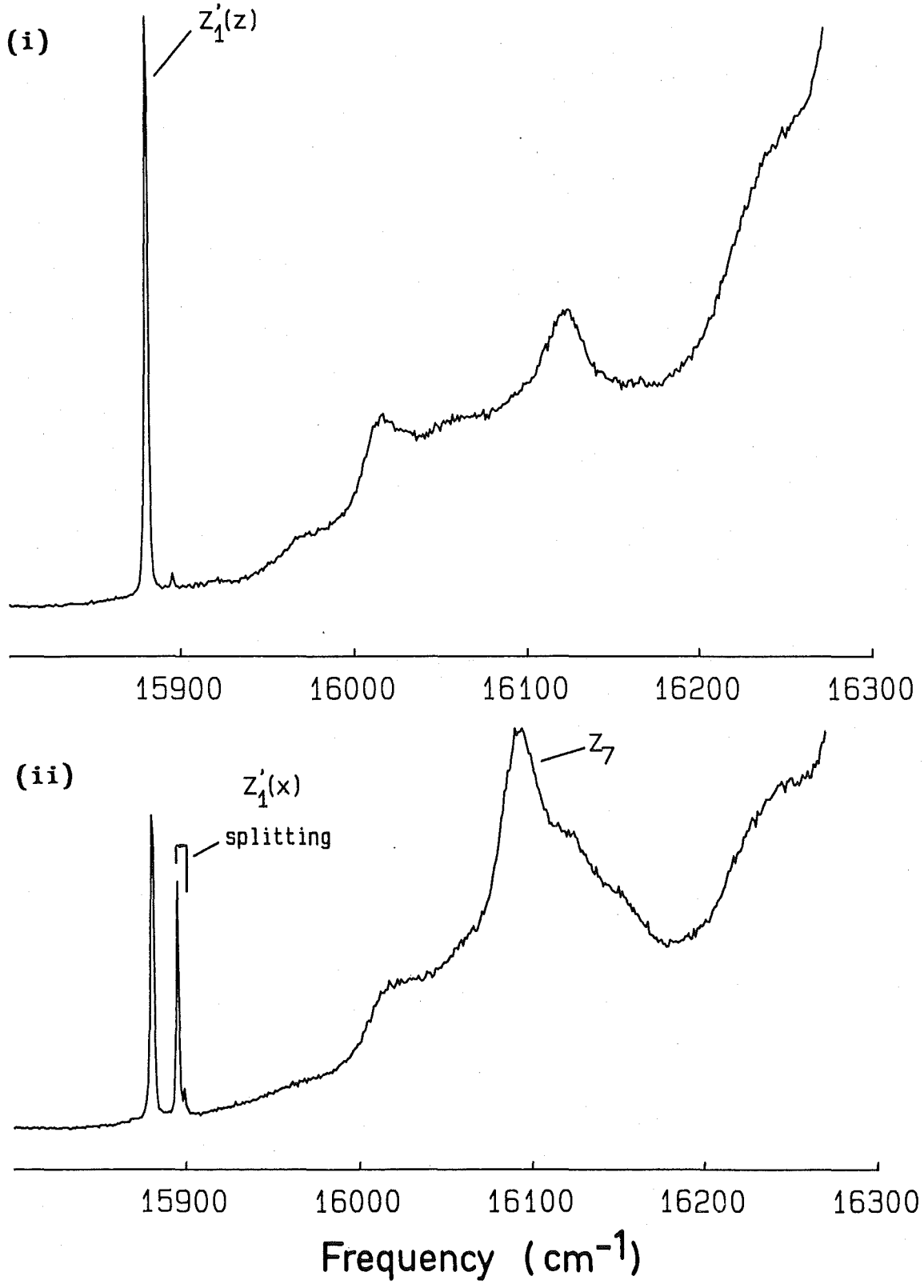

Figure VII.4.1(a) Polarised emission from the C_{4v} H^- site in $SrF_2:Pr^{3+}$ recorded at 14K for the; (i) x(yy)z and (ii) x(yx)z polarisation geometries showing spectral lines for transitions to the fundamental local mode vibronic levels. A splitting of $3.5cm^{-1}$ is apparent in the x,y vibronic line.

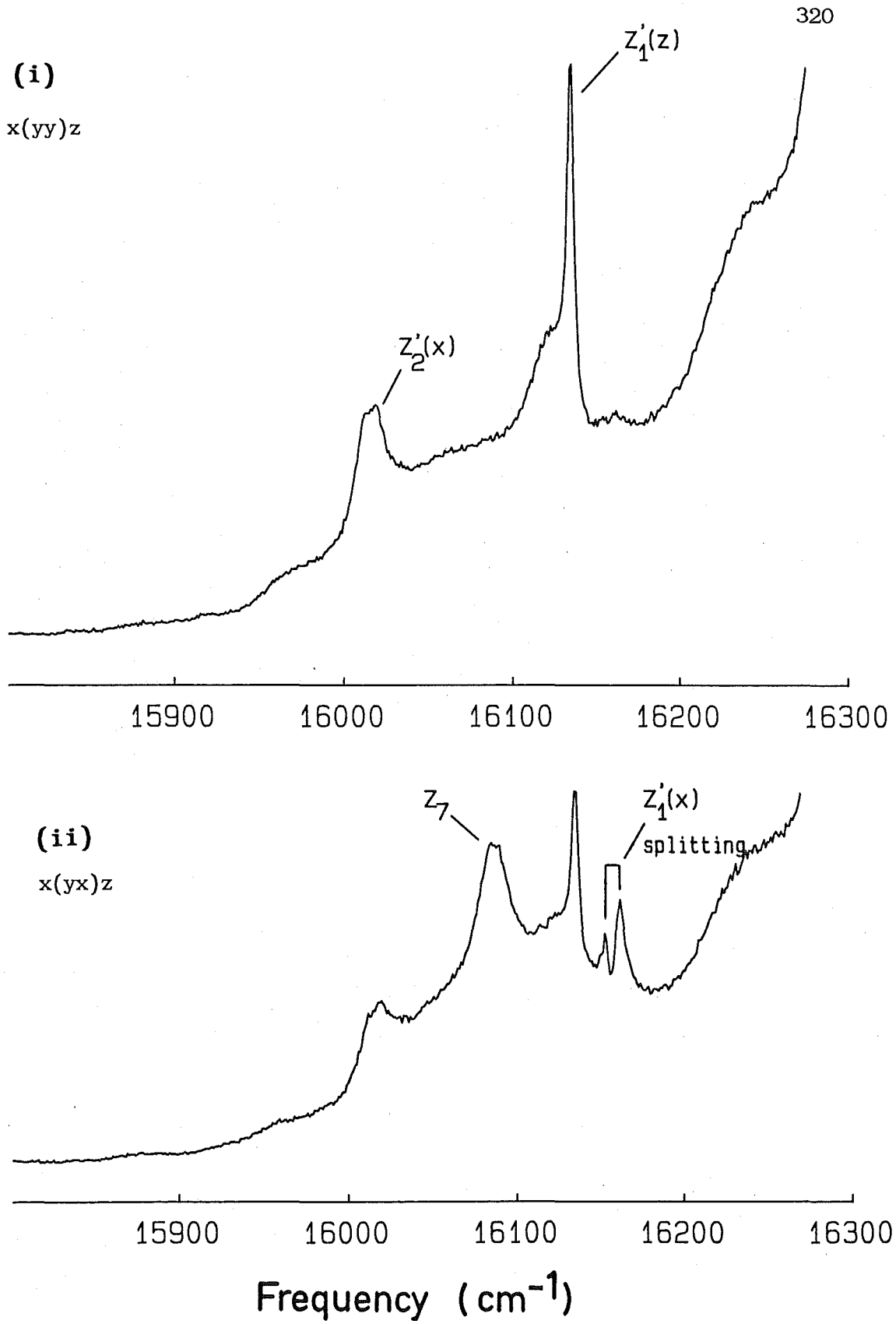

Figure VII.4.1(b) Polarised emission to the fundamental local mode vibronic levels of the C_{4v} D^- site in $SrF_2:Pr^{3+}$. A larger splitting of $8.5cm^{-1}$ is observed in the x,y vibronic line for this site.

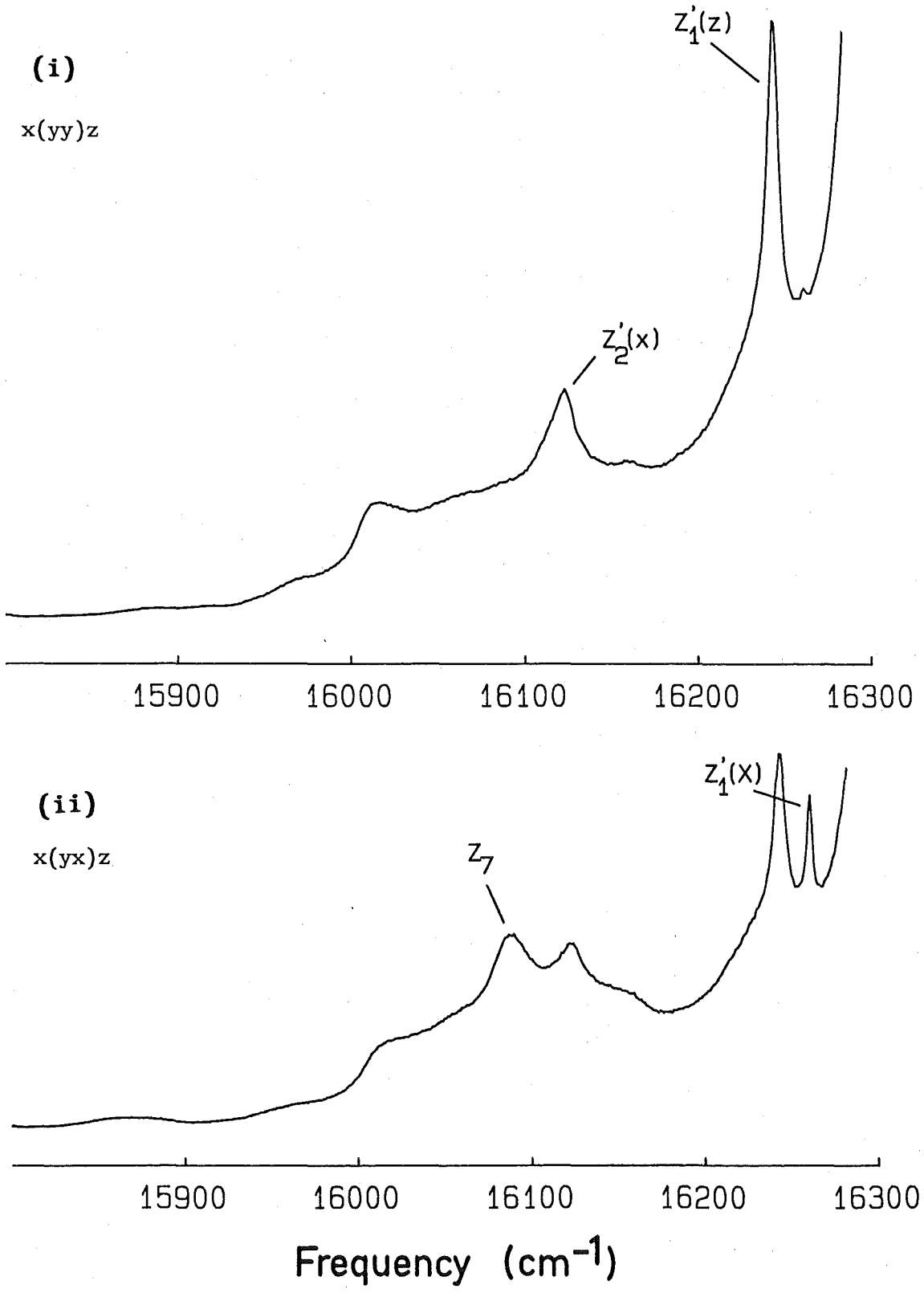

Figure VII.4.1(c) Polarised emission to the fundamental local mode vibronic levels of the C_{4v} T^- site in $SrF_2:Pr^{3+}$. There is no apparent splitting of the x,y vibronic line.

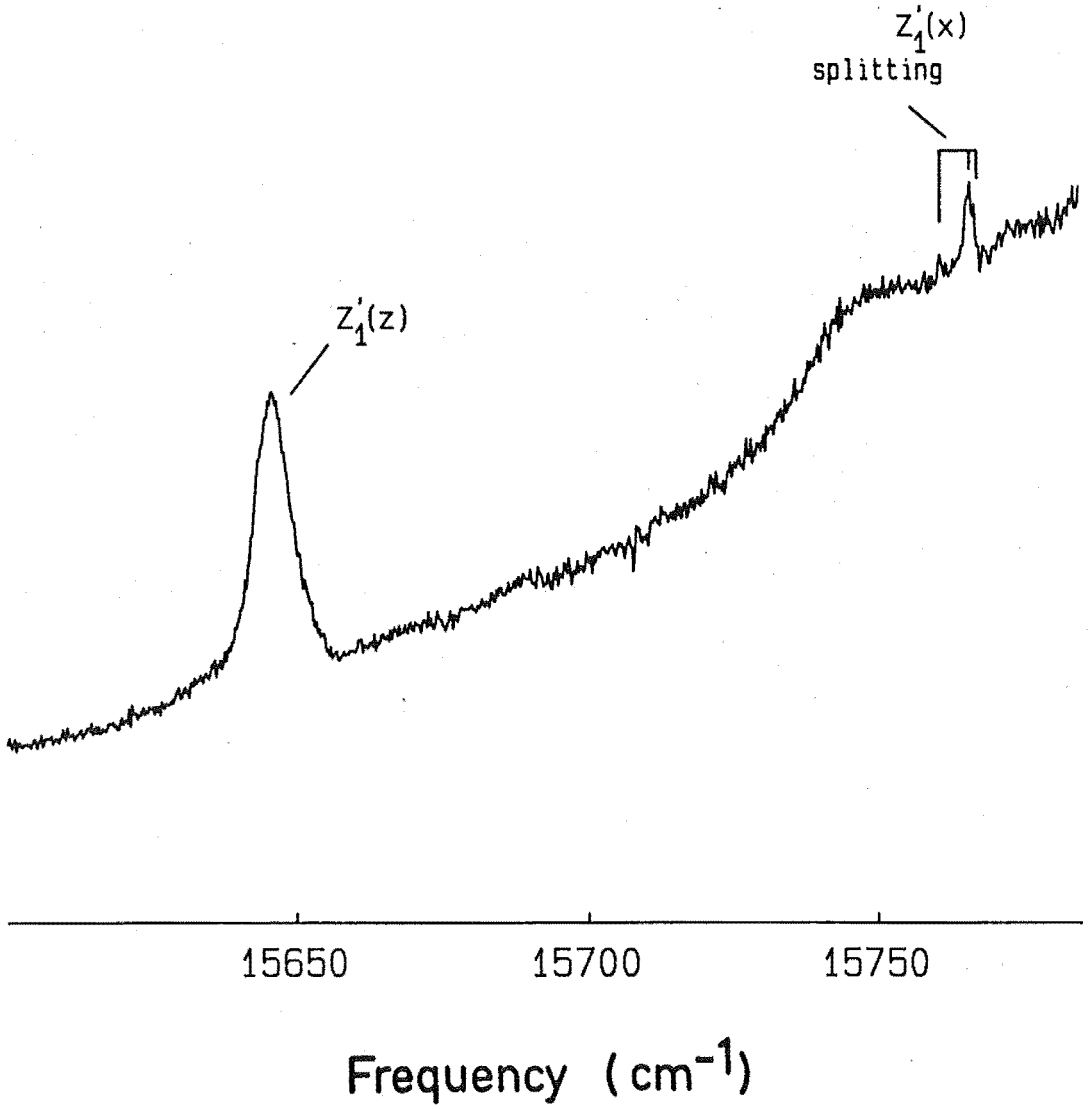

Figure VII.4.2(a) Fluorescence recorded at 14K from the C_{4v} H^- site in $CaF_2:Pr^{3+}$ showing the spectral lines for transitions to the fundamental local mode vibronic levels. A splitting of the x,y vibronic line into three components is apparent.

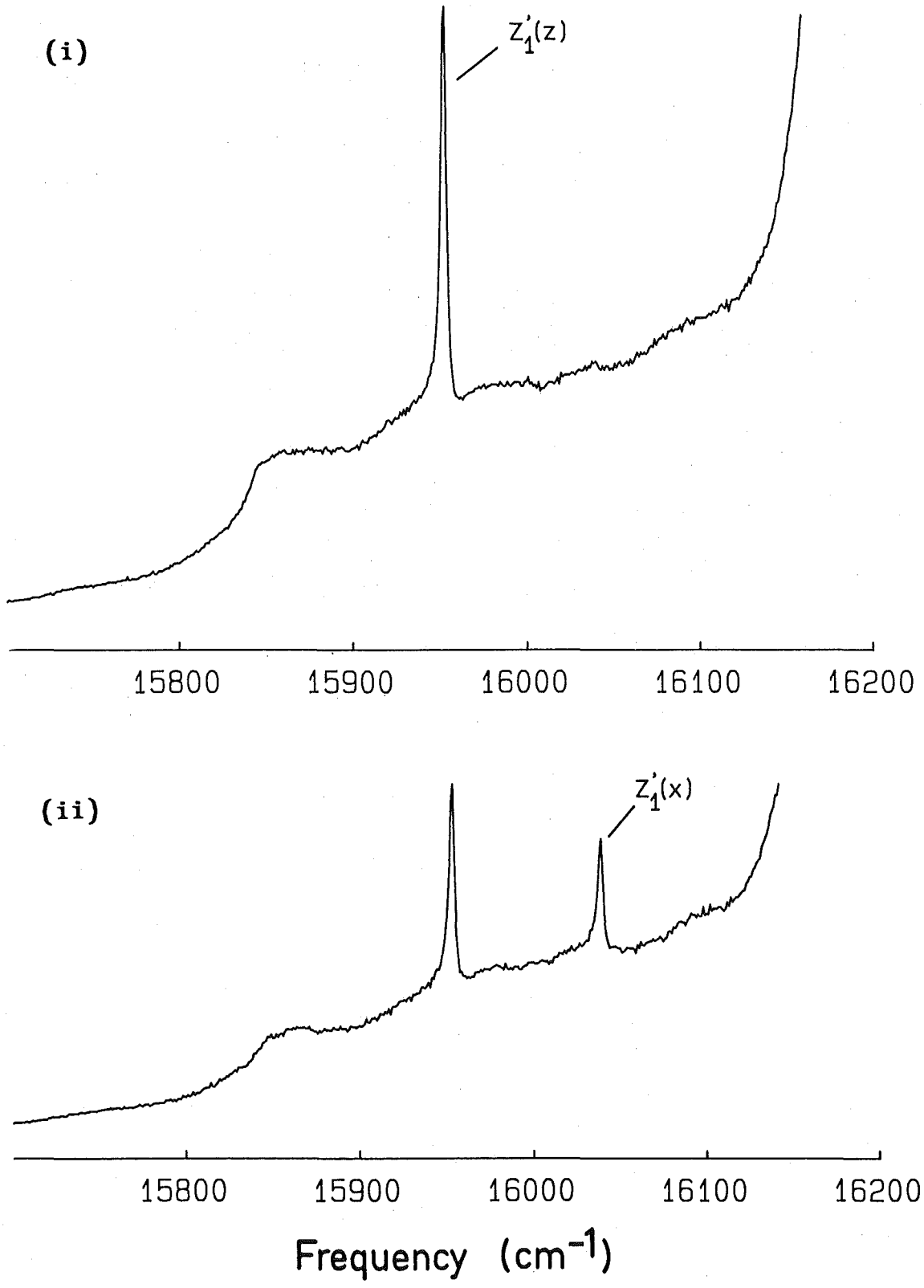

Figure VII.4.2(b) Polarised emission from the C_{4v} D^- site in $CaF_2:Pr^{3+}$ recorded at 14K for the; (i) x(yy)z and (ii) x(yx)z polarisation geometries showing transitions to fundamental local mode vibronic levels. No splitting of the x,y vibronic line is apparent.

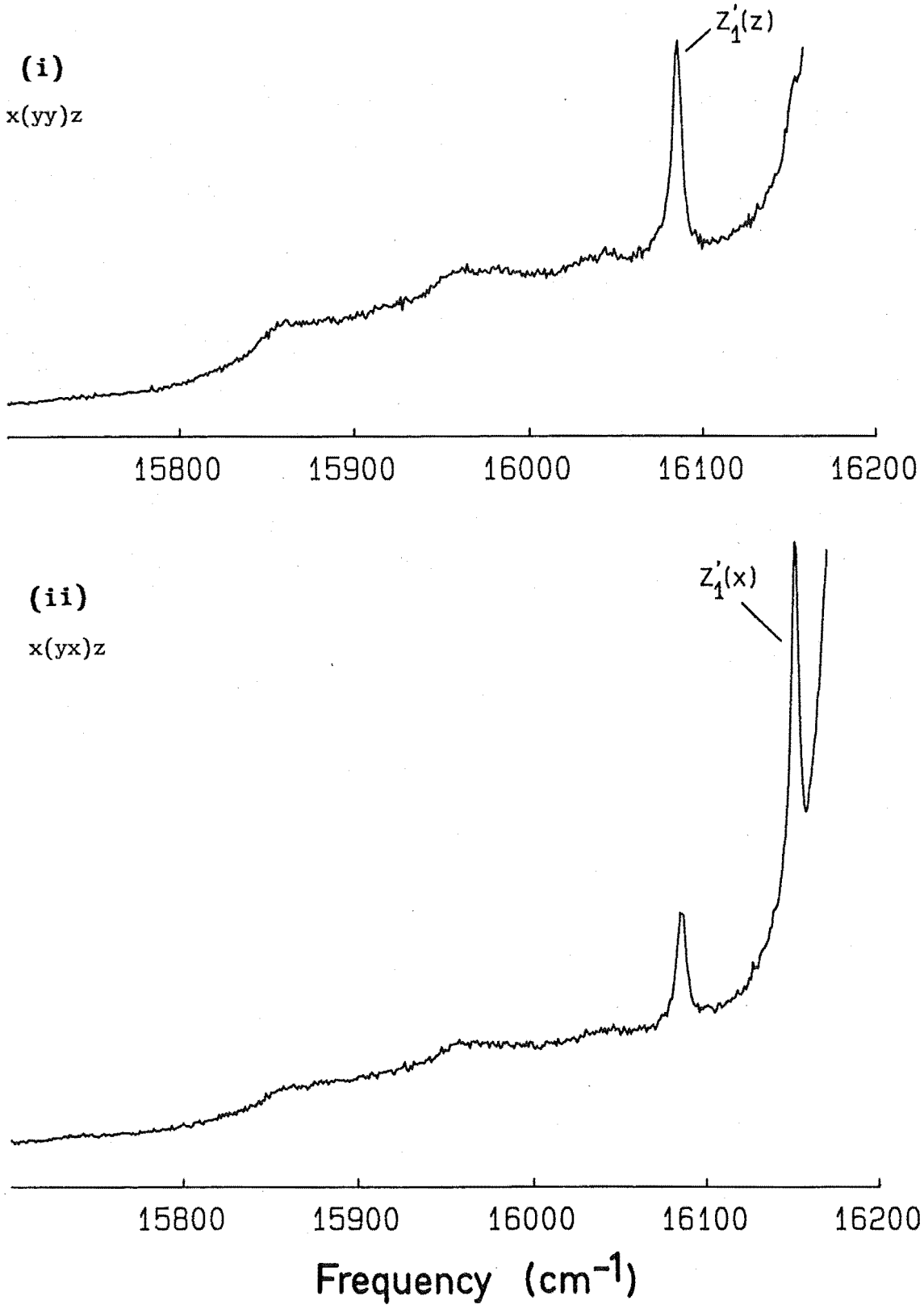

Figure VII.4.2(c) Polarised emission to the fundamental local mode vibronic levels of the C_{4v} T^- site in $CaF_2:Pr^{3+}$. No splitting of the x,y vibronic level is apparent.

effects, as the resolution in this work was inferior to that used in the infrared absorption experiments, and the different selection rules for transitions in the two techniques. In principle, electric dipole transitions to all four x,y vibronic states are observable from the γ_5 symmetry ground state but a lesser number are expected in emission from an excited state not having the same symmetry transformations.

Table VII.4.2

Fundamental local mode frequencies, measured from fluorescence transitions to vibronic levels, for the tetragonal Pr^{3+}-hydrogenic ion sites. The sample temperature was 14 K.

Crystal	Mode	Frequency (cm^{-1})
$SrF_2:Pr^{3+}:H^-$	w_{xy}	921.6 ± .5 925.1 ± .5
	w_z	939.6 ± .5
$SrF_2:Pr^{3+}:D^-$	w_{xy}	658.4 ± .5 666.9 ± .5
	w_z	684.9 ± .5
$SrF_2:Pr^{3+}:T^-$	w_{xy}	558 ± 1
	w_z	575 ± 1
$CaF_2:Pr^{3+}:H^-$	w_{xy}	996.5 ± .3 997.3 ± .3 1002.5 ± .3 *
	w_z	1117.5 ± .3
$CaF_2:Pr^{3+}:D^-$	w_{xy}	722.8 ± .3
	w_z	808.1 ± .3
$CaF_2:Pr^{3+}:T^-$	W_{xy}	606 ± 1
	W_z	673 ± 1

* tentative assignment

The electronic wavefunction of the praseodymium ion ground state transforms as the two-fold degenerate τ_5 irrep of the C_{4v} point group as does the x,y local mode wavefunction. Then since in the C_{4v} group

$$\tau_5 \times \tau_5 = \tau_1 + \tau_2 + \tau_3 + \tau_4 \qquad \text{(VII.4.1)}$$

the x,y local mode vibronic level is split into four components. For the z local mode vibronic level

$$\tau_5 \times \tau_1 = \tau_5 \qquad \text{(VII.4.2)}$$

and the level retains an electronic degeneracy. This is consistent with the polarisation observed in the fluorescence spectra where the transition to the z vibronic level has a x(yy)z:x(yx)z polarisation ratio of 2:1 indicating a σ-polarised transition. For the x,y vibronic level the split components show π-polarisation (Figure VII.4.1). The emission spectra of the hydrogenic sites in $SrF_2:Pr^{3+}$ crystals discussed in Chapter V, show electric dipole transitions terminating on electronic levels transforming as either a τ_1 or τ_3 irrep. The x,y local mode vibronic splitting observed here originates from separate transitions to the τ_1 and τ_3 vibronic levels. For the C_{4v} sites in $CaF_2:Pr^{3+}$ the same relaxation of transition selection rules was not apparent and a single line to the τ_1 vibronic level may be all that is observed even though the splitting appears greater (Table VII.4.1). Figure VII.4.3 summarises some of the levels of the combined electronic-local mode phonon system for the $^3H_4$ multiplet.

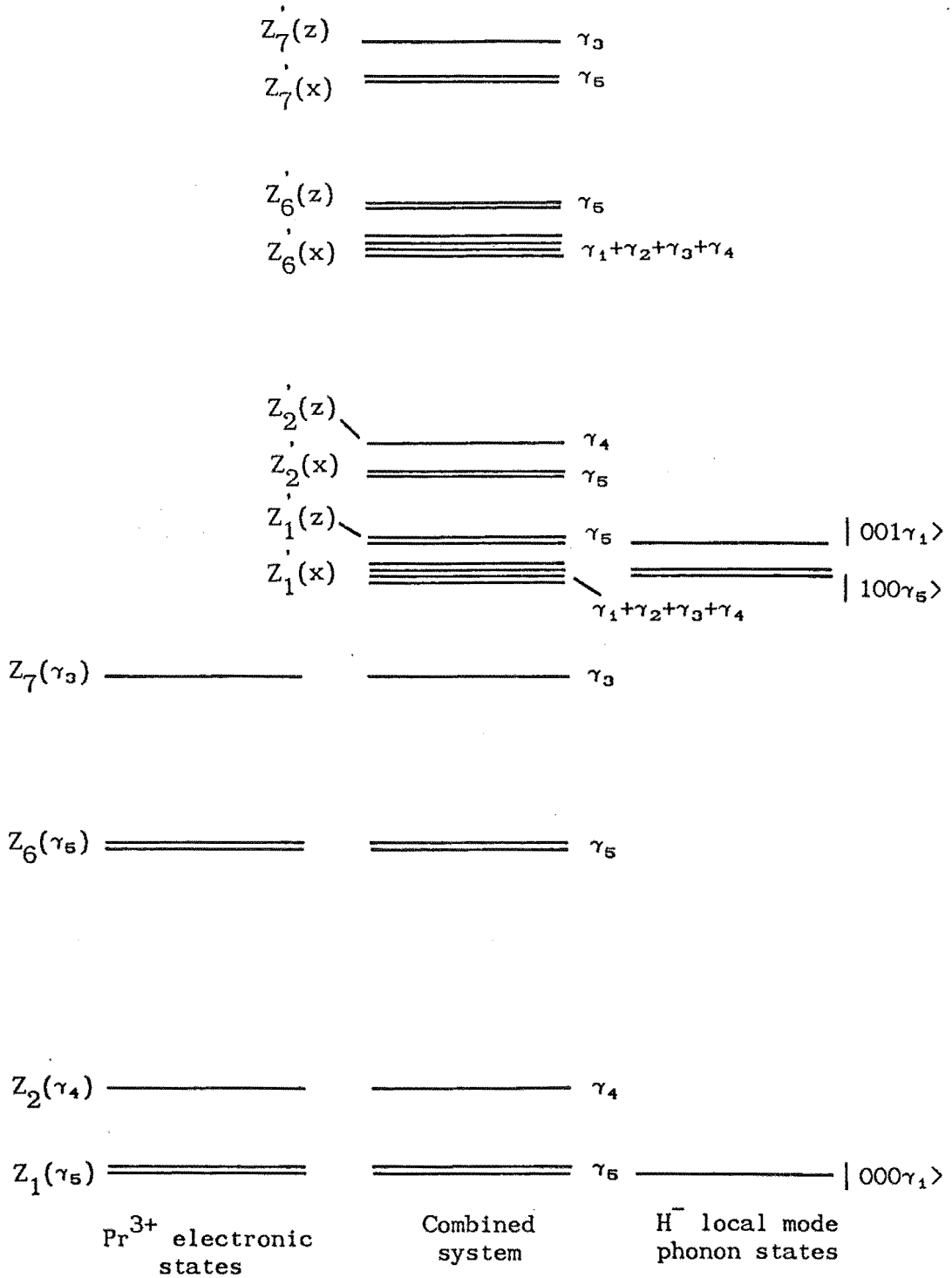

Figure VII.4.3 Some of the energy levels in the combined electronic-local mode phonon system for the $^3H_4$ multiplet of the Pr^{3+}-H^- C_{4v} site.

VII.4.2 Calculation of the First Order Splittings.

Using the Born-Oppenheimer approximation the zero order wavefunctions of the combined system (vibronic wave functions) take the product form

$$\Psi_{in} = \phi_i \psi_n \qquad \text{(VII.4.3)}$$

where ϕ_i and ψ_n are electronic and vibrational wavefunctions respectively. In the $|JM_J\rangle$ basis the cubic crystal field wavefunctions of the doubly degenerate $|^3H_4\Gamma_5\gamma_5\rangle$ Pr^{3+} ion electronic ground state are

$$\begin{aligned} \phi^+ &= \sqrt{\frac{7}{8}}\ |43\rangle - \sqrt{\frac{1}{8}}\ |4{-}1\rangle \\ \phi^- &= \sqrt{\frac{1}{8}}\ |4{-}3\rangle - \sqrt{\frac{7}{8}}\ |41\rangle \end{aligned} \qquad \text{(VII.4.4)}$$

The doubly degenerate x,y vibration of the H^- ion is labelled with states (100) and (010) corresponding to the occupation numbers of the harmonic oscillators. The four x,y vibronic states can be determined by diagonalising the 4x4 matrix formed from the electron-phonon interaction with the four zero order states, $\phi^+(100)$, $\phi^+(010)$, $\phi^-(100)$ and $\phi^-(010)$.

In the electron-phonon interaction, equation VII.3.3, the electronic functions f_i and g_{ij} act only on the electronic component of the vibronic wavefunctions and the X,Y,Z operators act as creation/annihilation operators on the phonon occupation numbers through the equation.

$$X|n\rangle = \sqrt{n+1}\ |\ n+1\rangle + \sqrt{n}\ |n-1\rangle\ . \qquad \text{(VII.4.5)}$$

With the four zero-order vibronic states having only a single non-zero occupation number, the operator in a first order perturbation treatment must be quadratic, i.e. only the operators g_{ij} contribute.

The elements of the 4x4 perturbation matrix are calculated as follows. For the first order perturbation effects being considered at this stage, the phonon operators that have non-zero elements are restricted to X^2+Y^2, X^2-Y^2 and XY as only x and y phonon states are involved. Furthermore the X^2+Y^2 and X^2-Y^2 operators will be strictly diagonal in the phonon states (100) and (010). Then using equation VII.4.5 the matrix elements are constructed and, for example, take the form

$$\langle\phi^+(100)|V_{ev}|\phi^-(100)\rangle = \langle\phi^+|g_{x^2-y^2}|\phi^-\rangle\frac{\hbar}{2mw_x} + \langle\phi^+|g_{x^2+y^2}|\phi^-\rangle\frac{2\hbar}{2mw_x}$$

$$\langle\phi^+(100)|V_{ev}|\phi^+(010)\rangle = \langle\phi^+|g_{xy}|\phi^+\rangle\frac{\hbar}{2mw_x} \qquad \text{(VII.4.6)}$$

Just as the form of the phonon operators limited the number of terms, symmetry arguments on the form of the g_{ij}, operators also restrict the number of non-zero elements. Using the tables of Koster [1963], the degenerate $\phi^{\pm}$ electronic states decompose to states transforming as $\hat{\gamma}_3 + \hat{\gamma}_4$ irreps of the C_4 group. The $g_{x^2+y^2}$ operator transforms as the totally symmetric representation, $\hat{\gamma}_1$, in this group and matrix elements of the form

$$\langle\phi^i|g_{x^2+y^2}|\phi^j\rangle$$

must be diagonal in the ϕ^i's to be non-vanishing. Similarly the γ_4 and γ_3 C_{4v} irreps of the g_{xy} and $g_{x^2-y^2}$ operators both decompose to

the $\hat{\gamma}_2$ irrep of C_4 and matrix elements of the form

$$\langle\phi^i|g_{xy}|\phi^j\rangle \quad \text{and} \quad \langle\phi^i|g_{x^2-y^2}|\phi^j\rangle$$

are non-vanishing only for $\phi^i \neq \phi^j$ as $\hat{\gamma}_4 \times \hat{\gamma}_2 = \hat{\gamma}_3$ in the C_4 group.

Using these restrictions and subtracting the diagonal elements which are now all equal, the first order perturbation matrix reduces to

	$\phi^+(100)$	$\phi^+(010)$	$\phi^-(100)$	$\phi^-(010)$
$\phi^+(100)$	0	0	A	-iB
$\phi^+(010)$	0	0	-iB	-A
$\phi^-(100)$	A	iB	0	0
$\phi^-(010)$	iB	-A	0	0

where

$$A = \langle\phi^+|g_{x^2-y^2}|\phi^-\rangle\frac{\hbar}{2mw_x}$$
$$iB = \langle\phi^+|g_{xy}|\phi^-\rangle\frac{\hbar}{2mw_x} \qquad \text{(VII.4.7)}$$

The four vibronic wavefunctions are the eigenfunctions of the matrix and will be linear combinations of the $\phi^{\pm}(100)$, $\phi^{\pm}(010)$ product states.

Using the operations and character table of the C_{4v} point group the vibronic wavefunctions are found to transform as the following particular representations of C_{4v}.

Vibronic State	Eigenvalue
$\Psi_1 = \sqrt{\frac{1}{2}}\,[\psi_\alpha(010) - i\psi_\beta(100)]$	-A+B
$\Psi_2 = \sqrt{\frac{1}{2}}\,[i\psi_\alpha(100) - \psi_\beta(010)]$	A-B
$\Psi_3 = \sqrt{\frac{1}{2}}\,[\psi_\alpha(010) + i\psi_\beta(100)]$	-A-B
$\Psi_4 = \sqrt{\frac{1}{2}}\,[i\psi_\alpha(100) + \psi_\beta(010)]$	A+B

where $$\psi_\alpha = \sqrt{\frac{1}{2}}\,(\phi^+ + \phi^-)$$

$$\psi_\beta = \sqrt{\frac{1}{2}}\,(\phi^+ - \phi^-)$$

Note that these linear combinations differ from those developed by Zdansky and listed by Jacobs [1971]. Using the coupling coefficients table of Koster [1963] the states ψ_α and ψ_β are seen here to transform as -iy and x respectively. The linear combinations derived in this work were checked using the first degree terms, $f_x X + f_y Y$, of V_{ev} in second order perturbation theory. The Hamiltonian, V_{ev}, transforms as the γ_1 irrep of C_{4v} and only intermediate states transforming as the same irrep as the vibronic wavefunction Ψ_r will contribute an energy shift to the vibronic level Ψ_r. The conflict between the wavefunctions derived here and those of Zdansky is resolved by noting that the form of f_x chosen by Zdansky [private communication] of

$$f_x \sim C_{-1}^{(n)} + C_1^{(n)}$$

differs from that chosen here of

$$f_x \sim C_{-1}^{(n)} - C_1^{(n)}$$

which is consistent with the definition of Wybourne [1965].

The problem of calculating the splittings of the four vibronic states reduces to evaluation of the two matrix elements

$$\langle \phi^+ | g_{x^2-y^2} | \phi^- \rangle$$

$$\langle \phi^+ | g_{xy} | \phi^- \rangle$$

The electronic operators $g_{x^2-y^2}$ and g_{xy} were shown to be (VII.3)

$$\begin{aligned} g_{xy} &= b_{2n} T^2_{n,y} \\ g_{x^2-y^2} &= c_{2n} T^2_{n,x} \end{aligned} \qquad \text{(VII.4.8)}$$

where the $T^2_{n,x}$ and $T^2_{n,y}$ are related to the tesseral harmonics and can be written in terms of Racah tensor operators as

$$\begin{aligned} T^2_{n,x} &= \frac{1}{2}\sqrt{\frac{(n+2)!}{(n-2)!}}\, r^n (C_2^{(n)} + C_{-2}^{(n)}) \\ T^2_{n,y} &= \frac{1}{2}\sqrt{\frac{(n+2)!}{(n-2)!}}\, r^n i (C_{-2}^{(n)} - C_2^{(n)}) \end{aligned} \qquad \text{(VII.4.9)}$$

The constants b_{2n} and c_{2n} depend upon the particular model for the interaction and are given by

$$b_{2n} = c_{2n} = \frac{eq}{D^{(n+3)}} \qquad \text{(VII.4.10)}$$

for the point charge model.

As the dominant contribution to the splitting will arise from the

n = 2 terms, only these terms will be considered for this calculation. The matrix elements are calculated using the equation (Wybourne [1965])

$$\langle SLJJ_z|C_2^{(k)}|SL'J'J'_z\rangle = (-1)^{J-J_z}\begin{pmatrix} J & k & J' \\ J_z & q & J'_z \end{pmatrix}\langle SLJ\|C^{(k)}\|SL'J'\rangle \qquad \text{(VII.4.11)}$$

and are

$$\begin{aligned} \langle\phi^+|C_2^{(2)} + C_{-2}^{(2)}|\phi^-\rangle &= \frac{2^4.13}{3.5^2.11}\frac{1}{\sqrt{6}} \\ \langle\phi^+|C_{-2}^{(2)} - C_2^{(2)}|\phi^-\rangle &= -\frac{2.13^2}{3.5^2.11} \end{aligned} \qquad \text{(VII.4.12)}$$

Thus for n = 2

$$\begin{aligned} A &= \frac{2.13^2}{3.5^2.11}\frac{eq\langle r^2\rangle}{D^5}\frac{\hbar}{2mw_x} \\ B &= -\frac{2.13^2}{3.5^2.11}\frac{eq\langle r^2\rangle}{D^5}\frac{\hbar}{2mw_x} \end{aligned} \qquad \text{(VII.4.13)}$$

Appropriate values for the terms in these equations are D_{SrF_2} = 2.93Å, D_{CaF_2} = 2.73Å, $\langle r^2\rangle_{4f}$ = 1 atomic unit = 0.528Å and e = q = 0.85e. Table VII.4.3 summarises the splittings of the four vibronic states for the three hydrogenic isotopes in the two lattices.

The results in the table show these first order shifts do not account for the observed splittings (Table VII.4.2). In reality the calculated splittings would be even smaller as the point charge value of $B_0^2 = \frac{eq\langle r^2\rangle}{D^3}$ used in the calculation here is approximately twice that measured from the crystal field splitting of the $^3P_1$ multiplet.

Table VII.4.3.

First order energy shifts, due to the electron-phonon interaction, to the x,y vibronic levels.

Crystal	Frequency $w_x(cm^{-1})$	Vibronic state shifts (cm^{-1})				$\Psi_3-\Psi_1$ splitting (cm^{-1})
		Ψ_2	Ψ_3	Ψ_4	Ψ_1	
$SrF_2:Pr^{3+}:H^-$	922	1.30	0.31	-.31	-1.30	1.61
$SrF_2:Pr^{3+}:D^-$	667	0.90	0.21	-.21	- .90	1.11
$SrF_2:Pr^{3+}:T^-$	558	0.46	0.11	-.11	- .46	0.57
$CaF_2:Pr^{3+}H^-$	997	1.71	.41	-.41	-1.71	2.12
$CaF_2:Pr^{3+}:H^-$	723	1.18	.28	-.28	-1.18	1.46
$CaF_2:Pr^{3+}:T^-$	606	.94	.22	- .22	- .94	1.16

VII.4.3 Calculation of the Second Order Splittings.

In addition to the first order splittings of the four x,y vibronic states there are second order splittings through the first degree terms $f_x X + f_y Y$ of the electron-phonon interaction. The matrix elements involved take the form

$$\Delta E_r = \frac{|\langle \Gamma_n \gamma_m(\ell_1 \ell_2 \ell_3) | f_x X + f_y Y | \Psi_r \rangle|^2}{E_{\Gamma_n \gamma_m(\ell_1 \ell_2 \ell_3)} - E_{\Psi_r}} \qquad \text{(VII.4.14)}$$

which gives the energy shift of the x,y vibronic level Ψ_r through the electron-phonon interaction with another vibronic state $\Gamma_n \gamma_m(\ell_1 \ell_2 \ell_3)$. As these second order perturbation shifts depend upon the energy denominater $E_{\Gamma_n \gamma_m(\ell_1 \ell_2 \ell_3)} - E_{\Psi_r}$ only nearby vibronic states will contribute significantly and intermediate states $\Gamma_n \gamma_m(\ell_1 \ell_2 \ell_3)$ can be restricted to the levels of the $^3H_4$ multiplet. The vibronic states Ψ_r have been constructed as linear combinations of the ground state electronic wavefunctions $\phi^{\pm}$ and x,y phonon wavefunctions (100) & (010) to transform as the irreps of the C_{4v} group. Then as V_{ev} transforms as the totally symmetric representation γ_1 of C_{4v}, only intermediate states transforming as the same irrep as Ψ_r will contribute an energy shift to the vibronic level Ψ_r.

In terms of $|JM_J\rangle$ states the cubic crystal field wavefunctions of the excited electronic states of the $^3H_4$ multiplet for the

praseodymium ion are

$$
\begin{aligned}
|\Gamma_5\gamma_4\rangle &= \sqrt{\tfrac{1}{2}}\,\{\ |2\rangle - |{-2}\rangle\ \} \\
|\Gamma_1\gamma_1\rangle &= \sqrt{\tfrac{5}{24}}\,|4\rangle + \sqrt{\tfrac{14}{24}}\,|0\rangle + \sqrt{\tfrac{5}{24}}\,|{-4}\rangle \\
|\Gamma_4\gamma_2\rangle &= \sqrt{\tfrac{1}{2}}\,\{\ |4\rangle - |{-4}\rangle\ \} \\
|\Gamma_3\gamma_1\rangle &= \sqrt{\tfrac{7}{24}}\,|4\rangle + \sqrt{\tfrac{10}{24}}\,|0\rangle + \sqrt{\tfrac{7}{24}}\,|{-4}\rangle \\
|\Gamma_4\gamma_5\rangle &= \sqrt{\tfrac{1}{8}}\,|\pm 3\rangle + \sqrt{\tfrac{7}{8}}\,|\mp 1\rangle \\
|\Gamma_3\gamma_3\rangle &= \sqrt{\tfrac{1}{2}}\,\{\ |2\rangle + |{-2}\rangle\ \}
\end{aligned}
\qquad \text{(VII.4.15)}
$$

Vibronic states, transforming as the γ_n irreps of the C_{4v} point group and constructed from these electronic states and the local mode phonon states (000), (110) and $\sqrt{\frac{1}{2}}\{(200) \pm (020)\}$, are listed in Table VII.4.4. Only those vibronic states listed in the column under each Ψ_r will contribute an energy shift to that vibronic state Ψ_r.

The first degree terms of the electron-phonon interaction that will act in second order perturbation on these particular states Ψ_r are

$$V_{ev} = f_x X + f_y Y$$

where f_x and f_y are electronic operators and X,Y phonon creation/annihilation operators.

The electronic operators f_x and f_y are related to the harmonic functions defined earlier by

$$
\begin{aligned}
f_x &= a_{1n}\, T_{n,x}^2 \\
f_y &= a_{1n}\, T_{n,y}^2
\end{aligned}
\qquad \text{(VII.4.16)}
$$

Table VII.4.4

Vibronic states of the $^3H_4$ multiplet in the hydrogenic C_{4v} Pr^{3+} site having the same transformation properties as the fundamental x,y vibronic levels Ψ_Γ.

Ψ_1	Ψ_2	Ψ_3	Ψ_4
$\|\Gamma_3\gamma_1\rangle$ (000) $\|\Gamma_1\gamma_1\rangle$ (000)	$\|\Gamma_4\gamma_2\rangle$ (000)	$\|\Gamma_3\gamma_3\rangle$ (000)	$\|\Gamma_5\gamma_4\rangle$ (000)
$\|\Gamma_5\gamma_4\rangle$(110)	$\|\Gamma_3\gamma_3\rangle$ (110)	$\|\Gamma_4\gamma_2\rangle$ (110)	$\|\Gamma_3\gamma_1\rangle$ (110) $\|R_1\gamma_1\rangle$ (110)
$\|\Gamma_3\gamma_1\rangle \frac{1}{\sqrt{2}}$ [(200)+(020)] $\|\Gamma_1\gamma_1\rangle \frac{1}{\sqrt{2}}$ [(200)+(020)]	$\|\Gamma_4\gamma_2\rangle \frac{1}{\sqrt{2}}$ [(200)+(020)]	$\|\Gamma_3\gamma_3\rangle \frac{1}{\sqrt{2}}$ [(200)+(020)]	$\|\Gamma_5\gamma_4\rangle \frac{1}{\sqrt{2}}$ [(200)+(020)]
$\|\Gamma_3\gamma_3\rangle \frac{1}{\sqrt{2}}$ [(200)+(020)]	$\|\Gamma_5\gamma_4\rangle \frac{1}{\sqrt{2}}$ [(200)+(020)]	$\|\Gamma_3\gamma_1\rangle \frac{1}{\sqrt{2}}$ [(200)+(020)] $\|\Gamma_1\gamma_1\rangle \frac{1}{\sqrt{2}}$ [(200)+(020)]	$\|\Gamma_4\gamma_2\rangle \frac{1}{\sqrt{2}}$ [(200)+(020)]

which in turn are expressed in Racah tensor operators by

$$T^{2}_{n,x} = \frac{1}{2}\sqrt{\frac{(n+1)!}{(n-1)!}}\, r^{n}(C^{(n)}_{-1} + C^{(n)}_{1})$$

$$T^{2}_{n,y} = \frac{1}{2}\sqrt{\frac{(n+1)!}{(n-1)!}}\, r^{n}\, i(C^{(n)}_{-1} + C^{(n)}_{1}) \qquad \text{(VII.4.17)}$$

The second order perturbation treatment involves calculating matrix elements of the form

$$\langle \Gamma_3\gamma_3(000)\,|\, f_x X + f_y Y\,|\Psi_3\rangle$$

for the second order shift to the Ψ_3 vibronic state due to the $|\Gamma_3\gamma_3(000)\rangle$ intermediate state. Expanding the vibronic state Ψ_3 as its linear combination of product states and taking the above form of operators f_x and f_y, this matrix element reduces to

$$\sqrt{\frac{\hbar}{2mw_x}}\sqrt{\frac{(n+1)!}{(n-1)!}}\, r^{n}\, i\langle \Gamma_3\gamma_3|C^{(n)}_{-1}|\phi^{+}\rangle \quad .$$

In the same way the energy shift to the vibronic states Ψ_r from the other intermediate states of Table VII.4.4 can be constructed. In general it can be shown that the shift ΔE_r to the state Ψ_r is given by

$$\Delta E_r = \frac{\hbar\,(n+1)!}{2mw_x(n-1)!}\,(a_{in}r^{n})^{2}\;|\langle \Gamma_\ell\gamma_m|C^{(n)}_{q}|\phi^{+}\rangle|^{2}$$

$$\times\ \left\{\frac{A}{E_{\Gamma_\ell\gamma_m} - \hbar w_x} + \frac{1}{E_{\Gamma_\ell\gamma_m} + \hbar w_x}\right\} \qquad \text{(VII.4.18)}$$

where

q = +1 for the electronic states $\Gamma_1\gamma_1$, $\Gamma_3\gamma_1$, $\Gamma_4\gamma_2$

= −1 for the electronic states $\Gamma_3\gamma_3$, $\Gamma_5\gamma_4$

and the constant A is given in Table VII.4.5.

Table VII.4.5

Constant A in equation VII.4.18 for the energy shifts ΔE_r of the vibronic states Ψ_r.

Ψ_r	Intermediate Electronic State	A
Ψ_1	$\Gamma_1\gamma_1$	1
	$\Gamma_3\gamma_1$	1
	$\Gamma_3\gamma_3$	0
	$\Gamma_5\gamma_4$	0
Ψ_2	$\Gamma_3\gamma_3$	0
	$\Gamma_4\gamma_2$	1
	$\Gamma_5\gamma_4$	0
Ψ_3	$\Gamma_1\gamma_1$	0
	$\Gamma_3\gamma_1$	0
	$\Gamma_3\gamma_3$	1
	$\Gamma_4\gamma_2$	0
Ψ_4	$\Gamma_1\gamma_1$	0
	$\Gamma_3\gamma_1$	0
	$\Gamma_4\gamma_2$	0
	$\Gamma_5\gamma_4$	1

The dominant second order contributions will originate from the $|\Gamma_3\gamma_3(000)\rangle$ and $|\Gamma_3\gamma_1(000)\rangle$ states as being those intermediate states lying closest to the Ψ_r vibronic levels. The energies for these levels have been determined from the optical spectra described in Chapter V and are reproduced in Table VII.4.6. Note that for $CaF_2:Pr^{3+}$ the $|\Gamma_3\gamma_3(000)\rangle$ level energy is inferred from the energy of the $|\Gamma_3\gamma_3(100)\rangle$ vibronic level and that the $|\Gamma_3\gamma_1(000)\rangle$ and $|\Gamma_4\gamma_5(000)\rangle$ levels appear to be coincident.

Table VII.4.6

Energies of the two closest levels to the fundamental x,y vibronic states.

Crystal	$\|\Gamma_3\gamma_3(000)\rangle$ (cm^{-1})	$\|\Gamma_3\gamma_1(000)\rangle$ (cm^{-1})
$SrF_2:Pr^{3+}:H^-$	729 ± 1	466 ± 1
$SrF_2:Pr^{3+}:D^-$	733 ± 1	467 ± 1
$SrF_2:Pr^{3+}:T^-$	732 ± 1	467 ± 1
$CaF_2:Pr^{3+}:H^-$	820 ± 5 (a)	560 ± 20 (b)
$CaF_2:Pr^{3+}:D^-$	836 ± 2	560 ± 20
$CaF_2:Pr^{3+}:T^-$	831 ± 2	560 ± 20

(a) position inferred from $|\Gamma_3\gamma_3(100)\rangle$ vibronic level

(b) level obscured by $D_1 \longrightarrow Z_6$ transition.

Using the wavefunctions of equation VII.4.15 in equation VII.4.11 the relevant matrix elements are

$$\langle\Gamma_3\gamma_3|C^{(2)}_{-1}|\phi^+\rangle = \frac{-2.13}{3^2.5^2}\sqrt{3}$$

$$\langle\Gamma_3\gamma_1|C^{(2)}_{1}|\phi^+\rangle = \frac{2.13}{3^2.5^2}$$

For the point charge model the constant a_{1n} in the definition of the operators f_x and f_y is

$$a_{1n} = \frac{eq}{D^{(n+2)}} \quad .$$

Table VII.4.7 lists the second order energy shifts for the various sites in the two lattices due to second order perturbation effects from the $|\Gamma_3\gamma_3(000)\rangle$ and $|\Gamma_3\gamma_1(000)\rangle$ intermediate states.

Table VII.4.7

Energy shifts to the Ψ_1 and Ψ_3 vibronic states due to second order effects from the $|\Gamma_3\gamma_3(000)\rangle$ and $|\Gamma_3\gamma_1(000)\rangle$ intermediate states.

Isotope	$SrF_2:Pr^{3+}$		$CaF_2:Pr^{3+}$	
	$\Delta E_3(cm^{-1})$	$\Delta E_1(cm^{-1})$	$\Delta E_3(cm^{-1})$	$\Delta E_1(cm^{-1})$
H^-	+2.2	+0.3	+4.0	+0.5
D^-	-4.6	+0.5	-4.4	+1.0
T^-	-1.4	+0.9	-1.7	+2.8

The change in sign of the shift from H^- to D^- and T^- arises as the x,y vibronic level changes from the high energy side of the $|\Gamma_3\gamma_3(000)\rangle$ level to the low energy side.

It is clear from Tables VII.4.3 and VII.4.7 that the dominant contribution to the observed x,y vibronic splittings originates through a second order effect due to the close proximity of the $|\Gamma_3\gamma_3(000)\rangle$ level and is particularly pronounced for the D^- sites where the energy separation is smallest. Table VII.4.8 combines the calculated first and second order shifts for the Ψ_1 and Ψ_3 vibronic states to give an overall splitting and compares this with the observed splittings.

The results from the table show the second order contributions to the energy shifts substantially improve the agreement between the calculated and observed splittings. The apparent lack of a splitting for the T^- site in $SrF_2:Pr^{3+}$ remains unaccounted for as if it follows the trend a splitting should be readily resolved. The broader spectral line due to the T^- local mode vibration extending further into the lattice may hide such a feature.

Table VII.4.8

Calculated x,y vibronic level splittings to second order perturbation theory.

$SrF_2:Pr^{3+}$	Calculated $\Psi_3-\Psi_1$ Splitting (cm^{-1})	Observed Splitting (cm^{-1})	
		this work	Jacobs[1971]
H^-	3.5	3.5	1.4
D^-	4.0	8.5	-
T^-	1.7	-	-

$CaF_2:Pr^{3+}$	Calculated $\Psi_3-\Psi_1$ Splitting (cm^{-1})	Observed Splitting (cm^{-1})	
		this work	Jacobs[1971]
H^-	5.6	5.2†	3.4
D^-	3.9	-	-
T^-	3.6	-	-

† tentative assignment only.

As it is difficult to observe this mode by infrared absorption, the recording of a high resolution fluorescence spectrum would be helpful to resolve this issue.

The calculated splittings for the $CaF_2:Pr^{3+}$ centres are greater than those for $SrF_2:Pr^{3+}$ and it is unfortunate that it appears to be adherence to selection rules that does not allow the various components to be seen in emission spectra. An emitting level transforming as the γ_5 irreducible representation is required for allowed transitions to all the x,y vibronic levels but unfortunately such a level does not occur in the optical region for the Pr^{3+} ion in these sites. To observe the splitting for the D^- and T^- centres using infrared absorption, thin samples would be needed to reduce the overlap from the lattice absorption.

CHAPTER VIII

TEMPORAL STUDIES AND UPCONVERSION IN HYDROGENATED $SrF_2:Pr^{3+}$ AND $CaF_2:Pr^{3+}$ CRYSTALS

VIII.1 Introduction

In any study of the optical spectra of rare-earth ions in crystals, some comment is appropriate on the dynamical processes associated with their optical excitation and decay. Results of a preliminary study into the role of hydrogenic ion local mode phonons in the decay of an electronically excited rare-earth ion will be presented. Fluorescent lifetimes of the C_{4v} Pr^{3+}-hydrogenic ion sites measured in $SrF_2:Pr^{3+}$ and $CaF_2:Pr^{3+}$ crystals show that the H^-, D^- or T^- ion local modes play a dominant role in dynamical processes involving the decay of the Pr^{3+} ion excitation. Multiphonon relaxation to lower energy multiplets through the local mode phonons is found to be the dominant process for non-radiative decay and strongly influences the quantum efficiency of the centres.

An unusual upconversion mechanism for single rare-earth ion centres has also been observed in the hydrogenic C_{4v} sites. The reduced efficiencies of upconversion in these centres can be explained using a model of a weak coupling between nearby equivalent centres.

VIII.1.1 Background

The origin of the sharp optical transitions in rare-earth salts first observed by Becquerel [1907], was explained by Van Vleck [1937], but it quickly became apparent that non-radiative relaxation phenomena had an important role in the luminescence properties of these ions. Hellewege [1942] recognised the influence of H_2O vibrations in the fluorescence quenching of some rare-earth ions in hydrated salts and explained the effect in terms of the number of vibrational quanta

required to bridge the energy separation between the excited level and the next lowest state. Early experimental results also went on to suggest that the non-radiative relaxation involves the simultaneous emission of several phonons as fluorescence stability was only achieved with energy separations several times the maximum available phonon energy. Temperature dependence studies (Partlow and Moos [1967], Weber [1968]) provided strong experimental evidence that the relaxation was a multiphonon process with the lowest order process dominating.

An excited paramagnetic ion in a crystal may relax by any combination of radiative and non-radiative processes with the fluorescent intensity being determined by the sum of the probabilities for these processes. As the non-radiative processes are not directly observable, their relative importance can be established by comparing the measured excited state lifetime with the total radiative lifetime, any difference being attributed to non-radiative transitions. The measured fluorescent lifetime of an excited state a is given by

$$\frac{1}{\tau_a} = \sum_b W_{ab}^R + \sum_b W_{ab}^{NR} \qquad \text{(VIII.1.1)}$$

where the summation is over all final states b and W^R, W^{NR} are the radiative and non-radiative probabilities respectively. In general the non-radiative probability W^{NR} includes relaxation by multiphonon emission and energy transfer to other ions, however at low rare-earth concentrations or for crystallographic sites consisting of single isolated ions the energy transfer contribution can be neglected. From equation VIII.1.1 the radiative quantum efficiency is defined as

$$\eta_a = \frac{\Sigma_b W_{ab}^R}{\Sigma_b W_{ab}^R + \Sigma_b W_{ab}^{NR}} = \tau_a \Sigma_b W_{ab}^R \qquad \text{(VIII.1.2)}$$

and may approach zero or unity depending upon the relative probabilities for radiative and non-radiative decay. If any two variables in equation VIII.1.2 are known the remaining two can be determined. A great deal of effort, both theoretical and experimental, has been spent deriving the values for these quantities. Probabilities for radiative transitions have been calculated theoretically using the phenomenological intensity parameters of the Judd-Ofelt approach (see for example Krupke [1966], Weber [1967], Partlow and Moos [1967], Weber [1968]). However using these methods the accuracy of the value of W^{NR} determined is open to question if the values of $^{1}/_{\tau}$ and the calculated W^{R} have the same order of magnitude. Other phenomenological treatments, initially by Kiel [1964] and later Riseberg and Moos [1968], Miyakawa and Dexter [1970b], Fong, Naberhuis and Miller [1972] have been used with some success to calculate multiphonon transition rates. The theoretical background to these calculations will not be elaborated on here as excellent descriptions are contained in the review articles of Riseberg and Weber [1976], Fong [1976] and Perlin and Kaminskii [1985].

Experimentally, the measurement of the excited state fluorescent lifetime is relatively easy and two approaches, each with its own difficulties, have been used to obtain a second quantity. Measurements of line strengths in absorption can be combined with the Einstein A and B coefficients to determine the emission probability W^{R}. Problems arise however, as knowledge of the impurity ion concentration is required as is the accurate calibration of the measurement system over the different spectral regions. Alternatively measurements can be made of the radiative quantum efficiency η by combining measurements of the absorption and fluorescence (or excitation) spectra. If such recordings are made simultaneously, the systematic errors associated with quantum efficiency measurements can be reduced. For a description of an experimental system, developed at

the University of Wisconsin, to record absorption and excitation simultaneously see Miller et al [1977] and the references therein.

VIII.2 Fluorescent lifetimes and non-radiative decay in the tetragonal site in $SrF_2:Pr^{3+}$ and $CaF_2:Pr^{3+}$

The fluorescent lifetimes of the $^1D_2$ and $^3P_0$ emitting levels were measured for a number of Pr^{3+} sites in $SrF_2:Pr^{3+}$ and $CaF_2:Pr^{3+}$ crystals. The pulsed laser and data collection system used to record these results has been described previously in Chapter III. Single crystals of $SrF_2:Pr^{3+}$ or $CaF_2:Pr^{3+}$ were cooled by a cryogenic refrigerator to 14 K in preparation for their irradiation by a nitrogen pumped tunable dye laser. Rare-earth ion concentrations in the range 0.05 - 0.1 mol% were used to reduce the effects of energy transfer. In all sites studied the laser was tuned to match the absorption transition from the ground state to the emitting level in question. In most cases, a spectrometer tuned to a transition from the emitting level to an excited level of the ground state multiplet was used to detect emission. It was found necessary for some weakly emitting sites, to tune the spectrometer into resonance with the laser frequency as this transition is generally the strongest. In these circumstances masking of the crystal was used to reduce the amount of scattered laser light detected.

Fluorescent lifetimes were measured for all the C_{4v} sites, including the hydrogenic varieties, in both $SrF_2:Pr^{3+}$ and $CaF_2:Pr^{3+}$ crystals and for both the $^1D_2$ and $^3P_0$ emitting levels. The results are summarised in Table VIII.2.1 along with the energy separation between levels and the minimum number of appropriate hydrogenic ion local mode phonons required to bridge the gap. Figure VIII.2.1 shows several fluorescent transients as examples of the type of recording obtained.

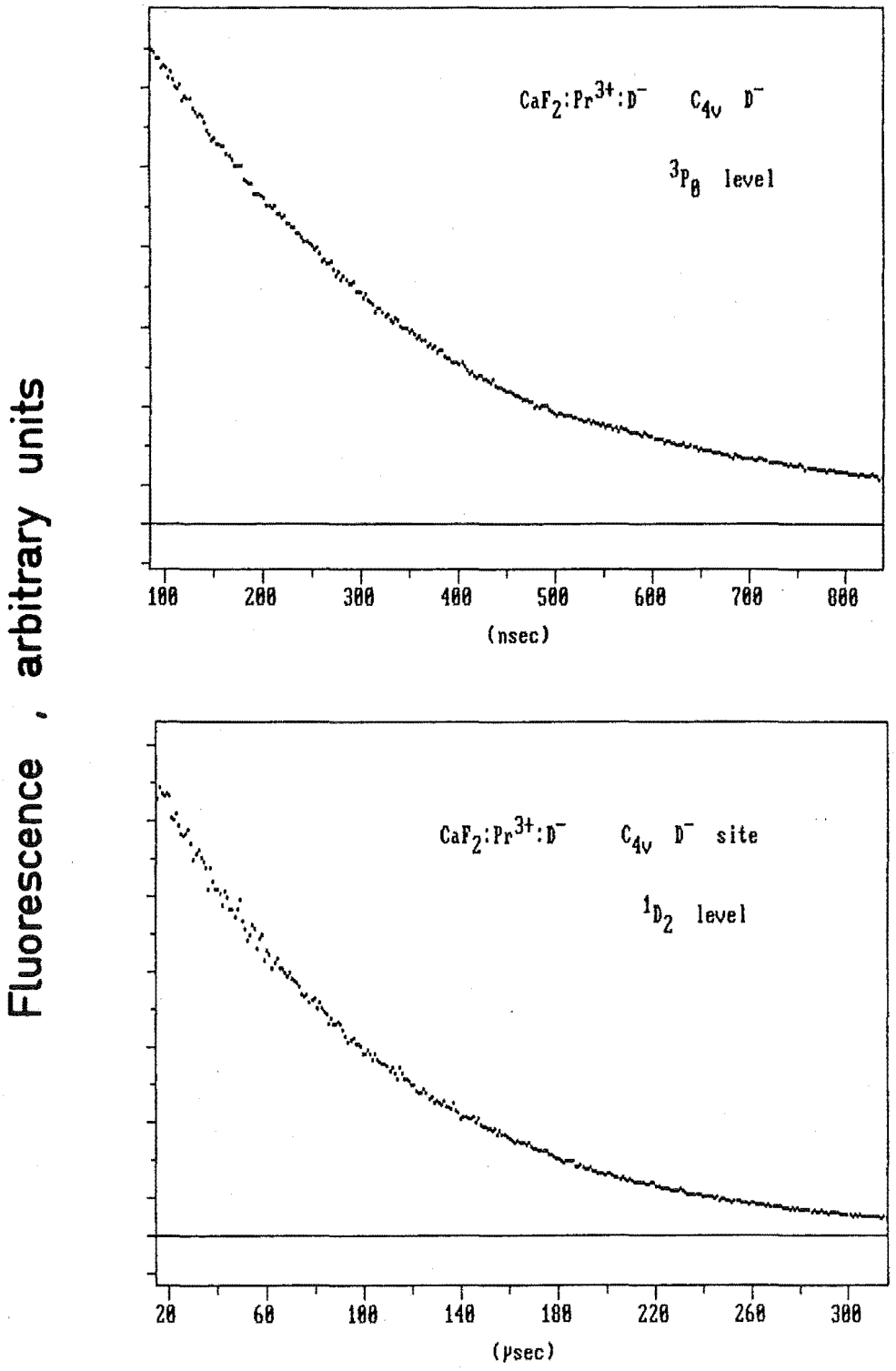

Figure VIII.2.1 Fluorescent transients recorded for the $^3P_0$ and $^1D_2$ emitting levels of the C_{4v} site in $CaF_2:Pr^{3+}:D^-$. The crystal temperature was 14K.

Table VIII.2.1

Fluorescent lifetimes measured at 14 K for the C_{4v} Pr^{3+} ion sites in SrF_2 and CaF_2 host crystals.

Crystal Host		$CaF_2:Pr^{3+}$		$SrF_2:Pr^{3+}$	
Transition		$^3P_0 \rightarrow {}^3H_4$	$^1D_2 \rightarrow {}^3H_4$	$^3P_0 \rightarrow {}^3H_4$	$^1D_2 \rightarrow {}^3H_4$
F^- C_{4v} Site		120±5 μsec	420±10 μsec	118±5 μsec	2.03±.05 msec
H^- C_{4v} Site		≤50 nsec	380±20 nsec	820±50 * nsec	2.69±.05 μsec
D^- C_{4v} Site		270±10 nsec	95±3 μsec	1.08±.05 μsec	405±10 μsec
T^- C_{4v} Site		-	-	16.3 μsec	360 μsec
Energy separation to the next lowest multiplet (cm^{-1})		3400	6100	3400	6100
Minimum number of local mode phonons to bridge gap	H^-	3	6	4	7
	D^-	4	8	5	9
	T^-	5	9	6	11

* tentative assignment.

One of the first things that becomes apparent when studying the fluorescence of the RE^{3+}-hydrogenic ion centres is the large variation in the efficiency of the emission. The D^- ion site fluorescence is much stronger than that for the corresponding H^- ion site even though it is the same electronic transition that is being excited. The results in Table VIII.2.1 graphically demonstrate the reasons for such

differences. The hydrogenic centre lifetimes, and consequently their quantum efficiencies, are observed to vary strongly with the particular charge compensation ion. The weakly fluorescing H^- ion sites have faster lifetimes than the D^- ion sites indicating a greater contribution to the level decay from non-radiative processes. As the H^- and D^- ion sites are electronically identical, the lifetime variations can only be accounted for by non-radiative processes involving the respective local mode phonons. Thus the electron-local mode phonon interaction that produces local mode vibronic lines in the optical spectra is also responsible for the relaxation of the ion and determines the relative importance of the radiative and non-radiative decay processes.

The results in the table for the T^- ion site in SrF_2Pr^{3+} require some comment. The $^3P_0$ lifetime follows the isotopic trend, having a lifetime slower than the D^- ion site value, however the $^1D_2$ value is faster than that for the D^- site. A possible reason for the shorter than expected $^1D_2$ lifetime is the unavoidable excitation of the C_{4v} H^- centres also present in these crystals. During the tritiation process H^- ions are also included into the crystals and compete with the T^- ions to form the hydrogenic charge compensating ion sites. The addition of a fast H^- component to the decay gives the appearance of a shorter lifetime than otherwise expected. The lifetime recorded for the $^3P_0$ level will be correct as for this level the H^--T^- isotope shift is ~ 3 cm^{-1} compared with ~ 0.1 cm^{-1} for the $^1D_2$ level and the laser can easily discriminate between the absorption lines for the sites of the two isotopes present.

Although having frequencies more than twice that of the lattice phonons, several hydrogenic ion local mode phonons still need to be created for energy conservation in the non-radiative relaxation of a

level. If p is the order of the process defined by

$$p = \frac{\Delta E}{\hbar\omega} \qquad \text{(VIII.2.1)}$$

where ΔE is the energy gap and $\hbar\omega$ the phonon frequency, then the rate for the p^{th} order multiphonon process can be written as (Moos [1970])

$$W^p = A\,\epsilon^p \qquad \text{(VIII.2.2)}$$

for constants A and $\epsilon << 1$ characteristic of the lattice. The form of this equation predicts the dominate non-radiative process to be that requiring the least number of phonons to bridge the energy gap to the next lowest level. As Table VIII.2.1 shows the lowest order process occurs in the H^- ion sites where the available phonon energy is greatest. Furthermore a consequence of the energy gap law represented by equations VIII.2.1 and VIII.2.2 is that similar multiphonon rates and consequently fluorescent lifetimes should be obtained for processes of the same order. For the C_{4v} Pr^{3+} sites, the order of the multiphonon decay of the $^3P_0$ level in the D^- ion sites is close to that of the decay of the $^1D_2$ level in the H^- ion sites (Table VIII.2.1). As predicted the lifetimes are similar with the differences correctly following the different orders of the processes. The comparison above appears to show the values of ϵ for the $^3P_0$ and $^1D_2$ levels are similar for this mode of non-radiative relaxation, supporting the contention of Moos [1970] that the constant ϵ is characteristic of the host crystal but not the rare-earth electronic state.

Additional evidence for the role of local mode phonons in the determination of site dynamics is provided by the rhombic $C_s(1)$ centre in $SrF_2:Pr^{3+}:D^-$. The $^1D_2$ lifetime for this centre was measured to be 60 μsec, substantially faster than the value of 405 μsec for the C_{4v}

D^- site. As discussed in Chapter VI, this centre contains two D^- ions within the close neighbourhood of the Pr^{3+} ion and has some very interesting bleaching characteristics. A model that satisfies the observed local mode vibronic spectrum and bleaching characteristics has the usual interstitial D^- ion and a second D^- ion replacing a lattice F^- ion in the first coordination shell. Strong local mode vibronics of the second D^- ion are observed in the optical spectra and provide evidence of a further non-radiative relaxation path for the Pr^{3+} ion. With a second path available the probability of non-radiative relaxation increases and the fluorescent lifetime is observed to be shorter.

The increased probability of non-radiative relaxation processes in Pr^{3+}-hydrogenic ion sites is further manifested in the radiation quenching of the $^3P_0$ level. Excitation to this state results in emission from both the $^3P_0$ and $^1D_2$ multiplets as strong quenching by local mode vibrations efficiently feeds the $^3P_0$ excitation to the lower $^1D_2$ multiplet. This effect was only very weakly observed in the fluorine ion sites (Chapter IV). The efficiency of the process is demonstrated by the rhombic C_s centres in $SrF_2:Pr^{3+}:D^-$ where the quenching is sufficiently strong to channel most of the excitation to the $^1D_2$ multiplet and preclude observation of emission from $^3P_0$.

The cascading of the excitation to the lower multiplet can be observed as a rise time of the fluorescence from the lower level. Figure VIII.2.2 shows the fluorescent transient obtained for $^1D_2 \longrightarrow {}^3H_4$ emission with $^3P_0$ excitation for the C_{4v} D^- and H^- sites in $SrF_2:Pr^{3+}$. The excitation decays from the $^1D_2$ level with the characteristic lifetime of this level, but as is apparent on an expanded scale shown in Figure VIII.2.3 for the same sites there is a risetime of ~1 μsec for the D^- site and very little (~50 nsec) for the H^- site. The risetime of this emission gives the non-radiative

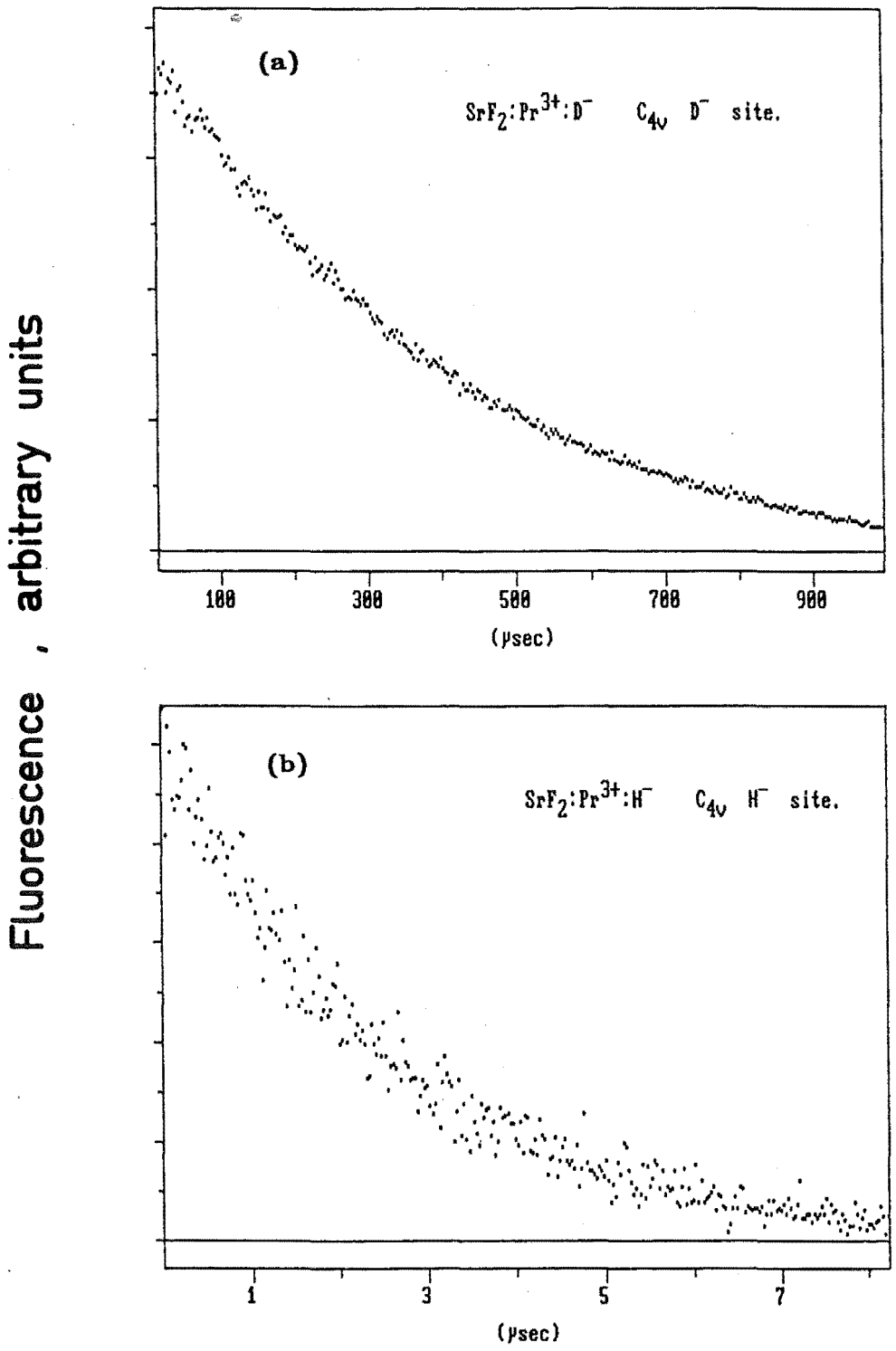

Figure VIII.2.2 Fluorescence decay, recorded at 14K, of the $^1D_2(D_1)$ emitting level with $^3H_4(Z_1) \rightarrow {}^3P_0$ excitation for the (a) C_{4v} D^- and (b) C_{4v} H^- sites in $SrF_2:Pr^{3+}$.

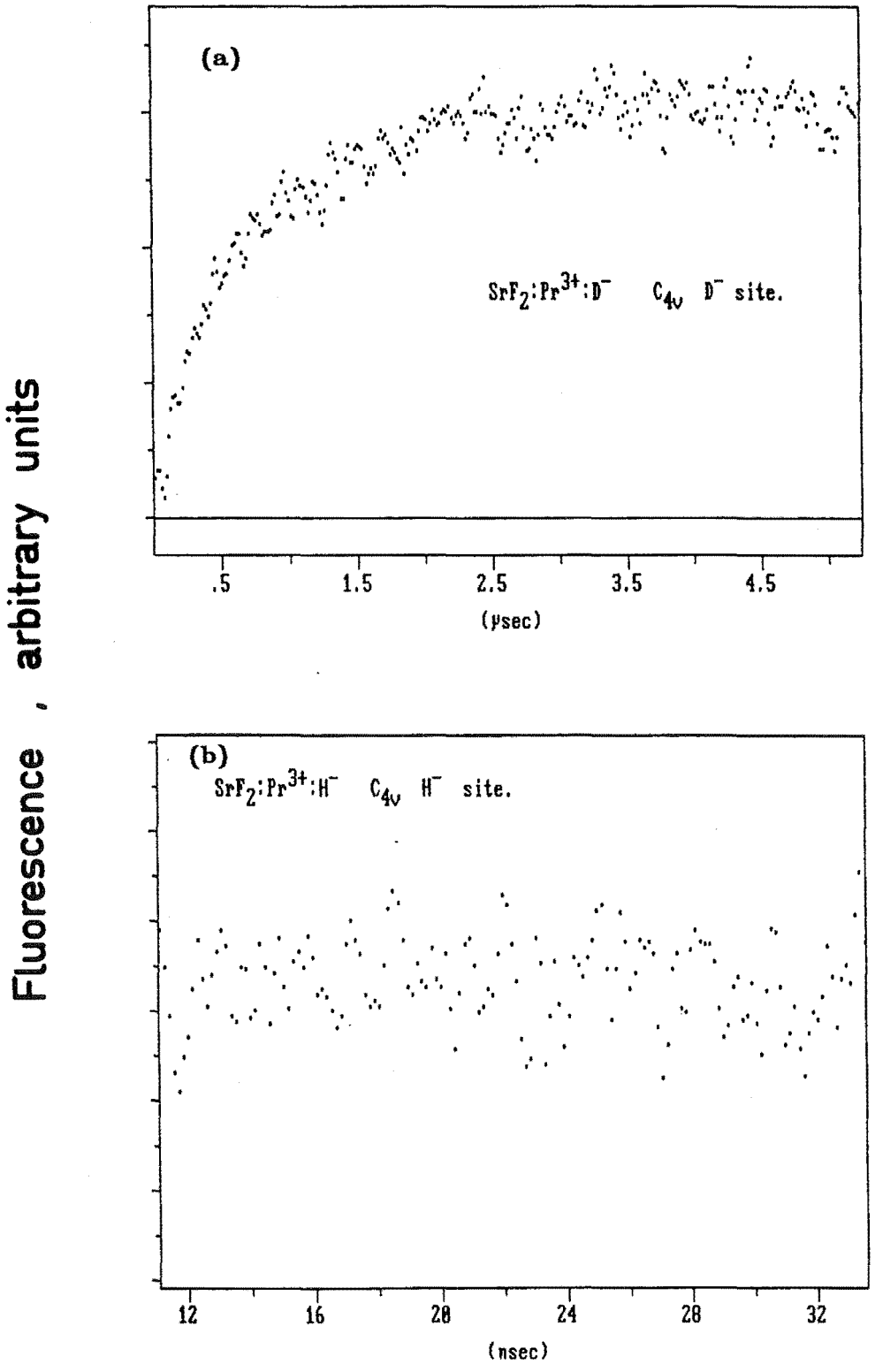

Figure VIII.2.3 Fluorescent transients of the $^1D_2$ level for the (a) C_{4v} D^- and (b) C_{4v} H^- sites in $SrF_2:Pr^{3+}$ on an expanded time scale showing the risetime for emission after $^3P_0$ excitation.

relaxation rate of the $^3P_0$ level (Perlin and Kaminskii [1985]) and has been used in some cases to obtain W^{NR} (Kushida and Geusic [1968], Zverev et al [1971]) although some care is needed to interpret the results correctly (Kushida et al [1982]).

With respect to the multiphonon relaxation rates of the hydrogenic ion sites, the emission for the C_{4v} F^- sites from the $^3P_0$ and even more so the $^1D_2$ levels can be considered as completely radiative. That this is not strictly true was shown in Chapter IV where a small amount of $^1D_2$ emission was observed with $^3P_0$ excitation, but for the purposes here the approximation is valid. Then from equation VIII.1.1

$$W^R(F^-) = \frac{1}{\tau(F^-)} \qquad \text{(VIII.2.3)}$$

as the non-radiative rate is zero. The radiative rates W^R for different C_{4v} sites can be simply related through the crystal field if the same levels are considered. As dipolar transition probabilties between electronic states involve terms of the form (Wybourne [1965])

$$|B_q^k \langle \phi | C_q^{(k)} | \psi \rangle|^2 \qquad \text{(VIII.2.4)}$$

where the B_q^k are crystal field parameters and $C_q^{(k)}$ Racah tensor operators, the relative rate of radiative decay between the same two states is related to the square of the crystal field. The validity of this approach is demonstrated by the results for the $^6P_{7/2} \rightarrow {}^8S_{7/2}$ transition of the Gd^{3+} ion in the C_{4v} sites of CaF_2. Jones et al [1969] measured the fluorescent lifetimes for the C_{4v} F^-, H^- and D^- sites and obtained the values 11±1, 4.0±.05 and 3 msec respectively. This transition has a frequency of 32000 cm^{-1} and evidently from the similar lifetimes can be considered as purely radiative. The second

order axial crystal field parameter for these sites has been measured to be B_0^2 = 650 and 1050 cm^{-1} (Edgar [1974]) for the F^- and H^- sites respectively. The change in B_0^2 gives the major difference in the crystal field between the F^- and H^- sites and can be used to estimate the change in fluorescent lifetime. Then the H^- site lifetime is related to that of the F^- site by

$$\tau(H^-) = \left| \frac{B_0^2(F^-)}{B_0^2(H^-)} \right|^2 \tau(F^-)$$

$$= 4.2 \pm .4 \text{ msec},$$

very close to that measured.

From equation VIII.2.3, assuming $W^{NR} = 0$ and using the fluorescent lifetime in the table, the radiative decay rate of the $^3P_0$ level in the C_{4v} F^- site of $SrF_2:Pr^{3+}$ is

$$W^R(F^-) = 8500 \text{ sec}^{-1} \qquad \text{(VIII.2.5)}$$

The crystal field of the hydrogenic sites increases by 70% over the F^- site and

$$W^R(H^-) = W^R(D^-) = W^R(T^-) = (1.7)^2 \times 8500 \text{ sec}^{-1}$$

$$= 24600 \text{ sec}^{-1} \qquad \text{(VIII.2.6)}$$

Rearranging equation VIII.1.1, the non-radiative relaxation rate for the $^3P_0$ level of the C_{4v} D^- site can then be written as

$$W^{NR}(D^-) = \frac{1}{\tau(D^-)} - W^R(D^-)$$

$$= 9.0 \times 10^5 \text{ sec}^{-1} \qquad \text{(VIII.2.7)}$$

The agreement with the value measured from the risetime of the fluorescent transient in Figure VIII.2.3 is remarkable. There the risetime was measured to be 1 μsec giving a non-radiative rate of 1×10^6 sec^{-1}. Using a similar analysis, the non-radiative rate for the $^3P_0$ level of the H^- site was calculated to be 1.2×10^6 sec^{-1}. At this rate the risetime of $^1D_2$ emission with $^3P_0$ excitation should be 840 nsec which contrasts sharply with the value observed in Figure VII.2.3 of $\leq$ 50 nsec. Working backwards, with this risetime the observed $^3P_0$ lifetime for the H^- site should be close to 50 nsec. Comparing the observed H^-, D^- and T^- $^3P_0$ lifetimes, the measured value of 820 nsec for H^- is much slower than would be expected using the simple model. The recording of transients is very difficult for those sites with fast lifetimes as the signals are weak by nature. The measured value for the $^3P_0$ site may well be in error as a component from some other site may be contributing to the transient. Clearly further investigations are required.

The multiphonon relaxation model can also be applied to the decay of the $^1D_2$ level. Taking the sites in $SrF_2:Pr^{3+}$ the radiative decay rate of the $^1D_2$ level in the F^- site is

$$W^R(F^-) = \frac{1}{\tau(F^-)} = 500 \text{ sec}^{-1} \qquad \text{(VIII.2.8)}$$

From the increase in the crystal field the rates for the H^- and D^- sites are calculated to be

$$W^R(H^-) = W^R(D^-) = 1450 \text{ sec}^{-1} \qquad \text{(VIII.2.9)}$$

Rearranging equation VIII.1.1 and using the results above and from the

table, the non-radiative rates are calculated to be

$$W^{NR}(H^-) = 3.7 \times 10^5 \text{ sec}^{-1}$$
$$W^{NR}(D^-) = 1.0 \times 10^3 \text{ sec}^{-1} \qquad \text{(VIII.2.10)}$$

The non-radiative relaxation rate was described by a phenomenological equation VIII.2.2. For the H^- and D^- sites the parameters can be assumed to be equal and the ratio of the relaxation rates is given by the single parameter ϵ raised to the power of the difference in the orders of the processes. Using the results from the table for the $^1D_2$ decay in the $SrF_2:Pr^{3+}$ sites it can be written that

$$\frac{W^{NR}(H^-)}{W^{NR}(D^-)} = \epsilon^{7-9} = \epsilon^{-2} \qquad \text{(VIII.2.11)}$$

and substituting the values from equation VIII.2.10

$$\epsilon = 0.05$$

A value of $\epsilon = 0.04$ is calculated from a similar analysis for the $CaF_2:Pr^{3+}$ sites. Using these values of ϵ and equations VIII.2.2 and VIII.1.1 the lifetimes of other levels can be predicted.

For the $^3P_0$ decay in $SrF_2:Pr^{3+}$, the difference in order of multiphonon relaxation for the H^- and D^- sites is one (Table VIII.2.1) and

$$W^{NR}(H^-) = \epsilon^{-1} W^{NR}(D^-)$$
$$= 1.8 \times 10^7 \text{ sec}^{-1} \qquad \text{(VIII.2.12)}$$

using the values $\epsilon = 0.05$ and $W^{NR}(D^-) = 9.0 \times 10^5 \text{ sec}^{-1}$ calculated above. A non-radiative decay of this order for the $^3P_0$ level would

correspond to a risetime of 56 nsec for the $^1D_2$ emission, close to the value of ~50 nsec observed. Such a fast non-radiative rate also predicts a $^3P_0$ lifetime of 56 nsec which is an order of magnitude faster than that observed but fits better to the isotopic trend.

The difference in order between the T^- and D^- sites is also one for the $^3P_0$ level (Table VIII.2.1) and

$$W^{NR}(T^-) = \epsilon\, W^{NR}(D^-) = 45000\ \text{sec}^{-1} \qquad \text{(VIII.2.13)}$$

Equation VIII.2.6 gives the radiative contribution as 24600 sec^{-1} and the lifetime of the $^3P_0$ level for the T^- site is calculated to be

$$\tau(T^-) = \frac{1}{45000 + 24600}\ \text{sec} = 14\ \mu\text{sec}\ , \qquad \text{(VIII.2.14)}$$

in excellent agreement with the measured lifetime of 16.3 μsec (Table VIII.2.1). A similar analysis for the $^1D_2$ level for this site yields a lifetime of

$$\tau(T^-) = 690\ \mu\text{sec} \qquad \text{(VIII.2.15)}$$

The measured lifetime is 360 μsec but as was discussed earlier the C_{4v} H^- site emission is expected to be contributing to this value.

In the C_{4v} sites of $CaF_2:Pr^{3+}$ three fluorescent lifetimes have yet to be measured before a complete set is obtained. An attempt was made to measure the $^3P_0$ decay of the C_{4v} H^- site but was unsuccessful due to the low signal. Consequently an upper limit of 50 nsec is placed on this value being the limit of the recording apparatus. The C_{4v} T^- sites in $CaF_2:Pr^{3+}$ were not examined during the period of this work.

Assuming radiative decay only from the $^1D_2$ level for the F^- site, the radiative rate is

$$W^R(F^-) = 2400 \text{ sec}^{-1}$$

and

$$W^R(H^-) = W^R(D^-) = W^R(T^-) = 6900 \text{ sec}^{-1}. \quad \text{(VIII.2.16)}$$

Then using the measured lifetimes (Table VIII.2.1) and equation VIII.1.1

$$\begin{aligned} W^{NR}(H^-) &= 2.6 \times 10^6 \text{ sec}^{-1} \\ W^{NR}(D^-) &= 3600 \text{ sec}^{-1} \end{aligned} \quad \text{(VIII.2.17)}$$

The difference in the order of the multiphonon relaxation between the H^- and D^- sites is 2 and

$$\epsilon^{-2} = \frac{W^{NR}(H^-)}{W^{NR}(D^-)}$$

or

$$\epsilon = 0.04 \quad \text{(VIII.2.18)}$$

The order of the D^- and T^- processes differ by one and

$$W^{NR}(T^-) = \epsilon\, W^{NR}(D^-) = 144 \text{ sec}^{-1} \quad \text{(VIII.2.19)}$$

Combining the radiative (VIII.2.16) and non-radiative (VIII.2.19) contributions the $^1D_2$ fluorescent lifetime of the T^- site is predicted

to be

$$\tau(T^-) = 140\ \mu sec \qquad \text{(VIII.2.20)}$$

The value of $\epsilon = 0.04$ determined above from the $^1D_2$ decay and the difference in the order of the relaxation processes can be used to estimate the missing $^3P_0$ lifetimes.

Assuming only radiative decay from the $^3P_0$ level for the F^- site

$$W^R(F^-) = 8300\ sec^{-1}$$

which increases to

$$W^R(H^-) = W^R(D^-) = W^R(T^-) = 24000\ sec^{-1} \qquad \text{(VIII.2.21)}$$

for the hydrogenic sites with the change in the crystal field. Then for the $^3P_0$ level of the D^- site

$$W^{NR}(D^-) = \frac{1}{\tau(D^-)} - W^R(D^-) = 3.7 \times 10^6\ sec^{-1} . \qquad \text{(VIII.2.22)}$$

The difference in the order of the multiphonon relaxation process for the H^- and T^- sites is one either side from that of the D^- site (Table VIII.1.1) and using the value $\epsilon = 0.04$

$$W^{NR}(H^-) = \epsilon^{-1}\ W^{NR}(D^-) = 9.3 \times 10^7\ sec^{-1} \qquad \text{(VIII.2.23)}$$
$$W^{NR}(T^-) = \epsilon\ W^{NR}(D^-) = 1.5 \times 10^5\ sec^{-1}$$

Substituting these multiphonon rates and the radiative rates of 24000 sec^{-1} (VIII.2.21) into equation VIII.1.1, the missing

fluorescent lifetimes of the $^3P_0$ level are predicted to be

$$\begin{aligned} \tau(H^-) &= 11 \text{ nsec} \\ \tau(T^-) &= 5.7 \ \mu\text{sec} \end{aligned} \qquad \text{(VIII.2.24)}$$

The results derived above show that a simple single-frequency phenomenological approach has a remarkable degree of success in analysing and predicting the relaxation of the hydrogenic C_{4v} sites. The local mode vibrations of the hydrogenic ions appear to totally determine the rates of decay for these sites. The discussion in this work has only just scratched the surface as a host of other effects can be considered. The multiphonon relaxation rates in other systems (Riseberg and Moos [1967], [1968], Weber [1968]) are known to be sensitive to the temprature as stimulated phonon emission becomes significant. Hydrogenic rare-earth systems do not often fluoresce at temperatures greater than 100 K and it is uncertain if local mode vibrations are responsible for the increased non-radiative decay rates. Also the dependence on host crystal and the universality of the phenomenological parameters are other areas yet to be addressed.

VIII.3 Upconversion in the C_{4v} Sites of $SrF_2:Pr^{3+}$ and $CaF_2:Pr^{3+}$ crystals.

From the first observation of energy transfer between donor and acceptor atoms (Cario and Franck [1923]) spectroscopists have focussed much attention in this area, culminating in the helium-neon laser as arguably the most practical application. Rare-earth ions have formed a major subset of this work over the years and although being slightly out of date in terms of current results, excellent discussions of the various processes can be found in the review articles of Wright [1976] and Riseberg and Weber [1976]. Current investigations of such

processes range from energy transfer within triads of ions giving ultraviolet fluorescence (Lezama et al [1985]) to the transfer amongst the ions distributed across an inhomogeneously broadened line after irradiation with a single frequency laser (Flach et al [1975], [1977]).

Energy transfer phenomena can be divided into two classes: (1) ion pair relaxation, and (2) upconversion. The ion pair relaxation occurs when only the donor ion is excited and relaxes by transferring all or part of its energy to the acceptor ion(s). Any energy mismatch is emitted as lattice phonons. However if two ions are initially excited one can decay by transferring its energy to the other which finishes with an energy greater than its initial excitation energy. It is this latter upconversion process that will be discussed in this section.

The upconversion process was first proposed by Bloembergen [1959] as having a stepwise mechanism but other mechanisms have since appeared where the process involves cooperative energy transfer amongst excited ions (see, for example, Miyakawa and Dexter [1970a]). These two mechanisms are frequently referred to in the literature as STEP (sequential two photon excitation process) and ETU (energy transfer upconversion).

Recently upconversion has been observed in the C_{4v} Pr^{3+}-F^- site in CaF_2:Pr^{3+} and SrF_2:Pr^{3+} crystals (Lezama et al [1986], Jones et al [1987]), and rather unexpectantly in the C_{4v} Pr^{3+}-hydrogenic ion sites in these same crystals (Reeves et al [1987]). Excitation of the Pr^{3+} ion to its $^1D_2$ multiplet yields fluorescence from the $^3P_0$ level that can be identified as belonging to the same site. Figure VIII.3.1 shows the energy level diagram of the C_{4v} Pr^{3+}-F^- site in SrF_2 determined from the results presented in Chapter IV. At first glance upconversion in the C_{4v} centres would be expected to follow the stepwise mechanism as the spectroscopy of these sites suggest they consist of isolated single rare-earth ions and their charge

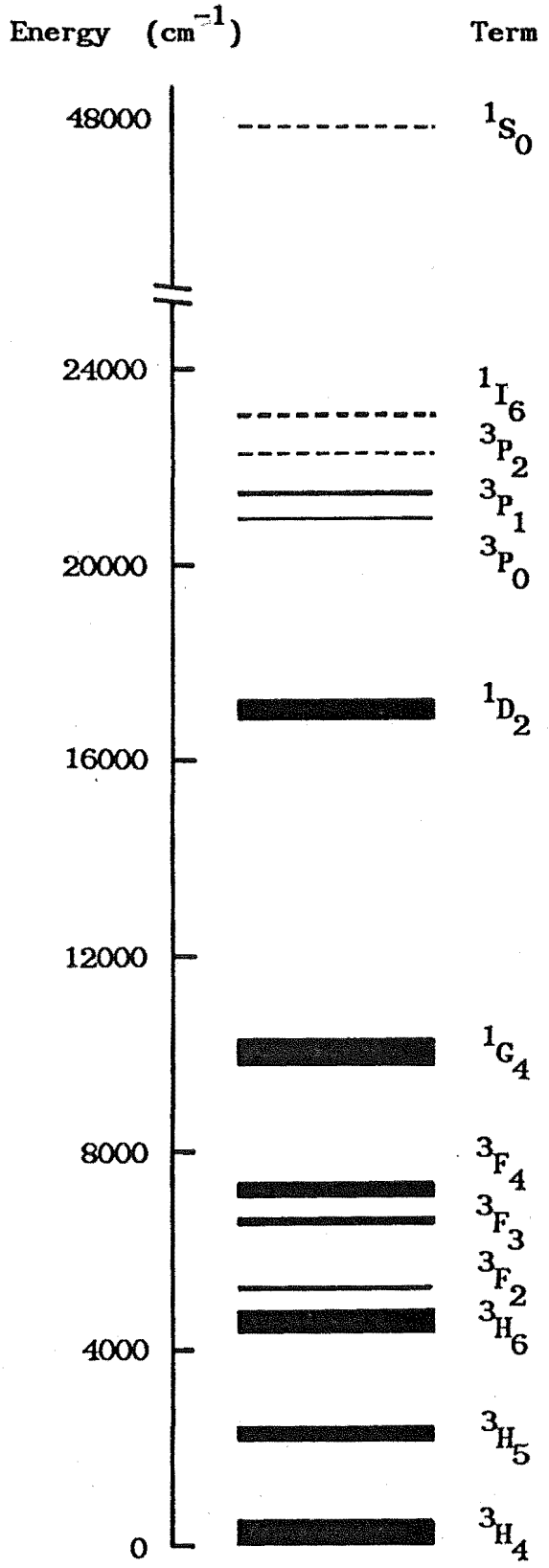

Figure VIII.3.1 Energy level diagram for the Pr^{3+} ion in the C_{4v} F^- site in SrF_2:Pr^{3+}. The positions have been measured for the ten lowest multiplets and their crystal field splitting is represented by the thickness of the line.

compensators. Results to be presented in this chapter suggest otherwise and the upconversion process involves energy transfer between the two ions of a pair of centres that form a specific subset of the regular C_{4v} site.

Upconverted emission from the $^3P_0$ level has been observed at temperatures up to 60 K, for the C_{4v} F^- sites in both $CaF_2:Pr^{3+}$ and $SrF_2:Pr^{3+}$ when pumping the $^1D_2$ level of each site. For the sites in $SrF_2:Pr^{3+}$ the upconversion emission intensities are factors 3×10^{-6}, 1×10^{-5} and 5×10^{-3} less than the intensity of the direct $^1D_2 \longrightarrow {}^3H_4$ transition for the C_{4v} D^-, T^- and F^- sites respectively. No upconversion was observed for the C_{4v} H^- site at a sensitivity 10^{-7} less than the direct $^1D_2 \longrightarrow {}^3H_4$ emission. The upconversion in the $CaF_2:Pr^{3+}$ C_{4v} F^- site is relatively more weak than for this site in $SrF_2:Pr^{3+}$. The corresponding upconversion efficiency ratio was measured to be 4×10^{-4}.

The near coincidence of the 476.5 nm argon ion laser line with the $^3P_0 \longrightarrow {}^3H_4$ transition of the C_{4v} F^- site in $SrF_2:Pr^{3+}$, can be used to selectively excite the Pr^{3+} ion in this site to the $^3P_0$ level. Figure VIII.3.2 shows the polarised upconverted $^3P_0 \longrightarrow {}^3H_4$ emission, recorded at 14 K from a <100> oriented crystal, for this site under $^1D_2$ excitation in the x(yy)z and x(yx)z polarisation geometries. Figure VIII.3.3 shows the $^3P_0 \longrightarrow {}^3H_4$ emission using direct excitation to $^3P_0$ with the argon ion laser. The upconverted emission for the hydrogenic C_{4v} sites was shown in Chapter V (Figure V.1.13 and V.1.14).

It was discussed in Chapter IV how the polarisation effects in these sites arise from the preferential excitation of only some of the orientations of the site. The identical polarisation observed in Figures VIII.3.2 and VIII.3.3 shows that either the same ion absorbs both photons to participate in upconversion or that two identical excited ions combine their excitation to give upconversion. This

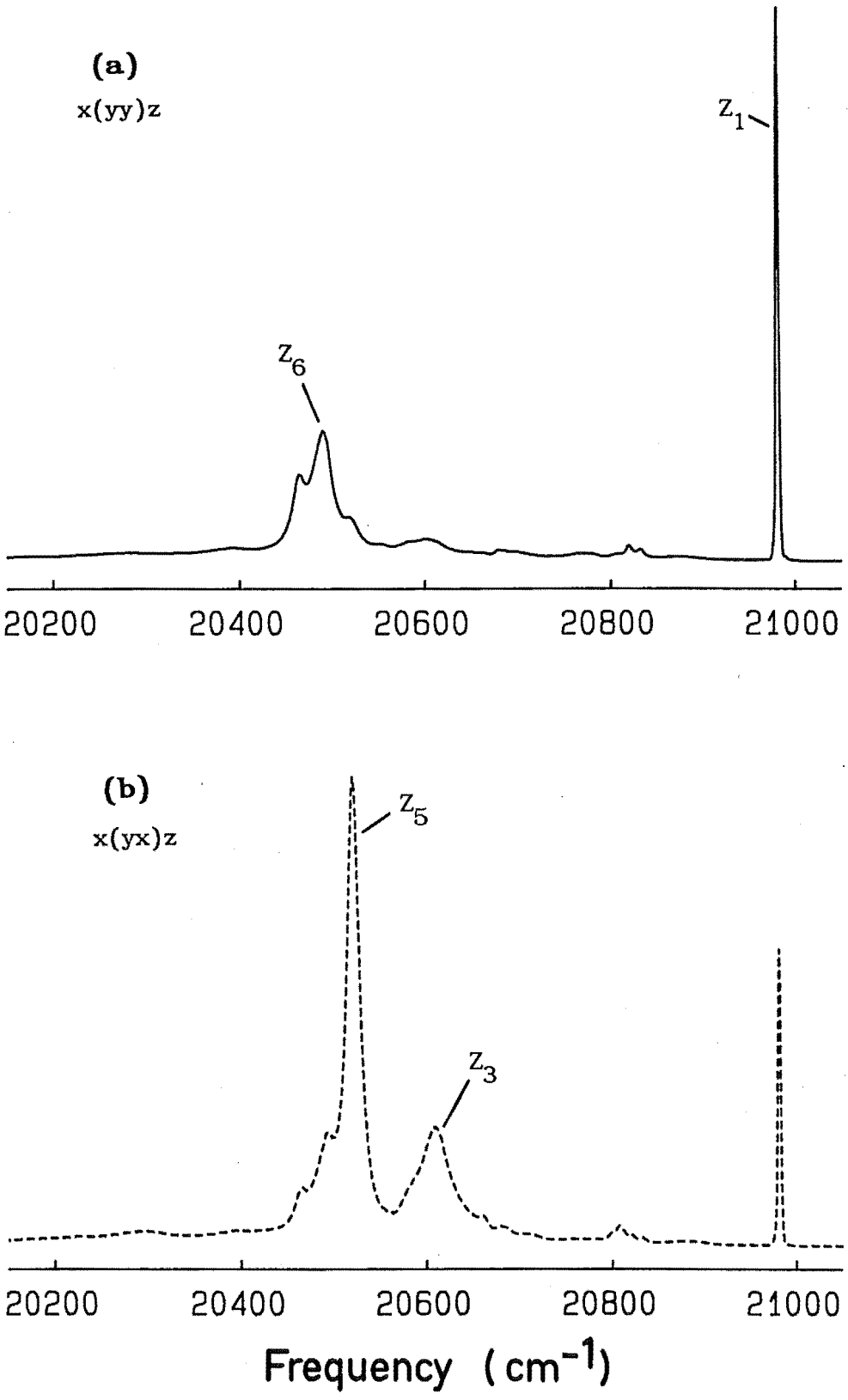

Figure VIII.3.2 Upconverted $^3P_0 \rightarrow {}^3H_4$ emission , at 14K, from the C_{4v} F^- site in $SrF_2:Pr^{3+}$ with $^3H_4(Z_1) \rightarrow {}^1D_2(D_1)$ excitation. The spectra show transitions for the (a) x(yy)z and (b) x(yx)z polarisation geometries in a <100> oriented crystal.

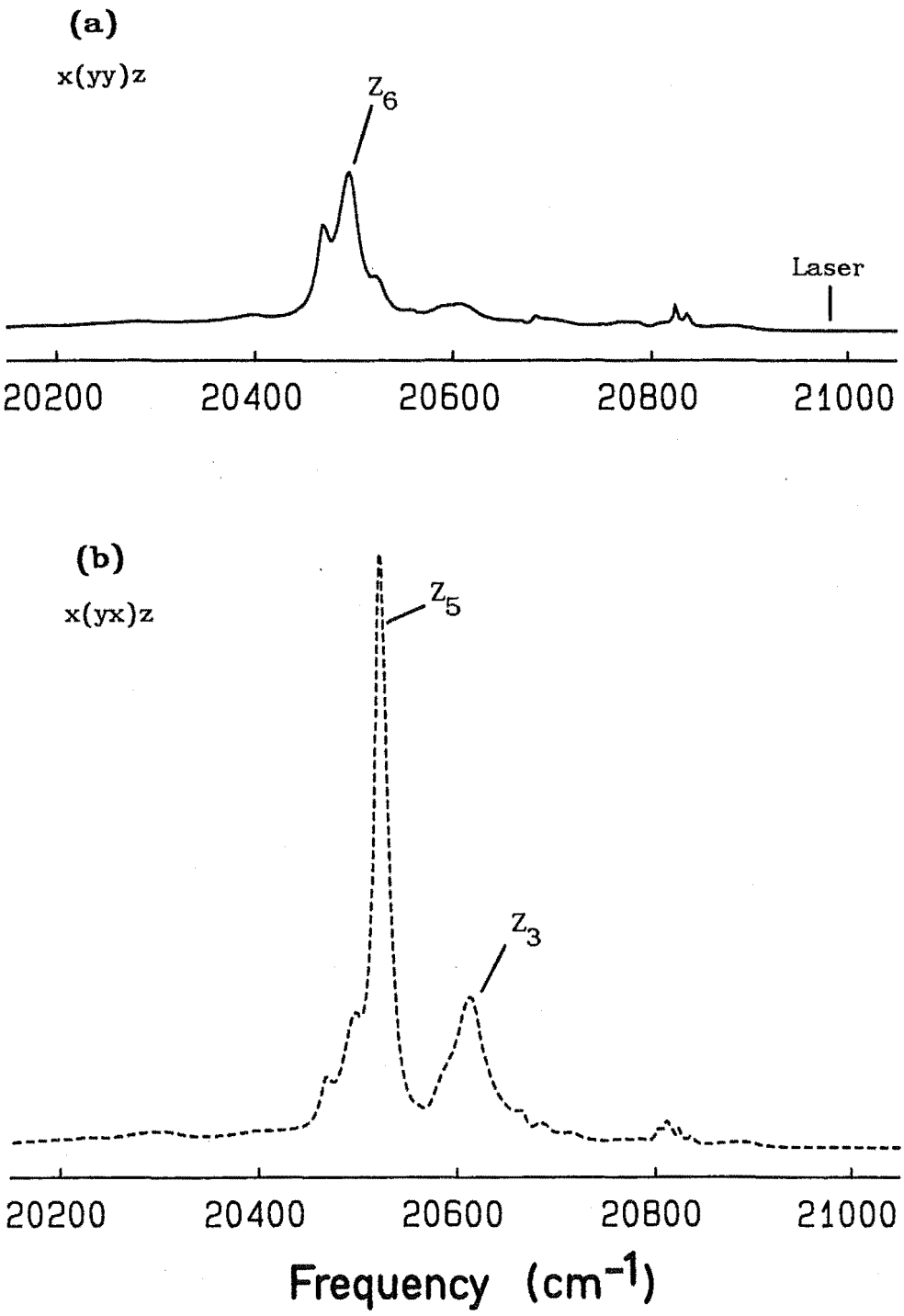

Figure VIII.3.3 Polarised $^3P_0 \rightarrow {}^3H_4$ emission from the C_{4v} F^- site in $SrF_2:Pr^{3+}$ with direct $^3P_0$ excitation using the argon ion laser.

first approach would require a STEP mechanism while an ETU process has to be invoked for the second. Examination of Figure VIII.3.1 shows that the $^1D_2$ level is unlikely to be an intermediate state in any STEP process as there is no energy level structure in the region of twice the photon frequency. The levels of the $^3H_6$ multiplet could act as intermediate states as the $^3P_0 \longrightarrow {}^3H_6$ frequency is close to the photon frequency and a time delay between absorption of the two photons would be expected.

The situation regarding the appropriate mechanism is clarified by the observation of upconversion under pulsed excitation conditions. A STEP process can be discounted as during the period of the laser pulse (~1 nsec) there is insufficient time for the ion to relax to an intermediate state in preparation for the absorption of the second photon. However this statement does not rule out the possibility of a STEP process if two photons of the correct, but differing energies are absorbed by the site. This is a different situation to the single photon frequency upconversion observed here and will not be discussed further.

The elimination of the stepwise process as the likely mechanism for the sites discussed here is consistent with the conclusion of Lezama et al [1986] that the upconversion in these C_{4v} sites proceeds by a weak long range interaction between pairs of C_{4v} centres. For the C_{4v} F^- site in $SrF_2:Pr^{3+}$, maximum upconversion intensity is measured to occur at a $^1D_2$ excitation frequency 0.25 cm^{-1} lower than that required for the strongest direct fluorescence. This difference indicates that a specific subset of the C_{4v} centres, slightly perturbed from the isolated C_{4v} centres, participate in upconversion.

The results of a two laser experiment also support ETU as the correct mechanism for upconversion. With a cw laser tuned to maximise the upconverted signal of the C_{4v} F^- site in $SrF_2:Pr^{3+}$, a second laser

having its beam exactly coincident with the first in the crystal was tuned across the $^1D_2$ excitation region. Extra upconversion was observed only when the frequency of the second laser matched a $^1D_2$ transition of the ion site. The interpretation is that both photons of the process are required to match a $^3H_4(Z_1) \longrightarrow {}^1D_2$ transition and that two ions have to be excited and combine their excitation before upconversion is observed.

At the sensitivities used in this experiment there were no other excitation lines visible that would indicate a stepwise process but this does not discount this mechanism as being possible in these sites under the right conditions. The C_{4v} F^- centres in $CaF_2:Nd^{3+}$ and $SrF_2:Nd^{3+}$ also participate in upconversion (Reeves et al [1987]) by the transfer mechanism but there is evidence of an additional stepwise process. A cw laser tuned to match the $^4F_{3/2} \longrightarrow {}^4D_{3/2}$ interval of 16507 cm^{-1} gives upconverted emission from this $^4D_{3/2}$ level at 28098 cm^{-1}. The intermediate state in this process is the $^4F_{3/2}$ level at 11591 cm^{-1} and is populated from the ground state by absorption of the laser into a phonon sideband of the $^4G_{5/2}$ multiplet. This particular process is much weaker than the energy transfer mechanism (Han [1987]). Presumably if the $^4F_{3/2}$ level could be populated more efficiently by tuning a second laser directly to this absorption the upconversion intensity would increase.

The observation of upconversion under pulsed excitation allows the concentration dependence of the exchange of energy between ions of the pair to be studied. The fluorescent lifetime of the upconverted $^3P_0$ state in the C_{4v} F^- site of $SrF_2:Pr^{3+}$ was measured for three concentrations of the Pr^{3+} ion. Upconverted lifetime values of 550±50, 470±20 and 220±20 μsec were measured for the $^3P_0$ level in crystals having Pr^{3+} ion concentrations of 0.05, 0.1 and 0.5 mol% respectively. Figure VIII.3.4 shows the fluorescent transients

Figure VIII.3.4 Fluorescence decay, at 14K, of the upconverted $^3P_0$ emission from the C_{4v} F^- site in $SrF_2:Pr^{3+}$ for Pr^{3+} ion concentrations of (a) 0.5 mol%, (b) 0.1 mol% and (c) 0.05 mol%.

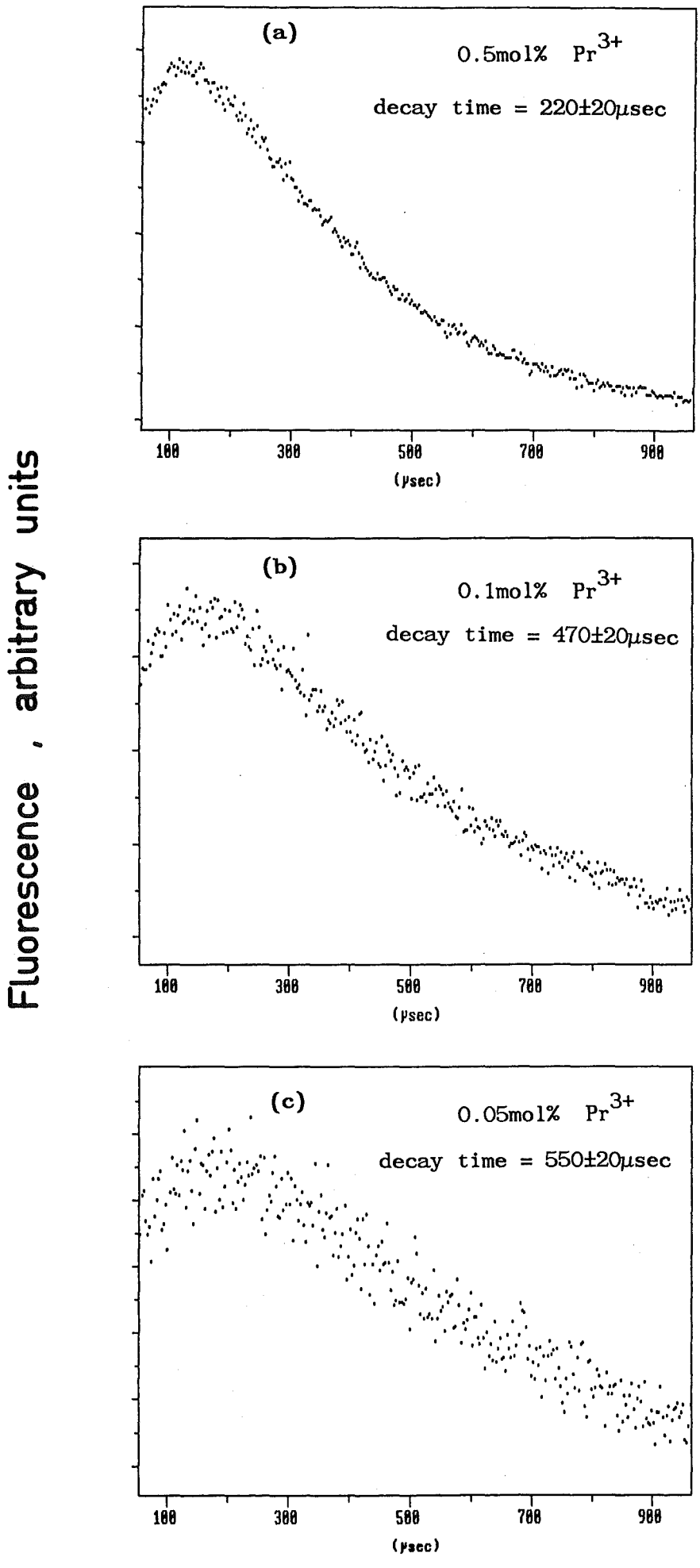
(a)
0.5mol% Pr^{3+}
decay time = 220±20μsec
100
300
500
700
900
(μsec)
(b)
0.1mol% Pr^{3+}
decay time = 470±20μsec
100
300
500
700
900
(μsec)
(c)
0.05mol% Pr^{3+}
decay time = 550±20μsec
100
300
500
700
900
(μsec)
Fluorescence , arbitrary units

obtained for these three crystals. That the upconversion is more efficient in the higher concentration crystals is apparent in the transients from both the shorter time for the decay and the superior signal to noise ratio.

The temporal behaviour of the upconversion process involving ion pairs in $LaF_3:Pr^{3+}$ has been discussed by Buisson and Vial [1981]. Upconversion in the C_{4v} sites follows a similar mechanism and their analysis is also appropriate here. If N_d is the number of ion pairs excited to the $^1D_2$ level by the laser pulse then the time evolution is given by

$$\frac{dN_d}{dt} = - 2 W_2 N_d - W_T N_d \qquad \text{(VIII.3.1)}$$

where W_T is the transfer rate and W_2 the decay rate of the $^1D_2$ level. The factor 2 arises as a pair that can participate in upconversion is destroyed as soon as one of its ions radiates. The number of ions N_3, excited into the $^3P_0$ level by the transfer varies as

$$\frac{dN_3}{dt} = W_T N_d - W_3 N_3 \qquad \text{(VIII.3.2)}$$

where W_3 is the decay rate from $^3P_0$. Solving VIII.3.1 and VIII.3.2 for N_3, the population of $^3P_0$ yields

$$N_3 = \frac{N^0_d W_T}{W_3 - 2W_2 - W_T} \left[e^{-(2W_2+W_T)t} - e^{-W_3 t} \right] \qquad \text{(VIII.3.3)}$$

where N^o_d is the initial number of excited pairs.

Two regimes for the upconversion can be identified corresponding to the transfer rate W_T having a large or small value. If the transfer rate is small, the decay of the upconverted emission is

determined by the first exponential term in equation VIII.3.3 and has a time constant of half the $^1D_2$ lifetime W_2. The second term then determines the risetime which will be of the order of W_3, the $^3P_0$ level lifetime. The second regime corresponds to W_T large and there is a sign change in the coefficient and the role of the exponetials reverse. The risetime of the upconverted emission will be of the order W_T^{-1} while the decay is determined by the lifetime of the $^3P_0$ state.

Evidence for these two regimes is provided by the concentration dependence of the decay of the upconverted $^3P_0$ emission measured here. At a low concentration the interacting centres are further apart and the transfer rate will be small. For the 0.05% crystal the measured decay is 550 μsec approaching the limiting case of 1 msec set by half the $^1D_2$ lifetime (Table VIII.2.1). In the other regime a large value of W_T is expected for the high concentration crystals as the intercentre distance shortens. Here the decay of the upconverted emission is determined by the $^3P_0$ lifetime (= 118 μsec, Table VIII.2.1) and was measured to be 220 μsec for the 0.5% crystal.

The theory of the transfer mechanism between interacting ions of a pair, was developed by Dexter [1953] where expressions for the transition probabilities and luminescence yield were derived as a function of concentration. The main interaction providing the means for energy transfer is the electric multipole coupling arising from the Coulomb interaction between the electron charge clouds of the two ions. The leading terms in this electrostatic coupling are the electric dipole-dipole, dipole-quadrupole and quadrupole-quadrupole interactions which have radial dependences of R^{-3}, R^{-4} and R^{-5} respectively. As the mean effective distance R between ions varies as the inverse cube root of the concentration, the order of the multipole interaction can be deduced from the concentration dependence of the fluorescence efficiency. For the upconversion observed here the

transfer occurs over a large distance and the electric dipole-dipole term is expected to be dominant. In the C_{4v} F^- site of $CaF_2:Pr^{3+}$, Lezama et al [1986] observed a transfer rate varying with R^{-6} consistent with electric dipole-dipole coupling.

In principle the form of the exchange can be calculated from the fluorescent transients observed here. For the 0.05% crystal in the small W_T regime, the transfer rate W_T is given by the decay of the upconverted fluorescence. From equation VIII.3.3 this decay lifetime is equal to

$$\tau = 2W_2 + W_T$$

and was measured to be 550 μsec. Substituting the $^1D_2$ lifetime of 2.03 msec (Table VIII.2.1) the transfer rate is

$$W_T = 830 \text{ sec}^{-1}.$$

For the 0.5% crystal in the large W_T regime, the risetime of the upconverted fluorescence determines the transfer rate. A value for this quantity is more difficult to determine than the decay time as it has to be measured from the observed transient rather than obtained from a computer generated exponential fit to the transient decay. The risetime estimated for the 0.5% crystal is 35 μsec which corresponds to a transfer rate of

$$W_T = 29000 \text{ sec}^{-1}$$

Since the 0.05 and 0.5% concentrations differ by a factor of 10, the inter-ion separations are related by

$$R(0.05\%) = 10^{1/3} R(0.5\%) \qquad \text{(VIII.3.3)}$$

For electric dipole-dipole coupling the transfer rate varies as $(R^{-3})^2$ and there will be a 100 fold increase in the transfer rate for the 0.5% crystal over the 0.05% crystal. In fact the observed increase is somewhat less than this. The order of the coupling for the upconversion observed here can be calculated as follows.

If the coupling is of the order $R^{-\alpha}$ then the transfer rate varies as $(R^{-\alpha})^2$ and

$$\frac{W_T(0.5\%)}{W_T(0.05\%)} = \frac{29000}{830} = \frac{R^{-2\alpha}(0.5\%)}{R^{-2\alpha}(0.05\%)} \qquad \text{(VIII.3.4)}$$

Then using equation VIII.3.3

$$10^{\frac{2\alpha}{3}} = \frac{29000}{830}$$

or

$$\alpha = 2.3$$

i.e. the measured coupling varies as $R^{-2.3}$. Other than the electric multipole interactions the only other transfer mechanism is the so called exchange interaction (Riseberg and Weber [1976]) which has only a short range radial dependence varying as exp(-R/L). Thus on the basis of these measurements the conclusion by Lezama et al [1986] of an electric dipole-dipole coupling appears valid.

The variation of the relative upconversion efficiencies between different sites can now be understood using this model. The number of ions excited to the upconverted state depends upon the number of pairs able to participate in the process which is itself dependent upon the $^1D_2$ lifetime. If the transfer rate is slower than the $^1D_2$ decay rate there will be fewer pairs to upconvert resulting in weaker upconversion efficiencies. This accounts for the difference between the C_{4v} F^- sites in $SrF_2:Pr^{3+}$ and $CaF_2:Pr^{3+}$ where, at the same

concentrations and thus the same inter-ion separation, the transfer rates would be expected to be similar. The differences in the efficiencies for the D^- and T^- sites are also influenced by the $^1D_2$ lifetime in the same way, however for the F^- to D^- sites some effect is expected from the lower absolute concentration of the D^- ion sites relative to the F^- sites. This arises as not all C_{4v} F^- centres are converted into hydrogenic ion sites during the crystal treatment.

Although at first glance upconversion in the C_{4v} sites appears to involve a new mechanism because of their single ion nature the results suggest the interaction is similar to those previously observed. Upconversion in these centres occurs through the exchange of energy between weakly coupled pairs of ions that form a specific subset of the regular C_{4v} sites. It would be interesting to examine the crystal environment of these pairs to see whether there are any fundamental differences from that of the main isolated sites. For the C_{4v} hydrogenic sites the transverse local mode vibration is degenerate and any influence from another closeby Pr^{3+} ion would be manifested in a splitting of the mode. Perhaps a more productive experiment would be to selectively excite the subset of ions participating in upconversion with the single frequency laser. A 0.3 cm^{-1} shift in the laser frequency was required to maximise between the upconverted or direct emission so an isolated transition may be apparent within the inhomogeneous linewidth corresponding to these pairs. If such a situation existed the sensitive ODNMR techniques described in the following chapter may be able to be used to map the positions of the ligand ions and determine any differences from the regular sites.

CHAPTER IX

SPECTRAL HOLEBURNING AND OPTICALLY DETECTED NUCLEAR MAGNETIC RESONANCE IN THE C_{4v} SITES OF $SrF_2:Pr^{3+}$ AND $CaF_2:Pr^{3+}$

IX.1 Introduction to spectral holeburning

With the advent of single frequency tunable lasers the spectroscopy of trivalent rare-earth ions has largely shifted from understanding the energy level structure to investigations within the transition linewidth. As a probe within the ~1 GHz optical transition linewidth the single frequency laser offers a resolution some 10^3 - 10^4 times that available from most spectrometers, giving information on effects previously hidden by the convential limits.

The broadening of spectral lines can be categorised as homogeneous or inhomogeneous broadening. Homogeneous broadening arises from dynamical perturbations to the transition frequency and is the same for all ions in the crystal having that transition. Some of the common contributions include the effects of lattice phonons and fluctuating nuclear or electron spins.

The presence of lattice strains inherent to all crystals introduces an inhomogeneous broadening to the transition linewidth. For the lowest crystal field level of a J multiplet the multiphonon relaxation required to bridge the energy gap to the next lowest multiplet results in long lifetimes and small homogeneous linewidths. For these levels the linewidth can be completely dominated by the inhomogeneous broadening and the resulting lineshape can be thought of as the envelope of homogeneous 'spin packets' as shown schematically in Figure IX.1.1.

One of the most common techniques introduced with single frequency lasers is spectral holeburning. In these experiments the laser is

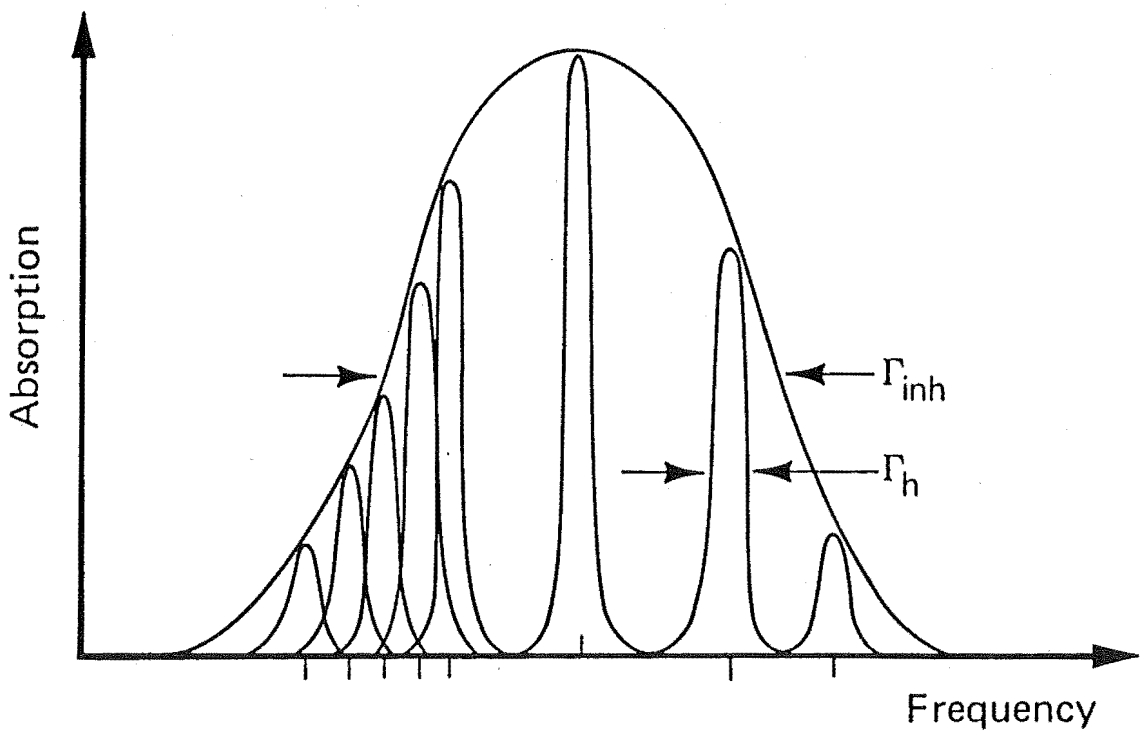

Figure IX.1.1 Schematic view of an inhomogeneously broadened spectral line formed from the envelope of much narrower homogeneous 'spin packets'.

used to selectively excite a narrow portion of the inhomogeneous line; within a single homogeneous linewidth if the laser bandwidth is sufficiently narrow. A dip in the inhomogeneous line profile or 'hole' forms as the ions resonant with the laser are removed from the ground state. Possible reservoirs for the population include the excited state itself, a metastable intermediate electronic state or spin levels and hyperfine splittings of the ground electronic state.

In a simple holeburning experiment the nuclear spin or hyperfine structure is determined by the splittings from the central 'hole' to the 'antiholes', i.e. to the levels showing enhanced populations. Such measurements are difficult since the features are quickly washed out by spin-lattice relaxation as the holeburning laser frequency is scanned to record the spectral line profile. Also the available resolution is limited by the laser bandwidth. A more satisfactory approach is to use double resonance techniques where a second radiation field is applied to the sample. For spin or hyperfine splittings an increase in fluorescence is apparent when an rf field is at resonance with the splittings as the displaced ion population is driven back into resonance with the laser. By sweeping the rf radiation this technique of optically detected nuclear magnetic resonance (ODNMR) can map out all the ground state spin levels and in some cases the excited state splittings.

IX.2 Review of previous work : ODNMR in the C_{4v} F^- site of $CaF_2:Pr^{3+}$

Recently a new holeburning mechanism by optical pumping of ground state superhyperfine levels has been observed in the 594.10 nm $^1D_2 \longleftrightarrow {}^3H_4$ transition of the C_{4v} F^- centre in $CaF_2:Pr^{3+}$ (Macfarlane et al [1981], Burum et al [1982]). The superhyperfine levels

originate from nuclear resonances of neighbouring ^{19}F nuclei IN the host lattice and the holeburning mechanism relies on the large difference in magnetic moment of the Pr^{3+} ion between the ground state and the lowest crystal field component of $^1D_2$. Using ODNMR techniques, resonance lines associated with spin flips of nearest neighbour (nn), next nearest neighbour (nnn) and the interstitial (i) ^{19}F ions were identified.

The 594.097 nm spectral line in $CaF_2:Pr^{3+}$ corresponds to the transition between the lowest crystal field levels of the $^1D_2$ and $^3H_4$ multiplets for the Pr^{3+} ion charge compensated by an interstitial F^- ion. In this site having C_{4v} point group symmetry the $^1D_2$ and $^3H_4$ levels are an electronic singlet and a non-Kramers doublet respectively. The non-zero electron orbital moment of the doublet contributes a large electronic magnetic moment to the Pr^{3+} ion in the ground state. Conversely for the excited singlet state the orbital moment is zero leaving only a nuclear quadrupole contribution and the net magnetic moment is reduced by $\sim 10^4$ to the moment of the bare ^{141}Pr nucleus (Macfarlane et al [1984]). The large magnetic interaction in the ground state produces a large first order hyperfine splitting that can be resolved outside the small inhomogeneous broadening of the transition. Figure IX.2.1 shows the hyperfine and superhyperfine levels for the Pr^{3+} ion of nuclear spin $I = {}^5/_2$.

A strong Pr^{3+} ion local field is set up by the large magnetic moment that inhibits spin flips of neighbouring ^{19}F nuclei while the ion is in the ground state. With the moment quenched when the Pr^{3+} ion is excited to the $^1D_2$ singlet state the ^{19}F nuclei are free to precess leading to a number of fluorine spin flips. Holeburning results when the ion returns to the ground state as its optical transition is shifted out of resonance with the laser by a new arrangement of neighbouring ^{19}F spins. Figure IX.2.2, reproduced from Burum et al [1982], summarizes the superhyperfine holeburning

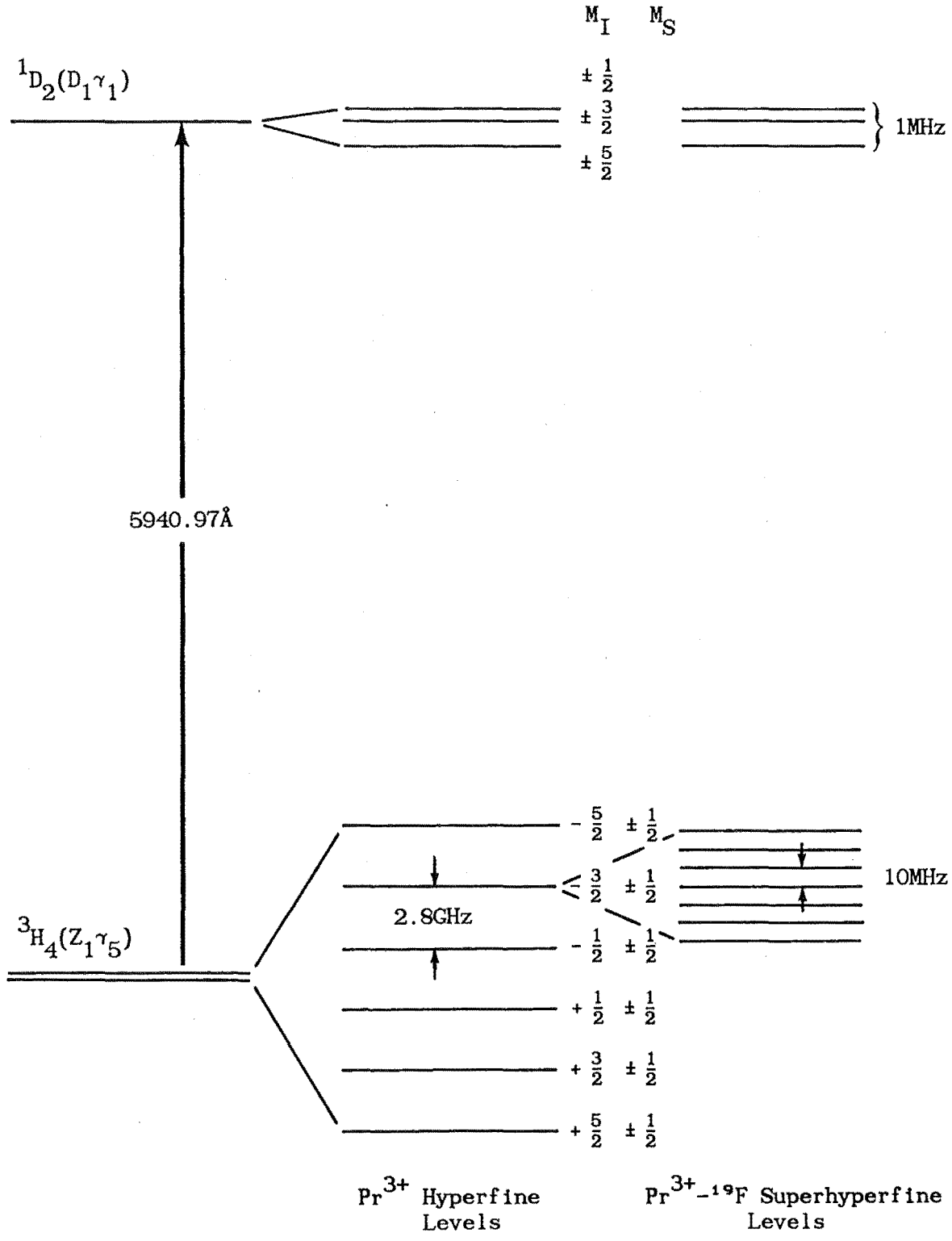

Figure IX.2.1 Energy level diagram of the Pr^{3+} ion, of nuclear spin $I = {}^5/_2$, in the C_{4v} symmetry site showing the hyperfine and superhyperfine levels.

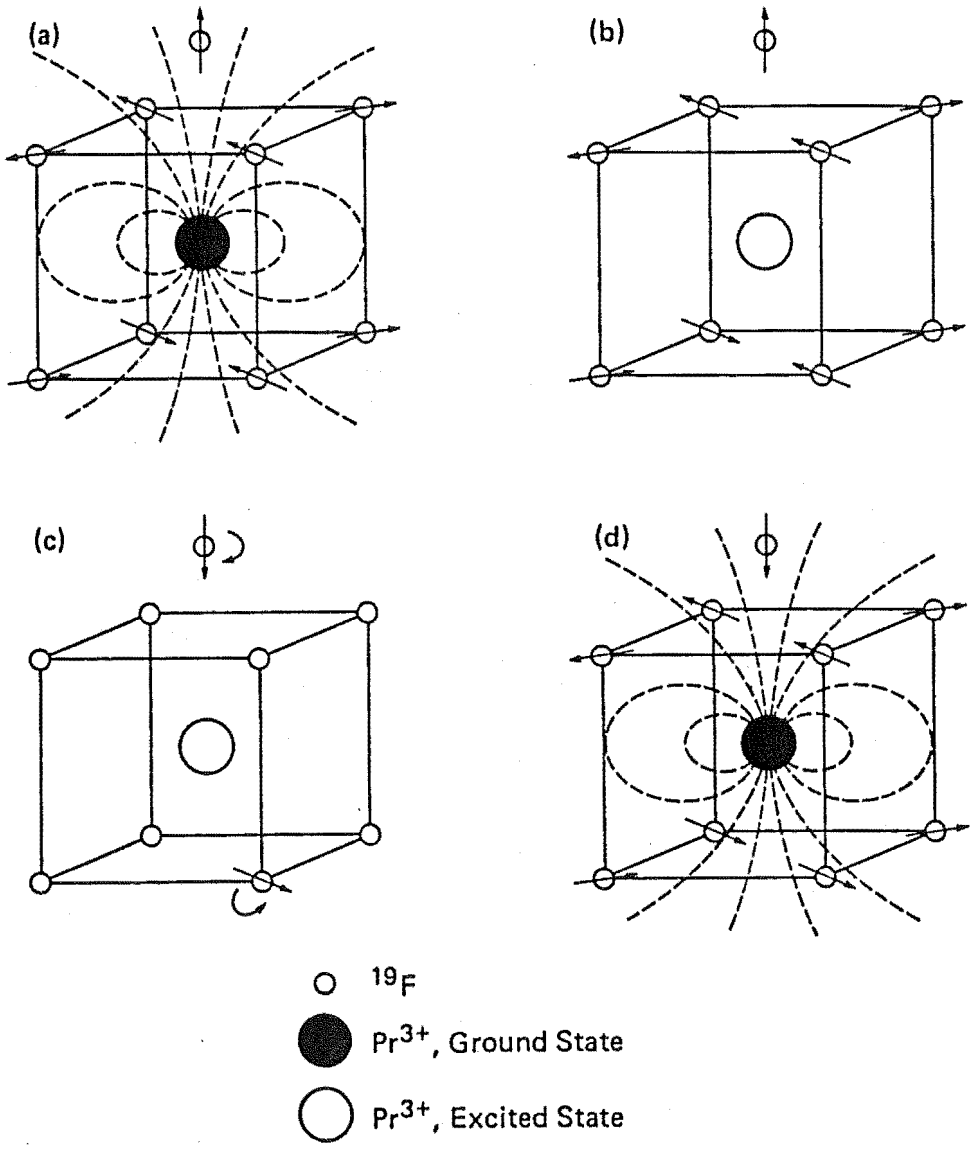

Figure IX.2.2 Pictorial reperesentation of the physical model for holeburning in the C_{4v} site.

(a) While the Pr^{3+} ion is in its ground state, spin flips of surrounding fluorine nuclei are inhibited due to strong coupling with the Pr^{3+} magnetic field.

(b) & (c) When optically excited the Pr^{3+} magnetic field all but vanishes and near neighbour fluorine nuclei are free to undergo spin flips.

(d) Holeburning results as the Pr^{3+} ion returns to its ground state and is out of resonance with the laser due to the energy shift caused by a new configuration of near neighbour fluorine nuclear spins.

mechanism.

Superhyperfine levels that have gained population during the holeburning process would show antiholes in the line profile at energy shifts from the central hole corresponding to the splitting between levels. Macfarlane et al [1981] found evidence of such antiholes ~10 MHz from the central hole, however the small separation and the broadening of the central hole by spin diffusion processes prevented measurement of the splittings. ODNMR techniques are ideal to study the structure as in these experiments the resolution is determined by the rf source rather than the laser.

Burum et al [1982] identified six ODNMR lines and assigned them as follows:-

0.87, 1.34, 1.40 MHz	Next nearest neighbour ^{19}F ions
9.20, 9.75 MHz	Nearest neighbour ^{19}F ions.
20.65 MHz	Interstitial ^{19}F ion.

The inclusion of the interstitial ion next to the Pr^{3+} ion destroys the equivalence of the eight nearest neighbour fluorines. The group of four ^{19}F ions closest to the interstitial will be in a slightly different field of the Pr^{3+} ion than the other four, leading to the observation of two ODNMR lines from nn ions. Note that in their paper the 9.20 MHz ODNMR line was incorrectly assigned to the group of nn fluorine ions furtherest from the interstitial.

The NMR frequency for a neighbouring ligand in the magnetic field H_e of the Pr^{3+} ion is given by

$$h\upsilon = g_N \mu_N H_e \qquad \text{(IX.2.1)}$$

where μ_N is the nuclear magneton and g_N is the ratio of the nuclear magnetic moment of the ligand nucleus in nuclear magnetons and its nuclear spin I. An external magnetic field will add vectorially to the Pr^{3+} ion local field at each of the ligand sites to produce a number of NMR frequencies. These frequencies are symmetrically shifted about the zero field value and correspond to the lifting of the degeneracy of ligands having the same internal field. From a measurement of these frequencies the internal field H_e at the ligand site can be evaluated.

The form of this hyperfine field will consist of two components; a dipolar field due to the electrons of the rare-earth ion acting as point magnetic dipoles and a covalent bonding effect. This latter contribution arises as the Pr^{3+} valence orbitals extend into the lattice to overlap with the orbitals of the neighbouring nuclei. The dipolar field at the ligand site at position $\underset{\sim}{r}$ relative to the rare-earth ion, can be expressed in terms of the magnetic moment $\underset{\sim}{\mu}$ of the Pr^{3+} ion as

$$\underset{\sim}{H}_e = \frac{\underset{\sim}{\mu}}{r^3} - \frac{3(\underset{\sim}{\mu}\cdot\underset{\sim}{r})\underset{\sim}{r}}{r^5} \qquad \text{(IX.2.2)}$$

Fortunately the covalent contributions to the internal field are confined largely to the first shell of neighbours and the assumption of a point dipolar form for the field at the second shell can provide information on ligand positions for these ions.

By measuring the splitting of their ODNMR lines and assuming a dipolar field where appropriate, Burum et al [1982] were able to calculate the positions of the neighbouring ligands of the Pr^{3+} ion in the C_{4v} site and illustrate the distortion of the lattice.

IX.3 ODNMR in hydrogenated crystals of $CaF_2:Pr^{3+}$ and $SrF_2:Pr^{3+}$

For the hydrogenic C_{4v} centres in $CaF_2:Pr^{3+}$ and $SrF_2:Pr^{3+}$ the same superhyperfine holeburning mechanism is expected as they retain the required ground state electronic degeneracy. Of interest in an ODNMR study of these sites is how the superhyperfine structure changes with the different characteristics of the various interstitial ions.

A collaborative study on spectral holeburning in the hydrogenic C_{4v} centres of Pr^{3+} doped crystals is continuing with Drs Neil Manson and Zameer Hasan of the Laser Physics Centre, Australian National University. In a series of preliminary experiments single crystals of hydrogenated and deuterated crystals of $CaF_2:Pr^{3+}$ and $SrF_2:Pr^{3+}$ were immersed in liquid helium at 1.6 K and surrounded by an rf coil. A Coherent model 699 cw single frequency stabilized laser, linewidth ~1 MHz, tuned to match the $^3H_4(Z_1) \longrightarrow {}^1D_2(D_1)$ absorption was used to irradiate the sample with about 30 mW of light. Sample fluorescence from $^1D_2$ to an upper crystal field level of $^3H_4$ was monitored while the rf field was applied. The fluorescence signal was recorded on a signal averager and processed over multiple sweeps of the rf frequency. ODNMR lines from spin flips of nearest neighbour and interstitial ions were observed and their frequencies are tabulated in Table IX.3.1.

The ODNMR line from the D^- interstitial in $SrF_2:Pr^{3+}$ was not observed at the sensitivities used including utilizing the signal enhancement technique of a second rf field recommended by Burum et al [1982]. Using the ratio of the H^- interstitial frequencies in the two lattices and the observed D^- frequency of 2.9 MHz in $CaF_2:Pr^{3+}$ the missing D^- frequency is expected to be ~2.5 MHz. As this frequency is approaching the laser stability, this ion resonance may be washed out.

Table IX.3.1

ODNMR frequencies for nearest neighbour ^{19}F nuclei and various interstitial ions for the tetragonal charge compensated sites in $CaF_2:Pr^{3+}$ and $SrF_2:Pr^{3+}$ crystals.

Crystal and interstitial ion.		ODNMR Measured Frequencyes in MHs for	
		Nearest Neighbour Ions	Interstitial Ions
$CaF_2:Pr^{3+}$	F^-	9.19 9.76	20.63
	H^-	9.33 9.58	17.6
	D^-	9.36 9.60	2.9
$SrF_2:Pr^{3+}$	F^-	8.03 8.9	16.84
	H^-	7.68 8.63	15.34
	D^-	8.25 8.9	-

Further evidence for this was the absence of any next nearest neighbour resonances, even those of the C_{4v} F^- site in $CaF_2:Pr^{3+}$ observed by Burum and coworkers. Figure IX.3.1 shows the ODNMR spectra obtained from the C_{4v} sites in $SrF_2:Pr^{3+}$ with F^- and H^- charge compensating ions. The lines are clearly broader than those observed by Burum et al [1982], probably due to instabilities in the laser frequency.

The six hyperfine lines apparent in the $CaF_2:Pr^{3+}$ C_{4v} F^- site were not observed for any of the other C_{4v} sites under study. The line profile in these cases had the appearance of a single line with linewidth qualitatively larger than the $CaF_2:Pr^{3+}$ C_{4v} F^- site. Reasons for no observable hyperfine structure may include a smaller

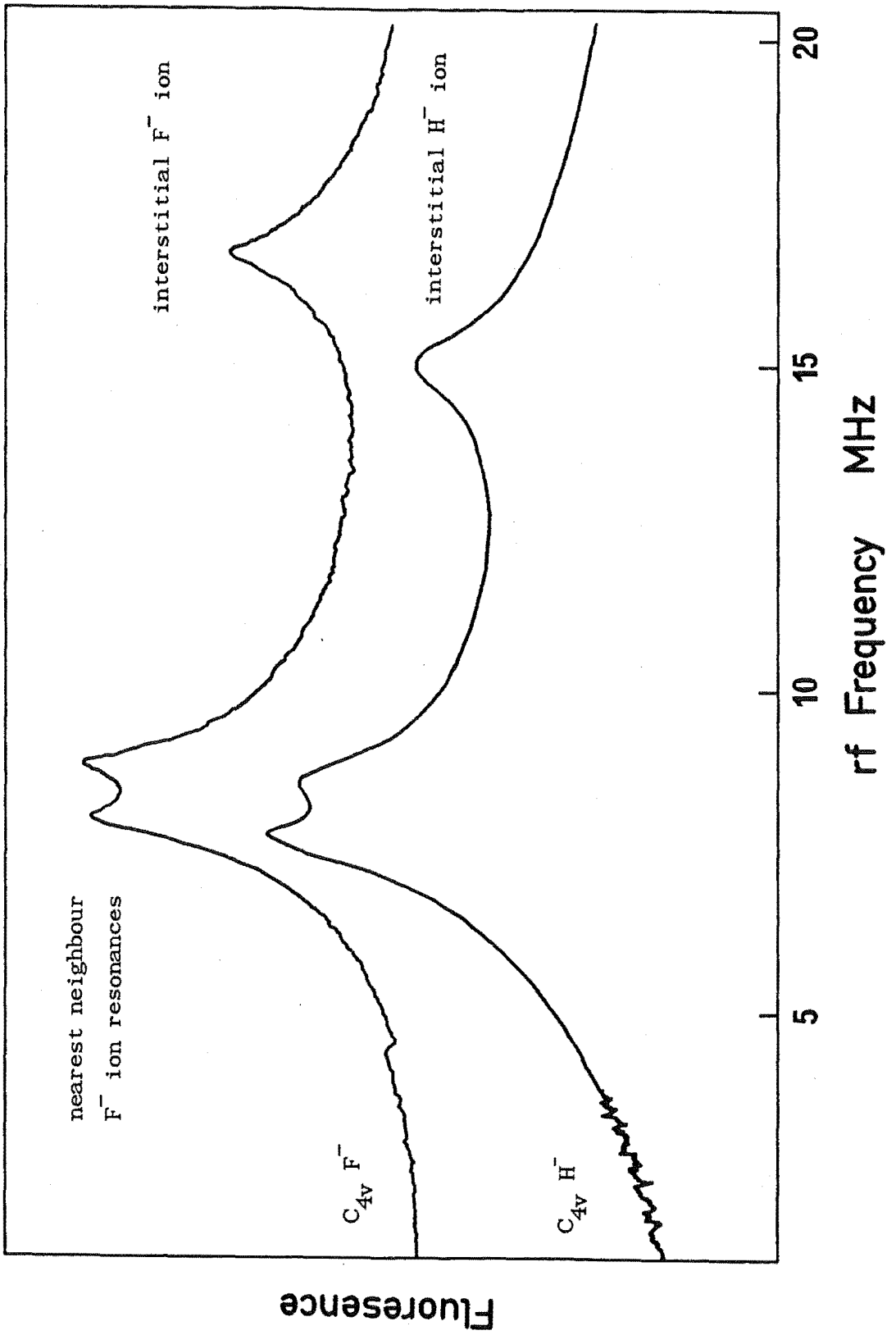

Figure IX.3.1 ODNMR lines from resonances of nearest neighbour ^{19}F nuclei and interstitial F^- and H^- ions in $SrF_2:Pr^{3+}$ crystals.

first order interaction in the other sites or that the structure was not resolvable outside the inhomogeneous broadening. As the crystals used in this study have been subject to stress as part of the hydrogenation or deuteration process, an increase in the inhomogeneous broadening is likely. Also the samples used contained typically 0.05 mol% praseodymium dopant; more than the 0.001 mol% used by Macfarlane et al [1981] to obtain the clearest resolution of the hyperfine structure.

The NMR frequency of ligand ions in the internal field of a paramagnetic ion was given in equation IX.2.1. Then for the C_{4v} sites under study the relative frequencies of the interstitial ion resonances can be estimated from their nuclear g values. Table IX.3.2 summarizes the interstitial ion frequencies observed and their expected relative ratios.

Of immediate interest is the observation of both H^- resonances at frequencies less than the ^{19}F frequencies, in contrast to the prediction from the g_N values. However the D^- interstitial ions appear to follow more closely the ^{19}F ions rather than the electronically similar H^- ions. Previous work using ENDOR on H^- and D^- interstitial ions (Baker, Davies and Reddy [1969], Kiro et al [1969a], [1969b], Kiro and Low [1969]) has shown that the RE^{3+}-interstitial ion distance decreases when H^- and D^- ions are substituted for F^- interstitial ions. Clearly additional effects are occurring as at the closer distance the hydrogenic ions experience a greater local field from the Pr^{3+} ion which should increase the NMR frequency relative to the ^{19}F interstitial ion. The solution to this contradiction probably lies in the large covalent bonding contribution to the observed frequency. Using the praseodymium g_N value of 5.44 MHz|Gauss for $CaF_2:Pr^{3+}$ (Macfarlane, et al [1984]) ,the point

Table IX.3.2

ODNMR frequencies and nuclear g values for the various interstitial ions in the C_{4v} sites of $CaF_2:Pr^{3+}$ and $SrF_2:Pr^{3+}$ crystals.

Interstitial Isotope	Nuclear g value g_N	Expected frequency ratio	Observed frequency (MHz) and ratio			
			$CaF_2:Pr^{3+}$		$SrF_2:Pr^{3+}$	
^{19}F	5.25454	1	20.63	1	16.84	1
H^-	5.58536	1.06	17.6	0.85	15.34	0.91
D^-	0.857387	0.16	2.9	0.14	[a] ≤2	≤0.12
T^-	5.95754	1.13	[b] ___		[b] ___	

[a] Upper limit of D^- resonance given by expected laser stability.

[b] Measurements on C_{4v} T^- sites are in progress.

dipole value for the interstitial fluorine frequency is 7.1 MHz. A large fraction of the observed NMR frequency originates in the covalent bonding, the degree of which will change from F^- to H^- due to their different electronic configurations $1s^2 2s^2 2p^6$ and $1s^2$ respectively. The difference in covalent bonding between H^- and D^- is not expected to be as great.

The differences in the $F^-:H^-:D^-$ interstitial ion positions in the lattice is clearly demonstrated by the frequencies of the nearest neighbour (nn) F^- ions. Figure IX.3.2 shows the ODNMR lines from the nn ^{19}F nuclei for sites with F^-, H^- and D^- charge compensating ions in $SrF_2:Pr^{3+}$ crystals. Covalent bonding will play a significant role in the observed NMR frequencies for the nn ^{19}F nuclei but the extent of the contribution should not change much between the sites with different interstitial ions. Thus any changes in these frequencies directly reflect changes in the positions of the nn nuclei. The group of four nn ^{19}F nuclei furtherest from the interstitial will have their positions and thus frequencies influenced less by the different interstitials. The high frequency nn ODNMR line from these nn nuclei does show less change with F^-, H^- or D^- ion than the low frequency line.

The low frequency ODNMR line corresponding to resonances of the nn ^{19}F nuclei closest to the interstitial shows different behaviour with H^- and D^- charge compensating ion. The frequency is lower for the H^- interstitial than for the F^- interstitial but higher in the case of D^-. The covalent bonding contribution to the frequencies is not expected to be significantly different so these changes are a direct result of the different positions of the interstitial ion. The electrostatic attraction between the RE^{3+} and the interstitial ion will be different for F^- and $H^-(D^-)$ and changes will occur, however H^-

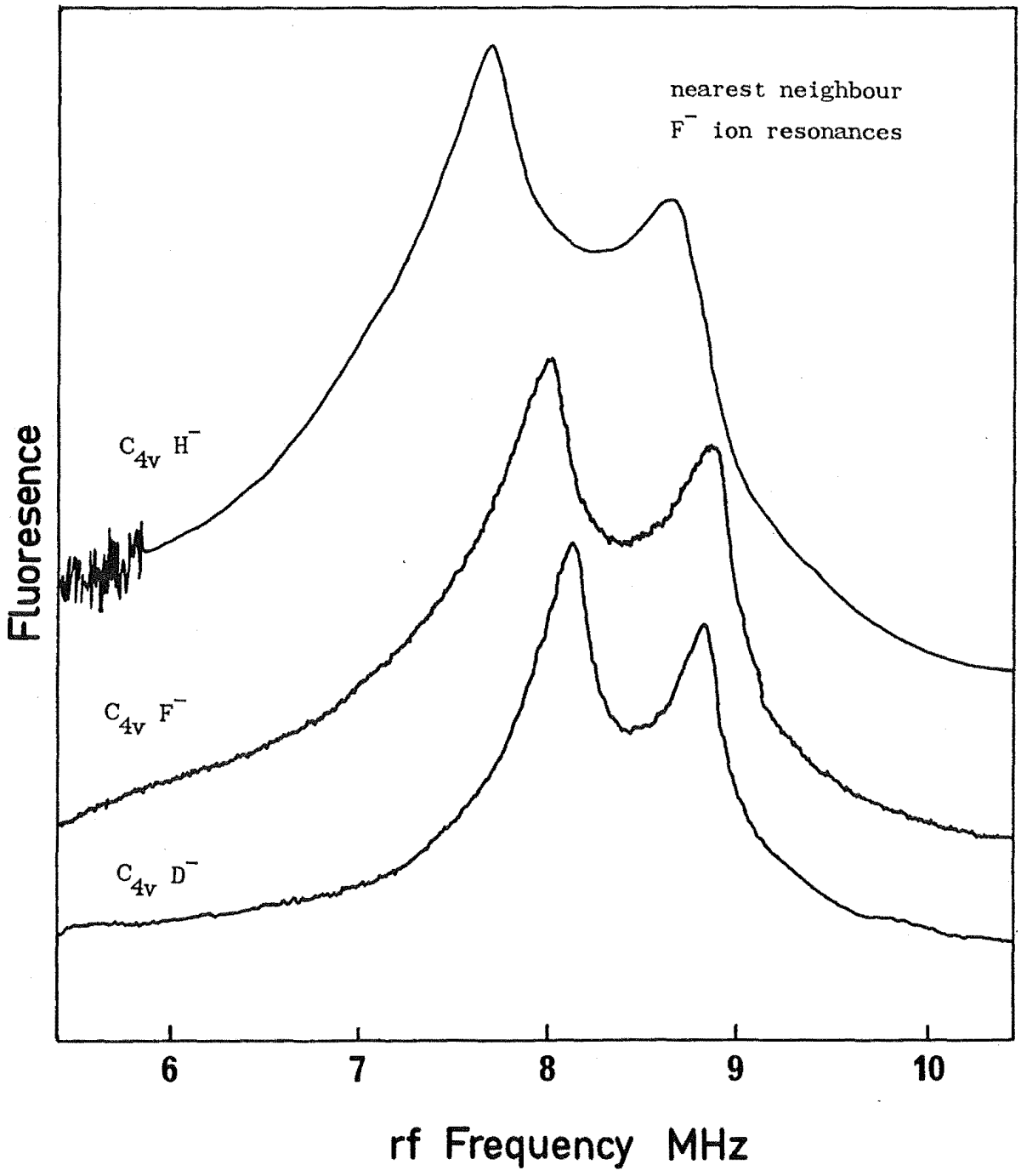

Figure IX.3.2 ODNMR lines from resonances of nearest neighbour ^{19}F nuclei for several C_{4v} sites in $SrF_2:Pr^{3+}$ crystals having different interstitial ions.

and D^- are electronically identical and the differences here may be due to the anharmonic shift associated with the asymmetric potential well of the ions (Jacobs et al [1971]). Investigations on this superhyperfine holeburning mechanism and associated lattice distortions are continuing with studies on the C_{4v} site with tritium ion charge compensation.

CHAPTER X

CONCLUSIONS AND SUGGESTIONS FOR FURTHER WORK

The powerful techniques of laser selective excitation have been successfully applied, and also extended using polarisation effects, to study a multitude of spectroscopic sites in hydrogenated crystals of $SrF_2:Pr^{3+}$ and $CaF_2:Pr^{3+}$. A survey of the tetragonally sited Pr^{3+} ions has established comprehensive sets of energy levels that hold promise for developing theories for the interactions in such crystals.

Several multiple hydrogenic ion sites have been found to exhibit interesting bleaching properties including reversible polarised bleaching and photoproduct formation. Site models have been developed that account for many of the observed features but more work is required for complete verification. Experiments using Stark or magnetic fields would isolate individual centres and predictions based on the models could be tested. Crystals containing both H^- and D^- ions would have bleaching centres with both isotopes and further information on the role of these ions in the bleaching mechanism and their positions may be revealed.

Calculations of the electron-phonon interaction show that the splitting observed in the fundamental x,y vibronic level in the C_{4v} Pr^{3+}- H^- sites is mostly due to a second order interaction with nearby electronic levels. Unfortunately, selection rules for fluorescent transitions restrict the number of lines observed. Infrared absorption spectra from deuterated and tritiated crystals are needed to verify the splittings observed in the optical region.

Temporal studies in hydrogenated crystals have shown that the relaxation properties of the Pr^{3+} ion are solely determined by the hydrogenic ions in the centre and the results fit closely to a simple

theory of multiphonon relaxation. Investigations in other RE^{3+} doped crystals would show whether the phenomenological parameters determined here are universal and if there is an underlying similarity to the relaxation of RE^{3+}- H^- centres.

Hydrogenic ions in rare-earth doped crystals have been studied for many years and have become an area of speciality at the University of Canterbury. The results presented in this work dispel any myths that these systems are well understood and the effects observed continue to surprise us.

REFERENCES

Abragam A. and Bleaney B. [1970], in *Electron Paramagnetic Resonance of Transition Ions*, (Clarendon Press, Oxford) pp 298.

Andeen C.G., Fontanella J.J., Wintersgill M.C., Welcher P.J., Kimble R.J. and Matthews G.E. [1981], J. Phys. C: **14**, 3557.

Baker J.M. and Bleaney B. [1958], Proc. Roy. Soc. (Lond) **A245**, 156.

Baker J.M., Davies E.R. and Reddy T.Rs [1969], Physics Letters **29A**, 118.

Becquerel J. [1907], Radium **4**, 328.

Bloembergen N. [1959], Phys. Rev. Letters **2**, 84.

Bollmans W., Görlich P., Hauk W. and Mothers H. [1970], Phys. Status Solidi A **2**, 157.

Buisson R. and Vial J.C. [1981], J. Physique (Paris) Letters **42**, L115.

Butler P.H. [1981], *Point Group Symmetry Applications*, (Plenum Press, New York and London).

Burum D.P., Shelby R.M. and Macfarlane R.M. [1982], Phys. Rev. **B25**, 3009.

Cario G. and Franck J. [1923], Z. Physik **17**, 202.

Carnall W.T., Fields P.R. and Rajnak K. [1968], J. Chem. Phys. **49**, 4424.

Catlow C.R.A. [1976], J. Phys. C: **9**, 1845.

Chrysochoos, J. [1984], J. Lumin. **31 & 32**, 172.

Cockroft N.J., Han T.P.J., Reeves R.J., Jones G.D. and Syme R.W.G. [1987a], Optics Letters **12**, 36.

Cockroft N.J., Thompson D., Jones G.D. and Syme R.W.G. [1987b], J. Chem. Phys. **86**, 521.

Condon E.U. and Shortley G.H. [1935], *The Theory of Atomic Spectra*, (Cambridge University Press, Cambridge).

Denham P., Field G.R., Morse P.L. and Wilkinson G.R. [1970], Proc. Roy. Soc. (Lond.) **A317**, 55.

Dexter D.L. [1953], J. Chem. Phys. **21**, 836.

Edgar A. [1974], Ph.D. Thesis, University of Canterbury.

Edgar A., Freeth C.A. and Jones G.D. [1977], Phys. Rev. **B15**, 5023.

Edgar A., Jones G.D. and Presland M.R. [1979], J. Phys. C: **12**, 1569.

Edgar A. and Welsh H.K. [1975], J. Phys. C: **8**, L336.

Elliott R.J., Hayes W., Jones G.D., Macdonald H.F. and Sennett C.T. [1965], Proc. Roy. Soc. (Lond.) **A289**, 1.

Feofilov P.P. and Kaplyanskii A.A. [1961], Opt. Spektrosk. **12**, 493. [Opt. Spectrosc. **12**, 272(1961).]

Flach R., Hamilton D.S., Selzer P.M. and Yen W.M. [1975], Phys. Rev. Letters **35**, 1034.

Flach R., Hamilton D.S., Selzer P.M. and Yen W.M. [1977], Phys. Rev. **B15**, 1248.

Fong F.K. [1976], in *Topics in Applied Physics*, Vol 15, ed F.K. Fong (Springer Verlag, Berlin, Heidelberg) pp 1-21.

Fong F.K., Naberhuis S.L. and Miller M.M. [1972], J. Chem. Phys. **56**, 4020.

Freeth C.A. [1974], M.Sc. Thesis, University of Canterbury.

Freeth C.A. and Jones G.D. [1982], J. Phys. C : **15**, 6833.

Friedrich J. and Haarer D. [1984], Angew. Chem. Int. Ed. Engl. **23**, 113.

Gorokhovskii A.A., Kaarli R.K. and Rebane L.A. [1974], Zh. ETF. Pis. Red. **20**, 474 [JETP Lett. **20**, 216(1974)].

Hall J.L. and Schumacher R.T. [1962], Phys. Rev. **127**, 1892.

Han T.P.J. [1987], Private communication, this laboratory.

Harrington J.A., Harley R.T. and Walker C.T. [1970], Solid State Commun. **8**, 407.

Hellewege K.H. [1942], Ann. d. Phys. **40**, 529.

Jacobs I.T. [1971], Ph.D. Thesis, University of Canterbury.

Jacobs I.T., Jones G.D., Zdansky K. and Satten R.A. [1971], Phys. Rev. **B3**, 2888.

Jones G.D., Cockroft N.J., Han T.P.J., Reeves R.J. and Syme R.W.G. [1987], in *Proceedings of the Second Asia-Pacific Physics Conference*, ed S. Chandrasekhar (World Scientific, Singapore) pp 648-655.

Jones G.D., Peled S., Rosenwaks S. and Yatsiv S. [1969], Phys. Rev. **183**, 353.

Judd B.R. [1963], *Operator Techniques in Atomic Spectroscopy* (McGraw-Hill, New York).

Kaiser W. Garrett G.B. and Wood D.L. [1961], Phys. Rev. **123**, 766.

Kiel A. [1964], *Multi-Phonon Spontaneous Emission in Paramagnetic Crystals*, in: Quantum Electronics, eds P. Grivet and N. Bleombergen (Columbia University Press, New York) pp 765-777.

Kiro D. and Low W. [1969], Physics Letters **29A**, 537.

Kiro D., Low W. and Kafri A. [1969a], Phys. Rev. Letters **22**;, 893.

Kiro D., Low W. and Schipper D.J. [1969b], Physics Letters **29A**, 586.

Kliava J., Evesque P. and Duran J. [1978], J. Phys. C : **11**, 3357.

Koster G.F., Dimmock J.D., Wheeler R.G. and Statz H. [1963] *Properties of the Thirty Two Point Groups*, (M.I.T. Press, Cambridge, Massachusetts).

Krupke W.F. [1966], Phys. Rev. **145**, 325.

Kushida T. and Geusic J.E. [1968], Phys. Rev. Letters **21**, 1172.

Kushida T., Kinoshita S., Ohtsuki T. and Yamada T. [1982], Solid State Commun. **44**, 1363.

Lea K.R., Leask M.J.M. and Wolf W.P. [1962], Phys. Chem. Solids **23**, 1381.

Lezama A., Oriá M. and de Araújo C.B. [1986], Phys. Rev. **B33**, 4493.

Lezama A., Oriá M., Rios Leite J.R. and de Araújo C.B. [1985], Phys. Rev. **B32**, 7139.

Macfarlane R.M., Shelby R.M. and Burum D.P. [1981], Optics Letters **6**, 593.

Macfarlane R.M., Burum D.P. and Shelby R.M. [1984], Phys. Rev. B29, 2390.

Macfarlane R.M., Reeves R.J. and Jones G.D. [1987], Accepted for publication in Sept. Issue of Optics Letters - also included in Appendix 1.

Miller M.P., Tallant D.R., Gustafson F.J. and Wright J.C. [1977], Anal. Chem. 49, 1474.

Maradudin A.A. and Peretti J. [1967], Phys. Rev. 161, 852.

Miyakawa T. and Dexter D.L. [1970a], Phys. Rev. B1, 70.

Miyakawa T. and Dexter D.L. [1970b], Phys. Rev. B1, 2961.

Moos H.W. [1970], J. Lumin. 142, 106.

Nauta-Leefers Z.C. and den Hartog H.W. [1979], Phys. Rev. B19, 4162.

Newman R.C. [1973], *Infra-red Studies of Crystal Defects* (Taylor & Francis, London).

Nielson C.W. and Koster G.F. [1963], *Spectroscopic Coefficients for* p^n, d^n *and* f^n *Configurations*, (M.I.T. Press, Cambridge, Mass.).

Partlow W.D. and Moos H.W. [1967], Phys. Rev. 157, 252.

Perlin Yu.E. and Kaminskii A.A. [1985], Phys. Stat. Sol. B. 132, 11.

Pollack S.A. and Satten R.A. [1962], J. Chem. Phys. 36, 804.

Rajnak K. and Wybourne B.G. [1963], Phys. Rev. 132, 280.

Reeves R.J., Jones G.D., Cockroft N.J., Han T.P.J. and Syme R.W.G. [1987], submitted for publication in Journal of Luminescence - also included in Appendix 1.

Riseberg L.A. and Moos H.W. [1967], Phys Rev. Letters 19, 1423.

Riseberg L.A. and Moos H.W. [1968], Phys. Rev. 174, 429.

Riseberg L.A. and Weber M.J. [1976], *Relaxation Phenomena in Rare Earth Luminescence*, in : Progress in Optics XIV, ed. E. Wolf (North Holland, Amsterdam) pp 89-159

Rotenberg M., Bivins R., Metropolis N. and Wooten J.K. [1959], *The 3-j and 6-j Symbols*, (Technology Press, Cambridge, Mass.).

Spitzer R.C., Ambrose W.P. and Seivers A.J. [1986], Optica Letters 11, 428.

Syme R.W.G., Reeves R.F. and Jones G.D. [1984], J. Lumin. 31 & 32, 248.

Teplov M.A. [1968], Zh. Eksp. Teor. Fiz. 53, 1510 (Sov. Phys JETF 26, 872 (1968)).

Tomblin C.W. [1983], Ph.D. Thesis, University of Canterbury.

Van Vleck J.A. [1937], J. Phys. Chem. 41, 67.

Volker S., Macfarlane R.M., Genack A.Z., Trommsdorff H.P. and Van der Waals J.H. [1977], J. Chem. Phys. 67, 1759.

Weber M.J. [1967], Phys. Rev. 157, 262.

Weber M.J. [1968], Phys. Rev. 171, 283.

Wigner E.P. [1959], *Group Theory* (Academic Press, New York).

Wood D.L. and Kaiser W. [1962], Phys. Rev. 126, 2079.

Wright J.C. [1976], *Upconversion and Excited State Energy Transfer in Rare-Earth Doped Materials*, in : Topics in Applied Physics Vol 15, (Springer Verlag, Berlin, Heidelberg) pp 239-295.

Wybourne B.G. [1965], *Spectroscopic Properties of Rare Earths* (Wiley Interscience, New York).

Zdansky K. and Edgar A. [1971], Phys. Rev. B3, 2133.

Zverev G.M., Kolodnii G.Ya. and Onishenko A.M. [1971], Sov. Phys. JETP 33, 497.

APPENDIX

PUBLICATIONS

1) Syme R.W.G., Reeves R.J. and Jones G.D., *Laser Selective Excitation of Fluorine and Hydrogenic Charge Compensation Sites in* $SrF_2:Pr^{3+}$, J. Lumin. 31 & 32 (1984), 248.

2) Cockroft N.J., Han T.P.J., Reeves R.J., Jones G.D. and Syme R.W.G., *Reversible Polarized Bleaching in Hydrogenated Rare-earth-doped Fluorides*, Optics Letters, **12** (1987), 36.

3) Macfarlane R.M., Reeves R.J. and Jones G.D., *Persistent Spectral Holeburning Due to Deuteron Tunneling in an Organic Material* $SrF_2:Pr^{3+}:D^-$, accepted for publication in Sept 1 issue of Optics Letters, 1987.

4) Reeves R.J., Jones G.D., Cockroft N.J., Han T.P.J. and Syme R.W.G., *Dynamical Processes Involving Local Modes for Rare-Earth Centres in* CaF_2, submitted for publication in Journal of Luminescence (1987).

Journal of Luminescence 31 & 32 (1984) 248-250
North-Holland, Amsterdam

LASER SELECTIVE EXCITATION OF FLUORINE AND HYDROGENIC CHARGE COMPENSATION SITES IN $SrF_2:Pr^{3+}$

R.W.G. Syme, R.J. Reeves and G.D. Jones

Department of Physics, University of Canterbury, Christchurch, New Zealand.

Two hydrogenic and two fluoride ion sites are identified. Fluorescence lines, local mode vibronics and two near coincidences with argon laser lines are discussed.

Hydride ions are well established as an alternative charge compensation species for trivalent rare earth ions in hydrogenated alkaline earth fluoride crystals. Andeen et al.[1] used audio frequency capacitance methods to determine the presence of the nearest neighbour tetragonal symmetry (C_{4v}) fluoride ion charge compensation site in SrF_2:0.1% Pr^{3+} crystals and a further dimer (RIV) site in the SrF_2:1% Pr^{3+} crystals. Edgar et al.[2] used infrared absorption and e.p.r. methods to establish the existence of two hydrogenic sites in hydrogenated SrF_2:0.05% Pr^{3+} cyrstals and assigned these to the hydrogen analogue of the C_{4v} site found in the parent crystals and to a rhombic symmetry (C_s) site, thought to be a modification of the hydrogenic C_{4v} site.

We have measured the optical absorption and laser selectively excited fluorescence spectra of SrF_2:0.05% Pr^{3+} crystals both before and after hydrogenation. The energy levels of the $4f^2$ configuration are appropriate to trivalent praseodymium ions and crystal field levels of the $^1D_2$ multiplet lie within the tuning range of a rhodamine 6G dye laser. These levels were selected for excitation of the fluorescence spectra of the various praseodymium sites determined by the optical absorption studies.

Before hydrogenation, the crystals show two distinct sites (identified in Figure 1) whose $^1D_2 \rightarrow {}^3H_4$ fluorescence spectra are presented in Figure 2. After hydrogenation, two hydrogenic sites are apparent (Figure 1) and these yield additional fluorescence spectra when selectively excited (Figure 2). The identification of these new sites as hydrogenic is confirmed both by the existence of an isotope shift in the Pr^{3+} ion electronic lines and by the observation of local mode vibronic lines (Figure 2). The hydrogenic C_{4v} site local mode vibronic intervals match those found in the infrared by Edgar et al.[2] to $\pm 2\ cm^{-1}$ while a tentative correlation of local mode vibronics with infrared local mode lines is obtained for the second hydrogenic site with the C_s site of Edgar et al.[2]

0022–2313/84/$03.00

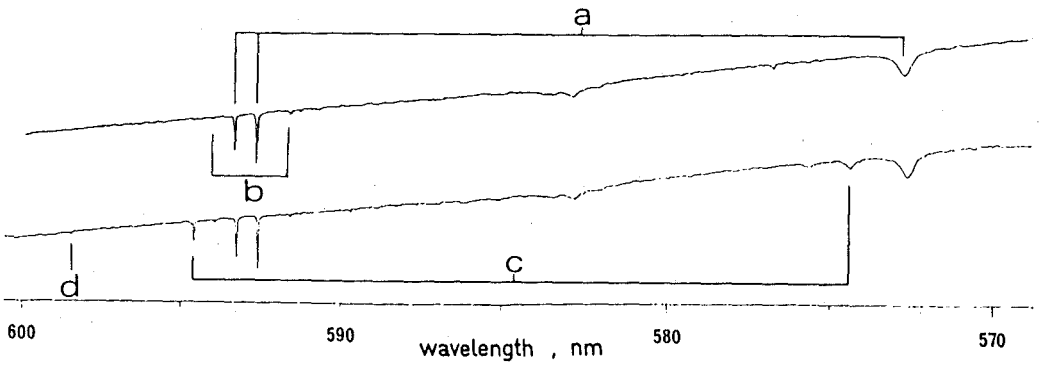

FIGURE 1

Optical transmission spectra of SrF_2:0.05% Pr^{3+} before and after hydrogenation. a and b identify the absorption lines of the fluoride ion C_{4v} and the second fluorine sites while c and d identify the hydrogenic C_{4v} and C_s sites respectively.

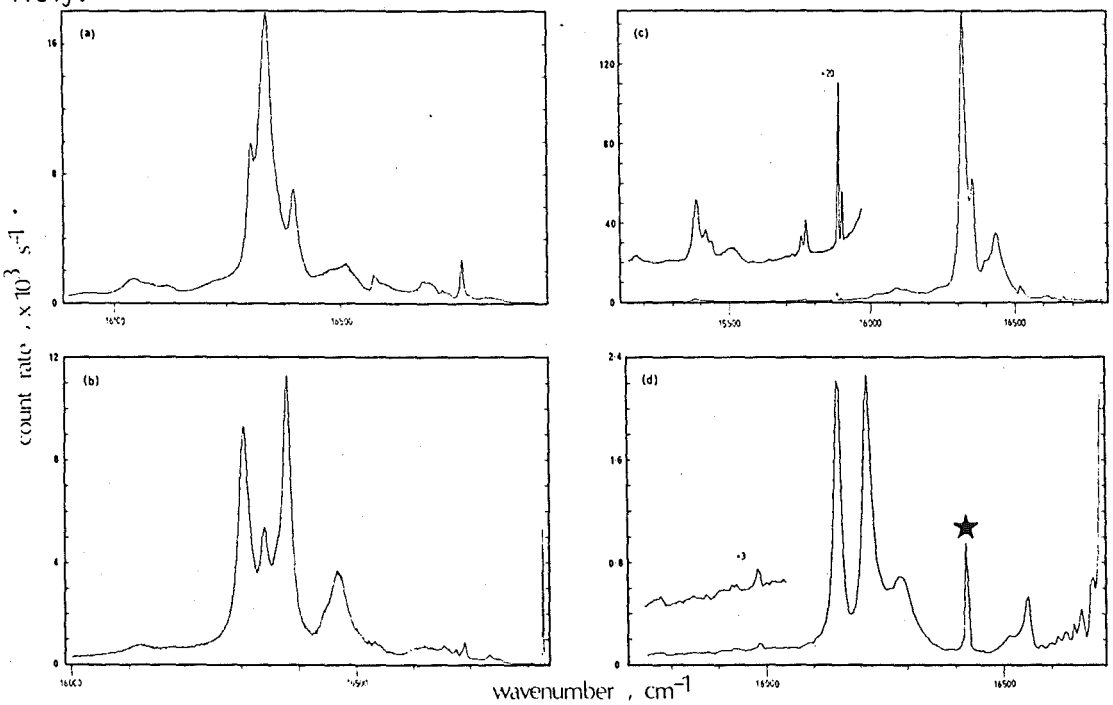

FIGURE 2

Laser selective fluorescence spectra of SrF_2:0.05% Pr^{3+} crystals before and after hydrogenation. The excitation wavenumbers are those at the extreme right hand side of each spectrum and the sharp peak marked * in (d) is the first-order Raman scattering line of the SrF_2 host crystal. (a) and (b) are the fluorescence spectra of the fluoride ion C_{4v} and the second fluorine sites respectively; (c) and (d) are those of the hydrogenic C_{4v} and C_s sites respectively. The expanded traces in (c) and (d) show details of the H^- local mode vibronics.

Fluorescence lifetime measurements were made on the transition from the lowest crystal field level of the $^1D_2$ multiplet for the fluoride, hydrogenic and deuterium C_{4v} sites by Dr. R.M. Macfarlane of the I.B.M. Research Laboratories, San José, California, who obtained values of 2.3 msecs for the fluoride C_{4v} site, 350 μsec for the deuterium C_{4v} site and 2.7 μsec for the hydrogenic C_{4v} site. Such results support a model for non-radiative decay to the $^1G_4$ multiplet some 6000 cm^{-1} lower in energy through the local mode phonons.

Preliminary measurements have been made on the analogous CaF_2:0.5% Pr^{3+} system. Results for the parent crystals have been published by Evesque et al.[4] among others. We find the hydrogenic spectra are more complex than in the hydrogenated SrF_2:0.05% Pr^{3+} system and comparable with the findings of Thompson[5] who identified six distinct hydrogenic sites in hydrogenated CaF_2:0.05% Er^{3+}. Further work is needed to correlate specific praseodymium sites with those identified for erbium.

Strontium fluoride crystals containing praseodymium feature two near coincidences for praseodymium site lines with two principal argon laser lines at 476.5 and 488.0 nm. The transition to the $^3P_0$ multiplet of the fluoride ion C_{4v} site is 0.3 nm longer wavelength than the 476.5 nm argon laser line, while the transition to the $^3P_0$ multiplet of an unidentified deuterium site produced in aged crystals falls within the profile of the 488.0 nm argon laser line. Such near coincidences offer the possibility of high resolution studies of these particular praseodymium site transitions by Zeeman sweeping them through a single mode argon laser line.

CONCLUSIONS

These preliminary measurements reveal the existence of hydrogenic sites whose identification, dynamics and thermal behaviour are under further study.

ACKNOWLEDGEMENTS

We wish to thank Dr. Roger Macfarlane for his active interest in this work and in providing his fluorescence lifetime measurements prior to publication.

REFERENCES

1) C.G. Andeen, J.J. Fontanella, M.C. Wintersgill, P.J. Welcher, R.J. Kimble and G.E. Matthews, J. Phys. C. 14 (1981) 3557.

2) A. Edgar, C.A. Freeth and G.D. Jones, Phys. Rev. B15 (1977) 5023.

3) C.A. Freeth and G.D. Jones, J. Phys. C. 15 (1982) 6833.

4) P. Evesque, J. Kliava and J. Duran, J. Luminescence 18/19 (1979) 646.

5) D. Thompson, M.Sc. Thesis (University of Canterbury 1983) unpublished.

Reversible polarized bleaching in hydrogenated rare-earth-doped fluorites

N. J. Cockroft, T. P. J. Han, R. J. Reeves, G. D. Jones, and R. W. G. Syme

Department of Physics, University of Canterbury, Christchurch, New Zealand

Received August 11, 1986; accepted October 15, 1986

By using site-selective laser spectroscopy, several sites in hydrogenated and deuterated rare-earth-doped fluorite crystals have been found to exhibit reversible bleaching. The site orientations can be switched between orthogonal directions by corresponding changes in the laser polarization. Such effects are a form of photochemical hole burning and are attributed to laser-induced migration of H^- or D^- ions between equivalent interstitial positions adjacent to the rare-earth ion.

An unusual phenomenon of reversible polarized bleaching has been observed for some hydrogenic sites in calcium and strontium fluorides containing 0.05% rare-earth ions. Previous studies of the hydrogenated and deuterated crystals reveal the existence of several low-symmetry sites derived from the hydrogenic C_{4v} site.[1] Recent laser-selective-excitation studies have shown that these sites (both H^- and D^- varieties) differ in the placement, relative to a ⟨100⟩ oriented RE^{3+}–H^- ion charge-compensation pair, of a second H^- ion substituting for an adjacent lattice F^- ion. Detailed spectroscopy of these sites will be presented elsewhere.

Many of these sites exhibit bleaching when studied by laser-selective excitation using a Spectra-Physics 375 tunable dye laser. On pumping appropriate rare-earth electronic transitions, with laser powers in the range 10 to 100 mW, the intensity of various fluorescence lines are observed to decrease by factors of up to 15 in times ranging from 10 sec to 5 min. Illuminating a different segment of the crystal restores the initial fluorescence level, which again rapidly decreases. Slightly shifting the laser frequency within the absorption contour gives a similar pattern of fluorescence response. Simultaneous monitoring of the transmitted laser light shows decreases in the absorption of up to 70% over the same period. This decreased absorption has been observed to persist at 15 K for 2 h, the longest period tested. Both H and D isotopes show the effect, and in all cases studied the H^- sites give a more rapid fluorescence decrease than the corresponding D^- sites.

Some of these bleachable sites exhibit a new phenomenon of reversible polarized bleaching. This effect is clearest for ⟨100⟩ oriented crystals with the laser light incident parallel to, say, the [100] unit cell edge. After bleaching with the laser polarized in the [001] direction, fluorescence could be substantially restored by switching the laser polarization to the [010] direction. Moreover, by suitable sequential pumping with the laser polarized in these two directions, an apparently indefinite sequence of bleaching and successive recovery of the fluorescence could be accomplished. Recovery levels of 95% or more are found for several sites after many cycles of successive bleaching [Fig. 1(a)]. Corresponding effects are seen in the transmission of the laser light. Subsequent pumping of the site with the laser polarized in the [011] direction gives a relatively stable intermediate level of fluorescence. Table 1 summarizes the number of bleachable centers found to date. Neither the hydrogenic C_{4v} site, from which nearly all these sites are derived, nor any of the fluoride ion charge-compensation sites studied have been observed to show this effect. Preliminary time-dependence studies of the bleaching rates reveal a mixture of single-exponential decay and two-body $1/t$ decay behavior,[2] depending on the site studied.

Temperature-dependence studies of the previously reported C_s site[3] in SrF_2:Pr^{3+} show bleaching times increasing with temperature until no bleaching effects are observed at a crystal temperature of 100 K. Preliminary studies of the same site at 2 K using a single-mode dye laser revealed a hole of width 800 MHz burned into the absorption contour, characteristic of photochemical hole burning.

The bleaching characteristics vary for different absorption lines of a given site. For a particular site in SrF_2:Nd^{3+}:D^- two of the three absorption transitions to the $^4G_{5/2}$ multiplet (at 17 026.3 and 17 153.5 cm^{-1} in vacuum) gave distinctly different fluorescence-decrease rates. Excitation of the third absorption transition (at 17 164.2 cm^{-1}) gave no sign of bleaching but removed any asymmetry induced by previous pumping of either of the two other transitions.

These reversible bleaching observations can be understood on a model of reorientation of ⟨100⟩ RE^{3+}–H^- ion pairs. The exact configuration of the sites showing reversible bleaching cannot be of critical significance, as a number of sites display the effect. A possible site configuration, derived from the well-established hydrogenic C_{4v} site, is presented in Fig. 2, which also shows a proposed reorientation mechanism.[4,5] Selective excitation with appropriately polarized laser light could result in the substitutional H^- ion's migrating to an adjacent empty interstitial posi-

0146-9592/87/010036-03$2.00/0

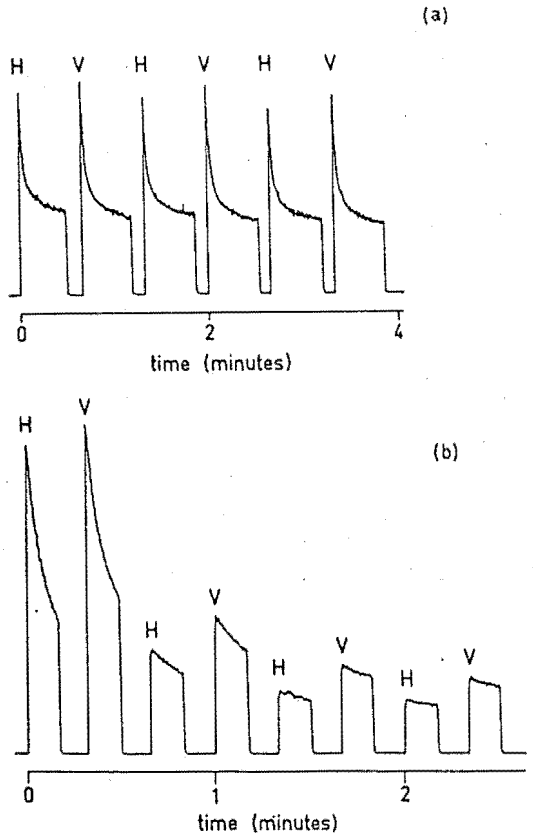

Fig. 1. Fluorescence intensity as a function of time for a sequence of laser excitations for two possible polarization directions, V[001] and H[010], of (a) the 16 612.8-cm^{-1} transition in a ⟨100⟩ oriented SrF_2:0.05% Pr^{3+}:D^- crystal showing bleaching and successive recovery of fluorescence and (b) the 16 667.0-cm^{-1} transition in a ⟨100⟩ oriented SrF_2:0.05%Pr^{3+}:D^- crystal showing independent bleaching of the different site orientations.

tion. The charge-compensating ion of this pair then occupies the vacated substitutional position, resulting in a preferential reorientation of the RE^{3+} H^- pair into the two directions at 90° to the original alignment. An alternative mechanism of direct interstitial H^- ion migration along a ⟨110⟩ direction could equally well be invoked.[4] The presence of the substitutional H^- ion adjacent to the RE^{3+} ion could permit ion displacements favorable for direct transfer of the interstitial H^- ion, whereas the simple H^- C_{4v} site shows no reorientation under the same excitation conditions.

Subsequent laser excitation of the reoriented RE^{3+}–H^- ion pair causes a return to the original alignment. As there are three equivalent ⟨100⟩ directions and only two laser-polarization directions, there is a preferential excitation of some site orientations. The extent of preferential orientation and recovery depends on the relative absorption coefficients of the transition being excited for laser light parallel (π type) and perpendicular (σ type) to the site's principal symmetry axis. The clearest polarization results are expected for Pr^{3+} ions, for which π- and σ-type transitions can be separately excited, whereas the odd-electron systems studied (Nd^{3+} and Er^{3+}) have either σ or mixed $\sigma\pi$ transitions. Nevertheless, all three ions show pronounced reversible bleaching and recovery effects.

The varied behavior of the previously mentioned SrF_2:Nd^{3+} site can be understood if the absorption transition yielding no bleaching effects has an isotropic absorption cross section whereas the other two are of predominantly σ type.

For the sites that do not exhibit the reversible phenomenon [Fig. 1(b)] there is no preferential reorientation of the RE^{3+}–H^- pairs, and the differently oriented pairs bleach independently. For these sites the H^- migration creates a new center with its absorption transition out of resonance with the laser. An example of site interconversion is seen to exist between two different sites in SrF_2:Nd^{3+}:H^-; there the bleaching of one site by laser irradiation at 17 085 cm^{-1} can be removed by subsequent irradiation of the absorption line at 17 096 cm^{-1} of the second closely related site and vice versa.

Table 1. Number of Bleachable Centers Established to Date in Hydrogenated Rare-Earth-Doped Fluorite Crystals[a]

Crystal	Number of Bleachable Centers	Number Showing Reversible Behavior
CaF_2:Pr^{3+}	3	2
SrF_2:Pr^{3+}	4	2
CaF_2:Nd^{3+}	1	–
SrF_2:Nd^{3+}	2	1
CaF_2:Er^{3+}	4	3

[a] Equivalent H^- and D^- varieties are not counted separately.

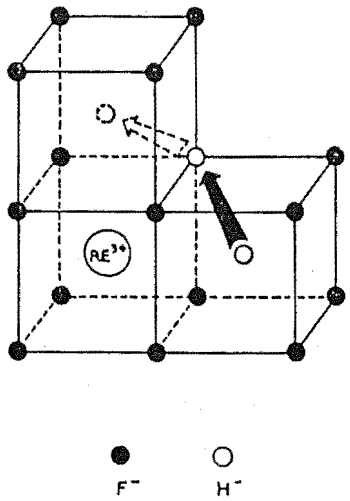

Fig. 2. A possible configuration for sites exhibiting reversible polarized bleaching. The arrows indicate one mechanism giving centers reoriented at 90° to the original alignment.

be determined by the time for the incident light flux to bleach all the absorbing centers of a given site. For the laser powers used, the fastest decay rates of the order of 1 sec observed here approach this limit. The rate of fluorescence decrease will depend also on the various diffusion processes and paths involved, with H^- sites reorienting more rapidly than the corresponding D^- ones because of the greater mobility of H^- ions.

This phenomenon of reversible bleaching is under more detailed study, as it offers a useful insight into the dynamics of light ion migration, is of interest for the redistribution in population of oriented sites, and could have application in the optical storage and retrieval of information.

This research was supported by research grants Zealand. N. J. Cockroft and R. J. Reeves acknowledge support by UGC postgraduate scholarships. We thank Ross Ritchie, Terry Rowe, and Wayne Smith for technical assistance and the Australian National University for access to equipment for the high-resolution measurements.

References

1. A. Edgar, G. D. Jones, and M. R. Presland, J. Phys. C 12, 1569 (1979).
2. B. Welber, J. Chem. Phys. 43, 3015 (1965).
3. R. W. G. Syme, R. J. Reeves, G. D. Jones, J. Lumin. 31, 248 (1984).
4. C. R. A. Catlow, J. Phys. C 9, 1845 (1976).
5. Z. C. Nauta-Leeffers and H. W. den Hartog, Phys. Rev. B 19, 4162 (1979).

PERSISTENT SPECTRAL HOLEBURNING DUE TO DEUTERON TUNNELING IN AN INORGANIC MATERIAL $SrF_2:Pr^{3+}:D^-$

R. M. Macfarlane

IBM Almaden Research Center
650 Harry Road
San Jose, California 95120

R. J. Reeves
G. D. Jones

Physics Department
University of Canterbury
Christchurch, New Zealand

ABSTRACT: We report the observation of persistent spectral holeburning due to a mechanism which is new to inorganic materials, *i.e.*, light induced deuteron (or proton) tunneling. Measurements were made on $^3H_4 \leftarrow \rightarrow {}^1D_2$ transitions of $SrF_2:Pr^{3+}$ centers having two D^- ions as near neighbors. The spectral holes exhibit hyperfine structure dominated by very large (~100 MHz) pseudoquadrupole splittings in the singlet ground state.

We report the observation of persistent spectral holeburning based on a mechanism which is new to inorganic materials, *i.e.*, light induced deuteron or proton motion. This is somewhat analogous to proton tautomerism in organic molecules which is known to lead to spectral holeburning in systems such as free-base phthalocyanine [1] and porphin [2]. Our measurements were made on deuterated Pr^{3+} centers in SrF_2. We used this effect to make the first observation of hyperfine structure in a persistent holeburning experiment and find the largest pseudoquadrupole splittings yet reported for Pr^{3+}. These large pseudoquadrupole splittings arise from the close proximity of the first excited electronic state to the ground state.

Previous uses of holeburning for hyperfine structure measurement used optical pumping of the hyperfine levels to produce a pattern of holes and antiholes due to redistribution of the ground state population [3]; this pattern then relaxes with the characteristic spin-lattice relaxation time. The present experiments differ in that a stable photoproduct is formed corresponding to centers having the Pr^{3+} ion in a different environment. No antiholes are produced since the photoproducts either absorb at frequencies distributed over the inhomogeneous line, or absorb in different zero-phonon lines. The high resolution capability of spectral holeburning provides a new probe of the structure and dynamics of centers associated with H^-, D^- and T^- ions in solids.

The broadband polarized bleaching of centers in deuterated SrF_2:Pr^{3+} was reported recently [4]. It appears that only centers containing two D^- (or H^-, T^-)ions exhibit persistent bleaching. Spectral data for the two principal sites of this kind are summarized in Table 1. These centers are assigned to Pr^{3+} ions in sites charge compensated by a D^- ion in the [100] interstitial position and having a second D^- ion substituting for a lattice F^- ion. Two possible configurations, with the substituting D^- ion in the nearest neighbor

shell are shown in Figure 1. In one site the substitutional D^- is on the side of the coordination cube closest to the interstitial (Fig. 1a) and in the other the substitutional D^- is opposite the interstitial (Fig. 1b). These centers are expected to have two sets of three D^- ion local-mode vibronics, with those of the D^- ion closer to the Pr^{3+} ion having greater intensity due to a stronger interaction between the electrons and the local-mode phonons. While the site configurations of Figure 1 are consistent with the major features of the observed lines, a completely unequivocal assignment cannot be made using the present vibronic data.

The presence of a charge compensating D^- ion in an approximately C_{4v} symmetry site is inferred from the observation of vibronic lines with frequencies similar to those which we have observed for the D^- C_{4v} site, viz., 658.4 and 666.9 cm^{-1} for the doubly degenerate (X,Y) local mode vibration [6] and 684.9 cm^{-1} for the Z local mode vibration (Table 1). The presence of a nearest neighbor substitutional D^- ion is inferred from the observation of three strong local mode lines. These have vibrational intervals whose mean frequency is close to the frequency, 642 cm^{-1}, of an isolated D^- ion in the regular T_d symmetry lattice anion sites [5]. For the configurations proposed, (Figure 1) the observed vibronic lines are assigned as follows. The three-fold degenerate T_d site line at 642 cm^{-1} of the isolated substitutional D^- ion is split into two components by the neighboring Pr^{3+} ion. The interstitial D^- ion further splits the doubly degenerate component to give a three line vibronic set. For the interstitial D^- ion, the neighboring ionic charge distribution is similar to that of the C_{4v} site and only relatively small deviations from the C_{4v} site line frequencies are found (Table 1).

The $C_s(1)$ and $C_s(2)$ centers both exhibit polarized bleaching, for their $^3H_4(Z_1) \rightarrow {}^1D_2(D_1)$ transitions, which can be largely reversed by rotating the polarization

of the laser from the [100] to [010] direction. This indicates that in both cases the main photoproducts are equivalent centers with local axes along [001] rotated from the original direction by 90 °. A model which exhibits this behavior is one where the charge compensating D^- ion moves to an equivalent position. After bleaching alternately in two orthogonal polarizations, intensity is eventually lost from the zero-phonon line. This is particularly pronounced in the case of the $C_s(2)$ center, and this loss is associated with a second bleaching mechanism which results in a photoproduct center absorbing at 5999.2 Å, labelled $C_s(2)^*$ in Figure 2. This center does not exist in the as-grown material. Some of the lost intensity can reside in the third orientation, polarized in the direction of the probe laser propagation. For the $C_s(1)$ center this may be the only process occurring as no photoproduct absorption has yet been found at a different wavelength. The photoproduct line $C_s(2)^*$ can be completely bleached and this restores almost all of the intensity in $C_s(2)$.

A noteworthy feature of the H^- , D^- or T^- ion substitution is the marked dependence of the bleaching rates on the particular isotope present. Under similar irradiation powers, the $2H^-$ centers bleach at a rate typically 50 times faster than the corresponding $2D^-$ centers. This behavior closely parallels the strong increase in non-radiative relaxation rates in going from D^- to H^- sites, as evidenced by much reduced fluorescence lifetimes and quantum yields. The C_{4v} site data is representative of the observed fluorescent lifetime trends. For the D^- C_{4v} site the $D_1 \rightarrow Z_1$ transition at 5945.35 Å is measured to have a radiative lifetime of 405 ± 5 μsec while the corresponding H^- C_{4v} site transition at 5945.46 Å has a lifetime of 2.74 ± 0.05 μsec. Both these lifetimes are substantially shorter than that of 1.90 ± 0.05 msec measured for the F^-C_{4v} site, for which non-radiative processes are negligible. The strong quenching of the H^- and D^- C_{4v} sites by non-radiative processes involving the respective local mode

phonons indicates that, in these sites, the Pr^{3+} electronic energy is efficiently channeled into the creation of local mode phonons. This may significantly enhance the tunneling rate of the D^- ion at low temperatures. Optical excitation provides an alternative way in which reorientation of the centers may occur without invoking tunneling. The pathway for the D^- ion motion is not yet known but since bleaching is not observed for either the D^- or H^- C_{4v} sites, the presence of the second D^- or H^- ion is essential to the process [4].

Persistent spectral holeburning was observed in the $Z_1 \rightarrow D_1$ absorption lines of the $C_s(1)$ and $C_s(2)$ centers at 1.6K. We attribute this persistent holeburning to the same mechanism proposed for the reversible polarized bleaching, i.e., rearrangement of the $Pr^{3+} - D^-$ ion bonds, with the additional requirement that the spectral line be inhomogeneously broadened.

A single frequency cw dye laser with a frequency jitter width of ~2 MHz was used to burn holes using exposures of ~1 sec × 100 mW/cm^2 and the holes were detected in a fluorescence excitation spectrum using ~100 $\mu W/cm^2$ in the probe beam. Figure 3 shows the holeburning spectra obtained. In addition to the hole at the laser frequency there are six side holes which have their origin in the hyperfine splittings in the ground and excited states.

These holes are observed to persist for at least one hour, the longest period tested. This is much longer than previously reported for optically pumped Pr^{3+} systems [3,7], where spin-lattice relaxation effects determine the hole lifetimes. In addition, antiholes which are characteristic of a hyperfine population reservoir, are not observed. The persistent holes we describe here, are therefore assigned to a new spectral holeburning mechanism.

The hyperfine structure observed in the holeburning spectra indicate that the $Z_1 \rightarrow D_1$ line is a transition between singlet electronic states. The C_{4v} symmetry site, from which the $2D^-$ centers are derived, has a doubly degenerate E ground state. The presence of the second D^- ion in the nearest neighbor shell lowers the Pr^{3+} ion site symmetry to C_s and produces a small splitting of the E level, which is 3.3 cm^{-1} for the $C_s(1)$ center and 7.6 cm^{-1} for $C_s(2)$.

A schematic diagram of the level structure is shown in Fig. 4, for electronic singlet states and the ^{141}Pr nuclear spin $I = 5/2$. For near axial symmetry, the hyperfine splittings are in the ratio 2:1 and the three transitions shown, which conserve M_I, are the strongest. The expected pattern of holes is shown in Fig. 4b, with the central hole three times as strong as the side holes. Because of the small separation between the two lowest electronic levels, the hyperfine splittings are dominated by the very large pseudoquadrupole [8] (2nd order hyperfine) contributions in the ground state. In the $CaF_2:Pr^{3+}$ $C_{4v}F^-$ site, the excited state has a very small hyperfine splitting of 0.44 MHz. [9] and similar values are expected here. Hence we make the reasonable assumption in what follows that $D^e = 0$.

The hyperfine Hamiltonian can be written

$$\mathcal{H} = D^{g,e}[I_z^{\,2} - I(I+1)/3] + E^{g,e}(I_x^{\,2} - I_y^{\,2}) \qquad (1)$$

where the superscripts g,e refer to ground and excited states. Because, to a good approximation, only the z-component of the magnetic dipole operator couples the two low lying levels (Z_1, Z_2), the system shows very close to axial behavior with [10]:

$$D^{g,e} = -A_J^{\,2} < 1|J_z|2 > < 2|J_z|1 > /\Delta, \quad E^{g,e} \approx 0 \ . \qquad (2)$$

Here $|1\rangle$ and $|2\rangle$ refer to the levels Z_1 and Z_2 and Δ is the energy separation between them. From this we see that the relative hyperfine splittings in the two sites should be inversely proportional to Δ since the matrix elements of J_z are not expected to change significantly from their purely axial values. This is, in fact, observed with $|D^g - D^e|_{5984}/|D^g - D^e|_{6018} = 2.6$, and $\Delta_{6018}/\Delta_{5984} = 2.3$. The absolute magnitude of D can be obtained using $A_J = 1093$ MHz [11] and assuming that the matrix element of J_z between the two lowest levels is $(g_{\parallel}\beta/2g_J)$ where $g_{\parallel}$ is the g-value of the doubly degenerate E ground state in the unperturbed C_{4v} sites. We use $g_{\parallel} = 3.9$ measured for the $C_{4v}F^-$ site of $CaF_2:Pr^{3+}$. [9] The results are shown in Table 2. Note that only the magnitude of D is determined experimentally, but this agrees very well with the calculated value. Such agreement is rather rare [12].

We have observed reversible polarized bleaching and persistent spectral holeburning in $SrF_2:Pr^{3+}:D^-$ crystals due to deuteron migration in centers containing $2D^-$ ions. The polarized bleaching results in photoproduct centers forming either within the line profile of the original centers or at different energies. This mechanism for the persistent holeburning is somewhat analogous to proton tautomerism in organic systems, but is new to inorganics. The mechanism appears insensitive to the nature of the trivalent impurity ion [4] and thus promises some degree of generality. We have used the persistent holes to determine the large pseudoquadrupole splittings in the ground state of two $Pr^{3+}(2D^-)$ centers and find excellent agreement with calculations of second order magnetic hyperfine interactions.

Table 1

10K spectral data for the two principal centers having $2D^-$ ions in their configuration, observed in SrF_2: $0.05\%Pr^{3+}$: D^- crystals

Center ($Z_1 \rightarrow D_1$ transition) ± 0.1Å	Ground State (Z_1) to first excited state (Z_2) splitting cm^{-1}	Local Mode Vibration Intervals interstitial ion (± 1 cm^{-1})	substitutional ion (± 1 cm^{-1})	D_1 excited state radiative lifetime μsec	Photoproduct Center $Z_1 \rightarrow D_1$ transition (Å) $Z_1 \rightarrow Z_2$ splitting (cm^{-1})
$C_s(1)$ 5984.0	3.3 ± 0.1	673 685	529 569 829	54 ± 5	—
$C_s(2)$ 6018.0	7.6 ± 0.2	658 682	480 533 554 812	20 ± 1	5999.2 ± 0.1 17 ± 1

Table 2

Hyperfine interaction parameter values for two $2D^-$ centers measured in SrF_2:0.05%Pr^{3+}:D^- crystals

Center	Wavelength Å	$2D^g$ (calc) (MHz)	$\|2(D^g - D^e)\|$ (obs)[a] (MHz)
$C_s(1)$	5984.0	−142	164
$C_s(2)$	6018.0	− 61	64

[a] D^e is expected to be negligible and the sign of D is not determined experimentally.

REFERENCES

1. A. A. Gorokhovskii, R. K. Kaarli and L. A. Rebane, *Zh. ETF Pis. Red.* **20**, 474 (1974); [*JETP Lett.* **20**, 216 (1974)].
2. S. Volker and J. H. van der Waals, *Mol. Phys.* **32**, 1703 (1976); S. Volker, R. M. Macfarlane, A. Z. Genack, H. P. Trommsdorff and J. H. van der Waals, *J. Chem. Phys.* **67**, 1759 (1977).
3. L. E. Erickson, *Phys. Rev.* **B16**, 4731 (1977).
4. N. J. Cockroft, T. P. J. Han, R. J. Reeves, G. D. Jones and R. W. G. Syme, *Opt. Lett.* **12**, 36 (1987).
5. J. A. Harrington, R. T. Harley and C. T. Walker, *Solid State Commun. 8*, 407 (1970).
6. I. T. Jacobs, G. D. Jones, K. Zdansky and R. A. Satten, *Phys. Rev.*, B. **3**, 2888 (1971).
7. D. P. Burum, R. M. Shelby and R. M. Macfarlane, *Phys. Rev.* B. **25**, 3009 (1982).
8. J. M. Baker and B. Bleaney, *Proc. Roy. Soc. (Lond)* **A245**, 156 (1958).
9. R. M. Macfarlane, D. P. Burum and R. M. Shelby, *Phys. Rev.* **B29**, 2390 (1984).
10. M. A. Teplov, *Zh. Eksp. Teor. Fiz.* **53**, 1510 (1968); [*Sov. Phys. JETP*, **26**, 872 (1968)]
11. A. Abragam and B. Bleaney in "Electron Paramagnetic Resonance of Transition Ions," Clarendon Press, Oxford (1970), p. 298.
12. R. M. Macfarlane and R. M. Shelby in "Spectroscopy of Crystals Containing Rare Earth Ions," eds., A. A. Kaplyanskii and R. M. Macfarlane, North Holland, Amsterdam, to be published, 1987.

FIGURE CAPTIONS

Figure 1. Probable configurations for two deuteron centers having near neighbor substitutional and interstitial D^- ions. The cross hatched circles denote Pr^{3+} ions, the full black circles D^-, and the open circles lattice fluorine ions.

Figure 2. Laser excitation of the two principal $2D^-$ centers in SrF_2: $0.05\%Pr^{3+}:D^-$ crystals at 10K. Z_1 and Z_2 label the initial states for the transitions to D_1. (a) The $C_s(1)$ center. Upper trace: before bleaching. Lower trace: after bleaching for several minutes at 50 mW laser power. No photoproduct of a different wavelength is observed. (b) The $C_s(2)$ center. Upper trace before bleaching. Lower trace: after bleaching as for $C_s(1)$. A photoproduct labelled $C_s(2)^*$ is produced at 5999.2Å. Irradiation into $C_s(2)^*$ restores $C_s(2)$.

Figure 3. Persistent spectral holes burned in the centers of SrF_2: $Pr^{3+}:D^-$ showing the large pseudoquadrupole splittings in the ground state a) the 5984.0A center b) the 6018.0Å center.

Figure 4. Schematic energy level diagram of the singlet electronic states of the $C_s(2D^-)$ centers which exhibit close to axial symmetry b) pattern of holes expected in the axial approximation.

(a)

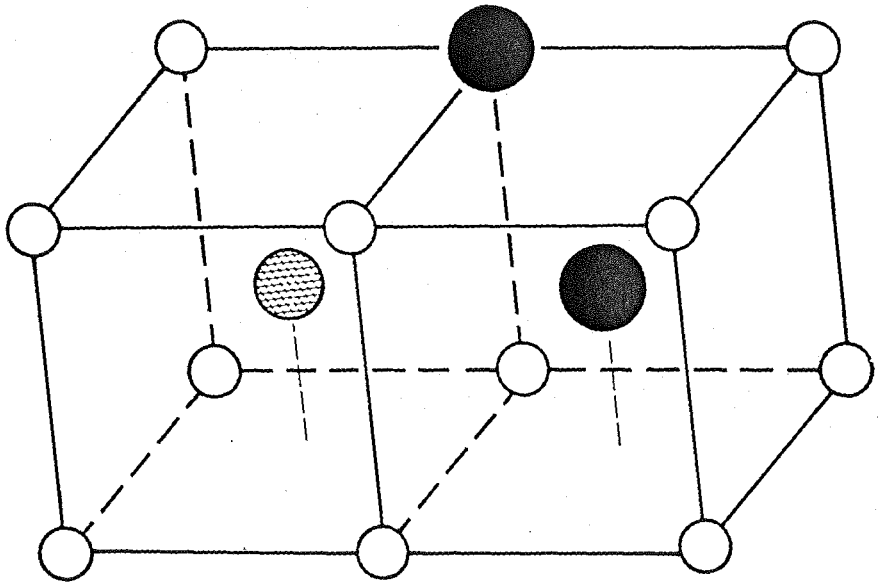

(b)

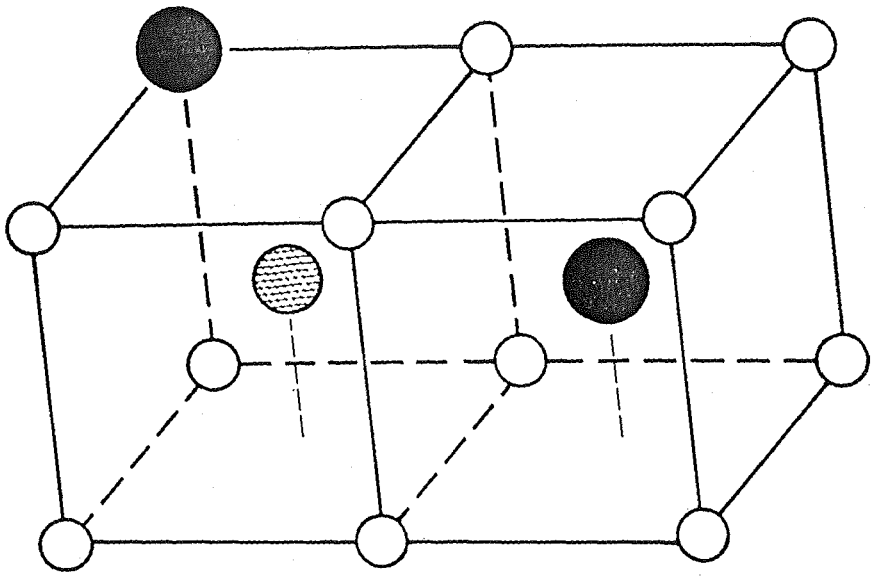

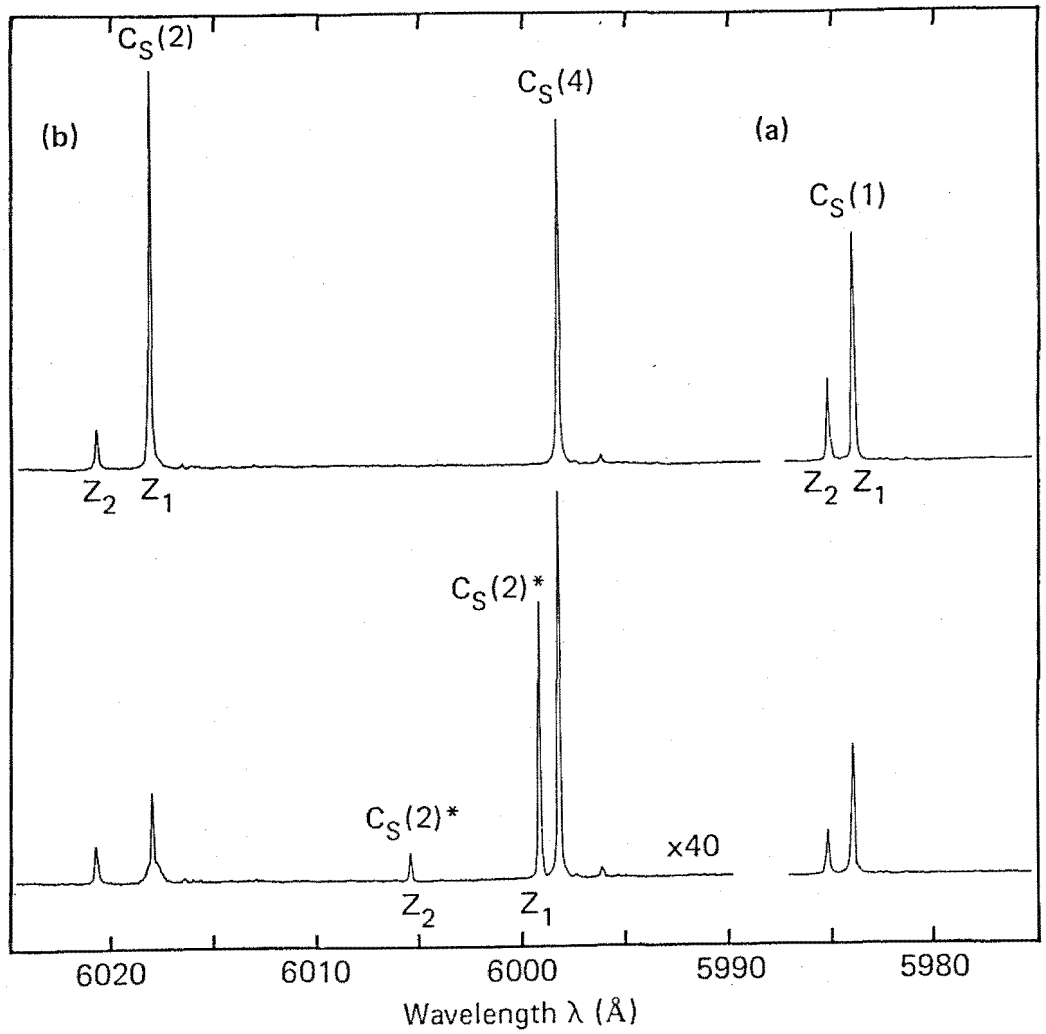
(b)
(a)
$C_S(2)$
$C_S(4)$
$C_S(1)$
Z_2
Z_1
Z_2
Z_1
$C_S(2)^*$
$C_S(2)^*$
x40
Z_2
Z_1
6020
6010
6000
5990
5980
Wavelength λ (Å)

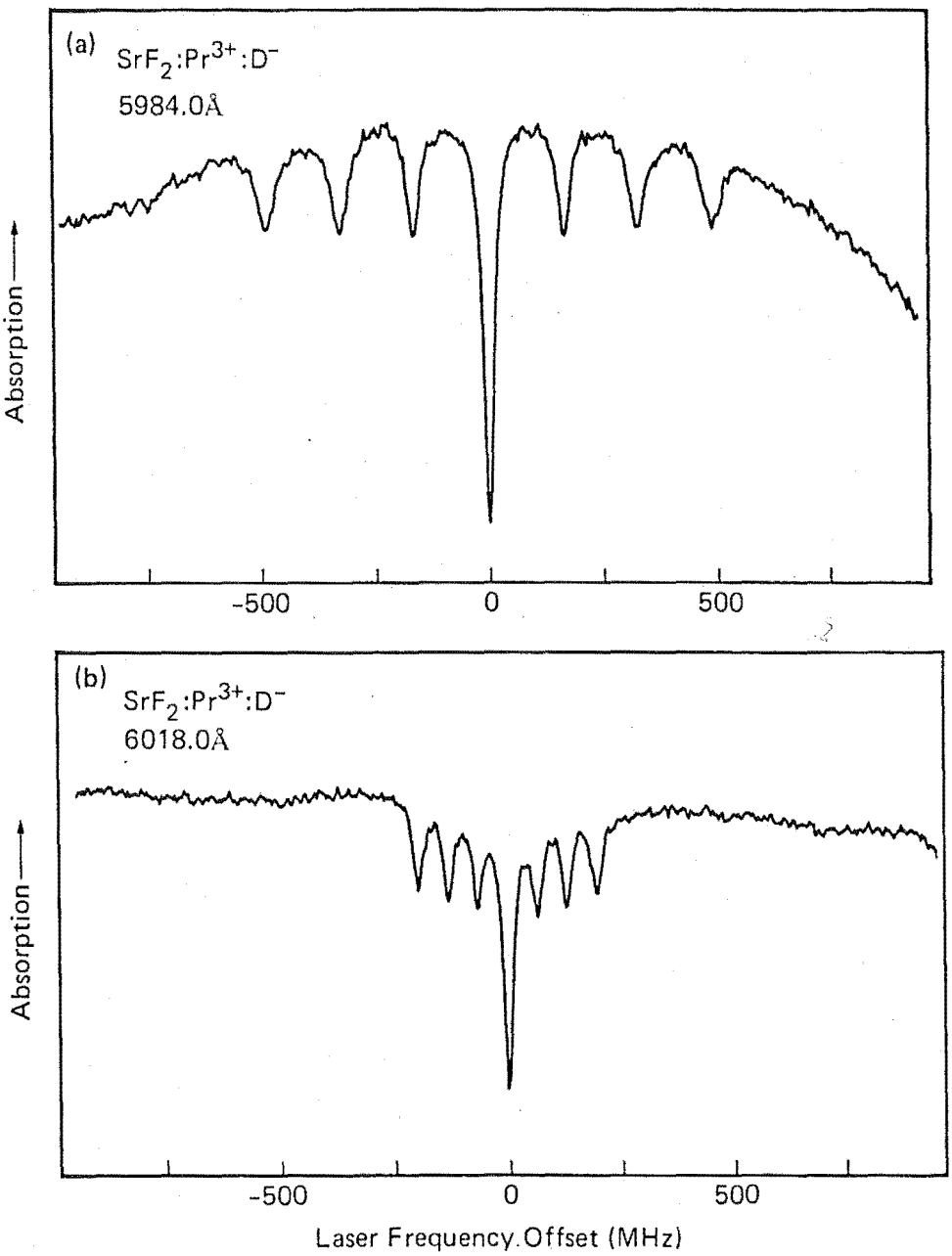
(a)
$SrF_2:Pr^{3+}:D^-$
5984.0Å
Absorption
-500
0
500
(b)
$SrF_2:Pr^{3+}:D^-$
6018.0Å
Absorption
-500
0
500
Laser Frequency Offset (MHz)

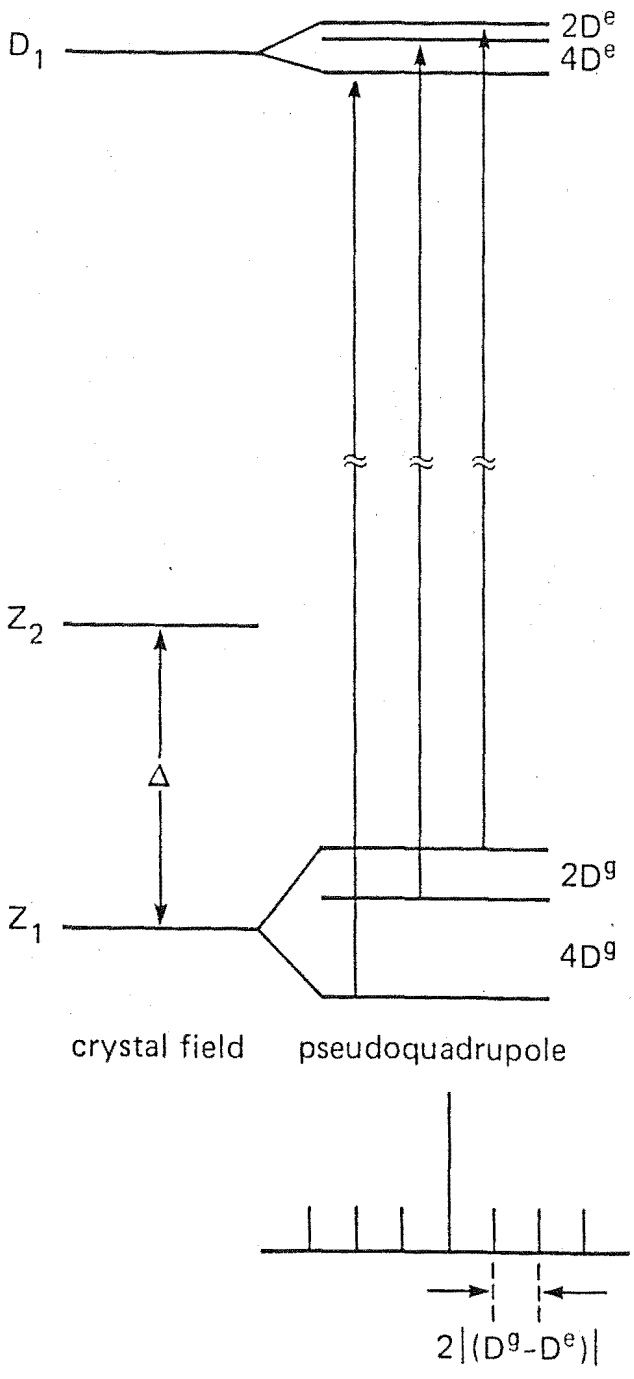
D1
2De
4De
Z2
Δ
Z1
2Dg
4Dg
crystal field
pseudoquadrupole
2|(Dg-De)|

DYNAMICAL PROCESSES INVOLVING LOCAL MODES FOR RARE EARTH CENTERS IN CaF_2

R.J. Reeves, G.D. Jones, N.J. Cockroft,
T.P.J. Han and R.W.G. Syme

Department of Physics,
University of Canterbury,
Christchurch, New Zealand.

Contact author: Dr. R.W.G. Syme,
Department of Physics,
University of Canterbury,
Christchurch,
New Zealand.

Telephone: New Zealand 03-482009 ext. 7564

ABSTRACT

H^-, D^- and T^- ion local modes play a significant role in dynamical processes involving laser excitation of hydrogenic rare-earth ion centers in CaF_2 and SrF_2. The hydrogenic varieties of a particular center are found to have substantially reduced fluorescence lifetimes supportive of models for non-radiative decay to lower energy multiplets through the respective local mode phonons. Likewise, upconversion efficiencies are reduced for the hydrogenic single rare-earth ion centers and are found to vary with inter-center separation consistent with a recent model for single ion upconversion involving a weak coupling between nearby equivalent centers.

The efficient channelling of the rare-earth ion excitation into the creation of local mode phonons can induce hydrogenic ion migration to produce re-oriented equivalent centers or new photoproduct centers with different excitation wavelengths.

Introduction

Local mode vibrations of hydrogen (H^-), deuterium (D^-) or tritium (T^-) anions play a significant role in the dynamical processes associated with laser excitation of hydrogenic rare-earth ion centers in CaF_2 and SrF_2. The results of fluorescence lifetime, upconversion, photoproduct formation and Raman scattering studies for several such centers will be discussed.

Fluorescence Lifetimes

Hydrogenic center lifetimes are determined by non-radiative decay processes involving the respective local mode phonons. The involvement of such phonons in the decay is shown by the greatly reduced H^- center lifetimes compared to those for the D^- centers (Table 1). A special case exists for Gd^{3+} where the energy gap to the next lowest level is sufficiently large that radiative decay is the dominant process as shown by the similar lifetimes for F^-, H^- and D^- centers. Additional evidence for the role of local mode phonons is shown in the hydrogenic Pr^{3+} ion centers where excitation of the ^3P_o multiplet results in emission from both ^3P_o and $^1D_2$ multiplets. Strong quenching by local modes efficiently feeds the ^3P_o level excitation to the lower $^1D_2$ multiplet. For the Cs(2) D^- center in $SrF_2:Pr^{3+}:D^-$ which is known to have more than one neighboring D^- ion [1], the quenching is sufficiently strong to channel most of the excitation to the $^1D_2$ multiplet thus precluding observation of emission from the ^3P_o level.

A model for multi-phonon non-radiative decay [2] predicts the dominance of processes requiring the least number of phonons to bridge the energy gap to the next lowest multiplet. It is expected and found

that states decaying by processes of similar order have similar lifetimes. For C_{4v} hydrogenic Pr^{3+} ion sites, the ^3P_o lifetimes of the D^- centers are similar to the $^1D_2$ lifetimes of the H^- centers in both CaF_2 and SrF_2 (Table 1). Some T^- center lifetimes measured were shorter than for the D^- center, but this is attributed to unavoidable excitation of the faster corresponding H^- centers also present in these samples.

Upconversion

Upconversion is common for multiple RE^{3+} ion clusters but has only recently been observed for a nominally single ion C_{4v} site [3,4]. In the work reported here upconversion has been observed for the F^- C_{4v} centers of Pr^{3+}, Nd^{3+} and Er^{3+} in both CaF_2 and SrF_2 and for the D^- and T^- C_{4v} centers in SrF_2:Pr^{3+}. Upconversion for H^- centers however, was immeasurably weak.

Upconversion for rare-earth ion centers is usually attributed either to sequential two photon excitation (STEP) processes, or to energy transfer (ETU) between identical ions [5,6]. The upconversion reported here for the C_{4v} Pr^{3+} ion centers is discussed as being representative.

a) As upconversion is observed under both pulsed (pulse width, ~1ns) and cw laser excitation, a STEP process involving relaxation between intermediate levels can be discounted. This conclusion was supported by the fact that no extra lines were seen in an upconversion excitation spectrum obtained by scanning the frequency of one laser while a second laser was tuned to the optimum upconversion frequency.

b) Maximum upconversion intensity occurs at a slightly different $^1D_2$ excitation frequency than that required for the strongest direct fluorescence. This difference (less than 0.3 cm^{-1}) indicates that a

subset of the C_{4v} centers, slightly perturbed from the isolated C_{4v} centers, participate in upconversion.

c) The variation of upconversion lifetimes with RE^{3+} concentration is as expected for a greater occurrence of sufficiently close C_{4v} centers at higher concentrations. For F^- C_{4v} centers in $SrF_2:Pr^{3+}$ the lifetimes of the upconverted ^3P_o level has values of 550±50, 470±20 and 220±20 μsec for Pr^{3+} ion concentrations of 0.05, 0.1 and 0.5 mol% respectively. These lifetimes all fall within the range of half the $^1D_2$ state lifetime (950 μsec) and the ^3P_o state lifetime (118 μsec) set by the limiting cases of small and large values for the upconversion transfer rate W_T [3].

d) The upconversion emission intensity of the $^3P_o \rightarrow {}^3H_4$ transition for the D^- C_{4v} site in $SrF_2:Pr^{3+}$ is a factor 3×10^{-6} less than the intensity of the direct $^1D_2 \rightarrow {}^3H_4$ emission transition. For the corresponding F^- C_{4v} center, the ratio is 5×10^{-3}. This result can be understood if the inter-center transfer rate W_T is slower than the fluorescent decay rates. The marked decrease in upconversion efficiency for the D^- center relative to the F^- center is attributed to both the five-fold change in respective lifetimes (Table 1) and, as evidenced by a weaker absorption for the D^- centers, to a reduced number of weakly coupled centers participating in upconversion.

e) The upconverted $^3P_o \rightarrow {}^3H_4$ fluorescence of the Pr^{3+} C_{4v} centers has the same polarisation as the fluorescence obtained by direct excitation of the ^3P_o multiplet. This contrasts to the case of Er^{3+}-F^- C_{4v} centers where polarisation reversals were reported [7]

All these observations are in agreement with a model [3] of a weak long range interaction between pairs of C_{4v} centers forming a specific subset of the isolated C_{4v} centers.

An additional upconversion process is apparent for Nd^{3+}-F^- C_{4v} centers in CaF_2, with evidence of a stepwise mechanism via the $^4F_{3/2}$ electronic level at 11591 cm^{-1}. A cw laser tuned to match the $^4F_{3/2} \rightarrow {}^4D_{3/2}$ interval of 16507 cm^{-1} gives emission from this $^4D_{3/2}$ level at 28098 cm^{-1}. The $^4F_{3/2}$ level is populated from the ground state by absorption of the laser into a phonon side-band of the $^4G_{9/2}$ multiplet.

Photoproduct Formation

Recently the bleaching characteristics of several multiple hydrogenic ion centers of Pr^{3+}, Nd^{3+} and Er^{3+} have been described [1,8]. Under constant excitation conditions the intensity of the rare-earth ion fluorescence decreases with time as physical motion of the constituent hydrogenic ions of a site remove that particular center from resonance with the laser. It appears that a second hydrogenic ion and the creation of local mode phonons are necessary to induce the ion motion as no bleaching properties are observed in any C_{4v} site studied.

The ion motion can produce equivalent centers reoriented by 90^o [8], or new photoproduct centers with different excitation wavelengths [1]. Figure 1 shows the formation of a photoproduct center absorbing at 16664 cm^{-1}, labelled $Cs(2)^*$, after bleaching the Cs(2) center at 16612 cm^{-1} in a $SrF_2:Pr^{3+}:D^-$ crystal. This ion motion is very nearly completely reversible as the photoproduct center $Cs(2)^*$ can be bleached to restore almost all of the intensity in Cs(2).

One hydrogenic site, the D^- R site of $CaF_2:Er^{3+}$ exhibits a similar frequency domain reversibility effect where each transition comprises two components within the linewidth observed. With the available laser bandwidth of 30 GHz an excitation spectrum

obtained by monitoring the broad band fluorescence showed that at 10 K the $Z_1 \rightarrow E_1$ (18439 cm^{-1}) and $Z_2 \rightarrow E_1$ (18430 cm^{-1}) transitions for the D^- R site each consist of two components separated by 15±6 GHz. Pumping either component resulted in an increase in intensity of the other with the effect appearing to be long lived at 10 K. This splitting is likely to be related to an effect recently observed by Macfarlane [10] where preliminary results of a high resolution laser study of the D^- and T^- ion R sites showed that the $Z_1 \rightarrow D_1$ transition (15293 cm^{-1}) comprised two components of 2 GHz linewidth separated by 11.5 GHz. Reversible interconversion between these components was seen, but only at temperatures below 4 K. This effect is consistent with the hydrogenic R site of $CaF_2:Er^{3+}$ having two slightly inequivalent, stable, interstitial hydrogenic ion positions within the same lattice cube. It is not obvious why exictation of the $Z_1 \rightarrow E_1$ transition should show reversibility between the two components at 10 K while a lower temperature is required to see the effect for $Z_1 \rightarrow D_1$ excitation [10].

Raman Scattering

As part of these studies Raman scattering [9] has been investigated as an alternative way of determining local modes of various hydrogenic RE^{3+} centers and has the added advantage of yielding D^- local mode frequencies not easily measured by infrared absorption. The preliminary spectra recorded show weak Raman scattering from hydrogenic local modes but also contain spurious electronic fluorescence from impurity rare-earth ions such as Sm^{2+}, at a comparable strength. By choice of optimum argon laser lines, the local mode frequencies of several H^- and D^- centers, including some from a multiple hydrogenic ion center, were identified.

Conclusion

The results described above clearly illustrate the importance of local mode vibrations of hydrogenic ions for dynamical processes in these systems. Spectroscopic investigation of such effects is being continued.

ACKNOWLEDGEMENTS

We thank W. van Dyk, University of Canterbury, for assistance with the Raman studies and Dr. R.M. Macfarlane, IBM Almaden Research Center, for communicating results prior to publication. This research was supported by Postgraduate Scholarships (RJR, NJC) and Research Grants from the New Zealand University Grants Committee.

REFERENCES

1. R.M. Macfarlane, R.J. Reeves and G.D. Jones, Optics Letters, (1987), in press.

2. L.A. Riseberg and M.J. Weber, Relaxation Phenomena in Rare Earth Luminescence in : Progress in Optics XIV, ed. E. Wolf (North Holland, Amsterdam, 1976) pp89-159

3. A. Lezama, M. Oriá and C.B. de Araujo, Phys. Rev. B, **33**, 4493 (1986).

4. G.D. Jones, N.J. Cockroft, T.P.J. Han, R.J. Reeves and R.W.G. Syme, Proceedings of the Second Asia-Pacific Physics Conference, ed. S. Chandrasekhar, (World Scientific, Singapore, 1987) pp648-655.

5. B.R. Reddy and P. Venkateswarlu, J. Chem. Phys., **79**, 5845 (1983).

6. For a review of upconversion processes see, for example,J.C. Wright, Upconversion and Excited State Energy Transfer in Rare-Earth Doped Materials in: Topics in Applied Physics, Vol. 15, ed. F.K. Fong, (Springer Verlag, Berlin, Heidelberg, 1976) pp239-295.

7. N.J. Cockroft, D. Thompson, G.D. Jones and R.W.G. Syme, J. Chem. Phys, **86**, 521 (1987).

8. N.J. Cockroft, T.P.J. Han, R.J. Reeves, G.D. Jones and R.W.G. Syme, Optics Letters, **12**, 36 (1987).

9. J.A. Harrington, R.T. Harley and C.T. Walker, Solid State Comm., **8**, 407 (1970)

10. R.M. Macfarlane (private communication).

11. G.D. Jones, S. Peled, S. Rosenwaks and S. Yatsiv, Phys. Rev., **183**, 353 (1969).

FIGURE CAPTION

Figure 1. Laser excitation of the Cs(2) center in a SrF_2:0.05% Pr^{3+}:D^- crystal at 10 K. (a) Before bleaching. (b) After bleaching for several minutes at 50 mW of laser power. A photoproduct labelled $Cs(2)^*$ is produced at 16664 cm^{-1}. Irradiation into $Cs(2)^*$ restores Cs(2).

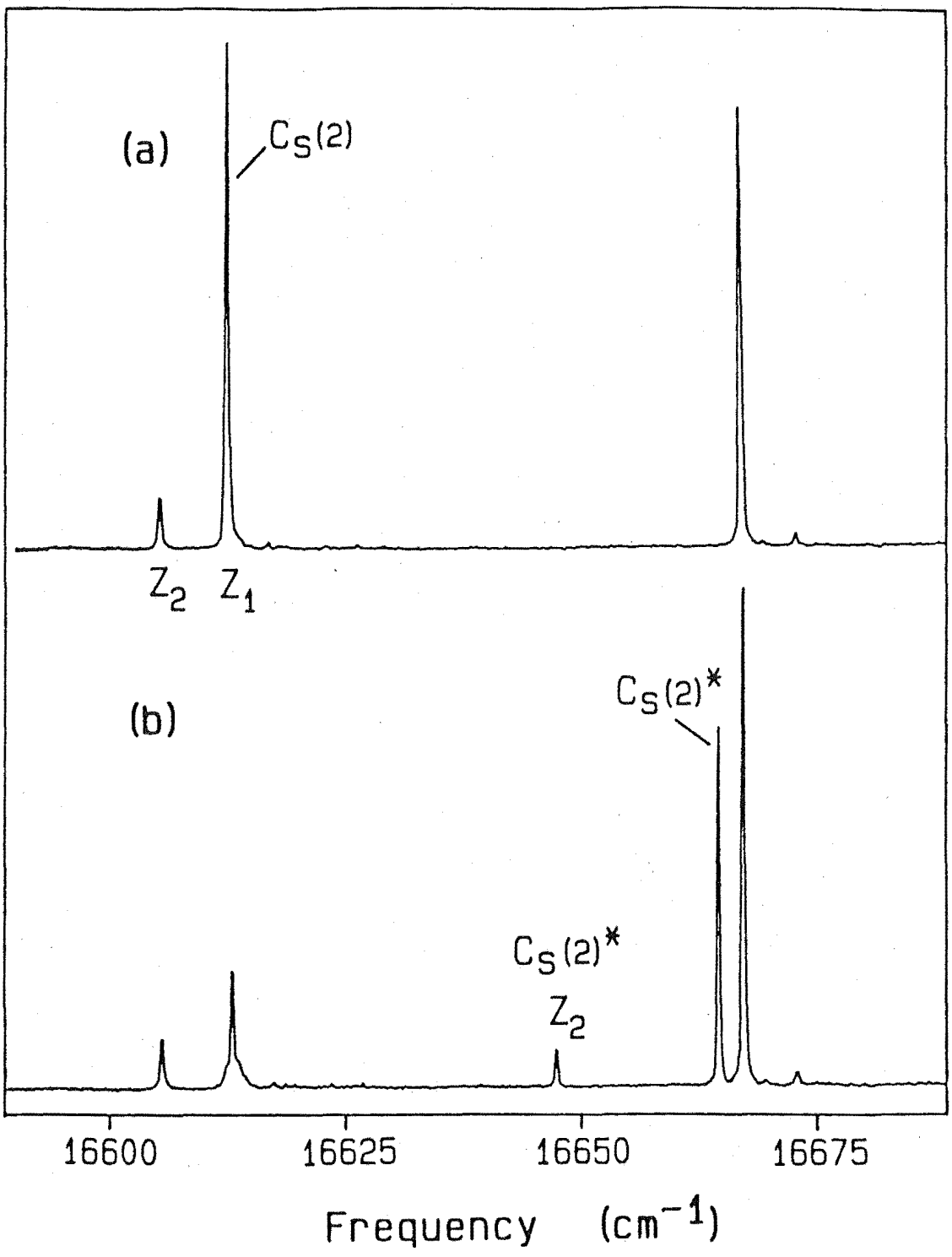
(a)
$C_S(2)$
Z_2
Z_1
(b)
$C_S(2)^*$
$C_S(2)^*$
Z_2
16600
16625
16650
16675
Frequency (cm^{-1})

Table 1 : Radiative lifetimes measured at 10 K for several rare-earth ion transitions in CaF_2 and SrF_2 host crystals

RARE EARTH		Pr^{3+}				Nd^{3+}		Gd^{3+}*
CRYSTAL HOST		CaF_2		SrF_2		CaF_2	SrF_2	CaF_2
TRANSITION		$^3P_o \rightarrow {}^3H_4$	$^1D_2 \rightarrow {}^3H_4$	$^3P_o \rightarrow {}^3H_4$	$^1D_2 \rightarrow {}^3H_4$	$^4F_{3/2} \rightarrow {}^4I_{9/2}$	$^4F_{3/2} \rightarrow {}^4I_{9/2}$	$^6P_{7/2} \rightarrow {}^8S_{7/2}$
F^- C_{4v} Site		120±5 μsec	420±10 μsec	118±5 μsec	2.03±.05 msec	1.3±.1 msec	1.6±.2 msec	11±1 msec
H^- C_{4v} Site		-	380±20 nsec	820±50 nsec	2.69±05 μsec	-	-	4±.05 msec
D^- C_{4v} Site		270±10 nsec	95±3 μsec	1.08±.05 μsec	405±10 μsec	2.2±.3 μsec	12±2 μsec	3 msec
Energy separation of next lowest multiplet (cm^{-1})		3400	6100	3400	6100	4900	5100	32000
Minimum number of phonons to bridge gap	H^-	3	6	4	7	5	6	29
	D^-	4	8	5	9	6	8	40

*Radiative lifetimes at 77 K for Gd^{3+} obtained from reference 11.